ESCUELA DE DOCTORADO

Programa de Doctorado en Infraestructuras de Transporte y Territorio

PhD Thesis

OVERTOPPING FLOW ON MOUND BREAKWATERS UNDER DEPTH-LIMITED BREAKING WAVE CONDITIONS

Author:

Patricia Mares Nasarre

Advisors:

Dr. Josep R. Medina Folgado
Dr. M. Esther Gómez Martín

Valencia, October 2020

Vive como si fueras a morir mañana. Aprende como si fueras a vivir para siempre.

Live as if you were to die tomorrow. Learn as if you were to live forever.

Mahatma Gandhi

Agradecimientos
Acknowledgements

Esta tesis doctoral es fruto de varios años de trabajo y como toda tesis, una carrera de obstáculos. Con estas líneas espero poder mostrar mi gratitud a todos aquellos que me han apoyado en la superación de cada uno de ellos y me han ayudado a llevarla a buen puerto. Mis disculpas de antemano para aquellos que mi memoria traicione; mi gratitud también va para vosotros.

A mi madre, mi eterno apoyo y mi mejor amiga. Gracias por dar sin condiciones; sé que siempre contaré contigo. Eres todo lo que debería ser una madre y mucho más. A mi padre, por enseñarme que con pensamiento positivo y trabajo todo se puede conseguir. A mi familia, por creer siempre en mí incondicionalmente.

A mis "chicas", a las de siempre, Andrea, Julieta, Alejandra, Cristina, Mónica y Laura, por no faltarme nunca. Gracias por perdonar mis ausencias, entenderme en los momentos bajos y demostrarme día a día lo increíble de las amigas que tengo. A Iñaki, por ser mi lugar seguro y hacerme recuperar la perspectiva cuando estoy perdida. A aquellos amigos que la carrera de Ingeniería de Caminos me ha regalado, Andrea A., Alex, Miguel Ángel, Dani C., Adrián, Jorge S., Natalia, y muchos más. Gracias por hacerme el camino más fácil.

A mis directores de tesis, Josep y Esther, por confiar en mí, aconsejarme y dedicarme vuestro tiempo siempre con una sonrisa. Gracias por transmitirme vuestra pasión por la

Ingeniería Marítima y demostrarme lo que es ser un gran investigador y una gran persona.

A los compañeros de la unidad de Ingeniería Marítima, por acogerme con los brazos abiertos. A Jorge M., por convertirte en un gran amigo estos años. Gracias por tu sinceridad, por tus consejos y por echarme una mano cuando más lo he necesitado. A Gloria, por acompañarme diariamente en el Laboratorio y remar conmigo por sacar adelante cada ensayo. A Carlos A., por tu ayuda diaria en el Laboratorio, por escucharme y por darme siempre la posibilidad de hablar con franqueza. A Jose Alberto, por enseñarme el camino hasta el Laboratorio en el que empecé mi aventura y hacerme confiar en que todo saldría bien. A Pepe A., Vicent y Pepe S. por hacer tan fácil trabajar con vosotros.

A mis compañeros de Departamento, por hacer un placer trabajar a vuestro lado. A Pablo M., por todos los buenos ratos de despacho compartido y todas las veces que te ha tocado escucharme. A Rosa, por escucharme y entenderme como sólo otra mujer podría. A Carla, por preocuparte por mí y compartir todas mis alegrías como si fuera tuyas. A Natxo, por aconsejarme y hacerme reír cuando más lo necesitaba. A Vito, por convertirte en una más. A Pablo S. y Kike, por todos los buenos momentos.

I also want to acknowledge Dr. Marcel R.A. van Gent for giving me the opportunity to collaborate with the Coastal Structures & Waves team in Deltares. It was a pleasure to work with you. Gracias también a Andrea F., me he llevado una gran amiga de la estancia.

Al Ministerio de Educación, Cultura y Deporte, por la financiación brindada con el programa de Formación de Profesorado Universitario (FPU16/05081).

Al Ministerio de Economía y Competitividad, por la financiación de los proyectos ESBECO (*__ES__tabilidad hidráulica del manto, __BE__rmas y __CO__ronación de diques en talud con rebase y rotura por fondo,* BIA2015-70436-R) y HOLOBREAK (*Estabilidad Hidráulica y Transmisión de Diques Rompeolas Homogéneos de Baja Cota Diseñados a Rotura por Fondo,* RTI2018-101073-B-I00-AR).

Abstract

Overtopping flow on mound breakwaters under depth-limited breaking wave conditions

Climate change and the social concern about the impact of infrastructures is leading to mound breakwaters with reduced crest freeboards facing higher extreme overtopping events. In addition, most mound breakwaters are built in the surf zone where depth-limited wave breaking takes place. Recent studies point out the need of considering not only the mean wave overtopping discharge (q) but also the maximum individual wave overtopping volume (V_{max}), the overtopping layer thickness (OLT) and the overtopping flow velocity (OFV) when designing mound breakwater crest elevation using overtopping criteria. However, few studies in the literature are focused on V_{max} on coastal structures under depth-limited breaking wave conditions. In addition, those few studies report contradictory conclusions regarding the significance of depth-limited breaking waves on V_{max}. With respect to OLT and OFV, no studies are found in the literature for their prediction on mound breakwaters.

In this PhD thesis, 2D physical model tests were conducted on overtopped mound breakwaters ($0.3 \leq R_c/H_{m0} \leq 2.5$) without a crown wall armored with three armor layers

(Cubipod®-1L, cube-2L and rock-2L) on two gentle bottom slopes (m=2% and 4%) in depth-limited breaking wave conditions ($0.2 \leq H_{m0}/h \leq 0.9$).

V_{max} together with q are the most recommended variables in the literature to design mound breakwater crest elevation based on overtopping criteria. In the present study, the 2-parameter Weibull distribution provides the best results when estimating $V_{max}^{*}=V_{max}/(gH_{m0}T_{01}^{2})$ with coefficient of determination R^2=0.833. During the design phase of a mound breakwater, q is needed to predict V_{max} using methods given in the literature. Thus, q must be estimated for design purposes when direct observations are not available. If CLASH NN is used to estimate q (R^2=0.636), the goodness-of-fit of the 2-parameter Weibull distribution proposed in this thesis to predict V_{max}^{*} is R^2=0.617. Hence, the ratio between the estimated and measured V_{max}^{*} falls within the range 1/2 to 2 (90% error band) when q is predicted using CLASH NN. The new estimators derived in this study provide satisfactory estimations of V_{max}^{*} with a method simpler than those found in the literature. Neither the bottom slope nor the depth-induced wave breaking seem to significantly influence the dimensionless V_{max}^{*} in this study.

OLT and OFV are directly related to the hydraulic stability of the armored crest and the pedestrian safety. Thus, OLT and OFV are required to properly design crest elevation using overtopping criteria. Neural Networks (NNs) are used in this study to develop new explicit unbiased estimators for the OLT and OFV exceeded by 2% of the incoming waves with a high coefficient of determination ($0.866 \leq R^2 \leq 0.867$). The appropriate number of significant figures of the empirical coefficients of such estimators is selected according to their variability. The optimum point where wave characteristics are determined to predict OLT and OFV was identified at a distance of $3h$ from the toe of the structure (where h is the water depth at the toe of the structure). The bottom slope does influence both OLT and OFV. The most extreme values of OLT and OFV are described with the 1-parameter Exponential and Rayleigh distribution functions, respectively, with satisfactory results ($0.803 \leq R^2 \leq 0.812$).

Resumen

Flujo de rebase sobre diques en talud sometidos a oleaje limitado por el fondo

El cambio climático y la conciencia social sobre el impacto de las infraestructuras en el medio está llevando a la necesidad de diseñar diques en talud con cotas de coronación reducidas frente a eventos de rebase más extremos. Además, la mayoría de estos diques se construyen en zonas de profundidades reducidas, donde el oleaje rompe a causa de la limitación por fondo. Estudios recientes apuntan a la necesidad de considerar no sólo la caudal medio de rebase (q) sino también el máximo volumen individual de rebase (V_{max}), el espesor de lámina de agua (OLT) y la velocidad del flujo de rebase (OFV) en el diseño de la cota de coronación de un dique en talud según criterios de rebase. No obstante, existen pocos estudios en la literatura científica centrados en V_{max} en estructuras costeras sometidas a oleaje limitado por fondo. Además, estos estudios proporcionan resultados contradictorios en relación a la influencia de la limitación por fondo del oleaje sobre V_{max}. En cuanto a OLT y OFV, no se han encontrado estudios en la literatura científica que permitan su predicción en diques en talud.

En esta tesis doctoral, se han realizado ensayos físicos 2D en diques en talud rebasables ($0.3 \leq R_c/H_{m0} \leq 2.5$) sin espaldón y con tres mantos principales (Cubípodo®-1L, cubo-2L y escollera-2L) sobre dos pendientes de fondo suaves (m=2% and 4%) en condiciones de oleaje limitado por fondo ($0.2 \leq H_{m0}/h \leq 0.9$).

V_{max} junto con q son las variables más recomendadas en la literatura científica para diseñar la cota de coronación de diques en talud según criterios de rebase. En el presente estudio, los mejores resultados en la estimación de $V_{max}^{*}=V_{max}/(gH_{m0}T_{01}^{2})$ se han obtenido empleando la función de distribución Weibull de dos parámetros con un coeficiente de determinación R^2=0.833. Durante la fase de diseño de un dique en talud, es necesario predecir q para calcular V_{max} cuando se emplean los métodos dados en la literatura científica. Por tanto, se debe estimar q con fines de diseño si no se dispone de observaciones directas. En caso de emplear la red neuronal CLASH NN para estimar q (R^2=0.636), la bondad de ajuste de la función de distribución Weibull de dos parámetros propuesta en esta tesis para predecir V_{max}^{*} es R^2=0.617. Así, el ratio entre V_{max}^{*} medido y estimado cae dentro del rango de 1/2 a 2 (banda de confianza del 90%) cuando se emplea q estimado con CLASH NN. Los nuevos estimadores desarrollados en la presente disertación proporcionan resultados satisfactorios en la predicción de V_{max}^{*} con un método más simple que aquellos propuestos en la literatura científica. No se ha encontrado una influencia significativa de la pendiente de fondo ni de la limitación por fondo del oleaje sobre V_{max}^{*} en este estudio.

OLT y OFV están directamente relacionados con la estabilidad hidráulica de la coronación del dique y la seguridad peatonal frente a rebase. Por tanto, se requiere estimar OLT y OFV en la coronación del dique para diseñar apropiadamente su cota de coronación empleando criterios de rebase. En este estudio, se han empleado redes neuronales para desarrollar nuevos estimadores explícitos que permiten predecir OLT y OFV superados por el 2% del oleaje incidente con un alto coeficiente de determinación ($0.866 \leq R^2 \leq 0.867$). El número de cifras significativas apropiado para los coeficientes experimentales de dichos estimadores se ha determinado en base a su variabilidad. El punto óptimo en el que las características del oleaje deben ser estimadas para predecir OLT y OFV se ha identificado a una distancia de $3h$ desde el pie de la estructura (siendo h la profundidad a pie de dique). La pendiente de fondo tiene influencia sobre OLT y OFV. Los valores más extremos de OLT y OFV se han descrito empleando las distribuciones Exponencial de un parámetro y Rayleigh, respectivamente, con resultados satisfactorios ($0.803 \leq R^2 \leq 0.812$).

Resum

Flux de sobrepasse de dics en talús sotmesos a onatge limitat per fons

El canvi climàtic i la consciència social sobre l'impacte de les infraestructures al medi està portant a la necessitat de dissenyar dics en talús amb cotes de coronació reduïdes front a esdeveniments d'ultrapassament més extrems. A més, la majoria dels dics es construeixen en zones amb profunditats reduïdes on l'onatge es trenca a causa de la limitació per fons. Estudis recents apunten a la necessitat de considerar no solament el cabal mitjà de sobrepasse (q) sinó també el màxim volum individual de sobrepasse (V_{max}), l'espessor de la làmina d'aigua (OLT) i la velocitat del flux de sobrepasse (OFV) pel disseny de la cota de coronació d'un dic en talús segons criteris de sobrepasse. No obstant, existeixen pocs estudis a la literatura científica centrats en V_{max} en estructures costeres sotmeses a onatge limitat per fons. Addicionalment, aquests estudis proporcionen resultats contradictoris en relació a la influència de la limitació per fons de l'onatge sobre V_{max}. Quant a OLT i OFV, no s'han trobat estudis a la literatura científica que permeten la seua predicció a dics en talús.

En aquesta tesi doctoral, s'han realitzat assajos físics 2D amb dics en talús amb sobrepassos rellevants ($0.3 \leq R_c/H_{m0} \leq 2.5$) sense espatlló i amb tres elements al mantell principal (Cubípode-1L, cubs-2L i esculleres-2L) ubicats sobre pendents de fons suaus (m=2% i 4%) en condicions d'onatge limitat pel fons ($0.2 \leq H_{m0}/h \leq 0.9$).

V_{max} conjuntament amb q són les variables més recomanades a la literatura científica per dissenyar la cota de coronació en dics en talús segons criteris d'ultrapassament. Al present estudi, els millors resultats en l'estimació de $V_{max}^*=V_{max}/(gH_{m0}T_{01}^2)$ s'han obtingut utilitzant la funció de distribució Weibull de dos paràmetres amb un elevat coeficient de determinació R^2=0.833. Durant la fase de disseny d'un dic en talús, és necessari predir q per calcular V_{max} quan s'utilitzen els mètodes donats a la literatura científica. Per tant, es deu estimar q amb fins de disseny si no es disposa d'observacions directes. Si s'aplica la xarxa neuronal de CLASH NN per estimar q (R^2=0.636), la bondat d'ajust de la funció de distribució Weibull de dos paràmetres proposada a aquesta tesi per predir V_{max}^* és R^2=0.617. Així doncs, el ràtio entre el V_{max}^* mesurat i estimat es troba dins del rang de 1/2 a 2 (banda de confiança del 90%) quan s'usa q predit amb CLASH NN. Els nous estimadors desenvolupats a aquesta dissertació proporcionen resultats satisfactoris en la predicció de V_{max}^* amb un mètode més senzill que aquells proposats a la literatura científica. No s'ha trobat una influència significativa de la pendent de fons ni de la limitació de l'onatge per fons sobre V_{max}^* a aquest estudi.

OLT i OFV estan directament relacionats amb l'estabilitat hidràulica de la coronació de dics i la seguretat de vianants front a ultrapassaments. Per tant, es requereix estimar OLT i OFV en la coronació de dics per dissenyar apropiadament la seua cota de coronació utilitzant criteris de sobrepasse. En aquest estudi, s'han usat xarxes neuronals per desenvolupar nous estimadors explícits que permeten predir OLT i OFV superats pel 2% de l'onatge incident amb un elevat coeficient de determinació ($0.866\leq R^2\leq 0.867$). El nombre de xifres significatives apropiat per als coeficients experimentals dels mencionats estimadors s'ha determinat basant-se en la seua variabilitat. El punt òptim on determinar les característiques de l'onatge deuen ser estimades per predir OLT i OFV s'ha identificat a una distància de $3h$ des del peu de l'estructura (on h és la profunditat a peu de dic). La pendent de fons té influència sobre OLT i OFV. Els valors més extrems de OLT i OFV s'han descrit amb les distribucions Exponencial d'un paràmetre i Rayleigh, respectivament, amb resultats satisfactoris ($0.803\leq R^2\leq 0.812$).

TABLE OF GENERAL CONTENTS

Chapter

TABLE OF CONTENTS

LIST OF FIGURES

LIST OF TABLES

NOTATION

Acronyms:

AWACS	= Active Wave Absorption System
CLASH	= EU-Project Crest Level Assessment of coastal Structures by full scale monitoring, neural network prediction and Hazard analysis on permissible wave overtopping
CLASH NN	= CLASH Neural Network given in (*van Gent et al., 2007*)
CV	= Coefficient of variation
LASA-V	= Local Approximation using Simulated Annealing given in *Figueres and Medina* (*2005*)
LPC-UPV	= Laboratory of Ports and Coasts (UPV)
MSE	= Mean squared error
MWL	= Mean water level
NN	= Neural Network
OLT	= Overtopping layer thickness
OFV	= Overtopping flow velocity
UPV	= Universitat Politècnica de València (ES)

Symbols:

B	= crest width
bias	= Relative bias
c	=$(gL/2\pi\ \tanh(2\pi h/L))^{0.5}$, wave celerity in intermediate waters
$\cot\alpha$ [-]	= armor slope
D_n [m] or [cm]	= $(W/\rho)^{1/3}$, concrete armor unit nominal diameter
D_{n50} [m] or [cm]	= $(W_{50}/\rho)^{1/3}$, rock nominal diameter
e_i	= estimated values

$\bar{e}$ = average of the estimated values

$f(u)$ [-] = Utility function

g [m/s^2] = gravitational acceleration

h [m] or [cm] = water depth

h_b [m] or [cm] = breaker water depth

$h_{A2\%}(z_A)$ [m] or [cm] = run-up layer thickness exceeded by 2% of the incoming waves

$h_c(x_c)$ [m] or [cm] = overtopping layer thickness with exceedance probabilities below 2%

$h_{c2\%}(x_c)$ [m] or [cm] = overtopping layer thickness exceeded by 2% of the incoming waves

H [m] or [cm] = wave height

H_b [m] or [cm] = breaker wave height

H_{max} [m] or [cm] = maximum wave height

H_{m0} [m] or [cm] $=4(m_0)^{0.5}$, spectral wave height

$H_{m0,g}$ [m] or [cm] = spectral wave height in the wave generation zone

$H_{m0,i}$ [m] or [cm] = incident spectral wave height

$H_{m0,m}$ [m] or [cm] = measured spectral wave height

$H_{m0,r}$ [m] or [cm] = reflected spectral wave height

H_{rms} [m] or [cm] = root mean square wave height

H_s [m] or [cm] = significant wave height or average wave height of the highest one-third waves, $H_{1/3}$

H_{s0} [m] or [cm] = deep water significant wave height

H_{tr} [m] or [cm] = transitional wave height

H_0 [m] or [cm] = deep water wave height

H_0' [m] or [cm] = equivalent deep water significant wave height

$H_{1/10}$ [m] or [cm] = average wave heigh of the highest tenth waves

$H_{0.1\%}$ [m] or [cm] = wave height exceeded by 0.1% of the incoming waves

$H_{1\%}$ [m] or [cm] = wave height exceeded by 1% of the incoming waves

$H_{2\%}$ [m] or [cm] = wave height exceeded by 2% of the incoming waves

Ir [-] = $\tan\alpha/(H/L_0)^{0.5}$, Iribarren number with the structure slope

Ir^* [-] = $m/(H/L_0)^{0.5}$, Iribarren number with the bottom slope

$Ir_{m-1,0}$ [-] = $\xi_{-1,0} = \tan\alpha/(H_{m0}/L_{m-1,0})^{0.5}$, Iribarren number or surf similarity parameter calculated with H_{m0} and $T_{m-1,0}$

Ir_g [-] = $Ir_{m-1,0}$ in the wave generation zone

k [rad/m] = $2\pi/L_m$, wave number

K_r [-] = $H_{m0,r}/H_{m0,i}$, reflection coefficient

K_s [-] = H/H_0', shoaling coefficient

L [m] or [cm] =$gT^2\tanh(2\pi h/L)/2\pi$, wave length

L_b [m] or [cm] = wave length calculated using the linear wave theory at a water depth h_b

L_{crest} [m] or [cm] = length of the wave crest

L_{jet} [m] or [cm] = length of the wave jet

$L_{m-1,0}$ [m] or [cm] = $gT_{m-1,0}^2/2\pi$, deep water wave length based on the spectral period, $T_{m-1,0}$

L_{m0} [m] or [cm] =$gT_m^2/2\pi$, deep water wave length based on the mean period, T_m

L_0 [m] or [cm] = $gT^2/2\pi$, deep water wave length

L_{0p} [m] or [cm] = $gT_p^2/2\pi$, deep water wave length based on the peak period, T_p

m [-] = bottom slope

m_i = i-th spectral moment

N_D [-] = number of data

N_h [-] = number of neurons in the hidden layer of NNs

N_i [-] = number of neurons in the input layer of NNs

N_o [-] = number of observations

N_{oL} [-] = number of neurons in the output layer of NNs

N_p [-] = number of parameters

N_{ow} [-] = number of overtopping events

N_v [-] = number of variables

N_w [-] = number of waves

o_i = observed values

$\bar{o}$ = average of the observed values

P [-] = number of free parameters in NNs

P_{ow} [-] = N_{ow}/N_w, proportion of overtopping waves

q [l/s/m] or [m^3/s/m] = mean wave overtopping discharge per meter of structure width

Q^* [-] = $q/(gH_{m0}T_{01})$, dimensionless mean wave overtopping discharge based on the spectral mean period, T_{01}

Q^{**} [-] = $q/(gH_{m0}T_{m-1,0})$, dimensionless mean wave overtopping discharge based on the spectral period, $T_{m-1,0}$

r = Correlation coefficient

R^2 = Coefficient of determination

R^2_{adj} = Adjusted coefficient of determination

R_c [m] or [cm] = crest freeboard

$Ru_{2\%}$ [m] or [cm] = wave run-up height exceeded by 2% of the incoming waves

s [-] =H/L, wave steepness

s_0 [-] =H_0/L_0, deep water wave steepness

s_{0p} [-] =H_{s0}/L_{0p}, deep water wave steepness based on the peak period, T_{p0}

S_{jet} [-] = L_{jet}/L_{crest}, breaking point parameter defined by *New et al.* (*1985*)

$S(f)$ = wave spectrum

t [s] = time

T [s] = wave period

T_m [s] = mean wave period

$T_{m-1,0}$ [s] = m_{-1}/m_0, spectral wave period based on the spectral moment, m_{-1}

T_p [s] = peak wave period

T_{p0} [s] = deep waters peak wave period

T_{01} [s] = m_0/m_1, mean spectral wave period

$T_{1/3}$ [s] = T_s, significant wave period

T-BLIND [-] = subset used for blind testing

TEST [-] = 15%*TR*, subset used for cross validation of the trained NNs as part of the Early Stopping Criterion

TR [-] = subset used for training NNs

TR-TRAIN [-] = 70%*TR*, subset used for the formal training of NNs as part of the Early Stopping Criterion

TR-VAL [-] = 15%*TR*, subset used for validation during the training of NNs as part of the Early Stopping Criterion

$u_{A2\%}(z_A)$ [m/s] or [cm/s] = run-up velocity

$u_c(x_c)$ [m/s] or [cm/s] = overtopping velocity with exceedance probabilities below 2%

$u_{c2\%}(x_c)$ [m/s] or [cm/s] = overtopping velocity exceeded by 2% of the incoming waves

V [l/m] or [m^3/m] = individual wave overtopping volume

$\bar{V}$ [l/m] or [m^3/m] = mean individual wave overtopping volume

V_{max} [l/m] or [m^3/m] = maximum individual wave overtopping volume

V_{max}^* [-] = $V_{max}/(gH_{m0}T_{01}^2)$, dimensionless maximum individual wave overtopping volume

W [t] or [g] = concrete armor unit mass

W_{50} [t] or [g] = rock mass corresponding to D_{n50}

x_c [m] or [cm] = horizontal coordinate along the crest from the seaward edge

x_e = estimated value by the linear regression

z_A [m] or [cm] = elevation on the MWL

ε [-] = error, difference between the estimated and the measured value

$\xi_{s,-1}$ [-] = $\tan\alpha/(H_s/L_{m-1,0})^{0.5}$, Iribarren number or surf similarity parameter calculated with H_s and $T_{m-1,0}$

ξ_0^* [-] = m/s_0, Iribarren number or surf similarity parameter with the bottom slope in deep waters

α [º] or [rad] = angle of the slope

σ [-] = variance of the estimated values by linear regression

γ [-] = parameter of the JONSWAP spectrum

γ_b [-] = H_b/h_b, breaker index

γ_{be} [-] = berm factor

γ_f [-] = roughness factor

γ_β [-] = obliquity factor

ρ [t/m^3] or [g/cm^3] = armor unit or rock density

$\Gamma(z)$ [-] = $\int_0^\infty t^{z-1}e^{-t}dt$, gamma function

Ω_b [-] = H_b/H_0, breaker height index

μ [-] = friction factor of dike crests according to *Schüttrumpf et al. (2002)*

μ_m [-]	= mean value of the Weibull distribution

“To reach a port we must set sail –
Sail, not tie at anchor
Sail, not drift”

Franklin D. Roosevelt

1

Introduction

Port of Valencia (Spain), May 2020

1.1. Introduction

Climate change is a new design factor for coastal engineers. Sea level rise (*IPCC*, *2019*) and stronger wave conditions (*Camus et al.*, *2019*) caused by climate change increase the risk of salinization and flooding in low lying areas, accelerate the erosion processes in exposed beaches and damage the existing coastal structures. Thus, coastal engineers are currently facing the challenge of designing and upgrading coastal structures considering climate change.

Since 1987, when sustainable development was first defined by the Brundtland Commission (*WCED*, *1987*), society is concerned about the impact of infrastructures: lower visual and environmental impacts are demanded. Crest elevation is a vital factor to optimize when designing a coastal structure due to its direct effect on the economic cost, the material consumption and the visual impact.

Both the consequences of climate change and the social demands lead to mound breakwaters with reduced crest freeboards facing higher extreme overtopping events. In addition, most research described in the literature refers to breakwaters in non-breaking conditions while real mound breakwaters are built in the surf zone where depth-limited wave breaking takes place. Therefore, new tools are needed to better design overtopped mound breakwaters under depth-limited breaking wave conditions.

Tolerable mean wave overtopping discharges (q) are the most common criteria when designing the crest elevation of mound breakwaters. However, *Franco et al.* (*1994*) pointed out that the overtopping hazard should be directly related with the individual wave overtopping events rather than with a mean overtopping rate; the mean individual wave overtopping volume ($\bar{V}$) may be much lower than the maximum individual wave overtopping volume (V_{max}). Consequently, recent studies (e.g.: *Bae et al.*, *2016*; *EurOtop*, *2018*) recommend considering not only q but also V_{max}, the overtopping layer thickness (OLT) and the overtopping flow velocity (OFV) when designing mound breakwater crest elevation.

Several prediction methods are found in the literature to estimate q (*van Gent et al.*, *2007; Molines and Medina*, *2016*), the number of overtopping events ($N_{ow} = N_w P_{ow}$) and V_{max} (*Bruce et al.*, *2009*; *Molines et al.*, *2019*) on mound breakwaters in non-breaking wave conditions. However, few studies in the literature are focused on N_{ow} and V_{max} on coastal structures under depth-limited breaking wave conditions. Such studies give contradictory results regarding the significance of depth-limited breaking waves on N_{ow} and V_{max}. *Gallach* (*2018*) carried out 2D physical tests with smooth impermeable steep sloped structures on bottom slopes m = 0 and 1/100 and did not find a significant effect of the depth-limited breakage of waves on V_{max}. On the other hand, *Nørgaard et al.* (*2014*) conducted 2D physical tests on mound breakwaters under depth-limited breaking wave conditions (m = 0) and observed that the existing formulas, which were developed for non-breaking wave conditions, underpredicted the measured N_{ow} and overpredicted the measured V_{max}. Therefore, no consensus exists in the literature regarding the significance of breaking waves on N_{ow} and V_{max}. *Herrera et al.* (*2017*) pointed out that the bottom slope may have a significant role in mound breakwaters design, since it influences the type of wave breaking at the toe of the structure. In addition, in depth-limited breaking wave conditions, the optimum point where wave characteristics is estimated becomes relevant for design and needs to be assessed. However, the effect of bottom slope on N_{ow} and V_{max} was not analyzed.

During extreme wave storms, overtopping occurs and water flows over the mound breakwater crest. The variables which better describe such flow, OLT and OFV, are directly related to the hydraulic stability of the armored crest (*Argente et al., 2018*) and the pedestrian safety when standing on the breakwater crest (*Bae et al., 2016*). Since pedestrians perform recreational activities on the breakwater crest such as fishing or taking pictures (see Figure 1.1), OLT and OFV should be included as a design criterion for determining the crest elevation of mound breakwaters.

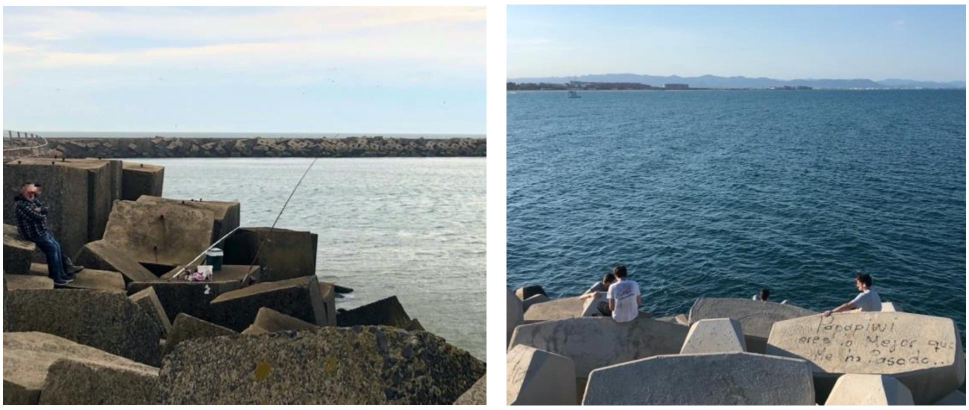

Fig. 1. 1. Pedestrians on mound breakwaters: (a) fishing at Scheveningen harbor (the Netherlands) and (b) sitting at Valencia port (Spain).

Recent studies (*Bae et al., 2016*; *Sandoval and Bruce*, *2017*) analyzed the stability of human bodies under overtopping flow conditions based on physical tests with anthropogenic dummies and video images. *Bae et al.* (*2016*) proposed tolerable limits for OLT and OFV for preventing pedestrian failure under overtopping flow conditions. Although several predictors exist in the literature to estimate OLT and OFV on dike crests, no studies were found for predicting OLT and OFV on mound breakwaters; the goal of this study is to fill these gaps of knowledge in the literature.

1.2. Research objectives

The present PhD thesis aimed to assess the existing estimators in the literature to predict the overtopping flow on sloping structures and to propose new design formulas to better explain this phenomenon on mound breakwaters. Special attention was given to the depth-limited breaking wave conditions and the influence of bottom slope. Based on the identified knowledge gaps, the following research questions were raised:

Q1. Do the existing methods in the literature satisfactorily describe the overtopping flow on mound breakwaters under depth-limited breaking wave conditions?

Q2. Can the methods given in the literature be improved to estimate N_{ow} *and* V_{max} *on mound breakwaters under depth-limited breaking wave conditions?*

Q3. Is it possible to develop explicit estimators to predict the extreme values of OLT and OFV on mound breakwater crests under depth-limited breaking wave conditions?

Q4. Where is the optimum point to estimate wave characteristics for predicting overtopping flow on mound breakwater crests under depth-limited breaking wave conditions?

Q5. Does the bottom slope play a significant role on the overtopping flow on mound breakwater crests under depth-limited breaking wave conditions?

The following objectives were stablished for this PhD thesis:

1. To review the existing literature regarding wave breaking and design criteria for determining crest elevation of mound breakwaters
2. To analyze the existing formulas for estimating the overtopping flow over sloping structures in order to identify the main significant explanatory variables.
3. To develop new design formulas to better estimate the overtopping flow on mound breakwaters under depth-limited breaking wave conditions.
4. To determine the optimum point where wave characteristics should be estimated for predicting the overtopping flow on mound breakwaters under depth-limited breaking wave conditions.
5. To evaluate the significance of bottom slope on the overtopping flow on mound breakwaters under depth-limited breaking wave conditions.

1.3. Background for the research

The present PhD thesis is the result of research conducted by the author and funded through the FPU program (*Formación de Profesorado Universitario*, grant FPU16/05081) by the Spanish Ministry of Education (*Ministerio de Educación, Cultura y Deporte*). Most of the results of this PhD thesis are based on the research project ESBECO (***ES****tabilidad hidráulica del manto,* ***BE****rmas y* ***Co****ronación de diques en talud con rebase y rotura por fondo – Hydraulic stability of the toe berm, armor and breakwater crest with overtopping and breaking wave conditions*, grant BIA2015-70436-R) awarded by the Spanish Ministry of Economy and Competitivity (*Ministerio de Economía y Competitividad*) and FEDER (*Fondo Europeo de Desarrollo Regional*).

Result of this PhD thesis have been published in the following papers:

1. Mares-Nasarre, P., Molines, J., Gómez-Martín, M.E., Medina, J.R., *2021*. Explicit Neural Network-derived formula for overtopping flow on mound breakwaters in depth-limited breaking wave conditions. Coast. Eng. 164, 103810. https://doi.org/10.1016/j.coastaleng.2020.103810
2. Mares-Nasarre, P., Gómez-Martín, M.E., Medina, J.R., *2020c*. Influencia de la pendiente de fondo sobre la seguridad de los peatones en diques en talud a rotura por fondo. XV Jornadas Españolas de Ingeniería de Costas y Puertos, 8 – 9 May 2019, Málaga (Spain) [in Spanish].
3. Mares-Nasarre, P., Molines, J., Gómez-Martín, M.E., Medina, J.R., *2020b*. Individual wave overtopping volumes on mound breakwaters in breaking wave conditions and gentle sea bottoms. Coast. Eng. 159, 103703. https://doi.org/10.1016/j.coastaleng.2020.103703
4. Mares-Nasarre, P., Gómez-Martín, M.E., Medina, J.R., *2020a*. Influence of Mild Bottom Slopes on the Overtopping Flow over Mound Breawaters under Depth-Limited Breaking Wave Conditions. J. Mar. Sci. Eng. 8 (1), 3. https://doi.org/10.3390/jmse8010003
5. Mares-Nasarre, P., Argente, G., Gómez-Martín, M.E., Medina, J.R., *2019*. Overtopping layer thickness and overtopping flow velocity on mound breakwaters. Coast. Eng. 154, 103561. https://doi.org/10.1016/j.coastaleng.2019.103561
6. Mares-Nasarre, P., Molines, J., Gómez-Martín, M.E., Medina, J.R., *2018*. Analysis of the overtopping layer thickness on low-crest mound breakwaters. Coastal 18. In: Proc. Of 7th CoastLab International Conference, 22-26th May 2018, Santander (Spain).
7. Mares-Nasarre, P., Herrera, M.P., Gómez-Martín, M.E., Medina, J.R., *2017*. Análisis de los eventos extremos de rebase y estabilidad de la coronación de diques en talud. XIV Jornadas Españolas de Ingeniería de Costas y Puertos, 24 – 25 May 2017, Alicante (Spain) [in Spanish].

During the present PhD thesis, a short stay in Deltares was funded by the mobility grant for FPU beneficiaries by the Spanish Ministry of Education (*Ministerio de Educación, Cultura y Deporte*). The following paper was the result of such short stay.

8. Mares-Nasarre, P., van Gent, M.R.A, *2020*. Oblique Wave Attack on Rubble Mound Breakwater Crest Walls of Finite Length. Water 12, Article number 353. https://doi.org/10.3390/w12020353

1.4. Dissertation structure

The dissertation presents the research structured into 6 chapters:

- **Chapter 1** describes the motivation, the research objectives and the main contributions of the actual PhD thesis.
- **Chapter 2** presents a literature review on wave breaking, paying special attention to depth-limited wave breaking, and overtopping criteria to design mound breakwater crest elevation. Methods in the literature to describe overtopping flow on coastal structures are also reported.
- **Chapter 3** describes the experimental methodology of the physical model tests conducted in this PhD thesis (ESBECO Project).
- **Chapter 4** introduces a new method to better estimate individual wave overtopping volumes on mound breakwaters under depth-limited breaking wave conditions.
- **Chapter 5** describes new predictors to estimate the extreme values of OLT and OFV on mound breakwater crests.
- **Chapter 6** summarizes the main conclusions from this PhD thesis answering the research questions raised in Chapter 1 and suggesting future lines of research.

“You cannot design a suitable model unless you understand the basic underlying physics/theory of what you are studying”

Henry L. Langhaar

2

Literature Review

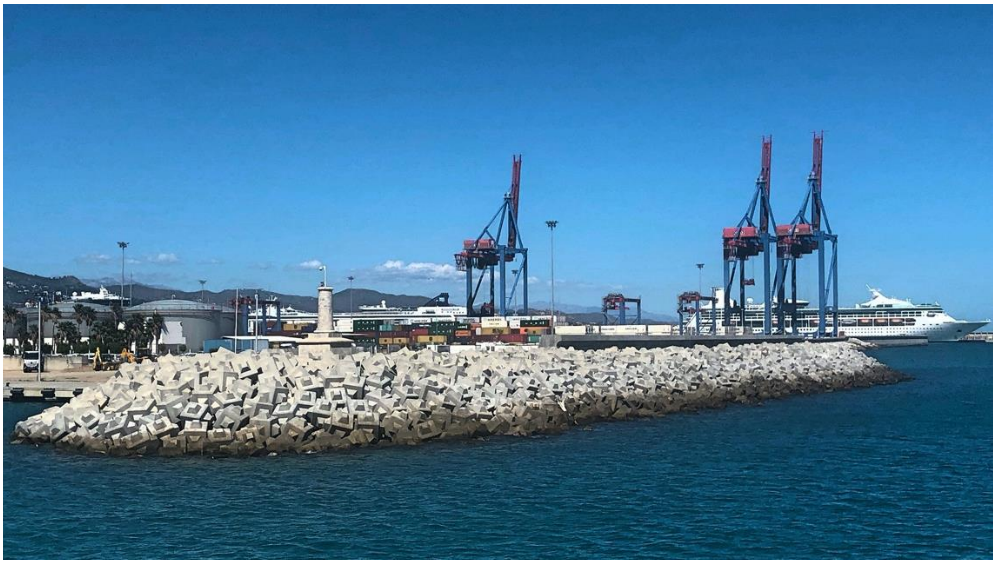

Port of Malaga (Spain), May 2019

2.1. Introduction

Crest elevation is a key parameter to be determined during the breakwater design process since it affects the cost and the risk, as well as many environmental and aesthetic factors. Typically, the tolerable mean overtopping discharge (q) is the criterion used to design crest elevation (*USACE, 2002*). However, more recent recommendations (*EurOtop, 2018*) point out the need of considering further criteria related to individual wave overtopping events; the maximum individual wave overtopping volume (V_{max}) may be much larger than the mean individual wave overtopping volume ($\bar{V}$). Therefore, it is obvious that overtopping flow characteristics need to be determined to better design the crest elevation of mound breakwaters.

Most mound breakwaters are built in the surf zone, where depth-limited wave breaking occurs. Wave forces and currents significantly change due to the depth-induced broken waves, since the larger waves break before reaching the structure. The incident wave characteristics in the depth-induced wave breaking zone are required to design mound breakwaters under depth-limited breaking wave conditions. For this reason, an extensive research exists on wave breaking characterization (*Ting and Kirby, 1995, 1996*). Nevertheless, most methods for estimating overtopping flow conditions do not consider the changes in the wave characteristics in the surf zone.

In this chapter, a brief review on wave breaking is first presented. Secondly, criteria given in the literature to determine crest elevation of mound breakwaters is reviewed. Thirdly, the methods in the literature to estimate individual wave overtopping volumes, overtopping layer thickness (OLT) and overtopping flow velocity (OFV) are analyzed. It should be noted that formulas to predict OLT and OFV on dike crests are reviewed, since no methods in the literature were found for mound breakwaters.

2.2. Waves in breaking conditions

Waves are usually the cause of the main loads on coastal structures. Thus, a proper coastal structure design requires an accurate estimation of wave characteristics. Waves propagate from deep water towards the coast suffering transformations due to refraction, shoaling, diffraction and breaking. Wave breaking is produced when the crest travels faster than the waveform, making the wave unstable with a significant dissipation of energy through turbulence.

2.2.1. Types of wave breaking mechanisms

Two types of wave breaking mechanisms are reported in the literature: (1) wave breaking due to an excessive wave steepness ($s = H/L$ too large, where H is the wave height and L the wave length) and (2) wave breaking due to water depth limitation (H/h too large, where h is the water depth). Most mound breakwaters are built in shallow water where wave breaking takes place due to depth-limitation (H/h too large).

Iribarren and Nogales (*1950*) defined the Iribarren number (Ir^*), also called surf similarity parameter (*Battjes*, *1974*), as

$$Ir^* = \frac{m}{\sqrt{\frac{H}{L_0}}} \tag{2.1}$$

where m is the bottom slope, $L_0 = gT^2/2\pi$ is the deep water wave length, g is the gravitational acceleration and T is the wave period. Ir^* has been widely applied for wave breaking classification (*Galvin*, *1968*; *Gourlay*, *1992*); four categories of wave breaking are usually considered for beaches and sloping structures: *spilling*, *plunging*, *collapsing* and *surging* (see Figure 2.1).

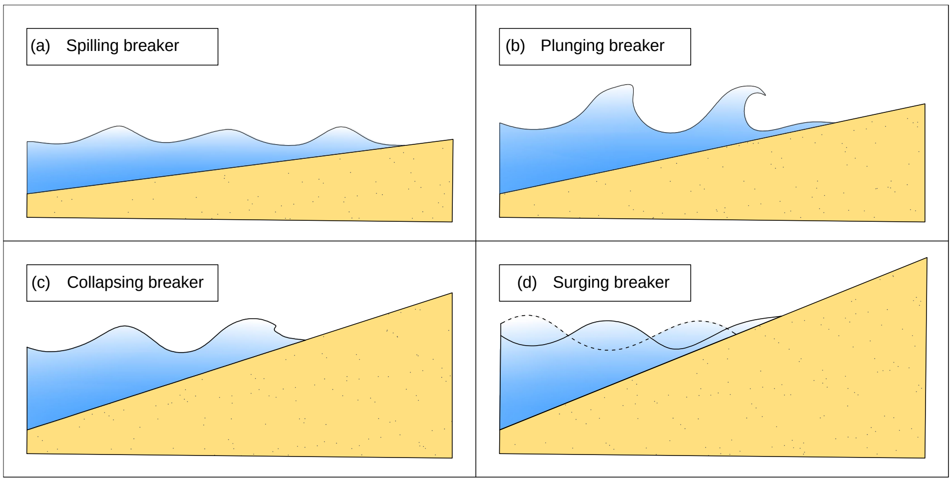

Fig. 2. 1. Wave breaker types.

Spilling breakers are characterized by symmetrical wave contours and a foamy water surface due to the unstable wave crest. *Spilling* waves are usually found on very gentle beach slopes.

Plunging waves are characterized by a high dissipation of energy, turbulence and air trapping. Their crest becomes first vertical, then curls over the shoreward face of the wave and finally falls on the trough of the wave with a violent impact. Plunging waves are usually found on gentle to intermediate beach slopes.

Collapsing breakers are between plunging and surging waves. They are similar to plunging waves but the crest is not breaking. The lower part of the shoreward face steepens and falls, creating an irregular turbulent water face.

Surging waves occur on very steep beaches, where waves do not break. *Surging* waves are usually considered on sloping structures because of the relatively larger forces generated by these breaking waves. *Surging* waves go up and down on the slope with minor breaking and a little bit of foamy water.

Table 2.1 shows the types of wave breakers according to *Iribarren and Nogales* (*1950*).

Breaker type	$Ir^{*}= m/(H/L_0)^{0.5}$
Spilling	< 0.5
Plunging	0.5 – 2.5
Collapsing	2.5 – 3.0
Surging	> 3.0

Table 2. 1. Wave breaker types as function of Ir^{*} according to *Iribarren and Nogales* (*1950*).

Although *Iribarren and Nogales* (*1950*) classification is the most common, its performance is not good in situations with complex bathymetry featuring steps, platforms and bars (*Smith and Kraus, 1991*; *Mead and Black, 2001*; *Scarfe et al., 2003*; *Blenkinsopp and Chaplin, 2008*).

Smith and Kraus (*1991*) found that the critical values of the surf similarity parameter were different on barred beaches and proposed a different classification based on the surf similarity parameter in deep waters ($\xi_0^{*} = m/s_0$, where $s_0 = H_0/L_0$ is the deep water wave steepness and H_0 is the deep water wave height). *Smith and Kraus* (*1991*) recommended $\xi_0^{*} < 0.4$ for *spilling* waves, $0.4 < \xi_0^{*} < 1.2$ for *plunging* waves and $\xi_0^{*} > 1.2$ for *collapsing* or *surging* waves.

Grilli et al. (*1997*) established new criteria to describe wave breaking of solitary waves based on $S_0 = 1.521\ m/H_0$. Since the period and wave length of solitary waves are theoretically infinite, they were not considered in the classification parameter S_0. *Grilli et al.* (*1997*) recommended $S_0 < 0.025$ for *spilling* waves, $0.025 < S_0 < 0.3$ for *plunging* waves and $0.3 < S_0 < 0.37$ for *collapsing* or *surging* waves.

Other classifications in the literature are based on the wave geometry at the breaking point (*Peregrine, 1983; New et al., 1985; Bonmarin, 1989*). *New et al.* (*1985*) proposed a criterion using the parameter $S_{jet} = L_{jet}/L_{crest}$, where L_{jet} is the length of the jet and L_{crest} is the length of the crest (see Figure 2.2). Based on S_{jet}, only two categories were distinguished: *spilling* breakers ($S_{jet} < 3/100$) and *plunging* breakers ($S_{jet} > 1/10$).

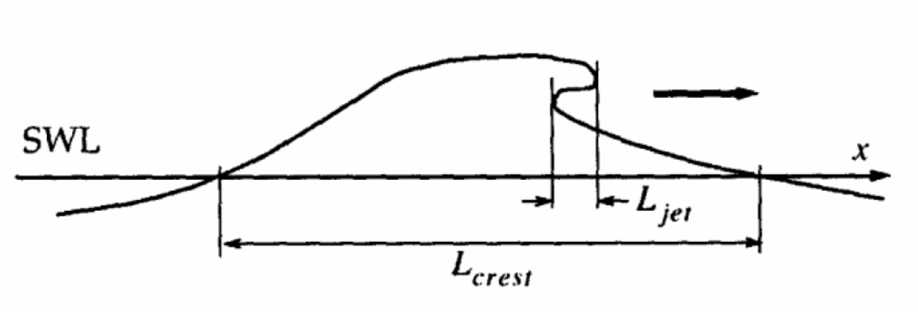

Fig. 2. 2. Breaking parameters according to *New et al.* (*1985*).

Breaking waves have also been classified by analyzing the wave plunge distances (*Smith and Kraus*, *1991*) and the wave vortex parameters (*Longuet-Higgins*, *1982*) with both empirical and numerical methods (*Vinje and Brevig*, *1981; Khayyer et al., 2008*).

Recently, *Díaz-Carrasco et al.* (*2020)* and *Moragues et al.* (*2020*) recommended using the logarithmic space log(*h/L*)-log(*H/L*) or the alternate slope similarity parameter, log(*h/L H/L*), to better analyze wave breaking and flow characteristics on slopes.

2.2.2. Wave breaking criteria

As mentioned in the previous section, two types of wave breaking exist: (1) wave breaking due to an excessive wave steepness ($s = H/L$ too large) and (2) wave breaking due to water depth limitation (H/h too large).

2.2.2.1 Wave steepness

Wave breaking due to an excessive wave steepness takes place mainly in deep and medium waters. *Michell* (*1893*) proposed the most well-known criterion for this type of wave breaking; the limiting wave steepness ($s = H/L$) was established as 0.142 in deep waters for waves with crest angles of 120º (see Figure 2.3)

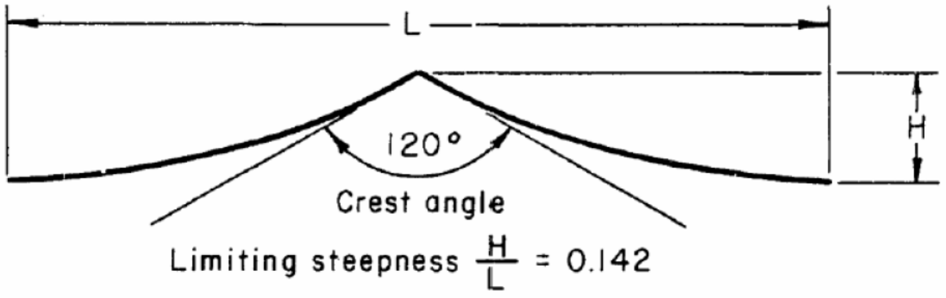

Fig. 2. 3. Limiting criterion for wave breaking due to excessive wave steepness (*USACE, 1984*).

Later, *Miche* (*1944*) provided a criterion for water depths shallower than $L_0/2$; the breaking limit was established at $(H/L)_{max} = 0.142\tanh(2\pi H/L)$. This criterion was adapted for horizontal sea bottoms by *Danel* (*1952*) who exchanged the constant 0.142 by 0.12. *Ostendorf and Madsen* (*1979*) also modified *Miche's* (*1944*) criterion in order to include the effect of the beach slope on the wave breaking point. Some studies based on laboratory tests indicated a limit for wave breaking of $H/gT^2 = 0.021$ while measurements in the North Sea established such limit at $H/gT^2 = 0.0067$. *Longuet-Higgins* (*1983*) established the breaking limit as function of the acceleration of the wave at the breaking point at $-0.388g$.

This thesis is focused on depth-limited breaking waves; thus, breaking waves in deep water are not considered in this research.

2.2.2.2 Water depth

Two common parameters are reported in the literature to define the wave breaking criterion caused by the water depth limitation: (1) the breaker index, γ_{br}, and (2) the breaker height index, Ω_b. The breaker index is defined as

$$\gamma_{br} = \left(\frac{H}{h}\right)_{max} = \left(\frac{H_b}{h_b}\right) \tag{2.2}$$

where H_b is the breaker wave height at a water depth h_b. The breaker height index is defined as

$$\Omega_b = \frac{H_b}{H_0} \tag{2.3}$$

where H_0 is the wave height in deep water.

Although the breaker index seems to be the most widely used, no consensus exists in the literature regarding the proper criteria to determine the breaking point (*Rattanapitikon and Shibayama, 2000*; *Robertson et al., 2013*). *Robertson et al.* (*2013*) classified in six categories the breaker index formulas found in the literature: (1) breaker index as a constant, (2) breaker index as function of bottom slope, (3) breaker index as function of Ir^*, (4) breaker index as function of the hyperbolic tangency of breaking wavelength and height, (5) breaker index as function of the bottom slope and the wave height and wavelength in deep waters, and (6) breaker index as function of an exponential of the bottom slope and the wave height and wavelength in deep waters. The main contributions in the literature are described in the following paragraphs.

The first criterion was given by *McCowan* (*1894*) for a solitary wave over an horizontal bottom; $\gamma_{br} = 0.78$. Such value was restated by *Munk* (*1949*). *Munk* (*1949*) also defined the breaker height index for a solitary wave as $\Omega_b = 1/(3.3s_0)^{1/3}$.

Based on physical tests, *Camfield and Street* (*1968)*, *Galvin* (*1968*) and *Collins* (*1969)* included the bottom slope in the breaker index definition. Later, *Le Roux* (*2007*) proposed an equation for the breaker index which included the bottom angle instead of the bottom slope based on *USACE* (*1984*) data.

Battjes (*1974*) was the first author who included the surf similarity parameter in the breaker index definition. *Battjes's* (*1974*) proposal was updated by *Sunamura* (*1981*) to make it applicable to a wider range of bottom slopes. Alternate proposals with better correlations can be found in *Kaminsky and Kraus* (*1993*).

Bottom slope and the wave height and wavelength in deep waters were first considered by *Le Méhauté and Koh* (*1967*). *Le Méhauté and Koh's* (*1967*) equation was later recalibrated by *Sunamura and Horikawa* (*1974*) using the experimental data given in *Goda* (*1970*). Similar proposals for estimating the breaker index can be found in *Ogawa and Shuto* (*1985*).

Gourlay (*1992*) did not find a significant effect of bottom slope on the breaker index. However, *Rattanapitikon and Shibayama* (*2000*) reported a poor performance of *Gourlay's* (*1992*) formula. *Tsai et al.* (*2005*) characterized breaking conditions on steep bottom slopes, since most of the existing studies were conducted in gentle to mild bottom slopes.

Based on laboratory data published in the literature, *Camenen and Larson* (*2007*) assessed the performance of the existing formulas. The authors concluded that the behavior in breaking conditions with steep bottom slopes was not properly described. Finally, *Camenen and Larson* (*2007*) proposed a new equation using trigonometric and deep water steepness relationships.

Yao et al. (*2012*) conducted new experiments in order to characterize depth-limited wave breaking on an idealized fringing reed (a plane sloping front reef and a horizontal submerged reef). The authors concluded that the ratio between the horizontal submerged reef depth and the wave height was a significant factor to describe wave breaking features.

Exponential relationships have been widely applied for estimating the breaker index or the breaking wave height. *Goda* (*1970*) conducted laboratory tests with regular waves on bottom slopes $5\% < m < 20\%$ and suggested an exponential dependence of the breaking wave height on the breaking water depth. Later, *Goda* (*1975*) modified such relationship for random irregular waves based on a new random wave breaking model. *Muttray and Oumeraci* (*2001*) recommended a new coefficient for *Goda's* (*1975*) formula which better described wave breaking on bottom slopes over 1/30. *Tsai et al.* (*2005*) observed that *Goda's* (*1975*) equation overestimated the wave height on steep bottom slopes. *Rattanapitikon and Shibayama* (*2000*) and *Goda* (*2010*) modified *Goda's* (*1975*) formula to improve its performance on steep slopes.

Weggel (*1972*) re-analyzed the breaking wave data in the literature and developed a new model for predicting the maximum breaker wave height to which a coastal structure may be subjected. *Weggel's* (*1972*) formula considered the water depth at which the wave breaks, the beach slope, the breaker steepness and the breaker travel distance given by *Galvin's* (*1968*) equation. *Camenen and Larson* (*2007*) confirmed that *Weggel* (*1972*) proposal overestimated the breaker wave height. *Smith and Kraus* (*1991*) re-calibrated the coefficients in *Weggel's* (*1972*) formula.

CIRIA/CUR/CETMEF (*2007*) recommended the formulas given in *Goda* (*1970*) and *Weggel* (*1972*) for estimating the breaker index for normally incident regular waves over a uniform slope (see Eqs. 2.4 and 2.5).

$$\gamma_{br} = \left(\frac{H_b}{h_b}\right) = 0.17\,\frac{L_0}{h_b}\left(1 - exp\left[-1.5\,\pi\,\frac{h_b}{L_0}\left\{1 + 15\,m^{4/3}\right\}\right]\right) \tag{2.4}$$

$$\gamma_{br} = \left(\frac{H_b}{h_b}\right) = \frac{b(m)}{1 + a(m)\,\dfrac{h_b}{L_0}} = b(m) - a(m)\,\frac{H_b}{L_0} \tag{2.5}$$

where $a(m) = 6.96(1–\exp[-19m])$ and $b(m) = 1.56(1+\exp[-19.5m])^{-1}$.

As previously mentioned, *Goda* (*1975*) suggested exchanging the coefficient 0.17 in Eq. 2.4 (valid for regular waves) for values between 0.18 and 0.12 for irregular random waves. *Goda* (*2010*) also reduced the coefficient 15 in Eq. 2.4 to 11 to better describe wave breaking on steep slopes.

Eq. 2.6 given by *Rattanapitikon and Shibayama (2000*) was also recommended in *CIRIA/CUR/CETMEF* (*2007*).

$$\left(\frac{H_b}{h_b}\right) = \left(-1.40\,m^2 + 0.57\,m + 0.23\right)\left(\frac{H_0}{L_0}\right)^{0.35} \tag{2.6}$$

where L_b is the wave length calculated using the linear wave theory at a water depth h_b.

2.2.3. Estimation of wave characteristics in shallow waters

Rayleigh distribution was proposed by *Longuet-Higgins* (*1952*) to describe wave height distribution in deep water, where wave surface elevation follows a Gaussian process. However, in shallow water, the water profile is distorted due to the wave transformation and the water surface elevation does not follow a Gaussian process any more. In the breaking zone, the wave height is limited; the waves which exceed the breaking limit, break. A comparison between the wave height distribution in deep waters and shallow waters is presented in Figure 2.4.

Since *Collins* (*1970*) proposed the first methodology for transforming wave characteristics in deep water into the corresponding breaking wave characteristics in shallow waters, several methods have been developed in the literature. A review on the statistical models to describe the distribution of the highest wave heights can be found in *Massel and Sobey* (*2000*).

Based on the energy dissipation produced by the depth-induced breaking phenomenon, *Battjes and Janssen* (*1978*) developed a bore-type dissipation model to estimate the transformation of random breaking waves in shallow water. During the following years, different methods (*Mase and Iwagaki*, *1982; Dally and Dean*, *1987*; *Dally*, *1990*, *1992*) were proposed to calculate the wave height distribution in shallow waters. A relevant contribution is the one by *Baldock et al.* (*1998*) who modified *Battjes and Janssen's* (*1978*) method to improve its performance on steep beaches. *Baldock et al.* (*1998*) also provided explicit expressions for the energy dissipation rate within the surf zone and for the fraction of broken waves.

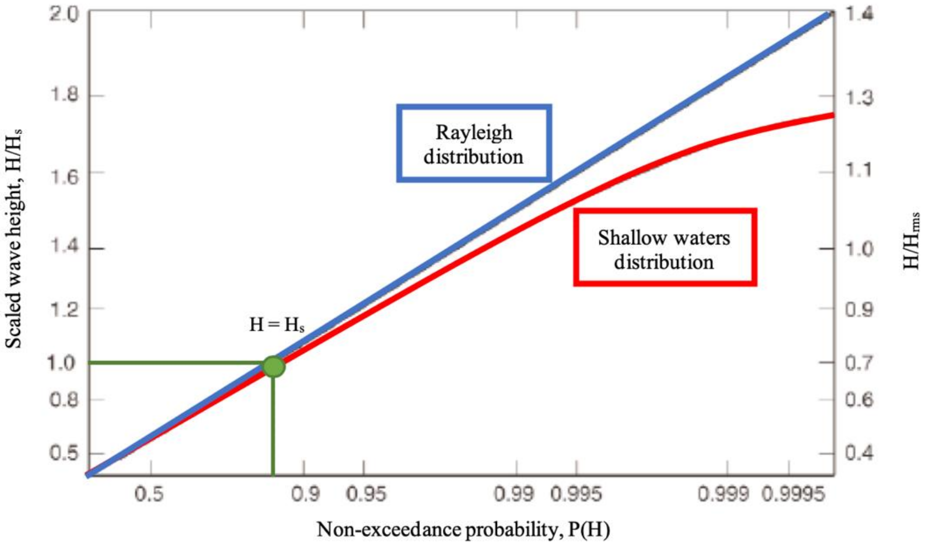

Fig. 2. 4. Comparison between the wave height distribution in deep water and shallow water.

Most methods in the literature (*Tayfun*, *1981; Hughes, S.A.*, *Borgman*, *1987*; *Klopman*, *1996*) characterize the wave height distribution in shallow water as empirical or semi-empirical variations of the Rayleigh distribution including the effects of wave breaking. *Battjes and Groenendijk* (*2000*) proposed the Composite Weibull Distribution to describe the individual wave height distribution for depth-limited waves (see Eq. 2.5). Later, such distribution was implemented in SwanOne model (*Verhagen et al.*, *2008*) which can be used for estimating wave characteristics in the surf zone for a given bathymetry and deep water wave conditions.

$$F(H) = \begin{cases} 1 - exp\left(-\left[\frac{H}{H_1}\right]^{k1}\right) \; if \; H \leq \; H_{tr} \\ 1 - exp\left(-\left[\frac{H}{H_2}\right]^{k2}\right) \; if \; H \geq \; H_{tr} \end{cases} \tag{2.7}$$

where H_1 and H_2 are the scale parameters, k_1 and k_2 are the exponents whose recommended values are $k_1 = 2.0$ and $k_2 = 3.6$ based on laboratory data with five bottom slopes, and $H_{tr} = (0.35+5.8m)h$ is the transitional wave height. The variance of the surface elevation (m_0) or the significant spectral wave height ($H_{m0} = 4m_0^{0.5}$) are needed to apply this method, since the root mean square wave height has to be calculated as $H_{rms} = m_0^{0.5}(2.69+3.24\ [m_0^{0.5}/h])$. Thus, *Battjes and Groenendijk* (*2000*) provided a table with the characteristic values for $H_{1/3}/\ H_{rms}$, $H_{1/10}/\ H_{rms}$, $H_{2\%}/\ H_{rms}$, $H_{1\%}\ H_{rms}$ and $H_{0.1\%}/\ H_{rms}$.

The Composite Weibull Distribution has been widely recommended in manuals such as *CIRIA/CUR/CETMEF* (*2007) or EurOtop* (*2018*). It has also been compared with field data from stations in the North Sea in *Mai et al.* (*2011*) with reasonable results. Nevertheless, *Caires and Van Gent* (*2012*) pointed out that high wave heights on horizontal bottom slopes were underestimated when using the Composite Weibull Distribution.

Formulas for estimating the significant wave height, $H_s = H_{1/3}$, and the maximum wave height, H_{max}, in the surf zone were given in *Goda* (*2000*) (see Eqs. 2.8 and 2.9).

$$H_{1/3} = \begin{cases} (K_s\, H_0')\; for\; h/L_0 \geq\; 0.2 \\ \min([\beta_0 H_0' + \beta_1 h], [\beta_{max} H_0'], [K_s\, H_0'])\; for\; h/L_0 \leq 0.2 \end{cases} \tag{2.8}$$

$$H_{max} = H_{1/250} = \begin{cases} (1.8\; K_s\, H_0')\; for\; h/L_0 \geq\; 0.2 \\ \min([\beta_0^* H_0' + \beta_1^* h], [\beta_{max}^* H_0'], [1.8\; K_s\, H_0'])\; for\; h/L_0 \leq 0.2 \end{cases} \tag{2.9}$$

where H_0' is the equivalent deep waters significant wave height, $K_s = H/H_0'$ is the shoaling coefficient, h/L_0 is based on the significant wave period ($T_{1/3}$) and β_0, β_1, β_{max}, β_0^*, β_1^*, β_{max}^* are coefficients calculated using the equations in Table 2.2.

Coefficients for $H_{1/3}$	**Coefficients for H_{max}**
$\beta_0 = 0.028(H_0'/L_0)^{-0.38} exp(20m^{1.5})$	$\beta_0^* = 0.052\left(H_0'/L_0\right)^{-0.38} exp\left(20m^{1.5}\right)$
$\beta_1 = 0.52 exp(4.2m)$	$\beta_1^* = 0.63 exp(3.8m)$
$\beta_{max} = max(0.92, 0.32[H_0'/L_0]^{-0.29} exp[2.4m])$	$\beta_{max}^* = max(1.65, 0.53[H_0'/L_0]^{-0.29} exp[2.4m])$

Table 2. 2. Coefficients for estimating $H_{1/3}$ and H_{max} in shallow waters according to *Goda* (*2000*).

Goda (*2000*) also provided diagrams for directly obtaining $H_{1/3}$ and H_{max} for bottom slopes $m = 1\%$, 3.33%, 5% and 10%.

CIRIA/CUR/CETMEF (*2007*) also provided five diagrams based on *Van der Meer* (*1990*) to determine H_{m0}/h in shallow waters as function of the wave steepness in deep waters (s_{0p}) and the ratio h/L_{0p} for $m < 2\%$, where $L_{0p}=gT_p^2/2\pi$ is the deep waters wave length based on the peak period, T_p.

As presented in this section, a wide variety of proposals exist in the literature since wave breaking is not a fully solved problem. Thus, more specific studies on wave breaking are still being developed, such as the characterization of the breaking depth for a determined type of breaker (*Xie et al., 2019*) or the development of new techniques for measuring wave breaking using video images (*Andriolo et al., 2020*) and remote sensing (*Díaz et al., 2017*). More recent proposals for wave height distribution in shallow waters can be found in *Mendez et al.* (*2004)* and *Méndez and Castanedo* (*2007*).

2.3. Criteria to assess the crest elevation of mound breakwaters

Coastal structure designs must ensure not only the structure integrity but also safe operational conditions during port activities. Although criteria based on tolerable mean wave overtopping discharge (q) are commonly applied, recent recommendations (*Bae et al., 2016*) point out the need of new criteria based on the individual wave overtopping events. This need was first stated by *Franco et al.* (*1994*), who noted that the mean individual wave overtopping volume ($\bar{V}$) may be much lower than the maximum individual wave overtopping volume (V_{max}). In this section, main criteria for designing mound breakwater crest elevation are reviewed.

Acceptable limits for mean wave overtopping discharges (q) were proposed by experts based on their subjective impressions when observing overtopping on prototype breakwaters (*Fukuda et al., 1974*; *Goda, 1985*). Those recommendations were included in manuals such as *British Standard (1991)* or *CIRIA/CUR* (*1991*). As shown in Figure 2.5, both the structural safety and the functional safety were considered.

Sigurdarson and Viggosson (*1994*) recommended a limit value of q = 0.42l/s/m in the 50-year design storm for preventing damage to equipment and cargo on quay. However, *Franco et al.* (*1994*) pointed out the lack of data related to safe operation of ports and ship mooring on the breakwater rear side. Moreover, these authors proposed the individual wave overtopping volumes as a better criterion for designing breakwater crest elevation. *Franco et al.* (*1994*) analyzed the effect of such overtopping volumes on model vehicles and model pedestrian in physical model tests with vertical and composite structures. The authors concluded that pedestrians were more stable than vehicles under the same overtopping event and that the admissible limits were dependent on the structure geometry; the same overtopping volume was more dangerous on vertical breakwaters (fast water jet) than on sloping structures (slower aerated flow). This may indicate that not only the overtopping volume but also the velocity of the overtopping flow resulted significant for pedestrian and vehicle safety. Figure 2.6 shows the risk curves for pedestrians obtained by *Franco et al. (1994)* for different structure geometries.

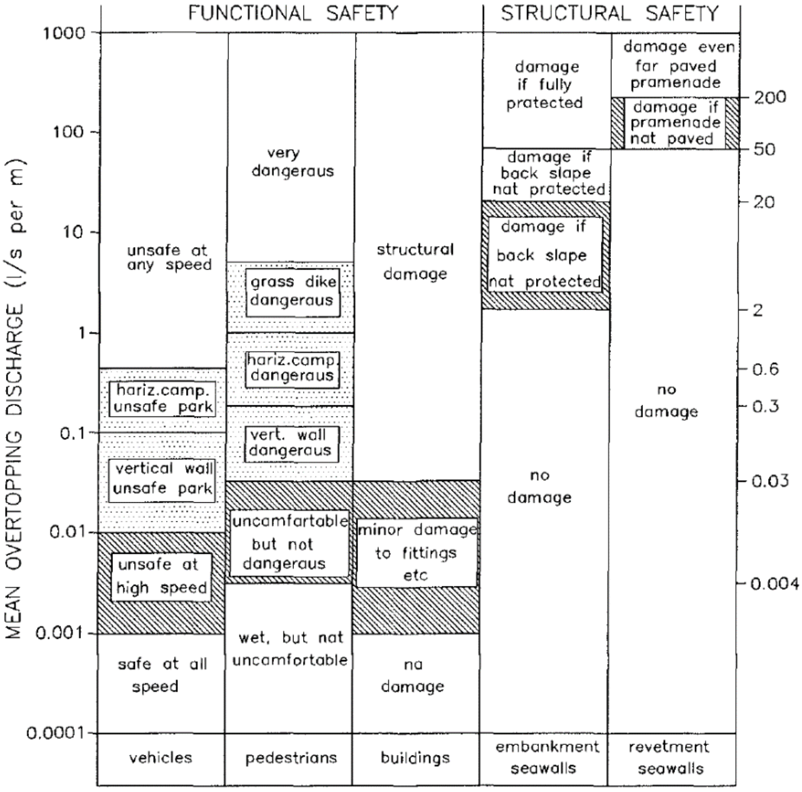

Fig. 2. 5. Admissible mean wave overtopping discharges according to the existing guidelines (*Franco et al., 1994*).

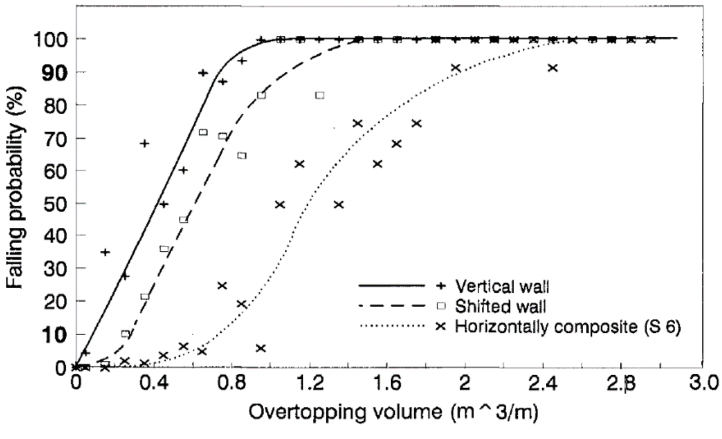

Fig. 2. 6. Overtopping risk curves for pedestrian according to *Franco et al. (1994)*.

USACE (*2002*) recommended admissible *q* equivalent to those reported in *British Standard (1991)* or *CIRIA/CUR* (*1991*) (see Figure 2.5). *Bruce et al.* (*2003*) highlighted the role of the velocity of the overtopping jet on human stability and proposed using both the individual wave overtopping volumes and the velocity of the overtopping jet as design criteria.

Geeraerts et al. (*2005*) measured forces caused by overtopping impact on dummies installed on the Zeebrugge mound breakwater (Belgium) in order to assess pedestrian safety. Later, *Geeraerts et al.* (*2007*) suggested the overtopping limits for vehicles and pedestrians in Table 2.3 based on previous works (*Fukuda et al., 1974*); admissible *q* and V_{max} were given accounting the location, the training level and attitude of the pedestrian when facing the overtopping event. *De Rouck et al.* (*2009*) added property limitations shown in Table 2.3 to recommendations given by *Geeraerts et al.* (*2007*). *Allsop et al.* (*2008*) also proposed admissible *q* and V_{max} similar to those recommended in *Geeraerts et al.* (*2007*) and *De Rouck et al.* (*2009*).

Hazard	***q* (l/s/m)**	**V_{max} (l/m)**
Unaware pedestrian, no clear view of the sea, relatively easily upset or frightened, narrow walkway or close proximity to edge	0.03	2 - 5
Aware pedestrian, clear view of the sea, not easily upset or frightened, able to tolerate getting wet, wider walkway	0.1	20 - 50
Trained staff, well shod and protected, expecting to get wet, overtopping flows al lower levels only, no falling jet, low danger or fall from walkway	1 - 10	500
Vehicles driving moderate or high speed, impulsive overtopping giving falling or high velocity jets	0.01 – 0.05	5
Vehicles driving at low speed, overtopping by pulsating flows at lower levels only, not falling jets	10 - 50	1,000
Sinking small boats set 5-10m from wall. Damage to larger yatchs	10	1,000 – 10,000
Significant damage or sinking of larger yatchs	50	5,000 – 50,000

Table 2. 3. Summary of the overtopping limits according to *Geeraerts et al.* (*2007*) and *De Rouck et al.* (*2009*).

Additional guidance on tolerable overtopping on buildings can be found in *Chen et al.* (*2017*).

Bae et al. (*2016*) were the first authors who explicitly assessed pedestrian safety under overtopping flow conditions using overtopping layer thickness (OLT) and overtopping flow velocity (OFV). The authors conducted physical tests with anthropomorphic dummies of several sizes (adults and children), weights (thin, standard and obese) and footwear and determined the admissible OLT and OFV. *Bae et al.* (*2016*) also compared their results with previous studies performed under steady flow conditions and concluded that humans were less stable under overtopping flow conditions. Figure 2.7 shows the thresholds for OLT and OFV given by *Bae et al.* (*2016*) as well as the experimental results of pedestrian accidents from different authors (*Abt et al.*, *1989*; *Endoh and Takahashi*, *1995*; *Karvonen et al.*, *2000*; *Jonkman and Penning-Rowsell*, *2008*; *Sandoval and Bruce*, *2017*). In this figure, open symbols correspond to steady flow observations while closed symbols correspond to overtopping flow observations.

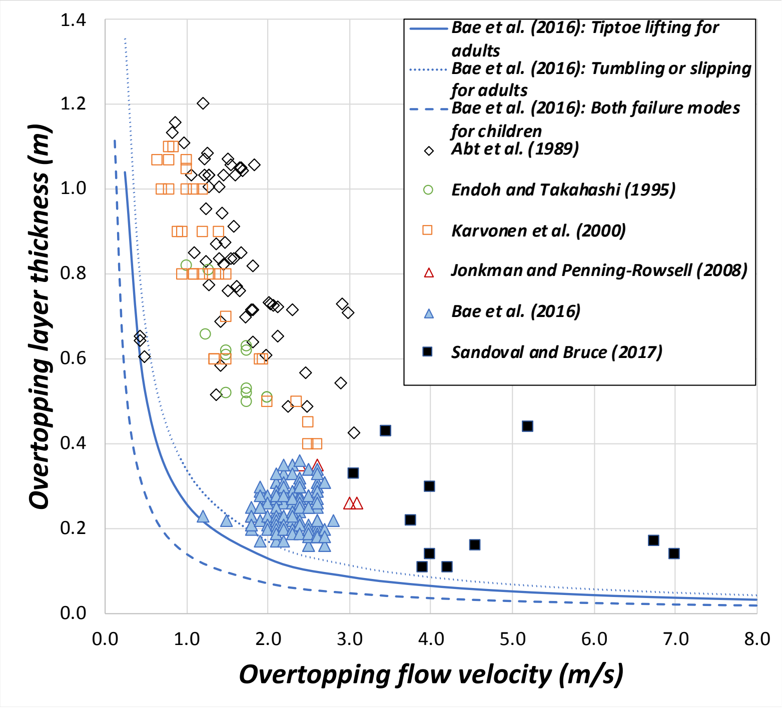

Fig. 2. 7. Experimental observations of pedestrian accidents in the literature and admissible overtopping layer thickness and overtopping flow velocity for pedestrian safety by *Bae et al.* (*2016*).

Sandoval and Bruce (*2017*) analyzed pedestrian safety as function of OLT and OFV using data from video images. The authors also observed that pedestrian were more unstable under overtopping flow conditions than under steady flow conditions, similar to *Bae et al.* (*2016*).

EurOtop (*2018*) considered both *q* and V_{max} to assess the hazards driven by wave overtopping and to give advice on tolerable wave overtopping. However, other overtopping variables such as overtopping velocities over the crest, OLT and overtopping falling distances were categorized as significant. *EurOtop* (*2018*) proposed wave overtopping limits based on the structural stability of the breakwater and the safety of the property, vehicles and people behind the coastal defense. Table 2.4 summarizes the limits for wave overtopping applicable to mound breakwater designs according to *EurOtop* (*2018*).

Hazard	***q* (l/s/m)**	**V_{max} (l/m)**
Rubble mound breakwaters facing H_{m0}>5m; no damage	1	2,000 – 3,000
Rubble mound breakwaters facing H_{m0}>5m; rear side designed for wave overtopping	5 - 10	10,000 – 20,000
Significant damage or sinking of larger yachts; H_{m0}>5m	>10	>5,000 – 30,000
Significant damage or sinking of larger yachts; H_{m0}=3-5m	>20	>5,000 – 30,000
Sinking small boats set 5-10m from wall, H_{m0}=3-5m. Damage to larger yatchs	>5	>3,000 – 5,000
Safe for larger yatchs; H_{m0}>5m	<5	<5,000
Safe for small boats set 5-10m from wall, H_{m0}=3-5m.	<1	<2,000
Building structure elements; H_{m0}=1-3m.	≤1	<1,000
Damage to equipment set back 5-10m	≤1	<1,000
People at seawall		
H_{m0}=3m	0.3	600
H_{m0}=2m	1	600
H_{m0}=1m	10 – 20	600
H_{m0}<0.5m	No limit	No limit
Cars on seawalls or railway close behind crest		
H_{m0}=3m	<5	2,000
H_{m0}=2m	10-20	2,000
H_{m0}=1m	<75	2,000

Table 2. 4. Summary of overtopping limits according to *EurOtop (2018*).

Recently, *Altomare et al.* (*2020*) analyzed the validity of the safety overtopping limits proposed in the literature for pedestrian using field data from the Catalan coast. The authors concluded that the pedestrian hazard is linked to the combination of the overtopping layer thickness and the overtopping flow velocity.

As shown in this section, acceptable limits for q and V_{max} seem to be appropriate criteria for designing mound breakwater crest when considering the structural safety and the hazard to building and properties in the protected area. However, recent studies (e.g.: *Altomare et al.*, *2020*) point out the need of considering overtopping layer thickness and the overtopping flow velocity when assessing vehicles and pedestrian safety.

2.4. Individual wave overtopping volumes on mound breakwaters

In the previous section, the maximum individual wave overtopping volume (V_{max}) was presented as one of the most relevant criteria to assess mound breakwater crest elevation. In this section, the methods given in the literature for estimating individual wave overtopping volumes are described.

2.4.1. Individual wave overtopping volumes distribution

Van der Meer and Janssen (*1994*) and *Franco et al. (1994)* were the first who described individual wave overtopping volumes using the Weibull distribution on dikes and vertical and composite structures, respectively. Later, the 2-parameter Weibull distribution (see Eq. 2.10) was widely applied in the literature to predict individual wave overtopping volumes for a variety of coastal structures.

$$F(V) = F(x \leq V) = 1 - exp\left(-\left[\frac{V}{a}\right]^{b}\right) \tag{2.10}$$

where $F(x \leq V)$ is the non-exceedance probability of the individual wave overtopping volume per wave, x is the individual wave overtopping volume, a is the dimensional scale factor and b is the shape factor. Eq. 2.10 can be rewritten as

$$F(V) = 1 - exp\left(-\left[\frac{V/\bar{V}}{A}\right]^{b}\right) \tag{2.11}$$

where $\bar{V}$ is the measured mean individual wave overtopping volume and $A=a/\bar{V}$ is the scale factor.

If the measured individual wave overtopping volumes followed an ideal Weibull distribution and all measured data were included in the analysis, $\bar{V}$ should be equal to the mean value of the Weibull distribution ($\mu_m = \bar{V}$). Under the described hypothesis, a relationship between A and b exists and is given by

$$A = \frac{a}{\overline{V}} = \frac{1}{\Gamma\left(1+\frac{1}{b}\right)} \tag{2.12}$$

where Γ is the gamma function, calculated as $\Gamma(z) = \int_0^\infty t^{z-1}e^{-t}dt$.

Van der Meer and Janssen (*1994*) and *Franco et al. (1994)* recommended a shape coefficient b = 0.75 for dikes and vertical and composite structures, respectively. According to Eq. 2.12, A = 0.84.

Besley (*1999*) investigated individual wave overtopping volumes on sloped structures, vertical walls and composite breakwaters. The author referred to the results in *Franco et al. (1994)* who observed that the shape factor b was about 0.1 lower for vertical walls than for sloping structures. *Franco et al. (1994)* also reported the significance of the wave steepness on the shape factor b for vertical walls. Thus, *Besley* (*1999*) proposed values for the shape factor b as function of the offshore wave steepness (s_{0p} = $2\pi H_{s0}/[gT_{p0}^2]$, where H_{s0} is the significant offshore wave height and T_{p0} is the deep waters peak period); b = 0.76 for s_{0p} = 0.02 and b = 0.92 for s_{0p} = 0.04.

Bruce et al. (*2009*) conducted 2D physical tests on mound breakwaters over horizontal bottoms with a wide variety of armor layers, both single- and double-layer. Main experimental ranges of such tests were $0.8 \le R_c/H_{m0} \le 1.3$ and $0.33 \le H_{m0}/h \le 0.40$, where R_c is the crest freeboard. *Bruce et al.* (*2009*) analyzed the individual wave overtopping volumes higher than $\overline{V}$ and proposed a shape factor b = 0.74. No significant differences were observed between the performance of the different tested armors.

Victor et al. (*2012*) analyzed individual wave overtopping volumes on smooth impermeable steep slopes ($0.36 \le cot\alpha \le 2.75$, where $cot\alpha$ is the armor slope) with $0.11 \le R_c/H_{m0} \le 1.69$ on horizontal bottoms. During the tests with large H_{m0}, the authors observed that the wave heights followed a Composite Weibull distribution, instead of a Rayleigh distribution, and concluded that such deviations were caused by the depth-induced breaking of the highest waves ($0.04 \le H_{m0}/h \le 0.37$). The authors also observed that both the shape factor b and V_{max} decreased when waves were not Rayleigh distributed. Furthermore, the effect of R_c/H_{m0}, $cot\alpha$ and s_{0p} was investigated; s_{0p} ($0.012 \le s_{0p} \le 0.041$) resulted negligible. Finally, they proposed Eq. 2.13 to estimate the shape factor b based on the individual wave overtopping volumes higher than $\overline{V}$.

$$b = exp\left(-2.0\ \frac{R_c}{H_{m0}}\right) + (0.56 + 0.15\ cot\alpha) \tag{2.13}$$

Zanuttigh et al. (*2013*) studied the shape factor b on rough and smooth low-crested structures ($0 \le R_c/H_{m0} \le 2$) using the individual wave overtopping volumes higher than $\overline{V}$. The authors observed that those formulas considering R_c/H_{m0} gave good results for smooth structures whereas poor performance was obtained for rubble mound breakwaters. Higher scatter of rubble mound breakwaters data was also observed. *Zanuttigh et al.* (*2013*) proposed Eq. 2.14 for estimating the shape factor b on rubble mound breakwaters based on the dimensionless mean wave overtopping discharge, $Q^{**}=q/(gH_{m0}T_{m-1,0})$ (where $T_{m-1,0} = m_{-1}/m_0$ and m_k is the k-th spectral moment, $m_k = \int_0^\infty S(f) f^k df$, and S(f) is the wave spectrum) similar to $Q^{*}=q/(gH_{m0}T_{01})$ (where $T_{01} = m_0/m_1$) recommended by *Besley* (*1999*). *EurOtop (2018*) also suggested Eq. 2.14 for rubble slopes and mounds.

$$b = 0.85 + 1500 {Q^{**}}^{1.3} \tag{2.14}$$

Nørgaard et al. (*2014*) carried out 2D physical tests on horizontal bottoms with rock-armored mound breakwaters with crown wall both in non-breaking and breaking conditions ($0.18 \le H_{m0}/h \le 0.50$) with $0.9 \le R_c/H_{m0} \le 2.0$. These authors assessed the performance of the formulas to estimate the shape factor *b* in the literature which were developed in non-breaking conditions using data in breaking conditions. *Nørgaard et al.* (*2014*) concluded that such formulas were overpredicting the largest overtopping wave volumes and proposed Eq. 2.15 based on 30% of the highest individual wave overtopping volumes.

$$b = \begin{cases} 0.75 & for\ \dfrac{H_{m0}}{H_{1/10}} \le 0.848\ or\ \dfrac{H_{m0}}{h} \le 0.2 \\ -6.1 + 8.08\,\dfrac{H_{m0}}{H_{1/10}} & for\ \dfrac{H_{m0}}{H_{1/10}} > 0.848\ and\ \dfrac{H_{m0}}{h} > 0.2 \end{cases} \tag{2.15}$$

where $H_{1/10}$ is the average of 10% of the highest waves in the test run.

Gallach (*2018*) conducted thousands of 2D physical tests with steep sloped and vertical structures with a wide range of crest freeboards ($0.0 \le R_c/H_{m0} \le 3.25$) on bottom slopes $m = 0$ and $m = 1/100$. The author found negligible the effect of depth-induced breaking waves ($0.03 \le H_{m0}/h \le 0.50$) on the shape factor *b*, contrary to the results reported in *Victor et al.* (*2012*) and *Nørgaard et al.* (*2014*). *Gallach* (*2018*) also noted that the roughness of the structured did not affect the shape factor *b* and proposed a new formula to estimate *b* as function of R_c/H_{m0} fitted with the largest 10% individual wave overtopping volumes. The author also fitted the scale factor *A* and obtained values significantly different from those given by Eq. 2.12.

Similar to *Pan et al.* (*2016*), *Molines et al.* (*2019*) pointed out the existing inconsistencies in the selection criteria regarding the number of overtopping events used to fit the 2-parameter Weibull distribution. *Molines et al.* (*2019*) used the 2D physical tests performed by *Smolka et al.* (*2009*) on conventional mound breakwaters ($1.25 \le R_c/H_{m0} \le 4.78$) with crown wall in non-breaking conditions ($0.10 \le H_{m0}/h \le 0.32$) to analyze the effect of the aforementioned selection criteria on the fit of the 2-parameter Weibull distribution. These authors fitted the scale *A* and shape factor *b* using 10%, 30% 50% and 100% (with a quadratic utility function) of the highest individual wave overtopping volumes. Utility functions are applied to consider the relative relevance of the observed data; special attention is given to the highest volumes when using the whole dataset with a quadratic utility function. The relationship between *A* and *b* was not described by Eq. 2.12. Small overtopping events are not relevant for practical applications but they significantly influence $\bar{V}$ and N_{ow} and, subsequently, the estimations of A given by Eq. 2.12. *Molines et al.* (*2019*) proposed Eqs. 2.16 and 2.17 for estimating the scale and shape factors, respectively, using the quadratic utility function on all observed individual wave overtopping volumes.

$$b = 0.63 + 1.25\, exp(-3.0 \cdot 10^5\, Q^*) \tag{2.16}$$

$$A = 1.4 - 0.4\, \frac{1}{b} \tag{2.17}$$

Additionally, *Molines et al.* (*2019*) reported a good performance of the 2-parameter Exponential distribution when describing the individual wave overtopping volumes, given by

$$F(V) = 1 - exp\left(-\left[\frac{V/\bar{V} - C}{D}\right]\right) \tag{2.18}$$

where

$$D = 2.6 + 2.6\, exp(-3.0 \cdot 10^5\, Q^*) \tag{2.19}$$

$$C = 1.2 - D - 0.2\, D^2 \tag{2.20}$$

2.4.2. Number of overtopping events

Makkonen (*2006*) recommended the Weibull plotting position formula (see Eq. 2.21) to assign an exceedance probability to every individual wave overtopping volume.

$$F(V) = \frac{i}{N_{ow} + 1} \tag{2.21}$$

where i is the rank of the individual wave overtopping volume, sorted in descending order (i=1 refers to V_{max}) and N_{ow} is the number of overtopping events.

Lykke Andersen et al. (*2009*) rewrite the Weibull distribution function using Eq. 2.21 as

$$V_i = A\bar{V}\left(-ln\left[\frac{i}{N_{ow} + 1}\right]\right)^{1/b} = A\bar{V}(ln[N_{ow} + 1] - \ln[i])^{1/b}\ with\ i = 1\ to\ N_{ow} \tag{2.22}$$

By setting i=1 in Eq. 2.22, V_{max} can be obtained as

$$V_i = A\bar{V}(ln[N_{ow} + 1])^{1/b} \tag{2.23}$$

Besley (*1999)* and *EurOtop (2018*) recommended Eq. 2.24 instead of Eq. 2.23.

$$V_i = A\bar{V}(ln[N_{ow}])^{1/b} \tag{2.24}$$

Since Eq. 2.24 uses N_{ow} instead of $N_{ow}+1$, $V_{max} = 0$ for $N_{ow} = 1$ (*Lykke Andersen et al., 2009*). Both the number of overtopping events (N_{ow}) and the mean individual wave overtopping volume ($\bar{V} = qT_{01}N_w/N_{ow}$, where N_w is the number of waves) need to be calculated for estimating V_{max} using either Eq. 2.23 or 2.24. To this end, *Besley* (*1999*) recommended Eqs. 2.25 and 2.26 for estimating N_{ow} for simple slopes and complex slopes with berms and return walls, respectively.

$$P_{ow} = \frac{N_{ow}}{N_w} = exp\left(-K_1\left[\frac{R_c}{T_{01}\sqrt{gH_{m0}}}\frac{1}{\gamma_f}\right]\right) \tag{2.25}$$

$$P_{ow} = \begin{cases} 55.4Q^{*0.634} & for\ 0 < Q^* < 8\cdot 10^{-4} \\ 2.5Q^{*0.199} & for\ 8\cdot 10^{-4} < Q^* < 10^{-2} \\ 1 & for\ Q^* > 10^{-2} \end{cases} \tag{2.26}$$

where P_{ow} is the proportion of overtopping waves, K_1 is an empirical coefficient and γ_f is the roughness factor. Note that $Q^*=q/(gH_{m0}T_{01})$ is used. *Besley* (*1999)* proposed K_1=37.8 for structure slope $cot\alpha$=2 and K_1=63.8 for structure slope $cot\alpha$=1. *Besley* (*1999)* proposed Eq. 2.27 for estimating q.

$$\frac{q}{gT_{01}H_{m0}} = K_2 exp\left(-K_3\frac{R_c}{T_{01}\sqrt{gH_{m0}}}\frac{1}{\gamma_f}\right) \tag{2.27}$$

where K_2 and K_3 are experimental coefficient to be calibrated as function of $cot\alpha$. For $cot\alpha$=1.5, K_2=8.84·10^{-5} and K_3=19.9.

Nørgaard et al. (*2014*) modified Eq. 2.26 to make it applicable to depth-limited breaking wave conditions for $0.006 \leq P_{ow} \leq 0.120$ and $7.3\cdot 10^{-7} \leq Q^* \leq 6.2\cdot 10^{-5}$. *Nørgaard et al.* (*2014*) proposed $P_{ow}=C_1$ *Eq.* 2.26.

$$C_1 = \begin{cases} 1 & for\ \frac{H_{m0}}{H_{1/10}} \leq 0.848\ or\ \frac{H_{m0}}{h} \leq 0.2 \\ -6.65 + 9.02\frac{H_{m0}}{H_{1/!0}} & for\ \frac{H_{m0}}{H_{1/10}} > 0.848\ and\ \frac{H_{m0}}{h} > 0.2 \end{cases} \tag{2.28}$$

Regarding the estimation of q, *Nørgaard et al.* (*2014*) suggested using CLASH Neural Network (CLASH NN) (*van Gent et al., 2007*).

EurOtop (2018) proposed Eq. 2.29 to estimate P_{ow} on mound breakwaters with permeable crest berms.

$$P_{ow} = exp\left(-\left[\sqrt{-ln0.02}\frac{R_c}{Ru_{2\%}}\right]^2\right) \tag{2.29}$$

where $Ru_{2\%}$ is the wave run-up heights exceeded by 2% of the incoming waves, calculated as

$$\frac{Ru_{2\%}}{H_{m0}} = 1.65\gamma_f\gamma_\beta\gamma_{be}\xi_{-1,0} \tag{2.30a}$$

with a maximum value of

$$\frac{Ru_{2\%}}{H_{m0}} = min\left(1.00\gamma_{f,surging}\gamma_\beta\left[4.00 - \frac{1.50}{\sqrt{\xi_{-1,0}}}\right], 2.0\right) \tag{2.30b}$$

where $\gamma_{f,surging}$= γ_f +($\xi_{-1,0}$-1.8)(1- γ_f)/8.2; γ_β is the oblique wave attack factor, γ_{be} is the influence factor for the presence of berms and $\xi_{-1,0}$ is the Iribarren number of surf similarity parameter calculated as

$$\xi_{-1,0} = tan\alpha/\sqrt{2\pi H_{m0}/(gT_{m-1,0}{}^2)} \tag{2.31}$$

EurOtop (2018) recommended Eq. 2.32 to estimate *q*.

$$\frac{q}{\sqrt{gH_{m0}{}^3}} = 0.09exp\left(-1.5\frac{R_c}{H_{m0}\gamma_f\gamma_\beta}\right) \tag{2.32}$$

Molines et al. (*2019*) proposed calculating P_{ow} using Eq. 2.33 for $0.001 \le P_{ow} \le 0.20$ and $7.0\cdot10^{-8} \le Q^* \le 6.4\cdot10^{-5}$.

$$P_{ow} = 480Q^{*0.8} \tag{2.33}$$

Similar to *Nørgaard et al.* (*2014*), *Molines et al.* (*2019*) suggested using CLASH NN to estimate *q*. A summary of the experimental ranges of the methods in the literature is given in Table 2.5.

As exposed in this section, most models in the literature to estimate individual wave overtopping volumes were developed under non-breaking conditions with horizontal or bottom slopes *m* = 1/100. On the other hand, those conducted under depth-limited breaking wave conditions reported opposite results. Thus, further research is needed on the effect of depth-limited wave breaking as well as on the influence of the bottom slope. A table showing the summary of the methods in the literature to estimate V_{max} on sloped structures or mound breakwaters is shown in Table 2.6.

Author	Structure	Crown wall	R_c/H_{m0}	H_{m0}/h_s	m	$cot\ \alpha$
Bruce et al. (2009)	Mound breakwaters	Yes	0.80 – 1.03	0.33 – 0.40	0	2
Victor et al. (2012)	Smooth impermeable steep slopes	No	0.11 – 1.69	0.04 – 0.37	0	0.36 – 2.75
Zanuttigh et al. (2013)	Smooth slopes and rubble mound breakwaters	-	0 – 2	–	–	2 – 4
Nørgaard et al. (2014)	Rubble mound breakwaters	Yes	0.9 – 2	0.18 – 0.50	0	1.5
Gallach (2018)	Steep slopes and vertical structures	No	0 – 3.25	0.03 – 0.50	0, 1/100	0 – 0.27, 1.5 – 2.75
Molines et al. (2019)	Mound breakwaters	Yes	1.25 – 4.78	0.10 – 0.32	0	1.5

Table 2. 5. Summary of the experimental ranges of the methods given in the literature to estimate V_{max}.

Variable	Besley (1999)	Nørgaard et al. (2014)	EurOtop (2018)	Molines et al. (2019)
***q* (l/s/m)**	Eq. 2.27	CLASH NN	Eq. 2.23	CLASH NN
P_{ow} (-)	Simple slopes: Eq. 2.25 Complex slopes: 2.26	Eq. 2.28	Eq. 2.29	Eq. 2.33
***b* (-)**	0.76 for s_{0p}=0.02 0.92 for s_{0p}=0.04	Eq. 2.15	Eq. 2.24	Eq. 2.26
***A* (-)**	Eq. 2.12	Eq. 2.12	Eq. 2.12	Eq. 2.17
V_{max} (l/m)	Eq. 2.24	Eq. 2.23	Eq. 2.24	Eq. 2.23

Table 2. 6. Summary of the methods given in the literature to calculate V_{max} on mound breakwaters and permeable slopes.

2.5. Overtopping layer thickness and overtopping flow velocity

In Section 2.2, overtopping layer thickness (OLT) and overtopping flow velocity (OFV) were presented as key variables to assess pedestrian safety when designing mound breakwaters. Since no methods were found in the literature that focused on OLT and OFV on mound breakwaters, the methods valid for dikes are also presented here. Special attention is given to the variables considered significant for describing OLT and OFV in the literature.

Van Gent (*2002*) and *Schüttrumpf et al.* (*2002*) measured OLT and OFV on dikes crests during 2D physical tests. Subsequently, *Schüttrumpf and Van Gent* (*2003*) combined the results of the two studies and described the overtopping flow on dike crests using two variables: (1) OLT on the dike crest exceeded by 2% of the incoming waves ($h_{c2\%}$), and (2) OFV on the dike crest exceeded by 2% of the incoming waves ($u_{c2\%}$). In addition, *Schüttrumpf and Van Gent* (*2003*) proposed a method to estimate $h_{c2\%}$ and $u_{c2\%}$ on dikes using $Ru_{2\%}$ calculated with *van Gent* (*2001*) as

$$\frac{Ru_{2\%}}{H_{m0}} = \begin{cases} c_0\,\xi_{s,-1} & if\ \xi_{s,-1} \le p \\ c_1 - \dfrac{c_2}{\xi_{s,-1}} & if\ \xi_{s,-1} \ge p \end{cases} \tag{2.34a}$$

$$c_2 = 0.25\frac{{c_1}^2}{c_0} \tag{2.34b}$$

$$p = 0.5\frac{c_1}{c_0} \tag{2.34c}$$

where c_0=1.35, c_1=4.0, c_2 and p are given by Eqs. 2.34b and 2.34c, respectively and c is the Iribarren number or surf similarity parameter obtained with $H_{1/3}$ and $T_{m-1,0}$ (see Eq. 2.31). Main variables involved in *Schüttrumpf and Van Gent* (*2003*) method are presented in Figure 2.8.

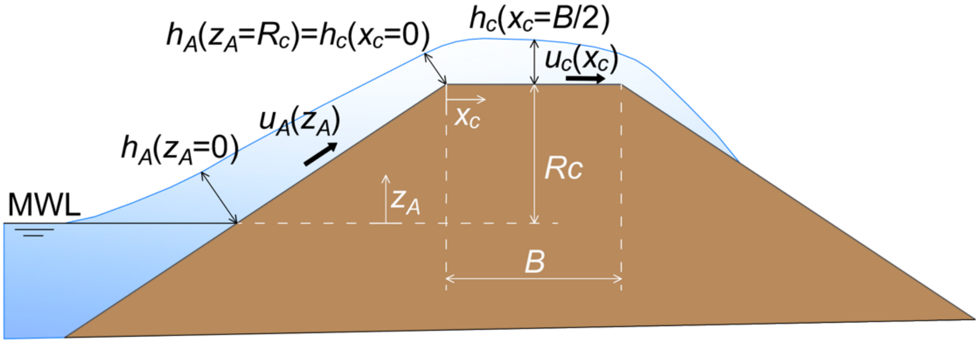

Fig. 2. 8. Definition of the variables considered by *Schüttrumpf and Van Gent* (*2003*) to estimate OLT and OFV on a dike.

Eqs. 2.35 and 2.36 were proposed by *Schüttrumpf and Van Gent* (*2003*) to calculate the OLT and OFV on the seaside slope of the dike ($0 \le z_A \le R_c$), respectively.

$$\frac{h_{A2\%}(z_A)}{H_{m0}} = c^*_{A,h}\left(\frac{Ru_{2\%} - z_A}{H_{m0}}\right) \tag{2.35}$$

$$\frac{u_{A2\%}(z_A)}{\sqrt{gH_{m0}}} = c^*_{A,u}\sqrt{\frac{Ru_{2\%} - z_A}{H_{m0}}} \tag{2.36}$$

where $h_{A2\%}(z_A)$ and $u_{A2\%}(z_A)$ are the run-up layer thickness and velocity along the seaside slope exceeded by 2% of the incoming waves, respectively, z_A is the elevation over the mean water level (MWL) and $c_{A,h}^*$ and $c_{A,u}^*$ are empirical coefficients shown in Table 2.7.

	van Gent (2002)	**Schüttrumpf et al. (2002)**	**Van der Meer et al. (2010)**	**Lorke et al. (2012)**	**Formentin et al. (2019)**
$\cot\alpha$	4	3, 4, 5	3	3, 6	2, 4
R_c/H_s	0.7-2.2	0.0-4.4	0.7-2.9	0.33-2.86	0, 0.5, 1.0
H_s/h	0.2-1.4	0.1-0.3	0.1-0.3	0.13-0.3	0.10 – 0.19
$c_{A,h}^*$	0.15	0.33	0.13	-	-
$c_{A,u}^*$	1.30	1.37	-	-	-
$c_{c,h}^*$	0.40	0.89	-	0.35 for $\cot\alpha$=3 0.54 for $\cot\alpha$=6	0.35 for $R_c \geq 0$ 0.18 for R_c<0
$c_{c,u}^*$	0.50	0.50	-	-	-

Table 2. 7. Summary of the experimental ranges and empirical coefficients of the methods in the literature to estimate OLT and OFV on dikes.

Following *Schüttrumpf and Van Gent* (*2003*) method, OLT and OFV on the dike crest ($0 \leq x_c \leq B$) can be determined as

$$\frac{h_{c2\%}(x_c)}{h_{A2\%}(z_A = R_c)} = exp\left(-c^*_{c,h}\frac{x_c}{B}\right) \tag{2.37}$$

$$\frac{u_{c2\%}(x_c)}{u_{A2\%}(z_A = R_c)} = exp\left(-c^*_{c,u}\frac{x_c\mu}{h_{c2\%}(x_c)}\right) \tag{2.38}$$

where $h_{c2\%}(x_c)$ and $u_{c2\%}(x_c)$ are the overtopping layer thickness and the overtopping flow velocity on the crest exceeded by 2% of the incoming waves, respectively, x_c is the distance to the intersection between the crest and the seaward slope, B is the crest width, μ is the friction coefficient and $c_{c,h}^*$ and $c_{c,u}^*$ are empirical coefficients shown in Table 2.7. *Schüttrumpf et al.* (*2002*) recommended μ=0.0058-0.02 for smooth slopes.

Van Gent (*2002*) and *Schüttrumpf et al.* (*2002*) proposed values for the empirical coefficients in Eqs. 2.35-2.38 based on their own physical tests. Although the range of application of the coefficients suggested in *Van Gent* (*2002*) falls within the range of application of those given by *Schüttrumpf et al.* (*2002*), relevant differences exist for $c_{A,h}^*$ and $c_{c,h}^*$. $h_{c2\%}(x_c)$ calculated using $c_{A,h}^*=0.15$ and $c_{c,h}^*=0.40$ suggested by *Van Gent* (*2002*) is 58%([0.15/0.33]×[exp{-0.40×1/2}/exp{-0.89×1/2}]) of the $h_{c2\%}(x_c)$ estimated using $c_{A,h}^*=0.33$ and $c_{c,h}^*=0.89$ recommended by *Schüttrumpf et al.* (*2002*). Even if the dike models were similar, estimations by *Schüttrumpf et al.* (*2002*) are almost twice the estimations by *Van Gent* (*2002*). Such differences may be caused by different experimental set ups (e.g. bottom slope) or different experimental ranges (see Table 2.7). However, these significant differences are hard to explain since both authors tested dikes under similar conditions.

Van der Meer et al. (*2010*) performed physical tests on dikes with $cot\alpha=3$ and measured OLT and OFV at the seaward edge and landward edge of the dike crest. Experimental ranges of *Van der Meer et al.* (*2010*) are given in Table 2.7. The authors combined their experimental results with those reported in *Van Gent* (*2002*) and *Schüttrumpf et al.* (*2002*) and proposed a new method to estimate OLT and OFV. Such method was also based on the difference between $Ru_{2\%}$ and R_c and is given in Eqs. 2.37 and 2.39-2.41.

$$h_{A2\%}(R_c) = 0.13(Ru_{2\%} - R_c) \tag{2.39}$$

$$u_{A2\%}(R_c) = 0.35cot\alpha\sqrt{g(Ru_{2\%} - R_c)} \tag{2.40}$$

$$\frac{u_{c2\%}(x_c)}{u_{A2\%}(R_c)} = exp\left(-1.4\frac{x_c}{L_{m-1,0}}\right) \tag{2.41}$$

where $L_{m-1,0}$ is the wave length based on $T_{m-1,0}$. Considering $z_A=R_c$ in Eqs. 2.35 and 2.39, $c_{A,h}^*=0.13$ given in Table 2.7 is obtained. *Van der Meer et al.* (*2010*) also recommended Rayleigh distribution to describe the OLT and OFV distribution functions.

Lorke et al. (*2012*) measured OLT and OFV on the landward edge of dike models with $cot\alpha=3$ and 6 in physical model tests focused on the effect of currents and wind on the overtopping. These authors used conventional wage gauges and miniature propellers to measure OLT and OFV, respectively. *Lorke et al.* (*2012*) proposed new values for $c_{c,h}^*$ in Eq. 2.37 given by *Schüttrumpf and Van Gent* (*2003*) based on their experimental observations; $c_{c,h}^*=0.35$ for $cot\alpha=3$ and $c_{c,h}^*=0.54$ for $cot\alpha=6$. Note that coefficients recommended by *Lorke et al.* (*2012*) are similar to those suggested by *Van Gent* (*2002*) for $cot\alpha=4$.

Hughes et al. (*2012*) analyzed the physical tests conducted by *Hughes and Nadal* (*2009*) on slightly submerged levees ($-0.32\leq R_c/H_s\leq -0.11$); OLT and OFV were measured on the crest close to the seaward and landward edges using pressure cells and Doppler velocimeters, respectively. Based on Eqs. 2.39 and 2.40 proposed by *Van der Meer et al.* (*2010*), *Hughes et al.* (*2012*) derived and calibrated a relationship between OLT and OFV given by

$$u_{A2\%}(R_c) = 1.53\sqrt{g\, h_{A2\%}(R_c)} \tag{2.42}$$

Hughes et al. (*2012*) also proposed the Rayleigh distribution function to describe the 10% upper values of OLT and OFV. No correlation was found between the OLT and OFV corresponding to the same overtopping event.

EurOtop (2018) recommended a method to estimate $h_{A2\%}$ and $h_{c2\%}$ on dike crests based on the difference between $Ru_{2\%}$ and R_c. First, $Ru_{2\%}$ is estimated using Eq. 2.43.

$$\frac{Ru_{2\%}}{H_s} = 1.65\gamma_f\gamma_\beta\gamma_{be}\xi_{s,-1} \tag{2.43a}$$

with a maximum value of

$$\frac{Ru_{2\%}}{H_s} = 1.0\gamma_f\gamma_\beta\left(4 - \frac{1.5}{\sqrt{\gamma_{be}\xi_{s,-1}}}\right) \tag{2.43b}$$

Once $Ru_{2\%}$ is determined, $h_{A2\%}(R_c)$ is calculated using Eq. 2.35 with $c_{A,h}^*=0.20$ for $cot\alpha=3$ and 4 and $c_{A,h}^*=0.30$ for $cot\alpha=6$. Finally, $h_{c2\%}(x_c>>0)=(2/3)h_{A2\%}(R_c)$ is assumed as constant on the crest of the dike not close to the seaside slope, after an initial zone of the crest where turbulence occurs.

Recently, *Formentin et al.* (*2019*) analyzed the existing methods in the literature to estimate OLT and OFV valid for dikes using numerical and experimental observations. OLT and OFV measured at the seaward edge of the dike crest were used. These authors found a non-negligible effect of the seaward slope on OLT and OFV. *Formentin et al.* (*2019*) proposed new formulas for estimating $h_{c2\%}(x_c=0)$ and $u_{c2\%}(x_c=0)$ based on the difference between $Ru_{2\%}$ and R_c (see Eqs. 2.44 and 2.45).

$$h_{c2\%}(x_c = 0) = 0.085cot\alpha(Ru_{2\%} - R_c)^{1.35} \tag{2.44}$$

$$u_{c2\%}(x_c = 0) = (0.12cot\alpha + 0.41)(g[Ru_{2\%} - R_c]^{0.5})^{1.35} \tag{2.45}$$

Regarding the evaluation of OLT along the dike crest, *Formentin et al.* (*2019*) observed a linear decay and refitted $c_{c,h}^*$ in Eq. 2.37 as

$$c_{c,h}^* = \begin{cases} 0.35\, for\ R_c \geq 0 \\ 0.18\, for\ R_c < 0 \end{cases} \tag{2.46}$$

These authors also investigated the evolution of OFV along the dike crest; different trends were observed for positive and negative freeboards. In case of positive freeboards, *Formentin et al.* (*2019*) recommended neglecting the decay of OFV along the dike crest, since it only occurred on very short crest widths. Such observations were contrary to those reported in previous studies (*Schüttrumpf and Van Gent, 2003*; *van Bergeijk et al., 2019*).

In this section, methods in the literature to estimate OLT and OFV on dike crests were presented. Such models proposed almost the same significant variables for describing OLT and OFV: H_s, $T_{m-1,0}$ and $cot\alpha$ gathered in the surf similarity parameter or Iribarren number ($\xi_{s,-1}$) and the crest freeboard. Thus, similar variables are expected to be relevant for describing OLT and OFV on mound breakwater crests. Table 2.8 summarizes the variables considered in the literature to describe OLT and OFV on dike crests.

Variable	**Author**	H_s	$T_{m-1,0}$	$cot\alpha$	R_c	B	$L_{m-1,0}$
$h_{c2\%}$	*Schüttrumpf and van Gent (2003)*	x	x	x	x	x	
	Lorke et al. (2012)	x	x	x	x		
	EurOtop (2018)	x	x	x	x		
	Formentin et al. (2019)	x	x	x	x	x	
$u_{c2\%}$	*Schüttrumpf and van Gent (2003)*	x	x	x	x	x	x
	Van der Meer et al. (2010)	x	x	x	x		x
	EurOtop (2018)	x	x	x	x		x
	Formentin et al. (2019)	x	x	x	x		

Table 2. 8. Summary of the variables considered to estimate OLT and OFV in the literature.

“Scale effects are to the experimenter what simplifying assumptions are to the theorist”

Alain Le Méhauté

3

Experimental methodology

Wave flume of the Laboratory of Ports and Coasts at the *Universitat Politècnica de València (Spain)*. September 2017

3.1. Introduction

Within the framework of the ESBECO project, 2D physical model tests on overtopped mound breakwaters under depth-limited breaking wave conditions were conducted in the wave flume of the Laboratory of Ports and Coasts at the *Universitat Politècnica de València* (LPC-UPV). Such physical model tests were focused on the characterization of the armor stability (*Argente et al.*, *2018*), rock toe berm stability (*Gómez-Martín et al.*, *2019*) and overtopping.

In this chapter, the experimental facilities and equipment are first described. Secondly, the experimental design of the model and the test matrix is presented. Thirdly, the instrumentation used during the tests is detailed. Fourthly, the results of the tests are analyzed. Wave analysis following *Herrera et al.* (*2017*) methodology is conducted while individual wave overtopping volume identification is performed applying the method proposed by *Molines et al.* (*2019*). Finally, the methodology applied in this thesis is summarized.

3.2. Experimental facilities

Two-dimensional physical model tests were performed at the LPC-UPV wave flume (30.0m×1.2m×1.2m) on mild bottom slopes (*m*=2% and 4%) and with a piston-type wavemaker. As shown in Figure 3.1, two bottom slope configurations were tested. First configuration was formed by a 6.3m-long *m*=4% ramp and a 9.0m-long *m*=2% ramp. Second configuration was composed of a continuous 15.3m-long bottom slope of *m*=4%. Both configurations show a 5.5m-long horizontal bottom at the wave generation zone.

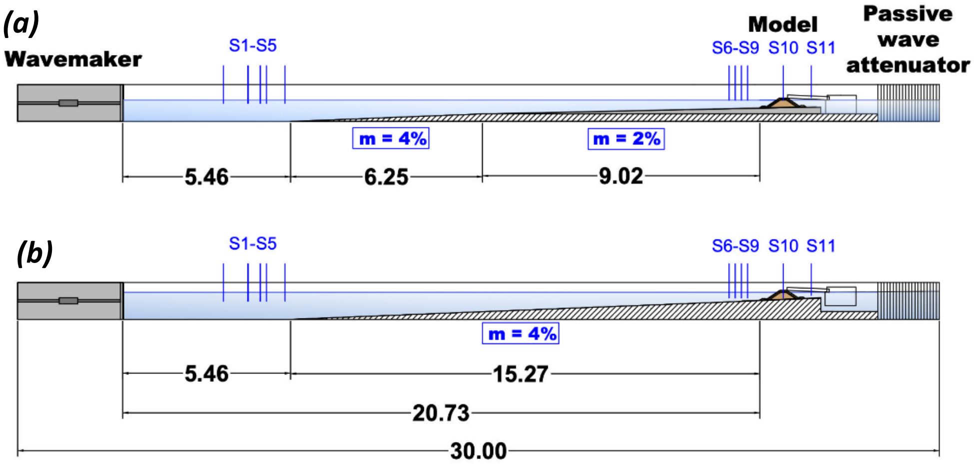

Fig. 3. 1. Longitudinal cross sections: (a) *m*=2% configuration and (b) *m*=4% configuration.

At one end of the wave flume, a piston-type wavemaker was installed while at the opposite end of the wave flume a passive wave attenuator was located to dissipate wave energy (see Figure 3.2). The physical model was built in front of the passive wave attenuator.

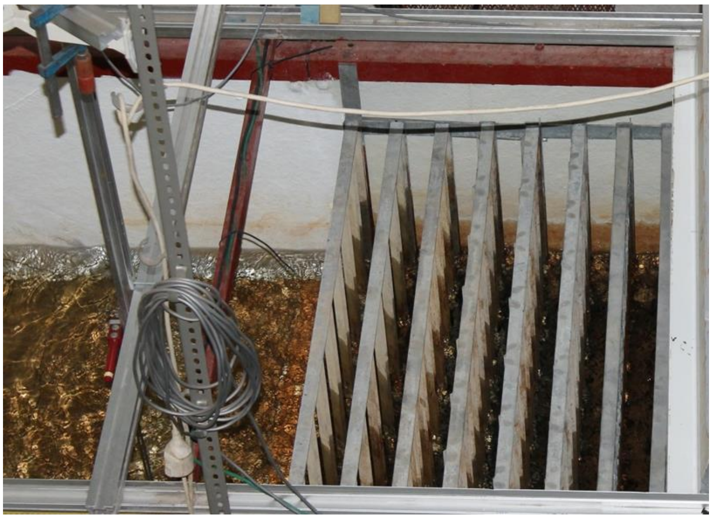

Fig. 3. 2. Passive wave attenuator.

The piston-type wavemaker (see Figure 3.3) had a maximum stroke of 0.9m and the AWACS (Active Wave Absorption System) was activated to prevent multi-reflections in the wave flume. Three wave generation types were available: (1) regular waves, (2) irregular waves (random seed number), and (3) irregular waves (given seed number).

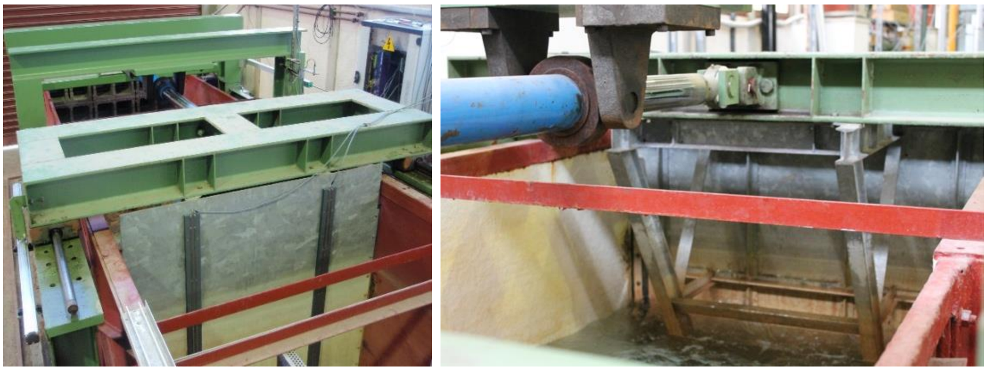

Fig. 3. 3. Piston-type wavemaker of the LPC-UPV wave flume.

The LPC-UPV wave flume has a double floor of 25cm which prevents wave breaking in the wave paddle and allows water recirculation to prevent piling-up. Piling-up is an undesirable effect which consists of an increase of the water depth in the model area due to the accumulation of water caused by slow currents and high overtopping rates. Neither piling-up (S11 in Fig. 3.1) nor low-frequency oscillations were significant during the tests conducted in this study.

3.3. Physical model

The tested cross-section depicted in Figure 3.4 corresponds to a mound breakwater (H/V=*cotα*=1.5) without crown wall and with rock toe berms.

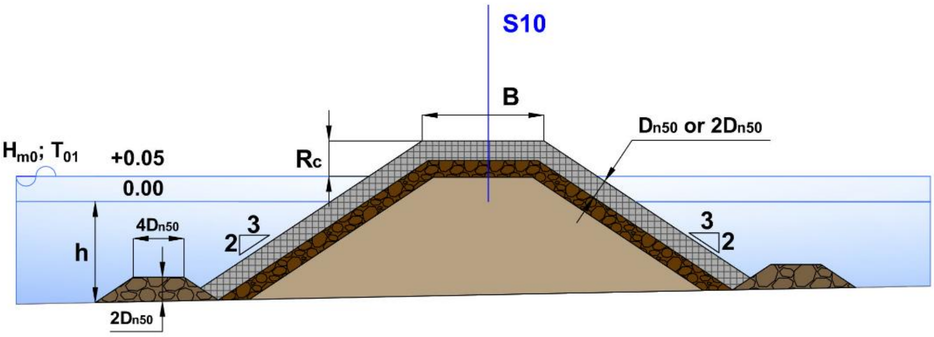

Fig. 3. 4. Cross-section tested in the LPC-UPV wave flume. Dimensions in m.

In order to ensure the toe berm hydraulic stability during the tests, different nominal median diameters or equivalent cube sizes (D_{n50}) of the stones were used as function of the bottom slope. Tests carried out on *m*=2% presented a medium-sized rock toe berm (D_{n50}=2.3cm) whereas tests conducted on *m*=4% required a larger rock toe berm (D_{n50}=3.9cm). Natural rocks with sharp edges and density *ρ*=2.6g/cm^3 were used. Figure 3.5 shows the nominal median diameter for the rocks in the toe berms.

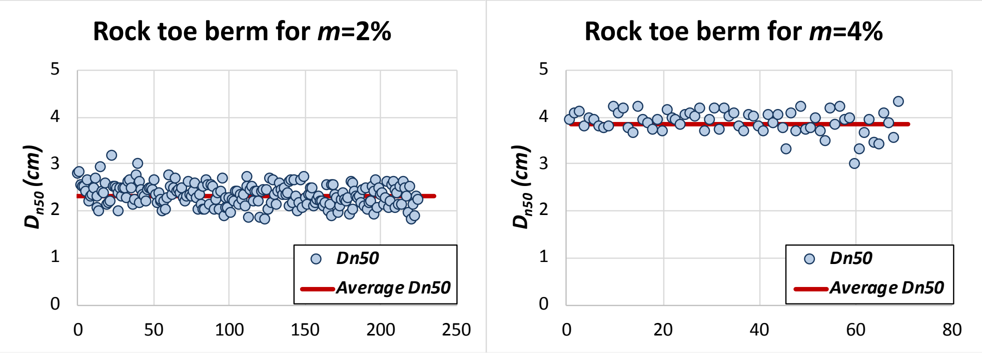

Fig. 3. 5. Nominal median diameter (D_{n50}) for rocks in the toe berms used in the experiments.

Three armor layers were considered: single-layer randomly-placed Cubipod® (Cubipod®-1L with nominal diameter or equivalent cube size D_n=3.79cm), double-layer randomly-placed cube (cube-2L with D_n=3.97cm) and double-layer randomly-placed rock (rock-2L with D_{n50}=3.11cm) armors. Figure 3.6 presents the nominal median diameter for the tested armor units while Table 3.1 summarizes the characteristics of the materials used in the tests.

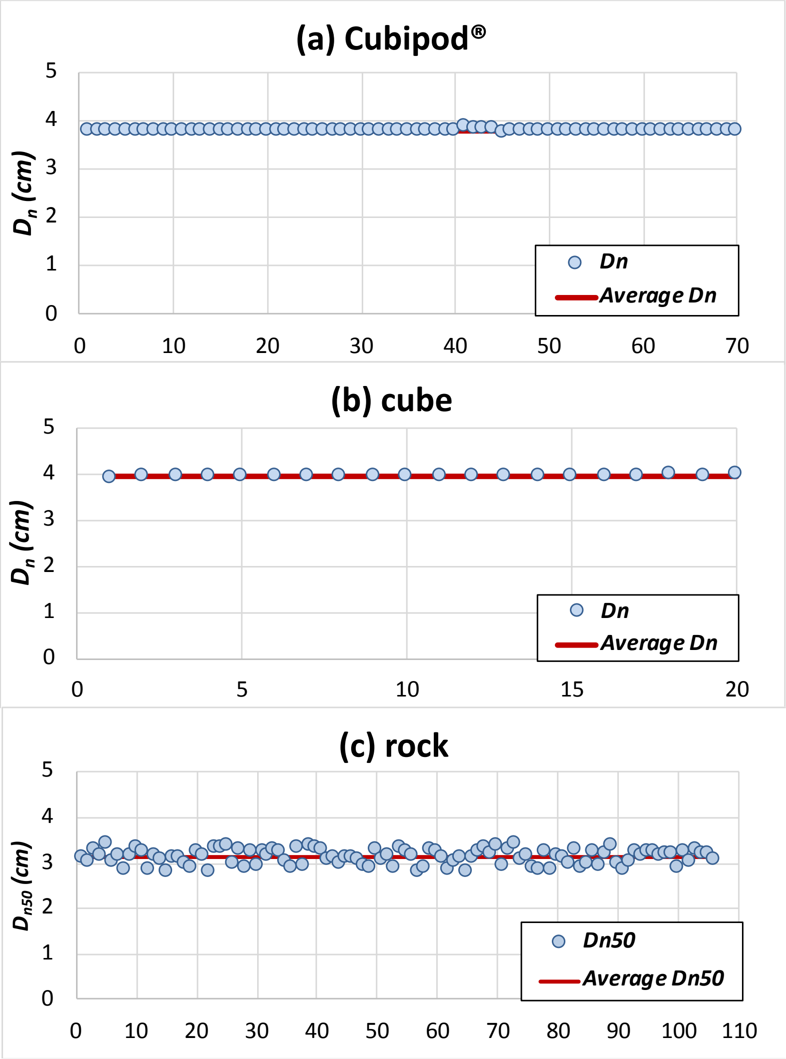

Fig. 3. 6. Nominal diameter or equivalent cube size of the tested armor layers: (a) Cubipod®, (b) cube, and (c) rock.

	Weight (g)	**Density (g/cm^3)**	**Nominal diameter (cm)**
Gravel 1 (core)	0.86	2.722	0.68
Gravel 2 (filter)	15.4	2.729	1.78
Cubipod®	121.1	2.21	3.79
cube	141.5	2.27	3.97
rock (armor)	81.1	2.66	3.11
rock (toe berm m=2%)	31.8	2.61	2.28
rock (toe berm m=4%)	153.1	2.63	3.86

Table 3. 1. Summary of the average characteristics of the materials used in the experiments.

Figure 3.7 shows the typical construction process of the tested physical models. First, the construction materials are washed and characterized; a sample splitter is used for rocks in order to obtain a representative sample. Secondly, the cross-section of the physical model is drawn on the walls of the wave flume. Thirdly, the core is built using Gravel 1. Note that the tube for wave gauge S10 needs to be inserted in the core. Fourthly, the rock toe berm and filter layer (Gravel 2) are constructed. Finally, the armor is placed. During the construction process of the different layers, a spirit level is used to check the geometry of the physical model.

Froude similarity (see Eq. 3.1) was applied with an approximate reference length scale 1:50. This implies that gravitational and inertial forces are properly represented in the model, while the others, namely surface tension or elastic forces, may be affected by scale effects.

$$\mathbb{F}r = \sqrt{\frac{u^2}{gl}} \tag{3.1}$$

where u is the velocity parameter, g is the gravitational acceleration and l is the length parameter.

Fig. 3. 7. Construction process: (a) characterization of the materials, (b) drawing the cross section, (c) construction of core, (d) construction of filter, (e) view of the model with core, filter and tube for S10 gauge, and (f) Cubipod®-1L physical model.

3.4. Tests

Random wave runs of 1,000 irregular waves were generated following a JONSWAP spectrum (γ=3.3). As previously mentioned, the AWACS wave absorption system was activated to prevent multi-reflections in the wave flume. On every foreshore configuration, two water depths at the toe of the structure (h) were tested. During the tests conducted on m=2%, h=20 and 25cm were tested with Cubipod® and rock armors while h=25 and 30cm were tested with cube armor. Those experiments conducted on m=4% were performed with h=20 and 25cm.

For each h, H_{m0} and T_p at the wave generation zone were determined in order to keep the wave steepness (s_{0p}=0.018 and 0.049) constant along the test series. For each s_{0p}, H_{m0} in the wave generation zone ($H_{m0,g}$) was increased in steps of 1cm from no damage until the armor layer failure or the breakage of waves in the wave generation zone. It shall be noted that the random seed to generate the wave runs was kept in order to repeat the same experiments with every armor layer and without structure.

Since one of the key explanatory variables of wave overtopping is the crest freeboard (R_c), an accurate measurement of R_c is required. Therefore, two corrections were applied in order to consider the water loss during the test series in the wave flume: (1) the natural evaporation and facility leakages, and (2) the overtopping volume pumped after each test accumulated during the working day. Such corrections led to a small increase in R_c on the order of 10mm for a long working day (a 3.9% variation in terms of water depth). The corrected crest freeboard was applied in the following calculations. A summary of the test characteristics is presented in Table 3.2. Note that not all the tests in Table 3.2 presented significant overtopping rates, so they could not be included in the analysis. Thus, in the following sections, the number of tests as well as the experimental ranges used in that section are indicated.

Tests without a structure were also conducted using an efficient passive wave attenuator assembly (see Figure 3.2) at the end of the wave flume in order to characterize wave conditions in the model zone, where depth-induced wave breaking takes place. In this manner, reflection caused by the model is avoided and wave energy was absorbed by the passive attenuator (reflection coefficient, $K_r=H_{m0,r}/H_{m0,i}<0.25$ in the wave generation zone, where $H_{m0,r}$ and $H_{m0,i}$ are the reflected and incident spectral significant wave height, respectively) and measured waves approximately corresponded to the incident waves.

m	Armor	B (m)	#tests	h (m)	R_c (m)	H_{m0} (m)	$T_{m-1,0}$ (s)	T_{01} (s)
2%	CC-1L	0.24	30	0.20	0.12	0.06-0.14	0.92-2.21	0.84-1.97
			30	0.25	0.07	0.06-0.16	0.97-2.24	0.89-2.02
	CB-2L	0.27	30	0.25	0.11	0.06-0.16	0.95-2.25	0.88-2.03
			24	0.30	0.06	0.06-0.18	0.92-2.05	0.85-1.88
	CE-2L	0.26	15	0.20	0.15	0.06-0.12	0.90-1.83	0.83-1.66
			15	0.25	0.10	0.06-0.13	0.91-1.87	0.84-1.71
4%	CC-1L	0.24	28	0.20	0.12	0.06-0.15	0.93-2.02	0.84-1.65
			30	0.25	0.07	0.06-0.18	0.91-2.33	0.82-2.11
	CB-2L	0.27	30	0.20	0.11	0.05-0.16	0.95-2.10	0.87-1.69
			30	0.25	0.06	0.06-0.17	0.96-2.34	0.87-2.12
	CE-2L	0.26	20	0.20	0.15	0.05-0.14	0.92-2.04	0.84-1.86
			17	0.25	0.10	0.05-0.14	0.88-2.05	0.80-1.88

Table 3. 2. Summary of characteristics of the physical tests. CC-1L, CB-2L and CE-2L represent Cubipod®-1L, cube-2L and rock-2L.

3.5. Instrumentation

Along the wave flume, 11 capacitive wave gauges arranged in two groups measured the water surface elevation. DHI capacitive wave gauges are composed by two parallel stainless-steel electrodes which measure the conductivity of the water volume located between them. This way, water surface was tracked at a frequency of 20Hz.

The first group of wave gauges (S1 to S5) was placed on the horizontal bottom near the wavemaker following *Mansard and Funke* (*1980*) recommendations (Eq. 3.2) in order to separate incident and reflected waves in the wave generation zone.

$$\begin{cases} d_1 \approx L/10 \\ L/6 < d_1 + d_2 < L/3 \\ d_1 + d_2 \neq L/5 \\ d_1 + d_2 \neq 3L/10 \end{cases} \tag{3.2}$$

where L is the wave length, d_1 is the distance between the first and second considered wave gauges and d_2 is the distance between the second and third considered wave gauges.

The second group (S6-S11) was located in the model zone: S6-S9 were placed in front of the model, S10 was installed on the model crest and S11 was located behind the model. Note that existing methods to separate incident and reflected waves are not reliable in the model zone, since depth-limited wave breaking takes place (see Figure 3.8). Wave gauges S6, S7, S8 and S9 were installed at distance of 5h, 4h, 3h and 2h from the model toe, respectively, where h is the water depth at the toe of the structure. Wave gauge S10 measured OLT in the middle of the mound breakwater crest while S11 was used to detect possible variations of the mean water level in the wave flume (piling-up).

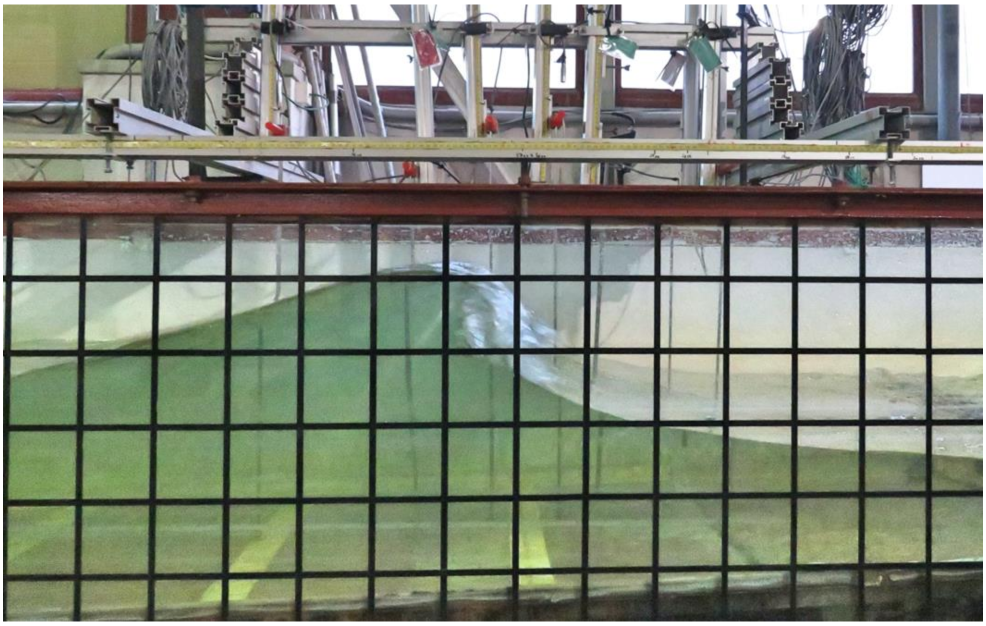

Fig. 3. 8. Wave breaking in the group of sensors located in the model zone.

As previously mentioned, wave gauge S10 was used to measure OLT at a frequency of 20Hz. Capacitive wave gauges need to be constantly submerged and their daily-calibrated reference level must be stable. Therefore, wave gauge S10 was inserted in a hollow cylinder filled up with water to ensure its submergence. On the top of the cylinder, a lid with a slot was located to prevent water loss during the tests. The cylinder was 8.5cm in diameter and 12cm in length. As shown in Figure 3.9, a clear water surface was observed during the visual inspection of the experiments. Thus, aeration was considered negligible.

Three miniature propellers were installed to measure OFV. Miniature propellers are composed by a head and tube. On the head of the propeller, a five bladed PFV helix is mounted on a stainless-steel shaft which is protected by a cage of 11.6mm in diameter. Such head is joined with the tube inside which there is a gold wire. When the propeller rotates due to the movement of a conductive liquid, the impedance between the wire and the tube changes. In this manner, movement is registered as pulses at a frequency of 20Hz.Those pulses are translated into velocity using calibrated relationships provided by the manufacturer. OFV was measured in three points along the model crest: (1) on the seaward edge of the crest, (2) at the middle of the crest, and (3) at the rear edge of the crest. Note that the propellers are located in a different longitudinal axis to avoid interferences between them. Figure 3.10 shows miniature propellers installed on the breakwater crest.

Fig. 3. 9. Overtopping layer thickness (OLT) measurement: (a) wave gauge S10, and (b) visual inspection of OLT.

Fig. 3. 10. Overtopping flow velocity (OFV) measurement using miniature propellers.

Overtopping discharges were recorded using a weighting system located behind the model in every test. Such weighting system consisted of a chute in the rear side line of the crest which led overtopping water to a collection tank over a load cell. A pump was also installed to drain the water after every test. The inner width of the chute was 5cm and its inner bottom face was aligned with the model crest to prevent too much overtopping loss. The load cell used in the tests measured at a frequency 5Hz and had a precision of 0.01kg. A continuous record of the accumulated overtopping volume was obtained (see Figure 3.11) after each test.

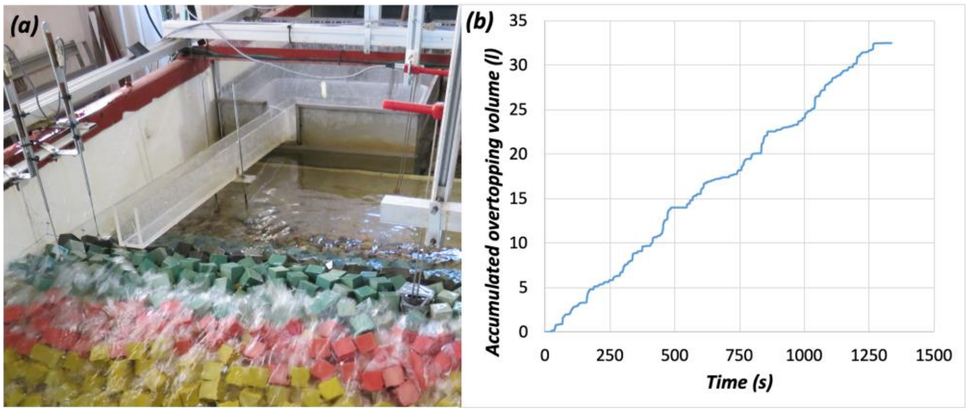

Fig. 3. 11. Overtopping measurement: (a) weighting system for overtopping collection, and (b) record of accumulated overtopping volume.

Three cameras were used to study the armor damage in the frontal slope, crest and rear side of the armor with the Virtual Net Method (*Gómez-Martín and Medina*, *2014*) as reported in *Argente et al.* (*2018*). Tests were also recorded using AXIS P1355 Network Cameras at a framerate FPS=5 in order to control the experiments and check possible outliers as well as to observe wave breaking and armor damage evolution during the tests (see Figure 3.12).

Fig. 3. 12. Video cameras recording the physical tests.

3.6. Data analysis

3.6.1. Goodness-of-fit metrics

In order to assess the goodness-of-fit in this study, the correlation coefficient (*r*), the coefficient of determination (R^2) and the relative bias (*bias*) are used. $0 \leq r \leq 1$ assesses the correlation, $0 \leq R^2 \leq 1$ estimates the proportion of the variance explained by the model and $-1 \leq bias \leq 1$ provides a dimensionless measure of the bias. Thus, the higher the *r*, the higher the R^2 and the closer the *bias* to 0, the better.

$$r = \frac{\sum_{i=1}^{N_o}(o_i - \bar{o})(e_i - \bar{e})}{\sqrt{\sum_{i=1}^{N_o}(o_i - \bar{o})^2 \sum_{i=1}^{N_o}(e_i - \bar{e})^2}} \tag{3.3}$$

$$R^2 = 1 - \frac{\frac{1}{N_o}\sum_{i=1}^{N_o}(o_i - e_i)^2}{\frac{1}{N_o}\sum_{i=1}^{N_o}(o_i - \bar{o})^2} \tag{3.4}$$

$$bias = \frac{1}{N_o}\sum_{i=1}^{N_o}\frac{(e_i - o_i)}{|o_i|} \tag{3.5}$$

where N_o is the number of observations, o_i and e_i are the observed and estimated values, and $\bar{o}$ is the average observed value.

3.6.2. Wave analysis

In this study, incident and reflected waves in the model zone cannot be accurately separated using methods in the literature, since tests were performed under depth-limited breaking wave conditions. Thus, the methodology applied in *Herrera et al.* (*2017*) was used. *Herrera et al.* (*2017*) proposed two methods for estimating H_{m0} under depth limited breaking wave conditions: (1) using the total wave records at the toe of the model (where wave breaking occurs) together with the reflection coefficients in the wave generation zone, and (2) using the SwanOne model (*Verhagen et al., 2008*). Such methodologies were validated by *Herrera et al.* (*2017*) using measurements in tests without a structure and are valid when reflection is relevant, but not dominant (reflection coefficient, $K_r=H_{m0,r}/H_{m0,i}<0.4$, where $H_{m0,r}$ and $H_{m0,i}$ are the reflected and incident spectral significant wave height, respectively). Reflection coefficients measured in the wave generation zone as function of the wave number ($k=2\pi/L_{m0}$, where L_{m0} is the mean deep waters wavelength calculated with T_{01}) in this study are presented in Figure 3.13.

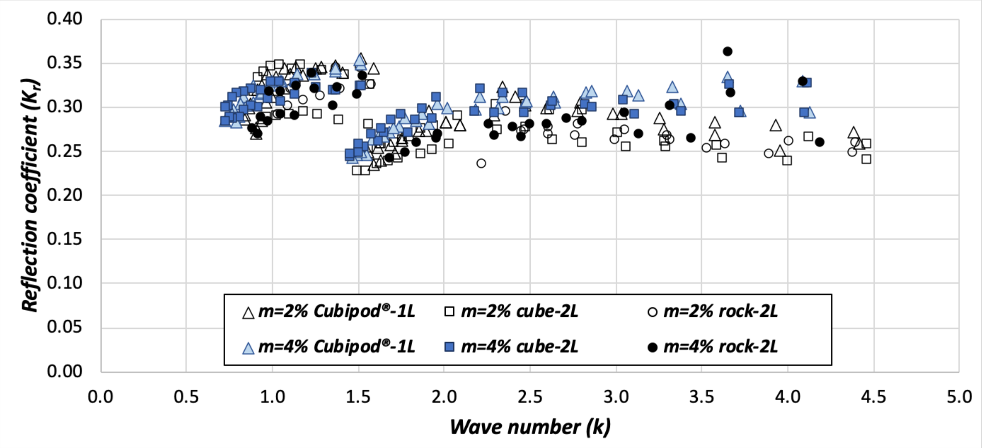

Fig. 3. 13. Reflection coefficients in the wave generation zone (K_r) as function of the wave number (k).

Therefore, the following steps were performed to analyze wave characteristics in this thesis. Firstly, incident and reflected waves were separated in the wave generation zone applying the LASA-V method (*Figueres and Medina*, *2005*) with wave gauges S1-S5. After that, H_{m0} was determined using both the reflection coefficient in the wave generation zone and the SwanOne model. A validation with tests without a structure was performed similar to *Herrera et al.* (*2017*). Finally, methodology with best results is selected for further analysis.

3.6.2.1 LASA-V. Wave separation in the wave generation zone.

The LASA-V method was applied to determine incident and reflected waves in the wave generation zone since it is valid for separating nonstationary and highly nonlinear irregular waves. Figure 3.14 shows the user interface of the LASA-V software.

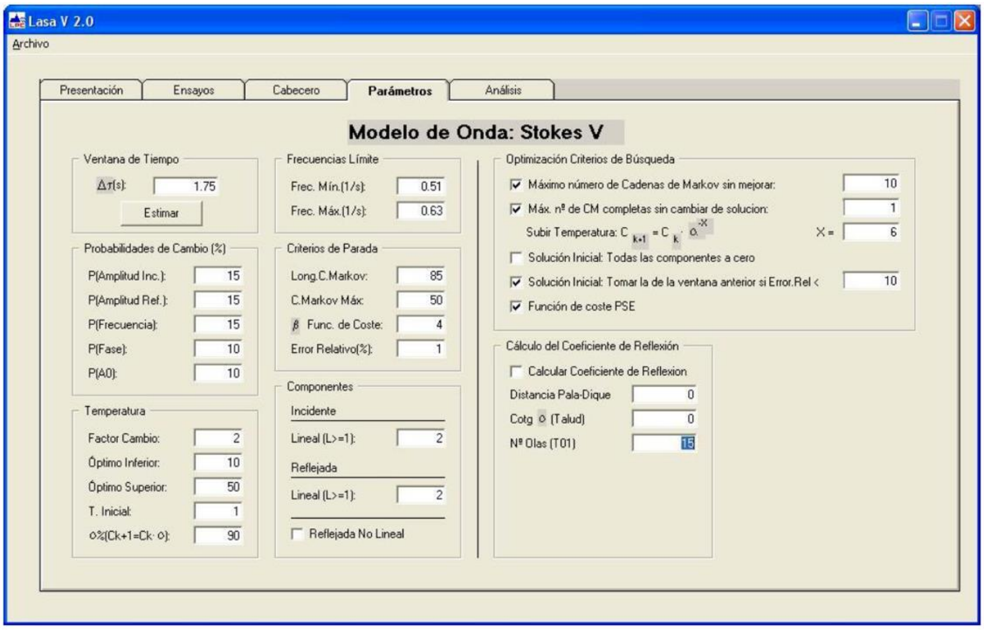

Modelo de Onda: Stokes V

Ventana de Tiempo
Δτ(s): 1.75

Probabilidades de Cambio (%)
P(Amplitud Inc.): 15
P(Amplitud Ref.): 15
P(Frecuencia): 15
P(Fase): 10
P(A0): 10

Temperatura
Factor Cambio: 2
Óptimo Inferior: 10
Óptimo Superior: 50
T. Inicial: 1
α%(Ck+1=Ck· α): 90

Frecuencias Límite
Frec. Mín.(1/s): 0.51
Frec. Máx.(1/s): 0.63

Criterios de Parada
Long.C.Markov: 85
C.Markov Máx: 50
β Func. de Coste: 4
Error Relativo(%): 1

Componentes
Incidente
Lineal (L>=1): 2
Reflejada
Lineal (L>=1): 2
☐ Reflejada No Lineal

Optimización Criterios de Búsqueda
☑ Máximo número de Cadenas de Markov sin mejorar: 10
☑ Máx. nº de CM completas sin cambiar de solucion: 1
Subir Temperatura: $C_{k+1} = C_k \cdot \alpha^{-X}$ X = 6
☐ Solución Inicial: Todas las componentes a cero
☑ Solución Inicial: Tomar la de la ventana anterior si Error.Rel < 10
☑ Función de coste PSE

Cálculo del Coeficiente de Reflexión
☐ Calcular Coeficiente de Reflexion
Distancia Pala-Dique 0
Cotg α (Talud) 0
Nº Olas (T01) 15

Fig. 3. 14. LASA-V software (*Figueres and Medina, 2005*).

The LASA (Local Approximation using Simulated Annealing) method analyzes the incident and reflected waves in the time domain using triangular windows with linear superposition. Note that other methods in the literature, such as the 2-point model by *Goda and Suzuki* (*1976*), conduct the analysis in the frequency domain without respecting the principle of casualty. The LASA method performs the following steps:

- Eliminate noise
- Define windows for estimating the central points
- Determine the local approach model

The empirical Stokes-V model, valid for highly asymmetric waves, is fitted for each window by minimizing the Mean Squared Error (see Eq. 3.6).

$$MSE = \frac{1}{N_o}\sum_{i=1}^{N_o}(o_i - e_i)^2 \tag{3.6}$$

Simulated annealing is used as optimization technique in order to reach the optimum model in an efficient manner and without stagnating in a local minimum. Therefore, a cost function and a mechanism of generation is required in the LASA method. The cost function assesses the validity of each possible solution while the generation mechanism provides a new possible solution to evaluate. The mentioned algorithm is developed in series, moving to a new solution or keeping the previous solution found, until the “crystallized” process converges to a global optimum.

3.6.2.2 SwanOne simulations

SwanOne is a free wave propagation model for 1D bathymetry (wave flume) developed by Delft University of Technology. The user interface of the SwanOne model is shown in Figure 3.15. The following physical phenomena are modeled by SwanOne:

- Wave propagation in time and space, including shoaling, refraction caused by depth and currents, and frequency shifting caused by non-stationary depth and currents.
- Nonlinear wave-wave interactions
- Wave generation by wind
- Depth-induced wave breaking
- Blocking of waves due to currents

Methods to separate incident and reflected waves are not reliable for breaking waves. In addition, measurements by wave gauges in breaking conditions are not accurate due to turbulence and air entrainment. Thus, simulations with the SwanOne model were performed to determine the incident wave characteristics in the model zone after the physical tests. Incident wave conditions in the wave generation zone were estimated for each physical test using the LASA-V method (Section 3.6.2.1). Both the incident wave conditions and the bottom slope profile were provided to the SwanOne model as input parameters. Based on these inputs, the model fitted a JONSWAP spectrum (γ=3.3) and propagated such spectrum along the virtual wave flume. The Composite Weibull Distribution (*Battjes and Groenendijk*, *2000*) was applied to describe the wave height distribution in shallow foreshores. This way, the SwanOne model provided the following outputs all along the wave flume: H_{m0}, $H_{1/10}$, $H_{2\%}$, T_p, T_{01} and $T_{m-1,0}$.

It should be noted that the SwanOne model considers frequencies between 0.03-0.8Hz since it is prepared for prototype scale wave conditions. Consequently, a reference scale 1/30 was assumed in this thesis.

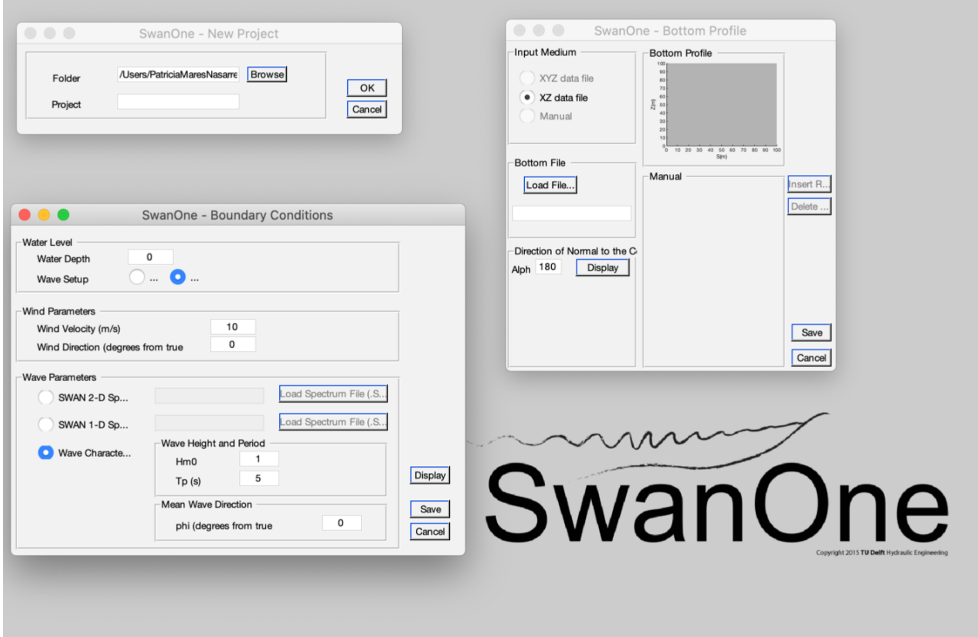

Folder /Users/PatriciaMaresNasarre
Project

Water Depth 0
Wave Setup ○ ... ● ...
Wind Velocity (m/s) 10
Wind Direction (degrees from true 0
○ SWAN 2-D Sp...
○ SWAN 1-D Sp...
● Wave Characte...
Hm0 1
Tp (s) 5
phi (degrees from true 0

○ XYZ data file
● XZ data file
○ Manual
Direction of Normal to the C
Alph 180

Fig. 3. 15. The SwanOne model interface.

3.6.2.3 Validation with tests without a structure

As mentioned in Section 3.4, tests without a structure were performed with the same wave generation conditions as the tests with the breakwater model. Wave energy was absorbed by an efficient passive wave attenuator at the opposite side of the flume (see Figures 3.1 and 3.2). Thus, measured waves approximately corresponded to the incident waves.

Tests without a structure were used to validate the two methodologies suggested by *Herrera et al.* (*2017*) to estimate the incident H_{m0} under depth-limited breaking wave conditions. The first methodology proposed by *Herrera et al.* (*2017*) consisted of assuming the reflection coefficient (K_r) in the wave generation zone as constant all along the wave flume and calculating the incident wave height in the model zone by applying this reflection coefficient to the total register measured in the model zone. A comparison between the measured H_{m0} ($H_{m0,m}$) in the tests without a structure and H_{m0} calculated using the measurements at the toe of the structure in the tests with model and K_r in the wave generation zone is presented in Figure 3.16. Good results were obtained (R^2=0.884), similar to those results reported in *Herrera et al.* (*2017*). Thus, H_{m0} estimated using K_r in the wave generation zone is a reasonable estimator of the actual H_{m0} under depth-limited breaking wave conditions when reflection is relatively small (K_r<0.4).

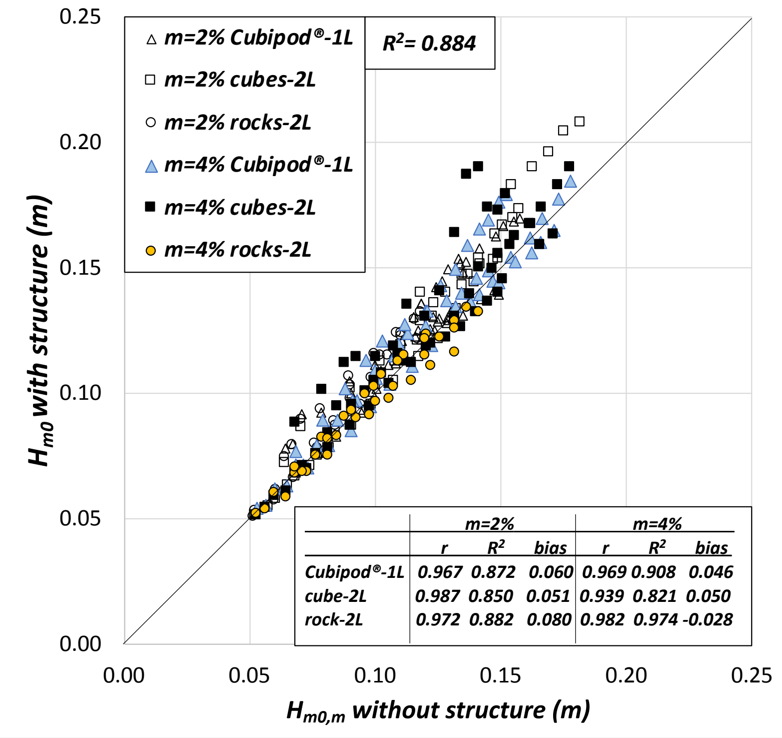

	m=2%			m=4%		
	r	R^2	bias	r	R^2	bias
Cubipod®-1L	0.967	0.872	0.060	0.969	0.908	0.046
cube-2L	0.987	0.850	0.051	0.939	0.821	0.050
rock-2L	0.972	0.882	0.080	0.982	0.974	-0.028

Fig. 3. 16. Comparison between the measured H_{m0} ($H_{m0,m}$) in the tests without a structure and H_{m0} calculated using measurements in tests with structure assuming K_r in the wave generation zone at the toe of the structure.

As exposed in the previous section, numerical simulations were conducted with the SwanOne model. The incident wave conditions in the wave generation zone and the bottom slope profile were given to the SwanOne model as input parameters. This way, wave characteristics were calculated all along the wave flume. A comparison between the measured H_{m0} ($H_{m0,m}$) in the tests without a structure and H_{m0} calculated using the SwanOne model in the wave generation zone and in the model zone is presented in Figures 3.17 and 3.18, respectively. Comparison in the wave generation zone represents the capability of the model to fit the JONSWAP spectrum in the wave generation zone to the input incident wave conditions. On the other hand, comparison in the model zone represents the capability of the model to reproduce the wave conditions when depth-induced wave breaking takes place. Although very good results were obtained (R^2>0.966), it should be noted that decreasing values of *bias* were obtained for H_{m0} in the model zone for increasing values of h: *bias* = 0.057 for h=0.20cm, *bias* = 0.021 for h=0.25cm and *bias* = -0.018 for h=0.30cm.

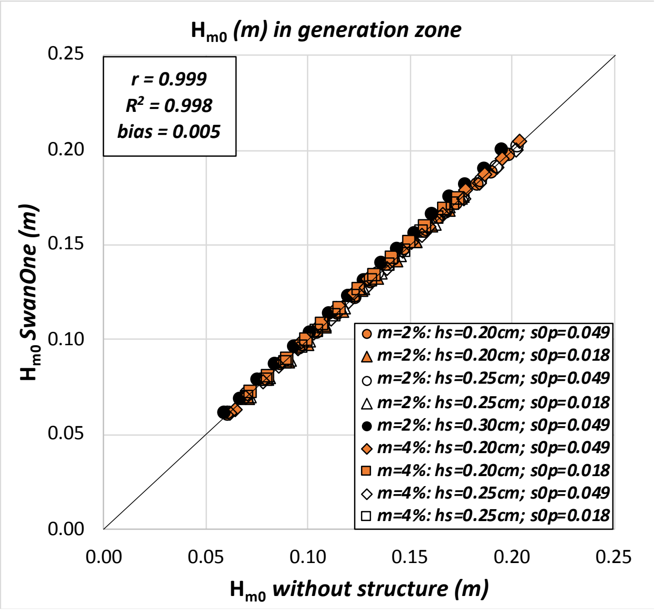

Fig. 3. 17. Comparison between the measured H_{m0} in tests without a structure and estimations given by the SwanOne model in the wave generation zone.

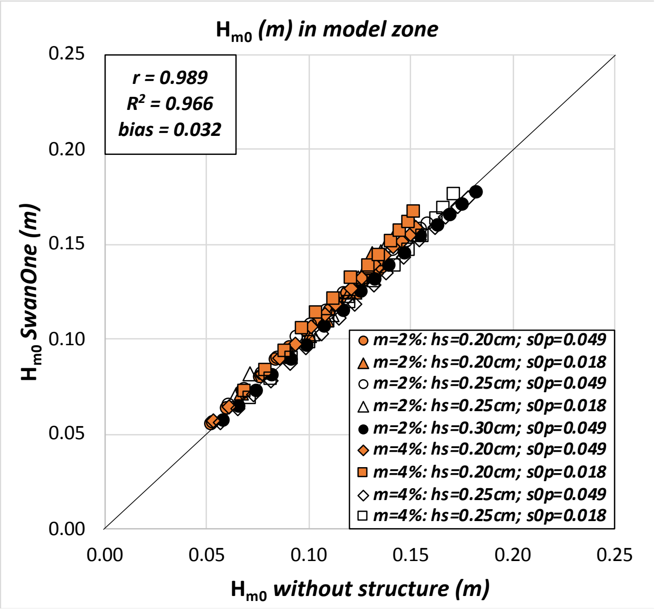

Fig. 3. 18. Comparison between the measured H_{m0} in tests without a structure and estimations given by the SwanOne model in the model zone.

The SwanOne model does not only provide H_{m0}; $T_{m-1,0}$ and T_{01} given by the SwanOne model were also compared to those measured in the tests without a structure in the wave generation zone and in the model zone (see Figures 3.19 to 3.22). As shown in Figures 3.19 and 3.20, reasonable results were obtained for $T_{m-1,0}$ in the wave generation zone (R^2=0.882), whereas poor results were obtained in the model zone (R^2=0.415). Note that the negative *bias* obtained in the model zone is approximately twice the *bias* obtained in the wave generation zone. Thus, the SwanOne model underestimates $T_{m-1,0}$ in the model zone. Regarding T_{01}, good results were obtained in the wave generation zone (R^2=0.954), while poor results were obtained in the model zone (R^2=0.245). Unlike $T_{m-1,0}$, the SwanOne model clearly overestimated T_{01} in the model zone (*bias*=0.059).

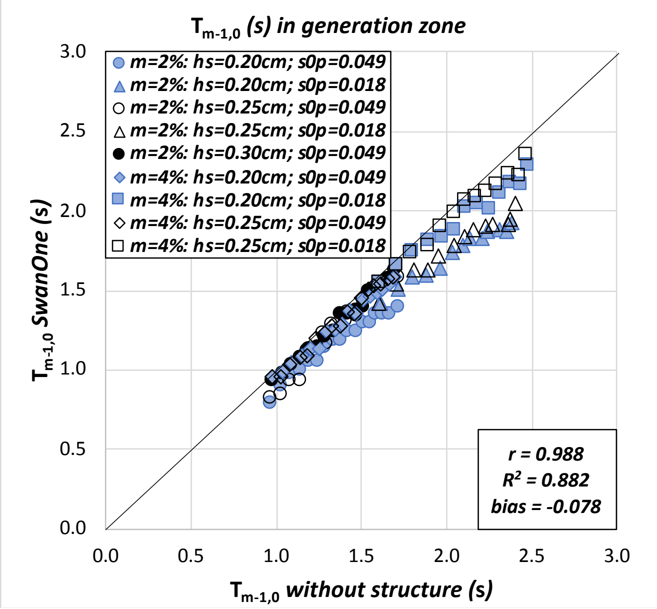

Fig. 3. 19. Comparison between the measured $T_{m-1,0}$ in tests without a structure and estimations given by the SwanOne model in the wave generation zone.

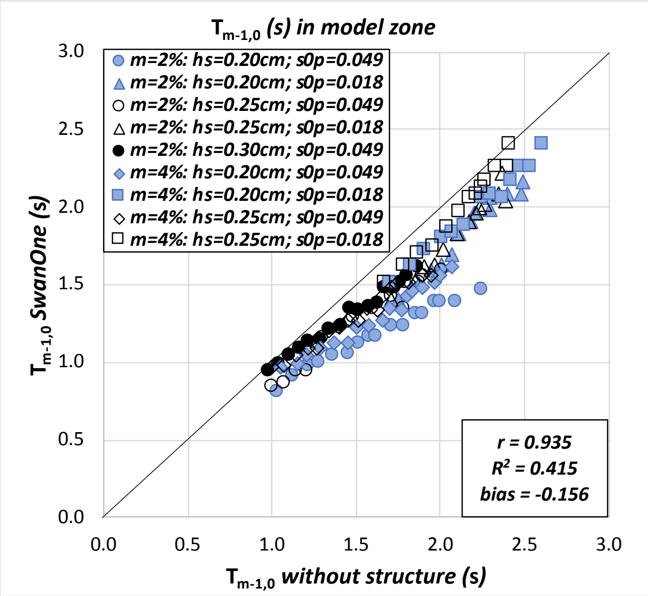

Fig. 3. 20. Comparison between the measured $T_{m-1,0}$ in tests without a structure and estimations given by the SwanOne model in the model zone.

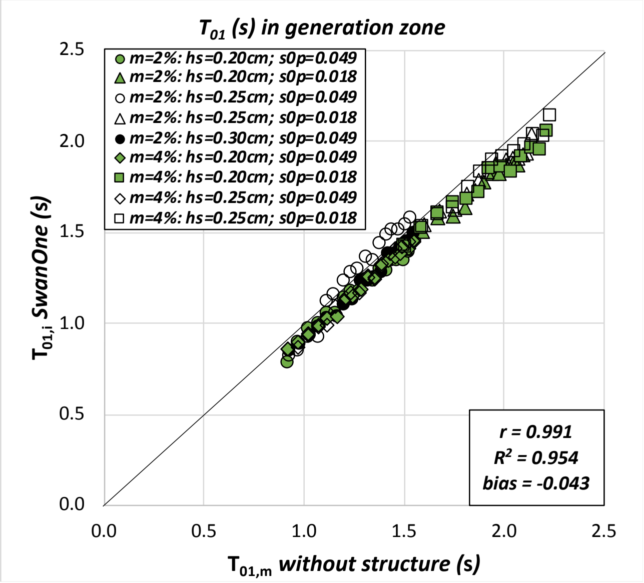

Fig. 3. 21. Comparison between the measured T_{01} in tests without a structure and estimations given by the SwanOne model in the wave generation zone.

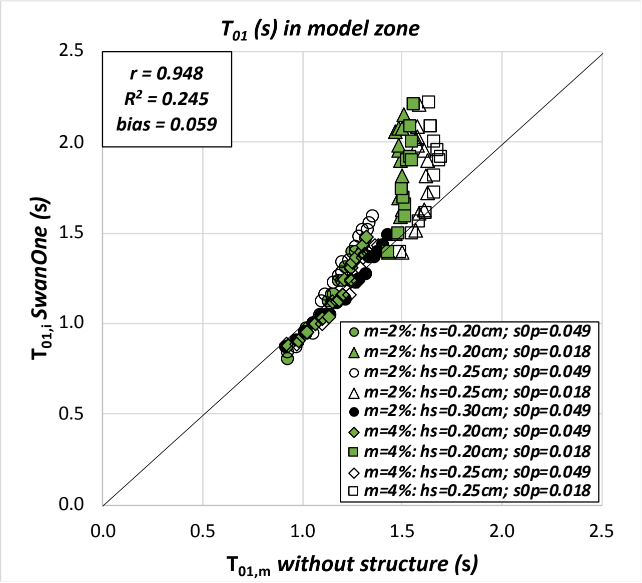

Fig. 3. 22. Comparison between the measured T_{01} in tests without a structure and estimations given by the SwanOne model in the model zone.

During the design phase of a mound breakwater, the design wave conditions (H_{m0}, $T_{m-1,0}$, T_{01}) at the location where the breakwater will be built need to be estimated. In addition, best results when estimating H_{m0} were obtained with the numerical simulations performed with the SwanOne model. Thus, H_{m0}, $T_{m-1,0}$ and T_{01} provided by the SwanOne model were used in this thesis.

3.6.3. Identification of individual wave overtopping volumes

Overtopping in physical tests is usually recorded using (1) wave gauges which measure the variations in the water level inside a collection tank, or (2) load cells located below the collection tank in order to measure the variations in weight. Wave gauges may be affected by the oscillations of the water level during the overtopping events whereas load cells may be affected by an added apparent mass caused by large overtopping events. Both measurement techniques provide a continuous accumulated overtopping volume register which is used to identify individual wave overtopping volumes. Different methods were proposed in the literature to this end, since an accurate identification of the individual wave overtopping volumes is key to avoid errors in the subsequent analyses. However, some authors (e.g. *Victor et al.*, *2012*; *Zanuttigh et al.*, *2013*) did not describe any explicit methodology to identify individual wave overtopping volumes.

Besley (*1999*) proposed a methodology based on two sensors to identify individual wave overtopping volumes. First, a wave gauge was located on the structure crest in order to identify the individual wave overtopping events. Second, if load cells were used, the individual wave overtopping volume was determined as the difference between two successive overtopping events. A time delay was accounted between the overtopping event detected by the wave gauge and the overtopping volume measured by the load cell. If water level gauges were used, the difference between the water levels before and after the overtopping event were considered to calculate te overtopping volume. In order to determine the reference baseline before the overtopping event, *Besley* (*1999*) recommended taking the average of the water level measured during the last few seconds before the arrival of the overtopping event.

Nørgaard et al. (*2014*) proposed using a water level gauge together with an algorithm to identify rapid changes in the water volume in a small collection tank. Results provided by the algorithm were compared with the time series of the accumulated overtopping volume after each test.

Molines et al. (*2019*) proposed a 10-step method to identify individual wave overtopping volumes, using load cells, which considered the water falling after a large overtopping event and the noise caused by dynamic loads. The ten steps of this methodology are described below.

1. **Step 1**. The weight record measured by the load cell, W (kg), is transformed into volume, V_{o1} (l).
2. **Step 2**. V_{o2} (l) is obtained by considering the pump operations; a non-decreasing record is obtained, $V_{o2}(t_{i-1}) \leq V_{o2}(t_i)$. The inner width of the chute (C=0.05m) is also accounted as $V_{o3}(t_i)= V_{o2}(t_i)/C$.
3. **Step 3**. The corrected accumulated volume register V_{o3} is derived according to Eq. 3.5. Overtopping water is discharged during the crest phase of the wave, which approximately corresponds to $T_{01}/2$. Thus, Eq. 3.7 is evaluated in intervals of $T_{01}/2$. The obtained derivative volume register, q_1 (l/s/m), presents local peaks close to the beginning of possible overtopping events.

$$q_1(t_i) = \frac{V_{o3}\left(t_i + \frac{T_{01}}{2}\right) - V_{o3}(t_i)}{\frac{T_{01}}{2}} \quad i = 1, \dots, L_1 \tag{3.7a}$$

$$L_1 = \max(i) - \mathrm{round}(5T_{01}/2) \tag{3.7b}$$

4. **Step 4**. The triangular moving average function given by Eq. 3.8 is applied to the derivative volume register q_1. Eq. 3.8 eliminates frequency noise higher than 3Hz caused by the dynamic loads of the large overtopping events falling into the collection tank. The length of the register of q_1 is denoted as L_2.

$$q_2(t_j) = 0.25q_1(t_{j-1}) + 0.5q_1(t_j) + 0.25q_1(t_{j+1}) \quad j = 2, \dots, L_2 - 1 \tag{3.8}$$

5. **Step 5**. The individual wave overtopping events are calculated using V_{o3} (Step 2) with Eq. 3.8. The number of local peaks in q_2 obtained in Step 4 is denoted

as N_{peak} while the time when q_2 presents a local peak and a possible overtopping event (Step 4) is represented as t_k.

$$V_1(t_k) = V_{o3}(t_{k+1}) - V_{o3}(t_k) \quad k = 1, \dots, N_{peak} \tag{3.9}$$

6. **Step 6**. The small values of V_1 (l/m) obtained in Step 5 do not always correspond to an actual small overtopping event, but to water constantly falling into the collection tank after a large overtopping event. Thus, a low threshold V_T (l/m)=0.25 is compared to the individual wave overtopping volumes (Step 5) to determine if they are real. If $V_1(t_k)>V_T$, $V_1(t_k)$ is considered a real overtopping event. On the other hand, if $V_1(t_k)<V_T$, $V_1(t_k)$ may correspond to a small overtopping or to water falling into the collection tank after another overtopping event. Note that the low threshold V_T (l/m)=0.25 would correspond to 625l/m ($0.25\times(50^3/50)$) assuming a reference scale 1/50. This value is close to the tolerability limit for pedestrian on seawall given by *EurOtop* (*2018*) (see Table 2.4).
7. **Step 7**. Values $V_1(t_k)<V_T$ are analyzed considering two scenarios: (1) $q_2(t_k)= q_2(t_{k+1})= q_2(t_{k+2})=\dots$ with an increasing time delay between the local peaks ($t_{k+1}-t_k \leq t_{k+2}-t_{k+1}$), and (2) small overtopping events with a local peak $q_2(t_k)$ surrounded by smaller local peaks. The first scenario is caused by water constantly falling into the collection tank after a large overtopping event. Thus, the time delay can be used to identify the starting time of the actual overtopping event, t_k(s). If a decreasing time delay is observed, the first time position of the sequence may correspond to an actual overtopping event. Regarding the second scenario, a small real overtopping event is considered when the local peak $q_2(t_k)$ is higher than the surrounding peaks, $q_2(t_k)> q_2(t_{k-1})$ and $q_2(t_k)> q_2(t_{k+1})$.
8. **Step 8**. Individual wave overtopping volumes, V_2(l/m), are again calculated using Eq. 3.9. The time positions and the number of real overtopping events obtained after Steps 6 and 7 are denoted as t_m(s) and N_{peak2}.

$$V_2(t_m) = V_{o3}(t_{m+1}) - V_{o3}(t_m) \quad m = 1, \dots, N_{peak2} \tag{3.10}$$

9. **Step 9**. The time delay between the overtopping events obtained after Step 7 is analyzed. Note that in Step 7 small overtopping events are added to those detected in Step 6. To this end, V_2(l/m) are sorted in descending order as $V_2(t_1)=\max(V_2(t_m);\ m=1 \text{ to } N_{peak2})$. Starting with $V_2(t_1)$, if another overtopping event is closer than $0.8T_{01}$, $|t_m-t_1|<0.8T_{01}$, the overtopping event corresponding to the time position t_m(s) is removed, since it is not possible to have two waves closer than T_{01}.
10. **Step 10**. The actual individual wave overtopping volumes are finally calculated according to Eq. 3.10. The time positions and the number of overtopping events obtained after Step 9 are denoted as t_n(s) and N_{ow}.

$$V(t_n) = V_{o3}(t_{n+1}) - V_{o3}(t_n) \quad n = 1, \dots, N_{ow} \tag{3.11}$$

In this thesis, the 10-step method given by *Molines et al.* (*2019*) was applied. $R^2 \approx 1$ when comparing the total measured V_{o3}(l/m) and the total V_{o3}(l/m) obtained after the reconstruction. A comparison between the measured V_{o3}(l/m) and the reconstructed V_{o3}(l/m) using the 10-step method for Test#17 is displayed in Figure 3.23.

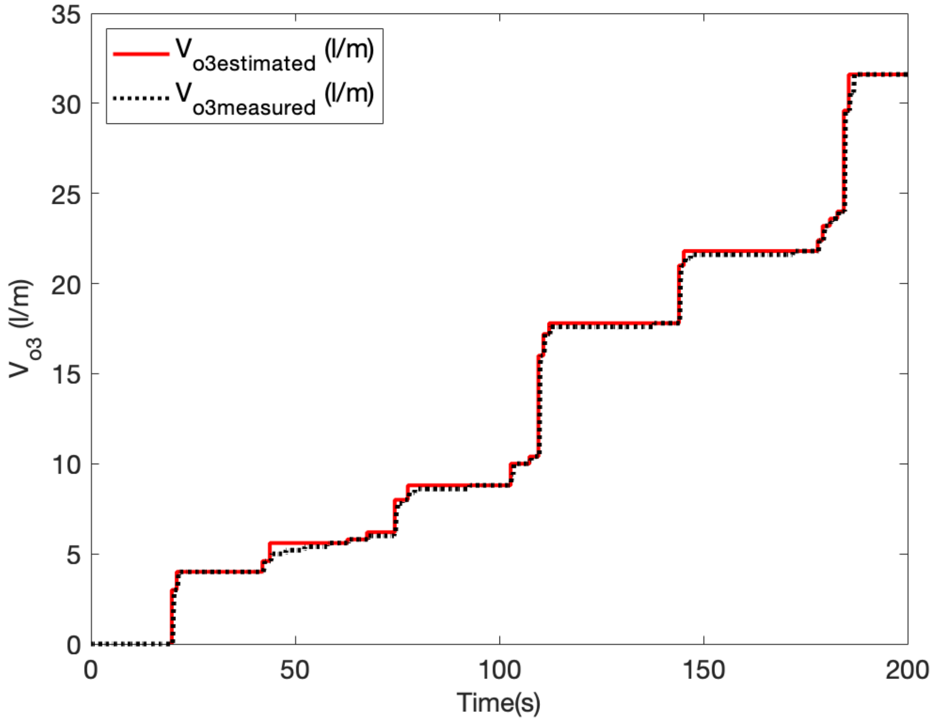

Fig. 3. 23. Comparison between the measured V_{o3}(l/m) and estimated V_{o3}(l/m) reconstructed with the 10-step method by *Molines et al.* (*2019*) for Test#17.

3.6.4. *Analysis of the identified individual wave overtopping volumes*

As shown in Section 2.4, the 2-parameter Weibull distribution is usually used to describe individual wave overtopping volumes. In order to fit such distribution, the Weibull plot is generated by taking logarithms on both sides of Eq. 2.11 twice:

$$\ln(-\ln[1-F(V)]) = b\left(\ln\left[\frac{V}{\overline{V}}\right] - \ln A\right) \tag{3.12}$$

Therefore, the Weibull plot can be represented with $\ln[V/\overline{V}]$ in the x-axis and $\ln(-\ln[1-F(V)])$ in the y-axis. Using the Weibull plot, the scale (A) and shape (b) factors can be estimated as the intercept and the slope of the fitted line.

In the literature, the shape factor (b) of the 2-parameter Weibull distribution is usually determined as the slope of the straight line in the Weibull plot while the scale factor (A) is calculated using Eq. 2.12. However, significant differences between the measured and estimated A given by Eq. 2.12 were observed in the literature (*Pan et al., 2016; Gallach, 2018*; *Molines et al., 2019*).

Distribution functions of individual wave overtopping volumes are usually fitted using the highest individual wave overtopping volumes, for instance, 10%, 30% or 50% of the highest volumes. Nevertheless, the low individual wave overtopping events are significant to estimate A when using Eq. 2.12. N_{ow} and the mean wave overtopping volume, $\bar{V} = V_{total}/N_{ow}$, affect the estimation of A but they are not easy to measure in laboratory tests. N_{ow} and $\bar{V}$ are subjected to a high uncertainty due to the low individual wave overtopping volumes, which are not relevant for most practical applications. As *Molines et al.* (*2019*) pointed out, both b and A need to be calibrated in order to provide an accurate description of the distribution of the highest individual wave overtopping events; in this case, Eq. 2.12 is not valid and the mean value of the distribution (μ_m) may be different from the measured $\bar{V}$.

If both b and A are calibrated, their value will depend on the number of data used to fit the Weibull distribution. As shown in the literature review, the number of data selected to fit such distribution depends on the author (highest 10%, 30%, 50%, etc.). In the present thesis, it is used the criterion given by *Molines et al.* (*2019*) who recommended using 100% of the individual wave overtopping volumes together with a quadratic utility function. In this manner, low individual wave overtopping volumes were included in the analysis while the relative relevance of the data was also considered.

3.6.4.1 Quadratic utility function

Utility functions, *f(u)*, are useful for considering the relative relevance of each datum in a dataset; the weights applied to the observed data to calibrate a mathematical model depend on *f(u)*. If the utility function concept is applied to studies in the literature, only step utility functions were used (see Figure 3.24) considering different cut-off thresholds $0 \leq V_p \leq V_{max}$, being p the percentage of volumes over the threshold, $V_i > V_p$. However, the criteria to determine the cut-off threshold is not clear nor easy to justify. Thus, a continuous and monotonically increasing utility function such as the quadratic utility function was proposed by *Molines et al.* (*2019*). This way, the higher V_i present the higher relevance in this analysis and the inconsistency in the step utility function is avoided.

The 2-parameter Weibull distribution was fitted using the weighted least squared methods using a 2-parameter Weibull plot; the Weibull distribution was represented by a straight line. Regarding the implementation of the quadratic utility function, each V_i was represented by a number of virtual points proportional to its weight.

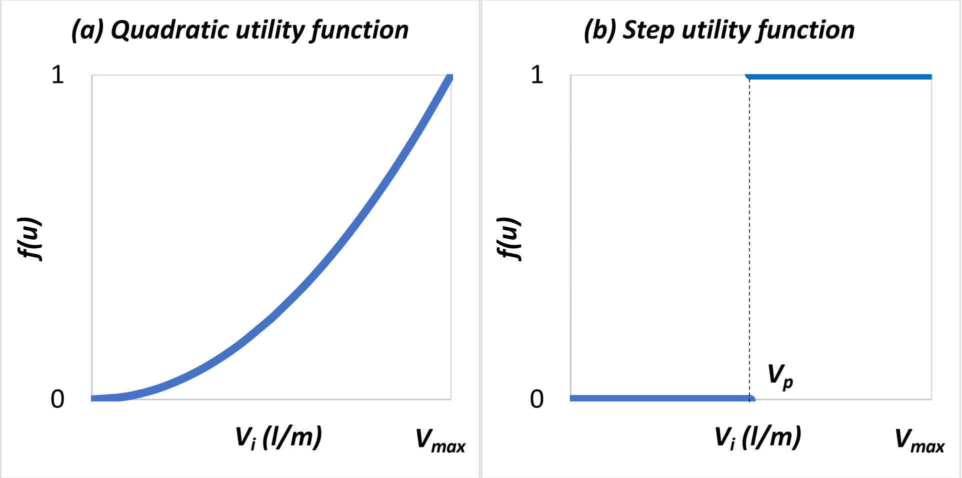

Fig. 3. 24. Utility function: (a) quadratic function, and (b) step function.

3.6.5. Overtopping layer thickness and overtopping flow velocity analysis

As mentioned in Section 3.5, OLT and OFV were measured on the model crest. Wave gauge S10 recorded OLT in the middle of the breakwater crest whereas three miniature propellers measured OFV along the breakwater crest. The performance of the wave gauge S10 was remarkable when measuring OLT; low noise as well as a low variation in the reference level was observed. In this study, the maximum OLT during each overtopping event was considered as illustrated in Figure 3.25.

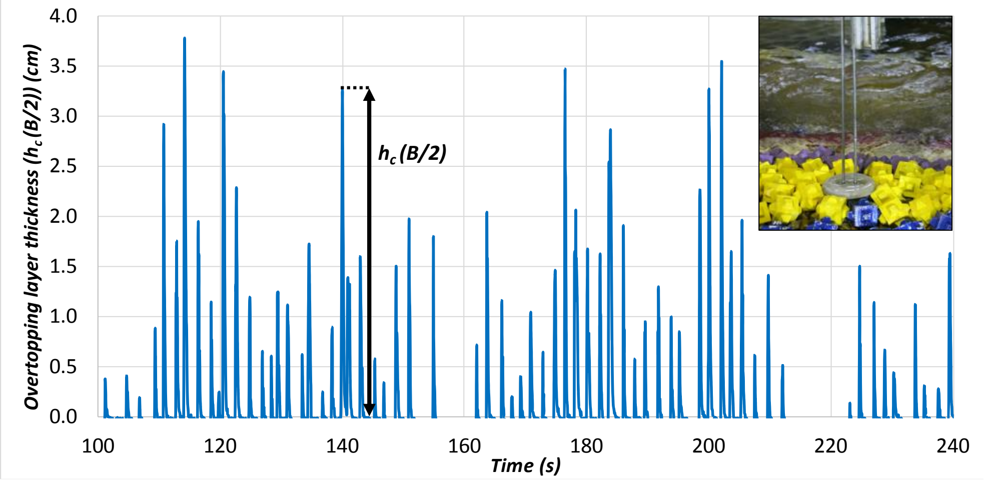

Fig. 3. 25. Example of the record of the OLT in the middle of the breakwater crest (Test#90).

Based on the miniature propellers measurements, OFV at the middle of the breakwater crest was further studied in this thesis. Miniature propellers are able to measure velocities between $0.15<u(\mathrm{m/s})<3.00$. Therefore, velocities under 0.15m/s are disregarded. Similar to the OLT, the maximum values of the OFV during each overtopping event were considered, as shown in Figure 3.26. The aforementioned operational threshold is also represented.

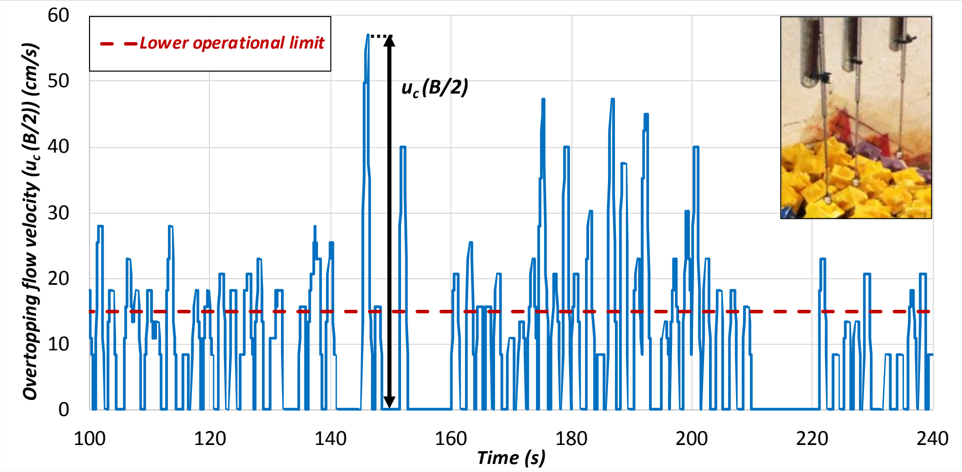

Fig. 3. 26. Example of the record of the OFV in the middle of the breakwater crest (Test#90).

3.6.6. Statistical methodology

One of the objectives of this thesis was to determine whether the bottom slope had a significant effect on the overtopping flow on mound breakwater crests. Since overtopping is a highly non-linear phenomenon, distributions different from Gaussian distribution were expected and non-parametric statistics needed to be applied.

In order to determine if the data followed a Gaussian distribution three criteria were applied: (1) asymmetry and kurtosis criteria, (2) Kolmogorov-Smirnov test (*Kolmogorov, 1933*; *Smirnov, 1939; Massey, 1952*; *Miller, 1956*) and (3) Shapiro-Wilk test (*Shapiro and Wilk, 1965*). When asymmetry and kurtosis were out of [-2, 2], data could not be considered Gaussian distributed. If asymmetry and kurtosis were within [-2, 2], Kolmogorov-Smirnov and Shapiro-Wilk tests were applied to verify the distribution shape.

Once the data was characterized as non-Gaussian distributed, significant differences between the mean values of the data were assessed using Mood test (*Mood, 1954*) or Kruskal-Wallis test (*Kruskal and Wallis, 1952*). Kruskal-Wallis test was applied when the hypothesis of same variance and same distribution of both datasets could be assumed. Significant differences between the variances were assessed using the Levene's test (*Levene, 1960*) while significant differences between the data distributions were assessed using Kolmogorov-Smirnov test and Mann-Whitney test (*Mann and Whitney*, *1947*). Kolmogorov-Smirnov test is based on the maximum distance between the cumulated distributions of both datasets while Mann-Whitney test uses the rank positions.

“Some people love the ocean. Some people fear it. I love it, hate it, fear it, respect it, cherish it, loathe it, and frequently curse it. It brings out the best in me and sometimes the worst.”

Rosalind “Roz” Savage

4

Individual wave overtopping volumes under depth-limited breaking wave conditions

Port of Palamós (Spain), September 2020

4.1. Introduction

The maximum individual wave overtopping volume (V_{max}) is widely recommended in the literature for designing mound breakwater crest elevation (*De Rouck et al., 2009*; *EurOtop, 2018*). Most of the studies focused on its estimation were conducted in non-breaking conditions, as exposed in Section 2.4. In this chapter, the performance of these methods is assessed using the experimental database in depth-limited breaking wave conditions described in Section 3. After that, a new method valid for depth-limited breaking waves is derived; the influence of the bottom slope on V_{max} is also examined. During the design phase of a mound breakwater, the mean wave overtopping discharge (q) needs to be estimated in order to calculate V_{max}, since no measurements are available. Thus, the proposed method to estimate V_{max} is finally evaluated using estimated q. Most results in this chapter were recently published in *Mares-Nasarre et al.* (*2020b*).

4.2. Estimation of the number of overtopping events, N_{ow}, and the maximum individual wave overtopping volume, V_{max}, using methods given in the literature

In this section, the performance of the methods to estimate V_{max} on mound breakwaters reviewed in Section 2.4 were evaluated. First, the mean wave overtopping volume, $\bar{V} = qT_{01}N_{ow}/N_w$, is required to calculate N_{ow}. Therefore, q needs to be estimated using methods given in the literature when direct observations are not available. As exposed in Section 2.4, estimators for q were recommended by the authors of the methods to estimate N_{ow} and V_{max}. Here, the goodness of fit of such estimators of q was assessed using the experimental database described in Section 3; 219 out of the total 299 physical tests were used ($N_{ow} \geq 2$; $Q^* = q/(gH_{m0}T_{01}) \geq 7 \cdot 10^{-7}$), since not all the physical tests performed in this study shown overtopping. A comparison between the measured and the estimated Q^* using the methods recommended in Section 2.4 is presented in Figure 4.1.

Besley (*1999*) suggested Eq. 2.27 together with γ_f=0.50 to estimate q for rock-2L. Since this author did not propose γ_f for Cubipod®-1L and cube-2L, it was only applied to data for rock-2L. Eq. 2.32 recommended by *EurOtop (2018*) was applied with γ_f=0.49, 0.47 and 0.40 to calculate q for Cubipod®-1L, cube-2L and rock-2L, respectively. CLASH NN was used with γ_f=0.48, 0.53 and 0.49 given by *Molines and Medina* (*2015*) for Cubipod®-1L, cube-2L and rock-2L, respectively. This predictor was applied on 189 physical tests within the range of application of CLASH NN.

It should be noted that quantitative goodness-of-fit metrics given in Figure 4.1 were calculated for lnQ^*. Methods proposed by *Besley* (*1999*) and *EurOtop (2018*) provided poor results (R^2<0). On the other hand, satisfactory results (R^2=0.636) were obtained with the predictor CLASH NN recommended by *Nørgaard et al.* (*2014*) and *Molines et al.* (*2019*).

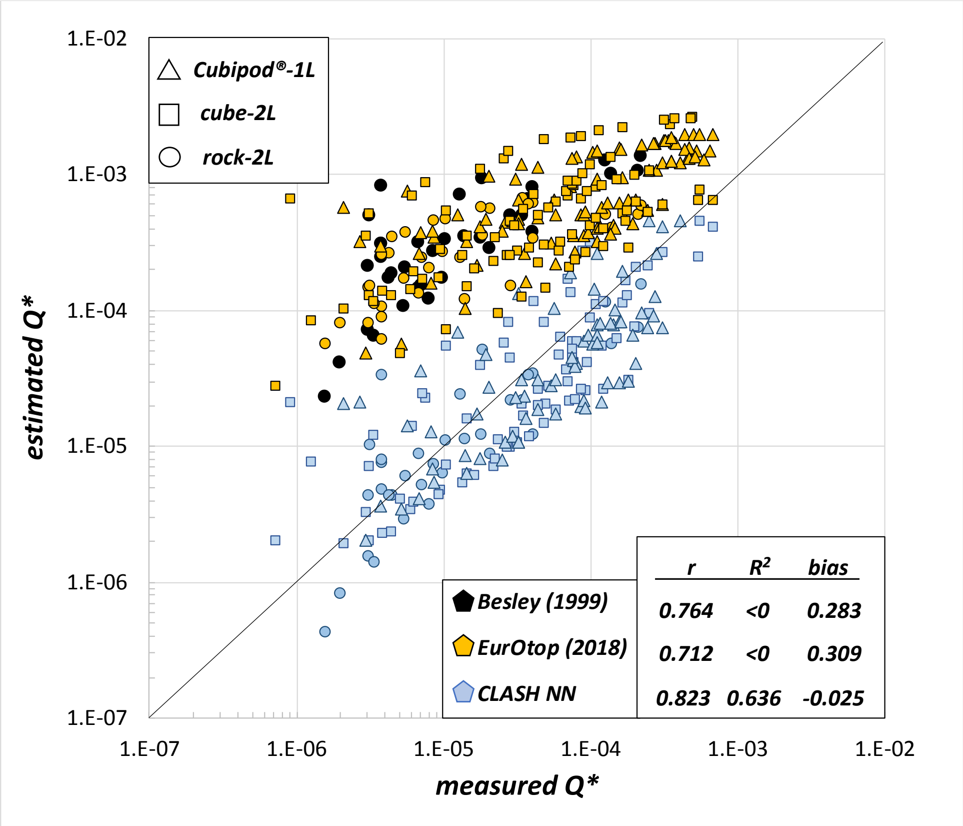

Fig. 4. 1. Comparison between measured and estimated $Q^*=q/(gH_{m0}T_{01})$ with methods in the literature.

4.2.1. Estimation of N_{ow} with existing methods given in the literature

Formulas to estimate N_{ow} presented in Section 2.4.2 are assessed in this section. A comparison between the observed and the estimated N_{ow} with methods in the literature valid for mound breakwaters is shown in Figure 4.2.

All formulas were applied no matter their application range. In order to simulate the design phase conditions, q estimated with the predictors suggested by the authors were applied. The predictor for N_{ow} given in Eq. 2.25 proposed by *Besley* (*1999*) was applied with γ_f=0.50 for rock-2L. Since this author did not propose γ_f for Cubipod®-1L and cube-2L, it was only applied to data for rock-2L. K_1=50.8 was used in Eq. 2.25 for $cot\alpha$=1.5, obtained from the interpolation between the values given for $cot\alpha$=1 and $cot\alpha$=2. Eq. 2.29 suggested by *EurOtop (2018*) was used together with γ_f=0.49, 0.47 and 0.40 to calculate q for Cubipod®-1L, cube-2L and rock-2L, respectively. CLASH NN, which was recommended by *Nørgaard et al.* (*2014*) and *Molines et al.* (*2019)*, was used to predict q with γ_f=0.48, 0.53 and 0.49 given by *Molines and Medina* (*2015*) for Cubipod®-1L, cube-2L and rock-2L, respectively.

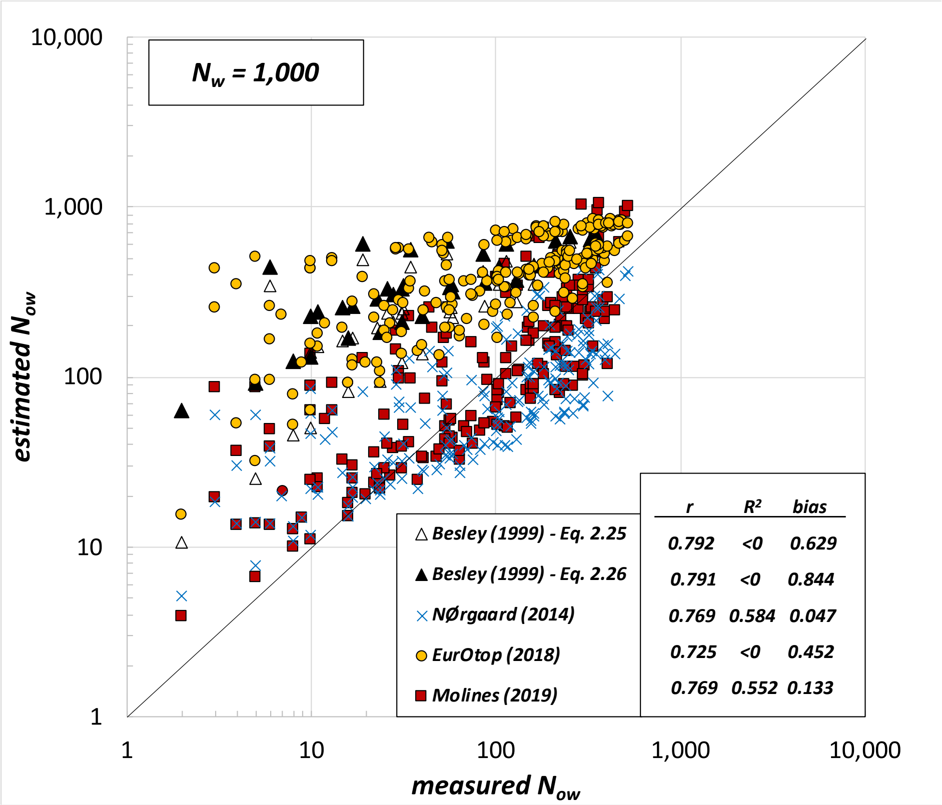

Fig. 4. 2. Comparison between measured and estimated N_{ow} with methods in the literature.

The quantitative goodness-of-fit metrics shown in Figure 4.2 are given for lnN_{ow}. The best agreement with experimental data was obtained with the methods by *Nørgaard et al.* (*2014*) and *Molines et al.* (*2019)* (0.55<R^2<0.59). In contrast, formulas proposed by *Besley* (*1999*) and *EurOtop (2018*) overpredicted the values of N_{ow}; poor results were obtained (R^2<0). Note that all the methods compared in Fig. 4.2 overpredicted the values of N_{ow}<100. Since none of the existing predictors of N_{ow} in the literature satisfactorily described N_{ow} within the experimental ranges of the present study, a new estimator for N_{ow} is developed in Section 4.3.

4.2.2. Estimation of V_{max} with existing methods given in the literature

In Section 2.4.1, formulas in the literature to estimate the shape factor *b* and the dimensionless scale factor *A* of the 2-parameter Weibull distribution were presented. In this section, the performance of the formulas valid for mound breakwaters are assessed when estimating V_{max}.

In this assessment, *q* and N_{ow} were estimated with the methods recommended by the authors (see Table 2.7). Note that such predictors of *q* and N_{ow} were previously evaluated in this section. The dimensionless scale factor *A* was estimated using Eq. 2.12 in the methods given by *Nørgaard et al.* (*2014*) and *EurOtop (2018*) while Eq. 2.17 was used in the method by *Molines et al.* (*2019)*. V_{max} was calculated using Eq. 2.23. A comparison between the observed and the estimated V_{max} with methods in the literature valid for mound breakwaters is shown in Figure 4.3.

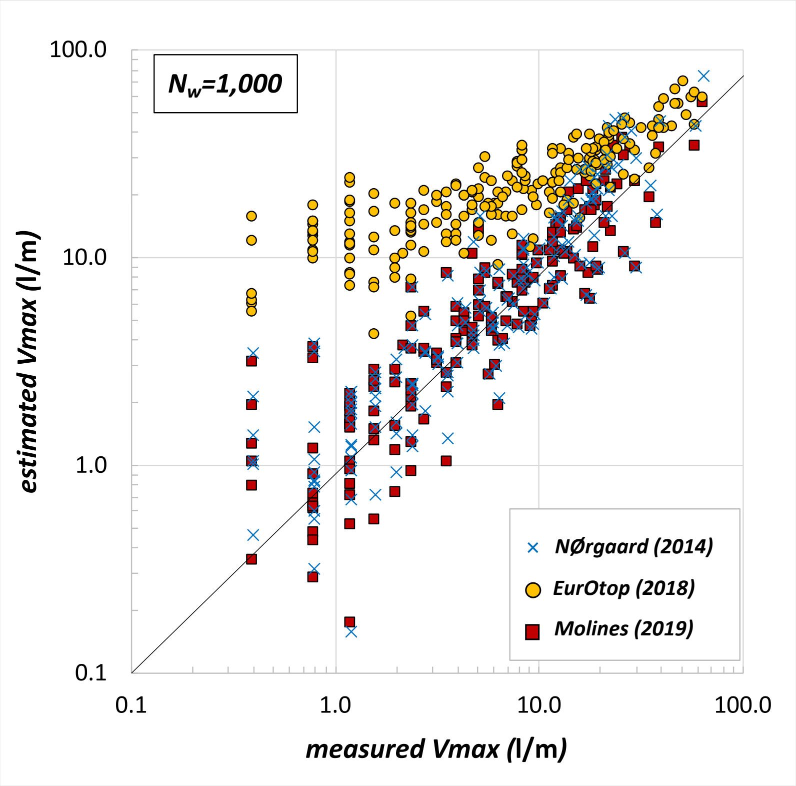

Fig. 4. 3. Comparison between measured and estimated V_{max} with methods in the literature.

Molines et al. (*2019)* proposed the dimensionless V_{max}, $V_{max}{}^{*}= V_{max}/(gH_{m0}T_{01}{}^{2})$, to better characterize the goodness of fit of the existing methods to estimate V_{max}. A comparison between the observed and the estimated V_{max}^* with methods in the literature valid for mound breakwaters is shown in Figure 4.4.

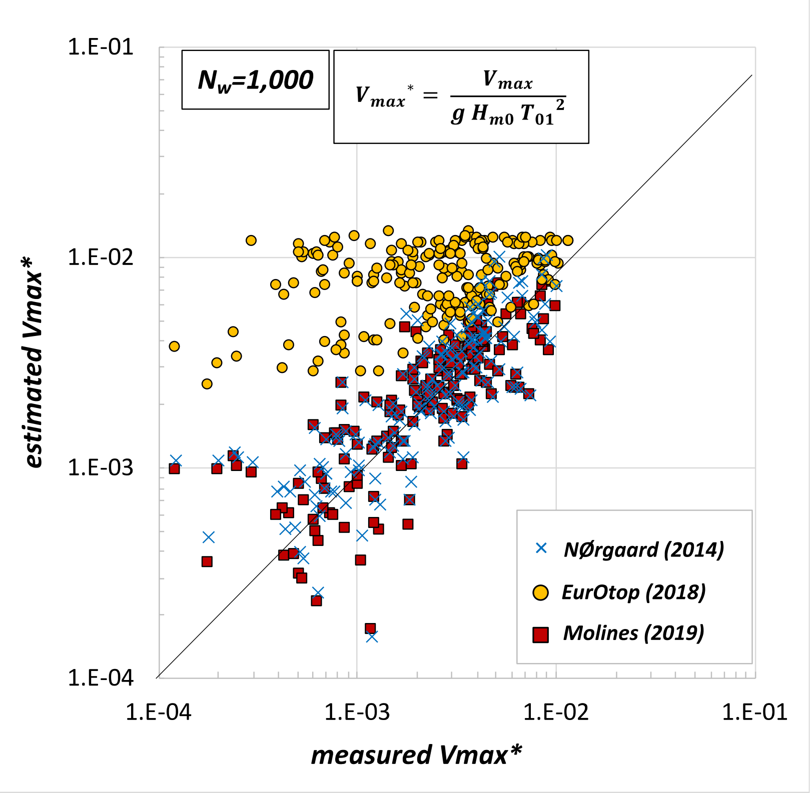

Fig. 4. 4. Comparison between measured and estimated V_{max}^* with methods in the literature.

The observed V_{max}^* in this study agreed well with the predictions given by the estimators in *Nørgaard et al.* (*2014*) and *Molines et al.* (*2019*). However, higher scatter was observed for V_{max}<5l/m and $V_{max}^*<2\cdot10^{-3}$. It should be noted that both *Nørgaard et al.* (*2014*) and *Molines et al.* (*2019)* tested mound breakwaters with crown wall and that *Molines et al.* (*2019)* conducted tests in non-breaking wave conditions. Hence, the presence of a crown wall and depth-limited wave breaking may not have a significant effect on V_{max}^*. The quantitative goodness-of-fit metrics for lnV_{max} and lnV_{max}^* as well as the number of variables and parameters of the methods shown in Figures 4.3 and 4.4 are presented in Table 4.1.

Author	#parameters	#variables	Metric	V_{max}(l/m)	V_{max}^*(-)
Nørgaard et al. (2014)	13	3	*r*	0.888	0.790
			R^2	0.784	0.618
			bias	0.148	-0.002
EurOtop (2018)	12	4	*r*	0.830	0.382
			R^2	<0	<0
			bias	2.222	0.173
Molines et al. (2019)	7	1	*r*	0.891	0.798
			R^2	0.788	0.630
			bias	-0.023	-0.017

Table 4. 1. Goodness-of-fit metrics for V_{max}^* estimated with methods in the literature.

4.3. A new method to estimate the number of overtopping events, N_{ow}, on mound breakwaters

In Section 4.2.1, methods in the literature to estimate N_{ow} on mound breakwaters were assessed using the experimental data in this study. None of the existing predictors of N_{ow} in the literature satisfactorily described N_{ow}, since all the compared methods overpredicted the values of $N_{ow}<100$. Therefore, a new estimator for N_{ow} is developed in this section; effect of the bottom slope on N_{ow} is also discussed.

4.3.1. Influence of the bottom slope on N_{ow}

In Section 3, two bottom slope configurations of the wave flume were described (m=2% and 4%). No significant differences were observed between both configurations in the scatter plot (see Figure 4.5). In addition, a statistical analysis was performed to guarantee that N_{ow} was equally distributed for different bottom slopes. Since data was not Gaussian distributed, Mann-Whitney tests was conducted (see Section 3.6.5). The null hypothesis corresponded to N_{ow} not being influenced by the bottom slope. Based on 103 tests with m=2% and 116 tests with m=4%, the null hypothesis was not rejected with a significance level of α_s=0.10. Thus, the bottom slope did not show a significant influence on N_{ow} in this study.

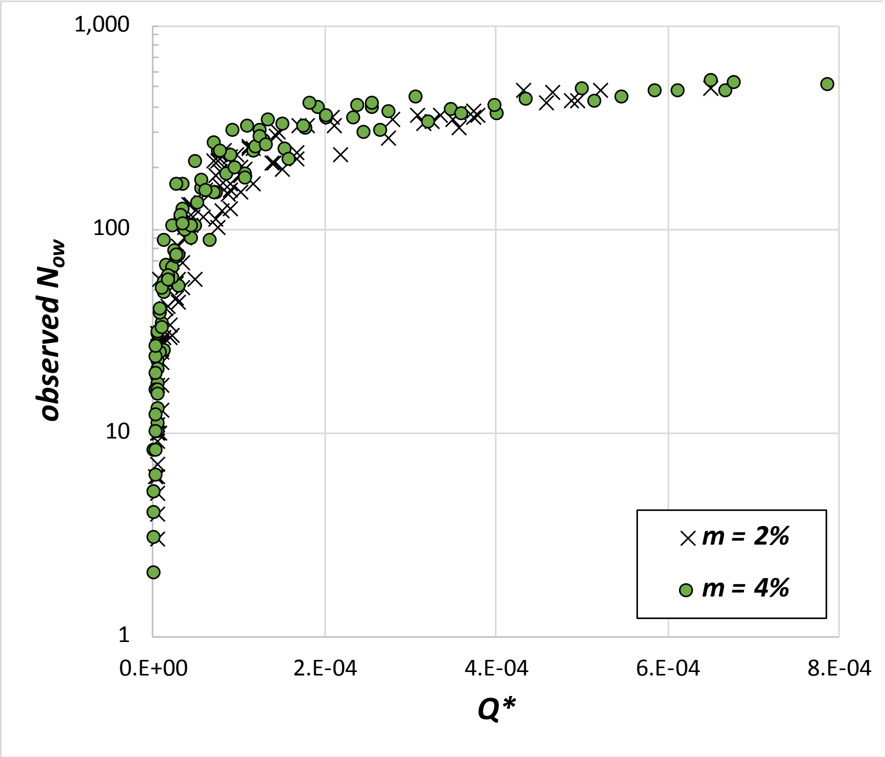

Fig. 4. 5. N_{ow} **as function of** $Q^*=q/(gH_{m0}T_{01})$**.**

4.3.2. A new method to estimate N_{ow}

As shown in Section 4.2.1, methods given in *Nørgaard et al.* (*2014*) and *Molines et al.* (*2019)* provided reasonable results within their range of application. However, they do not properly estimate P_{ow} for extreme values of Q^*. When Q^* is very low ($Q^*\rightarrow 0$), P_{ow} should also become very small ($P_{ow}\rightarrow 0$) whereas when Q^* is very large ($Q^*\rightarrow\infty$), P_{ow} should tend to 1. Thus, an exponential model may describe better P_{ow} than a power law of Q^*, since it considers the behavior of P_{ow} for extreme values of Q^*.

In the present study, a clear correlation between P_{ow} and Q^* was observed, as previously reported in the literature (*Besley*, *1999*; *Nørgaard et al.*, *2014; Molines et al.*, *2019*). Hence, an exponential function of Q^* was proposed as

$$P_{ow} = \frac{N_{ow}}{N_w} = \exp\left(\frac{-G_1}{Q^{*G_2}}\right) \tag{4.1}$$

where G_1 and G_2 are empirical coefficients to be calibrated. G_1 and G_2 were calibrated using 219 tests by minimizing the *MSE* (see Eq. 3.5) for lnN_{ow}. As mentioned in Section

1.1, the optimum point to determine wave characteristics becomes relevant when in depth-limited breaking wave conditions (*Herrera et al., 2017*). Hence, G_1 and G_2 were calibrated using $Q^*=q/(gH_{m0}T_{01})$ calculated with wave characteristics (H_{m0} and T_{01}) estimated at several distances from the model toe. H_{m0} and T_{01} were determined at distances from the structure toe of x=0, h, 2h, 3h, 4h, 5h and 6h. No significant differences were observed in the fitted values of G_1 and G_2; G_1=-0.1 and G_2=0.3 were obtained for H_{m0} and T_{01} estimated at distances between 0 to 6h from the model toe. Therefore, H_{m0} and T_{01} calculated at a distance of 3h from the structure toe were used in the presented study, following recommendations by *Herrera et al. (2017)*. No distinction was considered between the three armor units, following the results in *Bruce et al.* (*2009*).

A comparison between the observed and the estimated N_{ow} using Eq. 4.1 together with G_1=-0.1 and G_2=0.3 is shown in Figure 4.6. 90% error band as well as the goodness-of-fit metrics for lnN_{ow} are also presented in Figure 4.6. Good agreement is observed (R^2=0.919).

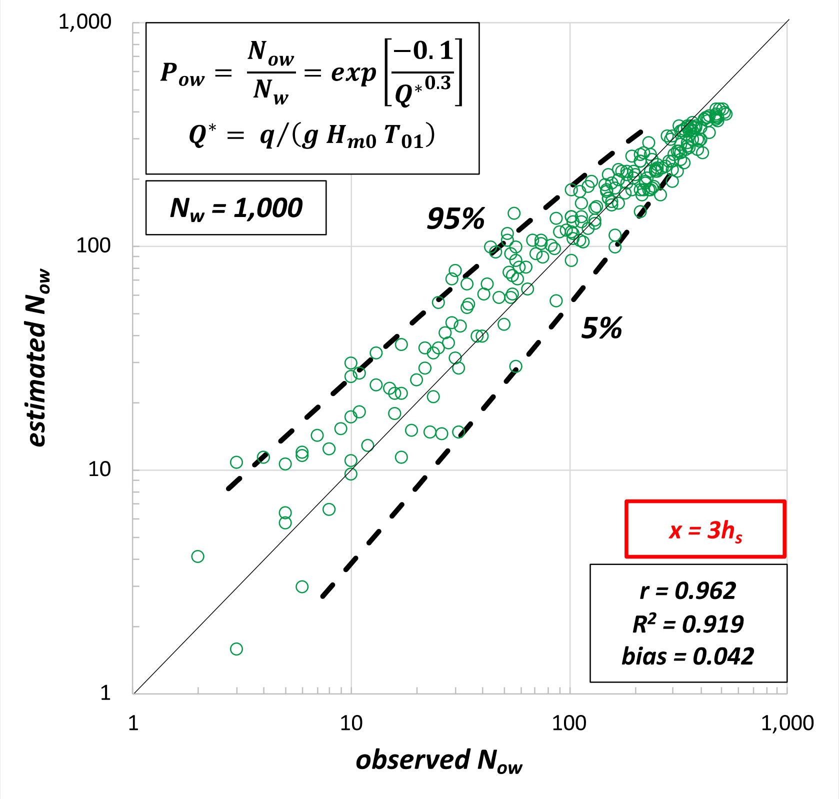

Fig. 4. 6. Comparison between measured and estimated N_{ow} using Eq. 4.1 together with wave characteristics calculated at a distance of 3*h* from the model toe.

The 90% error band was determined using the methodology by *Herrera and Medina* (*2015*), since *MSE* decreased for increasing values of lnN_{ow}. Error was assumed to be Gaussian distributed with 0 mean and variance given by

$$\sigma^2(\varepsilon) = 0.55 - 0.09 \ln N_{ow} \tag{4.2}$$

The 95% and 5% percentiles for lnN_{ow} can be calculated as

$$\ln N_{ow}\big|_{5\%}^{95\%} = \ln N_{ow} \pm 1.64\sqrt{0.55 - 0.09 \ln N_{ow}} \tag{4.3}$$

The range of application of Eq. 4.1 with G_1=-0.1 and G_2=0.3 is $0.002 \leq P_{ow} \leq 0.53$ and $7.2 \cdot 10^{-7} \leq Q^* \leq 6.9 \cdot 10^{-4}$. Note that Eq. 4.1 properly extrapolates the predictions for very small and very large values of Q^* ($P_{ow} \to 0$ when $Q^* \to 0$ and $P_{ow} \to 1$ when $Q^* \to \infty$).

4.4. A new method to estimate the maximum individual wave overtopping volume, V_{max}, on mound breakwaters

In Section 2.4.1, distribution functions to describe individual wave overtopping volumes were reviewed; the 2-parameter Weibull distribution and the 2-parameter Exponential distribution were recommended by authors in the literature (e.g.: *Franco et al.*, *1994*; *Molines et al.*, *2019*). In this section, both distribution functions are considered to fit *F(V)*; the quadratic utility function (see Section 3.6.4) proposed by *Molines et al.* (*2019)* is applied to account for the higher relevance of the largest individual wave overtopping volumes in practical applications. The influence of the bottom slope on the aforementioned distributions is also analyzed.

4.4.1. Influence of the bottom slope on the individual wave overtopping volumes

The 2-parameter Weibull distribution and the 2-parameter Exponential distribution proposed to describe *F(V)* are characterized by their coefficients: *b* and *A*, and *D* and *C*, respectively. Here, the influence of the bottom slope (*m*=2% and 4%) on the fitted values of these coefficients is analyzed.

No substantial differences were observed between the values of the coefficients from both bottom slope configurations in the scatter plot. Furthermore, Mann-Whitney test (see Section 3.6.5) was performed for each coefficient to determine if significant differences existed between both datasets. The null hypothesis corresponded to the coefficient (*b*, *A*, *D* or *C*) not being affected by the bottom slope. Based on 97 tests with *m*=2% and 106 tests with *m*=4%, the null hypothesis was not rejected with a significance level of α_s=0.10. Thus, the bottom slope did not show a significant influence on the distribution of individual wave overtopping volumes in this study.

4.4.2. A new method to estimate V_{max} using the 2-parameter Weibull distribution

If the 2-parameter Weibull distribution is used to describe the individual wave overtopping volumes, the maximum individual wave overtopping volume, V_{max}, is estimated with Eq. 2.23. Thus, N_{ow}, b and A, and $\bar{V}$ need to be calculated to predict V_{max}. As exposed in Section 3.6.4, a quadratic utility function was applied to the whole individual wave overtopping volume dataset of each test in order to fit b and A. Therefore, a value for b and A was obtained for each test. Tests with very low N_{ow} (N_{ow}<5) were disregarded to prevent inconsistencies due to the low number of observations; 209 were used to characterize b and A as

$$b = K_{B1} + \exp(K_{B2}Q^*) \tag{4.4}$$

$$A = 1.45 - 0.4b \tag{4.5}$$

Similar to Section 4.3.2, the empirical coefficients K_{B1} and K_{B2} were fitted considering wave characteristics (H_{m0} and T_{01}) in $Q^*= q/(gH_{m0}T_{01})$ at distances from the structure toe of x=0, h, 2h, 3h, 4h, 5h and 6h. $V_{max}{}^*=V_{max}/(gH_{m0}T_{01}{}^2)$ was calculated for each couple of values using Eqs. 2.23, 4.4 and 4.5 together with the measured N_{ow} and $\bar{V}$. The goodness-of-fit of these estimations of $V_{max}{}^*$ was assessed using r and R^2; best results were obtained for K_{B1}=0.8 and K_{B2}=-2·10^5 using wave characteristics determined at distances between x=2h and x=6h (r=0.92 and R^2=0.83). Hence, H_{m0} and T_{01} estimated at x=3h from the structure toe were used, following recommendations by *Herrera et al. (2017)*. Figure 4.7 relates Q^* and b and the least-squares fitting for b given by Eq. 4.4. Relationship between *1/b* and A as well as the least-squares fitting given by Eq. 4.5 is shown in Figure 4.8. Ranges of application for Eqs. 4.4 and 4.5 are 0.005≤P_{ow}≤0.53 and 1.3·10^{-6}≤Q^*≤6.9·10^{-4}.

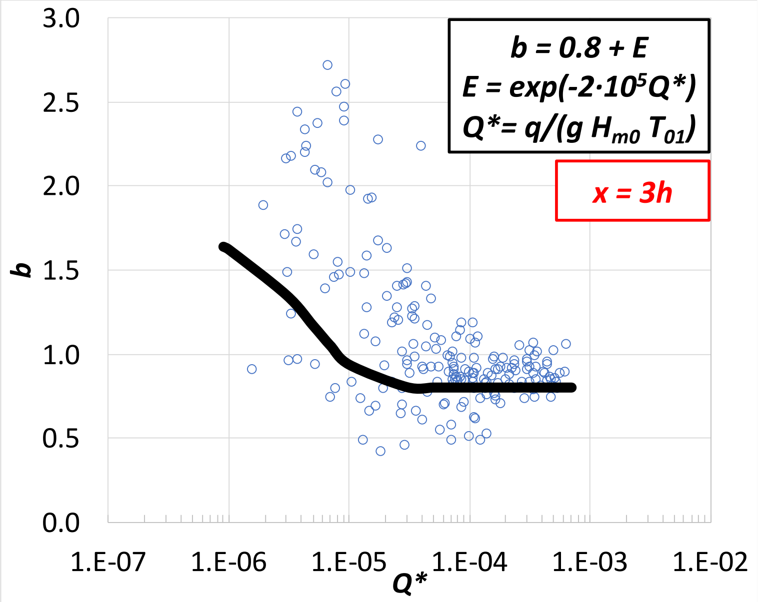

Fig. 4. 7. Relationship between the shape factor, *b*, of the 2-parameter Weibull distribution and Q^*.

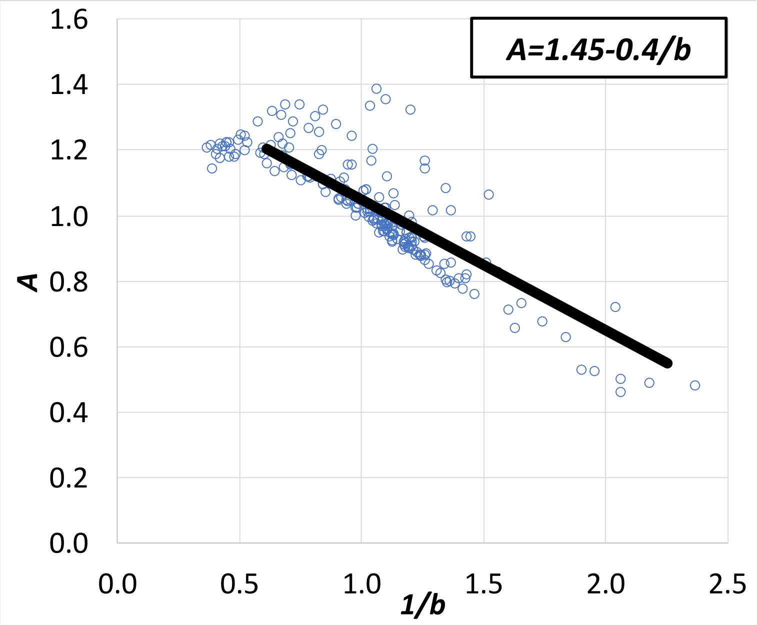

Fig. 4. 8. Relationship between the scale factor, *A*, and the shape factor, *b*, of the 2-parameter Weibull distribution.

The performance of Eq. 2.23 to estimate V_{max}^* using b and A calculated with Eq. 4.4 and 4.5, respectively, together with the measured N_{ow} and $\bar{V}$ is presented in Figure 4.9. The 95% and 5% percentiles for the predicted V_{max}^* are also shown in Figure 4.9. Satisfactory results were obtained (R^2=0.833).

Error of lnV_{max}^* was Gaussian distributed with 0 mean and constant variance $\sigma^2(\varepsilon)$=0.15. Thus, the 90% error band for the estimated V_{max}^* using Eqs. 2.25, 4.4 and 4.5 together with the measured N_{ow} and $\bar{V}$ is given by

$$\ln V_{max}^*|_{5\%}^{95\%} = \ln V_{max}^* \pm 0.63 \tag{4.6}$$

An example of the fitting of the 2-parameter Weibull distribution to the measured distribution of individual wave overtopping volumes is illustrated in Figure 4.9 for a randomly-selected test (#30). Figure 4.9 is presented in Weibull plot (see Eq. 3.11).

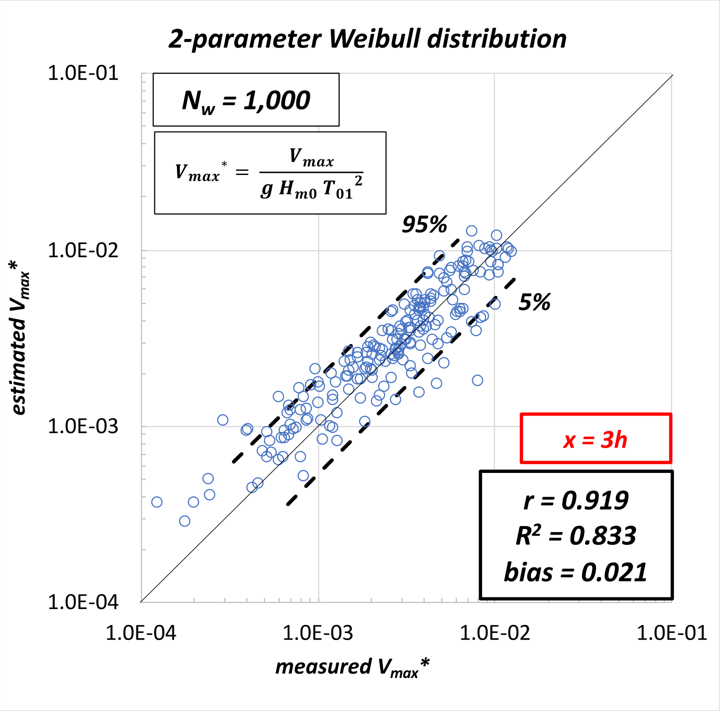

Fig. 4. 9. Comparison between the measured and estimated $V_{max}^*=V_{max}/(gH_{m0}T_{01}^2)$ using Eqs. 2.23, 4.4 and 4.5 together with wave characteristics calculated at a distance of 3*h* from the model toe.

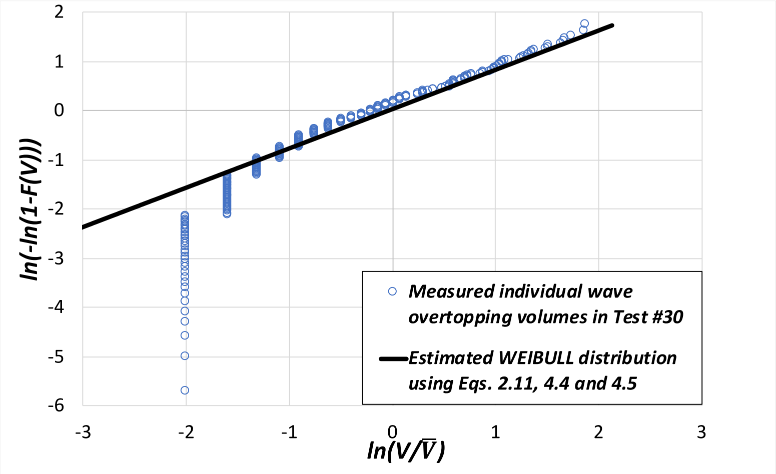

Fig. 4. 10. Comparison between measured and estimated individual wave overtopping volumes for Test#30 with Eqs. 2.11, 4.4 and 4.5.

4.4.3. A new method to estimate V_{max} using the 2-parameter Exponential distribution

As explained in Section 2.4.1, *Molines et al.* (*2019*) recommended the 2-parameter Exponential distribution (see Eq. 2.18) to describe *F(V)*. When using this distribution, V_{max} can be estimated as

$$V_{max} = D\bar{V}(\ln[N_{ow} + 1] + C/D) \qquad (4.7)$$

D and *C* coefficients were characterized as

$$D = K_{D1} - K_{D2}\exp(K_{D3}Q^{*}) \qquad (4.8)$$

$$C = 1 - D - 0.2D^{2} \qquad (4.9)$$

D and *C* fitted to the experimental dataset in this study applying a quadratic utility function (see Section 3.6.4). Tests with very low N_{ow} (N_{ow}<5) were not included in the analysis to avoid inconsistencies caused by the low number of observations, similar to Section 4.4.2. Wave characteristics (H_{m0} and T_{01}) were considered in $Q^{*}= q/(gH_{m0}T_{01})$ at distances from the structure toe of *x*=0, *h*, 2*h*, 3*h*, 4*h*, 5*h* and 6*h*. $V_{max}{}^{*}=V_{max}/(gH_{m0}T_{01}{}^{2})$ was estimated for each couple of values using Eqs. 4.7, 4.8 and 4.9 together with the measured N_{ow} and $\bar{V}$. Best goodness-of-fit metrics were obtained using H_{m0} and T_{01} estimated at distances between *x*=0 and *x*=3*h* with *r*=0.92 and R^2=0.85. Therefore, wave characteristics calculated at *x*=3*h* from the structure toe were used with K_{D1}=1.5, K_{D2}=1.5 and K_{D3}=-10^5, following recommendations by *Herrera et al. (2017)*. The relationship between Q^{*} and *D* as well as the least-squares fitting given in Eq. 4.8 are presented in Figure 4.11. The relationship between *D* and *C* and the least-squares fitting given in Eq. 4.9 are depicted in Figure 4.12.

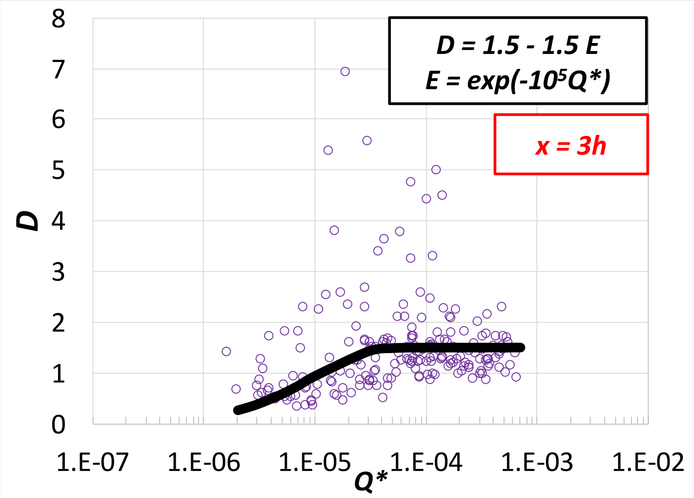

Fig. 4. 11. Relationship between the coefficient *D* of the 2-parameter Exponential distribution and Q^{*}.

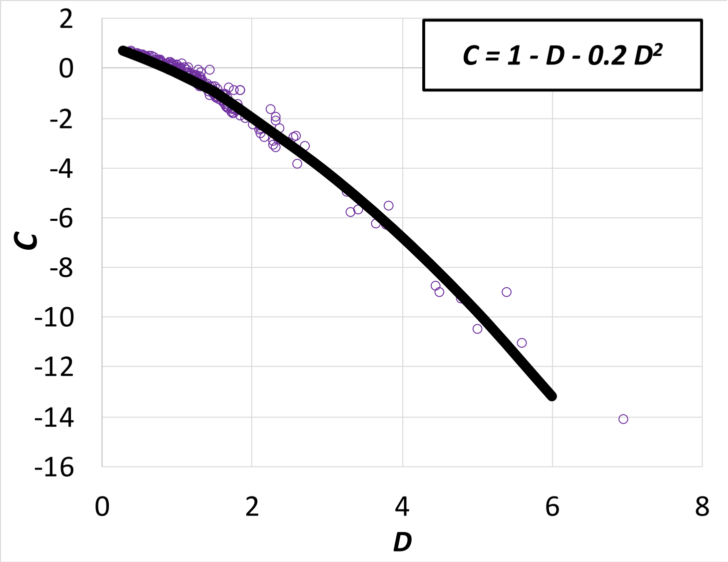

Fig. 4. 12. Relationship between the coefficients *D* and *C* of the 2-parameter Exponential distribution.

The performance of Eq. 4.7 to estimate V_{max}^* using C and D predicted with Eq. 4.8 and 4.9, respectively, together with the measured N_{ow} and $\bar{V}$ is presented in Figure 4.13. The 95% and 5% percentiles for the estimated V_{max}^* are also depicted in Figure 4.13. Satisfactory results were obtained (R^2=0.845), similar to those obtained with the 2-parameter Weibull distribution. Eqs. 4.8 and 4.9 are applicable within the ranges $0.005 \leq P_{ow} \leq 0.53$ and $1.3 \cdot 10^{-6} \leq Q^* \leq 6.9 \cdot 10^{-4}$.

Error of lnV_{max}^* followed a Gaussian distribution with 0 mean and constant variance $\sigma^2(\varepsilon)$=0.13. Therefore, the 90% error band for the estimated V_{max}^* using Eqs. 4.7, 4.8 and 4.9 together with the measured N_{ow} and $\bar{V}$ is given by

$$\ln V_{max}^*|_{5\%}^{95\%} = \ln V_{max}^* \pm 0.59 \qquad (4.10)$$

Figure 4.14 illustrates the fitting of the 2-parameter Exponential distribution to the measured distribution of individual wave overtopping volumes for the previous randomly-selected test (#30) in Figure 4.10. Figure 4.14 is presented in Exponential plot, generated as

$$\ln(1 - F(V)) = \frac{(V/\bar{V}) - C}{D} \qquad (4.11)$$

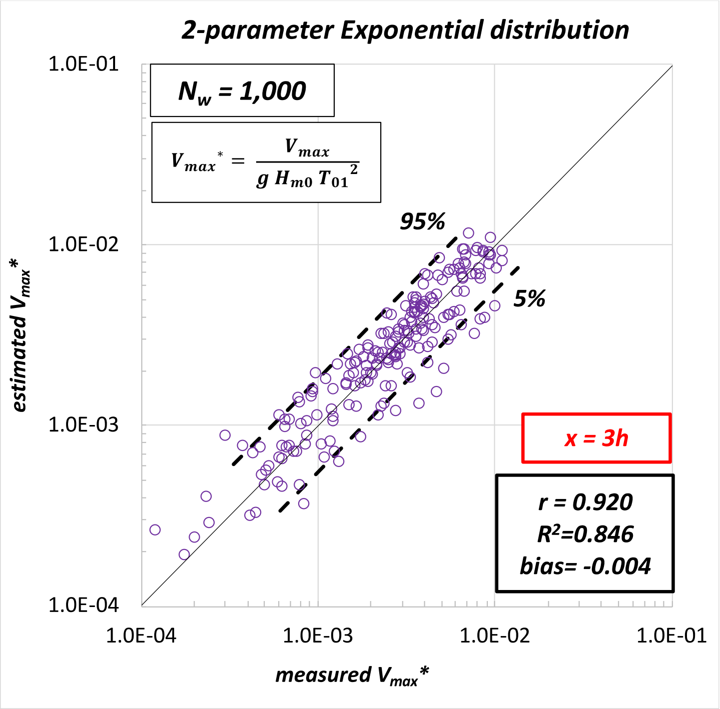

Fig. 4. 13. Comparison between the measured and estimated $V_{max}^*=V_{max}/(gH_{m0}T_{01}^2)$ using Eqs. 4.7, 4.8 and 4.9 together with wave characteristics calculated at a distance of 3h from the model toe.

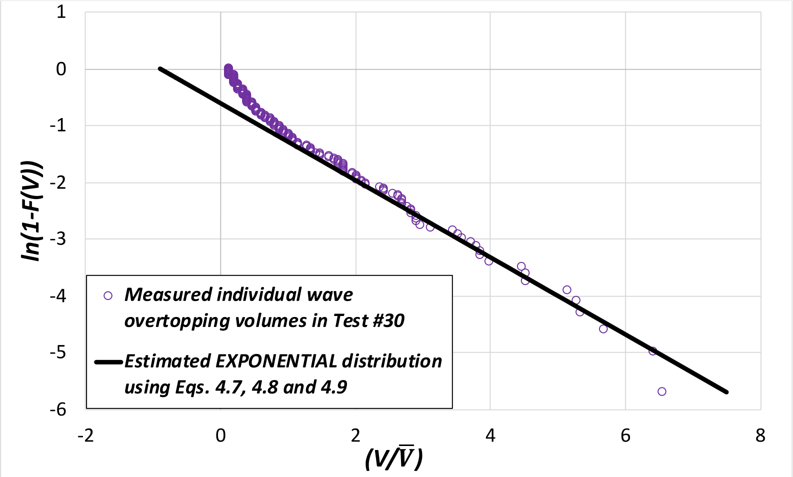

Fig. 4. 14. Comparison between measured and estimated individual wave overtopping volumes for Test#30 with Eqs. 4.7, 4.8 and 4.9.

4.5. Estimation of the maximum individual wave overtopping volume, V_{max}, for mound breakwater designs

During the design phase of a mound breakwater, the structural geometry and the design wave conditions (H_{m0} and T_{01}) are known. However, the mean individual wave overtopping volume ($\bar{V} = qT_{01}N_w/N_{ow}$) and the number of overtopping events (N_{ow}) are required to apply formulas in the literature to estimate V_{max}. Hence, q and N_{ow} need to be estimated using predictors in the literature when direct observations are not available. Methods recommended in the literature to estimate q were assessed in Section 4.2; best results to predict Q^* were obtained using CLASH NN (R^2=0.636). Thus, estimations provided by CLASH NN were used here for further analysis.

N_{ow} calculated using Eq. 4.1 developed in this thesis together with q predicted with CLASH NN provided R^2=0.584. This agreement is worse than R^2=0.919 obtained with measured q. Figure 4.15 illustrates the performance of Eq. 4.1 to estimate N_{ow} when q is predicted with CLASH NN; results of the methods in the literature to estimate N_{ow} with best results in Section 4.2.1 are also presented. The goodness-of-fit metrics in Figure 4.15 are given for lnN_{ow}.

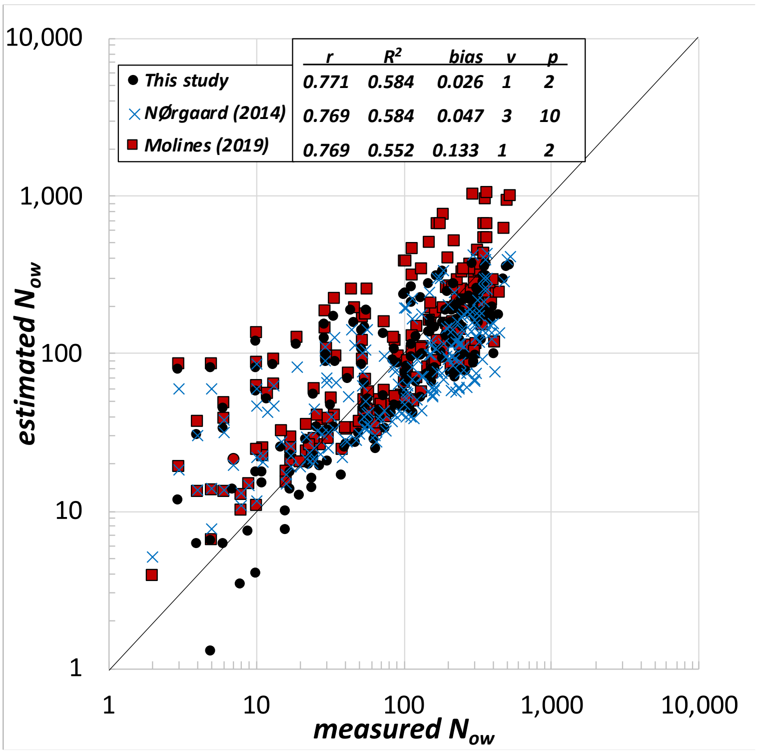

Fig. 4. 15. Comparison between the measured and the estimated number of overtopping events, N_{ow}, using estimated Q^*.

Note that the fitting of the new formula (Eq. 4.1) was equal to that obtained with the method given in *Nørgaard et al.* (*2014*), which provided the best fitting to the experimental data in this study in Section 4.2.1. Nevertheless, the method proposed by *Nørgaard et al.* (*2014*) to predict N_{ow} involves 3 variables and 10 parameters, while the method given in this thesis requires 1 variable and 2 parameters. In addition, lower *bias* and slightly higher *r* were obtained with the method proposed in the present thesis.

In Figure 4.16, $V_{max}^*=V_{max}/(gH_{m0}T_{01}^2)$ predicted using Eq. 2.23 (2-parameter Weibull distribution) together with Eqs. 4.4 and 4.5 to estimate *b* and *A*, respectively, is compared to the observed V_{max}^* in this study. The 90% error band is also given in Figure 4.16. Note that *q* and $\bar{V}$ were estimated using CLASH NN while N_{ow} was calculated using Eq. 4.1 developed in this thesis. The performance of the methods in the literature to predict V_{max} with best results in Section 4.2.1 are also shown. The goodness-of-fit metrics in Figure 4.16 are given for lnV_{max}^*.

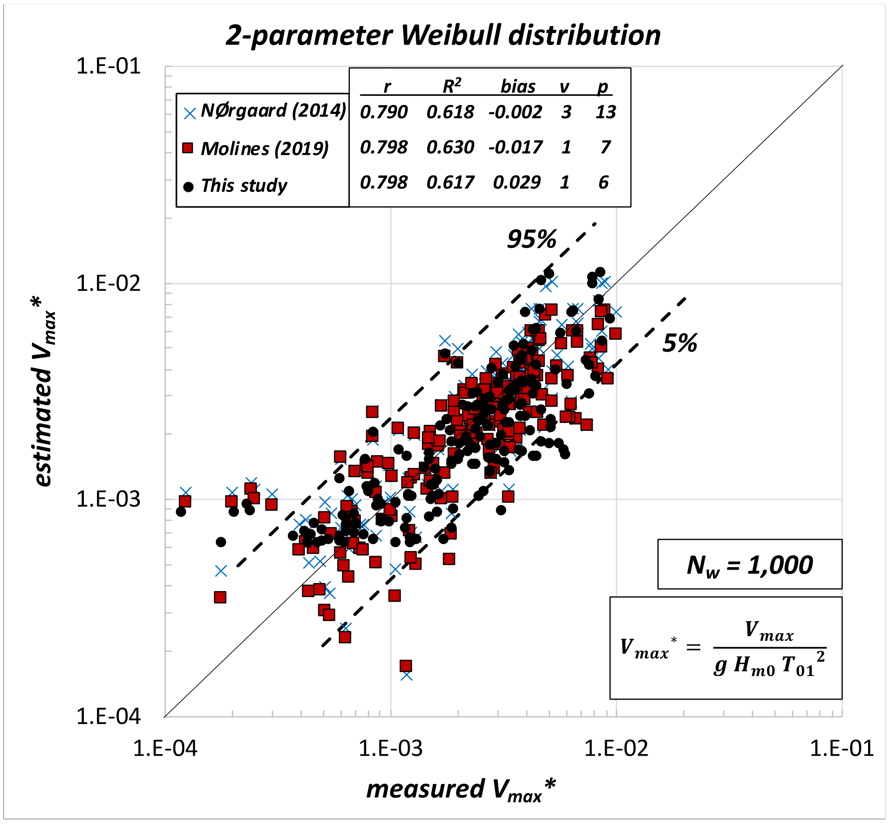

Fig. 4. 16. Comparison between the measured and the estimated dimensionless maximum individual wave overtopping volume, V_{max}^*, with the 2-parameter Weibull distribution using estimated N_{ow} and Q^*.

On the other hand, the performance of the 2-parameter Exponential distribution proposed in the present thesis using estimated q and N_{ow} is assessed in Figure 4.17. $V_{max}{}^*$ in Figure 4.17 is calculated using Eq. 4.7 together with Eqs. 4.8 and 4.9 to estimate C and D, respectively; the 90% error band is also presented. Note that q and $\bar{V}$ were calculated using CLASH NN whereas N_{ow} was determined using Eq. 4.1 recommended in this thesis. Similar to Figure 4.16, the results of the methods in the literature to predict V_{max} with best results in Section 4.2.1 are included in Figure 4.17. The goodness-of-fit metrics in Figure 4.17 are given for $lnV_{max}{}^*$.

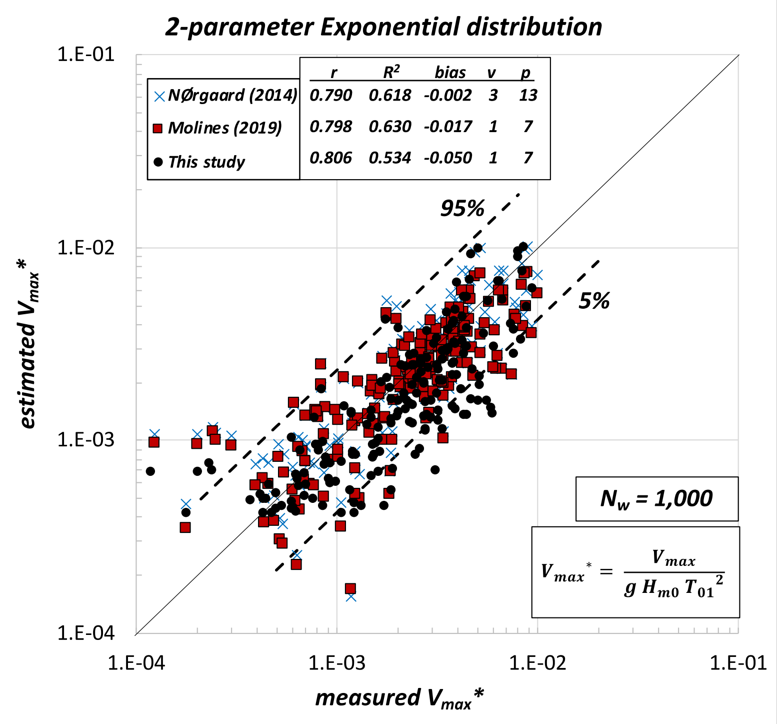

Fig. 4. 17. Comparison between the measured and the estimated dimensionless maximum individual wave overtopping volume, $V_{max}{}^*$, with the 2-parameter Exponential distribution using estimated N_{ow} and Q^*.

As shown in Figures 4.16 and 4.17, the goodness-of-fit of three of the four compared methods was similar ($0.617 \leq R^2 \leq 0.630$); the 2-parameter Exponential distribution provided worse results ($R^2=0.534$). Although methods given by *Nørgaard et al.* (*2014*) and *Molines et al.* (*2019*) provided similar results to those obtained with the 2-parameter Weibull distribution proposed in this thesis, the new method developed in the present study (1 variable, N_v, and 6 parameters, N_p) is much simpler than that recommended by *Nørgaard et al.* (*2014*) (N_v=3 and N_p=13) and simpler than that given in *Molines et al.* (*2019*) (N_v=1 and N_p=7). Thus, the 2-parameter Weibull distribution given in Eq. 2.11

with *b* and *A* calculated using Eqs. 4.4 and 4.5 is suggested in this thesis. Using such method, the ratio between the estimated and the measured V_{max}^* for design purposes falls within a factor of 2 (see the 90% error band in Figure 4.16).

4.6. Summary and conclusions

In this section, methods in the literature to estimate V_{max} were first evaluated using the experimental database in this study. Note that in the present thesis mound breakwaters without a crown wall under depth-limited breaking wave conditions were tested. Satisfactory results were provided when applying the methods given in *Nørgaard et al.* (*2014*) and *Molines et al.* (*2019*). Since these two studies were conducted on mound breakwaters with a crown wall, the presence of a crown wall seems to be negligible when estimating V_{max}. Best results were obtained using the formulas given by *Molines et al.* (*2019*), who performed tests in non breaking conditions. Thus, the influence of depth-limited breakage may not influence $V_{max.}$

Using the experimental database in this thesis, new equations were proposed to predict V_{max}. The two distribution functions in the literature were assumed to describe the individual wave overtopping volumes: (1) the 2-parameter Weibull distribution (Eqs. 2.11, 4.4 and 4.5) and, (2) the 2-parameter Exponential distribution (Eqs. 2.18, 4.8 and 4.9). Since q and N_{ow} are unknown during the design phase of a mound breakwater and need to be estimated, formulas developed in this study were assessed using estimated q and N_{ow}. Best results were obtained using the 2-parameter Weibull distribution with goodness-of-fit metrics similar to those obtained using the methods by *Nørgaard et al.* (*2014*) and *Molines et al.* (*2019*). Nevertheless, the new method developed in the present study using the 2-parameter Weibull distribution (N_v=1 and N_p=6) is much simpler than that recommended by *Nørgaard et al.* (*2014*) (N_v=3 and N_p=13) and simpler than that given in *Molines et al.* (*2019*) (N_v=1 and N_p=7). Consequently, the 2-parameter Weibull distribution given in Eq. 2.11 together with *b* and *A* calculated using Eqs. 4.4 and 4.5 is recommended here. For design purposes, the ratio between the estimated and the measured V_{max}^* falls within a factor of 2 (see the 90% error band in Figure 4.16).

"When dealing with water, first experiment then use judgement."

Leonardo Da Vinci

5

Overtopping layer thickness and overtopping flow velocity on mound breakwater crests

Port of Scheveningen (the Netherlands), October 2019

5.1. Introduction

During the last decades, pedestrian stability under steady flow conditions (*Abt et al., 1989*; *Endoh and Takahashi, 1995*) has been studied in order to better quantify the flood hazard for humans. In the current context of climate change, human stability under overtopping flow conditions has taken relevance; new studies focused on preventing pedestrian accidents under overtopping flow conditions (*Bae et al., 2016*; *Sandoval and Bruce, 2017*) have been developed. Such studies identified OLT and OFV as the significant flow variables to guarantee pedestrian safety. Several studies in the literature are focused on OLT and OFV prediction on dikes. However, no studies were found to estimate OLT and OFV on mound breakwaters.

In this chapter, the existing methods in the literature to estimate OLT on dikes (Section 2.5) were assessed using the data on mound breakwaters described in Section 3. Since the aforementioned methods developed for dikes (smooth impermeable slope) are not directly applicable to mound breakwaters (rough permeable slope where infiltration of overtopping water occurs), new estimators for mound breakwaters were proposed. Based on the literature, significant explanatory variables to describe OLT and OFV were selected and Neural Network models were trained. Using these models, the optimum point to estimate wave characteristics to calculate OLT and OFV under depth-limited breaking wave conditions was determined and bottom slope influence was analyzed. Finally, new explicit estimators to predict the extreme values of OLT and OFV were developed. Most results in this chapter have been recently published in (*Mares-Nasarre et al., 2019, 2020a, 2021*).

5.2. Comparison of the existing methods for estimating the overtopping layer thickness

In Section 2.5, formulas proposed in the literature to estimate OLT exceeded by 2% of the incoming waves, $h_{c2\%}$, on dikes were exposed. Although dikes are different to mound breakwaters, a comparison was conducted between the measured $h_{c2\%}$ in the middle of the breakwater crest, $h_{c2\%}(B/2)$, in this study and the predictions provided by the methods proposed for dikes (Section 2.5). Note that some methods were developed only for the seaward edge of the crest (*Van der Meer et al., 2010; Formentin et al., 2019*). Hence, only the methods valid to estimate $h_{c2\%}(B/2)$ were assessed.

A comparison between the measured and estimated $h_{c2\%}(B/2)$ using methods in the literature valid for dikes is presented in Figure 5.1 Roughness factors recommended in *EurOtop (2018*) were applied in the formulas proposed by such manual (Eqs. 2.25, 2.43 and $h_{c2\%}(B/2)=[2/3]h_{A2\%}(R_c)$): $\gamma_f = 0.49$, $\gamma_f = 0.47$, and $\gamma_f = 0.40$ for single-layer Cubipod® armors, double-layer randomly placed cube armors and double-layer rock armored structures with a permeable core, respectively. However, it should be noted that *Molines and Medina* (*2015*) pointed out that roughness factors depend on the experimental database and the formula; γ_f needs to be calibrated specifically for each database and formula. Therefore, comparison with the experimental data in this study was also performed considering γ_f=1.00. Eqs. 2.34, 2.35 and 2.37 given by *Schüttrumpf and Van Gent* (*2003*) were applied considering the experimental coefficients $c_{A,h}^*$ and $c_{c,h}^*$ proposed by *Schüttrumpf et al.* (*2002)* and *van Gent* (*2002*) (see Table 2.7).

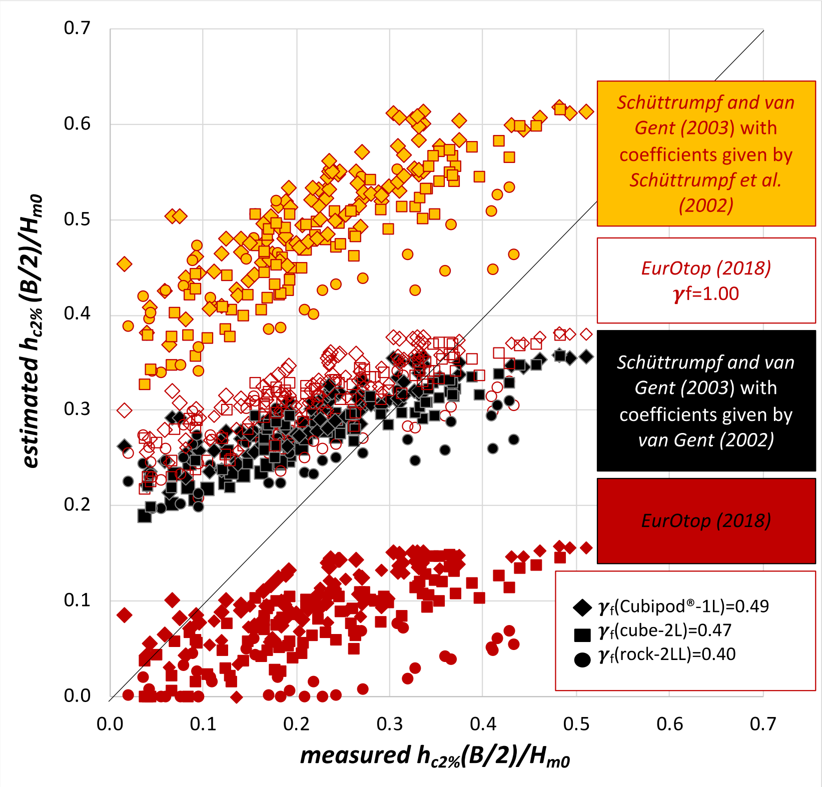

Fig. 5. 1. Comparison between the measured and the estimated overtopping layer thickness exceeded by 2% of the incoming waves in the middle of the breakwater crest, $h_{c2\%}(B/2)$, with the methods in the literature for dikes.

As shown in Figure 5.1, none of the existing estimators developed for dike crests provided satisfactory results (R^2<0.164). Significant discrepancies were also observed between the different estimators. As previously mentioned in Section 2.5, predictions of $h_{c2\%}(B/2)$ with Eqs. 2.34, 2.35 and 2.37 with coefficients by *van Gent* (*2002*) are almost half the estimations of $h_{c2\%}(B/2)$ when considering coefficients given in *Schüttrumpf et al.* (*2002)*. However, Eqs. 2.34, 2.35 and 2.37 (*Schüttrumpf and Van Gent, 2003*) together with coefficients proposed by *van Gent* (*2002*) provided similar results to Eqs. 2.25 and 2.43 with $h_{c2\%}(B/2)=[2/3]h_{A2\%}(R_c)$ given by *EurOtop (2018)* when γ_f=1.00 was considered. Thus, the prediction of $Ru_{2\%}/H_{m0}$ was the main reason for the aforementioned differences when roughness factors were considered in the method given by *EurOtop*

(2018). In order to illustrate the differences in the estimation of $Ru_{2\%}/H_{m0}$ using methods recommended in the literature, calculations of $Ru_{2\%}/H_{m0}$ are given here for test #121. In this test, H_{m0}=104mm, $T_{m-1,0}$=1.23s, $\gamma_b=\gamma_\beta=1$, γ_f=0.40 (rock-2L) and $cot\alpha$=1.5. Surf similarity parameter for this test can be calculated as

$$\xi_{s,-1} = (1/1.5)\Big/\sqrt{\left(\frac{[2\pi 0.104]}{9.81\ 1.23^2}\right)} = 3.18 \qquad (5.1)$$

Applying the method given in *EurOtop (2018)* (Eq. 2.43),

$$Ru_{2\%}/H_{m0} = 1.65 \times 1 \times 1 \times 0.40 \times 3.18 = 2.06 \qquad (5.2a)$$

with a maximum value of

$$Ru_{2\%}/H_{m0} = 1.0 \times 0.40 \times 1 \times \left(4 - \frac{1.5}{\sqrt{1 \times 3.18}}\right) = 1.26 \qquad (5.2b)$$

Using the equations proposed by *Schüttrumpf and Van Gent* (*2003)* (Eq. 2.34) with c_0=1.35 and c_1=4.0,

$$c_2 = 0.25 \times \frac{4.0^2}{1.35} = 2.96 \qquad (5.3a)$$

$$p = 0.5 \times \frac{4.0}{1.35} = 1.48 \qquad (5.3b)$$

Since $\xi_{s,-1}$=3.18<1.48=p, $Ru_{2\%}/H_{m0}$ can be calculated as

$$Ru_{2\%}/H_{m0} = 4.0 - 2.96/3.18 = 3.07 \qquad (5.3c)$$

Therefore, significant differences in the prediction of $Ru_{2\%}/H_{m0}$ were observed; $Ru_{2\%}/H_{m0}$(*van Gent*, *2001*)=3.07>>1.26= $Ru_{2\%}/H_{m0}$(*EurOtop*, *2018).*

The results of the present section confirmed that methods in the literature to estimate $h_{c2\%}(B/2)$ on dikes are not applicable to mound breakwaters. Such methods were based on $Ru_{2\%}$; significant inconsistencies were found when predicting $Ru_{2\%}$ using the recommended methods in the literature. Since the prediction of $u_{c2\%}(B/2)$ on dike crests using predictors in the literature is also based on $Ru_{2\%}$, similar incoherencies are expected. Thus, new explicit estimators for both $h_{c2\%}(B/2)$ and $u_{c2\%}(B/2)$ on mound breakwaters are needed.

5.3. Influence of bottom slope on overtopping layer thickness and overtopping flow velocity

As exposed in Section 2, only wave characteristics at the structure toe and geometric variables of the coastal structure were considered in the formulations in the literature to estimate $h_{c2\%}$ and $u_{c2\%}$ (see Table 2.8) on dike crests. When in depth-limited breaking wave conditions, the optimum point to determine wave characteristics needs to be assessed and bottom slope (*m*) results significant for mound breakwater designs (*Herrera and Medina, 2015; Herrera et al., 2017*). Thus, in this section, the optimum point to estimate wave characteristics to calculate $h_{c2\%}(B/2)$ and $u_{c2\%}(B/2)$ was evaluated and the effect of *m* on such variables was analyzed. To this end, Neural Networks (NNs) were applied.

5.3.1. Analysis using Neural Networks

Feedforward Neural Networks (NNs) are techniques from the artificial intelligence field which can be applied to model nonlinear relationships between explanatory variables (inputs of the model) and responses (outputs of the model). NNs have been widely applied in researches and practical applications related to overtopping (*van Gent et al., 2007*), since it is a highly nonlinear problem. NNs have also been satisfactorily used on smaller datasets with fewer input variables to identify the most significant variables to estimate crown wall forces (*Molines et al., 2018*), to define explicit overtopping formulae (*Molines and Medina, 2016*) or to assess the influence of the armor placement on the hydraulic stability of mound breakwater armors (*Herrera et al., 2015*). When the assumption of the linear relationship between variables is not possible, reliable results may be obtained using NNs rather than conventional methods. In this section, NNs were applied to determine the influence of the bottom slope on the overtopping layer thickness and the overtopping flow velocity on mound breakwaters in depth-limited breaking wave conditions (a highly nonlinear problem).

5.3.1.1 General outline

$h_{c2\%}(B/2)$ and $u_{c2\%}(B/2)$ were obtained from the 2D physical model tests described in Section 3. As mentioned in Section 3.6.5, $u_{c2\%}(B/2)$ values out of the operational range of the miniature propellers were disregarded. As a results, 235 values of $h_{c2\%}(B/2)$ (102, 93 and 40 for Cubipod®-1L, cube-2L and rock-2L, respectively) and 167 values of $u_{c2\%}(B/2)$ (57, 80 and 30 for Cubipod®-1L, cube-2L and rock-2L, respectively) were used in this study.

Each armor layer and overtopping variable ($h_{c2\%}(B/2)$ and $u_{c2\%}(B/2)$) was studied independently in order to keep the model as simple as possible. In case of including the three armor layers in only one NN, one or several extra input neurons would be necessary (e.g., armor element, number of armor layers). Additionally, a balanced dataset is required to guarantee a proper NN training. Thus, the same number of tests from each armor layer should be used in the training procedure, limiting the number of tests used to the minimum between the three armor layers. In other words, only 40 tests (N_D for rock-2L) would be used to train the NN for $h_{c2\%}(B/2)$ even if 102 and 93 tests were available for Cubipod®-1L and cube-2L, respectively. Therefore, since each armor layer was studied independently in this study, the following analysis were conducted 6 times (3 armor layers × 2 variables). Figure 5.2 illustrates the procedure of the analysis performed in this thesis using NNs.

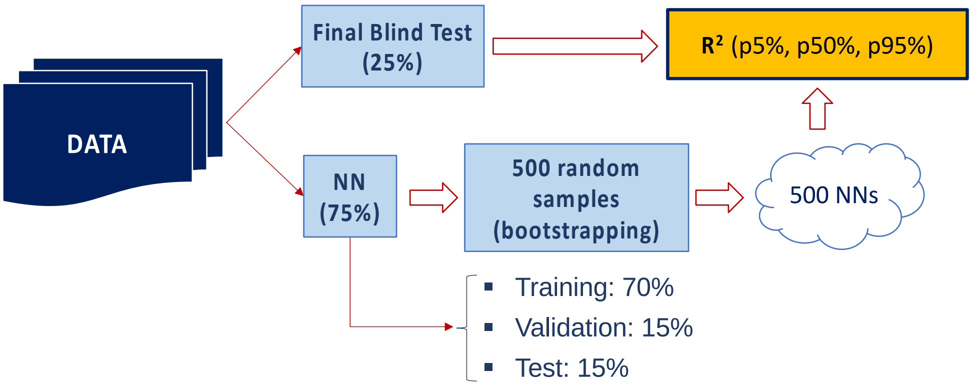

Fig. 5. 2. Diagram of the Neural Network (NNs) analysis conducted in this study.

First, every dataset was randomly divided in two sections: 75% of the data was used to train NNs (TR=75%×N_D) while 25% of the data was kept for a final blind test ($T\text{-}BLIND$=25%×N_D). 500 random datasets were generated applying the bootstrapping technique on the 75% of the data for training NNs. Bootstrap resample technique consists on the random selection of N_D data from a dataset with N_D data. Every data has a probability of 1/N_D to be selected each time. Hence, some data are not selected while some data are selected once or more than once in each resample. 500 NNs were trained based on the 500 random resamples and their goodness-of-fit was assessed on the *T-BLIND* dataset. In this manner, not only the average value of R^2 but also its variability could be obtained.

Multilayer feedforward NNs with one hidden layer were used with a hyperbolic tangent sigmoid transfer function. The NN structure was composed by three layers: (1) input layer with 4 neurons (N_i), (2) hidden layer with 3 neurons (N_h) and (3) output layer with one neuron (N_{oL}). Therefore, the number of free parameters of the NN model is $P = N_o + N_h (N_i + N_{oL} + 1) = 19$. In order to prevent overlearning, $P/TR < 1$ was ensured ($P/TR = 0.63$ in the worst case) and an early stopping criterion (*The MathWorks Inc., 2019*) was implemented. This early stopping criterion divided the data for training (TR=75%×N_D), in three sections: formal training ($TR\text{-}TRAIN$=75%×70%×N_D), validation ($TR\text{-}VAL$ 75%×15%×N_D) and test ($TEST$=75%×15%×N_D). Data in the training section (*TR-TRAIN*) was used to formally train the NN, updating the biases and weights. The error after each training step was monitored using the data in validation section (*TR-VAL*) in order to stop the training procedure once the error in this subset started growing (indicating possible overlearning). Data in the test section (*TEST*) was not used during the training procedure but as cross validation to compare different models.

5.3.1.2 Explanatory variables affecting $h_{c2\%}(B/2)$ *and* $u_{c2\%}(B/2)$

The structure of the used NN model is presented in Figure 5.3. Both $h_{c2\%}(B/2)$ and $u_{c2\%}(B/2)$ were made dimensionless for the analysis as $h_{c2\%}(B/2)/H_{m0}$ and $u_{c2\%}(B/2)/(H_{m0}/T_{m-1,0})$. Based on the literature (see Table 2.8), five input variables were considered: the spectral significant wave height (H_{m0}), the spectral wave period ($T_{m-1,0}$), the crest freeboard (R_c), the water depth at the toe of the structure (h) and the bottom slope (m). In order to prevent the NN model to be affected by the model scale, they were rearranged as four dimensionless variables to feed the NN model

- m, is the bottom slope.
- R_c/H_{m0}, is the dimensionless crest freeboard. This input variable is the most common and accepted variable for describing the mean wave overtopping discharge (e.g.: *van Gent et al., 2007,* or *Molines and Medina, 2016*).
- $Ir_{m-1,0}=\tan\alpha/(2\pi H_{m0}/g/T_{m-1,0}^2)$, is the Iribarren number or breaker parameter calculated using H_{m0} and $T_{m-1,0}$. $Ir_{m-1,0}$ represents the influence of the wave steepness and determines the type of wave breaking on the slope. Although, only $\tan\alpha=2/3$ was tested in this study, $Ir_{m-1,0}$ was used instead of the wave steepness since it was reported as significant for estimating $h_{c2\%}$ and $u_{c2\%}$ in the literature (*Schüttrumpf et al., 2002*; *van Gent, 2002; Schüttrumpf and Van Gent, 2003*).
- h/H_{m0}, is the dimensionless water depth calculated with the water depth at the toe of the structure and H_{m0}. h/H_{m0} is commonly used as breaking index to indicate if waves are depth-limited or not (*van Gent, 1999; Nørgaard et al., 2014*).

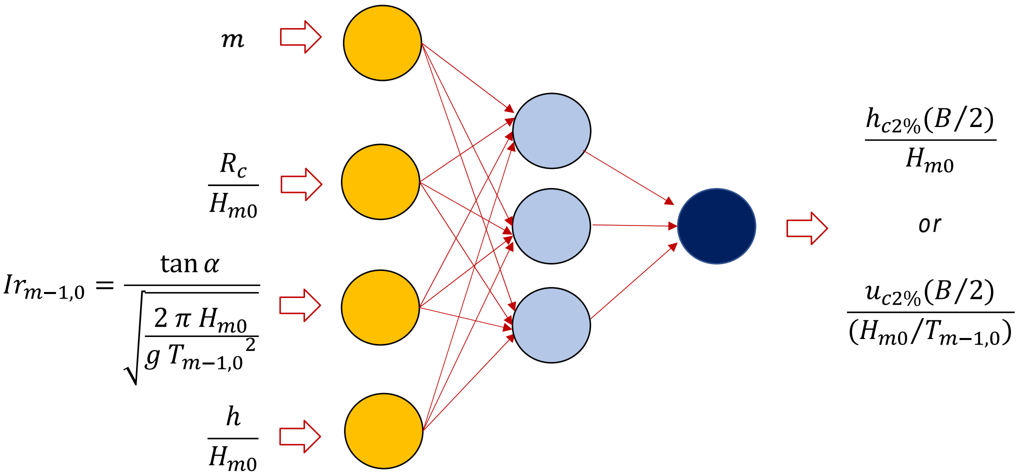

Fig. 5. 3. Structure of the neural networks (NNs) used in this study.

5.3.2. Optimum point to estimate wave parameters

The methodology presented in Figure 5.2 was repeated 7 times for each armor layer and overtopping variable (7 times × 3 armors × 2 variables = 42 times), modifying the wave characteristics (H_{m0} and $T_{m-1,0}$) considered to feed the model. Wave characteristics were estimated using SwanOne model (see Section 3.6.2) at the toe of the structure, at a distance of h from the toe of the structure, at a distance of $2h$ from the toe of the structure, and so on until $6h$ from the toe of the structure. Figure 5.4 illustrates the positions where wave characteristics were estimated for the configuration with bottom slope m=4%.

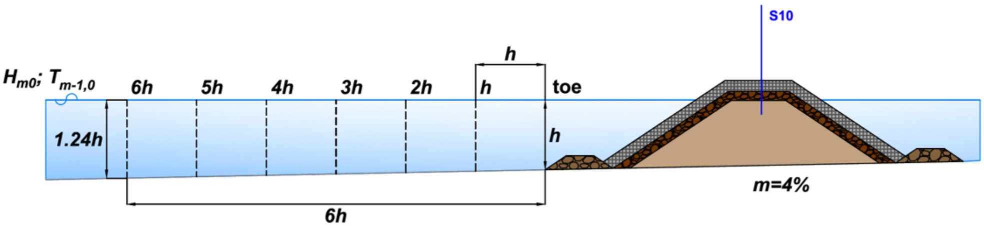

Fig. 5. 4. Locations where wave characteristics were estimated to assess the optimum point.

In this manner, percentiles 5%, 50% and 95% of R^2 on the *T-BLIND* dataset (p5%, p50% and p95%, respectively) could be calculated as a function of the distance from the toe of the model where wave characteristics were estimated. The evolution of p50% R^2 for $h_{c2\%}(B/2)/H_{m0}$ and $u_{c2\%}(B/2)/(H_{m0}/T_{m-1,0})$ is shown in Figures 5.5 and 5.6, respectively. In these figures, the x-axis represents the distance from the toe of the model to the point where wave characteristics were estimated while the y-axis represents the p50% R^2 on the *T-BLIND* dataset.

The highest R^2 for the dimensionless $h_{c2\%}(B/2)$ for the three studied armor layers was obtained when using wave characteristics (H_{m0} and $T_{m-1,0}$) estimated at a distance of $3h$ from the toe of the model. Regarding the dimensionless $u_{c2\%}(B/2)$, no clear tendency was found for Cubipod®-1L armor. This may be caused by the low number of tests for m = 2% (N_D = 13 for m = 2% and N_D = 44 for m = 4%). For cube-2L and rock-2L armors, the highest R^2 was obtained using wave characteristics estimated at a distance from the model toe between $3h$ and $4h$. Therefore, the optimum zone to estimate wave characteristics (H_{m0} and $T_{m-1,0}$) to calculate $h_{c2\%}(B/2)$ and $u_{c2\%}(B/2)$ was selected at a distance of $3h$ from the toe of the structure. Note that this point was also suggested by *Herrera et al. (2017)* to better describe the rock armor damage in depth-limited breaking wave conditions. In addition, this distance approximately corresponds to the distance of $5H_{m0}$ recommended by *Goda (1985)* to determine wave characteristics to design vertical breakwaters in breaking wave conditions. Later, *Melby (1999)* also suggested the distance proposed by *Goda (1985)* to better describe the armor damage progression of rubble mound breakwaters.

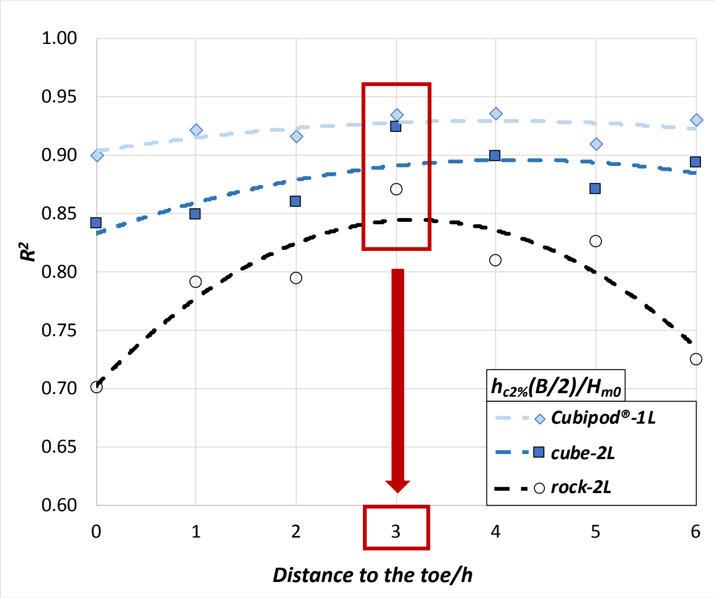

Fig. 5. 5. Median R^2 for dimensionless $h_{c2\%}(B/2)$ as a function of the relative distance to the structure.

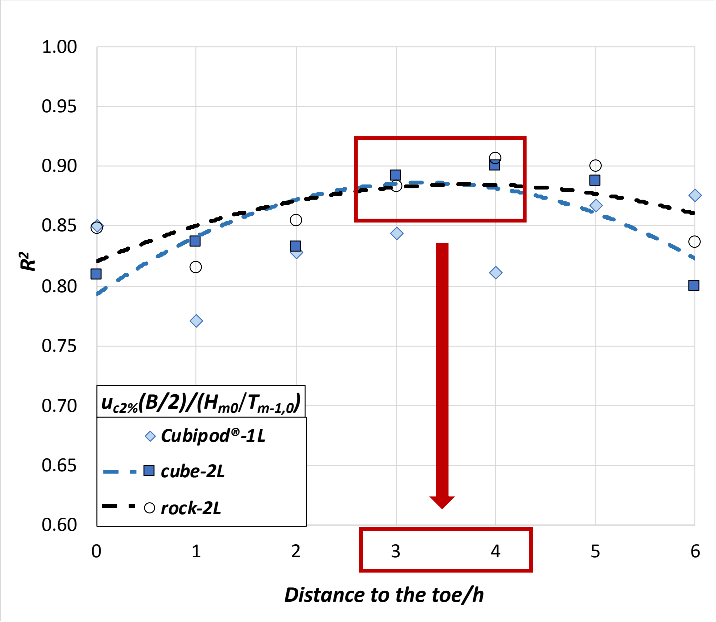

Fig. 5. 6. Median R^2 for dimensionless $u_{c2\%}(B/2)$ as a function of the relative distance to the structure.

5.3.3. Influence of bottom slope on $h_{c2\%}(B/2)$ and $u_{c2\%}(B/2)$

In the previous section, the zone where optimum wave characteristics (H_{m0} and $T_{m-1,0}$) are estimated for the calculation of $h_{c2\%}(B/2)$ and $u_{c2\%}(B/2)$ was identified at a distance of 3*h* from the toe of the model. Thus, the influence of *m* on $h_{c2\%}(B/2)$ and $u_{c2\%}(B/2)$ is evaluated here using the NNs trained with wave characteristics estimated at a distance of 3*h* from the model toe.

5.3.3.1 NN model performance

The performance of the NN models for $h_{c2\%}(B/2)/H_{m0}$ and $u_{c2\%}(B/2)/(H_{m0}/T_{m-1,0})$ using the training (*TR-TRAIN*), validation (*TR-VAL*) and test subset (*TEST*) is illustrated in Figures 5.7 and Figures 5.8. Good agreement was observed with the testing subset; R^2=0.903 and 0.789 for $h_{c2\%}(B/2)/H_{m0}$ and $u_{c2\%}(B/2)/(H_{m0}/T_{m-1,0})$, respectively. Note that R^2=0.164 was obtained for $u_{c2\%}(B/2)/(H_{m0}/T_{m-1,0})$ for the Cubipod®-1L armor due to the low variance of the randomly-selected testing subset; reasonable correlation (*r*=0.936) and bias (*bias*=0.017) were obtained. As previously mentioned in this section, *T-BLIND* subset was used to assess the goodness-of-fit of the trained NNs. Figures 5.9 and 5.10 illustrate the goodness-of-fit of the predictions given by the p50% NNs models for the *T-BLIND* subset. A good performance was observed with R^2=0.913 and 0.918 for $h_{c2\%}(B/2)/H_{m0}$ and $u_{c2\%}(B/2)/(H_{m0}/T_{m-1,0})$, respectively.

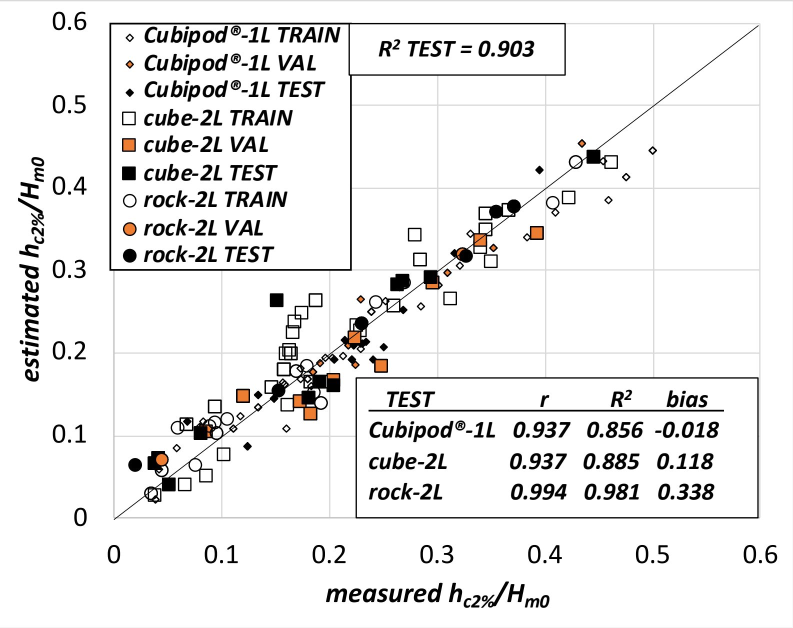

TEST	r	R²	bias
Cubipod®-1L	0.937	0.856	-0.018
cube-2L	0.937	0.885	0.118
rock-2L	0.994	0.981	0.338

Fig. 5. 7. Comparison between measured and estimated $h_{c2\%}(B/2)/H_{m0}$ with the NN models on the testing subset (*TEST*).

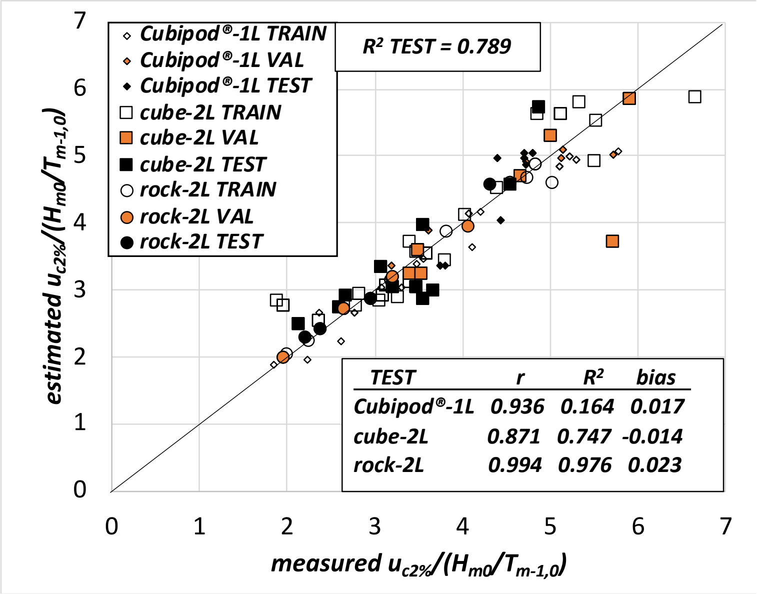

TEST	r	R²	bias
Cubipod®-1L	0.936	0.164	0.017
cube-2L	0.871	0.747	-0.014
rock-2L	0.994	0.976	0.023

Fig. 5. 8. Comparison between measured and estimated $u_{c2\%}(B/2)/(H_{m0}/T_{m-1,0})$ with the NN models on the testing subset (*TEST*).

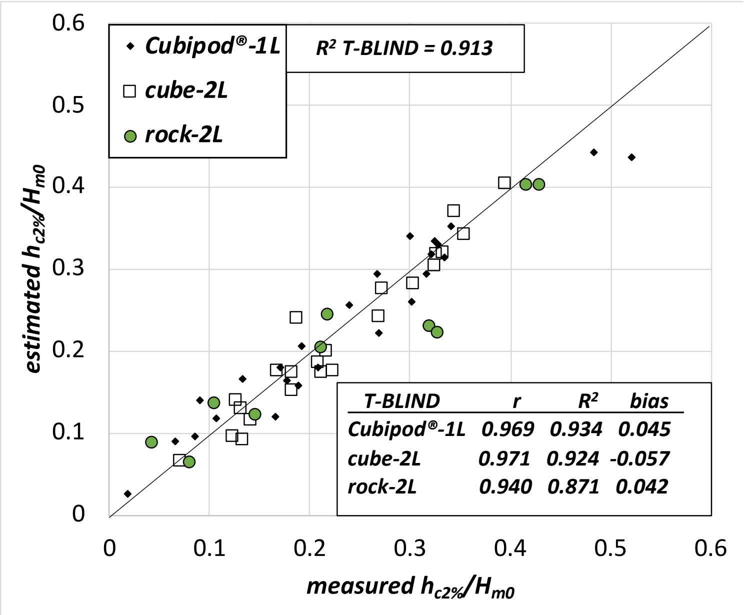

T-BLIND	r	R²	bias
Cubipod®-1L	0.969	0.934	0.045
cube-2L	0.971	0.924	-0.057
rock-2L	0.940	0.871	0.042

Fig. 5. 9. Comparison between measured and estimated $h_{c2\%}(B/2)/H_{m0}$ with the NN models on the final blind test subset (*T-BLIND*).

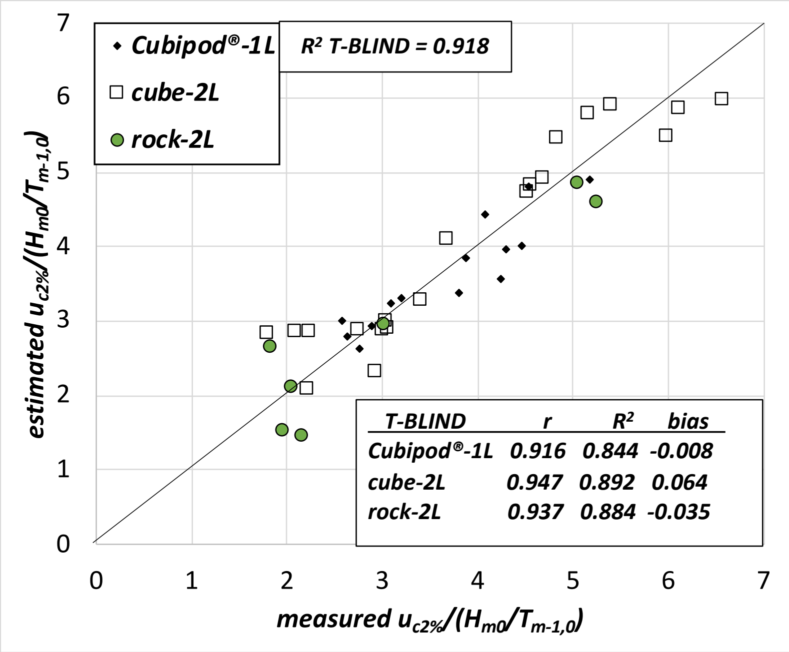

T-BLIND	r	R^2	bias
Cubipod®-1L	0.916	0.844	-0.008
cube-2L	0.947	0.892	0.064
rock-2L	0.937	0.884	-0.035

Fig. 5. 10. Comparison between measured and estimated $u_{c2\%}(B/2)/(H_{m0}/T_{m-1,0})$ with the NN models on the final blind test subset (*T-BLIND*).

5.3.3.2 Influence of m *on* $h_{c2\%}$(B/2) *and* $u_{c2\%}$(B/2)

In order to assess the influence of *m* on $h_{c2\%}(B/2)$ and $u_{c2\%}(B/2)$, wave conditions were selected in the wave generation zone (H_{m0} and $T_{m-1,0}$ in the wave generation zone, denoted here as $H_{m0,g}$ and $T_{m-1,0,g}$, respectively) and they were propagated along 5 numerical flumes using the SwanOne model (*Verhagen et al.*, *2008*) until a distance of 3*h* from the toe of the structure. Bottom slope (*m*) values were varied within the tested range (*m* = 2.0%, 2.5%, 3.0%, 3.5% and 4.0%). Figure 5.11 illustrates the wave flumes considered in this section.

After that, the propagated wave characteristics were used together with the p50% NNs to simulate $h_{c2\%}(B/2)$ and $u_{c2\%}(B/2)$. Consequently, $h_{c2\%}(B/2)$ and $u_{c2\%}(B/2)$ were calculated for 5 bottom slope configurations using the same wave characteristics in the wave generation zone. Figures 5.12 and 5.13 show the evolution of the dimensionless $h_{c2\%}(B/2)$ and $u_{c2\%}(B/2)$ as function of *m* for the three tested armor layers (Cubipod®-1L, cube-2L and rock-2L) and different wave conditions.

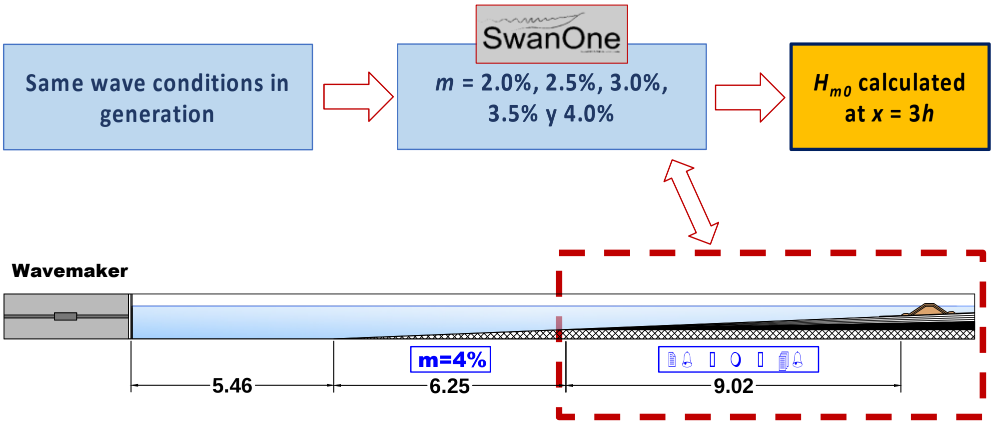

Fig. 5. 11. Scheme of the numerical flumes used for propagating with SwanOne.

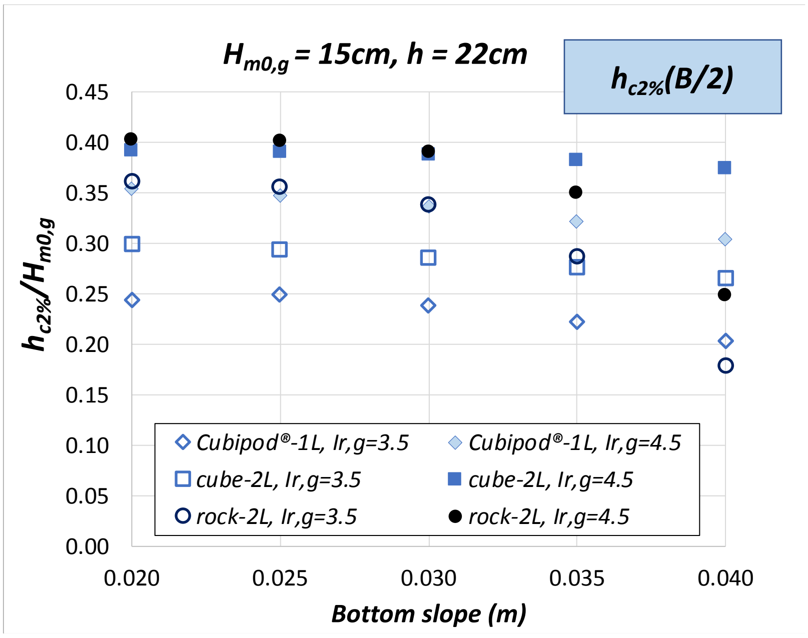

Fig. 5. 12. Influence of *m* on dimensionless $h_{c2\%}(B/2)$. *Ir,g* denotes the surf similarity parameter calculated using $H_{m0,g}$ and $T_{m-1,0,g}$.

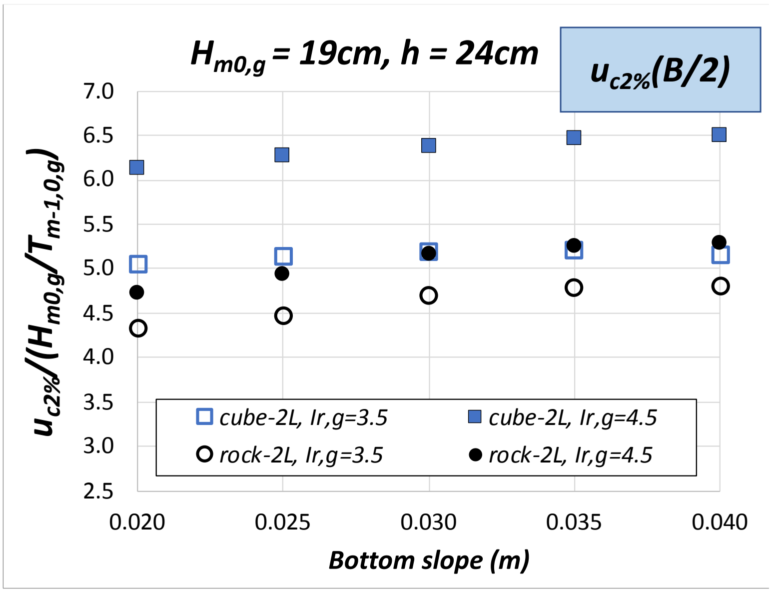

Fig. 5. 13. Influence of *m* on dimensionless $u_{c2\%}(B/2)$. *Ir,g* denotes the surf similarity parameter calculated using $H_{m0,g}$ and $T_{m-1,0,g}$.

As shown in Figures 5.12 and 5.13, *m* did affect both $h_{c2\%}(B/2)$ and $u_{c2\%}(B/2)$; the dimensionless $h_{c2\%}(B/2)$ decreased for increasing values of *m* whereas the dimensionless $u_{c2\%}(B/2)$ slightly increased for increasing values of *m*.

5.4. A new method to estimate the overtopping layer thickness (OLT) on mound breakwater crests

Mares-Nasarre et al. (2019) described a method to estimate $h_{c2\%}(B/2)$ and $h_c(B/2)$ on overtopped mound breakwaters under depth-limited breaking wave conditions with m = 2%. The present section presents new formulas to calculate $h_{c2\%}(B/2)$ and $h_c(B/2)$ on overtopped mound breakwaters under depth-limited breaking wave conditions considering the bottom slope effect (m = 2% and 4%).

5.4.1. OLT exceeded by 2% of the incoming waves, $h_{c2\%}$ (B/2)

Here, the methodology to build-up new estimators for $h_{c2\%}(B/2)$ is described. First, p50% NNs implemented in Section 5.3 were used to calculate the trends of the 4 dimensionless explanatory variables: m, R_c/H_s, $Ir_{m-1,0} = \tan\alpha/(2\pi H_{m0}/g/T_{m-1,0}^2)$ and h/H_s. An almost linear model was proposed. Second, linear regression was applied as a first approach to estimate the coefficients for the new models. Since negative values of $h_{c2\%}(B/2)$ are not allowed, the model was not fully linear. Thus, bootstrapping technic was used to determine the final coefficients of the new estimators as well as their variability. Linear regression results were used to determine the initial solution for the bootstrapping optimization procedure.

5.4.1.1 Influence of explanatory variables on $h_{c2\%}$ (B/2)/H_{m0}

Bottom slope (*m*) trend is presented using the simulations conducted with the p50% NN of Cubipod®-1L for R_c/H_{m0} = 0.5, 1.0 and 1.5, $Ir_{m-1,0}$ = 4.0 and h/H_{m0} = 2.0. As shown in Figure 5.14a, $h_{c2\%}(B/2)/H_{m0}$ decreased with increasing values of *m*. Since two values for *m* = 2% and 4% were tested, a linear approach is reasonable. Figure 5.14b illustrates the differences between the three armor layers: Cubipod®-1L, cube-2L and rock-2L for R_c/H_{m0} = 0.5. Trend for rock-2L seems steeper than that for Cubipod®-1L and cube-2L.

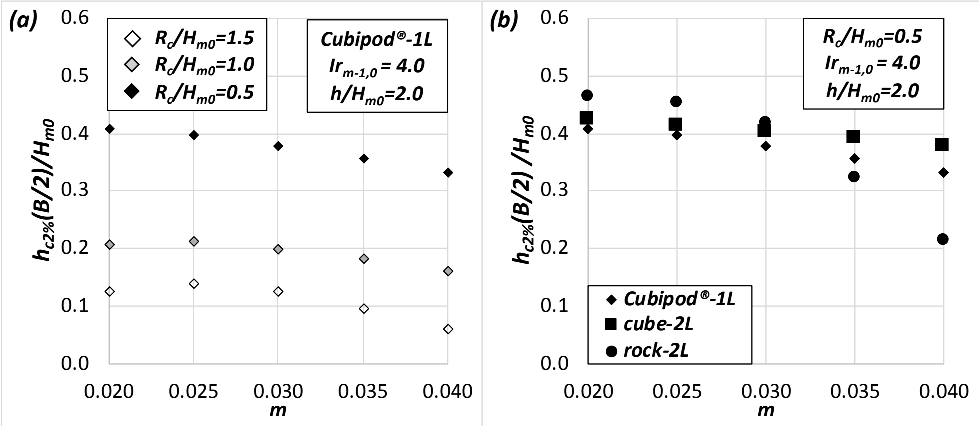

Fig. 5. 14. Influence of *m* on $h_{c2\%}(B/2)/H_{m0}$ with $Ir_{m-1,0}$ = 4.0, h/H_{m0} = 2.0 and constant R_c/H_{m0}.

Dimensionless crest freeboard (R_c/H_{m0}) was simulated first using the p50% NN of Cubipod®-1L for *m* = 4%, $Ir_{m-1,0}$ = 3.5, 4.0 and 4.5 and h/H_{m0} = 2.0. In Figure 5.15a, it is observed that $h_{c2\%}(B/2)/H_{m0}$ decreases for increasing values of R_c/H_{m0} in an approximately linear trend. In Figure 5.15b simulations using p50% NNs of the three armor layers were performed using $Ir_{m-1,0}$ = 4.0. No significant differences between the three armor layers were observed for high values of R_c/H_{m0}.

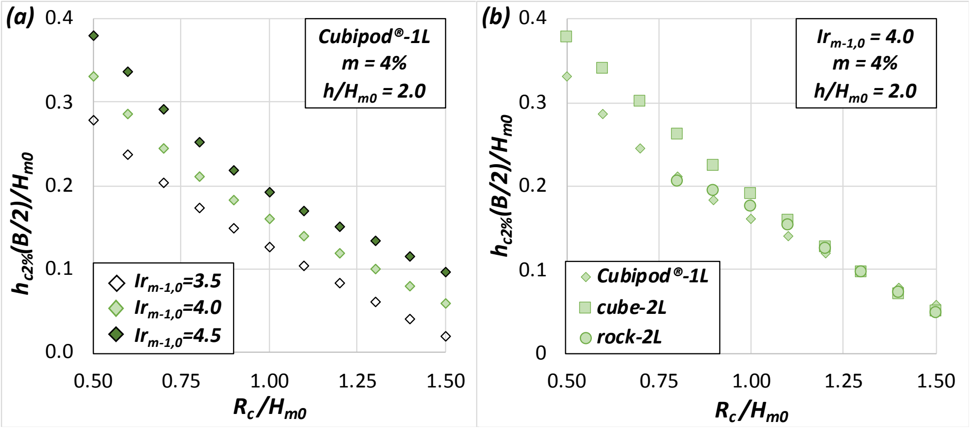

Fig. 5. 15. Influence of R_c/H_{m0} on $h_{c2\%}(B/2)/H_{m0}$ with m = 4%, h/H_{m0} = 2.0 and constant $Ir_{m-1,0}$.

The influence of the Iribarren's number or the breaker parameter ($Ir_{m-1,0}$) was analyzed using simulations conducted with the p50% NN of Cubipod®-1L for m = 2.5%, R_c/H_{m0} = 0.5, 1.0 and 1.5 and h/H_{m0} = 2.5. Figure 5.16a shows increasing values of $h_{c2\%}(B/2)/H_{m0}$ for increasing values $Ir_{m-1,0}$; a linear trend is observed. Difference between the three armor layers is illustrated in Figure 5.16b for R_c/H_{m0} = 1.0. Trend for rock-2L seems milder than that for Cubipod®-1L and cube-2L.

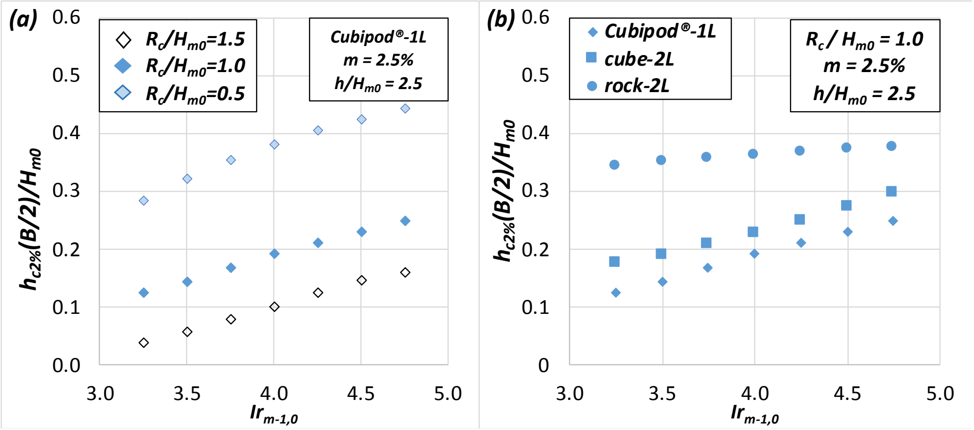

Fig. 5. 16. Influence of $Ir_{m-1,0}$ on $h_{c2\%}(B/2)/H_{m0}$ with for m = 2.5%, h/H_{m0} = 2.5 and constant R_c/H_{m0}.

Dimensionless water depth (h/H_{m0}) trend is presented in Figure 5.17 using the simulations performed with the p50% NN of Cubipod®-1L for m = 2.5%, R_c/H_{m0} = 0.5, 1.0 and 1.5 and $Ir_{m-1,0}$ = 3.5. Figure 5.17a shows how $h_{c2\%}(B/2)/H_{m0}$ decreases with increasing values of h/H_{m0}. Figure 5.17b presents the comparison between the three armor layers for R_c/H_{m0} = 0.5. h/H_{m0} had almost no effect on $h_{c2\%}(B/2)/H_{m0}$ for cube-2L and rock-2L armors.

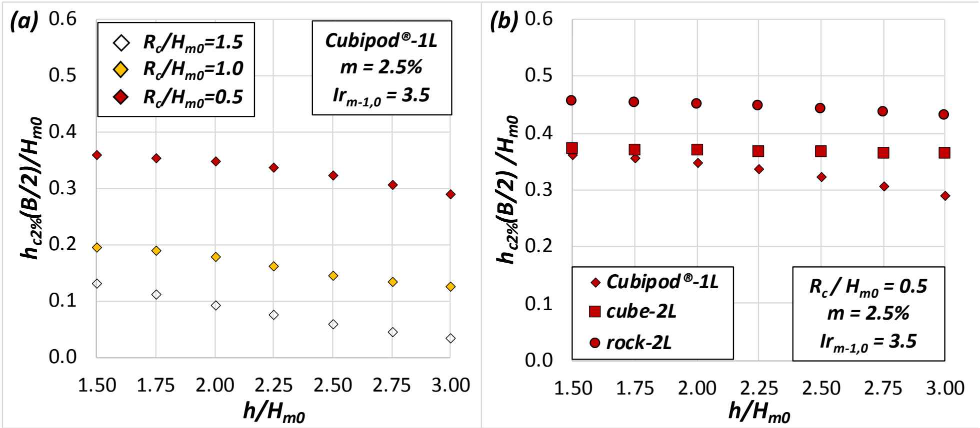

Fig. 5. 17. Influence of h/H_{m0} on $h_{c2\%}(B/2)/H_{m0}$ with for m = 2.5%, $Ir_{m-1,0}$ = 3.5 and constant R_c/H_{m0}.

5.4.1.2 A new method to estimate $h_{c2\%}$ (B/2)

In Section 5.4.1.1, approximately-linear trends were observed for the explanatory variables of $h_{c2\%}(B/2)/H_{m0}$. Here, a new model to better predict $h_{c2\%}(B/2)/H_{m0}$ is proposed as

$$\frac{h_{c2\%}(B/2)}{H_{m0}} = C1 + C2\,m + C3\left(\frac{R_c}{H_{m0}} - 1\right) + C4\,Ir_{m-1,0} + C5\,\frac{h}{H_{m0}} \geq 0 \qquad (5.4)$$

where *C1*, *C2*, *C3*, *C4* and *C5* are coefficients to be calibrated. *C1* to *C5* were fitted for each armor layer (Cubipod®-1L, cube-2L and rock-2L) since different behaviors were observed for the studied explanatory variables (see Figures 5.14 to 5.17). As negative values of $h_{c2\%}(B/2)/H_{m0}$ are not allowed, Eq. 5.4 is not fully linear and conventional linear regression techniques are not adequate to fit the coefficients *C1* to *C5*. Thus, *C1* to *C5* were calibrated using a nonlinear multivariable optimization algorithm without restrictions (*The MathWorks Inc., 2019*). This algorithm requires an initial solution to start the iterative optimization process, so conventional linear regression was conducted to obtain such initial solution. Tables 5.1 to 5.3 show the initial solutions obtained with the linear regression for each armor layer. As shown in Tables 5.1 to 5.3, some variables presented p-values>α_s=0.05. However, since Eq. 5.4 is not a fully linear model, no variables were discarded in this phase.

Coefficient	Variable	Estimation (x_e)	p-value
C1	Constant	0.010	0.65
C2	m	-4.075	0.00
C3	$R_c/H_{m0} - 1$	-0.323	0.00
C4	$Ir_{m-1,0}$	0.092	0.00
C5	h/H_{m0}	-0.029	0.00

Table 5. 1. Linear regression results for Cubipod®-1L.

Coefficient	Variable	Estimation (x_e)	p-value
C1	Constant	0.025	0.51
C2	m	-2.053	0.90
C3	$R_c/H_{m0} - 1$	-0.278	0.00
C4	$Ir_{m-1,0}$	0.082	0.00
C5	h/H_{m0}	-0.024	0.27

Table 5. 2. Linear regression results for cube-2L.

Coefficient	Variable	Estimation (x_e)	p-value
C1	Constant	0.331	0.00
C2	m	-9.935	0.00
C3	$R_c/H_{m0} - 1$	-0.432	0.00
C4	$Ir_{m-1,0}$	0.077	0.00
C5	h/H_{m0}	-0.028	0.50

Table 5. 3. Linear regression results for rock-2L.

The final nonlinear fitting coefficients $C1$ to $C5$ in Eq. 5.4 were obtained by minimizing the mean squared error (MSE), calculated as

$$MSE = \frac{1}{N_o} \sum_{i=1}^{N_o} (o_i - e_i)^2 \tag{5.5}$$

where N_o is the number of observations and o_i and e_i are the observed and estimated values. In order to assess the sensibility of the selected algorithm to the initial solution, 1,000 optimization processes were conducted on the original dataset. In each optimization, the initial solution was randomly calculated for each coefficient within the interval ($x_e - 3\sigma$, $x_e + 3\sigma$), where x_e represents the estimation provided by the linear regression process and σ, the variance of the estimation. The maximum number of iterations was set to 10,000 to ensure convergence ($\sigma < 0.01$). Low sensibility of the optimization algorithm to the given initial solution was observed.

Similarly to *van Gent et al.* (*2007*) and *Molines et al.* (*2018*) , the bootstrapping technique was applied together with the non-linear optimization algorithm to determine the coefficients *C1* to *C5* as well as their variability. The bootstrap resample technique involves the random selection of N_D data from a dataset with N_D data, so each datum has a probability of $1/N_D$ to be selected each time. Therefore, some data are not selected while other data may be selected once or more than once in each resample. Using this technique, p5%, p50% and p95% were obtained for the fitted coefficients (*C1* to *C5*) and the *MSE*.

In order to assess the significance of the considered explanatory variables, they were introduced one by one in the model following the structure in Eq. 5.4. First, four models composed by one of the explanatory variables and the constant term (*C1*) following Eq. 5.4 were optimized. The percentage of the variance explained by each model was also calculated. After that, the optimization process was repeated keeping the explanatory variable which explained the highest percentage of the variance in the previous step and adding each of the three missing explanatory variables. This process was repeated until the four explanatory variables were included in the model; a hierarchy of the influence of the explanatory variables on $h_{c2\%}(B/2)/H_{m0}$ was obtained. Finally, the significance of the constant term (*C1*) was assessed. In order to determine if an additional explanatory variable improved the prediction of $h_{c2\%}(B/2)/H_{m0}$, the adjusted coefficient of determination (R^2_{adj}) proposed by *Theil* (*1961*) was calculated using Eq. 5.6 in every step of the optimization process.

$$R^2_{adj} = 1 - (1 - R^2)\frac{N_D - 1}{N_D - N_P - 1} \tag{5.6}$$

where N_D is the number of data available and N_P is the number of explanatory variables. R^2_{adj} takes into account not only the goodness of fit but also the number of coefficients and data used to fit the model. Therefore, the model with the highest R^2_{adj} is selected for every armor layer; the five fitting coefficients will not always be included in the proposed model. The evolution of the median value of R^2_{adj} and its 90% error band along the aforementioned optimization process for each armor layer model is shown in Figures 5.18 to 5.20. The number of explanatory variables in the final model is highlighted in red and the explanatory variable which maximized R^2_{adj} in each step is also indicated.

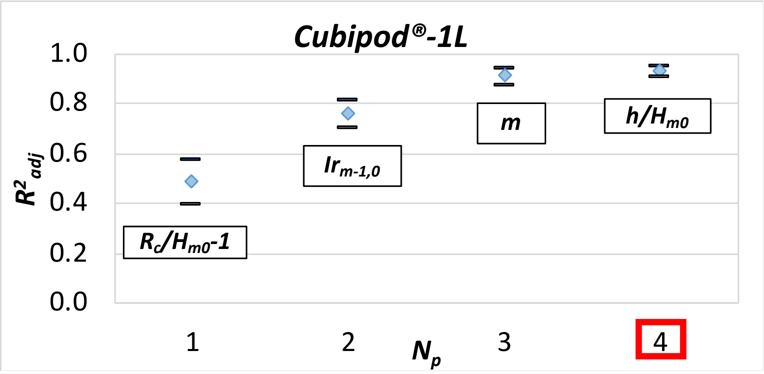

Fig. 5. 18. Influence of the number of explanatory variables (N_p) on R^2_{adj} for Cubipod®-1L to estimate $h_{c2\%}(B/2)/H_{m0}$.

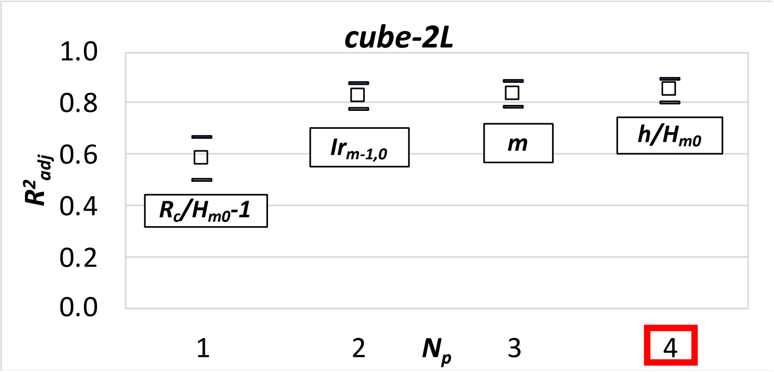

Fig. 5. 19. Influence of the number of explanatory variables (N_p) on R^2_{adj} for cube-2L to estimate $h_{c2\%}(B/2)/H_{m0}$.

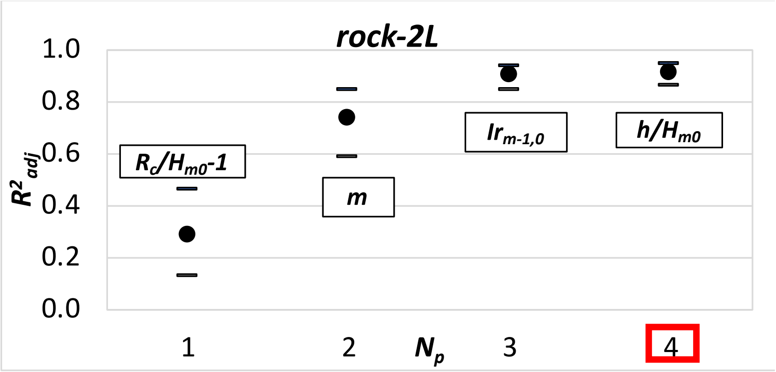

Fig. 5. 20. Influence of the number of explanatory variables (N_p) on R^2_{adj} for rock-2L to estimate $h_{c2\%}(B/2)/H_{m0}$.

As shown in Figures 5.18 to 5.20, the explanatory variable which explained the highest percentage of the variance was R_c/H_{m0} independently of the studied armor layer. Since the four explanatory variables resulted significant when applying R^2_{adj}, they were included in the model. Finally, the significance of the constant term (*C1*) was evaluated. The optimization process was repeated using $C1$=0 and R^2_{adj} was again applied. $C1 \neq 0$ was proposed for rock-2L armor whereas $C1$=0 was proposed for Cubipod®-1L and cube-2L armors.

The variability in the fitted coefficients from the bootstrapping resamples was considered to determine the number of significant figures in the coefficients (*C1* to *C5*) of the final formula. Only one significant figure was recommended for *C1*, *C2* and *C5* (coefficient of variation in the range: $7\% \leq CV \leq 45\%$) whereas a maximum of two significant figures was reasonable for *C3* and *C4* ($4\% \leq CV \leq 13\%$). Table 5.4 presents the final coefficients as well as the goodness-of-fit metrics for Eq. 5.4 for the three armor layers.

Armor layer	***C1***	***C2***	***C3***	***C4***	***C5***	***r***	R^2	***bias***
Cubipod®-1L	0	-4	-1/3	0.095	-0.03	0.957	0.914	0.030
cube-2L	0	-2	-0.3	0.085	-0.02	0.909	0.814	0.011
rock-2L	1/3	-10	-0.45	0.08	-0.03	0.951	0.903	0.072

Table 5. 4. Coefficients and goodness-of-fit metrics for Eq. 5.4.

Figure 5.21 shows the comparison between the measured and estimated $h_{c2\%}(B/2)/H_{m0}$ using the new predictors developed in this study (Eq. 5.4 with coefficients in Table 5.4) as well as the 90% error band. Good agreement is observed; R^2 = 0.876 and *bias* = 0.030.

The *MSE* remained stable with increasing values of $h_{c2\%}(B/2)/H_{m0}$. Therefore, assuming a Gaussian error distribution, the 90% error band can be estimated as

$$\left.\frac{h_{c2\%}(B/2)}{H_{m0}}\right|_{5\%}^{95\%} = \frac{h_{c2\%}(B/2)}{H_{m0}} \pm 1.64\sqrt{var(\varepsilon)} = \frac{h_{c2\%}(B/2)}{H_{m0}} \pm 0.064 \qquad (5.7)$$

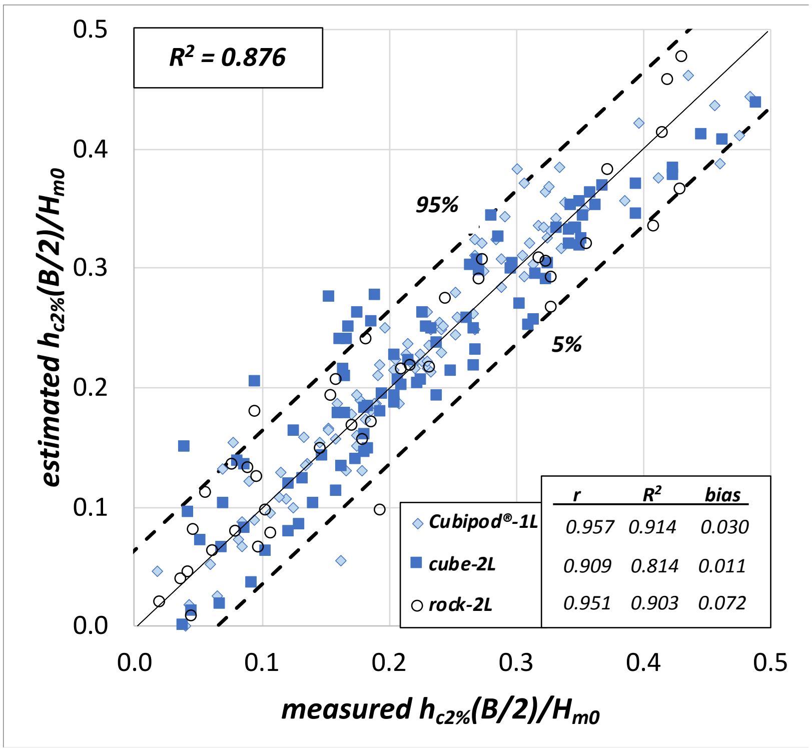

Fig. 5. 21. Comparison between measured and estimated $h_{c2\%}(B/2)/H_{m0}$ using Eq. 5.4 and coefficients in Table 5.4.

5.4.2. Distribution function for the extreme values of OLT, $h_c(B/2)$

An accurate description of extreme overtopping events is key to assess both the pedestrians' safety on mound breakwater crests and the hydraulic stability of mound breakwater crest and rare side. In Section 5.4.1, new predictors to estimate $h_{c2\%}(B/2)$ were developed. Therefore, the OLT distribution during the most severe wave storms is required for mound breakwater design. *Hughes et al. (2012)* pointed out that the extreme tail of the distribution is best described when only considering the low exceedance events. Hence, the distribution function to describe $h_c(B/2)$ with exceedance probabilities below 2% is proposed in this section.

As reported in *Mares-Nasarre et al. (2019)*, best results when describing the distribution function of $h_c(B/2)$ with exceedance probabilities below 2% were obtained with the 1-parameter Exponential distribution, given by

$$F\left(\frac{h_c(B/2)}{h_{c2\%}(B/2)}\right) = 1 - exp\left(-C_h\frac{h_c(B/2)}{h_{c2\%}(B/2)}\right) \qquad (5.8)$$

where $h_c(B/2)$ is the OLT value with exceedance probabilities under 2% and C_h is an empirical coefficient to be calibrated. C_h was estimated for each physical test using the 20 (1,000 waves × 2%) highest measured values of OLT. The exceedance probability assigned to each OLT value was calculated as $N_m/(N_w+1)$, where N_m is the rank of the OLT measured value and N_w represents the number of waves. Note that estimated $h_{c2\%}(B/2)$ using Eq. 5.4 with coefficients in Table 5.4 was applied. $h_{c2\%}(B/2) = 0$ for 3 tests, so they were not included in the analysis; 122 and 110 tests were used for $m = 2\%$ and 4%, respectively. The initial calibrated coefficients were C_h=4.04 for m=2% and C_h=3.91 for m=4%. The non-parametric Mood Median test (see Section 3.6.6) was applied in order to determine whether the difference between the median values of C_h for the two bottom slopes was significant. The null hypothesis (H_0) corresponded to both median being equal; H_0 was not rejected with a significance level α_s=0.05. Thus, best estimation was $C_h = 4$. Figure 5.22 presents the comparison between the measured and estimated $h_c(B/2)/H_{m0}$ using Eq. 5.8 together with $C_h = 4$. The 90% error band is also depicted. Good results were observed (R^2=0.811).

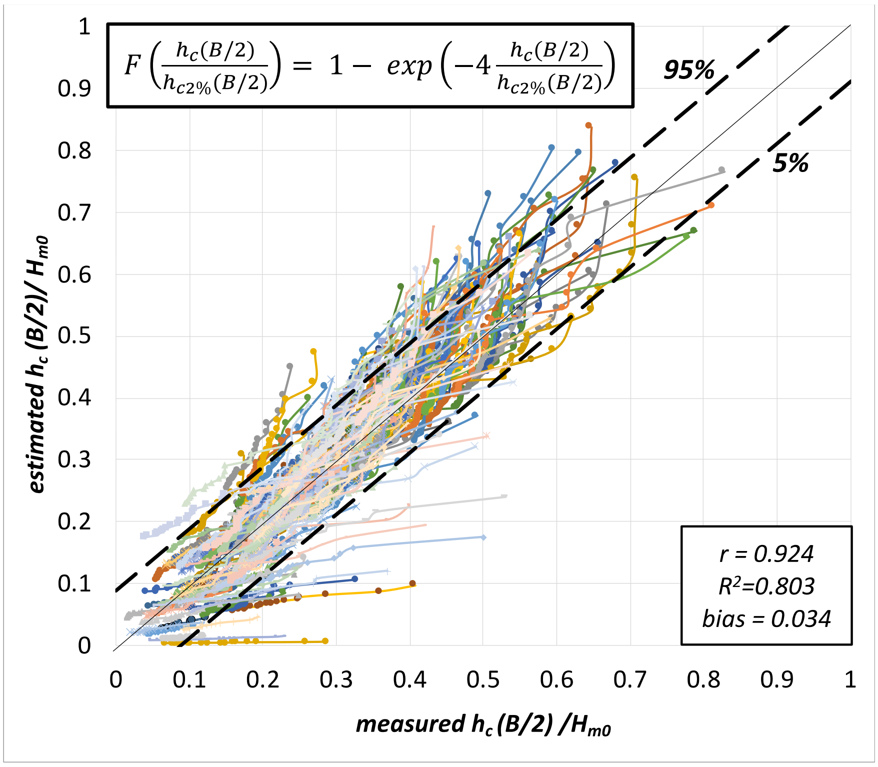

Fig. 5. 22. Comparison between measured and estimated $h_c(B/2)/H_{m0}$ using Eq. 5.8 with C_h = 4.

Since the *MSE* remained stable for increasing values of $h_c(B/2)/H_{m0}$, assuming a Gaussian error distribution, the 90% error band can be estimated as

$$\left.\frac{h_c(B/2)}{H_{m0}}\right|_{5\%}^{95\%} = \frac{h_c(B/2)}{H_{m0}} \pm 1.64\sqrt{var(\varepsilon)} = \frac{h_c(B/2)}{H_{m0}} \pm 0.087 \tag{5.9}$$

Figure 5.23 illustrates an example of the fitting of two datasets for Cubipod®-1L armor with the proposed 1-parameter Exponential distribution in exponential plot.

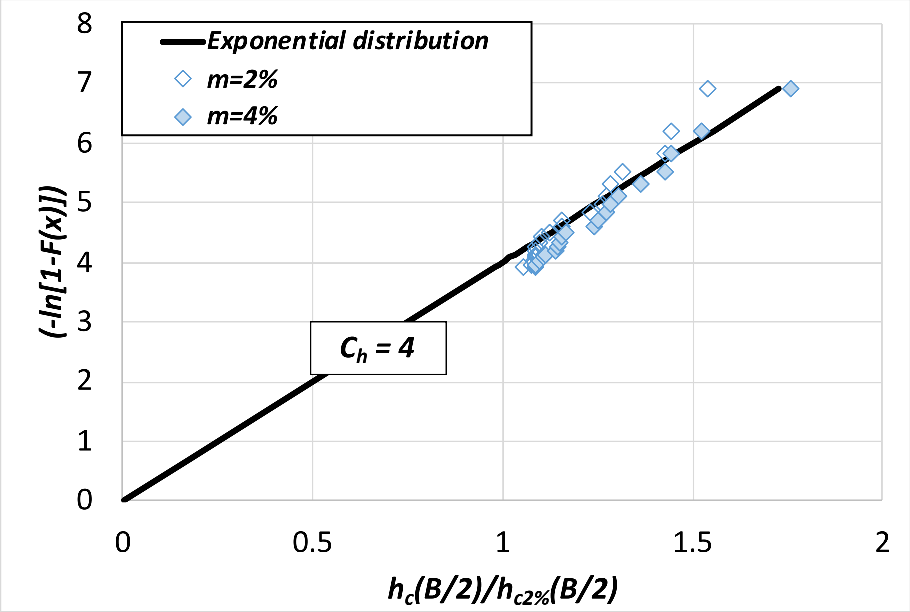

Fig. 5. 23. Example of cumulative distribution function of $h_c(B/2)$ in equivalent probability plot.

5.5. A new method to estimate overtopping flow velocity (OFV) on mound breakwaters crests

Methods in the literature to estimate OFV exceeded by 2% of the incoming waves, $u_{c2\%}(B/2)$, were reviewed in Section 2.5. Most of them (*Schüttrumpf and Van Gent, 2003; Mares-Nasarre et al., 2019*) were based on the correlation between the statistics of OLT and OFV, so they required to first estimate $h_{c2\%}(B/2)$ before calculating $u_{c2\%}(B/2)$ with the subsequent accumulated errors. Here, a new explicit empirical formula to estimate $u_{c2\%}(B/2)$ is developed based on the four input explanatory variables described in Section 5.3.1 (m, R_c/H_{m0}, $Ir_{m-1,0}$ and h/H_{m0}). The distribution of OFV during the most severe wave storms is also analyzed.

5.5.1. OFV exceeded by 2% of the incoming waves, $u_{c2\%}(B/2)$

In this section, a new predictor for $u_{c2\%}(B/2)$ was developed based on the dimensionless explanatory variables described in Section 5.3.1 (m, R_c/H_{m0}, $Ir_{m-1,0}$ and h/H_{m0}). Trends were identified using the simulations provided by the p50% NNs implemented in Section 5.3. Finally, the fitting procedure exposed in Section 5.4.1 was applied in order to detect the significant variables to calculate $u_{c2\%}(B/2)$ as well as to calibrate the final empirical coefficients.

5.5.1.1 *Influence of explanatory variables on* $u_{c2\%}(B/2)/(H_{m0}/T_{m-1,0})$

Bottom slope (m) trend is shown in Figure 5.24 using the simulations conducted with the p50% NN for cube-2L, R_c/H_{m0} = 0.5, 1.0 and 1.5, $Ir_{m-1,0}$ = 4.0 and h/H_{m0} = 2.0. In Figure 5.24a, it is observed how $u_{c2\%}(B/2)/(H_{m0}/T_{m-1,0})$ slightly decreases for increasing values of m. Figure 5.24b presents the differences between the three armor layers: Cubipod®-1L, cube-2L and rock-2L for R_c/H_{m0} = 0.5. $u_{c2\%}(B/2)/(H_{m0}/T_{m-1,0})$ decreases for increasing values of m for cube-2L and rock-2L while $u_{c2\%}(B/2)/(H_{m0}/T_{m-1,0})$ increases for increasing values of m for Cubipod®-1L. Note that $u_{c2\%}(B/2)/(H_{m0}/T_{m-1,0})$ also includes the effect of m through wave characteristics. Since two values of m were tested in this study, a linear trend of m is reasonable.

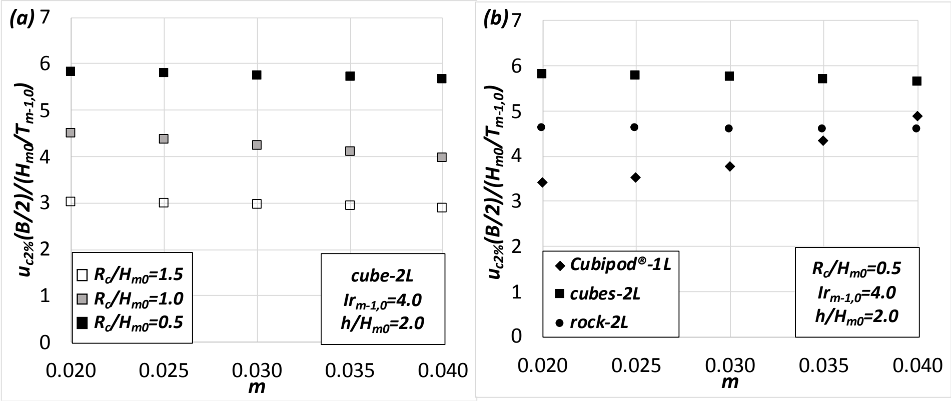

Fig. 5. 24. Influence of *m* on $u_{c2\%}(B/2)/(H_{m0}/T_{m-1,0})$ with $Ir_{m-1,0}$=4.0, h/H_{m0}=2.0 and constant R_c/H_{m0}.

Dimensionless crest freeboard (R_c/H_{m0}) was simulated first using the p50% NN of cube-2L for m = 3%, $Ir_{m-1,0}$ = 3.5, 4.0 and 4.5 and h/H_{m0} = 2.0. In Figure 5.25a is shown $u_{c2\%}(B/2)/(H_{m0}/T_{m-1,0})$ decreases for increasing values of R_c/H_{m0}. In Figure 5.25b simulations using the p50% NNs of the three armor layers were performed using $Ir_{m-1,0}$ = 4.0.

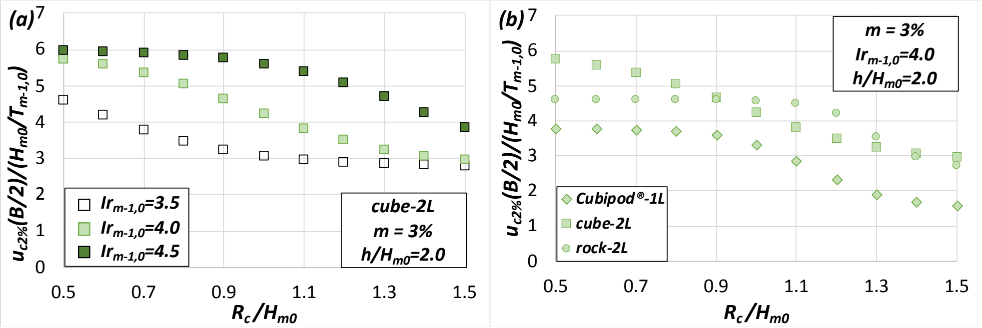

Fig. 5. 25. Influence of R_c/H_{m0} on $u_{c2\%}(B/2)/(H_{m0}/T_{m-1,0})$ with m=3%, h/H_{m0}=2.0 and constant $Ir_{m-1,0}$.

Iribarren's number or the breaker parameter ($Ir_{m-1,0}$) influence was analyzed using simulations conducted with the p50% NN of cube-2L for m = 2.5%, R_c/H_{m0} = 0.5, 1.0 and 1.5 and h/H_{m0} = 2.5. Figure 5.26a shows how $u_{c2\%}(B/2)/(H_{m0}/T_{m-1,0})$ grows for increasing values of $Ir_{m-1,0}$. A quadratic trend was observed. The difference between the three armor layers is illustrated in Figure 5.26b for R_c/H_{m0} = 1.5. The trend seemed to be similar for cube-2L and rock-2L.

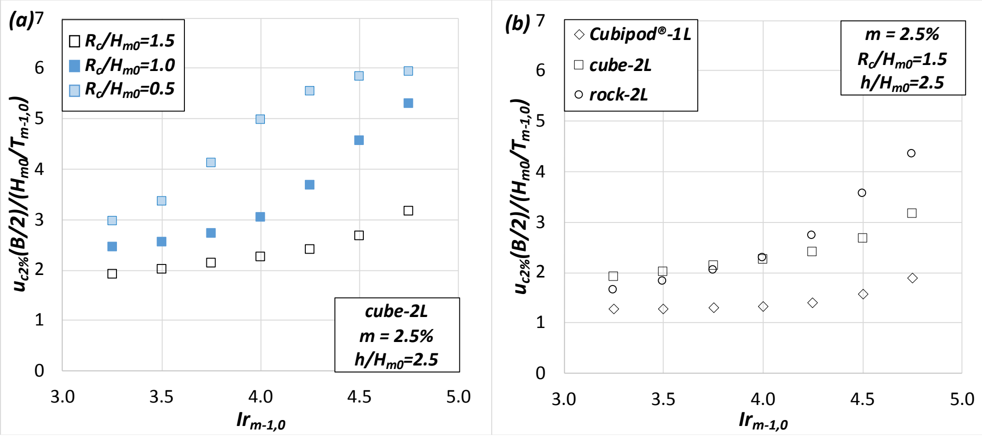

Fig. 5. 26. Influence of $Ir_{m-1,0}$ on $u_{c2\%}(B/2)/(H_{m0}/T_{m-1,0})$ with m=2.5%, h/H_{m0}=2.5 and constant R_c/H_{m0}.

The dimensionless water depth (h/H_{m0}) trend was simulated with the p50% NN of cube-2L for m = 2.5%, R_c/H_{m0} = 0.5, 1.0 and 1.5 and $Ir_{m-1,0}$ = 3.5. In Figure 5.27a, it is observed how $u_{c2\%}(B/2)/(H_{m0}/T_{m-1,0})$ decreases with increasing values of h/H_{m0}. Figure 5.27b illustrates the comparison between the three armor layers for R_c/H_{m0} = 1.0.

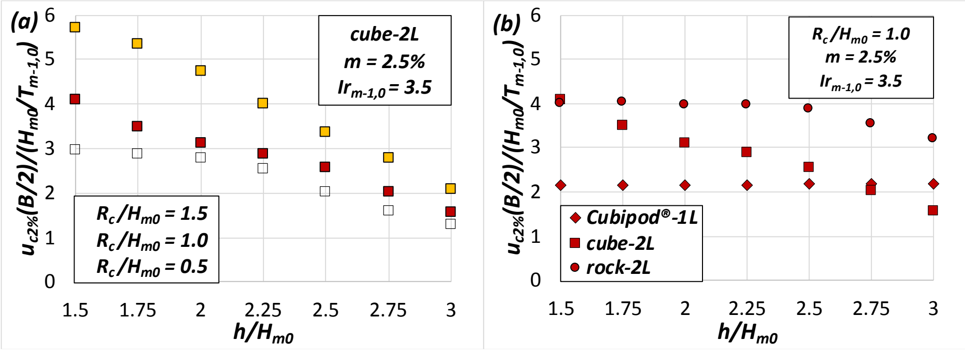

Fig. 5. 27. Influence of h/H_{m0} on $u_{c2\%}(B/2)/(H_{m0}/T_{m-1,0})$ with m=2.5%, $Ir_{m-1,0}$=3.5 and constant R_c/H_{m0}.

5.5.1.2 A new method to estimate $u_{c2\%}$ (B/2)

In Figures 5.24 to 5.27, the influence of the considered explanatory variables on $u_{c2\%}(B/2)/(H_{m0}/T_{m-1,0})$ was analyzed. Similar to Section 5.4.1, every armor layer was analyzed independently, since different behaviors were observed for the explanatory variables. Eq. 5.10 presents the initial model.

$$\frac{u_{c2\%}(B/2)}{\left(\frac{H_{m0}}{T_{m-1,0}}\right)} = D1 + D2\, m + D3\left(\frac{R_c}{H_{m0}} - 1\right) + D4\, {Ir_{m-1,0}}^2 + D5\frac{h}{H_{m0}} \geq 0 \qquad (5.10)$$

where $D1$, $D2$, $D3$, $D4$ and $D5$ are empirical coefficients to be calibrated. Since Eq. 5.10 is not linear, bootstrapping technique was applied to calculate the value of the final coefficients of the new estimators as well as their variability.

Following the procedure described in Section 5.4.1.2, the explanatory variables were introduced one by one in the model (see Eq. 5.10) and a hierarchy of their significance was derived based on R^2_{adj}. Finally, new predictors for $u_{c2\%}(B/2)$ were proposed for every armor layer. The evolution of the median value of R^2_{adj} and the 90% error band along the aforementioned process for each armor layer model is presented in Figures 5.28 to 5.30. The number of explanatory variables in the final model is emphasized in red and the explanatory variable which maximized R^2_{adj} in each step is also specified.

As shown in Figures 5.28 to 5.30, the explanatory variable which explained the highest percentage of the variance was $Ir_{m-1,0}$ in the three studied cases. The four explanatory variables resulted significant, so they were all included in the proposed model. In order to assess the significance of the constant term ($D1$) using R^2_{adj}, the optimization process was repeated considering $D1$=0. $D1 \neq 0$ was recommended for the three studied armor layers: Cubipod®-1L, cube-2L and rock-2L.

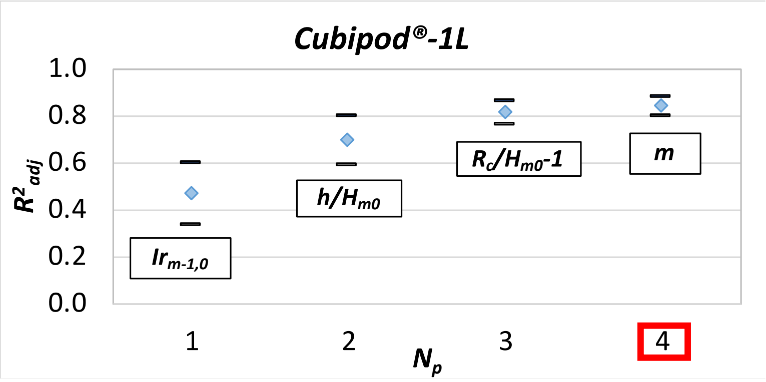

Fig. 5. 28. Influence of the number of explanatory variables (N_p) on R^2_{adj} for Cubipod®-1L to estimate $u_{c2\%}(B/2)/(H_{m0}/T_{m-1,0})$.

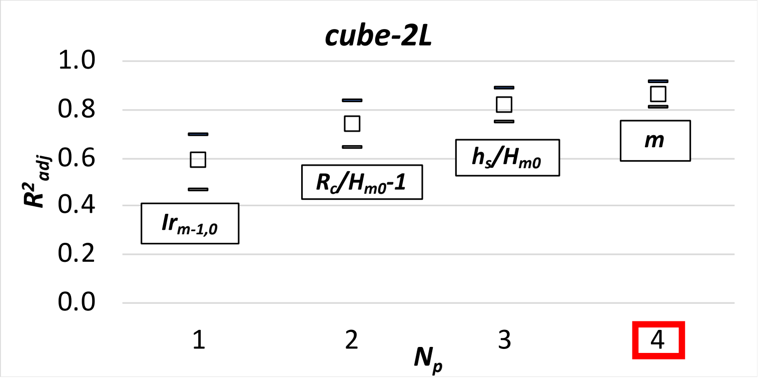

Fig. 5. 29. Influence of the number of explanatory variables (N_p) on R^2_{adj} for cube-2L to estimate $u_{c2\%}(B/2)/(H_{m0}/T_{m-1,0})$.

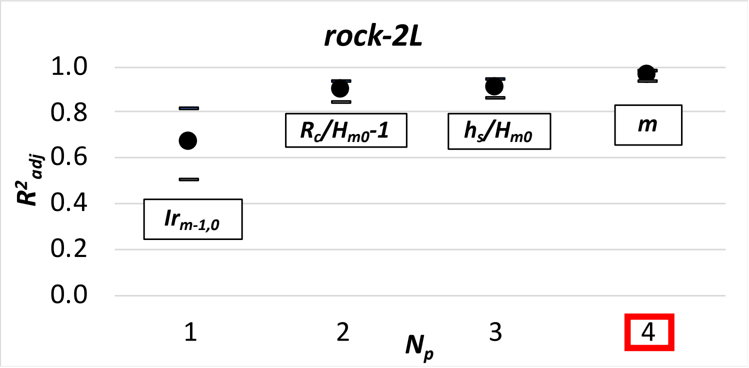

Fig. 5. 30. Influence of the number of explanatory variables (N_p) on R^2_{adj} for rock-2L to estimate $u_{c2\%}(B/2)/(H_{m0}/T_{m-1,0})$.

The number of significant figures in the final coefficients (*D1* to *D5*) was based on the variability from the bootstrapping resamples. Thus, only one significant figure was proposed for *D1*, *D2*, *D3* and *D5* (9%≤*CV*≤41%) whereas a maximum of two significant figures was reasonable for *D4* (5%≤*CV*≤9%). Table 5.5 presents the final coefficients as well as the goodness-of-fit metrics for Eq. 5.10 for the three armor layers.

Armor layer	*D1*	*D2*	*D3*	*D4*	*D5*	*r*	R^2	*bias*
Cubipod®-1L	2	20	-2	0.2	-1	0.920	0.832	-0.014
cube-2L	4	-30	-2	0.2	-1	0.917	0.845	0.011
rock-2L	2	-30	-3	0.25	-0.5	0.972	0.934	-0.023

Table 5. 5. Coefficients and goodness-of-fit metrics for Eq. 5.10.

Figure 5.31 illustrates the goodness-of-fit between the measured and estimated $u_{c2\%}(B/2)/(H_{m0}/T_{m-1,0})$ using the new predictors developed in this study (Eq. 5.10 with coefficients in Table 5.5). The 90% error band is also presented. Good agreement is observed (R^2 = 0.866 and *bias* = -0.005).

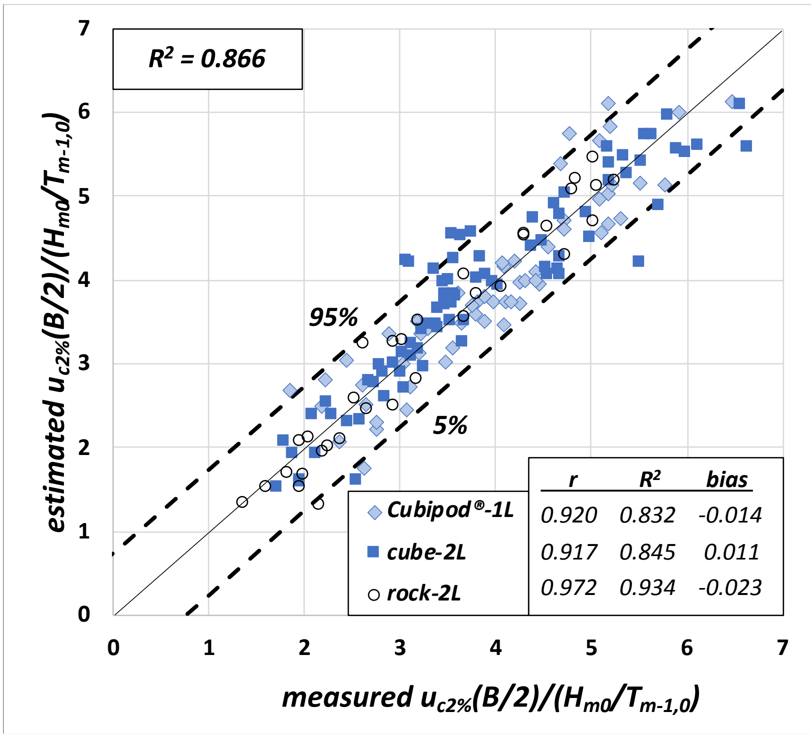

Fig. 5. 31. Comparison between measured and estimated $u_{c2\%}(B/2)/(H_{m0}/T_{m-1,0})$ using Eq. 5.10 and coefficients in Table 5.5.

As the *MSE* remained constant for increasing values of $u_{c2\%}(B/2)/(H_{m0}/T_{m-1,0})$, the 90% error band can be calculated assuming a Gaussian error distribution, as

$$\left.\frac{u_{c2\%}(B/2)}{(H_{m0}/T_{m-1,0})}\right|_{5\%}^{95\%} = \frac{u_{c2\%}(B/2)}{(H_{m0}/T_{m-1,0})} \pm 0.744 \tag{5.11}$$

5.5.2. Distribution function for the extreme values of OFV, $u_c(B/2)$

Similar to Section 5.4.2, the OFV during the most severe wave storms is characterized here; the distribution function to describe $u_c(B/2)$ with exceedance probabilities below 2% is proposed. *Mares-Nasarre et al. (2019)* recommended the Rayleigh distribution to describe the distribution function of $u_c(B/2)$ with exceedance probabilities below 2%, given by

$$F\left(\frac{u_c(B/2)}{u_{c2\%}(B/2)}\right) = 1 - exp\left(-C_u\left[\frac{u_c(B/2)}{u_{c2\%}(B/2)}\right]^2\right) \tag{5.12}$$

where $u_c(B/2)$ is the OFV value with exceedance probabilities under 2% and C_u is an empirical coefficient to be calibrated. C_u was calibrated using the 20 (1,000 waves × 2%) highest measured values of OFV during each physical test while the exceedance probability assigned to each OFV value was calculated as $N_m/(N_w+1)$. The estimated $u_{c2\%}(B/2)$ using Eq. 5.10 together with coefficients in Table 5.5 was used in order to simulate the design phase conditions of a mound breakwater when measured $u_{c2\%}(B/2)$ is not available. 66 and 105 tests for m = 2% and 4%, respectively, were used. The initial calibrated coefficients were C_u=3.62 for m=2% and C_h=3.46 for m=4%; C_u results were similar for both bottom slopes. Thus, Kruskal-Wallis test was used to determine if the difference between the mean values of C_u for both m was significant. The null hypothesis (H_0) corresponded to both means being equal; H_0 was not rejected with a significance level α_s=0.05. Thus, best estimation was C_u = 3.5. The comparison between the measured and estimated $u_c(B/2)/(H_{m0}/T_{m-1,0})$ using Eq 5.12 with C_u = 3.5 is shown in Figure 5.32. Good results were obtained (R^2=0.812 and *bias*=-0.013).

Since the *MSE* increased for increasing values of $u_c(B/2)/(H_{m0}/T_{m-1,0})$, methodology given in *Herrera and Medina (2015)* was used to estimate the 90% error band. A Gaussian error (ε) distribution was assumed with 0 mean and variance given by

$$\sigma^2(\varepsilon) = 0.08\,\frac{u_c(B/2)}{(H_{m0}/T_{m-1,0})} \tag{5.13}$$

The 90% error band was calculated as

$$\left.\frac{u_c(B/2)}{(H_{m0}/T_{m-1,0})}\right|_{5\%}^{95\%} = \frac{u_c(B/2)}{(H_{m0}/T_{m-1,0})} \pm 0.46\sqrt{\frac{u_c(B/2)}{(H_{m0}/T_{m-1,0})}} \tag{5.14}$$

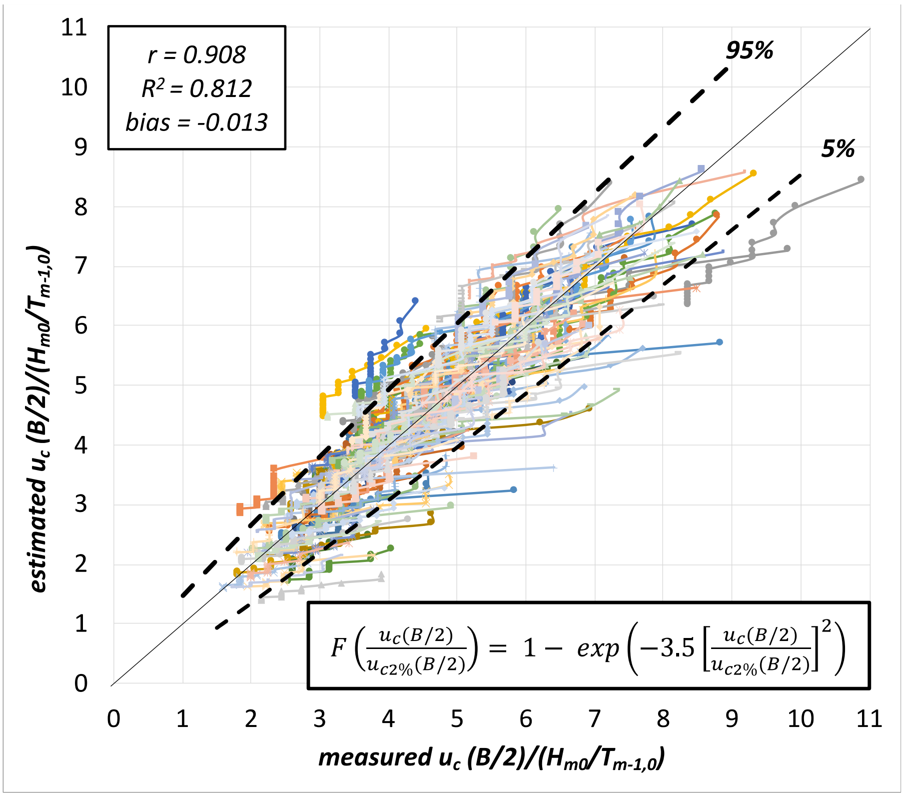

Fig. 5. 32. Comparison between measured and estimated dimensionless $u_c(B/2)$ using Eq. 5.12 and C_u = 3.5.

Figure 5.33 presents an example of the fitting of two datasets of cube-2L with the proposed Rayleigh distribution in Rayleigh probability plot.

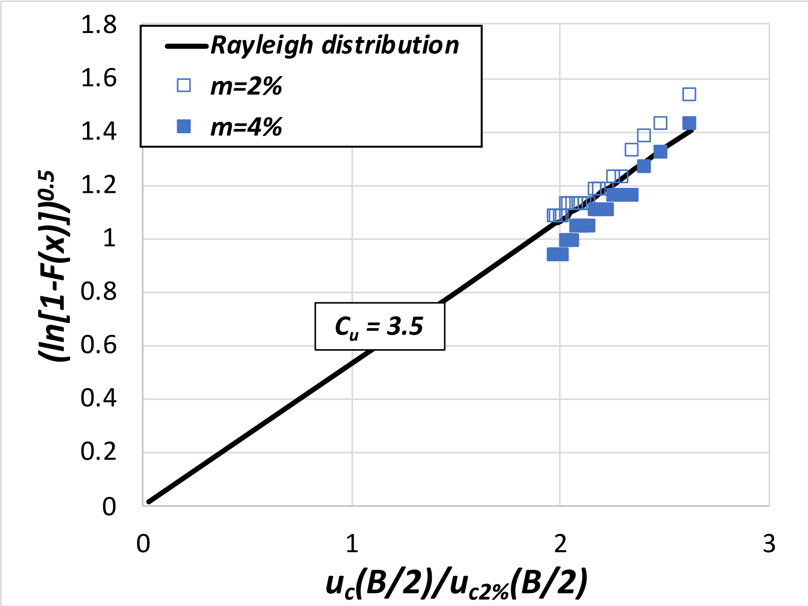

Fig. 5. 33. Examples of cumulative distribution function of $u_c(B/2)$ in equivalent probability plot.

5.6. Evaluation of the influence of the explanatory variables

As shown in Sections 5.4.1 and 5.5.1, the four selected explanatory variables (m, R_c/H_{m0}, $Ir_{m-1,0}$ and h/H_{m0}) were significant to estimate both $h_{c2\%}(B/2)$ and $u_{c2\%}(B/2)$. However, low influence of h/H_{m0} on $h_{c2\%}(B/2)$ and m on $u_{c2\%}(B/2)$ was observed. Thus, the performance of Eqs. 5.4 and 5.10 was assessed when h/H_{m0} and m were disregarded from such equations, respectively. The recalibrated coefficients as well as the goodness-of-fit metrics for Eq. 5.4 when h/H_{m0} is not considered in the model ($C5$=0) are listed in Table 5.6.

Armor layer	*C1*	*C2*	*C3*	*C4*	*C5*	*r*	R^2	*bias*
Cubipod®-1L	0	-4	-1/3	0.085	0	0.949	0.900	0.008
cube-2L	0	-2	-0.3	0.075	0	0.902	0.804	0.067
rock-2L	0.3	-10	-0.45	0.075	0	0.947	0.875	0.192

Table 5. 6. Sensitivity of the coefficients and goodness-of-fit metrics for $h_{c2\%}(B/2)/H_{m0}$ when h/H_{m0} is disregarded in Eq. 5.4.

Small variations in the calibrated coefficients *C1* and *C5* can be observed when comparing Tables 5.4 and 5.6. Nevertheless, most of the coefficients presented the same values. Likewise, the goodness-of-fit metrics slightly varied; R^2 decreased around 2% when *C5*=0. Table 5.7 shows the calibrated coefficients as well as the goodness-of-fit metrics for Eq. 5.10 when *m* is not included in the formula (*D2*=0).

Armor layer	*D1*	*D2*	*D3*	*D4*	*D5*	*r*	R^2	*bias*
Cubipod®-1L	3	0	-2	0.2	-1	0.909	0.785	0.068
cube-2L	2	0	-2	0.2	-0.5	0.901	0.796	-0.018
rock-2L	1	0	-3	0.2	-0.2	0.943	0.872	-0.039

Table 5. 7. Sensitivity of the coefficients and goodness-of-fit metrics for $u_{c2\%}(B/2)/(H_{m0}/T_{m-1,0})$ when *m* is disregarded in Eq. 5.10.

Coefficients *D1*, *D4* and *D5* presented small variations when comparing Tables 5.4 and 5.6. Similarly, R^2 decreased around 6% when *D2*=0. Note that *m* is still relevant even if it is not an explicit explanatory variable in the model, since the influence of *m* is also included through the wave conditions.

5.7. Summary and conclusions

The present section analyzed OLT and OFV on mound breakwater crests using the experimental database in this study (see Section 3). Thus, the conclusions and formulas derived in this section are valid within the experimental ranges 2% $\leq m \leq$ 4%, 0.3 $\leq R_c/H_{m0} \leq$1.8, 2.5 $\leq Ir_{m-1,0} \leq$4.6 and 0.2 $\leq H_{m0}/h \leq$ 0.9.

First, models for dike crests (smooth impermeable slope) were assessed using the aforementioned database, since no methods to estimate OLT and OFV on mound breakwaters (rough permeable slope where infiltration occurs) were found in the literature. Poor results (R^2<0.164) were obtained. Thus, a new method to better estimate $h_{c2\%}(B/2)$ and $u_{c2\%}(B/2)$ on mound breakwaters was needed.

Neural Networks (NNs) together with bootstrapping technique were used to study $h_{c2\%}(B/2)$ and $u_{c2\%}(B/2)$. Four dimensionless explanatory variables were considered to describe $h_{c2\%}(B/2)$ and $u_{c2\%}(B/2)$ based on the literature: the bottom slope, the dimensionless crest freeboard, the Iribarren number and the dimensionless water depth (m, R_c/H_{m0}, $Ir_{m-1,0}$ and h/H_{m0}).

These NNs were applied to determine the optimum point to estimate wave characteristics for predicting $h_{c2\%}(B/2)$ and $u_{c2\%}(B/2)$, following recommendations in *Herrera et al.* (*2017*). Such optimum point was found at a distance of 3*h* from the breakwater toe.

The influence of *m* on $h_{c2\%}(B/2)$ and $u_{c2\%}(B/2)$ was also analyzed using the trained NNs. Fixed wave conditions in the wave generation zone were propagated along numerical wave flumes with *m*=2.0%, 2.5%, 3.0%, 3.5% and 4.0% up to a distance of 3*h* from the breakwater toe using the SwanOne model (*Verhagen et al.*, *2008*). The obtained wave conditions were used as inputs of the trained NNs for simulating $h_{c2\%}(B/2)$ and $u_{c2\%}(B/2)$. It was observed how $h_{c2\%}(B/2)$ decreased for increasing values of m while $u_{c2\%}(B/2)$ slightly increased for rising values of m.

Further simulations were conducted with the trained NNs to analyze the influence of the selected explanatory variables. Based on these simulations, Eqs. 5.4 and 5.10 were proposed to estimate $h_{c2\%}(B/2)$ and $u_{c2\%}(B/2)$. Bootstrapping technique was applied in order to fit the empirical coefficients for each tested armor layer (Cubipod®-1L, cube-2L and rock-2L), as shown in Tables 5.4 and 5.5. The performance of the new proposed models was satisfactory ($0.866 \leq R^2 \leq 0.876$).

The significance of the selected explanatory variables was assessed using the adjusted coefficient of determination (Eq. 5.6). Dimensionless crest freeboard, R_c/H_{m0}, was the most significant explanatory variable to describe $h_{c2\%}(B/2)$ whereas the Iribarren number, $Ir_{m-1,0}$, was the most significant variable to describe $u_{c2\%}(B/2)$. Although all the selected explanatory variables resulted significant to describe $h_{c2\%}(B/2)$ and $u_{c2\%}(B/2)$, fitting between measured and estimated $h_{c2\%}(B/2)$ and $u_{c2\%}(B/2)$ was still satisfactory when neglecting the least significant explanatory variables (h/H_{m0} for $h_{c2\%}(B/2)$ and m for $u_{c2\%}(B/2)$).

The extreme values of OLT and OFV were also studied; the 1-parameter Exponential and Rayleigh distribution functions (Eqs. 5.8 and 5.12) were proposed to describe OLT and OFV with exceedance probabilities below 2%, $h_c(B/2)$ and $u_c(B/2)$, respectively. The agreement between the measured and estimated $h_c(B/2)$ and $u_c(B/2)$ using Eq. 5.8 with C_h=4 and Eq. 5.12 with C_u=3.5 was good ($0.803 \leq R^2 \leq 0.812$).

"The goal is to transform data into information, and information into insight."

Carly Fiorina

6

Conclusions and future research

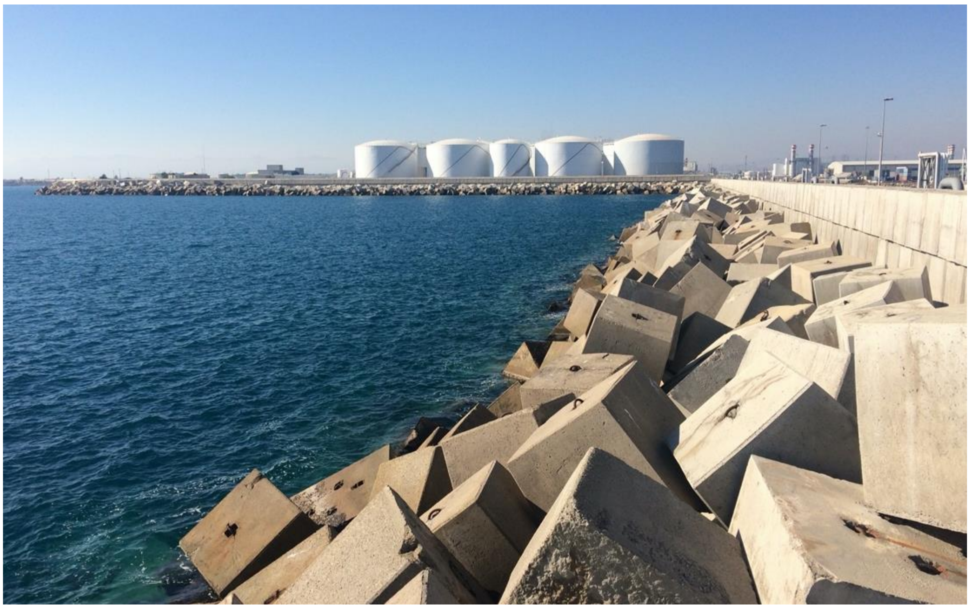

Port of Castellon (Spain), January 2019.

6.1. Introduction

Sea level rise caused by climate change, as well as the social concern about the impact of infrastructures, have led to coastal structures with reduced crest freeboards facing higher extreme overtopping events. In addition, most mound breakwaters are built in the surf zone where depth-limited wave breaking takes place. Thus, new tools are needed to better design overtopped mound breakwaters attacked by depth-limited breaking waves.

Authors in the literature (e.g.: *Franco et al., 1994*) emphasized the necessity of considering the individual wave overtopping events when designing the crest elevation of mound breakwaters. Recently, the maximum individual wave overtopping volume (V_{max}), the overtopping layer thickness (OLT) and the overtopping flow velocity (OFV) on the structure crest have been proposed as criteria for assessing overtopping hazard (*EurOtop, 2018; Altomare et al., 2020*).

Methods in the literature exist to estimate the mean wave overtopping discharge, q, (*van Gent et al., 2007; Molines and Medina, 2016*), the number of overtopping events, N_{ow}, and V_{max} (*Bruce et al., 2009*; *Molines et al., 2019*) on mound breakwaters in non-breaking wave conditions. However, few methods are available in the literature to predict N_{ow} and V_{max} on coastal structures under depth-limited breaking wave conditions. Regarding OLT and OFV, no studies were found for their prediction on mound breakwater crests, although several estimators exist to estimate OLT and OFV on dikes. Thus, new predictors are required to estimate N_{ow}, V_{max}, OLT and OFV on mound breakwaters with relevant overtopping discharges in depth-limited breaking wave conditions.

This dissertation proposes new methodologies for better design mound breakwater crest elevation based on overtopping criteria. Physical model tests on overtopped mound breakwaters protected with three armor layers (single-layer Cubipod® armor and double-layer cube and rock armors) were conducted under depth-limited breaking wave conditions. Using this experimental database, new unbiased explicit estimators for N_{ow}, V_{max}, OLT and OFV were developed. Special efforts were also put on the analysis of the influence of depth-limited breaking waves and the bottom slope influence.

6.2. Summary and conclusions

In this section, the five research questions raised in Section 1.2 are answered in order to summarize the findings in this PhD thesis.

Q1. Do the existing methods in the literature satisfactorily describe the overtopping flow on mound breakwaters under depth-limited breaking wave conditions?

In Section 4.2, methods in the literature to estimate N_{ow} and V_{max} were evaluated using the experimental database in depth-limited breaking wave conditions described in Section 3. Regarding the N_{ow}, best agreement with measured N_{ow} was obtained applying the methods by *Nørgaard et al.* (*2014*) and *Molines et al.* (*2019)* ($0.552<R^2<0.584$). It should be noted that both methods were based on the dimensionless mean overtopping discharge, $Q^*=q/(gH_{m0}T_{01})$, where q is estimated using CLASH NN. On the other hand, poor results (R^2<0) were obtained with the formulas given in *Besley* (*1999*) and *EurOtop (2018*). Since all the compared methods overpredicted the values of N_{ow}<100, a new estimator was needed to better describe N_{ow} within the experimental ranges of the present study.

With respect to V_{max}, the observed dimensionless V_{max}, $V_{max}^*=V_{max}/(gH_{m0}T_{01}^2)$, in this study agreed well with the estimations given by *Nørgaard et al.* (*2014*) and *Molines et al.* (*2019)* (0.618<R^2<0.630). Nevertheless, higher scatter was observed for V_{max}<5l/m and $V_{max}^*<2\cdot 10^{-3}$. In contrast, the formula given in *EurOtop (2018*) provided poor results (R^2<0). As *Nørgaard et al.* (*2014*) and *Molines et al.* (*2019)* tested mound breakwaters with a crown wall, the presence of a crown wall may not have a significant effect on V_{max}^*

As previously mentioned, no studies were found in the literature to estimate OLT and OFV on mound breakwaters. Therefore, in Section 5.1, predictors in the literature for dikes were compared with the experimental data in this study. The observed OLT exceeded by 2% of the incoming waves, $h_{c2\%}(B/2)$, was compared with the methods described in *Schüttrumpf and Van Gent* (*2003*) and *EurOtop (2018)*; poor agreement was obtained (R^2<0.164). In addition, noteworthy inconsistencies were observed both in the estimation of $Ru_{2\%}/H_{m0}$ and in the empirical coefficients proposed by *van Gent* (*2002*) and *Schüttrumpf et al.* (*2002)* for the method in *Schüttrumpf and Van Gent* (*2003*). Since the estimation of the OFV exceeded by 2% of the incoming waves, $u_{c2\%}(B/2)$, on dike crests using predictors in the literature was also based on $Ru_{2\%}$, similar incoherencies were expected.

In conclusion, methods in the literature did not accurately describe overtopping flow on mound breakwater crests within the experimental ranges of this thesis. Thus, new explicit estimators were required to properly assess overtopping hazard, as well as design mound breakwater crest elevation based on overtopping criteria.

Q2. Can the methods given in the literature be improved to estimate N_{ow} and V_{max} on mound breakwaters under depth-limited breaking wave conditions?

In this study, new models to better predict N_{ow} and V_{max} on mound breakwaters under depth-limited breaking wave conditions were developed. The new models provide estimations similar to those obtained with existing methods in the literature, but the number of variables and parameters has been reduced.

As mentioned in the previous research question, best results when estimating N_{ow} using methods in the literature were obtained applying the models by *Nørgaard et al.* (*2014*) and *Molines et al.* (*2019)*. Since those models are based on a power law of Q^*, they do not properly describe $P_{ow}=N_{ow}/N_w$ for extreme values of Q^* ($P_{ow}\rightarrow 0$ when $Q^*\rightarrow 0$ and $P_{ow}\rightarrow 1$ when $Q^*\rightarrow\infty$. Consequently, in this thesis, an exponential model with two empirical coefficients was proposed to better describe P_{ow} (see Eq. 4.1). Such empirical coefficients were calibrated using 219 tests; good agreement was obtained (R^2=0.919).

In order to describe the individual wave overtopping volumes, the two distribution functions proposed in the literature were applied: (1) the 2-parameter Weibull distribution (Eqs. 2.11, 4.4 and 4.5) and, (2) the 2-parameter Exponential distribution (Eqs. 2.18, 4.8 and 4.9). Their performance when estimating V_{max} was assessed simulating the design phase conditions of a mound breakwater; q and N_{ow} are unknown and need to be estimated. Hence, formulas developed in thesis were applied using q and N_{ow} estimated by CLASH NN and Eq. 4.1, respectively. Best results were obtained using the 2-parameter Weibull distribution (R^2=0.617). Although the obtained goodness-of-fit metrics were similar to those obtained using the methods by *Nørgaard et al.* (*2014*) and *Molines et al.* (*2019*), the new method developed in the present study using the 2-parameter Weibull distribution (v=1 and p=6) is much simpler than that recommended by *Nørgaard et al.* (*2014*) (v=3 and p=13) and simpler than that given in *Molines et al.* (*2019*) (v=1 and p=7). For design purposes, the ratio between the estimated and the measured V_{max}^* fell within a factor of 2 (see the 90% error band in Figure 4.16).

Q3. Is it possible to develop explicit estimators to predict the extreme values of OLT and OFV on mound breakwater crests under depth-limited breaking wave conditions?

The present thesis proposes new unprecedented empirical formulas to estimate the low-exceedance values of OLT and OFV on mound breakwater crests ($0.803 \leq R^2 \leq 0.876$). In Section 5.2, existing models to estimate $h_{c2\%}(B/2)$ and $u_{c2\%}(B/2)$ on dike crests were assessed using the experimental database on mound breakwaters in this thesis with poor results. Therefore, new models valid for mound breakwaters were needed.

First, $h_{c2\%}(B/2)$ and $u_{c2\%}(B/2)$ were analyzed using Neural Networks (NNs) together with the bootstrapping technique in Section 5. Four dimensionless explanatory variables were selected from the literature to describe $h_{c2\%}(B/2)$ and $u_{c2\%}(B/2)$: the bottom slope, the dimensionless crest freeboard, the Iribarren number and the dimensionless water depth (m, R_c/H_{m0}, $Ir_{m-1,0}$ and h/H_{m0}). Simulations conducted with the trained NNs were used to analyze the influence of the four selected explanatory variables on $h_{c2\%}(B/2)$ and $u_{c2\%}(B/2)$. Based on the identified trends, Eqs. 5.4 and 5.10 were proposed. The empirical coefficients in the new formulas were fitted for each armor layer (Cubipod®-1L, cube-2L and rock-2L) applying bootstrapping technique (see Tables 5.4 and 5.5). The fitting of the new models was satisfactory ($0.866 \leq R^2 \leq 0.876$).

The significance of the selected explanatory variables was evaluated using the adjusted coefficient of determination (Eq. 5.6). Although all the selected explanatory variables were significant to estimate $h_{c2\%}(B/2)$ and $u_{c2\%}(B/2)$, the agreement between measured and estimated $h_{c2\%}(B/2)$ and $u_{c2\%}(B/2)$ was still satisfactory when neglecting the least significant explanatory variables (h/H_{m0} for $h_{c2\%}(B/2)$ and m for $u_{c2\%}(B/2)$). Dimensionless crest freeboard, R_c/H_{m0}, was the most significant explanatory variable to describe $h_{c2\%}(B/2)$, while the Iribarren number, $Ir_{m-1,0}$, was the most significant variable to describe $u_{c2\%}(B/2)$. It should be mentioned that R_c/H_{m0} is is the most common and accepted variable for describing overtopping and it is related with the water level which reaches the breakwater crest. Thus, a direct relationship between $h_{c2\%}(B/2)$ and R_c/H_{m0} seems reasonable. On the other hand, $Ir_{m-1,0}$ is calculated using the wave length, so it is linked to the wave celerity (in intermediate waters, $0.05<h/L<0.5$: $c=(gL/2\pi \tanh(2\pi h/L))^{0.5}$). Therefore, correlation between $u_{c2\%}(B/2)$ and $Ir_{m-1,0}$ seems feasible.

After describing $h_{c2\%}(B/2)$ and $u_{c2\%}(B/2)$, the values of OLT and OFV with exceedance probabilities below 2%, $h_c(B/2)$ and $u_c(B/2)$, were studied. The 1-parameter Exponential and Rayleigh distribution functions (Eqs. 5.8 and 5.12) were proposed to describe $h_c(B/2)$ and $u_c(B/2)$, respectively. The fitting between the measured and estimated $h_c(B/2)$ and $u_c(B/2)$ using Eq. 5.8 with $C_h=4$ and Eq. 5.12 with $C_u=3.5$ was reasonable ($0.803 \leq R^2 \leq 0.812$).

In summary, new unbiased explicit estimators were developed in Section 5 using the experimental data described in Section 3 to better predict the extreme values of OLT and OFV.

Q4. Where is the optimum point to estimate wave characteristics for predicting overtopping flow on mound breakwater crests under depth-limited breaking wave conditions?

The point where wave characteristics are estimated becomes relevant when in depth-limited breaking wave conditions (*Herrera et al., 2017*). Therefore, such point was assessed in this thesis for the overtopping flow variables.

In the case of N_{ow} (Section 4.3.2), the empirical coefficients in the new formula developed in this study (G_1 and G_2 in Eq. 4.1) were fitted using $Q^*=q/(gH_{m0}T_{01})$ calculated with wave characteristics (H_{m0} and T_{01}) determined at several distances from the model toe: x=0, h, 2h, 3h, 4h, 5h and 6h. No significant differences were observed. Similar to N_{ow}, the empirical coefficients in the 2-parameter Weibull and Exponential distribution functions proposed to describe the individual wave overtopping volumes were fitted considering wave characteristics (H_{m0} and T_{01}) in Q^* at distances from the structure toe of x=0, h, 2h, 3h, 4h, 5h and 6h. $V_{max}^*=V_{max}/(gH_{m0}T_{01}^2)$ was also calculated for each couple of values. Best results were obtained using wave characteristics determined at distances between $x=2h$ and $x=6h$. Hence, H_{m0} and T_{01} estimated at $x=3h$ from the structure toe were used to estimate both N_{ow} and V_{max}^*, following recommendations by *Herrera et al. (2017)*.

With respect to OLT and OFV, NNs models were used to analyze $h_{c2\%}(B/2)$ and $u_{c2\%}(B/2)$, as described in Section 5.3. Those NNs were trained modifying the wave characteristics (H_{m0} and $T_{m-1,0}$) considered to feed the model and their goodness-of-fit was assessed. Similar to N_{ow} and V_{max}^*, wave characteristics at distances from the structure toe of x=0, h, 2h, 3h, 4h, 5h and 6h were considered. The highest R^2 for the $h_{c2\%}(B/2)/H_{m0}$ for the three studied armor layers was obtained when using wave characteristics (H_{m0} and $T_{m-1,0}$) estimated at a distance of 3h from the toe of the model.

Regarding $u_{c2\%}(B/2)/(H_{m0}/T_{m-1,0})$, the highest R^2 was obtained using wave characteristics estimated at a distance from the model toe between 3*h* and 4*h* for cube-2L and rock-2L armors. No clear tendency was found for Cubipod®-1L armor due the low number of tests for m = 2% (N_D = 13 for m = 2% and N_D = 44 for m = 4%). Thus, wave characteristics estimated at a distance of 3*h* were applied to estimate $h_{c2\%}(B/2)$ and $u_{c2\%}(B/2)$ in this thesis.

In conclusion, the optimum zone to estimate wave characteristics to describe overtopping flow on mound breakwaters was found at a distance of 3*h* from the toe of the structure. It should be noted that this point was also recommended by *Herrera et al. (2017)* to better describe the rock armor damage in depth-limited breaking wave conditions. Moreover, this distance approximately corresponds to the distance of $5H_{m0}$ suggested by *Goda (1985)* to determine wave characteristics to design vertical breakwaters in breaking wave conditions. Later, *Melby (1999)* also proposed the distance recommended in *Goda (1985)* to better describe the armor damage progression of rubble mound breakwaters.

Q5. Does the bottom slope play a significant role on the overtopping flow on mound breakwater crests under depth-limited breaking wave conditions?

Depth-induced breakage of waves significantly changes the wave forces and currents close to the coastal structure, since the larger waves break before reaching it. The type of wave breaking at the toe of the structure is influenced by the bottom slope. In addition, there is evidence that the role of depth-induced wave breaking and bottom slope is significant on mound breakwater design (*Herrera et al., 2017*). Hence, the influence of depth-induced wave breaking and bottom slope on the overtopping flow was evaluated in this thesis.

In Section 4.2, best results in the estimation of N_{ow} and V_{max}^* using methods in the literature were provided applying the method in *Molines et al.* (*2019*). Since *Molines et al.* (*2019*) performed tests in non-breaking conditions, the influence of depth-limited breakage may not influence N_{ow} and V_{max}^*. Regarding the influence of the bottom slope, Mann-Whitney tests were conducted using the experimental database in the present study and it was concluded that the bottom slope did not show a significant influence on N_{ow} or V_{max}^* in this study.

With respect to OLT and OFV, NNs models implemented in Section 5.3 were used to analyze the influence of the bottom slope on $h_{c2\%}(B/2)$ and $u_{c2\%}(B/2)$. Both $h_{c2\%}(B/2)$ and $u_{c2\%}(B/2)$ were influenced by the bottom slope; $h_{c2\%}(B/2)$ decreased for increasing values of the bottom slope while $u_{c2\%}(B/2)$ slightly increased for mounting values of the bottom slope. In addition, the bottom slope was one of the explanatory variables included in the new predictors for $h_{c2\%}(B/2)$ and $u_{c2\%}(B/2)$ developed in this thesis.

A possible explanation for the opposite results on the influence of the bottom slope may be that such influence is small enough not to be perceived for V_{max} in the experimental range tested in this dissertation ($2\% \leq m \leq 4\%$).

6.3. Future lines of research

Breaking waves and overtopping are wide and complex problems which cannot be covered in just one dissertation. Under such premise, future lines of research are given here considering the research gaps not covered by the present thesis.

Additional efforts should be put towards improving the estimation of wave characteristics in the surf zone, where depth-limited wave breaking takes place, to better design coastal structures. Special attention should be put on the estimation of wave periods.

Further physical model tests should be conducted considering gentler and steeper bottom slopes ($m<2\%$ and $m>4\%$) and different armor slopes ($\cot\alpha \neq 1.5$) in order to extend the conclusions in this study to a wider range. Tests performed in this thesis should also be repeated with different armor units on the main armor. In addition, the influence of the presence of a crown wall on the breakwater crest should be further studied to validate the conclusions in this thesis.

Several studies in the literature (*van Gent and van der Werf*, *2019; Mares-Nasarre and van Gent*, *2020*) highlight the significance of the oblique wave attack on the overtopping and the forces produced by this phenomenon. Thus, 3D physical model tests should be performed in order to characterize the influence of the oblique wave attack on the individual wave overtopping volumes, OLT and OFV.

The evolution of the OLT and OFV along the mound breakwater crest as well as the variation of OFV in depth should also be addressed. To this end, numerical modelling arises as a powerful tool to fill the gaps in the data from the physical tests.

Finally, the correlation between the overtopping variables during the same overtopping event should be studied. The relationship between the individual wave overtopping volume, the OLT and the OFV produced by a single wave can help to better understand the hydrodynamics of the overtopping phenomenon.

“Education is the most powerful weapon which you can use to change the world.”

Nelson Mandela

7

References

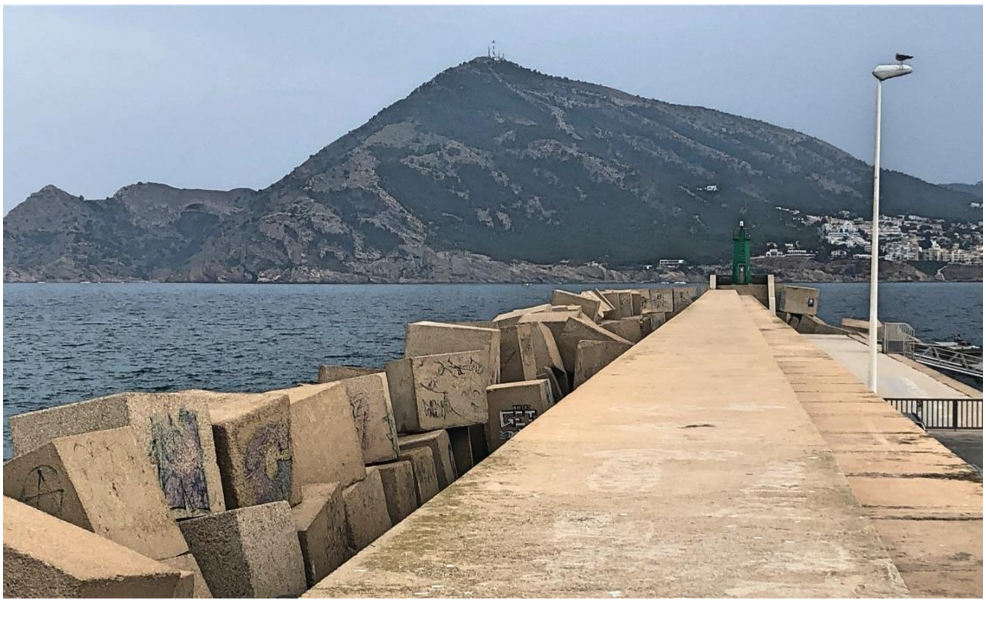

Port of Altea (Spain), July 2019

Abt, S.R., Wittier, R.J., Taylor, A., Love, D.J., *1989*. Human stability in a high flood hazard zone. JAWRA J. Am. Water Resour. Assoc. 25, 881–890. https://doi.org/10.1111/j.1752-1688.1989.tb05404.x

Allsop, N.W.H., Bruce, T., Pullen, T., Van der Meer, J.W., *2008*. Direct hazards from wave overtopping - the forgotten aspect of coastal flood risk assessment?, in: DEFRA, Proc. Flood and Coastal Management Conference.

Altomare, C., Gironella, X., Suzuki, T., Viccione, G., Saponieri, A., *2020*. Overtopping Metrics and Coastal Safety: A Case of Study from the Catalan Coast. J. Mar. Sci. Eng. 8, 556. https://doi.org/10.3390/jmse8080556

Andriolo, U., Mendes, D., Taborda, R., *2020*. Breaking Wave Height Estimation from Timex Images: Two Methods for Coastal Video Monitoring Systems. Remote Sens. 12, 204. https://doi.org/10.3390/rs12020204

Argente, G., Gómez-Martín, M.E., Medina, J.R., *2018*. Hydraulic stability of the armor layer of overtopped breakwaters. J. Mar. Sci. Eng. 6, 1–13. https://doi.org/10.3390/jmse6040143

Bae, H.U., Yun, K.M., Yoon, J.Y., Lim, N.H., *2016*. Human stability with respect to overtopping flow on the breakwater. Int. J. Appl. Eng. Res. 11, 111–119.

Baldock, T.E., Holmes, P., Bunker, S., Van Weert, P., *1998*. Cross-shore hydrodynamics within an unsaturated surf zone. Coast. Eng. 34, 173–196. https://doi.org/10.1016/S0378-3839(98)00017-9

Battjes, J.A., *1974*. SURF SIMILARITY. Proc. 14th Int. Conf. Coast. Eng. 1, 26. https://doi.org/10.9753/icce.v14.26

Battjes, J.A., Groenendijk, H.W., *2000*. Wave height distributions on shallow foreshores. Coast. Eng. 40, 161–182. https://doi.org/10.1016/S0378-3839(00)00007-7

Battjes, J.A., Janssen, J.P.F.M., *1978*. Energy Loss and Set-Up Due to Breaking of Random Waves, in: Proc. 16th International Conference on Coastal Engineering. American Society of Civil Engineers, New York, NY, pp. 569–587. https://doi.org/10.1061/9780872621909.034

Besley, P., *1999*. Overtopping of Sea-Walls Design and Assessment Manual. R&D Technical Report vol. 178, Environmental Agency, Bristol (UK).

Blenkinsopp, C.E., Chaplin, J.R., *2008*. The effect of relative crest submergence on wave breaking over submerged slopes. Coast. Eng. 55, 967–974. https://doi.org/10.1016/j.coastaleng.2008.03.004

Bonmarin, P., *1989*. Geometric properties of deep-water breaking waves. J. Fluid Mech. 209, 405–433. https://doi.org/10.1017/S0022112089003162

British Standard BS 6349 part 7, *1991*. Maritime Structures: Guide to the design and construction of breakwaters. London (UK).

Bruce, T., Pearson, J., Allsop, W., *2003*. HAZARDS AT COAST AND HARBOUR

SEAWALLS – VELOCITIES AND TRAJECTORIES OF VIOLENT OVERTOPPING JETS, in: Proc. 28th International Conference on Coastal Engineering. World Scientific Publishing Company, pp. 2216–2226. https://doi.org/10.1142/9789812791306_0186

Bruce, T., Van der Meer, J.W., Franco, L., Pearson, J.M., *2009*. Overtopping performance of different armour units for rubble mound breakwaters. Coast. Eng. 56, 166–179. https://doi.org/10.1016/j.coastaleng.2008.03.015

Caires, S., Van Gent, M.R.A., *2012*. WAVE HEIGHT DISTRIBUTION IN CONSTANT AND FINITE DEPTHS. Proc. 33rd Int. Conf. Coast. Eng. 1, 15. https://doi.org/10.9753/icce.v33.waves.15

Camenen, B., Larson, M., *2007*. Predictive Formulas for Breaker Depth Index and Breaker Type. J. Coast. Res. 234, 1028–1041. https://doi.org/10.2112/05-0566.1

Camfield, F., Street, R., *1968*. The effects of bottom configuration on the deformation, breaking and run-up of solitary waves., Proc. 10th International Conference on Coastal Engineering. London (UK).

Camus, P., Tomás, A., Díaz-Hernández, G., Rodríguez, B., Izaguirre, C., Losada, I.J., *2019*. Probabilistic assessment of port operation downtimes under climate change. Coast. Eng. 147, 12–24. https://doi.org/10.1016/j.coastaleng.2019.01.007

Chen, X., Jonkman, S., Pasterkamp, S., Suzuki, T., Altomare, C., *2017*. Vulnerability of Buildings on Coastal Dikes due to Wave Overtopping. Water 9, 394. https://doi.org/10.3390/w9060394

CIRIA/CUR/CETMEF, *2007*. The Rock Manual. The Use of Rock in Hydraulic Engineering (2nd edition). C683, CIRIA, London (UK).

CIRIA/CUR, *1991*. Manual on the use of rock in coastal and shoreline engineering.

Collins, J.I., *1970*. Probabilities of Breaking Wave Characteristics, in: Proc. 12th International Conference on Coastal Engineering. American Society of Civil Engineers, New York, NY, pp. 399–414. https://doi.org/10.1061/9780872620285.025

Collins, J.I., *1969*. Probabilities of wave characteristics in the surf zone. Tetra Technical Report, TC-149.

Dally, W.R., *1992*. Random breaking waves: Field verification of a wave-by-wave algorithm for engineering application. Coast. Eng. 16, 369–397. https://doi.org/10.1016/0378-3839(92)90060-8

Dally, W.R., *1990*. Random breaking waves: A closed-form solution for planar beaches. Coast. Eng. 14, 233–263. https://doi.org/10.1016/0378-3839(90)90026-S

Dally, W.R., Dean, R.G., *1987*. Transformation of Random Breaking Waves on Surf Beat, in: Proc. 20th International Conference on Coastal Engineering. American Society of Civil Engineers, New York, NY, pp. 109–123. https://doi.org/10.1061/9780872626003.009

Danel, P., *1952*. On the limiting clapotis, Gravity Waves. Natl. Bur. Stand. Circ. No. 521 35.

De Rouck, J., Verhaeghe, H., Geeraerts, J., *2009*. Crest level assessment of coastal structures — General overview. Coast. Eng. 56, 99–107. https://doi.org/10.1016/j.coastaleng.2008.03.014

Díaz-Carrasco, P., Moragues, M.V., Clavero, M., Losada, M.Á., *2020*. 2D water-wave interaction with permeable and impermeable slopes: Dimensional analysis and experimental overview. Coast. Eng. 158, 103682. https://doi.org/10.1016/j.coastaleng.2020.103682

Díaz, H., Catalán, P., Wilson, G., *2017*. Quantification of Two-Dimensional Wave Breaking Dissipation in the Surf Zone from Remote Sensing Data. Remote Sens. 10, 38. https://doi.org/10.3390/rs10010038

Endoh, K., Takahashi, S., *1995*. Numerically modeling personnel danger on a promenade breakwater due to overtopping waves, in: Proc. 24th International Conference on Coastal Engineering. pp. 1016–1029.

EurOtop. A manual on wave overtopping of sea defences and related structures. An overtopping manual largely based on European research but for worldwide Application, *2018*. Van der Meer, J. W.; Allsop, N.W.H.; Bruce, T.; De Rouck, J.; Kortenhaus, A.; Pullen, T.; Schüttrumpf, H.; Troch, P.; Zanuttigh, B. www.overtopping-manual.com.

Figueres, M., Medina, J.R., *2005*. Estimating incident and reflected waves using a fully nonlinear wave model, in: Proc. 29th International Conference on Coastal Engineering. Lisboa (Portugal), pp. 594–603. https://doi.org/10.1142/9789812701916-0047

Formentin, S.M., Gaeta, M.G., Palma, G., Zanuttigh, B., Guerrero, M., *2019*. Flow Depths and Velocities across a Smooth Dike Crest. Water 11, 2197. https://doi.org/10.3390/w11102197

Formentin, S.M., Zanuttigh, B., van der Meer, J.W., *2017*. A Neural Network Tool for Predicting Wave Reflection, Overtopping and Transmission. Coast. Eng. J. 59, 1750006-1-1750006–31. https://doi.org/10.1142/S0578563417500061

Franco, L., de Gerloni, M., Van der Meer, J.W., *1994*. Wave overtopping on vertical and composite breakwaters. Proc. 24th Int. Conf. Coast. Eng. 1, 1030–1044. https://doi.org/10.1061/9780784400890.076

Fukuda, N., Uno, T., Irie, I., *1974*. Field Observations of Wave Overtopping of Wave Absorbing Revetment. Coast. Eng. Japan 17, 117–128. https://doi.org/10.1080/05785634.1974.11924187

Gallach, D., *2018*. Experimental Study of Wave Overtopping Performance of Steep Low-Crested Structures. PhD Thesis. Ghent University.

Galvin, C.J., *1968*. Breaker type classification on three laboratory beaches. J. Geophys. Res. 73, 3651–3659. https://doi.org/10.1029/JB073i012p03651

Geeraerts, J., Boone, C., De Rouck, J., Kortenhaus, L., Van Damme, L., Franco, L., *2005*. Hazards from wave overtopping: field measurements on the Zeebrugge breakwater, in: Proc. 2nd International Coastal Symposium.

Geeraerts, J., Troch, P., De Rouck, J., Verhaeghe, H., Bouma, J.J., *2007*. Wave overtopping at coastal structures: prediction tools and related hazard analysis. J. Clean. Prod. 15, 1514–1521. https://doi.org/10.1016/j.jclepro.2006.07.050

Goda, Y., *2010*. Reanalysis of Regular and Random Breaking Wave Statistics. Coast. Eng. J. 52, 71–106. https://doi.org/10.1142/S0578563410002129

Goda, Y., *2000*. Random seas and design of maritime structures (2nd Edition). World Scientific Publishing, Singapore.

Goda, Y., *1985*. Random Seas and Design of Maritime Structures. University of Tokyo Press, Tokyo, Japan.

Goda, Y., *1975*. Irregular Wave Deformation in the Surf Zone. Coast. Eng. Japan 18, 13–26. https://doi.org/10.1080/05785634.1975.11924196

Goda, Y., *1970*. A SYNTHESIS OF BREAKER INDICES. Proc. Japan Soc. Civ. Eng. 39–49. https://doi.org/10.2208/jscej1969.1970.180_39

Goda, Y., Suzuki, T., *1976*. ESTIMATION OF INCIDENT AND REFLECTED WAVES IN RANDOM WAVE EXPERIMENTS, in: Proc. 15th International Conference on Coastal Engineering. p. 47. https://doi.org/10.9753/icce.v15.47

Gómez-Martín, M.E., Mares-Nasarre, P., Argente, G., Molines, J., Medina, J.R., *2019*. Influencia de la pendiente de fondo sobre la estabilidad hidráulica de la berma de pie en diques con oleaje rompiendo por fondo, in: XV Jornadas Españolas de Ingeniería de Costas y Puertos. 8-9 May 2019, Málaga (Spain) [in Spanish].

Gómez-Martín, M.E., Medina, J.R., *2014*. Heterogeneous Packing and Hydraulic Stability of Cube and Cubipod Armor Units. J. Waterw. Port, Coastal, Ocean Eng. 140, 100–108. https://doi.org/10.1061/(ASCE)WW.1943-5460.0000223

Gourlay, M.R., *1992*. Wave set-up, wave run-up and beach water table: Interaction between surf zone hydraulics and groundwater hydraulics. Coast. Eng. 17, 93–144. https://doi.org/10.1016/0378-3839(92)90015-M

Grilli, S.T., Svendsen, I.A., Subramanya, R., *1997*. Breaking Criterion and Characteristics for Solitary Waves on Slopes. J. Waterw. Port, Coastal, Ocean Eng. 123, 102–112. https://doi.org/10.1061/(ASCE)0733-950X(1997)123:3(102)

Herrera, M.P., Gómez-Martín, M.E., Medina, J.R., *2017*. Hydraulic stability of rock armors in breaking wave conditions. Coast. Eng. 127, 55–67. https://doi.org/10.1016/j.coastaleng.2017.06.010

Herrera, M.P., Hoyos, A., Molines, J., Medina, J.R., *2015*. Influence of the placement technique on double-layer cube armor stability of breakwaters constructed on steep foreshores, in: E-Proceedings of the 36th IAHR World Congress.

Herrera, M.P., Medina, J.R., *2015*. Toe berm design for very shallow waters on steep sea bottoms. Coast. Eng. 103, 67–77. https://doi.org/10.1016/j.coastaleng.2015.06.005

Hughes, S.A., Borgman, L.E., *1987*. Beta-Rayleigh distribution for shallow-water wave heights, in: Proc. International Conference on Coastal Hydrodynamics. pp. 17–31.

Hughes, S.A., Nadal, N.C., *2009*. Laboratory study of combined wave overtopping and storm surge overflow of a levee. Coast. Eng. 56, 244–259. https://doi.org/10.1016/j.coastaleng.2008.09.005

Hughes, S.A., Thornton, C.I., Van der Meer, J.W., Scholl, B., *2012*. Improvements in describing wave overtopping processes. Proc. 33rd Int. Conf. Coast. Eng. [SI], 1–15. https://doi.org/10.9753/icce.v33.waves.35

IPCC, *2019*. Special Report on the Ocean and Cryosphere in a Changing Climate. Chapter 4: Sea Level Rise and Implications for Low-Lying Islands, Coasts and Communities. https://doi.org/<https://www.ipcc.ch/site/assets/uploads/sites/3/2019/11/08_SROCC_Ch04_FINAL.pdf> [Accessed: 15th june 2020]

Iribarren, R., Nogales, C., *1950*. Generalización de la Fórmula para el Cálculo de los Diques de Escollera y Comprobación de sus Coeficientes. Rev. Obras Públicas (Madrid), 239–277.

Jonkman, S.N., Penning-Rowsell, E., *2008*. Human Instability in Flood Flows 1. JAWRA J. Am. Water Resour. Assoc. 44, 1208–1218. https://doi.org/10.1111/j.1752-1688.2008.00217.x

Kaminsky, G.M., Kraus, N.C., *1993*. Evaluation of depth-limited wave breaking criterion, in: Proc. 2nd International Symposium on Ocean Wave Measurement and Analysis. New Orleans (USA), pp. 437–448.

Karvonen, R.A., Hepojoki, A., Huhta, H.K., Louhio, A., *2000*. The Use of Physical Models in Dam-Break Analysis. RESCDAM Final Report. Helsinki University of Technology (Finland).

Khayyer, A., Gotoh, H., Shao, S.D., *2008*. Corrected Incompressible SPH method for accurate water-surface tracking in breaking waves. Coast. Eng. 55, 236–250. https://doi.org/10.1016/j.coastaleng.2007.10.001

Klopman, G., *1996*. Extreme wave heights in shallow water. Report H2486, WLr. Delft hydraulics, The Netherlands.

Kolmogorov, A.N., *1933*. Sulla determinazione empirica di una legge di distribuzione. G. dell'Instituto Ital. degli Attuari 4, 83–91.

Kruskal, W.H., Wallis, W.A., *1952*. Use of Ranks in One-Criterion Variance Analysis. J. Am. Stat. Assoc. 47, 583–621. https://doi.org/10.1080/01621459.1952.10483441

Le Méhauté, B., Koh, R.C.Y., *1967*. On The Breaking Of Waves Arriving At An Angle To The Shore. J. Hydraul. Res. 5, 67–88. https://doi.org/10.1080/00221686709500189

Le Roux, J.P., *2007*. A simple method to determine breaker height and depth for different deepwater wave height/length ratios and sea floor slopes. Coast. Eng. 54, 271–277. https://doi.org/10.1016/j.coastaleng.2006.10.001

Levene, H., *1960*. Robust tests for equality of variances. Stanford University Press.

Longuet-Higgins, M.S., *1983*. On the joint distribution of wave periods and amplitudes in a random wave field. Proc. R. Soc. London. A. Math. Phys. Sci. 389, 241–258. https://doi.org/10.1098/rspa.1983.0107

Longuet-Higgins, M.S., *1982*. Parametric solutions for breaking waves. J. Fluid Mech. 121, 403–424. https://doi.org/10.1017/S0022112082001967

Longuet-Higgins, M.S., *1952*. On the statistical distributions of heights of sea waves. J. Mar. Res. 11, 245 – 266.

Lorke, S., Scheres, B., Schüttrumpf, H., Bornschein, A., Pohl, R., *2012*. Physical model tests on wave overtopping and flow processes on dike crests influenced by wave-current interaction. Coast. Eng. Proc. 1–13. https://doi.org/10.9753/icce.v33.waves.34

Lykke Andersen, T., Burcharth, H.F., Gironella, F.X., *2009*. SINGLE WAVE OVERTOPPING VOLUMES AND THEIR TRAVEL DISTANCE FOR RUBBLE MOUND BREAKWATERS, in: Proc. 5th International Conference on Coastal Structures. World Scientific Publishing Company, pp. 1241–1252. https://doi.org/10.1142/9789814282024_0109

Mai, S., Wilhelmi, J., Barjenbruch, U., *2011*. WAVE HEIGHT DISTRIBUTIONS IN SHALLOW WATERS. Proc. 32nd Int. Conf. Coast. Eng. 1, 63. https://doi.org/10.9753/icce.v32.waves.63

Makkonen, L., *2006*. Plotting Positions in Extreme Value Analysis. J. Appl. Meteorol. Climatol. 45, 334–340. https://doi.org/10.1175/JAM2349.1

Mann, H.B., Whitney, D.R., *1947*. On a test of whether one of two random variables is stochastically larger than the other. Ann. Math. Stat. 18, 50-60(5.3).

Mansard, E.P.D., Funke, E.R., *1980*. The Measurement of Incident and Reflected Spectra Using a Least squares Method, in: Proc. 17th International Conference on Coastal Engineering. ASCE, pp. 154–172.

Mares-Nasarre, P., Argente, G., Gómez-Martín, M.E., Medina, J.R., *2019*. Overtopping layer thickness and overtopping flow velocity on mound breakwaters. Coast. Eng. 154, 103561. https://doi.org/10.1016/J.COASTALENG.2019.103561

Mares-Nasarre, P., Gómez-Martín, M.E., Medina, J.R., *2020a*. Influence of mild bottom slopes on the overtopping flow over mound breakwaters under depth-limited breaking wave conditions. J. Mar. Sci. Eng. 8. https://doi.org/10.3390/JMSE8010003

Mares-Nasarre, P., Molines, J., Gómez-Martín, M.E., Medina, J.R., *2020b*. Individual wave overtopping volumes on mound breakwaters in breaking wave conditions and gentle sea bottoms. Coast. Eng. 159, 103703. https://doi.org/10.1016/j.coastaleng.2020.103703

Mares-Nasarre, P., Molines, J., Gómez-Martín, M.E., Medina, J.R., *2021*. Explicit Neural Network-derived formula for overtopping flow on mound breakwaters in depth-limited breaking wave conditions. Coast. Eng. 164, 103810. https://doi.org/10.1016/j.coastaleng.2020.103810

Mares-Nasarre, P., van Gent, M.R.A., *2020*. Oblique wave attack on rubble mound breakwater crest walls of finite length. Water 12, Article number 353. https://doi.org/10.3390/w12020353

Mase, H., Iwagaki, Y., *1982*. Wave Height Distributions and Wave Grouping in Surf Zone, in: Proc. 18th International Conference on Coastal Engineering. American Society of Civil Engineers, New York, NY, pp. 58–76. https://doi.org/10.1061/9780872623736.004

Massel, S.R., Sobey, R.J., *2000*. Distribution of the Highest Wave in a Record. Coast. Eng. J. 42, 153–173. https://doi.org/10.1142/S0578563400000079

Massey, F.J., *1952*. Distribution table for the deviation between two sample cumulatives. Ann. Math. Stat. 23, 435–441.

McCowan, J., *1894*. XXXIX. On the highest wave of permanent type. London, Edinburgh, Dublin Philos. Mag. J. Sci. 38, 351–358. https://doi.org/10.1080/14786449408620643

Mead, S.T., Black, K.P., *2001*. Predicting the breaking intensity of surfing waves. Spec. Issue J. Coast. Res. Surfing 103–130.

Melby, J.A., *1999*. Damage progression on Rubble Mound Breakwaters. Vicksburg, MS, USA. Also Ph.D. Thesis, University of Delaware, Newark, DE, USA.

Méndez, F.J., Castanedo, S., *2007*. A probability distribution for depth-limited extreme wave heights in a sea state. Coast. Eng. 54, 878–882. https://doi.org/10.1016/j.coastaleng.2007.05.011

Mendez, F.J., Losada, I.J., Medina, R., *2004*. Transformation model of wave height distribution on planar beaches. Coast. Eng. 50, 97–115. https://doi.org/10.1016/j.coastaleng.2003.09.005

Miche, R., *1944*. Mouvements ondulatoires del la mer en profondeur constante ou décroissante. Ann. Ponts Chaussées 26–78.

Michell, J.H., *1893*. XLIV. The highest waves in water. London, Edinburgh, Dublin Philos. Mag. J. Sci. 36, 430–437. https://doi.org/10.1080/14786449308620499

Miller, L.H., *1956*. Table of percentage points of Kolmogorov statistics. J. Am. Stat. Assoc. 31, 111–121.

Molines, J., Herrera, M.P., Gómez-Martín, M.E., Medina, J.R., *2019*. Distribution of individual wave overtopping volumes on mound breakwaters. Coast. Eng. 149, 15–27. https://doi.org/10.1016/j.coastaleng.2019.03.006

Molines, J., Herrera, M.P., Medina, J.R., *2018*. Estimations of wave forces on crown walls based on wave overtopping rates. Coast. Eng. 132, 50–62.

https://doi.org/10.1016/j.coastaleng.2017.11.004

Molines, J., Medina, J.R., *2016*. Explicit wave-overtopping formula for mound breakwaters with crown walls using CLASH neural network-derived data. J. Waterw. Port, Coast. Ocean Eng. 142. https://doi.org/10.1061/(ASCE)WW.1943-5460.0000322

Molines, J., Medina, J.R., *2015*. Calibration of overtopping roughness factors for concrete armor units in non-breaking conditions using the CLASH database. Coast. Eng. 96, 62–70. https://doi.org/10.1016/j.coastaleng.2014.11.008

Mood, A.M., *1954*. On the Asymptotic Efficiency of Certain Nonparametric Two-Sample Tests. Ann. Math. Stat. 25, 514–522. https://doi.org/10.1214/aoms/1177728719

Moragues, M.V., Clavero, M., Losada, M.Á., *2020*. Wave Breaker Types on a Smooth and Impermeable 1:10 Slope. J. Mar. Sci. Eng. 8, 296. https://doi.org/10.3390/jmse8040296

Munk, W.H., *1949*. The Solitary Wave Theory and its Application to Surf Problems. Ann. N. Y. Acad. Sci. 51, 376–424. https://doi.org/10.1111/j.1749-6632.1949.tb27281.x

Muttray, M., Oumeraci, H., *2001*. Wave Transformation on the Foreshore of Coastal Structures, in: Proc. 27th International Conference on Coastal Engineering. American Society of Civil Engineers, Sydney, Australia, pp. 2178–2191. https://doi.org/10.1061/40549(276)170

New, A.L., McIver, P., Peregrine, D.H., *1985*. Computations of overturning waves. J. Fluid Mech. 150, 233–251. https://doi.org/10.1017/S0022112085000118

Nørgaard, J.Q.H., Lykke Andersen, T., Burcharth, H.F., *2014*. Distribution of individual wave overtopping volumes in shallow water wave conditions. Coast. Eng. 83, 15–23. https://doi.org/10.1016/j.coastaleng.2013.09.003

Ogawa, Y., Shuto, N., *1985*. Run-up of Periodic Waves on Beaches of Non-Uniform Slope, in: Coastal Engineering 1984. American Society of Civil Engineers, New York, NY, pp. 328–344. https://doi.org/10.1061/9780872624382.024

Ostendorf, D.W., Madsen, O.S., *1979*. An analysis of longshore currents and associated sediment transport in the surf zone. Report No. 241, Department of Civil Engineering, Massachusetts Institute of Technology.

Pan, Y., Li, L., Amini, F., Kuang, C.P., Chen, Y., *2016*. New Understanding on the Distribution of Individual Wave Overtopping Volumes over a Levee under Negative Freeboard. J. Coast. Res. 75, 1207–1211. https://doi.org/10.2112/si75-242.1

Peregrine, D.H., *1983*. Breaking Waves on Beaches. Annu. Rev. Fluid Mech. 15, 149–178. https://doi.org/10.1146/annurev.fl.15.010183.001053

Rattanapitikon, W., Shibayama, T., *2000*. Verification and Modification of Breaker Height Formulas. Coast. Eng. J. 42, 389–406. https://doi.org/10.1142/S0578563400000195

Robertson, B., Hall, K., Zytner, R., Nistor, I., *2013*. Breaking Waves: Review of Characteristic Relationships. Coast. Eng. J. 55.

https://doi.org/10.1142/S0578563413500022

Sandoval, C., Bruce, T., *2017*. Wave overtopping hazard to pedestrians: video evidence from real accidents, in: Proc. Of Coasts, Marine Structures and Breakwaters 2017. Realising the Potential. Liverpool Waterfront, UK, pp. 501–512.

Scarfe, B.E., Elwany, H.S., Mead, S.T., Black, K.P., *2003*. The science of surfing waves and surfing breaks - A review 1–12.

Schüttrumpf, H., Möller, J., Oumeraci, H., *2002*. OVERTOPPING FLOW PARAMETERS ON THE INNER SLOPE OF SEADIKES, in: Proc. 28th International Conference on Coastal Engineering. World Scientific Publishing Company, pp. 2116–2127. https://doi.org/10.1142/9789812791306_0178

Schüttrumpf, H., Van Gent, M.R.A., *2003*. Wave overtopping at seadikes, in: Coastal Structures 2003 - Proceedings of the Conference. pp. 431–443.

Shapiro, S.S., Wilk, M.B., *1965*. An analysis of variance test for normality (complete samples). Biometrika 52, 591–611. https://doi.org/10.1093/biomet/52.3-4.591

Sigurdarson, S., Viggosson, G., *1994*. Berm Breakwaters in Iceland, Practical Ecperiences, in: International Conference on Hydro-Technical Engineering for Port and Harbor Constructions. pp. 651–671.

Smirnov, N.V., *1939*. Estimate of deviation between empirical distribution functions in two independent samples (in Russian). Bull. Moscow Univ. 2, 3-16(6.1, 6.2).

Smith, E.R., Kraus, N.C., *1991*. Laboratory Study of Wave- Breaking over Bars and Artificial Reefs. J. Waterw. Port, Coastal, Ocean Eng. 117, 307–325. https://doi.org/10.1061/(ASCE)0733-950X(1991)117:4(307)

Smolka, E., Zarranz, G., Medina, J.R., *2009*. Estudio Esperimental del Rebase de un Dique en Talud de Cubípodos, Libro de las X Jornadas Españolas de Costas y Puertos (in Spanish). Universidad de Cantabria-Adif Congresos.

Sunamura, T., *1981*. A laboratory study of offshore transport of sediment for eroding beaches., in: Proc. 17th International Conference on Coastal Engineering. pp. 1051–1070.

Sunamura, T., Horikawa, K., *1974*. TWO-DIMENSIONAL BEACH TRANSFORMATION DUE TO WAVES. Coast. Eng. Proc. 1, 53. https://doi.org/10.9753/icce.v14.53

Tayfun, M.., *1981*. Breaking-limited wave heights. J. Waterw. Port, Coast. Ocean Eng. 107, 59–69.

The MathWorks Inc., *2019*. MATLAB®.

Theil, H., *1961*. Economic forecasts and policy. North, Amsterdam (Holland).

Ting, F.C.K., Kirby, J.T., *1996*. Dynamics of surf-zone turbulence in a spilling breaker. Coast. Eng. 27, 131–160. https://doi.org/10.1016/0378-3839(95)00037-2

Ting, F.C.K., Kirby, J.T., *1995*. Dynamics of surf-zone turbulence in a strong plunging breaker. Coast. Eng. 24, 177–204. https://doi.org/10.1016/0378-3839(94)00036-W

Tsai, C.-P., Chen, H.-B., Hwung, H.-H., Huang, M.-J., *2005*. Examination of empirical formulas for wave shoaling and breaking on steep slopes. Ocean Eng. 32, 469–483. https://doi.org/10.1016/j.oceaneng.2004.05.010

USACE, *2002*. Coastal Engineering Manual. Engineer Manual 1110-2-1100. U.S. Army Corps of Engineers, Washington D.C. (in 6 volumes).

USACE, *1984*. Shore Protection Manual, U.S. Army Coastal Engineering Research Center, U.S. Army Engineer Waterways Experiment Station, Vicksburg, Mississippi.

van Bergeijk, V.M., Warmink, J.J., van Gent, M.R.A., Hulscher, S.J.M.H., *2019*. An analytical model of wave overtopping flow velocities on dike crests and landward slopes. Coast. Eng. 149, 28–38. https://doi.org/10.1016/j.coastaleng.2019.03.001

Van der Meer, J.W., *1990*. Extreme shallow water wave conditions: Design curves for uniform sloping beaches. Report H198, Delft Hydraulics, Delft (the Netherlands).

Van der Meer, J.W., Hardeman, B., Steendam, G.J., Schüttrumpf, H., Verheij, H., *2010*. FLOW DEPTH AND FLOW VELOCITY AT CREST AND LANDWARD SLOPE OF A DIKE, IN THEORY AND WITH THE WAVE OVERTOPPING SIMULATOR. Coast. Eng. Proc. [SI]. https://doi.org/https://doi.org/10.9753/icce.v32.structures.10

Van der Meer, J.W., Janssen, J.P.F.M., *1994*. Wave run-up and wave overtopping at dikes and revetments. Report no. 485, Delft Hydraulics, Delft (the Netherlands).

van Gent, M.R.A., *2002*. WAVE OVERTOPPING EVENTS AT DIKES, in: Scientific, W. (Ed.), Proc. 28th International Conference on Coastal Engineering. World Scientific Publishing Company, Cardiff, UK, pp. 2203–2215. https://doi.org/10.1142/9789812791306_0185

van Gent, M.R.A., *2001*. Wave Runup on Dikes with Shallow Foreshores. J. Waterw. Port, Coastal, Ocean Eng. 127, 254–262. https://doi.org/10.1061/(ASCE)0733-950X(2001)127:5(254)

van Gent, M.R.A., *1999*. Physical model investigations on coastal structures with shallow foreshores. 2D model tests with single and double-peaked wave energy spectra. Technical Report, WL - Delft Hydraulics, Delft (The Netherlands).

van Gent, M.R.A., van den Boogaard, H.F.P., Pozueta, B., Medina, J.R., *2007*. Neural network modelling of wave overtopping at coastal structures. Coast. Eng. 54, 586–593. https://doi.org/10.1016/j.coastaleng.2006.12.001

van Gent, M.R.A., van der Werf, I.M., *2019*. Influence of oblique wave attack on wave overtopping and forces on rubble mound breakwater crest walls. Coast. Eng. 151, 78–96. https://doi.org/10.1016/j.coastaleng.2019.04.001

Verhagen, H.J., van Vledder, G., Arab, S.E., *2008*. A practical method for design of coastal structures in shallow water, in: Proc. 31st International Conference on Coastal Engineering. World Scientific Publishing Company, pp. 2912–2922.

https://doi.org/https://doi.org/10.1142/9789814277426_0241

Victor, L., Van der Meer, J.W., Troch, P., *2012*. Probability distribution of individual wave overtopping volumes for smooth impermeable steep slopes with low crest freeboards. Coast. Eng. 64, 87–101. https://doi.org/10.1016/j.coastaleng.2012.01.003

Vinje, T., Brevig, P., *1981*. Numerical simulation of breaking waves. Adv. Water Resour. 4, 77–82. https://doi.org/10.1016/0309-1708(81)90027-0

WCED, *1987*. Our Common Future. World Commission on Environment and Development. Oxford.

Weggel, J.R., *1972*. Maximum Breaker Height for Design, in: Proc. 13th International Conference on Coastal Engineering. American Society of Civil Engineers, New York (USA), pp. 419–432. https://doi.org/10.1061/9780872620490.024

Xie, W., Shibayama, T., Esteban, M., *2019*. A semi-empirical formula for calculating the breaking depth of plunging waves. Coast. Eng. J. 61, 199–209. https://doi.org/10.1080/21664250.2019.1579459

Yao, Y., Huang, Z., Monismith, S.G., Lo, E.Y.M., *2012*. Characteristics of Monochromatic Waves Breaking over Fringing Reefs. J. Coast. Res. 29, 94–104. https://doi.org/10.2112/JCOASTRES-D-12-00021.1

Zanuttigh, B., Van der Meer, J.W., Bruce, T., Hughes, S.A., *2013*. Statistical Characterisation of Extreme Overtopping Wave Volumes, in: Proc. Coasts, Marine Structures and Breakwaters. ICE Publishing, London (UK), pp. 442–452.

“We ourselves feel that what we are doing is just a drop in the ocean. But the ocean would be less because of that missing drop.”

Teresa de Calcuta

8

Appendix A. Scientific Publications

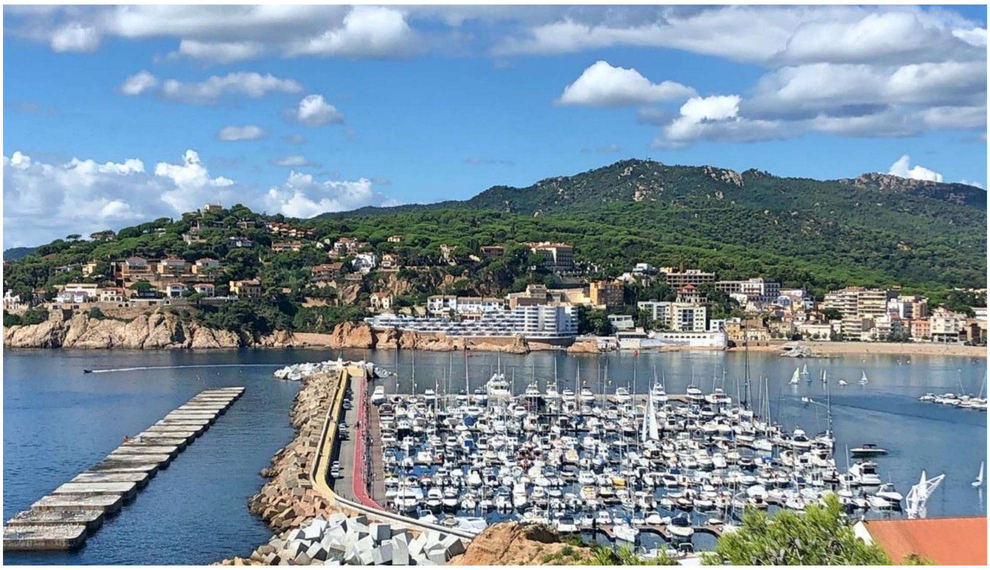

Port of Sant Feliu de Guixols (Spain), September 2020

1. **Mares-Nasarre, P., Argente, G., Gómez-Martín, M.E., Medina, J.R., 2019. Overtopping layer thickness and overtopping flow velocity on mound breakwaters. Coast. Eng. 154, 103561. https://doi.org/10.1016/j.coastaleng.2019.103561**

Overtopping layer thickness and overtopping flow velocity on mound breakwaters

Patricia Mares-Nasarre [1,] *, Gloria Argente[1], M. Esther Gómez-Martín[1] and Josep R. Medina[1]

[1]Lab. Ports and Coasts, Institute of Transport and Territory, Universitat Politècnica de València; patmana@cam.upv.es, jormollo@upv.es, mgomar00@upv.es, jrmedina@upv.es.

* Corresponding author: patmana@cam.upv.es

Abstract:

Mound breakwater design is evolving owing to rising sea levels caused by climate change and social concern regarding the visual impact of coastal structures. The crest freeboard of coastal structures tends to decrease while overtopping hazard increases over time. Pedestrian safety when facing overtopping events on coastal structures has been assessed considering the overtopping layer thickness (OLT) and overtopping flow velocity (OFV). This paper proposes a new method to estimate the OLT and OFV on mound breakwater crest during extreme overtopping events, based on 123 2D small-scale physical tests of conventional low-crested mound breakwaters with a single-layer Cubipod® and double-layer rock and cube armors. The new method to estimate OLT exceeded by 2% of incoming waves is based on formulas given in literature for dikes, but adapted and calibrated for mound breakwaters. The formula to estimate the OFV exceeded by 2% of incoming waves is based on the correlation between the statistics of the OLT and OFV, considering an empirical coefficient calibrated for each type of armor layer. Exponential and Rayleigh distribution functions are proposed for estimating the OLT and OFV with exceedance probabilities under 2%. Although the statistics of OLT and OFV depend on similar variables, contrary to intuition, specific OLT and OFV corresponding to the same overtopping event appear to be independent.

Keywords: mound breakwater, overtopping, overtopping layer thickness, overtopping flow velocity, Cubipod®, low-crested structures

1. Introduction

Crest elevation is a key factor in the design of mound breakwaters, as it affects the economic cost of the structure and its visual impact. The mean wave overtopping rate is typically considered for this end *[1]*; however, maximum individual volumes associated with the largest overtopping events are not directly characterized by the mean overtopping discharge. These extreme overtopping events are critical for the hydraulic stability of the breakwater crest and rear side *[2]*, as well as for pedestrian safety when standing on the structure.

Increasing social pressure to diminish the visual impact of coastal structures, and the sea level rise and stronger wave conditions caused by climate change *[3]* result in a reduction of the design dimensionless crest freeboard. Thus, overtopping rates and hazards to humans are expected to increase over time.

The overtopping layer thickness (OLT) and overtopping flow velocity (OFV) have been considered to estimate the overtopping hazard for humans (see *[4]* and *[5]*). Fig. 1 shows the thresholds for the OLT, h_c (m), and OFV, u_c (m/s), on the breakwater crests proposed by *Bae et al. [4]* for pedestrian safety, as well as the experimental results of pedestrian failure from different authors *[6, 7, 8 and 9]*. The referred limits were obtained from physical experiments using anthropomorphic dummies. In this figure, closed symbols correspond to overtopping flow observations, while the open symbols represent experiments conducted under constant flow conditions (floods).

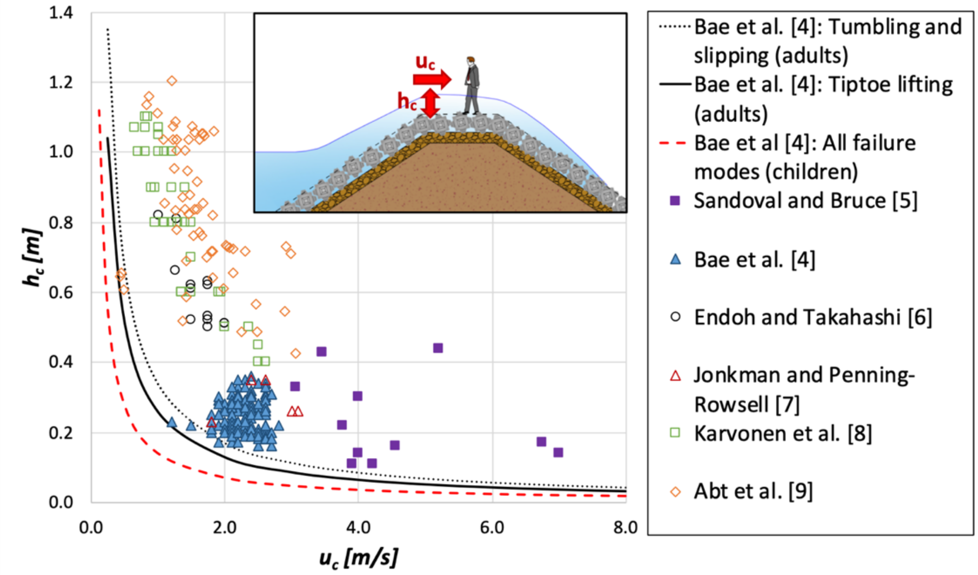

Fig. 1. Overtopping flow velocity, u_c and overtopping layer thickness, h_c limits for pedestrian stability given by *Bae et al. [4]* and other authors data.

The estimation of extreme OLT and OFV on breakwater crests is crucial to assess the hydraulic stability of the structure crest and pedestrian safety. Some studies in the literature are focused on the estimation of the OLT and OFV on dikes, but not on conventional mound breakwaters *[10]*. The objective of this study is to provide a method to estimate the OLT and OFV on conventional mound breakwaters during extreme overtopping events.

2. Literature review

Van Gent [11] proposed a method to estimate the wave run-up height exceeded by 2% of the incoming waves ($Ru_{2\%}$), estimated using Eqs. (1) to (4).

$$\begin{cases} \dfrac{Ru_{2\%}}{H_s} = c_0\, \xi_{s,-1} & if \quad \xi_{s,-1} \leq p \\ \dfrac{Ru_{2\%}}{H_s} = c_1 - \dfrac{c_2}{\xi_{s,-1}} & if \quad \xi_{s,-1} \geq p \end{cases} \tag{1}$$

where $c_0 = 1.35$, $c_1 = 4.0$, c_2 is given by Eq. (2), p is given by Eq. (3), $Ru_{2\%}$ is the wave run-up height exceeded by 2% of the incoming waves, $H_s=4(m_0)^{1/2}$ is the incident significant wave height at the toe of the structure, and $\xi_{s,-1}$ is the surf similarity parameter or Iribarren number given by Eq. (4), based on the spectral period $T_{m-1,0} = \frac{m_{-1}}{m_0}$, where m_i is the *i-th* spectral moment, $m_i = \int_0^\infty S(f) f_i df$, S(f) being the wave spectrum.

$$c_2 = 0.25\,\frac{{c_1}^2}{c_0} \tag{2}$$

$$p = 0.5\frac{c_1}{c_0} \tag{3}$$

$$\xi_{s,-1} = \frac{tan\ \alpha}{\sqrt{\dfrac{2\,\pi\,H_s}{g\,T_{m-1,0}^2}}} \tag{4}$$

Later, *Van Gent [12]* and *Schüttrumpf et al. [13]* performed physical tests focusing on the measurement of OLT and OFV on dike crests. Subsequently, *Schüttrumpf and Van Gent [14]* integrated the results of the two studies and described the overtopping flow on the dike crest using two variables: (1) the OLT on the crest exceeded by 2% of the incoming waves, $h_{c,2\%}$, and the OFV on the breakwater crest exceeded by 2% of the incoming waves, $u_{c,2\%}$. *Schüttrumpf and Van Gent [14]* also proposed a method to estimate the OLT and the OFV on dike crests based on the wave run-up height exceeded by 2% of the incoming waves ($Ru_{2\%}$), estimated using Eqs. (1) to (4), given by *Van Gent [11]*. According to *Schüttrumpf and Van Gent [13]*, $Ru_{2\%}$ is required to estimate the OLT and OFV on the seaside edge of the crest of the dike; $h_{A,2\%}(R_c)=h_A(z_A=R_c)$ and

$u_{A,2\%}(R_c)=u_A(z_A=R_c)$. Fig. 2 shows the key parameters and variables considered in the model given by the aforementioned authors, where MWL is the mean water level.

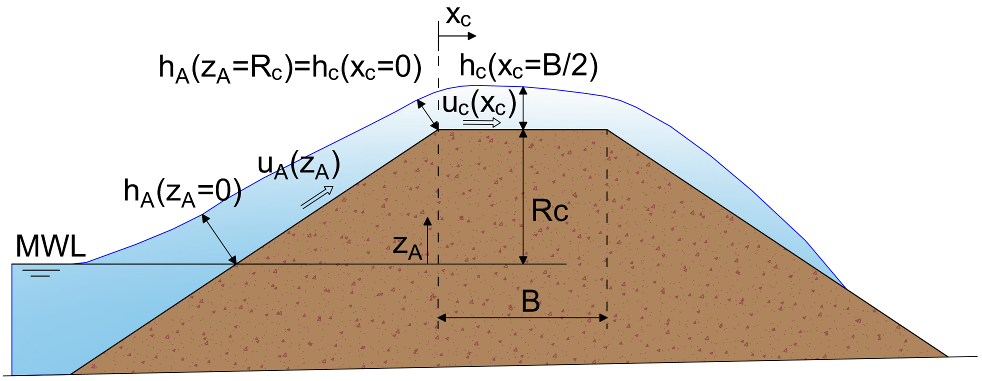

Fig. 2. Cross section defined by *Schüttrumpf and Van Gent [14]* to estimate overtopping layer thickness on dikes.

The OLT and OFV on the seaside slope of the dike ($0 \leq z_A \leq R_c$) can be estimated using Eq. (5) and Eq. (6), respectively.

$$\frac{h_{A,2\%}(z_A)}{H_s} = c^*_{A,h}\left(\frac{Ru_{2\%} - z_A}{H_s}\right) \tag{5}$$

$$\frac{u_{A,2\%}(z_A)}{\sqrt{g\,H_s}} = c^*_{A,u}\sqrt{\frac{Ru_{2\%} - z_A}{H_s}} \tag{6}$$

where $h_{A,2\%}(z_A)$ and $u_{A,2\%}(z_A)$ are the run-up layer thickness and velocity on the seaward slope exceeded by 2% of the incoming waves, respectively; z_A is the elevation on the MWL; $c_{A,h}{}^*$ and $c_{A,u}{}^*$ are the empirical coefficients given in Table 1.

According to *Schüttrumpf and Van Gent [14]*, the formulas to estimate the OLT and OFV on the crest of the dike ($0 \leq x_c \leq B$) are, respectively:

$$\frac{h_{c,2\%}(x_c)}{h_{A,2\%}(R_c)} = exp\left(-c^*_{c,h}\frac{x_c}{B}\right) \tag{7}$$

$$\frac{u_{c,2\%}(x_c)}{u_{A,2\%}(R_c)} = exp\left(-c^*_{c,u}\frac{x_c\,\mu}{h_{c,2\%}(x_c)}\right) \tag{8}$$

where $h_{c,2\%}$ and $u_{c,2\%}$ are the overtopping layer thickness and overtopping flow velocity on the crest exceeded by 2% of the incoming waves, respectively; x_c is the distance to the intersection of the crest and seaward slope; B is the crest width; μ is a friction coefficient; $c_{c,h}{}^*$ and $c_{c,u}{}^*$ are the empirical coefficients given in Table 1. *Schüttrumpf et* *al. [13]* discussed the influence of the bottom friction coefficient, μ, on the OFV on the dike crest, and provided some guidelines for μ.

Regarding the empirical coefficients, *Van Gent [12]* and *Schüttrumpf et al. [13]* proposed different coefficients, based on their own experimental results. Table 1 shows relevant differences in coefficients $c_{A,h}^*$ and $c_{c,h}^*$ used in Eqs. (5) and (7), respectively, while minor differences can be observed for coefficients $c_{A,u}^*$ and $c_{c,u}^*$ used in Eqs. (6) and (8), respectively. The range of applicability for dikes when using these coefficients is also listed in Table 1.

	Van Gent [12]	***Schüttrumpf et al. [13]***	***Van der Meer et al. [16]***
Slope (V/H)	1/4	1/3, 1/4, 1/6	1/3
R_c/H_s	0.7 - 2.2	0.0 - 4.4	0.7–2.9
H_s/h_s	0.2 – 1.4	0.1 – 0.3	0.1 – 0.3
$c_{A,h}^*$	0.15	0.33	0.13
$c_{A,u}^*$	1.30	1.37	-
$c_{c,h}^*$	0.40	0.89	-
$c_{c,u}^*$	0.50	0.50	-

Table 1. Range of applicability and empirical coefficients for dikes.

The range of applicability of the empirical coefficients given by *Van Gent [12]* falls within the range of application of the coefficients given by *Schüttrumpf et al. [13]*. However, $h_{c,2\%}(B/2)$ calculated with Eqs. (5) and (7) using $c_{A,h}^*=0.15$ and $c_{c,h}^*=0.40$ proposed by *Van Gent [12]* is 58% ([0.15/0.33]×[exp(-0.40*1/2)/ exp(-0.89*1/2)]) of the $h_{c,2\%}(B/2)$ calculated with the same equations using $c_{A,h}^*=0.33$ and $c_{c,h}^*=0.89$ proposed by *Schüttrumpf et al. [13]*. Although the tested dikes were similar, the estimations of $h_{c,2\%}(B/2)$ given by *Schuttrumpf et al. [13]* are almost twice the estimations given by Van Gent [12]. Different experimental designs (e.g. bottom slope) and different experimental ranges (see, structure slope and R_c/H_s ranges in Table 1) may explain some differences. Further discussion on slope angle influence can be found in *Bosman et al. [15]*. Nevertheless, this significant difference is hard to explain because both refer to dikes in similar conditions.

Van der Meer et al. [16] conducted physical tests on a dike with a V/H = 1/3 slope and measured the OLT and OFV at the seaward crest edge, and at the landward crest edge. The range of variables in these tests is shown in Table 1.

Van der Meer et al. [16] combined their experimental results with the observations obtained by *Van Gent [12]* and *Schüttrumpf et al. [13]*. Based on this new data base, *Van* *der Meer et al. [16]* proposed a new method for dikes also based on the difference between the run-up height exceeded by 2% of the incoming waves, $R_{u,2\%}$, and the crest freeboard, R_c. Eq. (9) was proposed to estimate the OLT exceeded by 2% of the incoming waves at the seaward crest, $h_{A,2\%}(R_c)$. Considering $z_A=R_c$ in Eq. (5), Eq. (9) leads to $c_{A,h}{}^*=0.15$ given in Table 1. Eqs. (10) and (11) describe the OFV exceeded by 2% of the incoming waves at the seaward crest, $u_{A,2\%}(R_c)$, and the OFV decay along the crest, $u_{c,2\%}(x_c)$, respectively:

$$h_{A,2\%}(R_c) = 0.13\,(Ru_{2\%} - R_c) \tag{9}$$

$$u_{A,2\%}(R_c) = 0.35\,\cot\alpha\,\sqrt{g\,(Ru_{2\%} - R_c)} \tag{10}$$

$$\frac{u_{c,2\%}(x_c)}{u_{A,2\%}(R_c)} = exp\left(-1.4\frac{x_c}{L_{m-1,0}}\right) \tag{11}$$

where α is the seaward slope angle, g is the gravity acceleration, and $L_{m-1,0}$ is the wave length based on the spectral period $T_{m-1,0}$. *Van der Meer et al. [16]* proposed a Rayleigh distribution to describe the distribution functions of the OLT and OFV.

Lorke et al. [17] performed physical model tests on dikes (V/H = 1/3 and 1/6), focusing on the effect of wind and currents on the overtopping on dikes with $0.33 \leq R_c/H_s \leq 2.86$ and $0.13 \leq H_s/h_s \leq 0.3$. These authors measured the OLT and OFV at the landward crest edge, using conventional wave gauges and miniature propellers. Based on their experimental observations, they proposed new values for the empirical coefficient $c_{c,h}{}^*$ of Eq. (7) given by *Schüttrumpf and Van Gent [14]* as a function of the seaside slope of the dike: $c_{c,h}{}^* = 0.35$ for V/H = 1/3 slope and $c_{c,h}{}^* = 0.54$ for V/H = 1/6 slope. It is noteworthy that these empirical coefficients were close to $c_{c,h}{}^* = 0.40$ proposed by *Van Gent [12]* for V/H=1/4.

Hughes et al. [18] analyzed the small-scale measurements on slightly submerged levees from *Hughes and Nadal [19]* within the range $-0.32 \leq R_c/H_s \leq -0.11$ and $R_c = -0.29$ m at the prototype scale (scale factor 1:25). During these tests, the OLT was measured on the crest close to the seaward side edge and landward edge using pressure cells, while the OFV was recorded using fiber-optic laser Doppler velocimeters at the same locations. From Eqs. (9) and (10) given by *Van der Meer [16]*, *Hughes et al. [18]* derived a relationship between $h_{A,2\%}(R_c)$ and $u_{A,2\%}(R_c)$ and proposed the Eq. (12) using the landward side edge measurements:

$$u_{A,2\%}(z_A = R_c) = 1.53\,\sqrt{g\,h_{A,2\%}(z_A = R_c)} \tag{12}$$

Hughes et al. [18] also investigated the correlation between the OLT and OFV corresponding to the same overtopping event. No correlation was found between the OLT and OFV corresponding to the same overtopping event. Additionally, the distribution functions for the overtopping variables were studied and their coefficients were fitted utilizing the 10% upper values to better describe the most extreme overtopping events. The Rayleigh distribution was recommended to describe the OLT and OFV distributions.

EurOtop [1] proposed a method for dikes to estimate $h_{A,2\%}$ and $h_{c,2\%}$ based on the difference between the estimated wave run-up ($Ru_{2\%}$) and the crest freeboard (R_c). The OLT on the seaside slope edge of the dike, $h_{A,2\%}(R_c)$, was estimated by Eq. (5) using the coefficient $c_{A,h}^*$ given in Table 2. $Ru_{2\%}$, was estimated by Eqs. (13)

$$\frac{Ru_{2\%}}{H_s} = 1.65\ \gamma_f\ \gamma_\beta\ \gamma_b\ \xi_{s,-1} \tag{13a}$$

with a maximum value of

$$\frac{Ru_{2\%}}{H_s} = 1.0\,\gamma_f\ \gamma_\beta\ \left(4\ -\ \frac{1.5}{\sqrt{\gamma_b\ \xi_{s,-1}}}\right) \tag{13b}$$

where γ_b is the influence factor for an existing toe berm, γ_f is the roughness factor, γ_β is the influence factor for oblique wave attack, and $\xi_{s,-1}$ is the breaker parameter given by Eq. (4). *EurOtop [1]* provided the roughness factors, γ_f.

Slope (V/H=1/3 and 1/4)	**Slope (V/H=1/6)**
0.20	0.30

Table 2. Empirical coefficient $c_{A,h}$* for Eq. (5) given by *EurOtop [1]*.

Once $Ru_{2\%}$ is estimated using Eqs. (13), $h_{A,2\%}(R_c)$ is calculated using Eq. (5) with the coefficient $c_{A,h}^*$ given in Table 2. Finally, $h_{c,2\%}(x_C)$ is assumed to be constant after an initial turbulent zone and approximately equal to $h_{c,2\%}(x_c>>0)=(2/3)h_{A,2\%}(R_c)$ on the crest of the dike not close to the seaside slope.

3. Experimental Methodology

Two-dimensional small-scale physical tests were conducted in the wave flume (30 m × 1.2 m × 1.2 m) of the Laboratory of Ports and Coasts of the *Universitat Politècnica de València* (LPC-UPV), using a piston-type wavemaker and a gentle bottom slope (m = 1/50). Fig. 3 shows a longitudinal cross-section of the LPC-UPV wave flume as well as the location of the wave gauges utilized in this study.

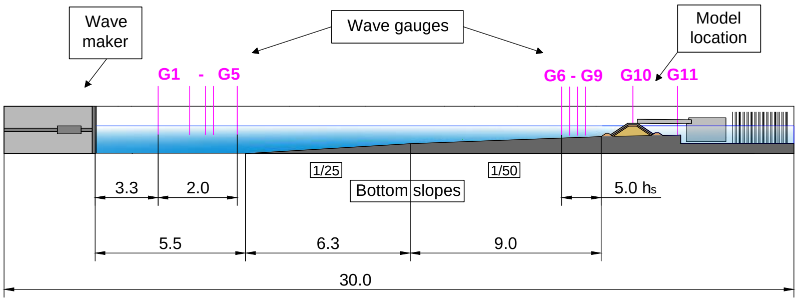

Fig. 3. Longitudinal cross section of the LPC-UPV wave flume (dimensions in meters).

The cross section of the model depicted in Fig. 4 corresponds to a mound breakwater with V/H = 2/3 slope and toe berms, protected with a single-layer Cubipod® armor, double-layer rock armor, and double-layer randomly-placed cube armor. In this study, the nominal diameters or equivalent cube sizes of the armor units were D_n = 37.9 mm for the Cubipod® units, D_n = 31.8 mm for rocks, and D_n= 39.7 mm for cubes. The range of variables in the tests is listed in Table 3; the test matrix is shown in Appendix A.

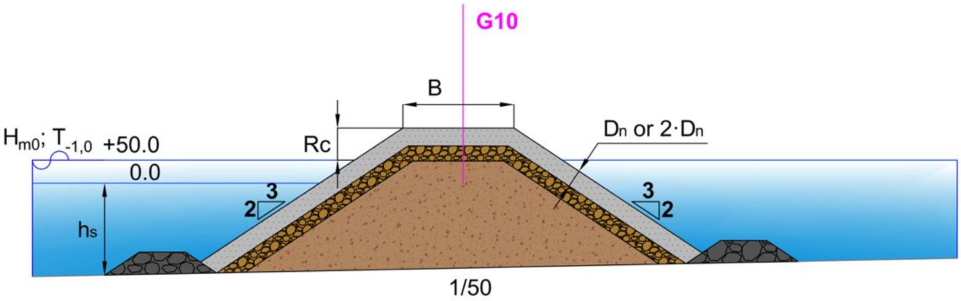

Fig. 4. Cross section of models tested in the LPC-UPV wave flume (dimensions in mm).

	Cubipod® (1L)	Rock (2L)	Cube (2L)
R_c/H_s	0.43–1.38	0.80–1.75	0.34–1.67
H_s/h_s	0.30–0.73	0.29–0.61	0.20–0.64
H_s/D_n	0.15–0.19	0.13–0.16	0.13–0.16
***B* (mm)**	240	259	265
D_n (mm)	37.9	31.8	39.7

Table 3. Range of variables of 2D physical tests at the LPC-UPV wave fume.

One thousand random waves were generated following the JONSWAP spectra (γ= 3.3). The active wave absorption system AWACS was activated to avoid multireflections.

Each test series was associated to the water depth at the toe of the structure (h_s). For a given h_s, the significant wave height at the wave generation zone (H_{sg}) and peak period (T_p) were calculated such that the Iribarren number was maintained approximately constant along each test series of wave runs ($Ir_p=T_p/cot\alpha(2\pi H_{sg}/g)^{1/2}\approx$ 3 or 5). For each Iribarren number, Ir_p, the values of the significant wave height at the wave generating zone (H_{sg}) were increased, from no damage to failure of the armor layer, or wave breaking at the generation zone. H_{sg} was increased within the range $80 \leq H_{sg}(\text{mm}) \leq 240$ in steps of 10 mm. The water depth at the toe of the model was h_s= 200 and 250 mm for the Cubipod® and rock armored models, and h_s = 250 and 300 mm for the cube armored model. Owing to the importance of the crest freeboard of the structure when studying overtopping, two corrections have been considered: (1) the accumulated overtopping volumes extracted during the test series on a working day, and (2) the natural evaporation and facilities leakages that resulted in a small increase in the crest freeboard. The correction was 9.9 mm in the worst case. Neither pilling-up (wave gauge G11) nor low-frequency oscillations were significant during the tests.

The water surface elevation was measured using 11 capacitive wave gauges. Wave gauges G1 to G5 were placed close to the wavemaker following *Mansard and Funke [20]* recommendations, and were used to separate incident and reflected waves in the wave generation zone. Wave gauges G6 to G9 were located along the flume near the model, where depth-induced wave breaking occurs and existing methods to separate incident and reflected waves are not reliable. Wave gauge G10 was placed on the model crest and G11 was located behind the model. The distances from G6, G7, G8, and G9 to the toe of the model were varied with the water depth at the toe, h_s. G6, G7, G8, and G9 were placed at distances $5h_s$, $4h_s$, $3h_s$, and $2h_s$ from the toe of the structure, respectively, according to *Herrera and Medina [21]*.

Armor damage was analyzed after each test by comparing the photographs captured perpendicular to the armor slope, using the Virtual Net method (*Gómez-Martín and Medina [22]*) in order to consider armor-unit extractions, sliding of the armor layer as a whole, and Heterogeneous Packing failure modes simultaneously (see *Gómez-Martín and Medina [23]*). Overtopping discharges were measured using a weighing system located in a collection tank behind the breakwater model during the test.

3.1. Measurement of overtopping layer thickness (OLT) and overtopping flow velocity (OFV)

As mentioned previously, the OLT was measured in the middle of the model crest using the capacitive wave gauge G10. These capacitive wave gauges must be partially submerged and they are calibrated with a certain reference level daily. To allow G10 to measure the OLT on the model crest, this wave gauge was introduced into a void vertical cylinder inserted in the model. This cylinder was 85 mm in diameter and 120 mm in length, and was filled up with water before the tests. Its upper part was closed with a lid covering the cylinder except for a slot to pass the wave gauge. Aeration was considered negligible because visual inspection of the overtopping events did not show significant aeration, but a clear water surface. The performance of the wave gauge G10 was excellent when measuring the OLT; low noise as well as low variations in the base level were observed (see Fig. 5). In this study, the maximum measured OLT of each overtopping event is considered the measured $h_c(B/2)$.

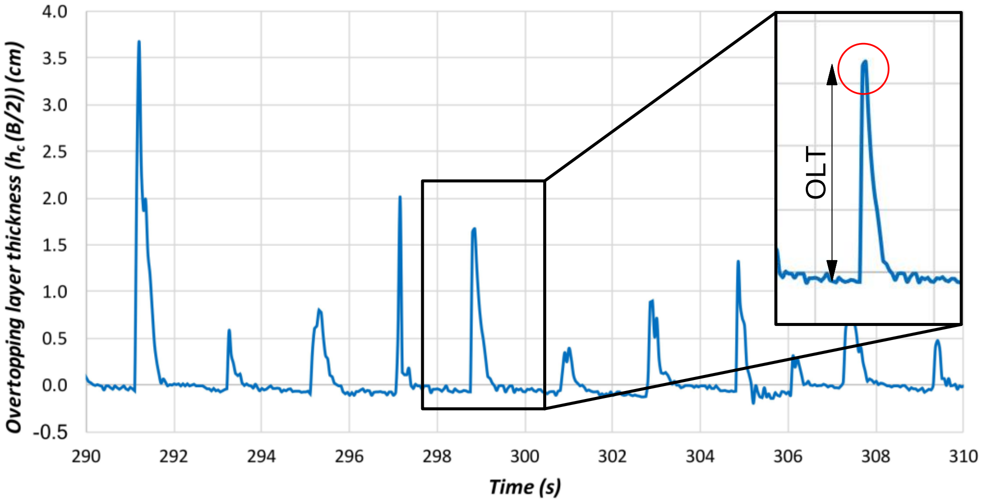

Fig. 5. Raw record of the OLT given by wave gauge G10.

The OFV were recorded in 66 out of 123 physical tests (13 tests with Cubipod®-1L armor, 14 test with rock-2L armor and 39 tests with cube-2L armor) using three miniature propellers installed on the model crest in three different positions: (1) seaward edge of the crest, (2) middle of the crest, and (3) landward edge of the crest. These propellers (11.6 mm in diameter) could measure the velocities within the range 0.15 m/s to 3.00 m/s. From the propeller measurements, the maximum measured values of the OFV of each overtopping event were obtained. Fig. 6 shows pictures of the aforementioned equipment.

3.2. Wave analysis

Using wave gauges G1 to G5 located at the wave generation zone, incident and reflected waves were separated using the LASA-V method (see *Figueres and Medina [24]*). Although the LASA-V method is valid for nonlinear and nonstationary irregular waves, it is not valid for breaking waves. According to *Battjes and Groenendijk [25]*, Composite Weibull distribution describes the wave height distribution on shallow foreshores. This distribution function is the one implemented in SwanOne software (see *Verhagen et al., [26]*). The incident significant wave height in the depth-induced breaking zone was estimated using the incident waves at the wave generation zone and the SwanOne numerical model (*Verhagen et al. [26]*). This methodology was validated by *Herrera and Medina [21]*, who compared the numerical SwanOne estimations with measurements in the wave flume without any structure. A similar comparison was also performed in this study; the results are depicted in Fig. 7.

The relative Mean Squared Error ($rMSE$) given by Eq. (14) was used to measure the goodness of fit. $0 \leq rMSE \leq 1$ estimates the proportion of variance not explained by the prediction technique; therefore, the lower r*MSE*, the better are the predictions. In this case, *rMSE* = 4.1%.

$$rMSE = \frac{MSE}{VAR} = \frac{\frac{1}{N_o}\sum_{i=1}^{N_o}(t_i - e_i)^2}{\frac{1}{N_o}\sum_{i=1}^{N_o}(t_i - \bar{t})^2} \qquad (14)$$

where *MSE* is the Mean Squared Error, VAR is the variance in the measured target values, N_o is the number of observations, t_i is the target value, e_i is the estimated value, and $\bar{t}$ is the average measured target value.

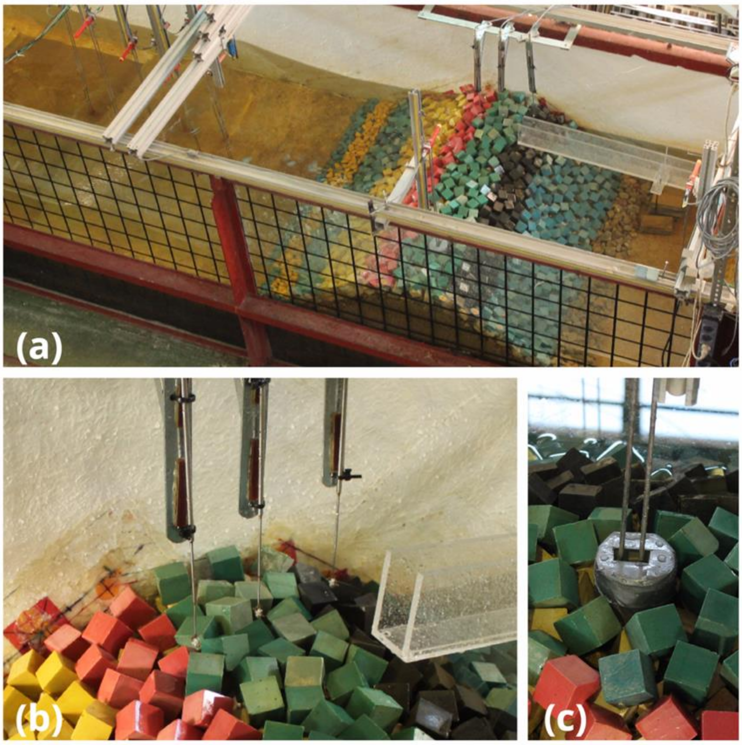

Fig. 6. Oblique view of the model in the LPC-UPV wave flume: (a) general view, (b) micro propellers and (c) wave gauge G10.

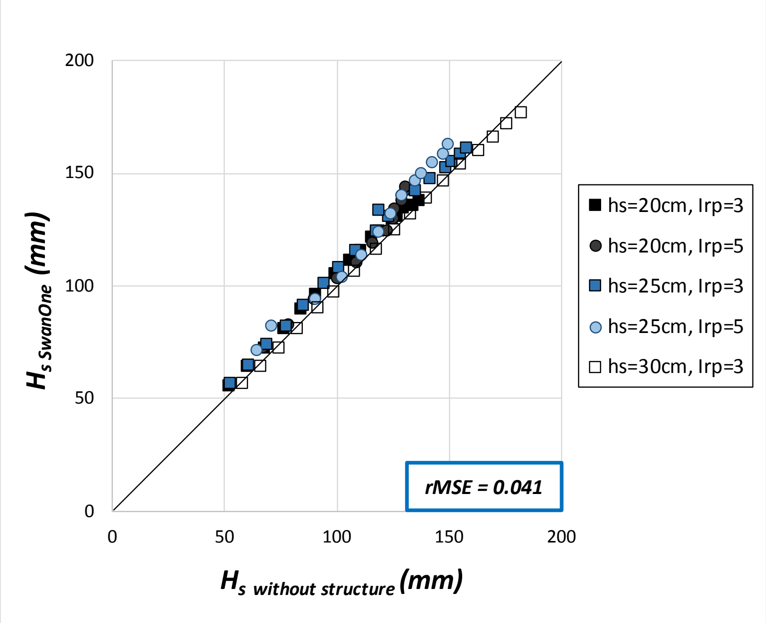

Fig. 7. Comparison of measured H_s without structure in the model zone and estimation given by SwanOne.

4. Comparison of the existing methods for estimating the overtopping layer thickness (OLT)

As mentioned in section 2, several methods are given in the literature to estimate the OLT exceeded by 2% of the incoming waves on the crest of a dike, $h_{c,2\%}$. Although they were proposed for dikes and not for conventional mound breakwaters, a comparison was performed between the OLT observed in this study on mound breakwater crests and the predictions by the aforementioned methods for dikes. To apply the *EurOtop [1]* formulas, the roughness factors recommended in the manual were used: $\gamma_f = 0.49$, $\gamma_f = 0.40$, and $\gamma_f = 0.47$ for single-layer Cubipod® armors, double-layer rock armored structures with a permeable core, and double-layer randomly-placed cube armors, respectively. However, it should be taken into account that *Molines and Medina [27]* pointed out that the roughness factors depend on the formula and experimental database; thus, γ_f should be calibrated specifically for each formula and database.

Fig. 8 compares the measured OLT exceeded by 2% of the incoming waves at the middle of the breakwater crest, $h_{c,2\%}(B/2)$, and the estimations given by Eqs. (5) and (7) (*Schüttrumpf and Van Gent [14]*) with coefficients $c_{A,h}^*$ and $c_{c,h}^*$ given in Table 1 (*Van Gent [12]*, data in white, and *Schüttrumpf et al. [13]*, data in blue) considering $Ru_{2\%}$ calculated with Eqs. (1) to (4) given by *Van Gent [11]*; and Eqs. (5) with coefficient $c_{A,h}^*$

given in Table 2 and $h_{c,2\%}(B/2)=(2/3)h_{A,2\%}(R_c)$, proposed by *EurOtop [1]*, considering $Ru_{2\%}$ given in Eqs. (13) (*EurOtop [1]*, data in red and black).

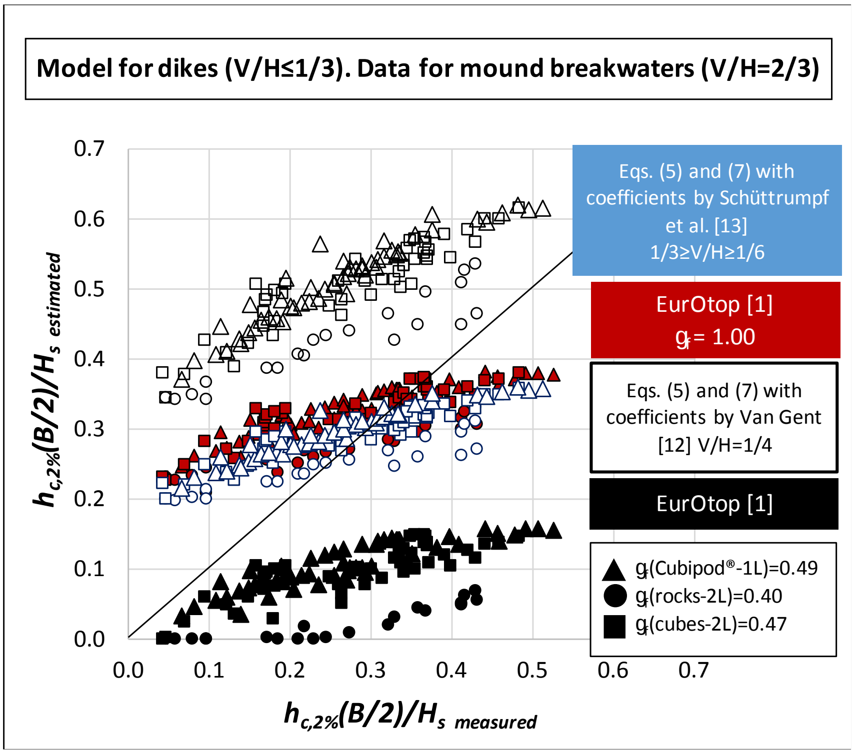

Fig. 8. Comparison of measured and estimated overtopping layer thickness, $h_{c,2\%}(B/2)$.

As mentioned in Section 2, estimations of $h_{c,2\%}(B/2)$ given by Eqs. (5) and (7) with coefficients $c_{A,h}{}^{*}$ and $c_{c,h}{}^{*}$ proposed by *Schüttrumpf et al. [13]* are almost twice the estimations obtained when considering the coefficients proposed by *Van Gent [12]*, due the differences in the empirical coefficients shown in Table 1.

Using Eqs. (1) to (4) proposed by *Van Gent [11]* to estimate $Ru_{2\%}$ and $h_{c,2\%}(B/2)$ calculated using Eqs. (5) with $c_{A,h}{}^{*}$=0.20 and $h_{c,2\%}(B/2)=(2/3)h_{A,2\%}(R_c)$ proposed by *EurOtop [1]*, $h_{c,2\%}(B/2)$ would be similar than that given by Eqs. (5) and (7) (*Schüttrumpf and Van Gent [14]*) with coefficients $c_{A,h}{}^{*}$=0.15 and $c_{c,h}{}^{*}$=0.40 proposed by *Van Gent [12]* (0.20/0.15×[(2/3)/exp(-0.40/2)]=1.09). As shown in Fig. 8, if Eqs. (13) proposed by *EurOtop [1]* with γ_f =1.00 are used to estimate $Ru_{2\%}$ (data in red), the estimation of $h_{c,2\%}(B/2)$ given by *EurOtop [1]* is also similar to that proposed by *Van Gent [12]*. However, if Eqs. (13) with γ_f proposed by *EurOtop [1]* are used to estimate $Ru_{2\%}$ (data in black), the estimation of $h_{c,2\%}(B/2)$ given by *EurOtop [1]* is much lower than $h_{c,2\%}(B/2)$ given by *Van Gent [12]*.

To show the differences in estimating $Ru_{2\%}/H_s$ when roughness factors *[1]* are used, calculations are given for Test #1 in Table A.2. (double layer rock armored model). In this case, H_s= 104 mm, $T_{m-1,0}$ = 1.23s, $\gamma_\beta = \gamma_b = 1$, $\gamma_f = 0.40$ and $tan\alpha = 2/3$.

$\xi_{s,-1} = (2/3)/\sqrt{[(2 \times \pi \times 0.104)/(9.81 \times 1.23^2)]} = 3.18$.

Using Eqs. (1) to (4) proposed by *Van Gent [11]* with c_0 = 1.35 and c_1 = 4.0.

$c_2 = 0.25 \times 4.0^2/1.35 = 2.96$ and $p = 0.5 \times 4.0/1.35 = 1.48$.

$\xi_{s,-1} > p$ and $Ru_{2\%}/H_s = 4.0 - 2.96/3.18 = 3.07$.

Using Eqs. (13) proposed by *EurOtop [1]*,

$Ru_{2\%}/H_s = 1.65 \times 1 \times 1 \times 0.40 \times 3.18 = 2.06$

With a maximum value of

$Ru_{2\%}/H_s = 1.0 \times 0.40 \times 1 \times \left(4 - 1.5/\sqrt{1 \times 3.18}\right) = 1.26$

$Ru_{2\%}/H_s$ (*Van Gent [11]*) = 3.07 >> 1.26 = $Ru_{2\%}/H_s$ (*EurOtop [1]*)

None of the existing estimators for dikes compared in Fig. 8 represent the OLT on mound breakwaters satisfactorily. Furthermore, significant differences are found between some methods given in the literature for dikes.

5. A new method to estimate the overtopping layer thickness (OLT) on mound breakwater crests

5.1. OLT exceeded by 2% of the incoming waves, $h_{c,2\%}$ (B/2)

The formulas proposed by *Schüttrumpf and Van Gent [14]* and *EurOtop [1]* to estimate the OLT exceeded by 2% of the incoming waves on the crest of dikes (smooth impermeable slope) are not directly applicable to typical mound breakwaters (rough permeable slope where infiltration occurs).

The methods proposed by *EurOtop [1]*, *Van Gent [12]* and *Schüttrumpf et al. [13]* to calculate the OLT on the crest of the dikes are based on the estimation of $Ru_{2\%}$. In this study on mound breakwaters, it is reasonable to use Eqs. (15) to estimate $Ru_{2\%}$, as indicated by *EurOtop [1]* for mound breakwaters, calibrating the roughness factor γ_f to the formula and experimental observations recorded in this study.

$$\frac{Ru_{2\%}}{H_s} = 1.65\, \gamma_f\, \gamma_\beta\, \gamma_b\, \xi_{s,-1} \tag{15a}$$

with a maximum value of

$$\frac{Ru_{2\%}}{H_s} = 1.00\, \gamma_{f,surging} \gamma_\beta\, \gamma_b \left(4.0 - \frac{1.5}{\sqrt{\xi_{s,-1}}}\right) \tag{15b}$$

where $\gamma_{f,surging}$ [-] is a coefficient that increases linearly up to 1.0 following

$$\gamma_{f,surging} = \gamma_f + (\xi_{s,-1} - 1.8)\frac{1 - \gamma_f}{8,2} \tag{15c}$$

The maximum $Ru_{2\%}/H_s$ is 2.0 for permeable core. In this case, $\gamma_\beta = \gamma_b = 1$.

It is convenient to point out that roughness factors, γ_f, is a fitting parameter and γ_f is different depending on the formula and database *[27]*. It is also reasonable to use Eqs. (5) and (7) proposed by *Schüttrumpf and Van Gent [14]*, calibrating the empirical coefficient $c_{A,h}^*$ with the experimental observations of this study.

Since OLT has been only measured in one site of the crest ($x_c=B/2$), $c_{c,h}^*$ cannot be calibrated in this study and the highest value of $c_{c,h}^*$ (maximum decay along the crest) found in the literature for dikes ($c_{c,h}^* = 0.89$) is assumed. If $c_{c,h}^*$ was calibrated in the future (for mound breakwaters), the optimum $c_{A,h}^*$ given in Table 4 should be modified to keep constant $c_{A,h}^* \times exp(-c_{c,h}^*/2)$.

Considering a specific estimator and a given dataset, the *rMSE* could be used to estimate the optimum values of the roughness factors and empirical coefficients. However, no information would be obtained regarding the uncertainty of their estimations. Hence, a bootstrap resample technique was applied in this study to assess the uncertainty of the estimations. This technique consists of the random selection of *N* data from *N* original datasets. The probability of each datum to be selected each time is 1/*N*; therefore, some data were selected once, or more than once while some other data were absent in a resample.

First, using the results from 123 physical tests performed at the LPC-UPV wave flume, 1,000 resamples were performed optimizing both the roughness factors and the empirical coefficient $c_{A,h}^*$. Thus, 1,000 values of roughness factors and empirical coefficients that minimize the *rMSE* were obtained, and they were used to statistically characterize the parameters using percentiles 5%, 50%, and 95% (see Table 4).

	P5%	**P50%**	**P95%**
$c_{A,h}^*$	0.49	0.52	0.54

Table 4. First level bootstrap resample results.

Subsequently, the empirical coefficient value was fixed to their 50% percentile ($c_{A,h}^* = 0.52$), and 1,000 bootstrap resamples were performed varying only the roughness factors, γ_f. The optimum roughness factors can be obtained for the model proposed using the 50% percentile for the empirical coefficients and the existing database. Using the obtained 1,000 values of each roughness factor, they were statistically characterized using the referred percentiles. Tables 4 and 5 show the results from both bootstrap resample levels.

		P5%	P50%	P95%	*rMSE*
Roughness factor (γ_f)	Cubipod® (1L)	0.32	0.33	0.34	0.149
	Rock (2L)	0.46	0.48	0.50	0.183
	Cube (2L)	0.33	0.35	0.36	0.159

Table 5. Second level bootstrap resample results using $c_{A,h}^* = 0.52$ and $c_{c,h}^* = 0.89$.

Fig. 9 shows the measured OLT at the middle of the breakwater crest, $h_{c,2\%}(B/2)$, as compared to the estimations given by Eqs. (15) and Eqs. (5) and (7) using the 50% percentile for the roughness factors and empirical coefficients given in Tables 4 and 5, as well as the 90% confidence interval. The *rMSE*, used to measure the goodness of fit, is given in Table 5.

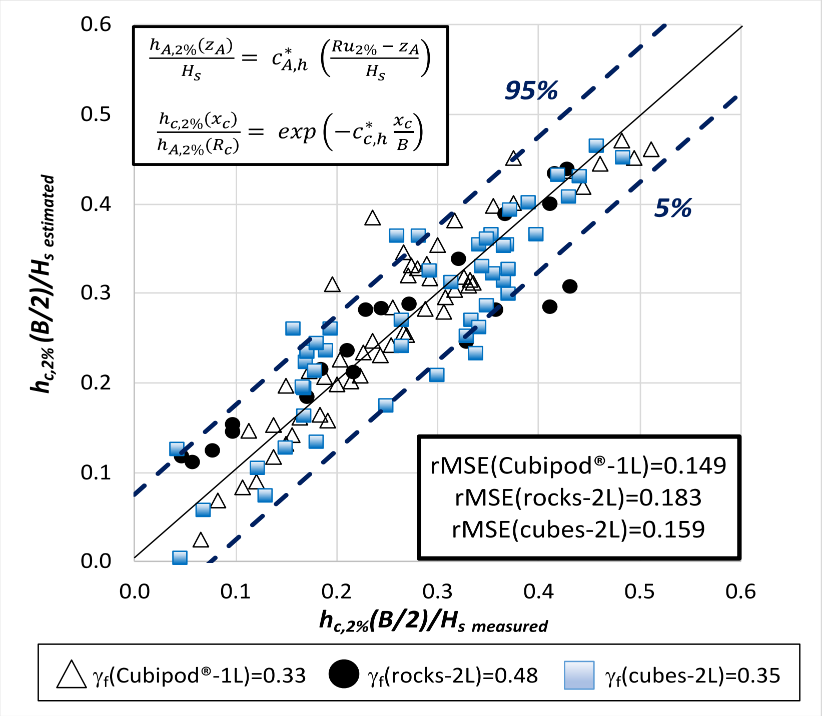

Fig. 9. Comparison of measured and estimated overtopping layer thickness, $h_{c,2\%}(B/2)$, and 90% confidence interval.

5.2. *Distribution of OLT,* $h_c(B/2)$

Extreme overtopping events are critical to assess the hydraulic stability of the breakwater crest and overtopping hazard to humans. Hence, it is necessary to describe not only the OLT exceeded by 2% of the incoming waves but also the OLT distribution in the most severe wave storms. As indicated by *Hughes et al. [18]*, the extreme tail of the distribution of the overtopping variables is described better when only considering the low exceedance events. Therefore, in this study, only the OLT values associated with exceedance probabilities below 2% are used for calibration purposes.

As presented in section 2, in previous studies, a Rayleigh distribution was suggested for describing the overtopping variable distributions. Nevertheless, in this study, the best results were obtained with an Exponential distribution, given by Eq. (16).

$$F\left(\frac{h_c(B/2)}{h_{c,2\%}(B/2)}\right) = 1 - exp\left(-K_1 \frac{h_c(B/2)}{h_{c,2\%}(B/2)}\right) \tag{16}$$

where $h_c(B/2)$ is the value of the OLT with exceedance probabilities under 2%, $h_{c,2\%}(B/2)$ is the OLT not exceeded by 2% of the incoming waves, and K_1 is an empirical coefficient to be calibrated. K_1 is estimated for each physical test based on the 20 (1,000 × 2%) highest measured values of the OLT. The exceedance probability assigned to each OLT value was obtained as $m/(N+1)$, where m is the rank of the OLT observation and N the number of waves. Based on 2,460 (20 × 123) values obtained from 123 physical model tests, the best estimation is K_1 = 4.2. This coefficient was calculated as the 50% percentile of the 123 values that minimize the *rMSE* for each of the 20 OLT datasets. Fig. 10 shows the variability of the best fit values for K_1.

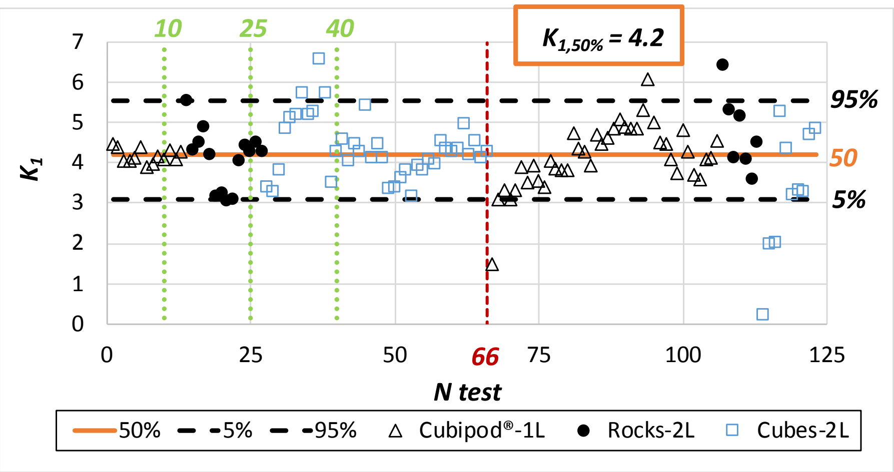

Fig. 10. 95%, 50%, and 5% percentile of K_1.

Fig. 11 presents three example datasets of the proposed Exponential distribution in probability plot, while Fig. 12 shows the measured OLT distribution for each test against the proposed distribution, as well as the 90% confidence interval. As a result *rMSE* = 0.162, indicating a good agreement with the experimental observations.

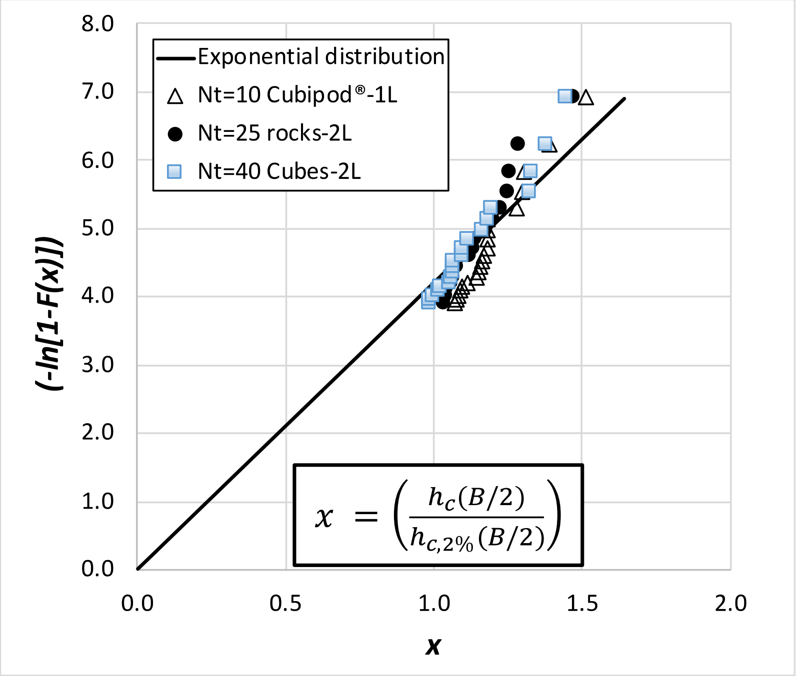

Fig. 11. Typical sample of cumulative distribution functions of OLT in equivalent probability plot.

6. A new method to estimate overtopping flow velocity (OFV) on mound breakwaters

6.1. *OFV exceeded by 2% of the incoming waves,* $u_{c,2\%}$ (B/2)

In section 2, different methods were presented to estimate the OFV exceeded by 2% of the incoming waves on the crest of a dike. Some of these proposals were based on the correlation between the statistics of the OLT and the statistics of the OFV (see Eqs. (8) and (12)). In this study, a new formula is proposed to estimate the OFV in the middle of the breakwater crest exceeded by 2% of the incoming waves, based on the relationship given by Eq. (17). It is noteworthy that the OLT exceeded by 2% of the incoming waves and OFV exceeded by 2% of the incoming waves do not always correspond to the same overtopping event.

$$u_{c,2\%}(B/2) = K_2\sqrt{g\, h_{c,2\%}(B/2)} \tag{17}$$

where $u_{c,2\%}(B/2)$ is the OFV at the middle of the breakwater crest exceeded by 2% of the incoming waves, K_2 is an empirical coefficient to be calibrated that depends on the armor unit, and $h_{c,2\%}(B/2)$ is the OLT at the middle of the breakwater crest exceeded by 2% of the incoming waves.

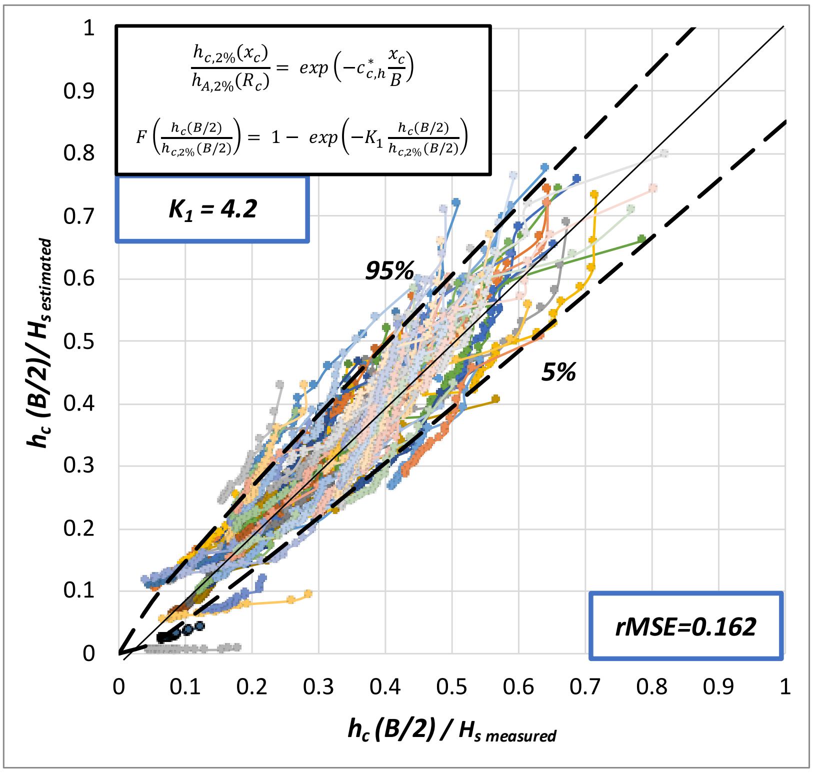

Fig. 12. Measured and estimated distribution of OLT in the middle of the breakwater crest, h_c (B/2), for each test and 90% confidence interval.

To obtain the best K_2 for each armor layer, the bootstrap resample technique was applied similarly to that described in section 4.1. Note that only the measured velocities within the operation range of the propellers (see section 3) have been used. First, 1,000 bootstrap resamples were created using the 66 OFV values. The optimum K_2 was determined for each sample as the one that minimizes the *rMSE*. Hence, 1,000 values of K_2 were obtained for each armor layer, such that they could be characterized statistically. The 5%, 50%, and 95% percentiles were used to this end and they are presented in Table 6 as well as *rMSE* values when using P50% of K_2. Fig. 13 compares the measured overtopping flow velocity exceeded by 2% of the incoming waves in the middle of the breakwater crest and the estimation given by Eq. (17) when using the 50% percentile of the K_2 coefficient.

K_2	P5%	P50%	P95%	*rMSE*
Cubipod® (1L)	0.56	0.57	0.59	0.228
Rock (2L)	0.46	0.47	0.49	0.114
Cube (2L)	0.57	0.60	0.63	0.233

Table 6. Statistical characterization of K_2 and *rMSE* values when using 50% percentile.

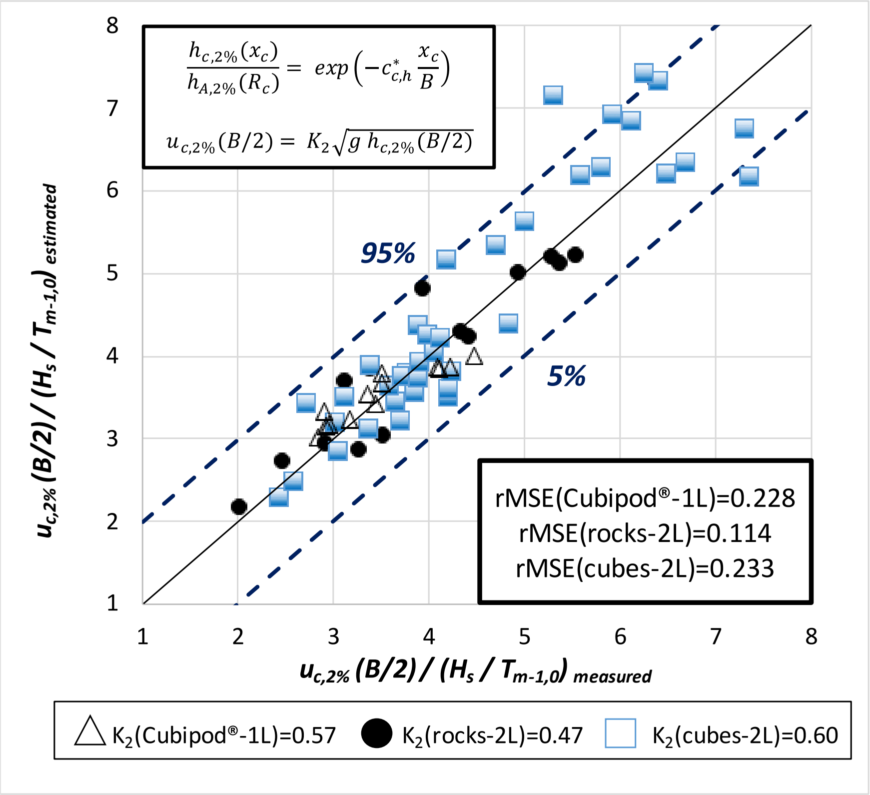

Fig. 13. Comparison of measured and estimated overtopping flow velocity, $u_{c,2\%}(B/2)$, and 90% confidence interval.

6.2. Distribution of OFV, u_c (B/2)

Eq. (17) shows a 1/2-power relationship between the OLT and OFV, and an Exponential distribution for the OLT has been proposed in section 5.2. Thus, a Rayleigh distribution is expected for the OFV, which is given by Eq. (18).

$$F\left(\frac{u_c(B/2)}{u_{c,2\%}(B/2)}\right) = 1 - exp\left(-K_3\left[\frac{u_c(B/2)}{u_{c,2\%}(B/2)}\right]^2\right) \qquad (18)$$

where $u_c(B/2)$ is the value of the OFV with an exceedance probability under 2%, $u_{c,2\%}(B/2)$ is the OFV not exceeded by 2% of the incoming waves, and K_3 is an empirical coefficient to be calibrated. K_3 is estimated similarly as described in section 4.2. Based on 1,320 (66 × 20) values from 66 physical tests, the empirical coefficient is K_3 = 3.6, calculated as the value that minimizes the *rMSE*. The variability of K_3 values is presented in Fig. 14. Fig. 15 presents three example datasets of the proposed Rayleigh distribution in probability plot, while Fig. 16 compares the measured distribution of the OFV for each test versus the proposed distribution, as well as the 90% confidence interval.

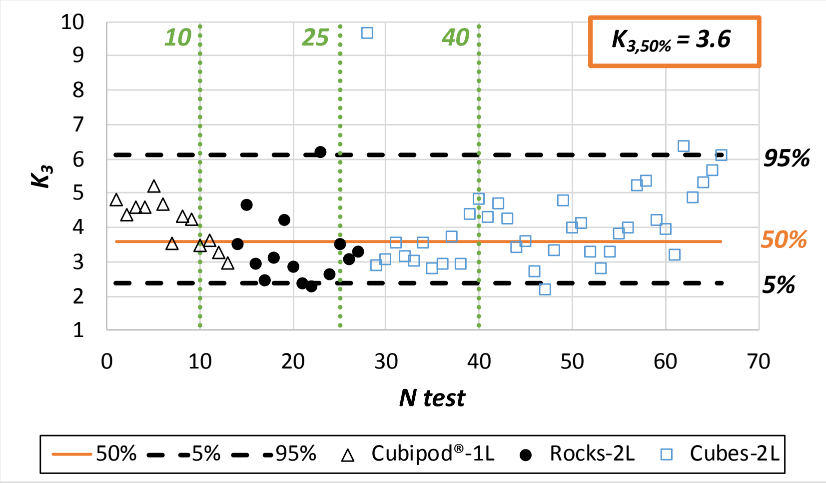

Fig. 14. 95%, 50%, and 5% percentile of K_3.

In this study, dimensionless OFV was $u_c(B/2)/(H_s/T_{m-1,0})$; $u_c(B/2)/(g\ H_s)^{0.5}$ and $u_c(B/2)/(g\ h_{c,2\%}(B/2))$ factors were also considered with poor results.

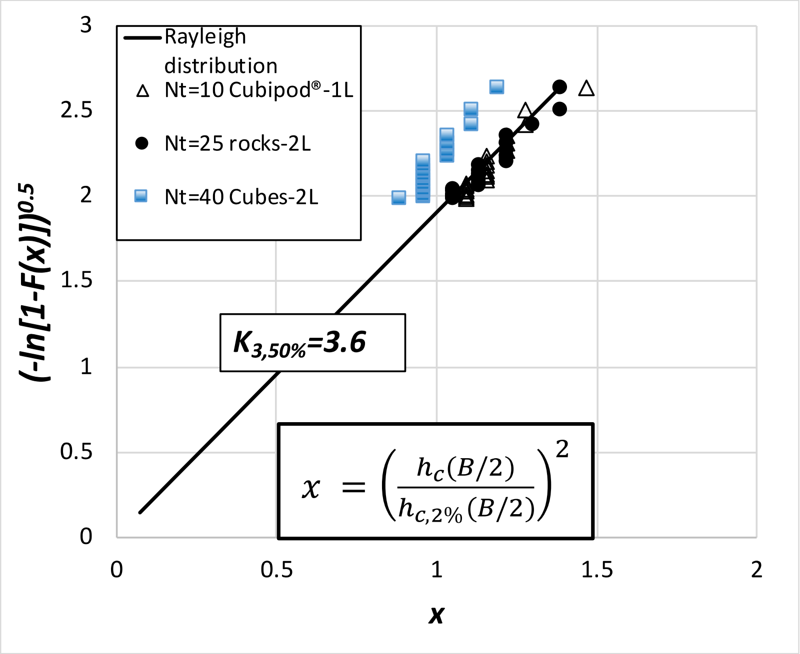

Fig. 15. Typical sample of cumulative distribution function of OFV in equivalent probability plot.

7. Relationship between overtopping layer thickness (OLT) and overtopping flow velocity (OFV) on mound breakwaters

In the previous sections, the statistics of the OLT and OFV were studied. However, the OLT and OFV values with the same exceedance probabilities may not correspond to the same overtopping event. Thus, in this section, the relationship between the OLT and OFV corresponding to the same overtopping event is studied. The highest 20 OLT values of each physical test (highest 2%) were selected, and the OFV values corresponding to the same overtopping event were determined, $h_c(B/2)$ and $u_{c,h}(B/2)$. The pairs of values where the velocity measurement is under 0.15 m/s were removed, as they were out of the operational range of the micro propellers (see section 3). Thus, not each physical test contains 20 pairs of $h_c(B/2)$ and $u_{c,h}(B/2)$. Fig. 17 shows the $h_c(B/2)$ values of each physical test compared to $u_{c,h}(B/2)$.

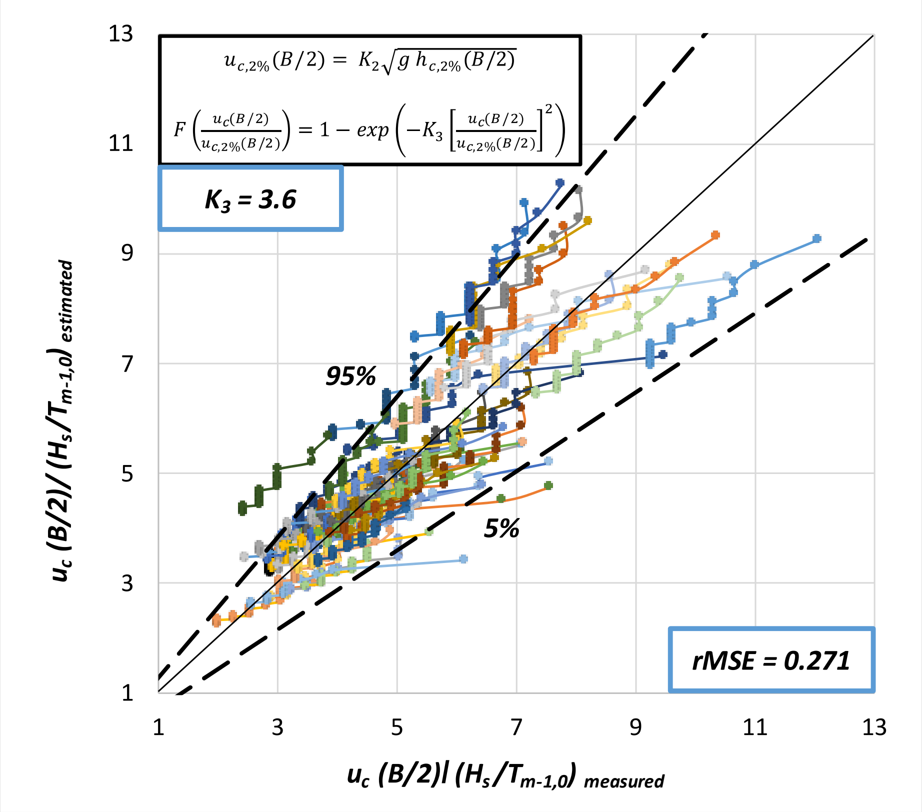

Fig. 16. Measured and estimated distribution of OFV in the middle of the breakwater crest, u_c (B/2), and 90% confidence interval.

Fig. 17 shows no clear correlation between measured $h_c(B/2)$ and $u_{c,h}(B/2)$. This result agrees with that of *Hughes et al. [18]*, where no correlation was found between the OLT and OFV corresponding to the same overtopping event. It is noteworthy that the OLT and OFV (peak values) of the same overtopping event may not be simultaneous in time.

In this study, a statistical analysis was conducted to analyze the possible dependency of the OLT and OFV in the same overtopping event. In this case, the data were not Gaussian distributed; therefore, nonparametric statistical methods were used.

First, a hypothesis test based on the nonparametric Wald–Wolfowitz randomness test was used *[28]*. The null hypothesis (H_0) corresponds to the independency of the maximum values of the OLT, $h_c(B/2)$, and the OFV corresponding to the same overtopping event, $u_{c,h}(B/2)$. To apply the Wald–Wolfowitz randomness test, a minimum of eight pairs of values is required; therefore, it is applicable only to 47 physical tests. Using the level of significance of α = 0.10, H_0 was only rejected in five cases. The number of rejected cases has a binomial distribution with N = 47 and probability of rejection of the null hypothesis p = 0.1 (q = 0.9). The mean value is $Np = 4.7$ and the standard deviation is $\sqrt{Npq} = 2.1$. Using a significance level of $\alpha = 0.10$, H_0 should be rejected only if the number of rejected tests is higher than seven cases (4.7 + 1.28 × 2.1); five (less than seven) rejected cases implies that the independence between $h_c(B/2)$ and $u_{c,h}(B/2)$ (H_0) is not rejected in this nonparametric test.

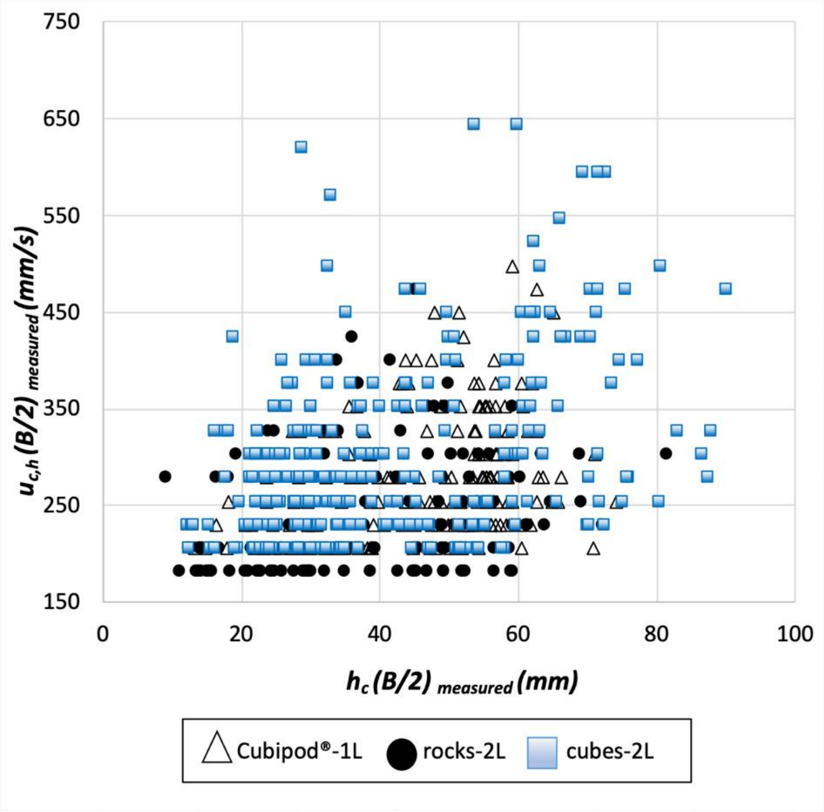

Fig. 17. Comparison of $h_c(B/2)$ and $u_{c,h}(B/2)$ corresponding to the same overtopping event.

An additional nonparametric correlation test is proposed in this study to verify the independency of $h_c(B/2)$ and $u_{c,h}(B/2)$. This second test is based on the idea that if a significant correlation exists between $h_c(B/2)$ and $u_{c,h}(B/2)$ corresponding to the same overtopping event, the mean value of their product is significantly higher than the one obtained randomly reordering $u_{c,h}(B/2)$ within each test. In this hypothesis test, the H_0 corresponds to the independence between $h_c(B/2)$ and $u_{c,h}(B/2)$. A scheme of the test is depicted in Fig. 18.

The N highest OLT values of each physical test $h_c(B/2)_{i,j}$, with the corresponding OFV values, $u_{c,h}(B/2)_{i,j}$ were selected, where i = 1,...,66 is the test order number and j = 1,...≤20 is the data rank. They were multiplied to obtain a fictitious overtopping discharge, $q_{i,j}$, and the average of these fictitious overtopping discharges within the same physical test was calculated $\bar{q}_i$. Subsequently, $u_{c,h}(B/2)_{i,j}$ values were randomly re-arranged within each test and associated to $h_c(B/2)_{i,j}$; this re-arrangement was repeated 100 times to obtain $(u_{c,h}(B/2)_{i,j})_k$, where k = 1,2,...,100 is the resample order number. New fictitious overtopping discharges were obtained, $(q_{i,j})_k$, and 100 new average fictitious overtopping discharges were calculated $(\bar{q}_i)_k$ for each physical test. Consequently, 6,600 (66 × 100) new average fictitious overtopping discharges $(\bar{q}_i)_k$ were obtained and compared to $\bar{q}_i$ obtained from the 66 tests without any re-arrangement.

If the OLT and OFV were correlated, $\bar{q}_i$ would be higher than $(\bar{q}_i)_k$ frequently. If $h_c(B/2)$ and $u_{c,h}(B/2)$ are independent (null hypothesis H_0), the number of cases where $\bar{q}_i > (\bar{q}_i)_k$ is a binomial distribution with N = 6,600, and the probabilities of acceptance and rejection of the hypothesis p = q = 0.5. The mean value is $Np =$3,300 and the standard deviation is $\sqrt{Npq} = 41$. The null hypothesis will be rejected if the number of cases with $\bar{q}_i > (\bar{q}_i)_k$ exceeds 3,352 (3,300 + 1.28 × 41), using a significance level α= 0.10. From 6,600 cases, only 3,172 (<3,352) cases have $\bar{q}_i > (\bar{q}_i)_k$. Subsequently, the H_0, i.e., independence between $h_c(B/2)$ and $u_{c,h}(B/2)$, is not rejected.

According to these results, the OLT and OFV corresponding to the same overtopping event are not correlated. This implies that the wave conditions and structure geometry determine the magnitude of the overtopping event (see sections 4 and 5); therefore, the OLT and OFV statistics tend to increase or decrease with similar variables. Nevertheless, contrary to intuition, a relatively high OLT during a specific overtopping event do not necessarily correspond to a relatively high OFV, and vice versa.

8. Conclusions

The increasing social concern on the visual impact of coastal structures and climate change effects on the coast (e.g., sea level rise) tends to reduce the crest freeboards and increase overtopping rates. The overtopping hazard must be considered in the design and adaptation of the existing coastal structures. The mean overtopping rate is typically considered to design the crest of mound breakwaters. The OLT and OFV on the crest are also relevant for the hydraulic stability of the armored crest and rear side, as well as pedestrian safety when standing on the breakwater crest.

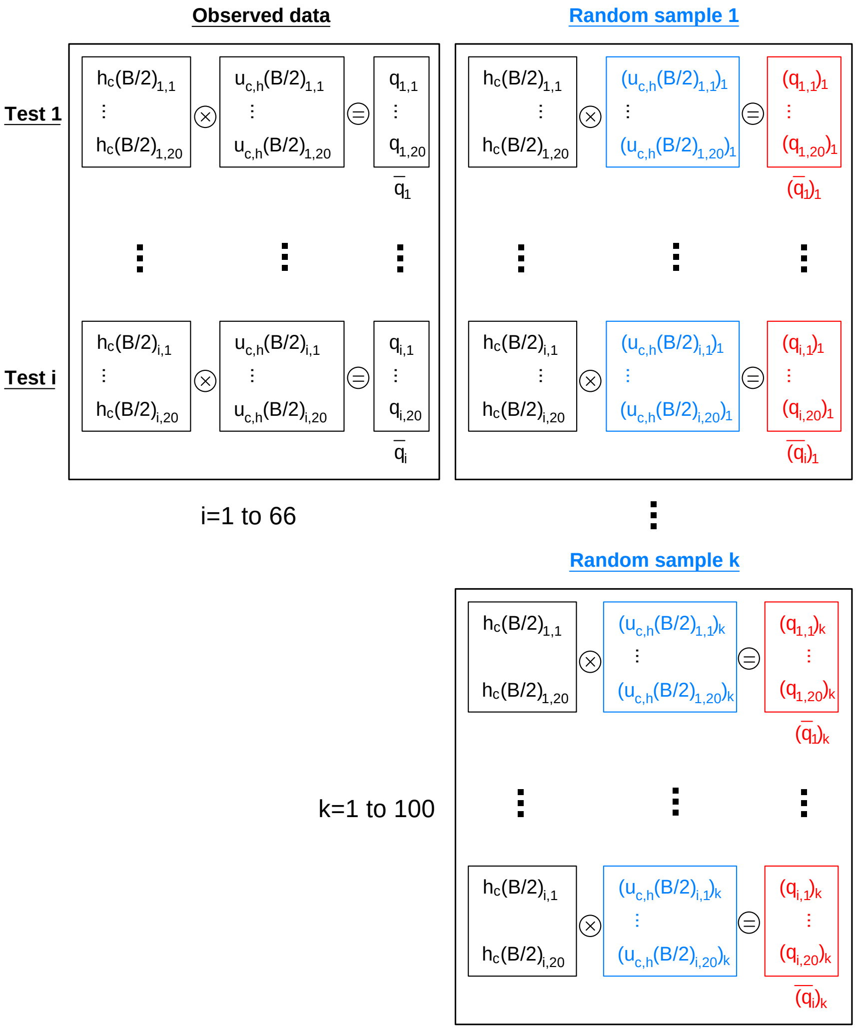

Fig. 18. Scheme of the correlation test.

In this study, 123 physical tests of conventional mound breakwaters using a single-layer Cubipod® armor, a double-layer rock armor, and a double-layer randomly-placed cube armor were performed on the LPC-UPV wave flume. 66 tests measured both the OLT and OFV, while 57 additional tests measured only the OLT. The OLT on the model crest was measured with a conventional capacitance wave gauge, providing reliable measurements with a low level of noise. The OFV on the crest was measured using three miniature propellers.

A new method is proposed to estimate the OLT exceeded by 2% of the incoming waves at the middle of the breakwater crest, $h_{c,2\%}(B/2)$. It is based on Eqs. (15) to estimate the run-up $Ru_{2\%}$ proposed by *EurOtop [1]* for mound breakwaters, but using roughness factors calibrated with the experimental results given in this study: $\gamma_f = 0.33$ (Cubipod®-1L), 0.48 (rocks-2L), and 0.35 (cubes-2L). The new method estimated $h_{c,2\%}(B/2)$ with Eqs. (5) and (7) proposed by *Schüttrumpf and Van Gent [14]* for dikes, but using the empirical coefficients $c_{A,h}^* = 0.52$ and $c_{c,h}^* = 0.89$ calibrated in this study. The relative Mean Squared Error was $0.149 < rMSE < 0.183$.

To describe the OLT distribution at the middle of the breakwater crest $h_c(B/2)$ with exceedance probabilities under 2%, an exponential distribution function ($K_1 = 4.2$) was proposed, as shown in Eq. (16). K_1 was calibrated using experimental observations ($rMSE = 0.162$).

A new method was also proposed to estimate the OFV exceeded by 2% of the incoming waves at the middle of the breakwater crest, $u_{c,2\%}(B/2)$. The formula to estimate $u_{c,2\%}(B/2)$ is given by Eq. (17). The empirical coefficient of the proposed model was calibrated using the experimental observations for each armor layer: $K_2 = 0.57$ (Cubipod®-1L), 0.47 (rocks-2L) and 0.60 (cubes-2L): $0.114 < rMSE < 0.233$.

The OFV distribution with exceedance probabilities under 2%, $u_c(B/2)$, was described with a Rayleigh distribution function ($K_3 = 3.6$), according to Eq. (18). K_3 was calibrated with the experimental data ($rMSE = 0.271$).

Finally, the correlation between OLT and OFV corresponding to the same extreme overtopping event was analyzed using two nonparametric tests. The statistics of the OLT and OFV were clearly related; however, contrary to intuition, the OLT and OFV values corresponding to the same overtopping event appeared to be independent; the null hypothesis of independence was not rejected at a significance level of 10%.

The results are valid for mound breakwaters ($0.34 \leq R_c/H_s \leq 1.75$) with armor slope V/H = 2/3 on a gentle sea bottom ($m = 1/50$).

Acknowledgements

The authors acknowledge the financial support from the *Ministerio de Economía y Competitividad* and the *Fondo Europeo de Desarrollo Regional (FEDER)* under grant BIA2015-70436-R, and from the *Conselleria d'Educació, Investigació, Cultura i Esport (Generalitat Valenciana)* under grant GV/2017/031. The first author was financially supported through the FPU program (*Formación de Profesorado Universitario*) funded by the *Ministerio de Educación, Cultura y Deporte* under grant FPU16/05081.

APPENDIX A. Test matrix

This appendix shows the test matrix used in this study. Wave runs of N_W=1,000 waves following a JONSWAP spectra ($\gamma = 3.3$) were generated. R_c is the crest freeboard, h_s is the water depth at the toe of the structure, H_{sg} is the significant wave height in the generation zone, $T_{m-1,0}$ is the spectral mean wave period, $H_s=4(m_0)^{1/2}$ is the significant wave height at the toe of the structure, $H_{1/10}$ is the average wave height of the highest tenth waves, $H_{2\%}$ is the wave height exceeded by 2% of the waves and $P_{OL}=N_{OL}/N_W$, where N_{OL} is the number of OLT events.

Test #	R_c (mm)	h_s (mm)	H_{sg} (mm)	$T_{m-1,0}$ (s)	H_s (mm)	$H_{1/10}/H_s$ (-)	$H_{2\%}/H_s$ (-)	P_{OL}
1	120.4	200.4	99.8	1.14	92.3	1.38	1.51	5.0%
2	120.5	200.5	108.6	1.22	100.0	1.39	1.53	8.2%
3	120.6	200.6	117.5	1.23	106.2	1.40	1.54	15.7%
4	120.8	200.8	125.6	1.22	110.6	1.41	1.55	21.1%
5	121.3	201.3	134.5	1.29	117.1	1.42	1.56	27.4%
6	121.5	201.5	145.2	1.32	122.1	1.43	1.57	33.1%
7	121.6	201.6	152.6	1.35	125.2	1.44	1.58	39.4%
8	121.7	201.7	161.8	1.41	129.4	1.45	1.59	45.0%
9	121.9	201.9	168.7	1.42	130.7	1.45	1.59	50.1%
10	122.1	202.1	180.2	1.39	131.2	1.45	1.59	58.4%
11	122.3	202.3	189.4	1.54	136.0	1.46	1.60	61.0%
12	120.0	200.0	198.4	1.53	136.1	1.46	1.60	68.4%
13	120.4	200.4	206.5	1.56	136.9	1.46	1.60	68.9%
14	120.1	200.1	86.0	1.60	89.0	1.35	1.48	5.2%
15	120.3	200.3	97.9	1.73	102.5	1.40	1.54	13.1%
16	120.4	200.4	108.3	1.73	110.9	1.41	1.55	23.5%
17	120.6	200.6	117.4	1.79	117.9	1.43	1.57	34.9%
18	120.9	200.9	127.2	1.79	124.5	1.44	1.58	42.2%
19	121.3	201.3	136.9	1.91	131.5	1.45	1.59	52.4%
20	121.8	201.8	143.8	2.05	134.3	1.45	1.60	61.2%

Test #	R_c **(mm)**	h_s **(mm)**	H_{sg} **(mm)**	$T_{m-1,0}$ **(s)**	H_s **(mm)**	$H_{1/10}/H_s$ **(-)**	$H_{2\%}/H_s$ **(-)**	P_{OL}
21	122.6	202.6	153.5	2.06	137.7	1.46	1.61	68.0%
22	120.0	200.0	158.3	2.08	139.2	1.46	1.61	74.7%
23	121.0	201.0	167.1	2.09	141.2	1.47	1.61	77.1%
24	122.0	202.0	176.1	2.08	142.6	1.47	1.62	83.0%
25	123.2	203.2	184.8	2.21	145.0	1.47	1.62	86.4%
26	70.2	250.2	81.49	1.02	74.7	1.32	1.45	6.3%
27	70.3	250.3	90.75	1.13	84.7	1.33	1.47	12.1%
28	70.4	250.4	98.59	1.14	91.8	1.34	1.48	20.8%
29	70.4	250.4	108.82	1.21	101.7	1.36	1.49	29.3%
30	70.6	250.6	118.04	1.19	108.8	1.37	1.50	42.2%
31	70.7	250.7	126.89	1.22	116.2	1.38	1.52	54.6%
32	71.0	251.0	136.09	1.27	124.3	1.39	1.53	65.6%
33	71.3	251.3	145.16	1.37	132.7	1.40	1.54	73.8%
34	71.8	251.8	152.58	1.36	137.9	1.41	1.55	83.9%
35	72.8	252.8	162.74	1.44	143.6	1.42	1.56	87.6%
36	73.8	253.8	173.02	1.49	149.3	1.43	1.57	98.9%
37	75.0	255.0	182.62	1.52	153.8	1.43	1.58	100.0%
38	76.7	256.7	192.63	1.58	158.3	1.44	1.58	100.0%
39	78.2	258.2	198.21	1.57	159.2	1.44	1.58	100.0%
40	79.9	259.9	205.67	1.60	161.3	1.45	1.59	100.0%
41	71.3	251.3	76.27	1.55	76.5	1.32	1.45	11.9%
42	71.6	251.6	87.19	1.65	88.6	1.34	1.47	26.6%
43	70.0	250.0	95.99	1.76	99.7	1.36	1.49	38.8%

Test #	R_c (mm)	h_s (mm)	H_{sg} (mm)	$T_{m-1,0}$ (s)	H_s (mm)	$H_{1/10}/H_s$ (-)	$H_{2\%}/H_s$ (-)	P_{OL}
44	70.3	250.3	106.51	1.75	110.2	1.37	1.51	54.3%
45	70.8	250.8	114.58	1.83	118.4	1.38	1.52	65.1%
46	71.9	251.9	125.29	1.87	128.8	1.40	1.54	82.9%
47	70.0	250.0	133.68	2.01	136.9	1.41	1.55	100.0 %
48	71.9	251.9	142.18	2.11	144.6	1.42	1.56	98.6%
49	74.0	254.0	150.71	2.00	148.7	1.43	1.57	100.0 %
50	70.0	250.0	160.75	2.09	154.0	1.43	1.58	100.0 %
51	70.3	250.3	168.62	2.17	158.0	1.44	1.58	100.0 %
52	70.6	250.6	177.19	2.14	161.7	1.45	1.59	100.0 %
53	71.3	251.3	181.92	2.24	164.4	1.45	1.59	100.0 %
54	120.0	200.0	62.78	0.91	57.0	1.31	1.44	<2%
55	120.2	200.2	71.75	1.00	65.9	1.33	1.46	<2%
56	120.3	200.3	80.79	1.03	74.3	1.35	1.48	<2%
57	120.3	200.3	90.65	1.14	84.8	1.37	1.50	<2%
58	120.0	200.0	75.22	1.54	77.3	1.35	1.48	<2%
59	70.0	150.0	62.13	0.96	56.7	1.29	1.42	<2%
60	70.1	150.1	72.71	0.94	66.1	1.31	1.44	<2%

Table A. 1. Test matrix for single-layer Cubipod® armored model.

Test #	R_c (mm)	h_s (mm)	H_{sg} (mm)	$T_{m-1,0}$ (s)	H_s (mm)	$H_{1/10}/H_s$ (-)	$H_{2\%}/H_s$ (-)	P_{OL}
1	151.4	200.3	113.9	1.23	103.9	1.40	1.54	6.40%

Test #	R_c (mm)	h_s (mm)	H_{sg} (mm)	$T_{m-1,0}$ (s)	H_s (mm)	$H_{1/10}/H_s$ (-)	$H_{2\%}/H_s$ (-)	P_{OL}
2	151.8	200.7	121.9	1.22	108.5	1.41	1.55	7.90%
3	151.1	200.0	130.9	1.27	114.9	1.42	1.56	12.80 %
4	151.3	200.2	83.5	1.60	86.9	1.37	1.50	3.20%
5	151.3	200.2	94.2	1.73	99.3	1.39	1.53	8.80%
6	151.5	200.4	104.6	1.73	108.0	1.41	1.55	18.20 %
7	151.9	200.8	113.2	1.79	116.5	1.42	1.56	29.60 %
8	152.1	201.0	121.8	1.79	121.9	1.43	1.57	37.90 %
9	102.1	251.0	79.0	1.02	72.5	1.32	1.45	2.30%
10	101.1	250.0	87.8	1.13	81.2	1.33	1.46	5.64%
11	101.7	250.6	96.6	1.14	89.7	1.34	1.47	9.83%
12	101.1	250.0	104.6	1.21	97.3	1.35	1.49	19.54 %
13	101.2	250.1	115.5	1.19	108.1	1.37	1.50	26.14 %
14	101.3	250.2	123.8	1.22	113.9	1.38	1.51	36.33 %
15	101.7	250.6	130.5	1.27	120.5	1.39	1.52	43.50 %
16	101.1	250.0	74.2	1.55	74.4	1.32	1.45	6.30%
17	101.2	250.1	84.8	1.65	86.2	1.34	1.47	15.80 %
18	101.4	250.3	95.4	1.76	99.2	1.36	1.49	30.10 %
19	101.1	250.0	105.2	1.75	109.0	1.37	1.50	51.40 %

Test #	**R_c (mm)**	**h_s (mm)**	**H_{sg} (mm)**	**$T_{m-1,0}$ (s)**	**H_s (mm)**	**$H_{1/10}/H_s$ (-)**	**$H_{2\%}/H_s$ (-)**	**P_{OL}**
20	101.2	250.1	111.9	1.83	117.2	1.38	1.52	60.40%
21	101.3	250.2	122.5	1.87	126.6	1.39	1.53	69.50%
22	151.1	200.0	62.7	0.89	57.0	1.31	1.44	<2%
23	151.4	199.7	71.1	1.00	65.4	1.33	1.46	<2%
24	151.7	199.5	79.7	1.00	73.1	1.34	1.48	<2%
25	151.1	200.0	86.9	1.10	80.7	1.36	1.49	<2%
26	151.2	199.9	96.5	1.16	89.8	1.37	1.51	<2%
27	151.3	199.8	105.0	1.20	97.0	1.39	1.52	<2%
28	151.1	200.0	73.1	1.54	75.2	1.35	1.48	<2%
29	101.1	250.0	60.4	0.91	55.1	1.29	1.42	<2%
30	101.6	249.6	69.4	0.96	63.3	1.30	1.43	<2%

Table A. 2. Test matrix for double-layer rock armored model.

Test #	**R_c (mm)**	**h_s (mm)**	**H_{sg} (mm)**	**$T_{m-1,0}$ (s)**	**H_s (mm)**	**$H_{1/10}/H_s$ (-)**	**$H_{2\%}/H_s$ (-)**	**P_{OL}**
1	111.7	249.4	81.7	1.09	75.6	1.32	1.45	2.8%
2	111.9	249.2	91.0	1.16	84.9	1.33	1.47	4.4%
3	112.0	249.1	97.9	1.15	91.2	1.34	1.48	7.3%
4	112.3	248.8	107.9	1.19	100.3	1.36	1.49	10.6%
5	112.4	248.7	116.4	1.21	108.1	1.37	1.50	14.0%
6	111.1	250.0	126.1	1.29	117.3	1.38	1.52	21.8%
7	111.3	249.8	137.1	1.37	127.0	1.40	1.53	27.1%
8	111.5	249.6	146.4	1.36	132.4	1.40	1.54	32.5%
9	111.8	249.3	155.0	1.45	140.0	1.41	1.55	36.9%

Test #	R_c (mm)	h_s (mm)	H_{sg} (mm)	$T_{m-1,0}$ (s)	H_s (mm)	$H_{1/10}/H_s$ (-)	$H_{2\%}/H_s$ (-)	P_{OL}
10	112.1	249.0	163.4	1.49	145.2	1.42	1.56	41.9%
11	112.5	248.6	175.3	1.49	150.0	1.43	1.57	48.9%
12	112.9	248.2	182.2	1.52	153.6	1.43	1.58	51.8%
13	111.1	250.0	186.6	1.57	156.5	1.44	1.58	55.8%
14	111.5	249.6	190.4	1.57	157.6	1.44	1.58	58.0%
15	111.1	250.0	69.3	1.55	69.5	1.31	1.44	2.2%
16	111.6	249.6	80.2	1.70	82.3	1.33	1.46	6.4%
17	111.9	249.2	91.7	1.72	94.7	1.35	1.48	12.9%
18	112.0	249.1	101.2	1.77	105.1	1.36	1.50	22.1%
19	111.1	250.0	107.9	1.95	114.3	1.38	1.51	30.7%
20	111.5	249.6	118.3	1.88	123.0	1.39	1.53	44.8%
21	111.9	249.2	126.9	2.04	132.1	1.40	1.54	52.9%
22	112.4	248.7	135.5	2.08	139.7	1.41	1.55	61.5%
23	113.2	247.9	141.5	2.08	144.0	1.42	1.56	100.0%
24	114.6	246.5	151.2	2.10	148.7	1.43	1.57	80.3%
25	116.1	245.0	162.0	2.24	155.3	1.44	1.58	87.4%
26	111.1	250.0	173.4	2.25	160.9	1.44	1.59	92.3%
54	61.2	299.9	72.7	0.91	66.8	1.29	1.42	2.4%
28	61.3	299.8	81.7	0.97	74.9	1.30	1.43	8.7%
29	61.4	299.7	89.3	1.04	82.4	1.31	1.44	16.1%
30	61.5	299.6	98.9	1.09	91.8	1.32	1.45	21.9%
31	61.9	299.2	107.6	1.12	99.9	1.33	1.46	27.7%
32	62.1	299.0	115.6	1.18	108.4	1.34	1.47	29.4%
33	62.2	298.9	124.2	1.23	114.8	1.35	1.48	32.6%
34	62.5	298.6	131.8	1.13	123.5	1.36	1.50	34.4%

Test **#**	R_c **(mm)**	h_s **(mm)**	H_{sg} **(mm)**	$T_{m-1,0}$ **(s)**	H_s **(mm)**	$H_{1/10}/H_s$ **(-)**	$H_{2\%}/H_s$ **(-)**	P_{OL}
35	62.7	298.4	137.3	1.28	128.7	1.37	1.50	38.4%
36	63.2	297.9	147.0	1.34	138.3	1.38	1.51	41.2%
37	63.7	297.4	154.7	1.40	143.3	1.38	1.52	43.8%
38	61.1	300.0	164.7	1.38	151.6	1.39	1.53	50.3%
39	62.5	298.6	173.4	1.55	160.0	1.40	1.54	50.3%
40	64.0	297.1	180.9	1.54	163.8	1.41	1.55	48.9%
41	65.8	295.3	190.1	1.55	169.0	1.42	1.56	45.8%
42	68.4	292.7	199.4	1.62	175.1	1.42	1.56	47.2%
43	61.1	300.0	70.5	1.54	69.5	1.29	1.42	10.0%
44	61.2	299.9	81.1	1.65	80.9	1.31	1.44	21.5%
45	61.3	299.8	90.8	1.76	92.5	1.32	1.45	34.5%
46	62.0	299.1	99.6	1.77	101.6	1.33	1.47	43.3%
47	62.7	298.4	108.6	1.92	112.9	1.35	1.48	59.9%
48	61.1	300.0	116.6	1.90	120.7	1.36	1.49	72.6%
49	62.0	299.1	126.0	2.05	131.5	1.37	1.51	82.2%
50	111.1	250.0	54.4	0.95	49.6	1.28	1.41	<2%
51	111.3	249.8	62.6	0.95	57.0	1.29	1.42	<2%
52	111.1	250.0	72.9	1.04	66.9	1.31	1.44	<2%
53	61.1	300.0	64.3	0.91	59.0	1.28	1.41	<2%

Table A. 3. Test matrix for double-layer cube armored model.

References

[1] EurOtop, 2018. *Manual on wave overtopping of sea defences and related structures*. An overtopping manual largely based on European research, but for worldwide application. Van der Meer, J.W., Allsop, N.W.H., Bruce, T., De Rouck, J., Kortenhaus, A., Pullen, T., Schüttrumpf, H., Troch, P. And Zanuttigh, B., www.overtopping-manual.com.

[2] Argente, G., Gómez-Martín, M.E., Medina, J.R., 2018. Hydraulic Stability of the Armor Layer of Overtopped Breakwaters. *Journal of Marine Science and Engineering 2018, 6(4), 143.* https://doi.org/10.3390/jmse6040143

[3] Camus, P., Tomás, A., Díaz-Hernández, G., Rodríguez, B., Izaguirre, C., Losada, I.J. (2019). Probabilistic assessment of port operation downtimes under climate change. *Coastal Engineering 147*, 12-24. https://doi.org/10.1016/j.coastaleng.2019.01.007

[4] Bae, H.U., Yun, K.M., Yoon, J.Y., Lim, N.H., 2016. Human Stability with respect to overtopping flow on the breakwater, *International Journal of Applied Engineering Research*, vol. 11, No. 1, 111-119.

[5] Sandoval, C., Bruce, T., 2017. Wave overtopping hazard to pedestrians: video evidence from real accidents, *Proc. of Coasts, Marine Structures and Breakwaters 2017. Realising the Potential*. 5 - 7 September 2017 - Liverpool Waterfront, UK. Paper 146. pp. 501-512.

[6] Endoh, K., Takahashi, S., 1995. Numerically modelling personnel danger on a promenade breakwater due to overtopping waves, *Proc. 24th International Conference on Coastal Engineering*, ASCE, 1016-1029.

[7] Jonkman, S.N., Penning-Rowsell, E., 2008. Human stability in flood flows, *Journal of American Water Resources Association (JAWRA)* 44(5), 1208-1218. https://doi.org/10.1111/j.1752-1688.2008.00217.x

[8] Karvonen, R.A., Hepojoki, A., Huhta, H.K., Louhio, A., 2000. The use of physical models in Dam-break analysis. *RESCDAM final report. Helsinki University of Technology*, Finland.

[9] Abt, S.R., Wittler, R.J., Taylor, A., Love, D.J., 1989. Human stability in a high flood hazard zone, *Water Resources Bulletin 25*, 4, 881-890.

[10] Mares-Nasarre, P., Molines, J., Gómez-Martín, M.E., Medina, J.R., 2018. Analysis of the overtopping layer thickness on low-crested mound breakwaters, *Coastlab18, Proc. of 7th CoastLab international conference*, 22-26th May 2018, Santander, Spain (in press).

[11] Van Gent, M., 2001. Wave runup on dikes with shallow foreshores, *Journal of Waterway, Port, Coastal and Ocean Engineering*, ASCE, vol. 127, No. 5, 254-262. https://doi.org/10.1061/(ASCE)0733-950X(2001)127:5(254)

[12] Van Gent, M., 2002. Wave overtopping events at dikes, *Proc. 28th International Conference on Coastal Engineering*, World Scientific, 2203 - 2215. https://doi.org/10.1142/9789812791306_0185

[13] Schüttrumpf, H., Möller, J., Oumeraci, H., 2002. Overtopping flow parameters on the inner slope of seadikes, *Proc. 28th International Conference on Coastal Engineering*, World Scientific, 2116-2127. https://doi.org/10.1142/9789812791306_0178

[14] Schüttrumpf, H., van Gent, M., 2003. Wave overtopping at seadikes, *Proc. Coastal Structures 2003*, ASCE, 431-443.

[15] Bosman, G., Van der Meer, J.W., Hoffmans, G., Schüttrumpf, H., Verhagen, H.J., 2009. Individual overtopping events at dikes, *Proc. 31st International Conference on Coastal Engineering*, World Scientific, 2944-2956. https://doi.org/10.1142/9789814277426_0244

[16] Van der Meer, J. W., Hardeman, B., Steendam, G., Schïuttrumpf, H., Verheij, H., 2010. Flow depths and velocities at crest and landward slope of a dike, in theory and with the wave overtopping simulator, *Coastal Engineering Proceedings, [S.I.], n. 32, p. structures.10, jan. 2011*. https://doi.org/10.9753/icce.v32.structures.10

[17] Lorke, S., Scheres, B., Schüttrumpf, H., Bornschein, A., Pohl, R., 2012. Physical model tests on wave overtopping and flow processes on dike crests influenced by wave-current interaction, *Coastal Engineering Proceedings, [S.I.],* n.33, p. waves.34, oct. 2012. https://doi.org/10.9753/icce.v33.waves.34

[18] Hughes, S.A., Thornton, C., Van der Meer, J., Scholl, B., 2012. Improvements in describing wave overtopping processes, *Coastal Engineering Proceedings, [S.I.], n.33, p. waves.35, oct. 2012*. https://doi.org/10.9753/icce.v33.waves.35.

[19] Hughes, S.A., Nadal, N.C., 2009. Laboratory study of combined wave overtopping and storm surge overflow of a levee, *Coastal Engineering 56*, 543-558. https://doi.org/10.1016/j.coastaleng.2008.09.005

[20] Mansard, R.P.D. and Funke, E.R. (1980). The measurement of incident and reflected spectra using a least squares method. *Proc. 17th International Conference on Coastal Engineering*, ASCE, 140(1), 100-108.

[21] Herrera, M.P., Medina, J.R., 2015. Toe berm design for very shallow waters, *Coastal Engineering 103*, 67-77. https://doi.org/10.1016/j.coastaleng.2015.06.005

[22] Gómez-Martín, M.E., Medina, J.R., 2006. Damage progression on cube armored breakwaters, *Proc. 30th International Conference on Coastal Engineering*, World Scientific, 5229-5240.

[23] Gómez-Martín, M.E., Medina, J.R., 2014. Heterogeneous packing and hydraulic stability of cube and Cubipod armor units, *Journal of Waterway, Port, Coastal and Ocean Engineering 140(1)*, 100-108. https://doi.org/10.1061/(ASCE)WW.1943-5460.0000223

[24] Figueres, M., Medina, J.R., 2004. Estimating incident and reflected waves using a fully nonlinear wave model, *Proc. 29th International Conference on Coastal Engineering*, World Scientific, 594-603. https://doi.org/10.1142/9789812701916-0047

[25] Battjes, J.A. and Groenendijk, H.W., 2000. Wave height distributions on shallow foreshores, *Coastal Engineering 40*, 161-182. https://doi.org/10.1016/S0378-3839(00)00007-7

[26]Verhagen, H.J., Van Vledder, G., Eslami Arab, S., 2008. A practical method for design of coastal structures in shallow water, *Proc. 31st International Conference on Coastal Engineering*, World Scientific, Vol. 4, 2912-2922. https://doi.org/10.1142/9789814277426_0241

[27]Molines, J., Medina, J.R., 2015. Calibration of overtopping roughness factors for concrete armour units in non-breaking conditions using the CLASH database. *Coastal Engineering 96,* 62-70. https://doi.org/ 10.1016/j.coastaleng.2014.11.008

[28]Conover, W.J., Practical nonparametric statistics, John Wiley & Sons Inc., New York, 1971.

2. **Mares-Nasarre, P., Gómez-Martín, M.E., Medina, J.R., 2020a. Influence of Mild Bottom Slopes on the Overtopping Flow over Mound Breakwaters under Depth-Limited Breaking Wave Conditions. J. Mar. Sci. Eng. 8 (1), 3. https://doi.org/10.3390/jmse8010003**

Influence of Mild Bottom Slopes on the Overtopping Flow over Mound Breakwaters under Depth-Limited Breaking Wave Conditions

Patricia Mares-Nasarre [1, *], M. Esther Gómez-Martín[1] and Josep R. Medina[1]

[1]Lab. Ports and Coasts, Institute of Transport and Territory, Universitat Politècnica de València; patmana@cam.upv.es, jormollo@upv.es, mgomar00@upv.es, jrmedina@upv.es.

* Corresponding author: patmana@cam.upv.es

Abstract:

The crest elevation of mound breakwaters is usually designed considering a tolerable mean wave overtopping discharge. However, pedestrian safety, characterized by the overtopping layer thickness (OLT) and the overtopping flow velocity (OFV), is becoming more relevant due to the reduction of the crest freeboards of coastal structures. Studies in the literature focusing on OLT and OFV do not consider the bottom slope effect, even if it has a remarkable impact on mound breakwater design under depth-limited breaking wave conditions. Therefore, this research focuses on the influence of the bottom slope on OLT and OFV exceeded by 2% of incoming waves, $h_{c,2\%}$ and $u_{c,2\%}$. A total of 235 2D physical tests were conducted on conventional mound breakwaters with a single-layer Cubipod® and double-layer rock and cube armors with 2% and 4% bottom slopes. Neural networks were used to determine the optimum point to estimate wave characteristics for $h_{c,2\%}$ and $u_{c,2\%}$ calculation; that point was located at a distance from the model toe of three times the water depth at the toe (h_s) of the structure. The influence of the bottom slope is studied using trained neural networks with fixed wave conditions in the wave generation zone; $h_{c,2\%}$ slightly decreases and $u_{c,2\%}$ increases as the gradient of the bottom slope increases.

Keywords: mound breakwater; overtopping; overtopping layer thickness; overtopping flow velocity; bottom slope; breaking waves

1. Introduction

Mound breakwater design criteria are evolving due to climate change effects (e.g., sea level rise) and increasing social pressure to reduce the visual impact of coastal structures. These phenomena lead to the reduction of their crest freeboards and an increase of the overtopping hazard. In this context, pedestrian safety becomes relevant due to the recreational activities that take place on the breakwater's crest (e.g., fishing and photography).

An admissible mean wave overtopping discharge, q ($m^3/s/m$), is usually the criteria considered for design purposes. Nevertheless, *Franco et al. [1]* suggested that the overtopping hazard should be more directly related to individual overtopping events, rather than mean values. When assessing the overtopping hazard to pedestrians standing on coastal structures during overtopping events, several authors (see *Bae et al. [2]* and *Sandoval and Bruce [3]*) have proposed using the overtopping layer thickness (OLT) and the overtopping flow velocity (OFV) as relevant variables.

There is extensive literature on q (see *EurOtop 2018 [4]* and *Molines and Medina [5]*) and individual wave overtopping volumes (see *Nørgaard et al. [6]* and *Molines et al. [7]*) on mound breakwaters. Nevertheless, few studies have focused on OLT and OFV on dikes (see *Schüttrumpf and Van Gent [8]*) or on mound breakwaters (see *Mares-Nasarre et al. [9])*. Those studies *[8,9]* considered variables related to wave characteristics and structure geometry as significant when estimating OLT and OFV. However, the bottom slope (m) has a significant influence on the type of wave breaking at the toe of the structure. *Herrera et al. [10]* pointed out that the bottom slope plays an important role in mound breakwater design; in depth-limited breaking-wave conditions, the optimum point where wave characteristics are estimated is relevant for design and needs to be determined.

This research focuses on the bottom slope influence on OLT and OFV during extreme overtopping events on mound breakwaters under depth-limited breaking-wave conditions. Two-dimensional physical tests were performed at the wave flume of the *Universitat Politècnica de València (Spain),* and data were analyzed using artificial neural networks (NNs). This paper is organized as follows. In Section 2, the variables considered in the formulas given in the literature to estimate OLT and OFV are presented. In Section 3, the experimental setup is presented. In Section 4, the analysis carried out with NNs is described; the optimum point to determine wave characteristics to estimate OLT and OFV is identified, and the bottom slope effect is assessed for both variables. Finally, in Section 5, conclusions are drawn.

2. Literature Review on Overtopping Layer Thickness (OLT) and Overtopping Flow Velocity (OFV)

Schüttrumpf and Van Gent [8] integrated the results of *Van Gent [11]* (m = 1% and $0.2 \leq H_s/h_s \leq 1.4$, H_s being the significant wave height at the toe of the structure and h_s the water depth at the toe) and *Schüttrumpf et al. [12]* (horizontal bottom and $0.1 \leq H_s/h_s \leq$

0.3) and described the overtopping flow on dike crests using two variables: (1) the OLT on the dike crest exceeded by 2% of the incoming waves, $h_{c,2\%}$, and (2) the OFV on the dike crest exceeded by 2% of the incoming waves, $u_{c,2\%}$. These authors also proposed a method to estimate $h_{c,2\%}$ and $u_{c,2\%}$ based on the wave run-up height exceeded by 2% of the incoming waves, $Ru_{2\%}$, obtained with the formulas proposed by Van Gent [13]. *Van Gent [13]* considered $Ru_{2\%}$ as a function of the surf similarity parameter or Iribarren number, $\xi_{s,-1}$, calculated with H_s and the spectral period $T_{m-1,0} = m_{-1}/m_0$, where m_i is the i-th spectral moment, and $m_i = \int_0^\infty S(f) f^i \, df$, being the wave spectrum $S(f)$. Following the *Schüttrumpf and Van Gent [8]* method, once $Ru_{2\%}$ is estimated, OLT and OFV on the seaward edge of the dike crest can be obtained: $h_{A,2\%}(R_c) = h_A(z_A=R_c)$ and $u_{A,2\%}(R_c) = u_A(z_A=R_c)$. Figure 1 shows the variables considered in the model proposed by the aforementioned authors, where MWL is the mean water level.

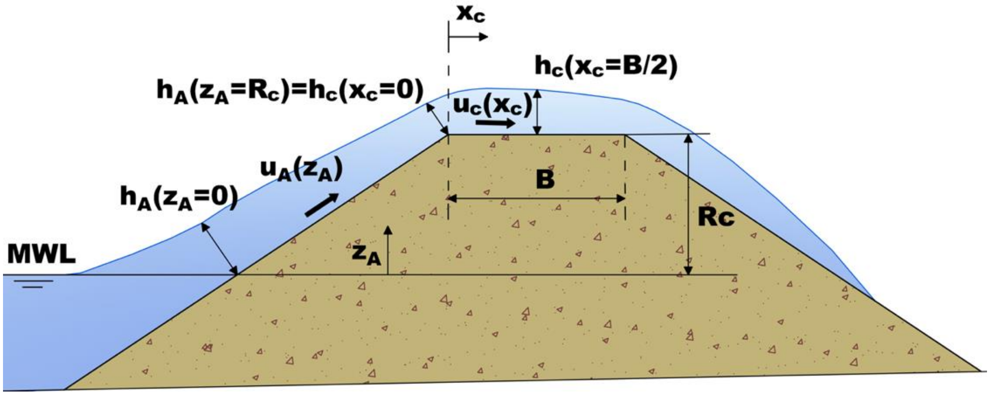

Figure 1. Definition of the variables considered by Schüttrumpf and Van Gent [8] to estimate overtopping layer thickness (OLT) and overtopping flow velocity (OFV) on a dike.

The OLT and OFV along the seaward slope of the dike depend on the $Ru_{2\%}$ calculated using the formula by *Van Gent [13]*, the elevation over the MWL, z_A, and the significant wave height at the toe of the structure, H_s.

Using the previously calculated values of $h_{A,2\%}(z_A = R_c)$ and $u_{A,2\%}(z_A = R_c)$, OLT and OFV on the crest of the dike, $h_{c,2\%}$ and $u_{c,2\%}$, are estimated using the distance from the intersection between the seaward slope and the crest, x_c, the crest width, B, and a friction coefficient, μ (see *[12]* for further guidance on this coefficient).

Van der Meer et al. [14] added their new test observations on dikes (using an overtopping simulator) to the data obtained by *Schüttrumpf and Van Gent [8]*. Based on the new dataset, *Van der Meer et al. [14]* proposed a new method to estimate OLT and OFV on dikes; $h_{A,2\%}$ and $u_{A,2\%}$ estimators considered the same variables as *Schüttrumpf and Van Gent [8]*. The $u_{c,2\%}$ formula included the wavelength based on the spectral period ($T_{m-1,0}$), $L_{m-1,0}$.

Lorke et al. [15] carried out physical model tests on dikes (horizontal bottom and $0.1 \leq H_s/h_s \leq 0.3$) focused on the effect of currents and wind on overtopping. Using this dataset, the authors proposed new empirical coefficients for the $h_{c,2\%}$ formulas obtained by *Schüttrumpf and Van Gent [8]* as a function of the seaward slope of the dike, α.

EurOtop [4] recommended a new method to estimate OLT and OFV on dikes. The formulas to estimate OLT and OFV along the seaward slope are equivalent to those proposed by *Schüttrumpf and Van Gent [8]* but consider different empirical coefficients. As *Lorke et al. [15]*, *EurOtop [4]* considers these empirical coefficients as a function of the seaward slope of the dike, α. Regarding $u_{c,2\%}$, *EurOtop [4]* suggests the formula given by *Van der Meer et al. [14]*.

Mares-Nasarre et al. [9] adapted the formulas given by *Schüttrumpf and Van Gent [8]* to estimate $h_{c,2\%}(x_c = B/2)$ on mound breakwaters with m = 2% and $0.2 \leq H_s/h_s \leq 0.7$. These authors proposed new empirical coefficients and roughness factors for three armor layers (Cubipod®-1Layer, randomly placed cube-2Layers, and rock-2Layers). Mound breakwaters (permeable structures) and dikes are different structures, but $h_{c,2\%}(x_c = B/2)$ seems to be related to the same variables. Regarding $u_{c,2\%}(x_c = B/2)$, it is calculated as a function of the squared root of $h_{c,2\%}(x_c = B/2)$.

Table 1 summarizes the variables considered in the models proposed by the aforementioned authors to estimate $h_{c,2\%}$ and $u_{c,2\%}$.

It can be concluded from Table 1 that only geometric variables of the coastal structure and wave characteristics at the structure toe were considered in the formulations given in the literature to estimate $h_{c,2\%}$ and $u_{c,2\%}$. Even if V*an Gent [11]*, *Schüttrumpf and Van Gent [8]*, and *van der Meer et al. [14]* were considering physical tests under depth-limited breaking-wave conditions, none of them considered the bottom slope (m) as a significant variable or analyzed the optimum point for measuring wave characteristics. Here, the optimum point to estimate incident wave characteristics is considered to be the point where the error in the estimation of OLT and OFV is lowest.

3. Experimental Methodology

Two-dimensional small-scale physical tests were carried out in the wave flume (30 m × 1.2 m × 1.2 m) of the Laboratory of Ports and Coasts at the *Universitat Politècnica de València* (LPC-UPV), with a piston-type wave maker and two bottom slope (m) configurations. The first configuration corresponded to a continuous ramp of m = 4% all along the flume. The second configuration was composed by two ramps: one 6.3 m long and of which m = 4%, and one 9.0 m long and of which m = 2%. Figure 2 presents the longitudinal cross-sections of the LPC-UPV wave flume configurations as well as the location of the free surface wave gauges.

	Author	H_s	$T_{m-1,0}$	α	R_c	B	μ	$L_{m-1,0}$	m
$h_{A,2\%}$	Schüttrumpf and Van Gent [8]	x	x	x					
	Van der Meer et al. [14]	x	x	x					
	EurOtop [8]	x	x	x					
$u_{A,2\%}$	Schüttrumpf and Van Gent [8]	x	x	x					
	Van der Meer et al. [14]	x	x	x					
	EurOtop [8]	x	x	x					
$h_{c,2\%}$	Schüttrumpf and Van Gent [8]	x	x	x	x	x			
	Lorke et al. [15]	x	x	x	x				
	EurOtop [8]	x	x	x	x				
	Mares-Nasarre et al. [9]	x	x	x	x	x			
$u_{c,2\%}$	Schüttrumpf and Van Gent [8]	x	x	x	x		x		
	Van der Meer et al. [14]	x	x	x	x			x	
	EurOtop [8]	x	x	x	x			x	
	Mares-Nasarre et al. [9]	x	x	x	x	x			

Table 1. Summary of the variables considered for the estimation of OLT and OFV in the literature.

The tested cross section depicted in Figure 3 corresponds to a mound breakwater with a cotα = 1.5 slope and rock toe berms. Three armor layers were tested: a single-layer Cubipod® armor, a double-layer randomly placed cube armor, and a double-layer rock armor. The nominal diameters or equivalent cube sizes were Dn = 3.79 cm (Cubipod®-1L), Dn = 3.97 cm (cube-2L), and Dn = 3.18 cm (rock-2L). The rock toe berm was designed to guarantee its stability. Thus, tests in which m = 2% were performed with a medium-sized rock toe berm (Dn_{50} = 2.6 cm), while tests in which m = 4% were conducted with a larger rock toe berm (Dn_{50} = 3.9 cm).

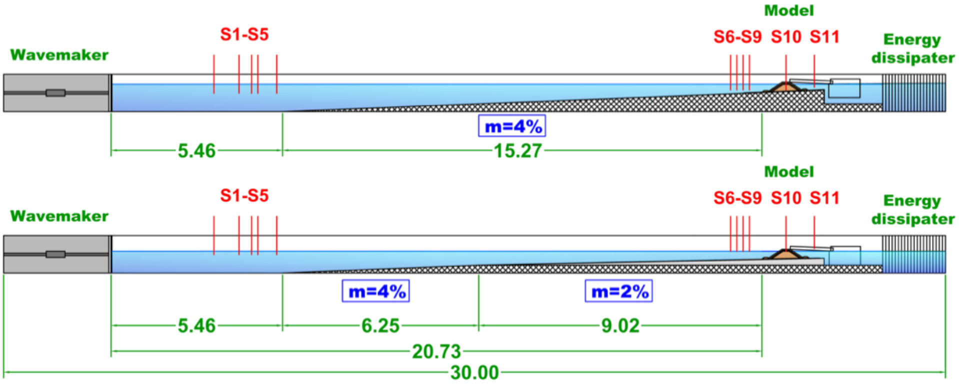

Figure 2. Longitudinal cross section of the Laboratory of Ports and Coasts at the Universitat Politècnica de València (LPC-UPV) wave flume. Dimensions are in meters.

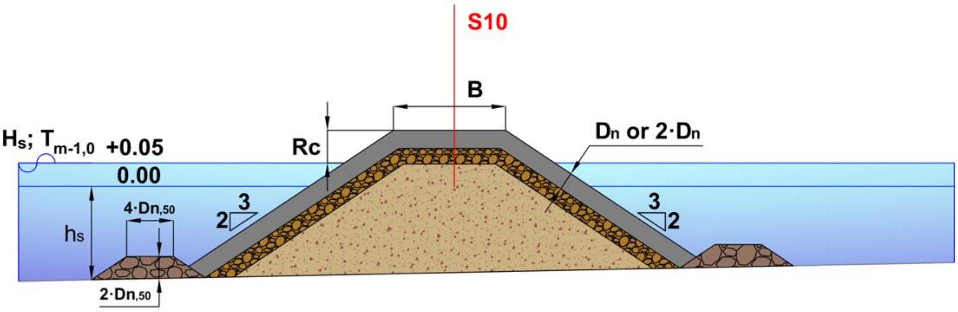

Figure 3. Cross section of the tested models in the LPC-UPV wave flume (dimensions in meters).

Two water depths (h_s) at the toe of the structure were tested for each mound breakwater model on every foreshore configuration. In the tests for which m = 4%, h_s equaled either 20 or 25 cm. For the tests with the Cubipod® and rock armored models, when m = 2%, h_s was either 20 or 25 cm. For the tests with the cube armored model, when m = 2%, h_s equaled either 25 or 30 cm.

For each h_s, the significant wave height ($H_s = 4(m_0)^{0.5}$) and peak period (T_p) at the wave generation zone were calculated so as to keep the Iribarren number approximately constant along the test series ($Ir_p=\tan\alpha/[2\pi H_s/(g\ T_p^2)]^{0.5}$). For each Ir_p, H_s at the generation zone (H_{sg}) was increased in steps of 1 cm from no damage until the armor layer failed or waves broke at the wave generation zone.

One thousand irregular waves were generated during each test following a JONSWAP spectrum (γ = 3.3). Thus, the tests lasted approximately 15 to 35 min, depending on the mean wave period. The AWACS (Active Wave Absorption Control System) system was activated to avoid multireflections. Neither low-frequency oscillations nor piling-up (wave gauge S11) were significant during the tests.

As explained in *Mares-Nasarre et al. [9]*, two corrections were applied to the crest freeboard because of its impact on wave overtopping: (1) the extracted accumulated overtopping volumes during a working day, and (2) the natural evaporation and facility leakages. These corrections produced a small increase in the considered crest freeboard over time on the order of 10 mm for a long working day (a 3.9% variation in terms of water depth). The crest freeboard obtained after the two previous considerations is the one applied in the following analysis. A summary of the geometry and wave characteristics in the test is presented in Table 2.

Armor	m[-]	R_c [m]	B [m]	h_s [m]	H_s [m]	T_p [s]	$T_{m-1,0}$ [s]	#tests
Cubipod ®-1L	2%	0.07–0.12	0.24	0.20 and 0.25	0.06–0.18	1.25–2.68	1.03–2.24	53
	4%	0.07–0.12		0.20 and 0.25	0.07–0.18	1.12–2.69	1.03–2.21	49
Cube-2L	2%	0.08–0.17	0.27	0.25 and 0.30	0.06–0.18	1.00–2.68	0.91–2.25	49
	4%	0.06–0.12		0.20 and 0.25	0.09–0.17	1.25–2.69	1.17–2.33	44
Rock-2L	2%	0.10–0.15	0.26	0.20 and 0.25	0.07–0.13	1.12–2.15	0.99–1.88	21
	4%	0.10–0.15		0.20 and 0.25	0.09–0.14	1.25–2.40	1.19–2.06	19

Table 2. Summary of geometry and wave characteristics in the LPC-UPV tests.

A total of 11 capacitive wave gauges were located along the flume to measure the water surface elevation (see Figure 2). Wave gauges S1–S5 were placed in the wave generation zone following *Mansard and Funke [16]* recommendations, while wave gauges S6–S9 were placed close to the model. In order to minimize the error in the separation of incident and reflected waves, *Mansard and Funke [16]* proposed several criteria to calculate the distance between wave gauges as a function of the wavelength in order to separate incident and reflected waves. Nevertheless, methods in the literature to separate incident and reflected waves are not reliable in breaking conditions. Thus, in the model zone where depth-limited breaking takes place, they are not applicable. The distances from S6–S9 to the model toe were a function of the water depth at the toe of the structure, h_s. S6, S7, S8, and S9 were placed at distances $5h_s$, $4h_s$, $3h_s$ and $2h_s$ from the toe of the model, respectively, following the recommendations given by *Herrera and Medina [17]*. Wave gauge S10 was located in the middle of the model crest, and S11 was located behind the model.

The experimental set up also included three cameras to analyze the armor damage in the frontal slope, on the crest, and at the rare side of the armor using the virtual net method

[18] as explained in *Argente et al. [19]* and *Gómez-Martín et al. [20]*. Overtopping discharges were collected and measured using a collection tank and a weighing system behind the model during each test.

3.1. Wave Analysis

Waves were analyzed following the methodology for depth-limited breaking waves proposed by *Herrera and Medina [17]* and *Herrera et al. [10]*, and similar validations to those proposed by the authors were conducted. Note that this methodology is applicable when reflection is relevant but not dominant (reflection coefficient $K_r = H_{s,r}/H_{s,i} < 0.4$, where $H_{s,r}$ and $H_{s,i}$ are the reflected and incident spectral significant wave height, respectively). Figure 4 shows the reflection coefficients measured in the wave generation zone as a function of the wave number ($k = 2\pi/L_{m0}$, where L_{m0} is the mean deep waters wavelength, obtained from the spectral mean wave period, $T_{01} = m_0/m_1$).

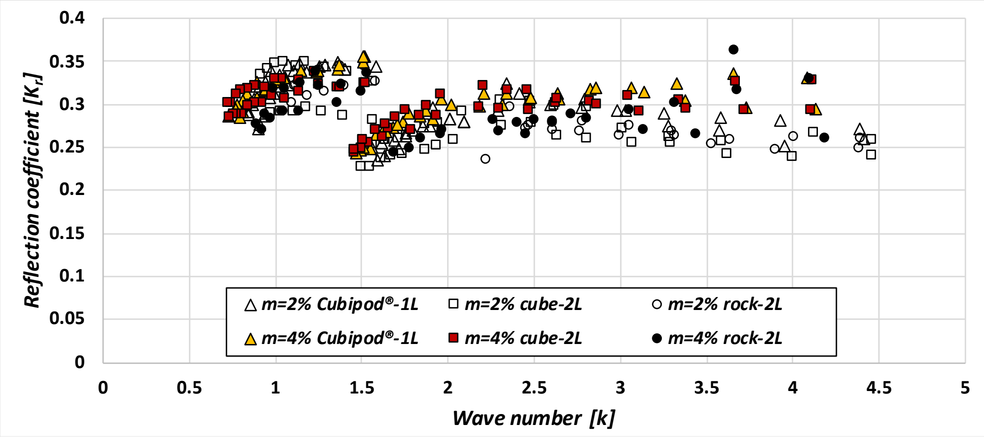

Figure 4. Reflection coefficient, K_r, as a function of the wave number, *k*.

The LASA-V method *[21]* (Local Approximation using Simulated Annealing) was applied in the wave generation zone to separate incident and reflected waves using wave gauges S1–S5. Although the LASA-V method is applicable to nonlinear and nonstationary irregular waves, it is not valid for breaking waves. Thus, it is not applicable in the model zone where breaking occurs, as is the case with other existing methods in the literature. Incident waves were estimated in the model zone from the total wave gauge records, considering the reflection coefficient ($K_r = H_{s,r}/H_{s,i} < 0.4$, $H_{s,r}$ and $H_{s,i}$ being the reflected and incident spectral significant wave height, respectively) measured in the wave generation zone. Tests without a structure were conducted in this study using an efficient wave absorption assembly located at the end of the flume ($K_r < 0.25$ measured in the wave generation zone). Thus, the measured waves directly corresponded to the incident waves. Figure 5a compares the incident significant wave height in the model zone from the tests conducted with a structure (assuming the measured K_r in the generation zone as constant) and the incident significant wave height in the model zone from the tests without a structure. To quantify the goodness of fit, the relative mean squared error (*rMSE*) and the correlation coefficient (*r*) were used. The proportion of the variance not explained by the model is estimated by 0% < *rMSE* < 100%, whereas $0 < r < 1$ assesses the correlation between the variables. Thus, the lower the *rMSE* is and the higher *r* is, the better the estimation. *rMSE* and *r* are given by Equations (1) and (2), respectively,

$$rMSE = \frac{MSE}{var} = \frac{\frac{1}{N_o}\sum_{i=1}^{N_o}(o_i - e_i)^2}{\frac{1}{N_o}\sum_{i=1}^{N_o}(o_i - \bar{o})^2} \tag{1}$$

$$r = \frac{\sum_{i=1}^{N_o}(o_i - \bar{o})(e_i - \bar{e})}{\sqrt{\sum_{i=1}^{N_o}(o_i - \bar{o})^2 \sum_{i=1}^{N_o}(e_i - \bar{e})^2}} \tag{2}$$

where *MSE* is the mean squared error, *var* is the variance of the observations, N_o is the number of observations, o_i is the observed value, e_i is the estimation value, $\bar{o}$ is the average of the observations, and $\bar{e}$ is the average of the estimations.

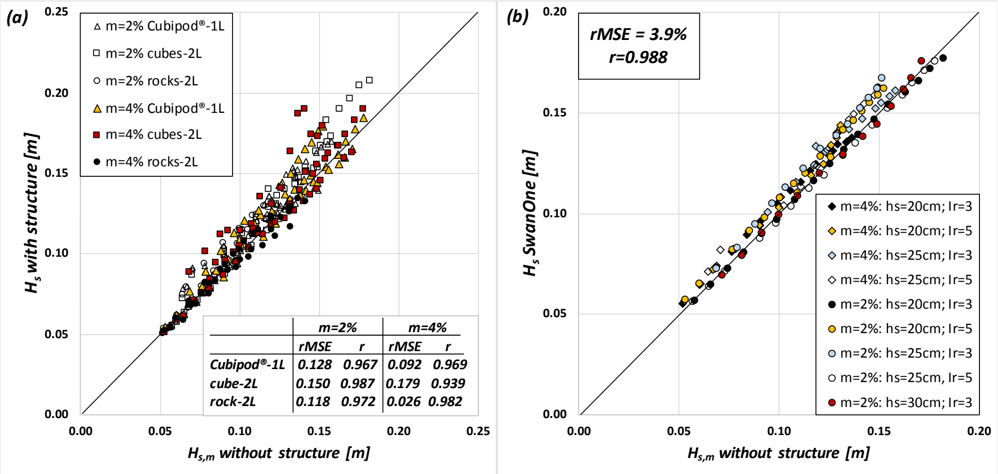

	m=2%		*m=4%*	
	rMSE	*r*	*rMSE*	*r*
Cubipod®-1L	*0.128*	*0.967*	*0.092*	*0.969*
cube-2L	*0.150*	*0.987*	*0.179*	*0.939*
rock-2L	*0.118*	*0.972*	*0.026*	*0.982*

Figure 5. Comparison of the measured significant wave height in the model zone from the tests without a structure with (a) the incident significant wave height in the model zone from the tests conducted with a structure using K_r and (b) the incident wave height obtained using SwanOne.

As shown in Figure 5a, a high correlation was found between the incident wave heights obtained from tests with and without a structure. Therefore, when reflection is small ($K_r < 0.4$), the incident significant wave height obtained from the K_r measured in the wave generation zone is a good estimator of the actual incident significant wave height. This result agrees with those reported in *[10]* and *[17]*. However, as those authors *[17]* pointed out, measurements without a structure are more reliable when estimating incident waves, and they were the ones used for the following analysis.

The composite Weibull distribution suggested by *Battjes and Groenendijk [22]* to describe the wave height distribution in shallow foreshores has been widely validated in the studies of mound breakwaters in depth-limited breaking-wave conditions (i.e., *[6]* or *[23]*). This distribution was implemented in the *SwanOne software [24]*, which was proposed by *Herrera and Medina [17]* as an alternative for tests conducted without a structure. *Herrera and Medina [17]* applied the SwanOne model to estimate the incident wave height in the model zone by introducing the incident waves at the wave generation zone. They validated this methodology comparing the measurements in the wave flume without a structure with the results from the numerical SwanOne simulations. A similar comparison was conducted in this study and it is presented in Figure 5b. A high correlation was found between the experimental measurements and the predictions given by the SwanOne model ($rMSE$ = 3.9%, r = 0.988). Thus, the SwanOne model is a very good estimator of the actual incident significant wave height. Since the SwanOne model provided better results than those obtained from the experimental measurements with a structure, the SwanOne predictions were used for the following analysis.

3.2. Overtopping Layer Thickness (OLT) and Overtopping Flow Velocity (OFV) Measurement

As shown in Figure 2, the capacitive wave gauge S10 was located in the middle of the breakwater crest to measure OLT. S10 was introduced into a hollow cylinder inserted in the model; S10 was filled up with water, so as to keep the capacitive wave gauge partially submerged. In order to keep the daily calibrated reference level constant, the upper part of the cylinder was closed using a lid with a slot to pass the wave gauge. The cylinder was 85 mm in diameter and 120 mm in length. Visual inspection showed a clear water surface during the overtopping events, so aeration was considered negligible. Low noise and low variation in the reference level were observed; the performance of S10 was excellent. In this study, the maximum measured OLT during each overtopping event was considered the observed $h_c(B/2)$, as shown in Figure 6a.

The OFV was measured in 178 out of 235 physical tests using three miniature propellers on the model crest. Miniature propellers were installed in three different positions: (1) on the seaward edge of the model crest, (2) at the middle of the model crest, and (3) on the leeward edge of the crest. These miniature propellers were able to measure velocities between 0.15 and 3.00 m/s and were able to record instantaneous velocities to a frequency of 20 Hz. From the propeller recordings, the maximum values of the OFV for each overtopping event were obtained similarly to the OLT, as displayed in Figure 6b.

4. Analysis Using Neural Networks

Feedforward neural networks (NNs) are techniques from the artificial intelligence field that can be used to model nonlinear relationships between the input (explanatory) and output (response) variables. Since overtopping is a highly nonlinear problem, NNs have been applied in research and practical applications such as CLASH NN *[25]*. NNs have also been applied with fewer input variables and smaller datasets, with satisfactory results, to define explicit overtopping formulae *[5]*, to assess the influence of armor placement on hydraulic stability *[26]*, or to identify the most relevant variables to estimate forces on the crown wall *[27]*. Thus, when the assumption of linear relationships between variables is not valid, acceptable and reliable results may be obtained when applying NNs rather than conventional methods, such as the case of the influence of bottom slope on the overtopping layer thickness and overtopping flow velocity on mound breakwaters in depth-limited breaking-wave conditions (a highly nonlinear problem).

From the experimental data presented in Section 3, OLT exceeded by 2% of the incoming waves in the middle of the model crest, $h_{c,2\%}(B/2)$, and OFV exceeded by 2% of the incoming waves in the middle of the model crest, $u_{c,2\%}(B/2)$, were determined. Note that the velocity values out of the operational range of the miniature propellers were disregarded. As a result, 57, 30, and 80 values of $u_{c,2\%}(B/2)$ were considered for Cubipod®-1L, rock-2L, and cube-2L models, respectively.

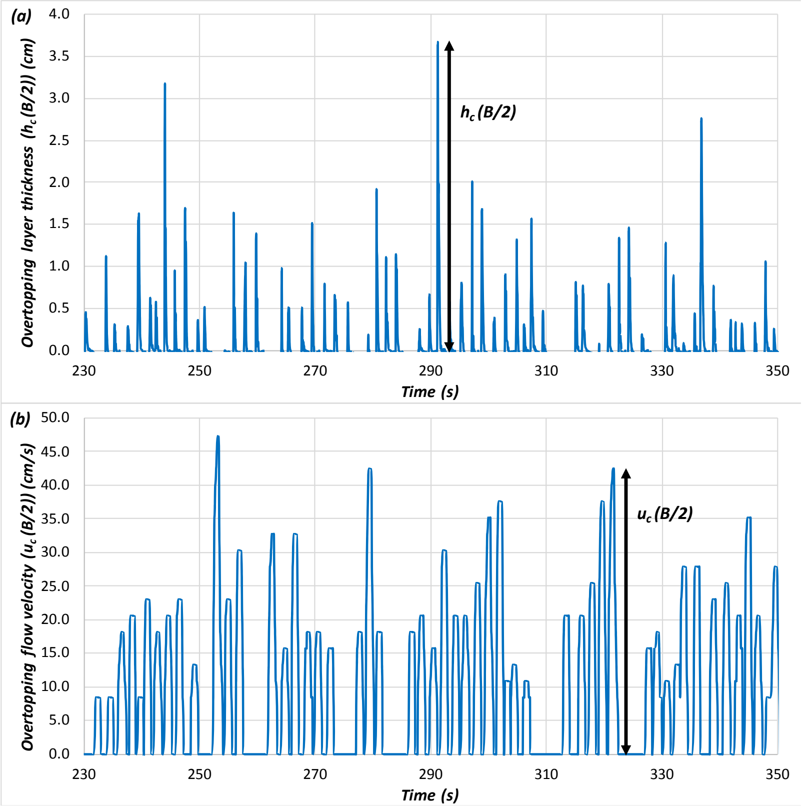

Figure 6. Example of raw records of (a) OLT in the middle of the breakwater crest, $h_c(B/2)$, and (b) OFV in the middle of the breakwater crest, $u_c(B/2)$.

Each armor layer and overtopping variable ($h_{c,2\%}(B/2)$ and $u_{c,2\%}(B/2)$) was studied independently, so the analyses described in the following paragraphs are repeated three times (Cubipod®-1L, rock-2L, and cube-2L) for each overtopping variable ($h_{c,2\%}(B/2)$ and $u_{c,2\%}(B/2)$). The three armor units were studied independently to keep the model as simple as possible. The diagram of this analysis is illustrated in Figure 7.

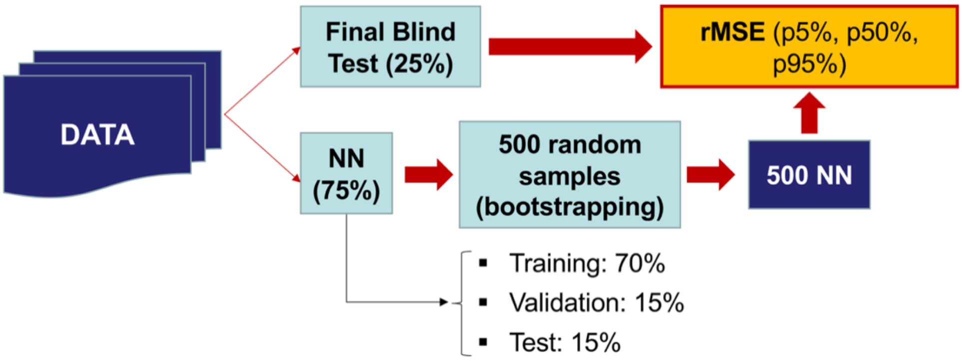

Figure 7. Diagram of the neural network (NN) analysis conducted in this study.

Initially, the data of each armor were divided in two sections: 25% of the data was kept for a final blind test (*FBT*), and 75% of the data was used for the NN training (*T*). The bootstrapping technique is applied to the 75% of the data for training to generate 500 random datasets. This technique consists of the random selection of *N* data from *N* original datasets with a probability of each datum to be selected each time of $1/N$. Thus, some data were absent in a resample, whereas some data were chosen once or more than once. The 500 random datasets were used to train 500 NNs. The goodness of fit of these NNs was evaluated using *FBT* data with *rMSE*. The average value of *rMSE* and its variability is obtained.

Multi-layer feed-forward NNs with only one hidden layer were used, and a hyperbolic tangent sigmoid transfer function was applied. The NN structure was composed of one input layer of four neurons (N_i), one hidden layer of three neurons (N_h), and one output layer of one neuron (N_o). The number of free parameters of the NN model is given by $P = N_o + N_h (N_i + N_o + 1) = 19$. Overlearning is likely to occur when $P/T \geq 1$, when $P/T = 0.63$ in the worst case. Additionally, an early stopping criterion was applied to prevent overlearning (see MATLAB® [28]), dividing the 75% dataset used for training (*T*) into three sections: training (75% × 70%), validation (75% × 15%), and test (75% × 15%). Data in the training section were used to formally train the NN, updating the biases and weights. Data in the validation section were used to monitor the error after each training step and to stop the training when the error on this subset starts growing (an indication of overlearning). Data in the test section were not used during the training process, but to compare different models as a cross validation. As previously mentioned, every armor layer was studied independently to maintain the simplest NN; in the case of including the three armor layers in one NN, one or several extra input neurons would be needed (e.g., armor element, number of armor layers). In addition, to guarantee a proper NN training, a balance dataset is needed, so the same number of tests from each armor layer should be used. Therefore, the number of tests used should be limited to the number of cases of the smallest dataset. In other words, only 40 tests would be used (rock-2L), even if 102 and 93 cases are available for Cubipod®-1L and cube-2L, respectively.

As shown in Figure 8, both $h_{c,2\%}(B/2)$ and $u_{c,2\%}(B/2)$ were analyzed as dimensionless variables ($h_{c,2\%}(B/2)/H_s$ and $u_{c,2\%}(B/2)/(H_s/T_{m-1,0})$). Five input variables were considered as significant to describe OLT and OFV: the significant wave height (H_s), the spectral period ($T_{m-1,0}$), the crest freeboard (R_c), the water depth at the toe of the structure (h_s), and the bottom slope (m). Nevertheless, only four dimensionless variables were considered to feed the NN model (see Figure 8): m, R_c/H_s, $Ir = \tan\alpha/(2\pi H_s/g/T_{m-1,0}^2)$ and h_s/H_s.

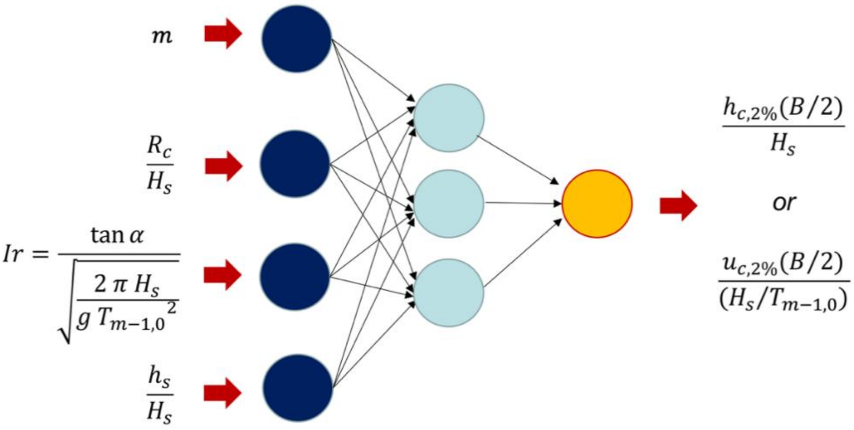

Figure 8. Diagram of the neural networks (NNs) used in this study.

4.1. Optimum Point to Estimate Wave Parameters

The method shown in Figure 7 is repeated seven times for each armor layer and overtopping variable (7 × 3 × 2 = 42 times), modifying the incident wave height (H_s) given to feed the model. The considered H_s values were H_s estimated at the toe of the structure, H_s estimated at a distance of h_s from the toe of the model, H_s at $2h_s$ from the toe of the model, as so on until $6h_s$ from the breakwater toe.

As a result, the evolution of the percentiles of *rMSE* can be obtained as a function of the distance from the model toe where H_s is calculated. Percentiles 5%, 50%, and 95% were used to characterize *rMSE*. Figure 9 presents the *rMSE* of the NN p50% for $h_{c,2\%}(B/2)$ while Figure 10 shows the results for $u_{c,2\%}(B/2)$. Here, the *x*-axis represents the distance from the toe to the structure to the point where H_s is calculated as a multiple of h_s, whereas the *y*-axis presents the median *rMSE* (p50% NN).

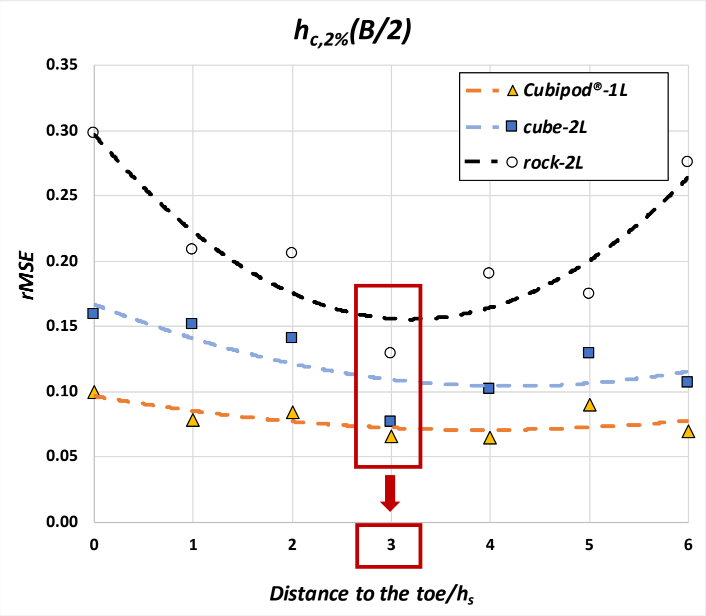

Figure 9. Median relative mean squared error, *rMSE*, (p50% NN) of $h_{c,2\%}(B/2)$ as a function of the relative distance to the structure toe.

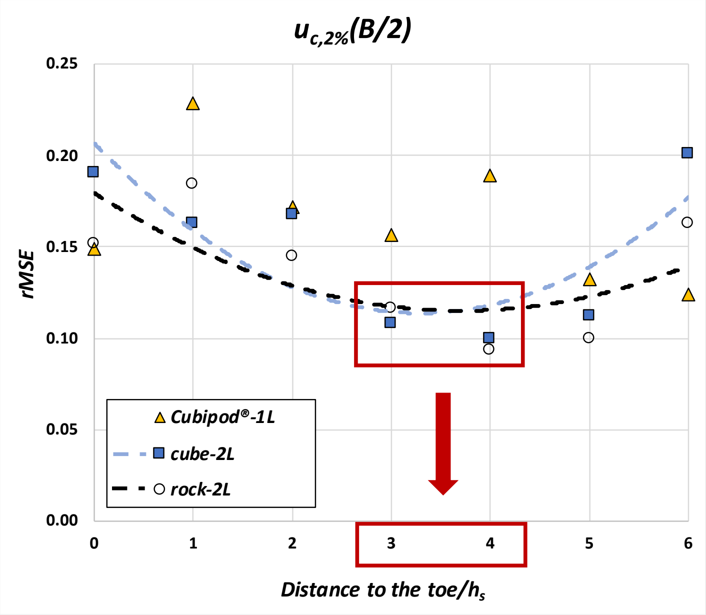

Figure 10. Median *rMSE* (p50% NN) of $u_{c,2\%}(B/2)$ as a function of the relative distance to the structure toe.

The lowest *rMSE* for $h_{c,2\%}(B/2)$ for the three armor layers was obtained around the zone of H_s estimated at a distance of $3h_s$ from the breakwater toe, as shown in Figure 9. In the case of $u_{c,2\%}(B/2)$, no clear tendency was identified for the Cubipod®-1L armor. This may be due to the low number of values for the 2% bottom slope ($N = 13$ for $m = 2\%$, and $N = 44$ for $m = 4\%$). For rock-2L and cube-2L armors, the optimum point to estimate H_s was located between $3h_s$ and $4h_s$ from the toe of the model (see Figure 10). Thus, a distance of $3h_s$ from the model toe was selected as the optimum zone to estimate H_s for the calculation of $h_{c,2\%}(B/2)$ and $u_{c,2\%}(B/2)$. This point was also selected by *Herrera et al. [10]* to better describe the hydraulic stability of rock-armored rubble mound breakwaters in depth-limited wave conditions. This distance approximately corresponds to the distance of $5H_s$ proposed by *Goda [29]* and recommended by *Melby [30]* to determine wave parameters, when considering H_s in breaking wave conditions for vertical breakwaters.

4.2. Influence of the Bottom Slope on OLT and OFV

In the previous section, the optimum zone to estimate H_s for the calculation of $h_{c,2\%}(B/2)$ and $u_{c,2\%}(B/2)$ was identified at a distance of $3h_s$ from the model toe. Here, the influence of bottom slope on $h_{c,2\%}(B/2)$ and $u_{c,2\%}(B/2)$ is assessed. To this end, wave conditions were considered in the wave generation zone ($H_{s,g}$ and Ir_g), and they were propagated along the wave flume using the SwanOne model [24] up to a distance of $3h_s$ from the structure toe. Five numerical flumes (see Figure 11) were considered in this propagation, and the gradient of their bottom slope varied within the tested range (m = 2.0%, 2.5%, 3.0%, 3.5%, and 4.0%).

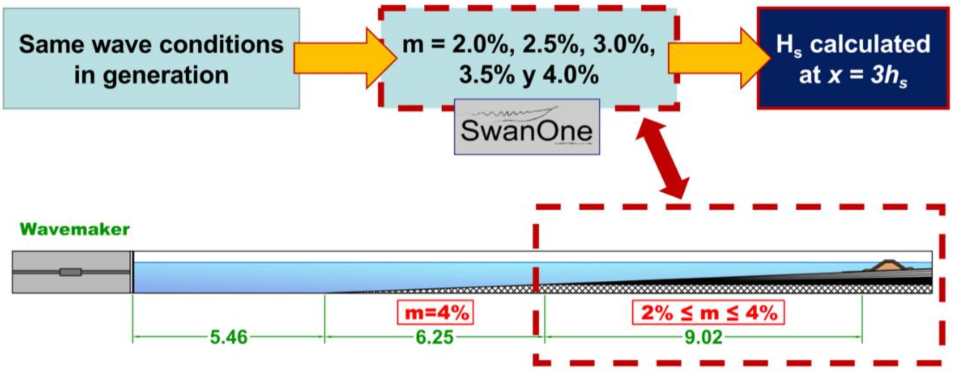

Figure 11. Scheme of the numerical flumes considered for wave propagation using SwanOne.

Using the wave characteristics obtained from the propagation, simulations were conducted using NN p50%. Thus, $h_{c,2\%}(B/2)$ and $u_{c,2\%}(B/2)$ were obtained for five different bottom slopes and the same wave conditions in the wave generation zone. Figure 12 shows the cross-validation of NNs p50% with the final blind test data. The agreement between p50% NNs and the final blind-test data was very good ($0.937 \leq r \leq 0.971$; $0.066 \leq rMSE \leq 0.129$).

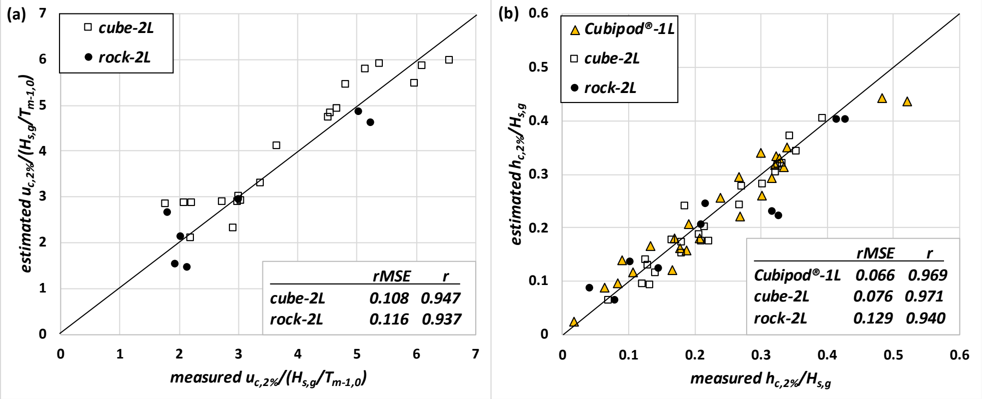

Figure 12. Comparison between measured and estimated blind test data using NN p50% for (a) dimensionless $u_{c,2\%}$, and (b) dimensionless $h_{c,2\%}$.

Figure 13 illustrates the evolution of $h_{c,2\%}(B/2)$ as a function of m for different wave conditions and the three armor layers (Cubipod®-1L, cube-2L, and rock-2L). $h_{c,2\%}(B/2)$ decreased for increasing values of m.

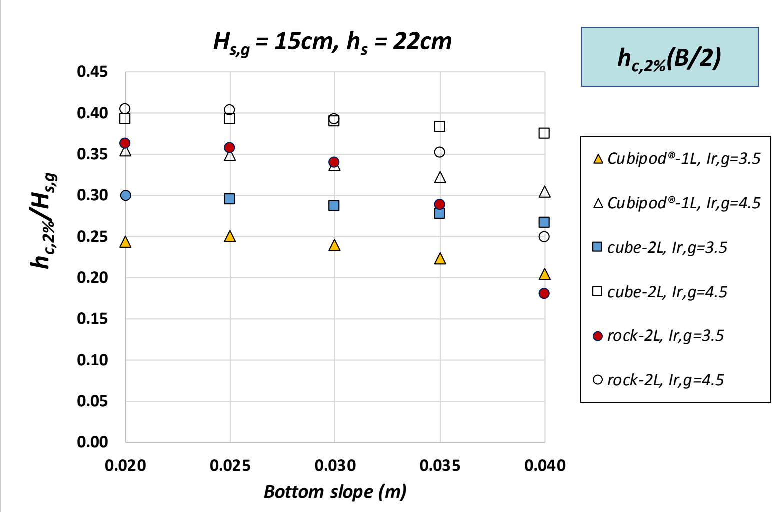

Figure 13. Influence of the bottom slope (m) on OLT exceeded by 2% of the incoming waves ($h_{c,2\%}(B/2)$).

Figure 14 shows the progression of $u_{c,2\%}(B/2)$ for cube and rock armors when varying m for different wave conditions and two of the three studied armor layers. $u_{c,2\%}(B/2)$ slightly increased with increasing values of m.

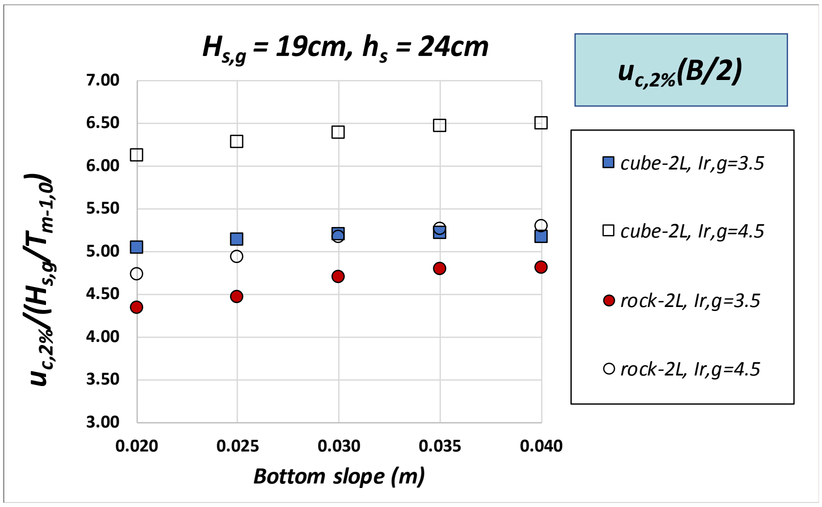

Figure 14. Influence of the bottom slope (*m*) on OFV exceeded by 2% of the incoming waves ($u_{c,2\%}(B/2)$).

5. Conclusions

Overtopping is an increasing risk on coastal structures because of the rising sea levels caused by climate change and social demands to reduce the visual impacts. The safety of pedestrians is a relevant issue during recreational activities on the breakwater crest (e.g., fishing and photography). In order to assess pedestrians' risk, the overtopping layer thickness (OLT) and the overtopping flow velocity (OFV) have been proposed as significant variables.

Few studies are focused on OLT and OFV estimation on coastal structures. These studies only considered variables related to geometry and wave conditions for OLT and OFV calculation. However, most of the mound breakwaters are built in the surf zone, and the bottom slope is an important factor in depth-limited breaking-wave conditions.

In this study, 235 2D physical tests were conducted at the LPC-UPV wave flume with two bottom slopes (m = 2% and m = 4%) and models of mound breakwaters with a single-layer Cubipod® armor, a double-layer rock armor, and a double-layer randomly placed cube armor. A total of 178 tests measured both OLT and OFV, while an additional 57 tests only measured OLT. OLT was measured using a capacitance wave gauge, while OFV was measured using miniature propellers.

Using neural networks (NNs) and bootstrapping techniques, the optimum point to estimate the significant wave height (H_s) to calculate the OLT exceeded by 2% of incoming waves ($h_{c,2\%}(B/2)$) and the OFV exceeded by 2% of incoming waves ($u_{c,2\%}(B/2)$) was studied for each armor. A distance of $3h_s$ from the breakwater toe was determined as the optimum zone to estimate H_s for the calculation of $h_{c,2\%}(B/2)$ and $u_{c,2\%}(B/2)$.

In order to analyze the influence of m on $h_{c,2\%}(B/2)$ and $u_{c,2\%}(B/2)$, fixed wave conditions in the wave generation zone were propagated along five numerical wave flumes with different bottom slopes (m = 2.0%, 2.5%, 3.0%, 3.5%, and 4.0%) using the SwanOne software *[24]* up to a distance of $3h_s$ from the model toe. Using the median *rMSE* NNs (p50% NN), it is observed how $h_{c,2\%}(B/2)$ decreases and $u_{c,2\%}(B/2)$ slightly increases as the gradient of the bottom slope increases.

Author Contributions: P.M.-N. wrote the original draft and was responsible for the conceptualization, experimental methodology, and analysis. M.E.G.-M. and J.R.M. supervised the investigation, review, and approved the manuscript.

Funding: This research was funded by *Ministerio de Economía y Competitividad* and the *Fondo Europeo de Desarrollo Regional (FEDER)* under grant BIA2015-70436-R and RTI2018-101073-B-I00. The first author was also financially supported by the *Ministerio de Educación, Cultura y Deporte* through the FPU program (*Formación de Profesorado Universitario*) under grant FPU16/05081.

Acknowledgments: The authors wish to thank all their funders for their generous support.

Conflicts of Interest: The authors declare no conflicts of interest.

References

[1] Franco, L.; de Gerloni, M.; van der Meer, J.W. Wave overtopping on vertical and composite breakwaters. In Proceedings of the 24th International Conference on Coastal Engineering, Kobe, Japan, 23–28 October 1994; ASCE: USA, 1994; pp. 1030–1044.

[2] Bae, H.U.; Yun, K.M.; Yoon, J.Y.; Lim, N.H. Human Stability with respect to overtopping flow on the breakwater, *Int. J. Appl. Eng. Res.* 2016, *11*, 111–119.

[3] Sandoval, C.; Bruce, T. Wave overtopping hazard to pedestrians: Video evidence from real accidents. In Proceedings of the Coasts, Marine Structures and Breakwaters 2017, Liverpool, UK, 5–7 September 2017; ICE Publishing: Scotland, UK, 2017; pp. 501–512.

[4] EurOtop. *Manual on Wave Overtopping of Sea Defences and Related Structures*; An overtopping manual largely based on European research, but for worldwide application; Van der Meer, J.W., Allsop, N.W.H., Bruce, T., De Rouck, J., Kortenhaus, A., Pullen, T., Schüttrumpf, H., Troch, P., Zanuttigh, B., Eds.; EurOtop: 2018. Available online: www.overtopping-manual.com (accessed on march, 2019).

[5] Molines, J.; Medina, J.R. Explicit wave overtopping formula for mound breakwaters with crown walls using CLASH neural network derived-data. *J. Waterw. Port Coast. Ocean Eng*. 2015, *142*, 04015024. doi:10.1061/(ASCE)WW.1943-5460.0000322.

[6] Nørgaard, J.Q.H.; Lykke-Andersen, T.; Burcharth, H.F. Distribution of individual wave overtopping volumes in shallow water wave conditions. *Coast. Eng.* 2014, *83*, 15–23. doi:10.1016/j.coastaleng.2013.09.003.

[7] Molines, J.; Herrera, M.P.; Gómez-Martín, M.E.; Medina, J.R. Distribution of individual wave overtopping volumes on mound breakwaters, *Coast. Eng.* 2019, *149*, 15–27. doi:10.1016/j.coastaleng.2019.03.006.

[8] Schüttrumpf, H.; van Gent, M. Wave overtopping at seadikes. In Proceedings of the Coastal Structures, Portland, OR, USA, 26–30 August 2003; ASCE: USA, 2003; pp. 431–443.

[9] Mares-Nasarre, P.; Argente, G.; Gómez-Martín, M.E.; Medina, J.R. Overtopping layer thickness and overtopping flow velocity on mound breakwaters. *Coast. Eng.* 2019, *154*, 103561. doi:10.1016/j.coastaleng.2019.103561.

[10] Herrera, M.P.; Gómez-Martín, M.E.; Medina, J.R. Hydraulic stability of rock armors in breaking wave conditions. *Coast. Eng.* 2017, *127*, 55–67. doi:10.1016/j.coastaleng.2017.06.010.

[11] Van Gent, M. Wave overtopping events at dikes. In Proceedings of the 28th International Conference on Coastal Engineering, Cardiff, UK, 7–12 July 2002; World Scientific: Singapore, 2002; pp. 2203–2215. doi:10.1142/9789812791306_0185.

[12] Schüttrumpf, H.; Möller, J.; Oumeraci, H. Overtopping flow parameters on the inner slope of seadikes. In Proceedings of the 28th International Conference on Coastal Engineering, Cardiff, UK, 7–12 July 2002; World Scientific: Singapore, 2002; pp. 2116–2127. doi:10.1142/9789812791306_0178.

[13] Van Gent, M. Wave runup on dikes with shallow foreshores. *J. Waterw. Port Coast. Ocean Eng.* 2001, *127*, 254–262. doi:10.1061/(ASCE)0733-950X(2001)127:5(254).

[14] Van der Meer, J.W.; Hardeman, B.; Steendam, G.; Schïuttrumpf, H.; Verheij, H. Flow depths and velocities at crest and landward slope of a dike, in theory and with the wave overtopping simulator. In Proceedings of the 32nd International Conference on Coastal Engineering, Shanghai, China, 30 June–5 July 2010; World Scientific: Singapore, 2010; p. 2728. doi:10.9753/icce.v32.structures.10.

[15] Lorke, S.; Scheres, B.; Schüttrumpf, H.; Bornschein, A.; Pohl, R. Physical model tests on wave overtopping and flow processes on dike crests influenced by wave-current interaction. In Proceedings of the 33rd International Conference on Coastal Engineering, Santander, Spain, 1–6 July 2012; World Scientific: Singapore, 2012; p. 1770. doi:10.9753/icce.v33.waves.34.

[16] Mansard, R.P.D.; Funke, E.R. The measurement of incident and reflected spectra using a least squares method. In Proceedings of the 17th International Conference on Coastal Engineering, Sydney, Australia, 23–28 March 1980; ASCE: USA, 1980; pp. 100–108.

[17] Herrera, M.P.; Medina, J.R. Toe berm design for very shallow waters. *Coast. Eng.* 2015, *103*, 67–77. doi:10.1016/j.coastaleng.2015.06.005.

[18] Gómez-Martín, M.E.; Medina, J.R. Heterogeneous packing and hydraulic stability of cube and Cubipod® armor units. *J. Waterw. Port Coast. Ocean Eng.* 2014, *140*, 100–108. doi:10.1061/(ASCE)WW.1943-5460.0000223.

[19] Argente, G.; Gómez-Martín, M.E.; Medina, J.R. Hydraulic Stability of the Armor Layer of Overtopped Breakwaters. *J. Mar. Sci. Eng.* 2018, *6*, 143. doi:10.3390/jmse6040143.

[20] Gómez-Martín, M.E.; Herrera, M.P.; Gónzalez-Escriva, J.A.; Medina, J.R. Cubipod® Armor Design in Depth-Limited Regular Wave-Breaking Conditions. *J. Mar. Sci. Eng.* 2018, *6*, 150. doi:10.3390/jmse6040150.

[21] Figueres, M.; Medina, J.R. Estimating incident and reflected waves using a fully nonlinear wave model. In Proceedings of the 29th International Conference on Coastal Engineering, Lisbon, Portugal, 19–24 September 2004; World Scientific: Singapore, 2004; pp. 594–603. doi:10.1142/9789812701916-0047.

[22] Battjes, J.A.; Groenendijk, H.W. Wave height distributions on shallow foreshores. *Coast. Eng.* 2000, *40*, 161–182. doi:10.1016/S0378-3839(00)00007-7.

[23] Victor, L.; van der Meer, J.W.; Troch, P. Probability distribution of individual wave overtopping volumes for smooth impermeable steep slopes with low crest freeboards. *Coast. Eng.* 2012, *64*, 87–101. doi:10.1016/j.coastaleng.2012.01.003.

[24] Verhagen, H.J.; Van Vledder, G.; Eslami Arab, S. A practical method for design of coastal structures in shallow water. In Proceedings of the 31st International Conference on Coastal Engineering, Hamburg, Germany, 31 August–5 September 2008; World Scientific: Singapore, 2008; pp. 2912–2922. doi:10.1142/9789814277426_0241.

[25] Van Gent, M.R.A.; Van den Boogaard, H.F.P.; Pozueta, B.; Medina, J.R. Neural network modelling of wave overtopping at coastal structures. *Coast. Eng.* 2007, *54*, 586–593. doi:10.1016/j.coastaleng.2006.12.001.

[26] Herrera, M.P.; Hoyos, A.; Molines, J.; Medina, J.R. Influence of placement technique on double-layer cube armor stability of breakwaters constructed on steep foreshores. In Proceedings of the 36th IAHR World Congress, The Hague, The Netherlands, 28 June–3 July 2015.

[27] Molines, J.; Herrera, M.P.; Medina, J.R. Estimations of wave forces on crown walls based on wave overtopping rates. *Coast. Eng.* 2018, *132*, 50–62.

[28] *MATLAB® 2015a*; The MathWorks Inc.: Natick, MA, USA, 2015.

[29] Goda, Y. *Random Seas and Design of Maritime Structures*; University of Tokyo Press: Tokyo, Japan, 1985.

[30] Melby, J.A. *Damage Progression on Rubble Mound Breakwaters*; Technical Report CHL-99-17; U.S. Army Engineer Research and Development Center: Vicksburg, MS, USA, 1999. Also Ph.D. Thesis, University of Delaware, Newark, DE, USA, 1999.

3. **Mares-Nasarre, P., Molines, J., Gómez-Martín, M.E., Medina, J.R., 2020b. Individual wave overtopping volumes on mound breakwaters in breaking wave conditions and gentle sea bottoms. Coast. Eng. 159, 103703. https://doi.org/10.1016/j.coastaleng.2020.103703**

Individual wave overtopping volumes on mound breakwaters in breaking wave conditions and gentle sea bottoms

Patricia Mares-Nasarre [1,] *, Jorge Molines[1], M. Esther Gómez-Martín[1] and Josep R. Medina[1]

[1]Lab. Ports and Coasts, Institute of Transport and Territory, Universitat Politècnica de València; patmana@cam.upv.es, jormollo@upv.es, mgomar00@upv.es, jrmedina@upv.es.

***** Corresponding author: patmana@cam.upv.es

Abstract:

Mound breakwaters are usually designed to limit the mean wave overtopping rate (*q*) or the maximum individual wave overtopping volume (V_{max}). However, rarely do studies focus on wave overtopping volumes on breakwaters in depth-limited breaking wave conditions. This study analyzes 2D physical tests on mound breakwaters with relevant overtopping rates ($0.33 \leq R_c/H_{m0} \leq 2.83$) and three armor layers (Cubipod®-1L, rock-2L and cube-2L) in depth-limited breaking wave conditions ($0.20 \leq H_{m0}/h_s \leq 0.90$) and with two bottom slopes (m = 1/25 and m = 1/50). The 2-parameter Weibull distribution was used to estimate $V_{max}^* = V_{max}/(g\, H_{m0}\, T_{01}^2)$ with coefficient of determination $R^2 = 83.3\%$. In this study, the bottom slope (m = 1/50 and m = 1/25) did not significantly influence V_{max} or the number of overtopping events, N_{ow}. During the design phase of a mound breakwater, *q* is required to use the methods given in the literature to estimate V_{max}. Thus, *q* must be estimated for design purposes when measured *q* is not available. In this study, CLASH Neural Network (CLASH NN) was used to estimate *q* with $R^2 = 63.6\%$. If the 2-parameter Weibull distribution proposed in this study is used to estimate V_{max} with *q* estimated using CLASH NN, the prediction error of V_{max}^* is $R^2 = 61.7\%$. With the method presented in this study, the ratio between estimated and measured V_{max}^* falls within the range 1/2 to 2 (90% error band) when *q* is estimated with CLASH NN. The new estimators derived in this study provide good predictions of N_{ow} and V_{max} with a method simpler than those in the literature on overtopped mound breakwaters in depth-limited breaking wave conditions on gentle sea bottoms ($1/50 \leq m \leq 1/25$).

Keywords: mound breakwater; wave overtopping; individual wave overtopping volumes; depth-limited breaking wave conditions; bottom slope; proportion of overtopping events

1. Introduction

Crest elevation is a key parameter when designing mound breakwaters due to its direct effect on construction costs as well as visual and environmental impact. Climate change effects (e.g., sea level rise) and increasing social concern about the visual impact of coastal structures are leading to reductions in crest freeboards and increases in the overtopping hazard. In this situation, coastal structure designs with reduced crest freeboards and relevant overtopping discharges become significant. In addition, most mound breakwaters are built in the surf zone, where they are attacked by waves breaking on the sea bottom.

Tolerable mean overtopping discharges, q (m^3/s/m), are commonly considered to design crest elevation of coastal structures. However, the mean individual overtopping volume ($\bar{V}$) may be much lower than the maximum individual wave overtopping volume, V_{max} (m^3/m). For this reason, *Franco et al. (1994)* suggested that overtopping hazard should be directly related with individual wave overtopping events, rather than the mean overtopping rate.

Several prediction methods exist to estimate q (e.g. *Molines and Medina, 2015a,* and *EurOtop, 2018*), the number of overtopping events ($N_{ow} = N_w P_{ow}$) and V_{max} (see Molines et al., 2019) on mound breakwaters in non-breaking conditions. *Victor et al. (2012)* conducted 2D physical tests on smooth impermeable structures under depth-limited breaking wave conditions with horizontal bottom slope and concluded that wave breaking had a significant impact on N_{ow} and V_{max}. *Gallach (2018)* carried out 2D physical tests on smooth impermeable steep sloped structures in depth-limited breaking wave conditions and two bottom slopes ($m = 0$ and $m = 1/100$). However, *Gallach (2018)* did not find a significant effect of the breaking waves conditions on V_{max}. *Nørgaard et al. (2014)* performed 2D physical tests on rubble mound breakwaters ($\cot\alpha = 1.5$, where $\cot\,\alpha$ is the armor slope) in depth-limited breaking wave conditions with horizontal bottom slope. They evaluated the performance of the existing formulations, valid for non-breaking wave conditions, for observations in breaking wave conditions and concluded that existing formulas were underpredicting N_{ow} and overpredicting V_{max}. Therefore, the depth-limited breaking wave conditions of the incoming waves may be a significant factor to consider.

The bottom slope highly affects the type of wave breaking at the toe of the structure. *Herrera et al. (2017)* pointed out that bottom slope directly influences mound breakwater design; the optimum point where wave characteristics are estimated needs to be determined when in depth-limited breaking wave conditions. *Mares-Nasarre et al. (2020)* found a significant effect of bottom slope on the overtopping layer thickness (h_c) and the overtopping flow velocity (u_c). *Mares-Nasarre et al. (2020)* also determined that the optimum point to estimate wave characteristics to calculate h_c and u_c was located at a distance of 3 times the water depth from the toe of the structure. However, the influence of the bottom slope on V_{max} has not yet been analyzed.

This research focuses on the distribution of individual wave overtopping volumes *F(V)* in depth-limited breaking wave conditions for mound breakwaters and the influence of bottom slope on V_{max}. This paper is organized as follows. In section 2, the literature on individual wave overtopping volumes is examined. Neither the optimum point to estimate wave characteristics nor the effect of bottom slope on N_{ow} and V_{max} was assessed by the studies in the literature. Section 3 describes the experimental setup with two bottom slopes (m = 1/25 and m = 1/50) and the experimental data analysis. 2D small-scale tests on mound breakwaters in depth-limited breaking wave conditions ($0.20 \leq H_{m0}/h_s \leq 0.90$) and three armor layers (Cubipod®-1L, rock-2L and cube-2L) were conducted. Section 4 assesses existing estimators for N_{ow} and V_{max}. None of the existing estimators for mound breakwaters satisfactory describes N_{ow} for very low q. In section 5, the optimum point to estimate wave characteristics when calculating N_{ow} is determined and a new N_{ow} estimator is developed. In section 6, the 2-parameter Weibull distribution is considered to fit *F(V)*; the influence of bottom slope on the two-parameter Weibull distribution is also investigated. The quadratic utility function proposed by *Molines et al. (2019)* is used in this study to take into account the higher relevance of the largest individual wave overtopping volumes for practical applications. In section 7, the performance of the new N_{ow} and V_{max} estimators is validated using q estimators given in the literature. Finally, in section 8, conclusions are drawn.

2. Literature review

2.1. Individual wave overtopping volumes

Van der Meer and Janssen (1994) and *Franco et al. (1994)* first introduced the Weibull distribution to describe individual wave overtopping volumes for dikes, and vertical and composite breakwaters, respectively. Later, the 2-parameter Weibull distribution was proposed by different authors (e.g., *Besley, 1999* or *Victor et al., 2012*) to analyze individual wave overtopping volumes in a variety of coastal structures. The 2-parameter Weibull distribution is given by

$$F(V) = F(x \leq V) = 1 - exp\left[-\left(\frac{V}{a}\right)^{b}\right] \tag{1}$$

where $F(x \leq V)$ is the non-exceedance probability of the individual wave overtopping volume per wave, x is the individual wave overtopping volume, a is the dimensional scale factor and b is the shape factor. Eq. (1) can also be found as:

$$F(V) = 1 - exp\left[-\left(\frac{V/\bar{V}}{A}\right)^{b}\right] \tag{2}$$

where $A = a/\bar{V}$ is the scale factor and $\bar{V}$ is the measured mean individual wave overtopping volume.

If all the measured data were used for the analysis and they followed a perfect Weibull distribution, the mean individual wave overtopping volume, $\bar{V}$, would be equal to the mean value of the Weibull distribution, μ ($\mu = \bar{V}$). Under the previous hypothesis, a relationship between A and b exists and is described by

$$A = \frac{a}{\bar{V}} = \frac{1}{\Gamma\left(1 + \frac{1}{b}\right)} \tag{3}$$

where Γ is the gamma function, given by $\Gamma(\mathrm{z}) = \int_0^\infty t^{z-1}\, e^{-t}\, dt$. *Van der Meer and Janssen (1994)* and *Franco et al. (1994)* recommended a value of $b = 0.75$ for dikes, and vertical and composite breakwaters, respectively, which corresponds to $A = 0.84$ according to Eq. (3).

Besley et al. (1999) studied individual wave overtopping volumes for sloped structures, vertical walls and composite breakwaters. These authors also referred to the results reported by *Franco et al. (1996)*, who highlighted the influence of wave steepness on shape factor b for vertical walls. *Franco et al. (1996)* also noticed that the shape factor b was around 0.1 higher for sloping structures than for vertical walls. Regarding sloped structures, *Besley et al. (1999)* recommended values for the shape factor b as a function of the offshore wave steepness, $s_{0p} = 2\pi H_{s0}/(gT_{p0}^2)$, where H_{s0} is the significant offshore wave height and T_{p0} is the deep water peak period. These authors suggested $b = 0.76$ for $s_{op} = 0.02$ and $b = 0.92$ for $s_{op} = 0.04$.

Bruce et al. (2009) carried out 2D physical tests on mound breakwaters with horizontal bottoms, $0.8 \leq R_c/H_{m0} \leq 1.3$ and $0.33 \leq H_{m0}/h_s \leq 0.40$, where R_c is the crest freeboard, $H_{m0} = 4(m_0)^{1/2}$ is the significant wave height, and h_s is the water depth at the toe of the structure. These authors tested a wide variety of armor units, both double- and single-layer armors, and analyzed the individual wave overtopping volumes higher than $\bar{V}$. *Bruce et al. (2009)* suggested a shape factor $b = 0.74$ and concluded that no significant differences could be observed between the different armor units.

Victor et al. (2012) investigated individual wave overtopping volumes on smooth impermeable steep slopes ($0.36 \leq cot\ \alpha \leq 2.75$) with horizontal bottoms and $0.11 \leq R_c/H_{m0} \leq 1.69$. The authors observed that the wave heights during the tests with large H_{m0} did not fit a Rayleigh distribution ($0.04 \leq H_{m0}/h_s \leq 0.37$), but a Composite Weibull distribution, and they concluded that deviations were caused by depth-induced breaking of the largest waves. *Victor et al. (2012)* also observed that this wave breaking process limited the value of the maximum individual wave overtopping volumes and decreased the shape factor *b*. Moreover, these authors investigated the effect of the relative crest freeboard, R_c/H_{m0}, slope angle, α, and s_{0p}. They concluded that the effect of s_{0p} ($0.012 \leq s_{0p} \leq 0.041$) was negligible and proposed Eq. (4) to estimate the shape factor *b* considering the individual wave overtopping volumes higher than $\bar{V}$.

$$b = exp\left(-2.0\,\frac{R_c}{H_{m0}}\right) + (0.56 + 0.15\cot\alpha) \tag{4}$$

Zanuttigh et al. (2013) analyzed the shape factor *b* for rough and smooth low-crested structures ($0 \leq R_c/H_{m0} \leq 2$), using the individual wave overtopping volumes higher than $\bar{V}$. These authors reported higher scatter in the data for rubble mound breakwaters than in the data for smooth slopes. *Zanuttigh et al. (2013)* also pointed out that, even if formulas considering the dimensionless crest freeboard (R_c/H_{m0}) gave good results for smooth structures, they were not adequate for rubble mound breakwaters. The shape factor *b* for rubble mound breakwaters was found to be related to a dimensionless mean wave overtopping discharge, $Q^{**}=q/(g\,H_{m0}\,T_{m-1,0})$ (where $T_{m-1,0} = \frac{m_{-1}}{m_0}$ and m_k is the *k-th* spectral moment, $m_k = \int_0^\infty S(f) f^k df$, and *S(f)* is the wave spectrum) similar to $Q^{*}=q/(g\,H_{m0}\,T_{01})$ (where $T_{01} = \frac{m_0}{m_1}$) proposed by *Besley (1999)*, and Eq. (5) was derived. *EurOtop (2018)* also recommends Eq. (5) for estimating the shape factor *b* for armored rubble slopes and mounds.

$$b = 0.85 + 1500\,Q^{**1.3} \tag{5}$$

Nørgaard et al. (2014) conducted 2D physical tests on rock-armored mound breakwaters with crown wall both in non-breaking and breaking wave conditions ($0.18 \leq H_{m0}/h_s \leq 0.50$) with horizontal bottoms and $0.9 \leq R_c/H_{m0} \leq 2.0$. These authors assessed the existing formulas in the literature for the shape factor *b* in non-breaking wave conditions and concluded that they were overpredicting the largest overtopping wave volumes in depth-limited breaking wave conditions. *Nørgaard et al. (2014)* proposed Eq. (6) based on 30% of the highest individual wave overtopping volumes.

$$b = \begin{cases} 0.75 & for\ \frac{H_{m0}}{H_{1/10}} \leq 0.848\ or\ \frac{H_{m0}}{h_s} \leq 0.2 \\ -6.1 + 8.08\,\frac{H_{m0}}{H_{1/10}} & for\ \frac{H_{m0}}{H_{1/10}} > 0.848\ and\ \frac{H_{m0}}{h_s} > 0.2 \end{cases} \tag{6}$$

where $H_{1/10}$ is the average of 10% of the highest waves in the test run.

Gallach (2018) carried out thousands of 2D physical tests using bottom slopes $m = 0$ and $m = 1/100$ for steep slopes and vertical structures in a wide range of crest freeboards ($0.0 \leq R_c/H_{m0} \leq 3.25$). The author investigated the effect of depth-limited breaking wave conditions ($0.03 \leq H_{m0}/h_s \leq 0.50$) on the shape factor b and found it negligible, contrary to results published by *Victor et al. (2012)* and *Nørgaard et al. (2014)*. *Gallach (2018)* also noticed that the shape factor b was not affected by the roughness of the structure and proposed a new formula to estimate b as function of R_c/H_{m0} and the structure slope, using the largest 10% individual wave overtopping volumes. Regarding the scale factor A, *Gallach (2018)* found that the best fit values were significantly different than those given by Eq. (3).

Molines et al. (2019) analyzed the 2D physical tests conducted by *Smolka et al. (2009)* on conventional mound breakwaters ($1.25 \leq R_c/H_{m0} \leq 4.78$) with crown wall in non-breaking conditions ($0.10 \leq H_{m0}/h_s \leq 0.32$) and reported the inconsistencies in the selection criteria of the number of overtopping events used to fit the scale and shape factors identified by *Pan et al. (2016)*. *Molines et al. (2019)* compared the fitting of A and b of the 2-parameter Weibull distribution using 10%, 30% 50%, and 100% (with quadratic utility function) of the highest individual wave overtopping volumes. Utility functions are used to consider the relative relevance of the observed data; using the whole dataset with a quadratic utility function, all the observations are used but special attention is paid to the highest volumes. The relationship between A and b was not given any more by Eq. (3). Note that small overtopping events significantly affect $\bar{V}$ and N_{ow}; the estimations of A based on Eq. (3) are sensitive to small overtopping events which are not significant for practical applications. The shape factor, b, is given as function of the dimensionless mean wave overtopping discharge, $Q^* = q/(g\, H_{m0}\, T_{01})$, whereas the scale factor A depends on the shape factor b, as shown in Eqs. (7) and (8), respectively, when applying the quadratic utility function to all observed individual wave overtopping volumes.

$$b = 0.63 + 1.25 \exp(-3.0 \cdot 10^5\, Q^*) \tag{7}$$

$$A = 1.4 - 0.4\,\frac{1}{b} \tag{8}$$

Additionally, *Molines et al. (2019)* proposed a 2-parameter Exponential distribution to describe individual wave overtopping volumes, given by

$$F(V) = 1 - exp\left[-\left(\frac{V/\bar{V} - C}{D}\right)\right] \tag{9}$$

where

$$D = 2.6 - 2.6\exp(-3.0 \cdot 10^5\, Q^*) \tag{10}$$

$$C = 1.2 - D - 0.2\, D^2 \tag{11}$$

2.2. Number of overtopping events

In order to assign an exceedance probability to every individual wave overtopping volume, *Makkonen (2006)* recommended the Weibull plotting position formula, given by

$$F(V) = 1 - \frac{i}{N_{ow} + 1} \tag{12}$$

where *F(V)* is the exceedance probability of the individual wave overtopping volume per wave, *i* is the rank of the individual volume, sorted in descending order (*i* = 1 corresponds to V_{max}) and N_{ow} is the number of overtopping events.

Lykke-Andersen et al. (2009) applied Eq. (12) to rewrite the Weibull distribution function as:

$$V_i = A\bar{V}\left[-\ln\left(\frac{i}{N_{ow} + 1}\right)\right]^{1/b} = A\bar{V}\,[\ln(N_{ow} + 1) - \ln(i)]^{1/b} \quad with\ i = 1\ to\ N_{ow} \tag{13}$$

By setting *i* = 1 in Eq. (13), V_{max} can be calculated as

$$V_{max} = A\bar{V}\,[\ln(N_{ow} + 1)]^{1/b} \tag{14}$$

Besley (1999), *EurOtop (2007)* and *EurOtop (2018)* proposed Eq. (15), which uses N_{ow} instead of N_{ow}+1.

$$V_{max} = A\bar{V}\,[\ln(N_{ow})]^{1/b} \tag{15}$$

Lykke-Andersen et al. (2009) warned that Eq. (15) would predict an inconsistent V_{max}=0 for N_{ow}=1. To estimate V_{max}, not only N_{ow} has to be estimated, using either Eq. (14) or Eq. (15), but also the mean individual wave overtopping volume ($\bar{V} = qT_{01}N_w/N_{ow}$, where q is the mean overtopping discharge). Thus, q has to be estimated in order to calculate V_{max}. To this end, *Besley (1999)* proposed Eqs. (16) and (17) for simple slopes, and complex slope structures with return walls or berms, respectively.

$$P_{ow} = \frac{N_{ow}}{N_w} = exp\left[-K_1\left(\frac{R_c}{T_{01}\sqrt{g\,H_{m0}}}\,\frac{1}{\gamma_f}\right)^2\right] \tag{16}$$

$$\begin{cases} P_{ow} = 55.4\, Q^{*0.634} & for\ 0 < Q^* < 8\cdot 10^{-4} \\ P_{ow} = 2.5\, Q^{*0.199} & for\ 8\cdot 10^{-4} < Q^* < 10^{-2} \\ P_{ow} = 1 & for\ Q^* > 10^{-2} \end{cases} \tag{17}$$

where P_{ow} is the proportion of overtopping waves, N_{ow} is the number of overtopping events and N_w is the number of incoming waves, γ_f is the roughness factor, H_{m0} is the spectral significant wave height, $Q^*=q/(gH_{m0}T_{01})$ and q are the dimensionless and dimensional mean overtopping discharges, respectively. *Besley (1999)* recommended K_1=37.8 for structure slope $cot\alpha$=2 and K_1=63.8 for $cot\alpha$=1. *Besley (1999)* proposed Eq. (18) to estimate q.

$$\frac{q}{g\, T_{01}\, H_{m0}} = K_2\, exp\left[-K_3 \frac{R_c}{T_{01}\sqrt{g\, H_{m0}}}\frac{1}{\gamma_f}\right] \tag{18}$$

where K_2 and K_3 are experimental coefficients function of α. For $cot\alpha$=1.5, $K_2=8.84\cdot 10^{-5}$ and K_3 =19.9.

Nørgaard et al. (2014) proposed a variation of Eq. (19) to extend the application of this equation to depth-limited breaking wave conditions for $0.006\leq P_{ow}\leq 0.120$ and $7.3\cdot 10^{-7}\leq Q^*\leq 6.2\cdot 10^{-5}$, given by

$$N_{ow} = C_1\, Eq.(17)$$
$$C_1 = \begin{cases} 1 & for\ H_{m0}/H_{1/10} \leq 0.848\ or\ H_{m0}/h_s \leq 0.2 \\ -6.65 + 9.02\, \dfrac{H_{m0}}{H_{\frac{1}{10}}} & for\ H_{m0}/H_{1/10} > 0.848\ and\ H_{m0}/h_s > 0.2 \end{cases} \tag{19}$$

Nørgaard et al. (2014) recommended using CLASH Neural Network (CLASH NN), described by *Van Gent et al. (2007)*, for q estimation.

EurOtop (2018) recommended Eq. (20) for mound breakwaters with permeable crest berms.

$$P_{ow} = exp\left[-\left(\sqrt{-\ln 0.02}\, \frac{R_c}{Ru_{2\%}}\right)^2\right] \tag{20}$$

where $Ru_{2\%}$ is the wave run-up height exceeded by 2% of the incoming waves, calculated as

$$\frac{Ru_{2\%}}{H_{m0}} = 1.65\, \gamma_f\, \gamma_\beta\, \gamma_b\, \xi_{-1,0} \tag{21a}$$

with a maximum value of

$$\frac{Ru_{2\%}}{H_{m0}} = \min\left(1.00\,\gamma_{fsurging}\,\gamma_\beta\,\left[4.00 - \frac{1.50}{\sqrt{\xi_{-1,0}}}\right], 2.0\right) \tag{21b}$$

where $\gamma_{fsurging} = \gamma_f + \left(Ir_{-1,0} - 1.8\right)(1 - \gamma_f)/8.2$; γ_β, the oblique wave attack factor and $\xi_{-1,0} = \tan\alpha/\sqrt{2\pi H_{m0}/(g\,{T_{m-1,0}}^2)}$.

EurOtop (2018) suggested Eq. (22) to estimate q.

$$\frac{q}{\sqrt{g\,{H_{m0}}^3}} = 0.09\exp\left(-1.5\,\frac{R_c}{H_{m0}\,\gamma_f\,\gamma_\beta}\right) \tag{22}$$

Molines et al. (2019) recently proposed to estimate the proportion of overtopping waves, P_{ow}, valid for $0.001 \leq P_{ow} \leq 0.20$ and $7.0 \cdot 10^{-8} \leq Q^* \leq 6.4 \cdot 10^{-5}$, using

$$P_{ow} = 480\,Q^{*0.8} \tag{23}$$

Similar to *Nørgaard et al. (2014)*, *Molines et al. (2019)* recommended using CLASH NN for estimating q. Table 1 summarizes the experimental ranges of the methods found in the literature.

Table 2 presents a summary of the methods in literature to estimate V_{max} on mound breakwaters or permeable slopes.

3.1. Experimental setup

2D physical tests were conducted in the wave flume (30.0 m × 1.2 m × 1.2 m) of the Laboratory of Ports and Coasts at the *Universitat Politècnica de València* (LPC-UPV), with two bottom slope configurations and a piston-type wave maker. The first configuration involved a continuous ramp of 4% slope (m = 1/25) all along the flume. The second configuration was formed by two ramps: a 6.3 m-long m = 1/25 bottom slope, and a 9.0 m-long m = 1/50 bottom slope. Figure 1 shows the longitudinal cross-sections of the LPC-UPV wave flume for both configurations as well as the locations of the wave gauges.

Author	**Structure**	**Crown wall**	R_c/H_{m0} **[-]**	H_{m0}/h_s **[-]**	m **[-]**	$\cot\alpha$ **[-]**
Bruce et al. (2009)	Mound breakwaters	Yes	0.80 – 1.03	0.33 – 0.40	0	2
Victor et al. (2012)	Smooth impermeable steep slopes	No	0.11 – 1.69	0.04 – 0.37	0	0.36 – 2.75
Zanuttigh et al. (2013)	Smooth slopes and rubble mound breakwaters	-	0 – 2	–	–	2 – 4
Nørgaard et al. (2014)	Rubble mound breakwaters	Yes	0.9 – 2	0.18 – 0.50	0	1.5
Gallach (2018)	Steep slopes and vertical structures	No	0 – 3.25	0.03 – 0.50	0, 1/100	0 – 0.27, 1.5 – 2.75
Molines et al. (2019)	Mound breakwaters	Yes	1.25 – 4.78	0.10 – 0.32	0	1.5

Table 1. Summary of the experimental ranges of the methods to estimate V_{max} in the literature.

Author	q [m^3/s/m]	P_{ow} [-]	b [-]	A [-]	V_{max} [l/m]
Besley (1999)	$g\, T_{01}\, H_{m0}\, K_2\, exp\left[-K_3 \frac{R_c}{T_{01}\sqrt{g\, H_{m0}}} \frac{1}{\gamma_f}\right]^{*,1}$	*Simple slopes:* $exp\left[-K_1\left(\frac{R_c}{T_{01}\sqrt{g\, H_{m0}}} \frac{1}{\gamma_f}\right)^2\right]$ *Complex slopes*: $\begin{cases} 55.4\, Q^{*0.634} & 0 < Q^* < 8\, 10^{-4} \\ 2.5\, Q^{*0.199} & 8\, 10^{-4} < Q^* < 10^{-2} \\ 1 & Q^* > 10^{-2} \end{cases}$	0.76 for s_{op} = 0.02 0.92 for s_{op} = 0.04	$\frac{1}{\Gamma\left(1+\frac{1}{b}\right)}$	$A\bar{V}[\ln(N_{ow})]^{1/b}$
EurOtop (2018)	$0.09\, \exp\left(-1.5 \frac{R_c}{H_{m0}\, \gamma_f\, \gamma_\beta}\right)\sqrt{g\, H_{m0}{}^3}$	$exp\left[-\left(\sqrt{-\ln 0.02}\, \frac{R_c}{Ru_{2\%}}\right)^2\right]$	$0.85 + 1500\, Q^{**1.3}$	$\frac{1}{\Gamma\left(1+\frac{1}{b}\right)}$	$A\bar{V}[\ln(N_{ow})]^{1/b}$
Nørgaard et al. (2014)	CLASH NN	$C_1 \times (Besley, 1999; compl.sl.)$ Where: $C_1 = -6.65 + 9.02\, \frac{H_{m0}}{H_{\frac{1}{10}}}{}^{*,2}$	$-6.1 + 8.08\, \frac{H_{m0}}{H_{1/10}}{}^{*,3}$	$\frac{1}{\Gamma\left(1+\frac{1}{b}\right)}$	$A\bar{V}[\ln(N_{ow}+1)]^{1/b}$
Molines et al. (2019)	CLASH NN	$\mathbf{480\, Q^{*0.8}}$	$0.63 + 1.25\, \exp(-3\, 10^5 Q^*)$	$1.4 - 0.4\frac{1}{b}$	$A\bar{V}[\ln(N_{ow}+1)]^{1/b}$

Notes:

[*,1] K_2 and K_3 are empirical coefficients function of α. Here, for cot(α)=1.5, K_2 = 8.84· 10^{-5} and K_3 = 19.9

[*,2] for $\frac{H_{m0}}{H_{\frac{1}{10}}} > 0.848\ and\ \frac{H_{m0}}{h_s} > 0.2$; elsewise C_1=1.

[*,3] for $\frac{H_{m0}}{H_{\frac{1}{10}}} > 0.848\ and\ \frac{H_{m0}}{h_s} > 0.2$; elsewise b=0.75.

Table 2. Summary of the methods in the literature to estimate V_{max} for mound breakwaters or slopes structures.

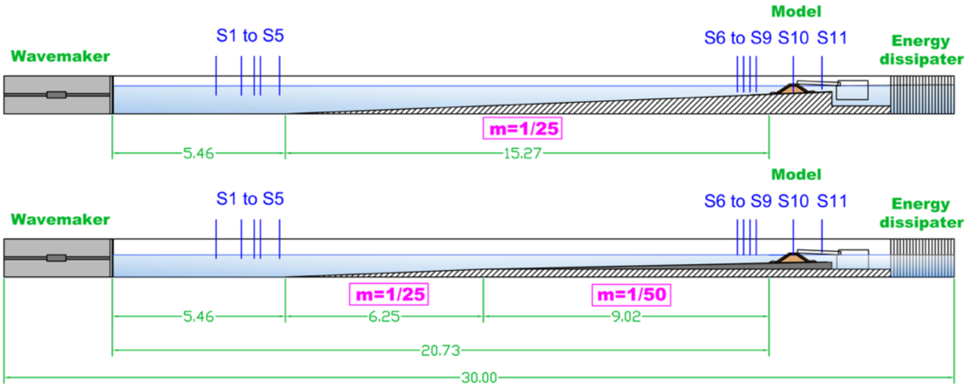

Figure 1. Longitudinal cross-section of the LPC-UPV wave flume (dimensions in meters).

In order to measure the water surface elevation, 11 capacitive wave gauges were placed along the flume. Wave gauges S1 to S5 were located in the wave generation zone, and these were used to separate incident and reflected waves in the wave generation zone using the LASA-V method (see *Figueres and Medina, 2004*). Wave gauges S6 to S9 were placed close to the model, where depth-limited wave breaking occurs and existing methods to separate incident and reflected waves are not reliable. The distances from the structure toe to S6, S7, S8 and S9 were modified with the water depth at the toe of the structure, h_s. S6, S7, S8 and S9 were located at distances $5h_s$, $4h_s$, $3h_s$ and $2h_s$ from the toe of the breakwater, respectively, following the recommendations given by *Herrera and Medina (2015)*. Wave gauge S10 was placed in the middle of the structure crest, and S11 was located behind the model.

Random wave runs of 1,000 waves were generated following a JONSWAP spectrum (γ=3.3). The AWACS wave absorption system was activated to avoid multireflections. Neither low-frequency oscillations nor piling-up (wave gauge S11) were significant during the tests. Piling-up consists of an increase of the water depth around the model caused by the accumulation of water when high overtopping rates occur. The LPC-UPV wave flume allows the water to be recirculated through a double floor of 25 cm to prevent it.

Test series were associated to the water depth at the toe of the model (h_s). For each h_s, T_p and $H_{m0} = 4(m_0)^{0.5}$ at the wave generation zone were calculated so as to keep the wave steepness approximately constant throughout each test series (s_{0p} = 0.018 and 0.049). For each s_{0p}, H_{m0} at the wave generation zone ($H_{m0,g}$) was increased in steps of 1 cm from no damage to failure of the armor layer or wave breaking at the wave generation zone. The water depths at the toe of the structure were h_s = 20 and 25 cm for the tests carried out with a bottom slope m = 1/25. The water depths were h_s = 20 and 25 cm for the single-layer Cubipod® and double-layer rock armored models with a bottom slope $m = 1/50$. The water depths were $h_s = 25$ and 30 cm for the double-layer cube armored model with a bottom slope $m = 1/50$.

Due to the importance of crest freeboard on overtopping, two corrections were made: (1) the natural evaporation and facility leakages during the tests and (2) the extracted accumulated overtopping volumes during the working day (overtopping volumes in the collection tank were pumped out of the flume). These lead to a small increase in the crest freeboard along time of the order of 10 mm for a long working day.

The tested breakwater model corresponds to a mound breakwater with $\cot\alpha = 1.5$ slope and toe berms (see Figure 2). Three armor layers were tested: a single-layer Cubipod® armor, a double-layer rock armor and a double-layer randomly-placed cube armor. The nominal diameters or equivalent cube sizes were: $Dn = 3.79$ cm (Cubipod®-1L), $Dn = 3.18$ cm (rock-2L) and $Dn = 3.97$ cm (cube-2L). Tests with the bottom slope $m = 1/50$ were conducted with a medium size rock toe berm ($D_{n,50} = 2.6$ cm), while tests with the bottom slope $m = 1/25$ were carried out with a larger rock toe berm ($D_{n,50} = 3.9$ cm) to guarantee the toe berm stability. The range of the variables in the test is shown in Table 3. Note that wave conditions in the model zone are estimated using the SwanOne model (see Verhagen et al., 2008), as explained in section 3.2.

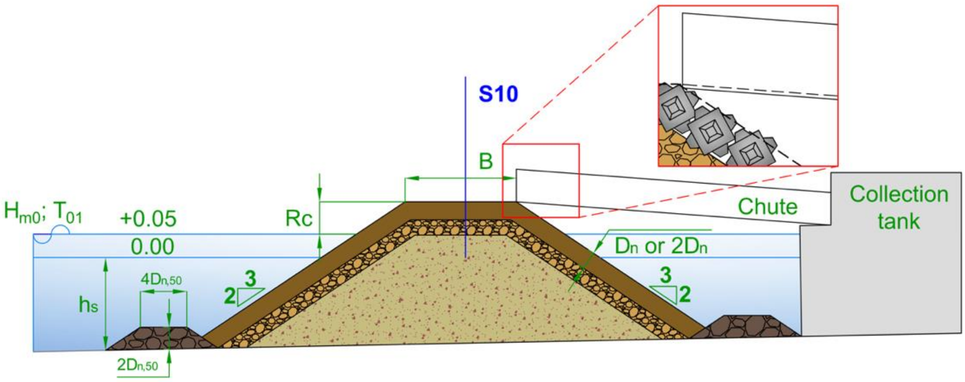

Figure 2. Cross-section of the breakwater model tested in LPC-UPV wave flume (dimensions in meters).

Overtopping discharges were measured using a weighing system placed in a collection tank behind the model during each test. Overtopping was collected using a chute in the rear side line of the crest. The inner border of the base of the chute was aligned with the armor layer to prevent too much wave overtopping losses. Individual wave overtopping volumes were identified following the method developed by *Molines et al. (2019)*, based on a continuous record of accumulated overtopping volume. This method uses the derivative of the overtopping record to identify the overtopping volumes. Figure 3 shows a photo of the experimental set up with the Cubipod®-1L armored breakwater model.

m	**Armor**	**#tests**	B **[m]**	h_s **[m]**	R_c **[m]**	$H_{m0,g}$ **[m]**	H_{m0} **[m]**	T_{01} **[s]**
1/50	CC-1L	47	0.24	0.20	0.12	0.06 – 0.21	0.06 – 0.15	0.83 – 1.97
				0.25	0.07	0.06 – 0.21	0.06 – 0.16	0.87 – 2.02
	CB-2L	45	0.27	0.25	0.11	0.06 – 0.19	0.05 – 0.16	0.86 – 2.03
				0.30	0.06	0.06 – 0.20	0.06 – 0.18	0.83 – 1.88
	CE-2L	13	0.26	0.20	0.15	0.06 – 0.13	0.06 – 0.12	0.81 – 1.66
				0.25	0.10	0.06 – 0.13	0.06 – 0.13	0.82 – 1.71
1/25	CC-1L	46	0.24	0.20	0.12	0.07 – 0.21	0.06 – 0.15	0.84 – 1.65
				0.25	0.07	0.07 – 0.21	0.06 – 0.18	0.82 – 2.11
	CB-2L	47	0.27	0.20	0.11	0.06 – 0.20	0.05 – 0.16	0.87 – 1.69
				0.25	0.06	0.06 – 0.21	0.06 – 0.17	0.87 – 2.12
	CE-2L	21	0.26	0.20	0.15	0.06 – 0.16	0.05 – 0.14	0.84 – 1.86
				0.25	0.10	0.06 – 0.13	0.05 – 0.14	0.80 – 1.88

Table 3. Dimensions and wave conditions at the toe of the structure in 2D physical tests at the LPC-UPV wave flume: CC-1L, CB-2L and CE-2L correspond to Cubipod® - 1L, cube-2L and rock-2L armors.

Figure 3. Experimental set up with the Cubipod$^{®}$-1L armored breakwater model.

3.2. Wave analysis

Incident and reflected waves were separated in the wave generation zone using wave gauges S1 to S5 applying the LASA-V method (see *Figueres and Medina, 2004*). Although the LASA-V method is applicable to nonstationary and nonlinear irregular waves, it is not valid for breaking waves.

In order to estimate the incident wave conditions in the model zone, where wave breaking takes place, SwanOne software was used. This model assumes a Composite Weibull distribution to describe the wave height distribution in shallow foreshores, as suggested by *Battjes and Groenendijk (2000).* Following the methodology proposed by *Herrera and Medina (2015)*, the incident wave height in the depth-induced wave breaking zone was estimated with the SwanOne model using the incident waves at the wave generation zone. SwanOne model fits a JONSWAP spectrum (γ=3.3) based on the given incident wave conditions in the wave generation zone and propagates such fitted wave conditions along a given bathymetry. *Herrera and Medina (2015)* validated this method comparing the numerical SwanOne simulations with the measurements in the wave flume conducted without any structure. The results of the validation in this study are given in Figure 4 for both the wave generation zone (Figure 4 (a) and (c)) and the model zone (Figure 4 (b) and (d)).

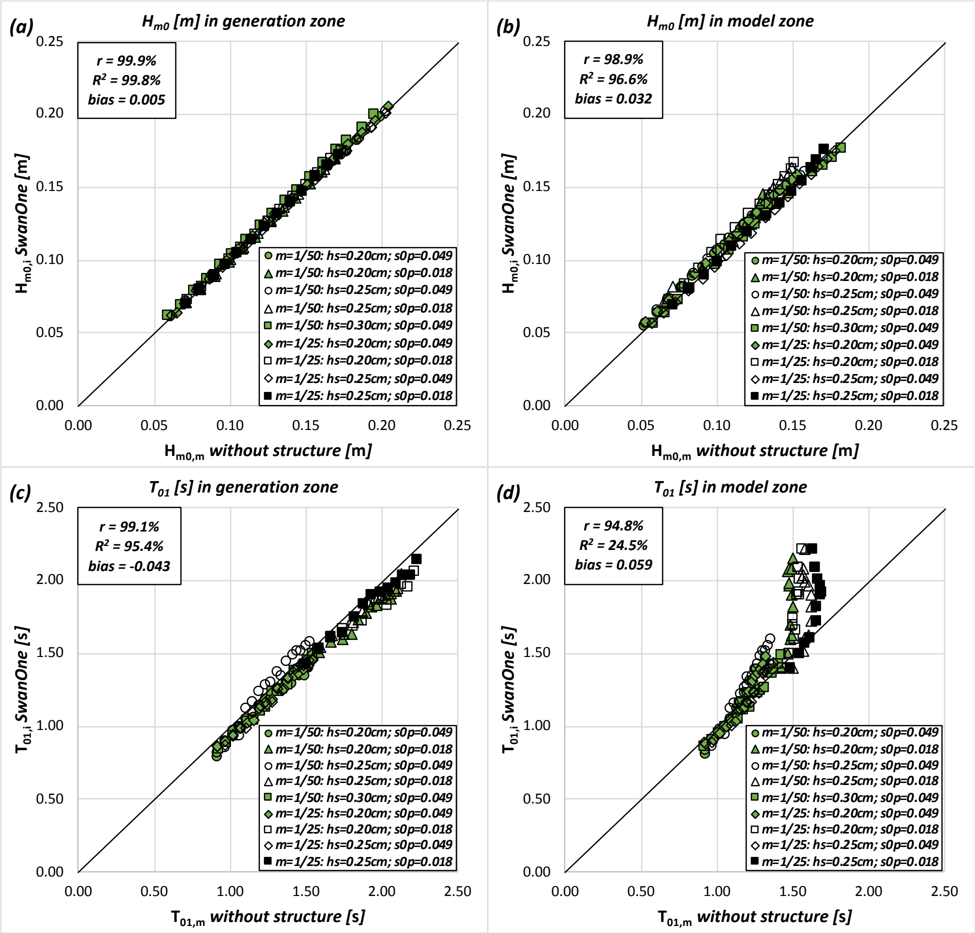

Figure 4. Comparison between: (a) the incident wave height obtained with the SwanOne and the measured significant wave height without a structure in generation zone, (b) the incident wave height obtained with the SwanOne and the measured significant wave height without a structure in model zone, (c) the incident mean period obtained with the SwanOne and the measured mean period without a structure in generation zone and (d) the incident mean period obtained with the SwanOne and the measured mean period without a structure in model zone.

To quantify the goodness of fit in this study, the correlation coefficient (*r*), the coefficient of determination (R^2) and the relative bias (*bias*) were calculated. $0 \leq r \leq 1$ assesses the correlation, $0 \leq R^2 \leq 1$ estimates the proportion of the variance explained by the model and $-1 \leq bias \leq 1$ provides a dimensionless measure of the bias. Thus, the higher the *r*, the higher the R^2 and the closer the *bias* to 0, the better.

$$r = \frac{\sum_{i=1}^{N_o}(o_i - \bar{o})(e_i - \bar{e})}{\sqrt{\sum_{i=1}^{N_o}(o_i - \bar{o})^2 \sum_{i=1}^{N_o}(e_i - \bar{e})^2}} \tag{24}$$

$$R^2 = 1 - \frac{\frac{1}{N_o}\sum_{i=1}^{N_o}(o_i - e_i)^2}{\frac{1}{N_o}\sum_{i=1}^{N_o}(o_i - \bar{o})^2} \tag{25}$$

$$bias = \frac{1}{N_o}\sum_{i=1}^{N_o}\frac{(e_i - o_i)}{|o_i|} \tag{26}$$

where N_o is the number of observations, o_i and e_i are the observed and estimated values, and $\bar{o}$ is the average observed value. Figure 4 shows that the agreement is very good for the fitted conditions in the wave generation zone ($R^2 > 95.4\%$). On the other hand, in the model zone good agreement is obtained for H_{m0} ($R^2 = 96.6\%$) whereas poor results are observed for T_{01} ($R^2 = 24.5\%$). Note that decreasing values of $bias$ were observed for H_{m0} in the model zone for increasing values of h_s: $bias = 0.057$ for $h_s = 0.20$cm, $bias = 0.021$ for $h_s = 0.25$cm and $bias = -0.018$ for $h_s = 0.30$cm. SwanOne clearly overestimates T_{01} measured at the model area.

During the design phase of a mound breakwater, the design wave conditions (H_{m0} and T_{01}) in the location where the structure will be built need to be estimated. Thus, in this study, both H_{m0} and T_{01} estimated by SwanOne were used.

4. Estimations of N_{ow} and V_{max} with methods given in the literature

In this section, the performance of the formulas to estimate N_{ow} and V_{max} presented in Section 2 is analyzed using the experimental data described in Section 3. As mentioned in Section 2.2, the formulas given in the literature for estimating N_{ow} and V_{max} require knowing the mean individual wave overtopping volume, $\bar{V} = q\, T_{01}\, N_w / N_{ow}$. Therefore, q needs to be estimated using formulas in the literature when direct observations are not available. As shown in Table 2, estimators for q are suggested by the different authors of the methods to estimate N_{ow} and V_{max} on mound breakwaters. The goodness of fit of such estimators of q was assessed using the experimental data presented in Section 3. Figure 5 compares the observed and predicted Q^* using the estimators in Table 2.

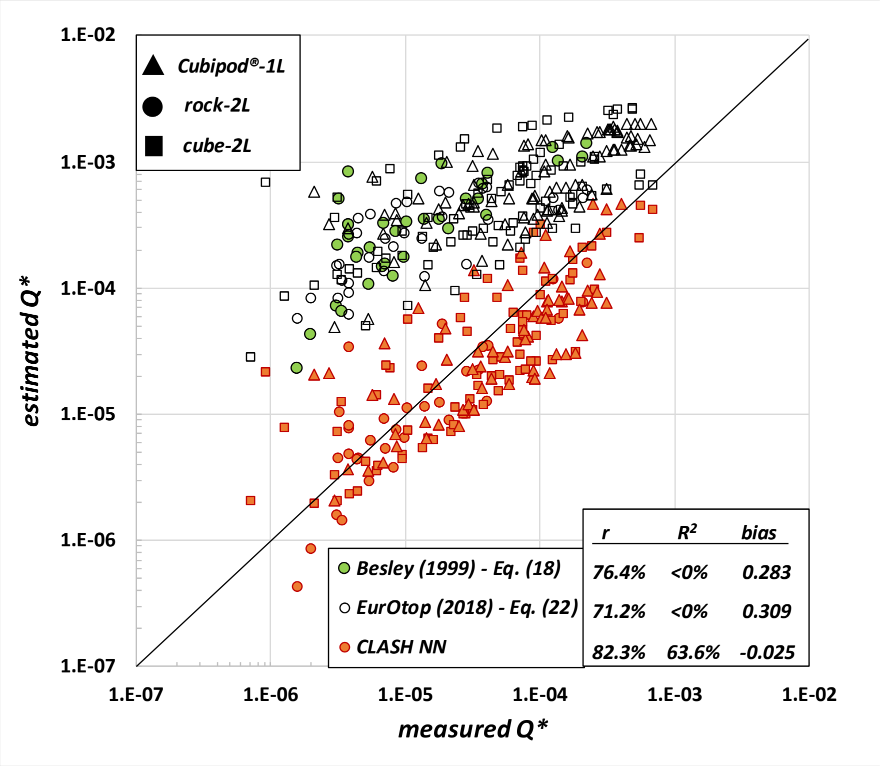

Figure 5. Comparison between measured and estimated $Q^{*}= q/(g\ H_{m0}\ T_{01})$.

The q estimator recommended by *Besley (1999)* - Eq. (18) was applied using γ_f = 0.50 for rock-2L. Since this author did not propose γ_f for Cubipod®-1L and cube-2L, it was not applied on those data. The q estimator proposed by *EurOtop (2018)* - Eq. (22) was used with γ_f = 0.49, 0.40 and 0.47 for Cubipod®-1L, rock-2L and cube-2L, respectively. CLASH NN was applied with γ_f recommemded by *Molines and Medina (2015b)*: γ_f = 0.48, 0.49 and 0.53 for Cubipod®-1L, rock-2L and cube-2L, respectively. q was estimated for 189 physical tests within the range of application of CLASH NN.

Note that the quantitative goodness-of-fit metrics in Figure 5 are given for $ln(Q^{*})$. As shown in Figure 5, poor results (R^2 < 0%) were obtained with the formulas given by *Besley (1999)* - Eq. (18) and *EurOtop (2018)* - Eq. (22). On the other hand, the predictor CLASH NN for Q^{*} suggested by *Molines et al. (2019)* and *Nørgaard et al. (2014)* provided good results with R^2 = 63.6%.

4.1. Estimating N$_{ow}$ *with existing methods*

In this section, the performance of the formulas to estimate N_{ow} presented in Section 2.2 is assessed. Figure 6 compares the observed N_{ow} with different estimators valid for mound breakwaters.

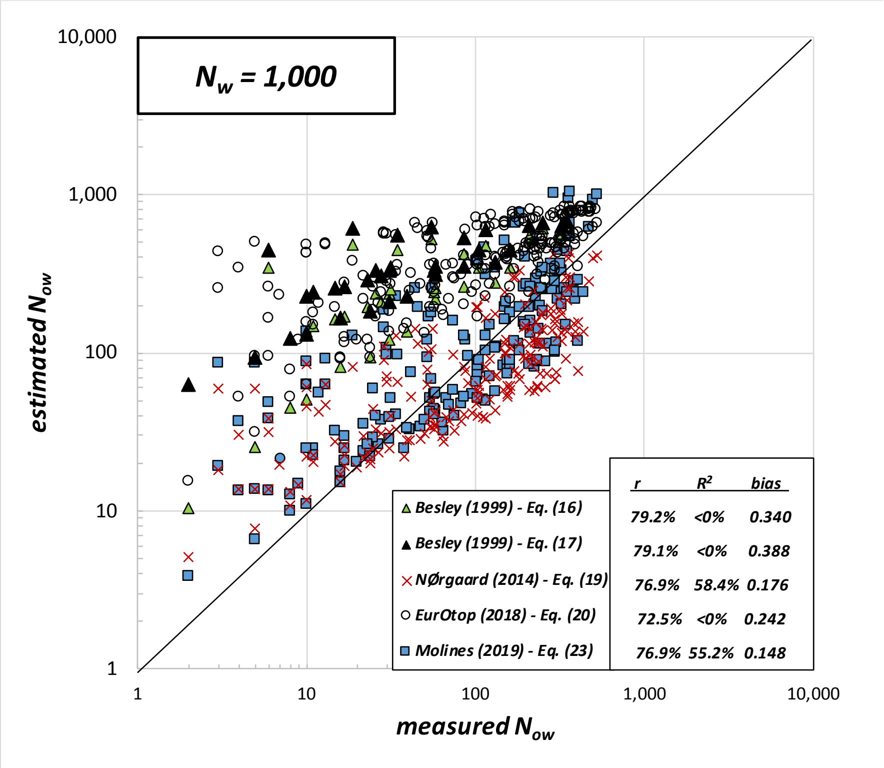

Figure 6. Comparison between measured and estimated N_{ow} with methods given in the literature.

All formulas were applied no matter the application range. Note that estimated q suggested by the authors of these formulas was used in the N_{ow} predictors given by *Besley (1999)* - Eq. (17), *Nørgaard et al. (2014)* - Eq. (19) and *Molines et al. (2019)* - Eq. (23). The N_{ow} estimator presented in Eq. (16) by *Besley (1999)* was applied using the roughness factor γ_f = 0.50 for rock-2L. Since this author did not recommended γ_f for Cubipod®-1L and cube-2L, it was not applied on those data. *K1* = 50.8 was used with Eq. (16) for *cot α* = 1.5, obtained from the interpolation of the values given for *cot α* = 2 and *cotα* = 1. Eq. (20) was applied using γ_f given by *EurOtop (2018)*: γ_f = 0.49, 0.40 and 0.47 for Cubipod®-1L, rock-2L and cube-2L, respectively.

The quantitative goodness-of-fit metrics are given for *ln*(N_{ow}). Eqs. (19) and (23) proposed by *Nørgaard et al. (2014)* and *Molines et al. (2019)*, respectively, provided the best agreement with experimental data (55.2% < R^2 < 58.4%). *Besley (1999)* - Eqs. (16) and (17) and *EurOtop (2018)* – Eq. (20) overpredicted the values of N_{ow} and provided poor results (R^2 < 0%). Note that all the compared methods from the literature overpredicted the values of N_{ow} < 100. Figure 6 shows that that none of the existing N_{ow} estimators properly describe N_{ow} for the range of variables analyzed in this study. For this reason, a new N_{ow} estimator is developed in Section 5.

4.2. Estimating $\mathrm{V}_{\mathrm{max}}$ *with existing methods*

In Section 2, several formulas to estimate the shape factor *b* were presented. Nevertheless, most of them are not valid for mound breakwaters. For this reason, only the formulas for mound breakwaters will be considered in the following comparison with the V_{max} measured in this study.

In this analysis, N_{ow} and *q* are estimated with the methods proposed by the authors (see Table 2). The estimators for N_{ow} and *q* have been previously assessed in this Section. The scale factor, *A*, was calculated using Eq. (3) for *Nørgaard et al. (2014)* and *EurOtop (2018)*, while Eq. (8) was applied for *Molines et al. (2019)*. V_{max} was estimated by Eq. (15).

Figure 7 compares the measured and the estimated dimensional V_{max} (l/m) and the dimensionless $V_{max}{}^{*}=V_{max}/(gH_{m0}T_{01}{}^{2})$ using the methods valid for mound breakwaters.

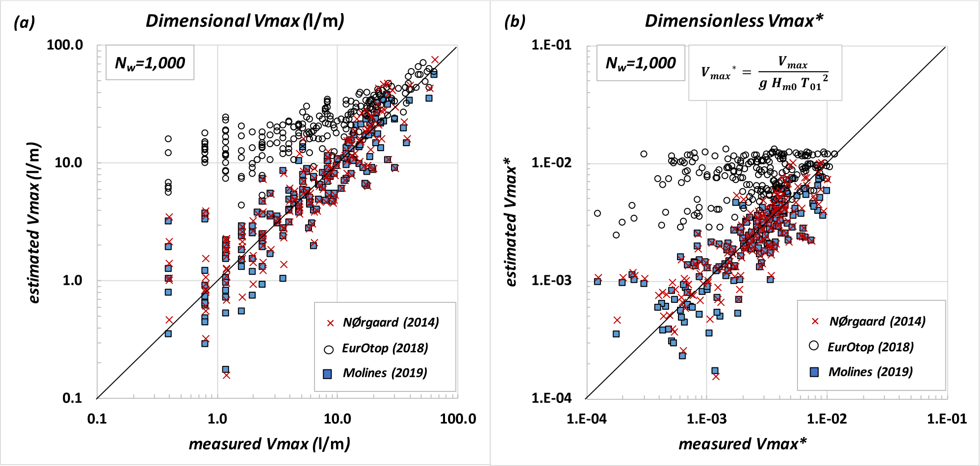

Figure 7. Comparison between measured and estimated (a) V_{max} (l/m) and (b) dimensionless $V_{max}{}^{*}$.

V_{max}^* measured in this study agreed well with estimations given by *Nørgaard et al. (2014)* and *Molines et al. (2019)* with higher scatter for $V_{max} < 5$ l/m and $V_{max}^* < 2 \cdot 10^{-3}$. Note that *Molines et al. (2019)* was developed for mound breakwaters with crown wall in non-breaking wave conditions. Thus, depth-limited breaking may not have a significant effect on V_{max}^*. Table 4 presents the quantitative measurements of the goodness of fit as well as the number of variables and parameters of the methods shown in Figure 7. The quantitative goodness-of-fit metrics in Table 4 are given for $ln(V_{max})$ and $ln(V_{max}^*)$.

Author		**V_{max} (l/m)**	**V_{max}^* (-)**	**# parameters**	**# variables**
Nørgaard et al. (2014)	*r*	88.8%	79.0%	13	3
	R^2	78.4%	61.8%		
	bias	0.148	-0.002		
EurOtop (2018)	*r*	83.0%	38.2%	12	4
	R^2	< 0%	< 0%		
	bias	2.222	0.173		
Molines et al. (2019)	*r*	89.1%	79.8%	7	1
	R^2	78.8%	63.0%		
	bias	-0.023	-0.017		

Table 4. Goodness-of-fit metrics for the methods in the literature to estimate V_{max}.

5. Estimating of the number of overtopping events, N_{ow}

5.1. A new formula to estimate N_{ow}

As shown in Section 2, most of the existing estimators of $P_{ow} = N_{ow}/N_w$ are a function of a power of Q^*, as Eqs. (17), (19) and (23). Methods by *Nørgaard et al. (2014)* - Eq. (19) and *Molines et al. (2019)* - Eq. (23) provide good results within their range of application, but they do not properly estimate P_{ow} for very low or very large Q^*. When Q^* is very small, P_{ow} should tend to 0, and when Q^* is very large, P_{ow} should tend to 1. Therefore, an exponential model may be better than a power law of P_{ow}, because it is good for very low and very high values of Q^*.

In this study, a clear correlation was found between P_{ow} and Q^*, as previously observed by *Besley (1999)*, *Nørgaard et al. (2014)* and *Molines et al. (2019)*. Therefore, an exponential function of Q^* was proposed and G_1 and G_2 in $P_{ow} = exp\ (-G_1/\ Q^{*G2})$ were calibrated based on the 219 tests maximizing R^2 of lnN_{ow}. The three armor layers tested in this study are not distinguished in the analysis (*Bruce et al., 2009*).

As exposed in Section 1, in depth-limited breaking wave conditions, the optimum point where wave characteristics are estimated is relevant for design and needs to be determined (*Mares-Nasarre et al., 2020*). Thus, G_1 and G_2 were calibrated considering wave characteristics at several distances from the structure toe in $Q^*= q/(g\ H_{m0}\ T_{01})$. H_{m0} and T_{01} were estimated with SwanOne at distances x=0, h_s, 2h_s, 3h_s, 4h_s, 5h_s and 6h_s from the model toe. No significant differences were observed; G_1=-0.1 and G_2=0.3 were obtained for H_{m0} and T_{01} estimated between the model toe and at 6h_s from the model toe. In this study, wave characteristics estimated at a distance of 3h_s from the model toe are used, following *Herrera et al. (2017)* and *Mares-Nasarre et al. (2020)* recommendations. Note that this distance is approximately the same as x=5H_{m0}, suggested by *Melby (1999)* and *Goda (1985)* to determine wave characteristics in breaking wave conditions. Figure 8 compares the experimental data and Eq. (27) with R^2 = 91.9%, as well as the 90% error band.

$$P_{ow} = \frac{N_{ow}}{N_w} = exp\left(\frac{-0.1}{Q^{*0.3}}\right) \tag{27}$$

where P_{ow}=N_{ow}/N_w is the proportion of overtopping waves and Q^* is the dimensionless wave overtopping discharge, $Q^*= q/(gH_{m0}T_{01})$.

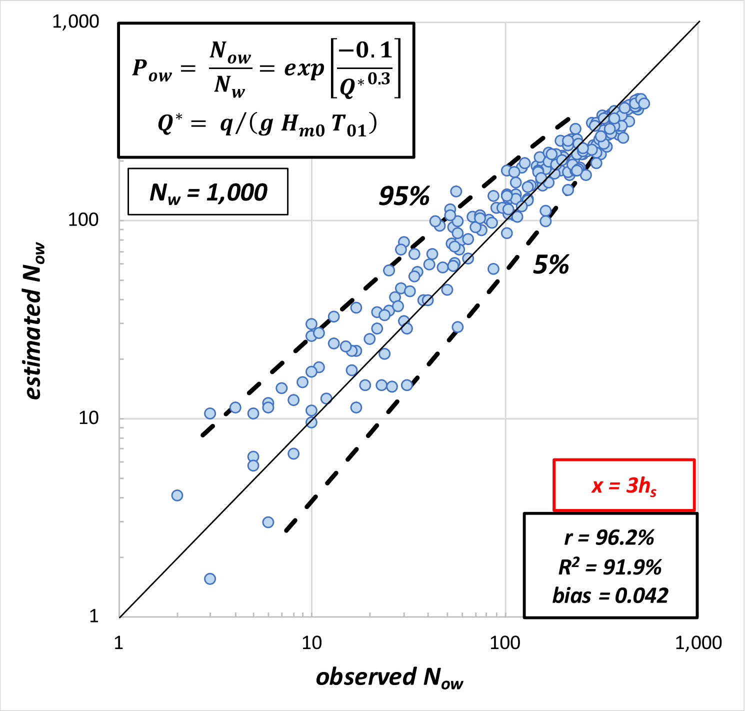

Figure 8. Comparison between observed number of overtopping events, N_{ow}, and estimated N_{ow} given by Eq. (27) using wave characteristics estimated at a distance of 3h_s from the model.

In this study, the methodology given in *Herrera and Medina (2015)* and applied in works such as *Mares-Nasarre et al. (2019)* is used to estimate the 90% error band. Thus, a Gaussian distribution of the error (ε) is assumed, with 0 mean and the variance given by

$$\sigma^2(\varepsilon) = 0.55 - 0.09\ lnN_{ow} \tag{28}$$

The 95% and 5% percentiles for the N_{ow} predicted by Eq. (27) can be calculated using Eq. (29).

$$lnN_{ow}|_{5\%}^{95\%} = lnN_{ow}\ \pm 1.64\sqrt{0.55 - 0.09\ lnN_{ow}} \tag{29}$$

The range of application of Eq. (26) is $0.002 \leq P_{ow} \leq 0.53$ and $7.2 \cdot 10^{-7} \leq Q^* \leq 6.9 \cdot 10^{-4}$. Eq. (26) properly extrapolates the prediction of P_{ow}=0 when Q^*=0 and P_{ow}=1 when $Q^* \rightarrow \infty$.

5.2. Influence of bottom slope on N_{ow}

In Section 3, the experimental setup using two bottom slope configurations with m = 1/50 and m = 1/25 was described. No significant difference between bottom slopes m = 1/50 and m = 1/25 was observed in the scatter plot. A statistical analysis was performed to determine if N_{ow} are equally distributed for different bottom slopes. Since the data were not Gaussian distributed, a nonparametric Mann-Whitney test (*Mann and Whitney, 1947*) was applied. In this test, the null hypothesis (H_0) corresponded to N_{ow} not being affected by the bottom slope. Based on 103 tests with a bottom slope m = 1/50 and 116 tests with a bottom slope m = 1/25, H_0 was not rejected using a significance level α = 0.10. Thus, in this study the bottom slope does not show any significant influence on N_{ow}.

6. Estimating of the maximum individual wave overtopping volume, V_{max}

6.1. A new method to estimate V_{max} using the 2-parameter Weibull distribution

The maximum individual wave overtopping volume, V_{max}, is estimated using Eq. (15). Then, V_{max} depends on the number of overtopping events, N_{ow}, shape and scale factors of the Weibull distribution, A and b, and $\bar{V} = V_{total}/N_{ow}$. As previously mentioned, both A and b obtained for each test are fitted using a quadratic utility function applied to the whole individual wave overtopping volume dataset. Tests with very low values of N_{ow} ($N_{ow} < 5$) were not used in this analysis to prevent inconsistencies caused by a very low number of observations. Eqs. (30) and (31) were proposed to characterize A and b

$$b = K_{B1} + \exp(K_{B2}\, Q^*) \tag{30}$$

$$A = 1.45 - 0.4/b \tag{31}$$

Similar to Section 5.1, K_{B1} and K_{B2} were calibrated considering wave characteristics at several distances from the structure toe in $Q^* = q/(g\ H_{m0}\ T_{01})$. H_{m0} and T_{01} were determined with SwanOne at distances x = 0, h_s, $2h_s$, $3h_s$, $4h_s$, $5h_s$ and $6h_s$ from the structure toe. The goodness-of-fit of $V_{max}^* = V_{max}/(g\ H_{m0}\ T_{01}^2)$ was assessed for every couple of coefficients calculated using Eqs. (15), (30) and (31) with the measured N_{ow} and $\bar{V}$. Best fit was obtained between $x = 2h_s$ and $x = 6h_s$, $K_{B1} = 0.8$ and K_{B2} = = $-2\cdot10^5$ were obtained with r = 92% and R^2 = 83%. Wave characteristics were decided to be estimated at $x = 3h_s$.

Figure 9a illustrates the relationship between Q^* and b and the least-squares fitting given by Eq. (30). Figure 9b relates A and $1/b$ and the least-squares fitting given by Eq. (31). The range of application of Eqs. (30) and (31) is $0.005 \leq P_{ow} \leq 0.53$ and $1.3\cdot10^{-6} \leq Q^* \leq 6.9\cdot10^{-4}$.

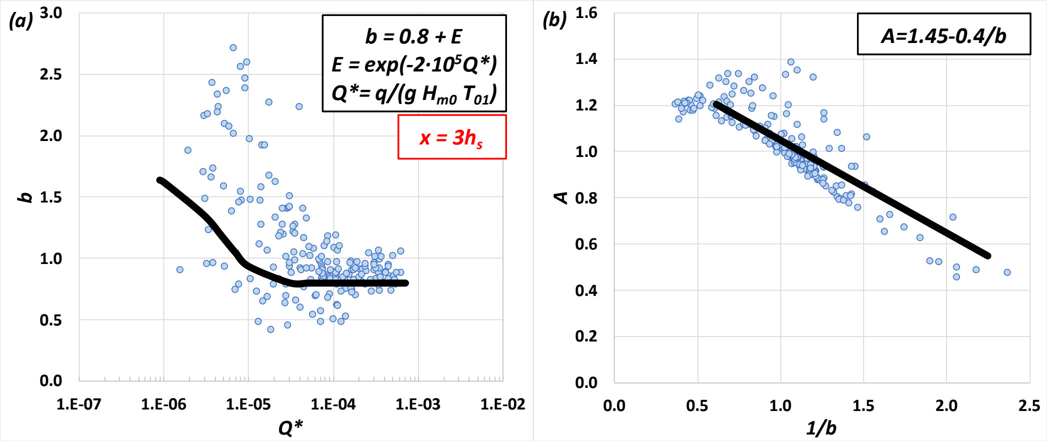

Figure 9. Relationship between explanatory variables and the least-squares fitting of Weibull distribution factors: (a) Weibull's shape factor, *b*, in Eq. (30) and (b) Weibull's scale factor, *A*, in Eq. (31).

Figure 10 illustrates the performance of Eq. (15) to estimate $V_{max}^*=V_{max}/(gH_{m0}T_{01}^2)$ when using A and b obtained from Eqs. (30) and (31) and measured N_{ow} and $\bar{V}$. The agreement was good; R^2 = 83.3%.

The variance of the error (e) of lnV_{max}^* is $s^2(\varepsilon) = 0.15$. Thus, the 95% and 5% percentiles for the predicted V_{max}^* by Eq. (15) are given by

$$lnV_{max}^*|_{5\%}^{95\%} = lnV_{max}^* \pm 0.63 \qquad (32)$$

Figure 11 shows an example of the fit of the 2-parameter Weibull distribution to the measured individual wave overtopping volumes for a randomly-selected test (#22). Figure 11 is presented in a Weibull plot:

$$\ln\big(-\ln\big(1-F(V)\big)\big) = b(\ln(V/\bar{V}) - \ln(A)) \qquad (33)$$

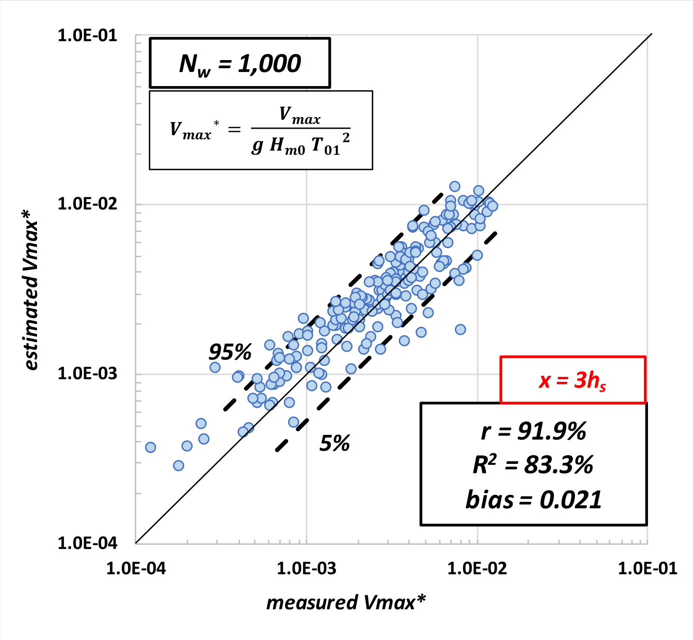

Figure 10. Comparison between the measured and estimated dimensionless $V_{max}{}^*$ by the 2-parameter Weibull distribution with shape and scale factors given by Eqs. (30) and (31).

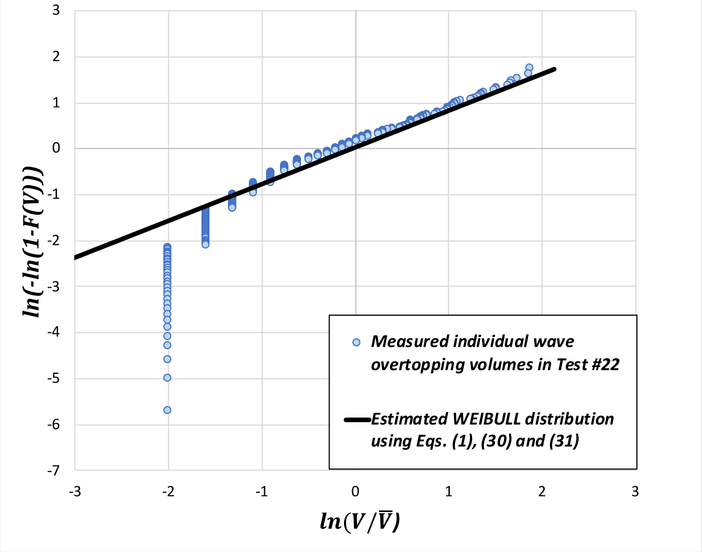

Figure 11. Comparison of measured and estimated individual wave overtopping volumes for Test #22 using Eqs. (1), (30) and (31).

As explained in Section 2, *Molines et al. (2019)* proposed a 2-parameter Exponential distribution given by Eq. (9) to describe $F(V)$. In this study, the 2-parameter Exponential distribution was also fitted with good results.

6.2. Influence of bottom slope on the 2-parameter Weibull distribution

As presented in section 5.2, the influence of bottom slope on b and A estimated by Eqs. (30) and (31) is studied here. No relevant differences between the bottom slopes m = 1/50 and m = 1/25 were found. The Mann-Whitney test was applied for each parameter, as described in section 5.2. The null hypothesis (H_0) corresponded to b and A not being influenced by the bottom slope. Based on 97 tests with a bottom slope m = 1/50 and 106 tests with a bottom slope m = 1/25, H_0 was not rejected using a significance level α = 0.10. Thus, in this case bottom slope does not show any significantly influence on V_{max}.

7. Estimation of V_{max} for mound breakwater designs

During the design phase of a mound breakwater, the design wave conditions (H_{m0} and T_{01}) and the structural geometry are given. The formulas given in the literature require knowing the mean individual wave overtopping volume, $\bar{V}=qT_{01}N_w/N_{ow}$, and the number of overtopping events, N_{ow}. Therefore, q and N_{ow} need to be estimated using formulas in the literature when direct observations (e.g. sections 5 and 6) are not available. Methods suggested in the literature to estimate q were assessed in Section 4. The best fit was given by CLASH NN with R^2 = 63.6%. Thus, Q^* estimated with CLASH NN was used in the following. When using Eq. (27) developed in this study to calculate N_{ow} estimating q with CLASH NN, r = 77.1%, R^2 = 58.4% and *bias* = 0.026. The agreement was worse than R^2 = 91.9% (see Figure 8) obtained when q is measured and not estimated. Note that the fitting of the new formula is equal to the one obtained with the method proposed by *Nørgaard et al. (2014)* (see Figure 6). However, the method proposed by *Nørgaard et al. (2014)* to estimate N_{ow} requires 3 variables and 10 parameters, while the method developed in this study uses 1 variable and 2 parameters.

Figure 12 illustrates the goodness of fit of Eq. (15) to estimate V_{max} based on the estimations of N_{ow} and $\bar{V}$ when q is estimated using CLASH NN. Eqs. (30) and (31) were applied to estimate the Weibull parameters (A, b). R^2 = 61.7% was obtained for $V_{max}^* = V_{max}/(gH_{m0}T_{01}^2)$. Figure 12 also presents the estimations given by *Nørgaard et al. (2014)* and *Molines et al. (2019)* as well as the 90% error band.

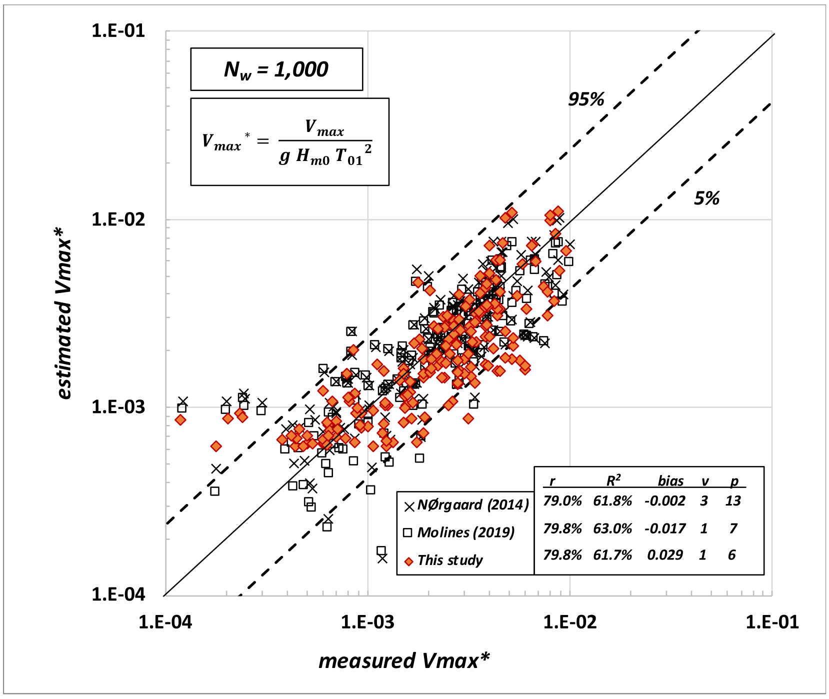

Figure 12. Comparison of measured dimensionless maximum individual wave overtopping volume, V_{max}^{*}, and the estimated V_{max}* for the Weibull distribution model using Eqs. (15), (30) and (31) and the methods for mound breakwaters in the literature.

As shown in Figure 12, the goodness of fit of the three compared methods is similar. However, the method proposed in the present study (1 variable (v) and 6 parameters (p)) is much simpler than the method proposed by *Nørgaard et al. (2014)* (v = 3 and p = 13) and simpler than the method proposed by *Molines et al. (2019)* (v = 1 and p = 7). Using the method proposed in this study, the ratio between estimated and measured V_{max}^{*} for design purposes falls within a factor of 2.0 (90% error band).

8. Conclusions

Crest elevation of mound breakwaters is usually designed to limit the mean wave overtopping rate (q) or the maximum individual wave overtopping volume (V_{max}). Furthermore, rising sea levels caused by climate change and mounting social pressure to minimize the visual impact of coastal structures mean lower crest freeboards and increased overtopping hazards. Thus, coastal structure designs with relevant overtopping rates attacked by waves breaking on the sea bottom become relevant. Few studies have been conducted in depth-limited breaking wave conditions. This research is focused on mound breakwaters with significant overtopping rates ($0.002 \leq P_{ow} \leq 0.53$ and $7.2 \cdot 10^{-7}$

$\leq Q^*=q/(gH_{m0}T_{01}) \leq 6.9 \cdot 10^{-4}$) and intermediate crest elevations ($0.33 \leq R_c/H_{m0} \leq 2.83$) with armor slope $cot\alpha=1.5$ in depth-limited breaking wave conditions ($0.2 \leq H_{m0}/h_s \leq 0.9$), considering two bottom slopes (m = 1/50 and m = 1/25).

In this study, 105 physical tests with a bottom slope m = 1/50 and 114 tests with m = 1/25 were conducted at the LPC-UPV wave flume. Individual wave overtopping volumes were analyzed using *Molines et al. (2019)* methodology, based on a continuous record of accumulated overtopping volume. In order to estimate the incident wave conditions in the model zone, where breaking occurs, SwanOne model was used. The performance of SwanOne when estimating wave characteristics under depth-limited breaking wave conditions was assessed using tests without structure. The agreement was good for H_{m0} (R^2=96.6%), but some bias was observed for the shallowest water depth (*bias* = 0.057). The agreement was poor for T_{01} (R^2=23.3%); SwanOne overestimated the measured T_{01} in the model zone.

Estimators for P_{ow} given in the literature were assessed using the experimental data; it was observed that most existing formulas overpredict P_{ow} for P_{ow} < 10%. Most of the existing P_{ow} estimators are a function of a power of Q^*, so they cannot fit the boundary limits ($P_{ow}\rightarrow 0$ when $Q^*\rightarrow 0$ and $P_{ow}\rightarrow 1$ when $Q^*\rightarrow\infty$). Hence, a new exponential estimator is given for P_{ow} valid for depth-limited breaking wave conditions in Eq. (27) (R^2 = 91.9%).

The quadratic utility function proposed by *Molines et al. (2019)* was applied in this study to all the data to fit the 2-parameter Weibull distribution for individual wave overtopping volumes, $F(V)$. Estimators were taken from *Nørgaard et al. (2014)*, *EurOtop (2018)* and *Molines et al. (2019)* for the scale (A) and shape (b) factors of the Weibull distribution to compare with the measured data, obtaining $0\% \leq R^2 \leq 63.0\%$ for the dimensionless maximum individual wave overtopping volume, $V_{max}^*=V_{max}/(gH_{m0}T_{01}^2)$. Best results using methods given in the literature were obtained for *Molines et al. (2019)* whose method was developed for mound breakwaters with crown wall in non-breaking wave conditions. Thus, the influence of the depth-induced wave breaking or the presence of the crest wall may not be significant.

New estimators for the factors A and b of the Weibull distribution were fitted using the experimental data. The new Weibull (Eqs. (30) and (31)) distribution provide estimations of V_{max}^* with R^2 = 83.3% and a number of variables and parameters lower than those of the methods in the literature. In this study, no significant influence of bottom slope ($1/50 \leq m \leq 1/25$) was found on N_{ow} and V_{max}.

During the design phase of a mound breakwater, the mean individual wave overtopping volume ($\bar{V}=qT_{01}N_w/N_{ow}$) is required to estimate V_{max}. But q and N_{ow} are unknown, and they have to be estimated using methods in the literature when direct observations are not available. Here, CLASH Neural Network (CLASH NN) was used to estimate q with $R^2 = 63.6\%$. Using q estimated by the CLASH NN and the new N_{ow} estimator given in Eq. (27), V_{max}^* was estimated with the 2-parameter Weibull distribution proposed in this study. The prediction error of V_{max}^* dropped from $R^2 = 83.3\%$ when q and N_{ow} were measured in the laboratory to $R^2 = 61.7\%$ when q was estimated with CLASH NN. The ratio between estimated and measured V_{max}^* falls within a factor of 2.0 (90% error band) for design purposes.

The estimators and conclusions derived here are valid within the experimental ranges of this study. Therefore, it is encouraged to check their validity out of these experimental ranges, paying special attention to the significance of the depth-limited breakage of waves and the presence of a crown wall.

Acknowledgements

The authors acknowledge the financial support from the *Ministerio de Economía y Competitividad* and *Fondo Europeo de Desarrollo Regional* (FEDER) under grant RTI2018-101073-B-I00, *Universitat Politècnica de València* (Grant SP20180111), *Primeros Proyectos de Investigación* (PAID-06-18), *Vicerrectorado de Investigación, Innovación y Transferencia de la Universitat Politècnica de València* and *Generalitat Valenciana* (Grant AEST/2019/004). The first author was also financially supported through the FPU program (*Formación de Profesorado Universitario*) funded by *Ministerio de Educación, Cultura y Deporte* under grant FPU16/05081. The authors thank Debra Westall for revising the manuscript.

References

Battjes, J.A., Groenendijk, H.W., 2000. Wave height distributions on shallow foreshores, *Coastal Engineering* 40, 161-182. https://doi.org/10.1016/S0378-3839(00)00007-7

Besley, P., 1999. Overtopping of Sea-Walls-Design and Assessment Manual. R & D Technical Report, vol. 178 Environment Agency, Bristol, UK.

Bruce, T., van der Meer, J.W., Franco, L., Pearson, J.M., 2009. Overtopping performance of different armour units for rubble mound breakwaters. *Coastal Engineering* 56, 166–179. https://doi.org/10.1016/j.coastaleng.2008.03.015

EurOtop, 2007. *Wave Overtopping of Sea Defences and Related Structures: Assessment Manual (EurOtop Manual).* Environment Agency, UK/ENW Expertise Netwerk Waterkeren, NL/KFKI Kuratorium für Forschung im Küsteningenieurwesen, Germany, pp. 193; Pullen, T., Allsop, N.W.H., Bruce, T., Kortenhaus, A., Schüttrumpf, H., Van der Meer, J.W.

EurOtop, 2018. *Manual on wave overtopping of sea defences and related structures*. An overtopping manual largely based on European research, but for worldwide application. Van der Meer, J.W., Allsop, N.W.H., Bruce, T., De Rouck, J., Kortenhaus, A., Pullen, T., Schüttrumpf, H., Troch, P., Zanuttigh, B., www.overtopping-manual.com.

Figueres, M., Medina, J.R., 2004. Estimating incident and reflected waves using a fully nonlinear wave model, *Proc. 29th International Conference on Coastal Engineering*, World Scientific, 594-603. https://doi.org/10.1142/9789812701916-0047

Franco, L., de Gerloni, M., van der Meer, J.W., 1994. Wave overtopping on vertical and composite breakwaters. *Proc. 24th International Conference on Coastal Engineering*, ASCE, 1030-1044.

Gallach, D., 2018. Experimental Study of Wave Overtopping Performance of Steep Low-Crested Structures. PhD Thesis. Ghent University.

Goda, Y., 1985. *Random Seas and Design of Maritime Structures*; University of Tokyo Press: Tokyo, Japan.

Herrera, M.P., Medina, J.R., 2015. Toe berm design for very shallow waters, *Coastal Engineering* 103, 67-77. https://doi.org/10.1016/j.coastaleng.2015.06.005

Herrera, M.P.; Gómez-Martín, M.E.; Medina, J.R., 2017. Hydraulic stability of rock armors in breaking wave conditions. *Coastal Engineering* 127, 55–67. https://doi.org/10.1016/j.coastaleng.2017.06.010.

Lykke-Andersen, T., Burcharth, H.F., Gironella, F.X., 2009. Single wave overtopping volumes and their travel distance for rubble mound breakwaters. *Proc. 5th International Conference Coastal Structures 2007,* World Scientific, 1241–1252. https://doi.org/10.1142/9789814282024_0109

Makkonen, L., 2006. Plotting positions in extreme values analysis. *Journal of Applied Meteorology and climatology,* 45, 334–340. https://doi.org/10.1175/JAM2349.1

Mann, H.B., Whitney, D.R., 1947. On a test of whether one of two random variables is stochastically larger than the other. *The Annals of Mathematical Statistics* 18, 50-60 (5.3).

Mares-Nasarre, P., Gómez-Martín, M.E., Medina, J.R., 2020. Influence of Mild Bottom Slopes on the Overtopping Flow over Mound Breakwaters under Depth-Limited Breaking Wave Conditions. *Journal of Marine Science and Engineering* 8(1), 3. https://doi.org/10.3390/jmse8010003

Mares-Nasarre, P., Argente, G., Gómez-Martín, M.E., Medina, J.R., 2019. Overtopping layer thickness and overtopping flow velocity on mound breakwaters. *Coastal Engineering* 154, 103561. https://doi.org/10.1016/j.coastaleng.2019.103561

Melby, J.A., 1999. Damage Progression on Rubble Mound Breakwaters; Technical Report CHL-99-17; U.S. Army Engineer Research and Development Center:

Vicksburg, MS, USA. Also Ph.D. Thesis, University of Delaware, Newark, DE, USA.

Molines, J., Medina, J.R., 2015a. Explicit wave overtopping formula for mound breakwaters with crown walls using CLASH neural network derived-data. *Journal of Waterway, Port, Coastal and Ocean Engineering.* 142 (3), 04015024. https://doi.org/10.1061/(ASCE)WW.1943-5460.0000322.

Molines, J., Medina, J.R., 2015b. Calibration of overtopping roughness factors for concrete armor units in non-breaking conditions using the CLASH database. *Coastal Engineering* 96, 65–70. https://doi.org/10.1016/j.coastaleng.2014.11.008

Molines, J., Herrera, M.P., Gómez-Martín, M.E., Medina, J.R., 2019. Distribution of individual wave overtopping volumes on mound breakwaters, *Coastal Engineering* 149, 15-27. https://doi.org/10.1016/j.coastaleng.2019.03.006

Nørgaard, J.Q.H., Lykke-Andersen, T., Burcharth, H.F., 2014. Distribution of individual wave overtopping volumes in shallow water wave conditions. *Coastal Engineering* 83, 15–23. https://doi.org/10.1016/j.coastaleng.2013.09.003

Pan, Y., Lin, L., Amini, F., Kuang, C., Chen, Y., 2016. New understanding on the distribution of individual wave overtopping volumes over a levee under negative freeboard. *Journal of Coastal Research*, 75, 1207–1211. https://doi.org/10.2112/SI75-242.1

Smolka, E., Zarranz, G., Medina, J.R., 2009. Estudio Experimental del Rebase de un Dique en Talud de Cubípodos. *Libro de las X Jornadas Españolas de Costas y Puertos*. Universidad de Cantabria-Adif Congresos, 803–809 (in Spanish).

Van der Meer, J.W., Janssen, J.P.F.M., 1994. Wave Run-Up and Wave Overtopping at Dikes, Delft Hydraulics No. 485, 22.

Van Gent, M.R.A., Van den Boogaard, H.F.P., Pozueta, B., Medina, J.R., 2007. Neural network modelling of wave overtopping at coastal structures. *Coastal Engineering* 54 (8), 586–593. https://doi.org/10.1016/j.coastaleng.2006.12.001.

Available: https://www.deltares.nl/en/software/overtopping-neural-network/, Accessed: 26 June 2019.

Verhagen, H.J., Van Vledder, G., Eslami Arab, S., 2008. A practical method for design of coastal structures in shallow water, *Proc. 31st International Conference on Coastal Engineering*, World Scientific, 2912-2922. https://doi.org/10.1142/9789814277426_0241

Victor, L., van der Meer, J.W., Troch, P., 2012. Probability distribution of individual wave overtopping volumes for smooth impermeable steep slopes with low crest freeboards. *Coastal Engineering* 64, 87–101. https://doi.org/10.1016/j.coastaleng.2012.01.003

Zanuttigh, B., van der Meer, J.W., Bruce, T., Hughes, S., 2013. Statistical characterization of extreme overtopping wave volumes. *Proc. Coasts, Marine Structures and Breakwaters*. 2014. ICE Publishing, (London, UK), 1, 442–452. https://doi.org/10.1680/fsts.59757.0442

4. **Mares-Nasarre, P., Molines, J., Gómez-Martín, M.E., Medina, J.R., 2021. Explicit Neural Network-derived formula for overtopping flow on mound breakwaters in depth-limited breaking wave conditions. Coast. Eng. 103810. https://doi.org/10.1016/j.coastaleng.2020.103810**

Explicit Neural Network-derived formula for overtopping flow on mound breakwaters in depth-limited breaking wave conditions

Patricia Mares-Nasarre[1, *], Jorge Molines[1], M. Esther Gómez-Martín[1] and Josep R. Medina[1]

[1]Lab. Ports and Coasts, Institute of Transport and Territory, Universitat Politècnica de València; patmana@cam.upv.es, jormollo@upv.es, mgomar00@upv.es, jrmedina@upv.es.

***** Corresponding author: patmana@cam.upv.es

Abstract:

Sea level rise due to climate change, as well as social pressure to decrease the visual impact of coastal structures, have led to reduced crest freeboards, and this increases the overtopping hazard. In previous studies, pedestrian safety during overtopping events was assessed considering the overtopping layer thickness (OLT) and the overtopping flow velocity (OFV). This study analyzed the statistics of OLT and OFV on mound breakwaters without crown walls during severe wave storms. Small-scale 2D physical tests were conducted on mound breakwaters with dimensionless crest freeboards between 0.29 and 1.77, testing three armor layers (single-layer Cubipod®, and double-layer cubes and rocks) in depth-limited breaking wave conditions and with two bottom slopes. Neural Networks were used to develop new estimators for the OLT and OFV exceeded by 2% of the incoming waves with a high coefficient of determination ($0.866 \leq R^2 \leq 0.876$). The best number of significant figures in the empirical coefficients of the new estimators was determined according to their variability. The 1-parameter Exponential and Rayleigh distribution functions were proposed to estimate the extreme values of OLT and OFV with $0.803 \leq R^2 \leq 0.812$, respectively.

Keywords: mound breakwater; wave overtopping; overtopping layer thickness; overtopping flow velocity; depth-limited breaking wave conditions; Cubipod®

1. Introduction

Coastal hazards are increasing due to the sea level rise and stronger wave storms caused by climate change (*Camus et al.*, *2019*). In addition, new social concerns demand decreasing visual and environmental impacts of infrastructures. The consequences of climate change and the satisfaction of new social demands influence coastal structure design; reduced design dimensionless crest freeboards and higher overtopping rates must be considered. Higher extreme overtopping events and overtopping risks are expected, leading to the need for new tools to better consider the current design conditions. In addition, most mound breakwaters are built in the surf zone in depth-limited breaking wave conditions.

During extreme wave overtopping events, overtopping water flows over the breakwater crest. The characteristics of such flow, overtopping layer thickness (OLT) and overtopping flow velocity (OFV), are directly related to the hydraulic stability of the breakwater crest and rear side (*Argente et al.*, *2018*), but also to pedestrian safety on the breakwater crest (*Bae et al.*, *2016*). Pedestrian safety becomes relevant as recreational activities such as fishing, walking or taking pictures often take place on the breakwater (see Figure 1).

Fig. 1. Pedestrians on mound breakwaters: (a) fishing in Scheveningen (the Netherlands) and (b) taking photos in Altea (Spain).

There is extensive literature on the tolerable limits of water depth and flow velocity for pedestrian safety under constant flow conditions (*Abt et al.*, *1989*; *Endoh and Takahashi*, *1995*). Recently, *Bae et al.* (*2016)* and *Sandoval and Bruce* (*2017*) analyzed the stability of human bodies under overtopping flow conditions based on physical experiments with dummies and video images, respectively. *Bae et al.* (*2016*) also proposed tolerable limits for OLT and OFV for pedestrian accidents under overtopping flow conditions. Several predictors exist for OLT and OFV on dike crests (*Schüttrumpf and Van Gent*, *2003*; *van Bergeijk et al.*, *2019*). However, few studies are focused on OLT and OFV on mound breakwater crests (*Mares-Nasarre et al.*, *2020a*, *2019*). *Mares-Nasarre et al.* (*2020a*) demonstrated that the bottom slope (m) is a significant variable for estimating OLT and OFV, but m is not considered as an explanatory variable in the estimators found in the literature. Thus, methods given in the literature should be reviewed since none of the studies considered the bottom slope as an explanatory variable to estimate OLT and OFV.

This study examines the statistics of OLT and OFV on overtopped mound breakwaters (armor slope H/V = 3/2) without crown walls during extreme overtopping events under depth-limited breaking wave conditions and proposes new simple empirical formulas to estimate OLT and OFV exceeded by 2% of the incoming waves in the middle of the breakwater crest. In Section 2, the literature on OLT and OFV is analyzed, focusing on studies conducted on mound breakwaters. In Section 3, the experimental setup and data analysis are described; tests reported in *Mares-Nasarre et al.* (*2020a*) are used to fit the proposed empirical formulas and distribution functions. Small-scale models of mound breakwaters with single-layer randomly-placed Cubipod® (Cubipod®-1L), double-layer randomly-placed cube (cube-2L) and double-layer randomly-placed rock (rock-2L) armors were tested in the wave flume of the *Universitat Politècnica de València* (Spain) with two bottom slope configurations (m = 2% and 4%). Section 4 describes the Neural Network (NN) methodology used in this study to build up the empirical formulas with five explanatory variables for OLT and OFV. New estimators for OLT exceeded by 2% of the incoming waves as well as the statistical distribution function for the highest OLT (with exceedance probabilities under 2%) are described in Section 5. In Section 6, new estimators for OFV exceeded by 2% of the incoming waves and a statistical distribution function for OFV (with exceedance probabilities under 2%) are proposed. Finally, conclusions are drawn in Section 7.

2. Literature review on overtopping flow on mound breakwaters without crown wall

Few studies (*Mares-Nasarre et al., 2019, 2020a*) can be found in the literature focused on OLT and OFV on mound breakwater crests. Thus, studies performed on sloping structures such as dikes are also reviewed in this section. It should be noted that dikes are sloping impermeable structures with smooth gentle slopes (seaward slope H/V > 3), whereas mound breakwaters are permeable structures (where infiltration occurs) with steeper slopes (seaward slope H/V ≤ 2).

Schüttrumpf et al. (*2002*) and *Van Gent* (*2002*) conducted the first studies analyzing OLT and OFV on dikes mainly in non-breaking conditions. *Schüttrumpf and Van Gent* (*2003*) combined their previous results and described the overtopping flow on a dike using two variables: (1) the OLT exceeded by 2% of the incoming waves ($h_{c2\%}$) and (2) the OFV exceeded by 2% of the incoming waves ($u_{c2\%}$). *Schüttrumpf and Van Gent* (*2003*) also proposed an empirical method to estimate $h_{c2\%}$ and $u_{c2\%}$ based on the wave run-up height exceeded by 2% of the incoming waves ($Ru_{2\%}$) calculated using the formulas in *Van Gent* (*2001*). *Van Gent* (*2001*) considered $Ru_{2\%}$ to be a function of the surf similarity parameter or Iribarren number ($Ir_{m-1,0}$) calculated with the significant wave height (H_s =

$H_{1/3}$) and the spectral wave period $T_{m-1,0} = m_{-1}/m_0$, where m_i is the i-th spectral moment $m_i = \int_0^{\infty} S(f) f^i df$, being the wave spectrum $S(f)$. The main variables considered by *Schüttrumpf and Van Gent* (*2003*) are specified in Figure 2.

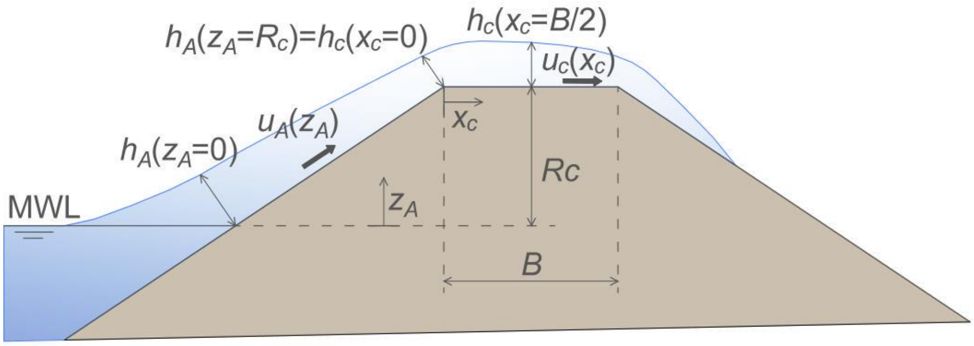

Fig. 2. Definition of the variables considered by *Schüttrumpf and Van Gent (2003)* on a dike cross-section.

According to *Schüttrumpf and Van Gent* (*2003*), OLT and OFV exceeded by 2% of the incoming waves at the seaward edge of the crest of the dike, $h_{A2\%}(z_A = R_c)$ and $u_{A2\%}(z_A = R_c)$, are estimated as

$$\frac{h_{A2\%}(z_A)}{H_s} = c^*_{A,h} \left(\frac{Ru_{2\%} - z_A}{H_s} \right) \tag{1}$$

$$\frac{u_{A2\%}(z_A)}{\sqrt{g\, H_s}} = c^*_{A,u} \sqrt{\frac{Ru_{2\%} - z_A}{H_s}} \tag{2}$$

where $c_{A,h}{}^*$ and $c_{A,u}{}^*$ are the empirical coefficients given in Table 1 and z_A is the elevation over the mean water level ($0 \leq z_A \leq R_c$). Once $h_{A2\%}(z_A = R_c)$ and $u_{A2\%}(z_A = R_c)$ are estimated using Eqs. (1) and (2), $h_{c2\%}$ and $u_{c2\%}$ can be calculated using Eqs. (3) and (4).

$$\frac{h_{c2\%}(x_c)}{h_{A2\%}(R_c)} = exp\left(-c^*_{c,h} \frac{x_c}{B} \right) \tag{3}$$

$$\frac{u_{c2\%}(x_c)}{u_{A2\%}(R_c)} = exp\left(-c^*_{c,u} \frac{x_c\, \mu}{h_{c2\%}(x_c)} \right) \tag{4}$$

where $c_{c,h}{}^*$ and $c_{c,u}{}^*$ are the empirical coefficients given in Table 1, x_c is the distance from the seaward side edge, B is the crest width and μ is the bottom friction coefficient. *Schüttrumpf et al.* (*2003*) proposed values of μ between 0.0058 and 0.02 for smooth slopes.

	Van Gent (2003)	**Schüttrumpf et al. (2003)**
R_c/H_{m0}	0.7 – 2.2	0.0 – 4.4
H_{m0}/h_s	0.2 – 1.4	0.1 – 0.3
Seaward slope (tanα=V/H)	1/4	1/3, 1/4, 1/6
c_{A,h^*}	0.15	0.33
c_{A,u^*}	1.30	1.37
c_{c,h^*}	0.40	0.89
c_{c,u^*}	0.50	0.50

Table 1. Experimental ranges and empirical coefficients for Eqs. (1) to (4).

Therefore, $h_{c2\%}$ and $u_{c2\%}$ estimated using the methods described in *Schüttrumpf and Van Gent* (*2003*) depend on H_s and $T_{m-1,0}$ as well as the seaward slope, tanα, the crest freeboard, R_c, and the crest width of the dike, *B*.

Van der Meer et al. (*2010*) considered the same variables as *Schüttrumpf and Van Gent* (*2003*) to explain $h_{c2\%}$ when analyzing new tests in the overtopping simulator. Regarding $u_{c2\%}$, *Van der Meer et al.* (*2010*) included $L_{m-1,0}$, the wavelength based on $T_{m-1,0}$. *Lorke et al.* (*2012*) and *Formentin et al.* (*2019*) proposed new formulas to estimate $h_{c2\%}$ and $u_{c2\%}$ on dikes with no additional explanatory variables.

Mares-Nasarre et al. (*2019*) was the first study focusing on OLT and OFV on overtopped mound breakwaters; the experimental range of the dimensionless crest freeboard was $0.34 \leq R_c/H_{m0} \leq 1.75$, where $H_{m0} = 4(m_0)^{0.5}$ is the spectral significant wave height, and three armor layers (Cubipod®-1L, cube-2L and rock-2L) were tested under depth-limited breaking wave conditions ($0.20 \leq H_{m0}/h_s \leq 0.73$, where h_s is the water depth at the toe of the structure). *Mares-Nasarre et al.* (*2019*) performed tests with a bottom slope m = 2% and measured OLT and OFV in the middle of the breakwater crest. These researchers adapted Eqs. (1) and (3) proposed by *Schüttrumpf and Van Gent* (*2003*) to estimate $h_{c2\%}$ in the middle of the breakwater crest, $h_{c2\%}(B/2)$. Since the formulas given by *Schüttrumpf and Van Gent* (*2003*) are based on $Ru_{2\%}$, *Mares-Nasarre et al.* (*2019*) recommended Eq. (5) given by *EurOtop* (*2018*) to estimate $Ru_{2\%}$.

$$\frac{Ru_{2\%}}{H_s} = 1.65\,\gamma_f\,\gamma_\beta\,\gamma_b\,Ir_{m-1,0} \tag{5a}$$

with a maximum value of

$$\frac{Ru_{2\%}}{H_s} = 1.00\,\gamma_{f,surging}\gamma_\beta\,\gamma_b\left(4.0 - \frac{1.5}{\sqrt{Ir_{m-1,0}}}\right) \tag{5b}$$

where γ_f is the roughness coefficient depending on the type of armor, γ_β is the factor which takes into account the effect of oblique wave attack, γ_b is the influence factor for berms and $\gamma_{f,surging}$ [-] is the roughness coefficient that increases linearly up to 1.0 following

$$\gamma_{f,surging} = \gamma_f + \left(Ir_{m-1,0} - 1.8\right)\frac{1 - \gamma_f}{8{,}2} \tag{5c}$$

The maximum $Ru_{2\%}/H_s$ is 2.0 for permeable core. In *Mares-Nasarre et al.* (*2019*), $\gamma_\beta = \gamma_b = 1$.

Mares-Nasarre et al. (*2019*) calibrated $c_{A,h}$*, $c_{c,h}$* and γ_f following the recommendations by *Molines and Medina* (*2015*) and proposed $c_{A,h}* = 0.52$, $c_{c,h}* = 0.89$ and $\gamma_f = 0.33$, 0.35 and 0.48 for Cubipod®-1L, cube-2L and rock-2L, respectively, in Eqs. (1) and (3). *Mares-Nasarre et al.* (*2019*) calculated $u_{c2\%}$ in the middle of the breakwater crest, $u_{c2\%}(B/2)$, as function of the squared root of $h_{c2\%}(B/2)$; $u_{c2\%}(B/2) = K_2\ (gh_{c2\%}(B/2))^{0.5}$, where K_2 was calibrated for each armor layer. $K_2 = 0.57$, 0.60 and 0.47 were proposed for Cubipod®-1L, cube-2L and rock-2L, respectively. These authors also described the highest values of OLT and OFV in the middle of the breakwater crest using the 1-parameter Exponential and Rayleigh distributions.

Mares-Nasarre et al. (*2020a*) recently expanded the database used in *Mares-Nasarre et al.* (*2019*) conducting 2D physical tests with m = 4%. Similar to *Mares-Nasarre et al.* (*2019*), overtopped mound breakwaters were tested with the same three armor layers (Cubipod®-1L, cube-2L and rock-2L) under depth-limited breaking wave conditions ($0.20 \leq H_{m0}/h_s \leq 0.90$). As pointed out by *Herrera et al.* (*2017*), in depth-limited breaking wave conditions, the optimum point to estimate the incident wave characteristics is relevant. Thus, *Mares-Nasarre et al.* (*2020a*) analyzed the optimum point to estimate wave characteristics in order to calculate $h_{c2\%}(B/2)$ and $u_{c2\%}(B/2)$; the optimum point was found at a distance of $3h_s$ from the toe of the structure. This distance was also recommended by *Herrera et al.* (*2017*) and approximately corresponds to $5H_s$ suggested by *Goda* (*1985)* and *Melby* (*1999*). It was found that $h_{c2\%}(B/2)$ decreased while $u_{c2\%}(B/2)$ slightly increased for increasing values of m; therefore, m is a significant variable to consider when estimating $h_{c2\%}(B/2)$ and $u_{c2\%}(B/2)$ on mound breakwater crests.

3. Experimental methodology

3.1. Experimental setup

Mares-Nasarre et al. (*2019* and *2020a*) carried out 2D physical tests in the wave flume (30 m × 1.2 m × 1.2 m) of the Laboratory of Ports and Coasts at the *Universitat Politècnica de València* (LPC-UPV), with two mild bottom slope configurations. The first configuration was composed of two ramps: one 6.25 m-long m = 4% bottom slope, and another 9.0 m-long m = 2% bottom slope. The second configuration consisted of a continuous ramp of m = 4% all along the wave flume. Figure 3 shows the longitudinal cross-sections of the LPC-UPV wave flume for the two configurations with the locations of the wave gauges.

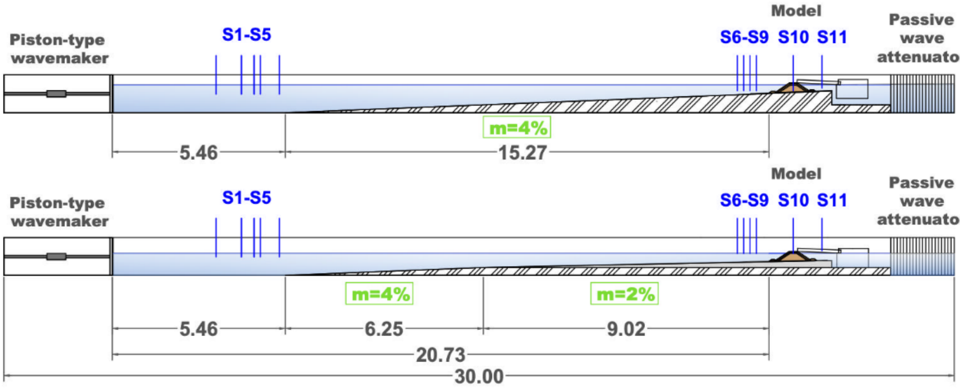

Fig. 3. Longitudinal cross-sections of the LPC-UPV wave flume.

11 capacitive wave gauges were placed along the flume to measure the water surface elevation. Wave gauges S1 to S5 were installed in the wave generation zone following the recommendations by *Mansard and Funke* (*1980*) in order to separate incident and reflected waves in the wave generation zone. Wave gauges S6 to S9 were located close to the model. Note that close to the model, depth-limited wave breaking occurs, and the existing methods to separate incident and reflected waves are not reliable. The distances from S6, S7, S8 and S9 to the model toe were $5h_s$, $4h_s$, $3h_s$ and $2h_s$, respectively. Wave gauge S10 was placed in the middle of the breakwater crest in order to analyze OLT, while S11 was installed behind the model to detect possible phenomena of water piling-up.

Irregular wave tests with 1,000 waves were generated following a JONSWAP spectrum ($\gamma = 3.3$). The AWACS wave absorption system was activated during the tests to avoid multireflections. Neither low-frequency oscillations nor piling-up (S11) were significant during the tests. Piling-up is an undesirable phenomenon which consists of an increase in the water depth behind the model due to the accumulation of water caused by high overtopping rates and other effects. The LPC-UPV wave flume prevents piling-up by allowing the water to recirculate through a double floor.

The tested cross-section depicted in Figure 4 corresponds to a mound breakwater with armor slope H/V = 3/2 and rock toe berms. Three armor layers were tested: single-layer Cubipod® (Cubipod®-1L with nominal median diameter or equivalent cube size Dn_{50}= 3.79 cm), double-layer randomly-placed cube (cube-2L with Dn_{50} = 3.97 cm) and double-layer randomly-placed rock (rock-2L with Dn_{50} = 3.18 cm) armors. Tests conducted with m = 2% were performed with a medium-sized rock toe berm (Dn_{50} = 2.6

cm) while tests carried out with m = 4% were conducted with a larger rock toe berm (Dn_{50} = 3.9 cm) in order to guarantee the toe berm hydraulic stability during the tests.

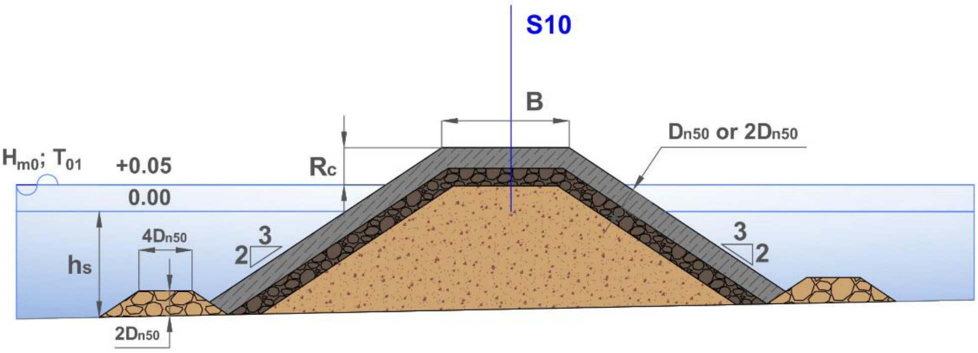

Fig. 4. Cross-section of the models tested in the LPC-UPV wave flume. Dimensions in m.

Each breakwater model was built on bottom flume configurations m = 2% and 4% and two water depths (h_s) at the toe of the structure were considered. h_s = 20 cm and 25 cm were tested for all the cases except the test series corresponding to cube-2L with m = 2%; in these specific case test series, h_s = 25 cm and 30 cm were tested. For each water depth (h_s), H_{m0} and peak period (T_p) were calculated at the wave generation zone, in order to keep the wave steepness ($s_{0p} = H_{m0}/L_{0p} = 2\pi H_{m0}/(gT_p^2)$) approximately constant through each test series (s_{0p} = 0.02 and 0.05). For each s_{0p}, H_{m0} at the wave generation zone ($H_{m0,g}$) was increased in steps of 1 cm from no damage to initiation of damage of the armor layer or wave breaking at the wave generation zone. Table 2 shows the range of the main variables considered during the tests. Note that wave characteristics (H_{m0} and $T_{m-1,0}$) are provided at a distance of $3h_s$ from the toe of the structure following recommendations by *Mares-Nasarre et al.* (*2020a*).

Three cameras were also installed in order to analyze the armor damage in the frontal slope, crest and rear side of the armor using the Virtual Net Method (*Gómez-Martín and Medina*, *2014*). Overtopping discharges were collected using a chute and a weighing system placed in a collection tank behind the model (*Mares-Nasarre et al.*, *2020b*).

m	Armor	B [m]	#tests	h_s [m]	R_c [m]	H_{m0} [m]	$T_{m-1,0}$ [s]
1/50	Cubipod® - 1L	0.24	25	0.20	0.12	0.08 – 0.15	1.04 – 1.98
			28	0.25	0.07	0.07 – 0.17	0.93 – 2.04
	cube – 2L	0.27	26	0.25	0.11	0.07 – 0.16	0.95 – 2.05
			23	0.30	0.06	0.07 – 0.18	0.89 – 1.89
	rock – 2L	0.26	8	0.20	0.15	0.09 – 0.13	1.12 – 1.70
			13	0.25	0.10	0.07 – 0.13	0.89 – 1.73
1/25	Cubipod® - 1L	0.24	21	0.20	0.12	0.09 – 0.17	1.04 – 1.88
			28	0.25	0.07	0.07 – 0.18	0.94 – 2.15
	cube – 2L	0.27	21	0.20	0.11	0.10 – 0.17	1.14 – 1.87
			23	0.25	0.06	0.09 – 0.18	1.06 – 2.15
	rock – 2L	0.26	8	0.20	0.15	0.10 – 0.14	1.25 – 1.89
			11	0.25	0.10	0.09 – 0.14	1.08 – 1.91

Table 2. Structural and wave characteristics of the 2D tests corresponding to single (1L) and double-layer (2L) armors.

3.2. Wave analysis

Waves in the wave generation zone were separated using the measurements taken by wave gauges S1 to S5 and the LASA-V method (*Figueres and Medina, 2005*). The LASA-V method is applicable to nonstationary and nonlinear irregular waves. However, the existing methods given in the literature are not valid for breaking waves. Thus, to estimate incident waves in the model zone, where wave breaking occurs, the SwanOne propagation model (*Verhagen et al., 2008*) was used. The SwanOne model fits a JONSWAP spectrum (γ=3.3) based on the input incident wave conditions in the wave generation zone. This spectrum is propagated along the bathymetry of the wave flume and the Composite Weibull distribution recommended by *Battjes and Groenendijk* (*2000*) is applied to describe the wave height distribution in shallow foreshores. Note that the SwanOne model analyzes frequencies within the range 0.03 – 0.8 Hz, since it is prepared for prototype scale wave conditions; in this study, a reference scale 1/30 was assumed.

Herrera and Medina (*2015*) validated the SwanOne model using tests without a structure. In the present study, a similar validation was conducted; tests without a structure were performed using an efficient passive wave absorption system at the end of the flume ($K_r = H_{m0,r}/H_{m0,i} < 0.25$). The measurements of the tests without a structure (total waves) were compared with the SwanOne model simulations at both the wave generation zone (Figure 5a and 5c) and the model zone (Figure 5b and 5d). Note that SwanOne simulations at the wave generation zone represent the fitting to the input incident waves obtained after separating incident and reflected waves using measurements taken by wave gauges S1 to S5.

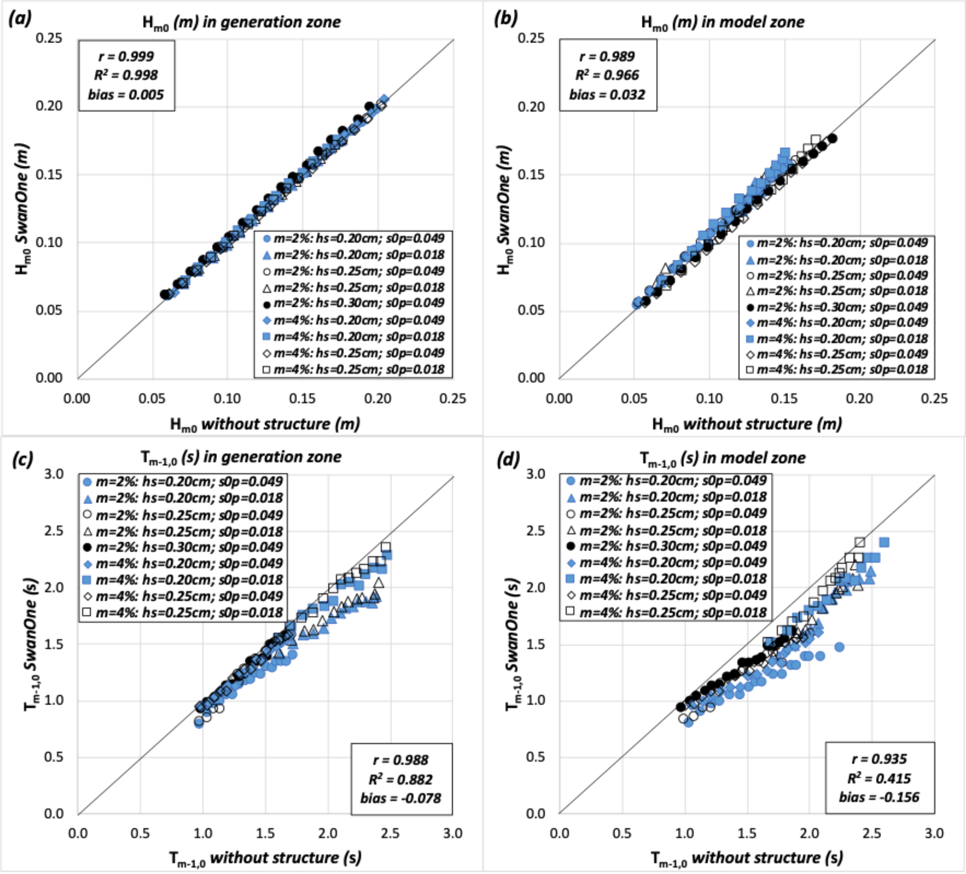

Fig. 5. Comparison between the measured wave characteristics in the tests without a structure and the estimations for incident waves given by the SwanOne model for: (a) significant wave height in the generation zone, (b) significant wave height in the model zone, (c) spectral period $T_{m-1,0}$ in the generation zone and (d) spectral period $T_{m-1,0}$ in the model zone.

Correlation coefficient (*r*), coefficient of determination (R^2) and relative bias (*bias*) were considered to quantify the goodness of fit in this study. $0 \le r \le 1$ assesses the correlation,

$0 \leq R^2 \leq 1$ estimates the proportion of variance explained by the model and $-1 \leq bias \leq 1$ provides a dimensionless quantification of the bias. Thus, the higher the *r*, the higher the R^2 and the closer the *bias* to 0, the better.

$$r = \frac{\sum_{i=1}^{N_o}(o_i - \bar{o})(e_i - \bar{e})}{\sqrt{\sum_{i=1}^{N_o}(o_i - \bar{o})^2 \sum_{i=1}^{N_o}(e_i - \bar{e})^2}} \tag{6}$$

$$R^2 = 1 - \frac{\frac{1}{N_o}\sum_{i=1}^{N_o}(o_i - e_i)^2}{\frac{1}{N_o}\sum_{i=1}^{N_o}(o_i - \bar{o})^2} \tag{7}$$

$$bias = \frac{1}{N_o}\sum_{i=1}^{N_o}\frac{(e_i - o_i)}{|o_i|} \tag{8}$$

where N_{ob} is the number of observations, o_i and e_i are the observed and estimated values, and $\bar{o}$ is the average observed value. As shown in Figure 5, agreement was reasonable for the fitted conditions in the wave generation zone ($R^2 \geq 0.882$). Regarding the model zone, good agreement was observed for H_{m0} ($R^2 = 0.966$) while poor results were obtained for $T_{m-1,0}$ ($R^2 = 0.415$). As reported in *Mares-Nasarre et al.* (*2020b*), decreasing values of *bias* were observed for H_{m0} in the model zone for increasing values of h_s.

During the design phase of a mound breakwater, the design wave conditions (H_{m0} and $T_{m-1,0}$) must be estimated at the location where the mound breakwater will be built; thus, both H_{m0} and $T_{m-1,0}$ estimated by SwanOne are applied in this study.

3.3. Overtopping layer thickness (OLT) and Overtopping flow velocity (OFV) measurement

OLT was recorded in 57 physical tests, while OLT and OFV were measured in an additional 178 physical tests. OLT was measured using a capacitive wave gauge (S10) located in the middle of the breakwater crest (see Figures 3 and 4). S10 was inserted into a hollow cylinder filled with water in order to keep the sensor partially submerged. A lid with a slot was installed in the upper part of the cylinder to prevent water loss and to maintain the daily-calibrated reference level. The cylinder was 12 cm in length and 8.5 cm in diameter. Visual inspection of the OLT during overtopping events showed a clear water surface (see Figure 6). Thus, aeration was considered negligible. Little variation in the reference level was seen and little noise was measured, as shown in Figure 7.

Fig. 6. Visual inspection of the overtopping layer thickness (OLT) during the physical tests.

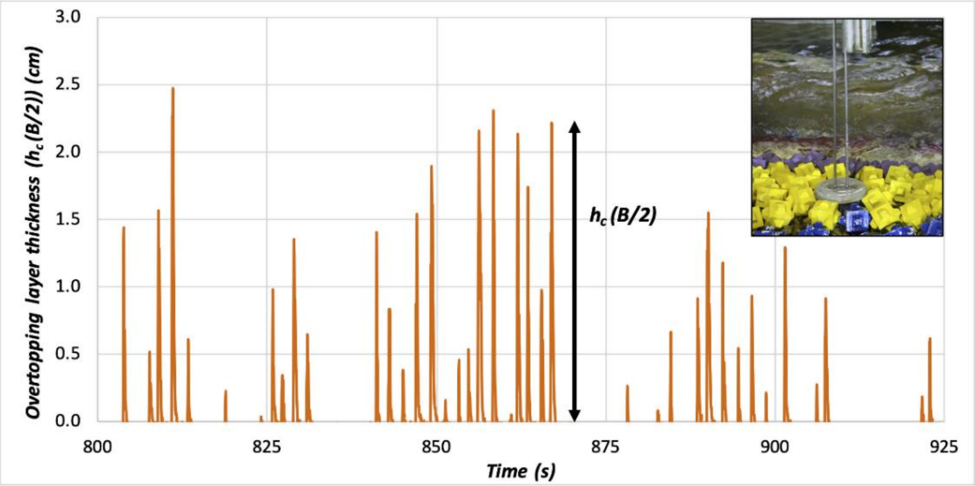

Fig. 7. Example of a raw record taken by wave gauge S10.

The OFV was measured at a frequency of 20 Hz using three miniature propellers installed along the crest: (1) on the seaward edge of the model crest, (2) in the middle of the model crest, and (3) on the leeward edge of the model crest. In this study, the measurements taken in the middle of the breakwater crest were used. The operational range of these miniature propellers was $0.15 < u(\text{m/s}) < 3.00$. Thus, OFV values below 0.15 m/s were disregarded. Figure 8 displays an example of a record from a miniature propeller.

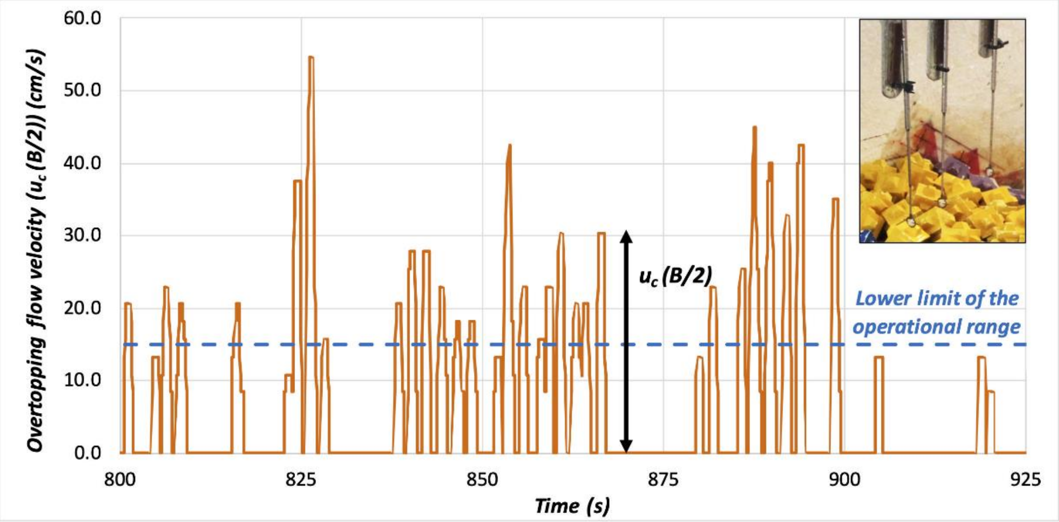

Fig. 8. Example of a raw record of a miniature propeller.

4. Methodology of analysis using Neural Networks (NNs)

Feedforward Neural Network (NN) models are commonly used in the artificial intelligence field to model nonlinear relationships between explanatory variables (input) and response variables (output). During the last two decades, NN models have been applied successfully by researchers and practitioners to estimate wave overtopping, wave reflection or wave forces on coastal structures. NN models have also been used in practical applications with a large database of wave overtopping tests (*van Gent et al., 2007; Formentin et al., 2017*) and with smaller datasets to identify the most relevant variables to estimate wave forces on crown walls (*Molines et al., 2018*), or to define explicit wave overtopping formulae (*Molines and Medina, 2016*). In this research, Multi-layer feedforward NN models were used to analyze the influence of a set of explanatory variables on $h_{c2\%}(B/2)$ and $u_{c2\%}(B/2)$.

4.1. Explanatory variables affecting $\mathrm{h_{c2\%}(B/2)}$ *and* $\mathrm{u_{c2\%}(B/2)}$

Based on the literature, the explanatory variables which might influence $h_{c2\%}(B/2)$ and $u_{c2\%}(B/2)$ are m, R_c, H_{m0}, $T_{m-1,0}$ and h_s (with H_{m0} and $T_{m-1,0}$ located at a distance of $3h_s$ from the toe of the structure). These explanatory variables consider the wave conditions at the toe of the structure and the crest freeboard. In order to ensure a NN model is not affected by the model scale, the aforementioned explanatory variables were made dimensionless as:

- R_c/H_{m0}, is the dimensionless crest freeboard and is the most common and widely accepted dimensionless variable that governs the mean wave overtopping discharge.

- $Ir_{m-1,0}=tan\alpha/(H_{m0}/L_{m-1,0})^{0.5}$, is the Iribarren number or breaker parameter calculated using H_{m0} and $T_{m-1,0}$ at a distance of $3h_s$ from the toe of the structure. $Ir_{-m1,0}$ considers the influence of the wave steepness and armor slope and determines the type of wave breaking on the slope. In this study, only tanα=2/3 was tested; however, $Ir_{m-1,0}$ was selected instead of wave steepness, since *Schüttrumpf and Van Gent* (*2003*) reported $Ir_{m-1,0}$ as significant. The influence of $Ir_{-m1,0}$ on wave overtopping was also reported in studies such as *Molines and Medina* (*2016*).
- *m*, is the bottom slope, which determines the type of wave breaking on the toe of the structure. *Mares-Nasarre et al.* (*2020a*) determined that *m* plays a significant role in the estimation of OLT and OFV.
- h_s/H_{m0}, is the dimensionless water depth using the water depth at the toe of the structure and H_{m0} at a distance of $3h_s$ from the toe of the structure. h_s/H_{m0} is commonly used as a breaking index to indicate if waves are depth-limited or not (*Nørgaard et al.*, *2014*; *van Gent*, *1999*).

Both $h_{c2\%}(B/2)$ and $u_{c2\%}(B/2)$ were also analyzed as dimensionless variables: $h_{c2\%}(B/2)/H_{m0}$ and $u_{c2\%}(B/2)/(H_{m0}/T_{m-1,0})$.

4.2. General outline

For each type of armor (Cubipod®-1L, cube-2L and rock-2L), a NN model was trained to estimate $h_{c2\%}(B/2)$ and $u_{c2\%}(B/2)$ independently. Thus, six NN models were developed (3 types of armors x 2 output variables).

For each NN model, the dataset (*N* cases) was randomly divided in two parts: *TR*=75%x*N* to develop the NN model and *T*=25%x*N* for a final blind test (*T-BLIND*) in which the NN model performance was evaluated with data not used to develop the NN model. The NN models connected neurons using a hyperbolic tangent sigmoid transfer function; the NN models presented an input layer with 4 neurons (N_i), a hidden layer with 3 neurons (N_h) and an output layer with 1 neuron (N_o), see Figure 9. Thus, the number of free parameters in the NN model is given by $P = N_o + N_h (N_i + N_o + 1) = 19$.

In this study, $P/TR < 0.63$ and the Early Stopping Criterion were applied to prevent overlearning (see *The MathWorks Inc.*, *2019*). The Early Stopping Criterion randomly divides the dataset *TR* in three categories: (1) training of the NN (70% × *TR=TRAIN*), (2) validation (15% × *TR=VAL*) and (3) testing (15% × *TR=TEST*). Data in the training subset were used to update the biases and weights of the NN. Data in the validation subset were used to monitor the error after each training step and to stop the training process once the error in this validation subset started growing (indicating possible overlearning). Data in the testing subset were used as cross validation to compare different models, since they were not included in the training process.

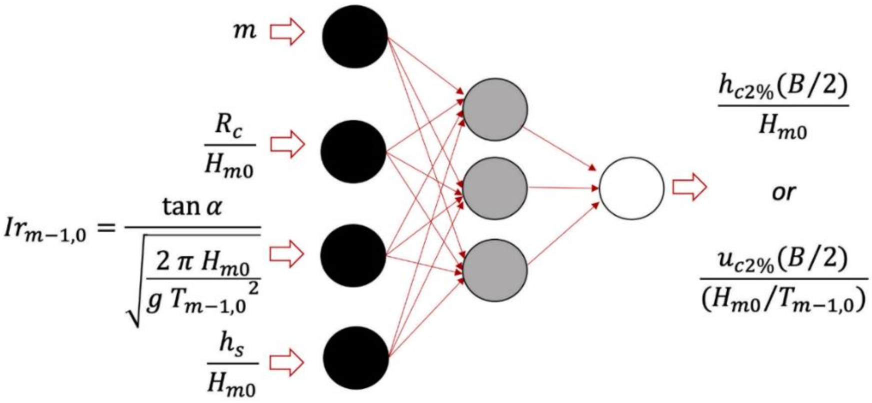

Fig. 9. Architecture of the Neural Network models used in this study.

4.3. NN model results

Figures 10a and 10b illustrate the performance of the NN models for $h_{c2\%}(B/2)/H_{m0}$ and $u_{c2\%}(B/2)/(H_{m0}/T_{m-1,0})$ using the training (*TRAIN*), validation (*VAL*) and testing (*TEST*) subset. A good performance was observed in the testing subset with $R^2 = 0.903$ and 0.789 for $h_{c2\%}(B/2)/H_{m0}$ and $u_{c2\%}(B/2)/(H_{m0}/T_{m-1,0})$, respectively. Figures 10c and 10d compare the measured and estimated $h_{c2\%}(B/2)/H_{m0}$ and $u_{c2\%}(B/2)/(H_{m0}/T_{m-1,0})$ using the NN models on the 25% experimental data reserved for the final blind test (*T-BLIND*). A good agreement was found with $R^2 = 0.913$ for $h_{c2\%}(B/2)/H_{m0}$ and $R^2 = 0.918$ for $u_{c2\%}(B/2)/(H_{m0}/T_{m-1,0})$. Note that $R^2 = 0.164$ was obtained when assessing the goodness-of-fit of the NN developed for $u_{c2\%}(B/2)/(H_{m0}/T_{-1,0})$ on Cubipod®-1L using the *TEST* subset due to the low variance of the randomly selected testing subset (variance of the *TEST* subset was 0.15 while the variance of the whole *TR* dataset was 0.90).

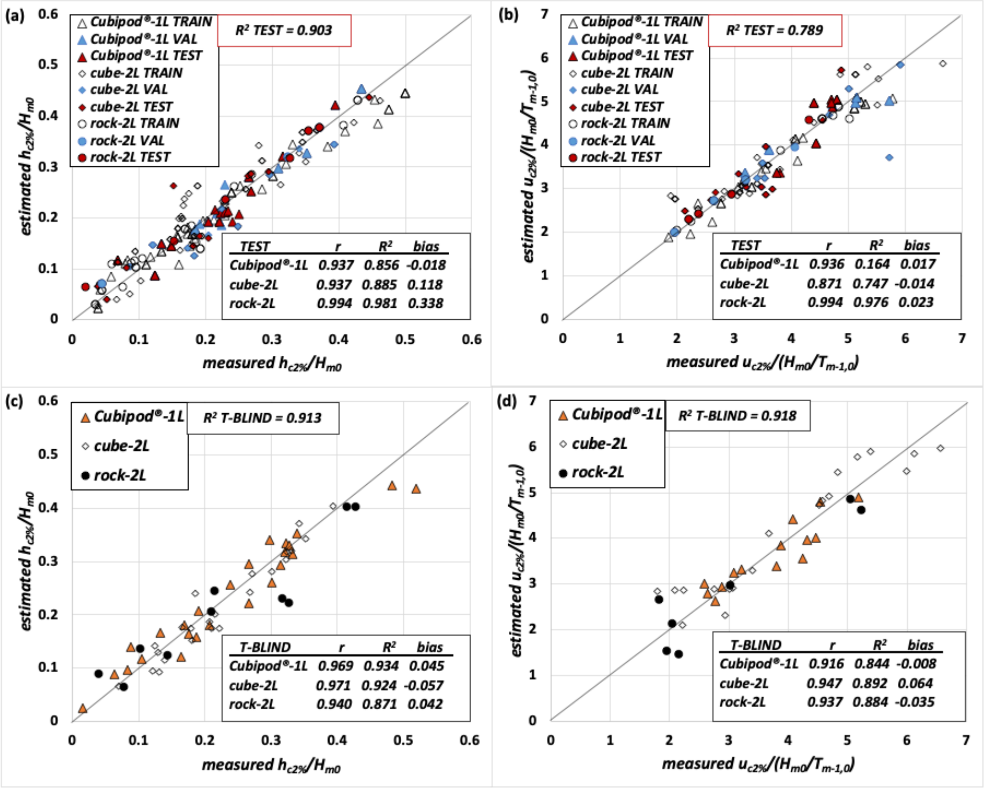

Fig. 10. Comparison between measured and estimated OLT and OFV with the NN models: (a) $h_{c2\%}(B/2)/H_{m0}$ on the testing subset (TEST), (b) $u_{c2\%}(B/2)/(H_{m0}/T_{m-1,0})$ on the testing subset (TEST), (c) $h_{c2\%}(B/2)/H_{m0}$ on the final blind test subset (T-BLIND) and (d) $u_{c2\%}(B/2)/(H_{m0}/T_{m-1,0})$ on the final blind test subset (T-BLIND).

4.4. Influence of the explanatory variables on $h_{c2\%}(B/2)/H_{m0}$ *and* $u_{c2\%}(B/2)/(H_{m0}/T_{m-1,0})$

NN models trained in Sections 4.1 to 4.3 were used here to analyze the influence of the four explanatory dimensionless variables (m, R_c/H_{m0}, $Ir_{m-1,0}$ and h_s/H_{m0}) on $h_{c2\%}(B/2)/H_{m0}$ and $u_{c2\%}(B/2)/(H_{m0}/T_{m-1,0})$. To this end, simulations were performed with variations in only one input variable while keeping the value of the other input variables constant. Figure 11 illustrates the influence of R_c/H_{m0} on $h_{c2\%}(B/2)/H_{m0}$. Figure 11a shows the simulations performed using the NN model for Cubipod®-1L armor corresponding to the inputs m = 4%, $Ir_{m-1,0}$ = 3.5, 4.0 and 4.5, and h_s/H_{m0} = 2.0. Figure 11b shows the differences between NN simulations corresponding to Cubipod®-1L, cube-2L and rock-2L armors for m = 4%, $Ir_{m-1,0}$ = 4.0 and h_s/H_{m0} = 2.0. Figure 11 shows that a linear model is suitable to describe the influence of R_c/H_{m0} on $h_{c2\%}(B/2)/H_{m0}$. Similar figures were obtained to describe the influence of m, R_c/H_{m0} and h_s/H_{m0} on $h_{c2\%}(B/2)/H_{m0}$; thus, a linear model was found to be suitable to describe the influence of the four dimensionless input variables on $h_{c2\%}(B/2)/H_{m0}$. Note that only linear relationships between m and the studied variables, namely $h_{c2\%}(B/2)/H_{m0}$ and $u_{c2\%}(B/2)/(H_{m0}/T_{m-1,0})$, were reasonable, since only two values of m were tested in this study, and the model is only valid in the range $2\% \leq m \leq 4\%$.

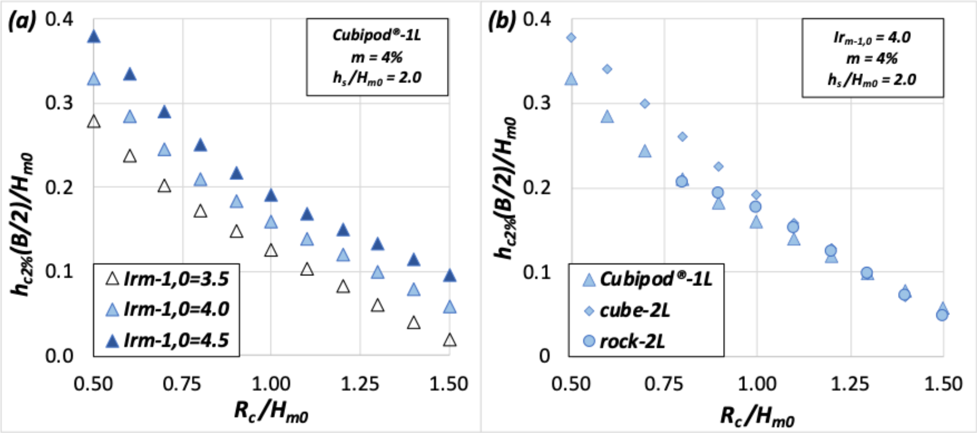

Fig. 11. Influence of R_c/H_{m0} on $h_{c2\%}(B/2)/H_{m0}$ with m=4%, h_s/H_{m0}=2.0 and constant $Ir_{m-1,0}$.

Figure 12a shows the NN simulations conducted for cube-2L with m = 2%, R_c/H_{m0} = 0.5, 1.0 and 1.5 and h_s/H_{m0} = 2.5. Figure 12b illustrates the differences between NN simulations corresponding to Cubipod®-1L, cube-2L and rock-2L armors for m = 2%, R_c/H_{m0} = 1.5 and h_s/H_{m0} = 2.5. Figure 12 illustrates that the influence of $Ir_{m-1,0}$ on $u_{c2\%}(B/2)/(H_{m0}/T_{m-1,0})$ followed a quadratic relationship. On the other hand, a linear relationship was observed between m, R_c/H_{m0} and h_s/H_{m0} and $u_{c2\%}(B/2)/(H_{m0}/T_{m-1,0})$.

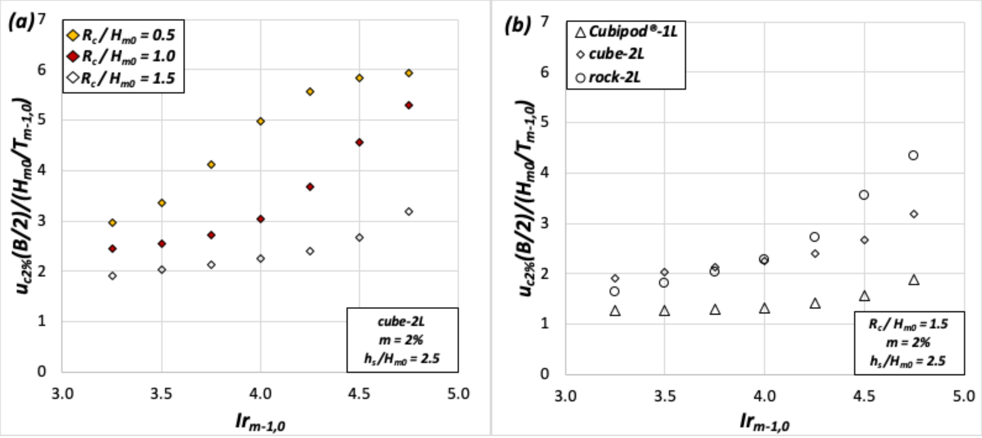

Fig. 12. Influence of $Ir_{m-1,0}$ on $u_{c2\%}(B/2)/(H_{m0}/T_{m-1,0})$ with m=2%, h_s/H_{m0}=2.5 and constant R_c/H_{m0}.

5. Estimating overtopping layer thickness (OLT) on mound breakwaters

5.1. Overtopping layer thickness (OLT) exceeded by 2% of the incoming waves

In Section 4.4, the simulations conducted with NN models were used to analyze the influence of the explanatory variables on $h_{c2\%}(B/2)/H_{m0}$. Since linear influence was observed in most cases, Eq. (9) is proposed to estimate $h_{c2\%}(B/2)/H_{m0}$.

$$\frac{h_{c2\%}(B/2)}{H_{m0}} = C1 + C2\,m + C3\left(\frac{R_c}{H_{m0}} - 1\right) + C4\,Ir_{m-1,0} + C5\,\frac{h_s}{H_{m0}} \geq 0 \qquad (9)$$

where *C1*, *C2*, *C3*, *C4* and *C5* are coefficients to be fitted for each armor layer (Cubipod®-1L, cube-2L and rock-2L). Eq. (9) is not a fully linear model, since negative values are not allowed, so conventional linear regression techniques are not adequate to determine the coefficients *C1* to *C5* in Eq. (9). In order to estimate *C1* to *C5* in Eq. (9), a nonlinear multivariable optimization algorithm without restrictions (see *The MathWorks Inc., 2019*) was used. Since this algorithm requires an initial solution to start the iterative optimization process, conventional linear regression was performed first to provide the initial solution. The final nonlinear fitting of coefficients *C1* to *C5* in Eq. (9) were calibrated by minimizing the Mean Squared Error (*MSE)*, calculated as

$$MSE = \frac{1}{N_o}\sum_{i=1}^{N_o}(o_i - e_i)^2 \qquad (10)$$

where N_{ob} is the number of observations and o_i and e_i are the observed and estimated values. The sensitivity of the nonlinear multivariable optimization algorithm without restrictions to the initial solution was assessed. A low sensitivity of the optimization algorithm to the initial solution was observed.

Similarly to *van Gent et al.* (*2007*) and *Molines et al.* (*2018*), the bootstrapping technique was applied together with the aforementioned nonlinear optimization algorithm to characterize the variability of the coefficients in Eq. (9). The bootstrap resample technique consists in the random selection of *N* data from a dataset with *N* data, so each datum has a probability of 1/ *N* to be selected each time. Hence, some data are not selected while other data may be selected once or more than once in each resample. Using this technique, 5%, 50% and 95% percentiles were obtained for the fitted coefficients (*C1* to *C5*) and the *MSE*.

The explanatory variables were introduced one by one in the model following the structure in Eq. (11) in order to assess their significance. First, four models composed of the constant term (*C1*) and each one of the four explanatory variables were optimized. Thus, the percentage of variance explained by each model could be calculated. After that, the process was repeated keeping the explanatory variable which explained the highest percentage of the variance in the previous step and adding one of the three missing explanatory variables. This procedure was repeated until the four explanatory variables were included in the model. Once the hierarchy of the influence of each explanatory variable was obtained, the influence of the constant term (*C1*) in the explained variance was evaluated. The adjusted coefficient of determination (R^2_{adj}) defined by *Theil* (*1961*) was calculated in every step to decide if an additional explanatory variable improved the prediction model.

$$R^2_{adj} = 1 - (1 - R^2)\frac{N - 1}{N - N_P - 1} \tag{11}$$

where N is the number of data available and N_P is the number of explanatory variables. R^2_{adj} considers not only the goodness of fit but also the number of data used to fit the model. In this study, the model with the highest R^2_{adj} was selected for every armor layer; the five fitting coefficients will not always be included in the model. Figures 13 to 15 show the evolution of the median value and 90% confidence band of the R^2_{adj} depending on the number of explanatory variables considered in Eq. (9) for every armor layer model. The explanatory variable which maximized R^2_{adj} in every step, is indicated and the final number of selected explanatory variables to be included in Eq. (9) is highlighted in red.

As shown in Figures 13 to 15, R_c/H_{m0} explained the highest percentage of the variance for the three armor layers. The four selected explanatory variables were significant and were included in the model. Finally, the significance of the constant term (*C1*) was assessed by repeating the optimization procedure with $C1 = 0$. $C1 = 0$ was proposed for Cubipod®-1L and cube-2L armors, while $C1 \neq 0$ was proposed for rock-2L armor.

The number of significant figures or significant numbers of the coefficients in the final empirical formula depended on the variability in the fitted coefficients from the bootstrapping resamples. Only one significant figure or number was reasonable for *C1*, *C2* and *C5* (coefficient of variation in the range: $7\% \leq CV \leq 45\%$) while a maximum of two significant figures or numbers were recommended for *C3* and *C4* ($4\% \leq CV \leq 13\%$). Table 3 presents the coefficients *C1* to *C5* with the correct number of significant figures or numbers, as well as the goodness-of-fit metrics for Eq. (9) corresponding to Cubipod®-1L, cube-2L and rock-2L armors.

Figure 16 compares the measured and estimated $h_{c2\%}(B/2)/H_{m0}$ using Eq. (9) and the coefficients given in Table 3. The 90% error band is also shown in Figure 16. Good agreement is observed ($R^2 = 0.876$).

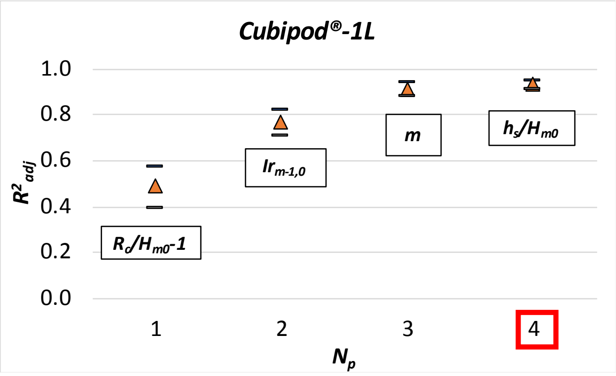

Fig. 13. Influence of the number of explanatory variables (N_p) on R^2_{adj} for Cubipod®-1L to estimate $h_{c2\%}(B/2)/H_{m0}$.

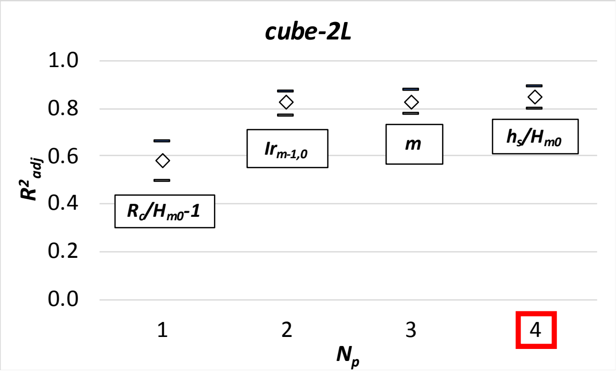

Fig. 14. Influence of the number of explanatory variables (N_p) on R^2_{adj} for cube-2L to estimate $h_{c2\%}(B/2)/H_{m0}$.

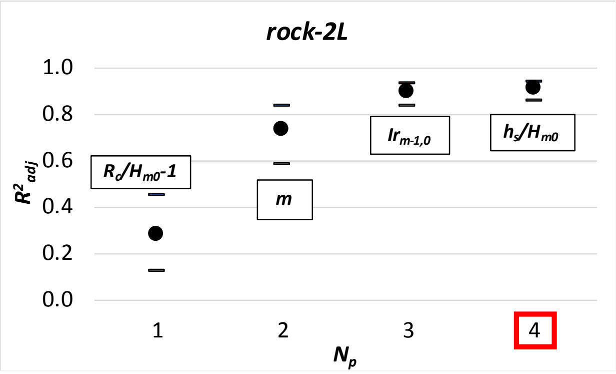

Fig. 15. Influence of the number of explanatory variables (N_p) on R^2_{adj} for rock-2L to estimate $h_{c2\%}(B/2)/H_{m0}$.

Armor layer	*C1*	*C2*	*C3*	*C4*	*C5*	*r*	*R^2*	*bias*
Cubipod®-1L	0	-4	-1/3	0.095	-0.03	0.957	0.914	0.030
cube-2L	0	-2	-0.3	0.085	-0.02	0.909	0.814	0.011
rock-2L	1/3	-10	-0.45	0.08	-0.03	0.951	0.903	0.072

Table 3. Coefficients and goodness-of-fit metrics for Eq. (9).

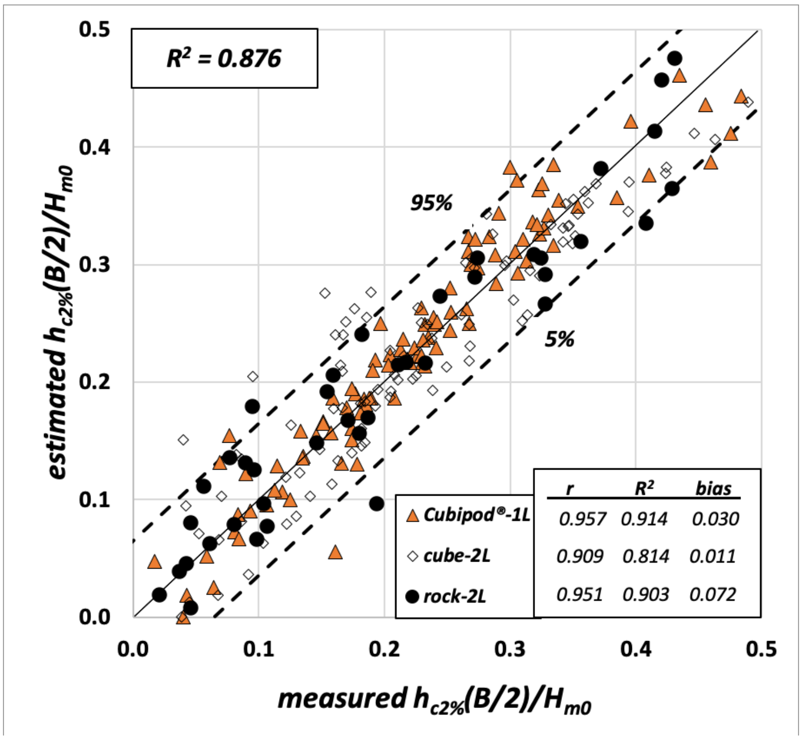

Fig. 16. Comparison between measured and estimated dimensionless $h_{c2\%}(B/2)$ using Eq. (9) and Table 3.

Assuming a Gaussian error distribution, the 90% error band can be estimated as

$$\left.\frac{h_{c2\%}(B/2)}{H_{m0}}\right|_{5\%}^{95\%} = \frac{h_{c2\%}(B/2)}{H_{m0}} \pm 1.64\sqrt{var(\varepsilon)} = \frac{h_{c2\%}(B/2)}{H_{m0}} \pm 0.064 \qquad (12)$$

5.2. Distribution function for extreme values of overtopping layer thickness (OLT)

As much the assessment of pedestrians' safety on mound breakwater crests as the hydraulic stability of the armor layer of mound breakwater crests require a detailed description of extreme overtopping events. Thus, the OLT distribution in the most severe wave storms must be known for the breakwater design. *Hughes et al.* (*2012*) pointed out that the extreme tail of a distribution is best described when only considering the low probability exceedance events. Hence, the distribution function of $h_c(B/2)$ with exceedance probabilities below 2% is studied here.

As reported in *Mares-Nasarre et al.* (*2019*), the best results when describing the distribution function of $h_c(B/2)$ with exceedance probabilities below 2% were obtained with a 1-parameter Exponential distribution,

$$F\left(\frac{h_c(B/2)}{h_{c2\%}(B/2)}\right) = 1 - exp\left(-C_h \frac{h_c(B/2)}{h_{c2\%}(B/2)}\right) \qquad (13)$$

where $h_c(B/2)$ is the OLT value with exceedance probabilities under 2% and C_h is an empirical coefficient to be calibrated. *Mares-Nasarre et al.* (*2019*) proposed $C_h = 4.2$ when $m = 2\%$. C_h was calibrated for each physical test using the 20 (1,000 waves × 2%) highest OLT measured values. $h_{c2\%}(B/2)$ estimated with Eq. (9) and coefficients in Table 3 was used in this study. The exceedance probability assigned to each OLT measured value was calculated as $N_m/(N_w+1)$, where N_m is the rank of the OLT measured value and N_w is the number of waves. The initial calibrated coefficients were $C_h = 4.04$ for $m = 2\%$ and $C_h = 3.91$ for $m = 4\%$. The non-parametric Mood Median Test was conducted to determine if the difference between these median values of C_h was significant; the null hypothesis (H_0) corresponded to both medians being equal. Since H_0 was not rejected with a significance level □ = 0.05, the final value $C_h = 4$ was proposed for both bottom slopes. The bottom slope does not have an influence on C_h but it does influence the estimation of $h_{c2\%}(B/2)$. Figure 17 compares measured and estimated $h_c(B/2)$ using Eq. (13) with $C_h = 4$. The 90% error band is also presented. Each alignment in Figure 17 corresponds to the data for one test. A good agreement ($R^2 = 0.803$) was obtained.

Assuming a Gaussian error distribution, the 90% error band can be estimated as

$$\left.\frac{h_c(B/2)}{H_{m0}}\right|_{5\%}^{95\%} = \frac{h_c(B/2)}{H_{m0}} \pm 0.087 \qquad (14)$$

Figure 18 illustrates the fitting of two sample datasets to the proposed 1-parameter Exponential distribution in an exponential plot.

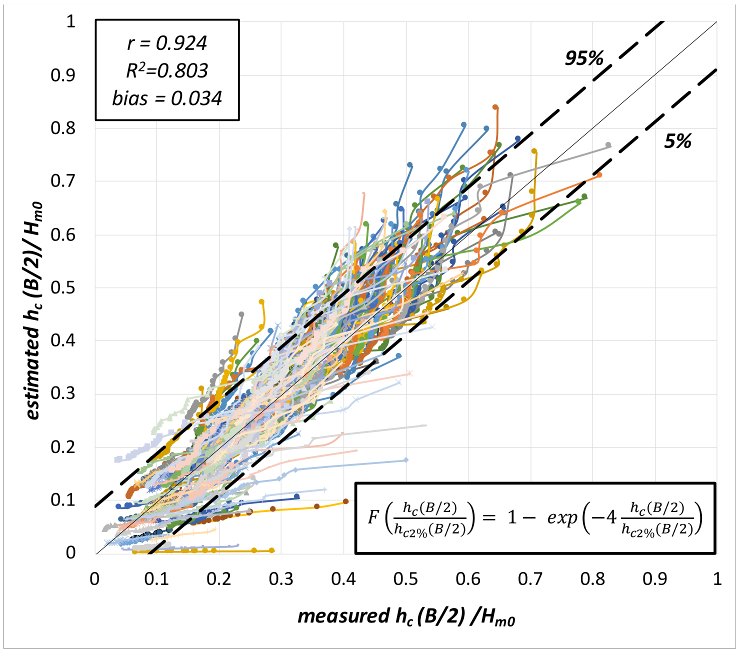

Fig. 17. Comparison between measured and estimated dimensionless $h_c(B/2)$ using Eq. (13) with C_h = 4.

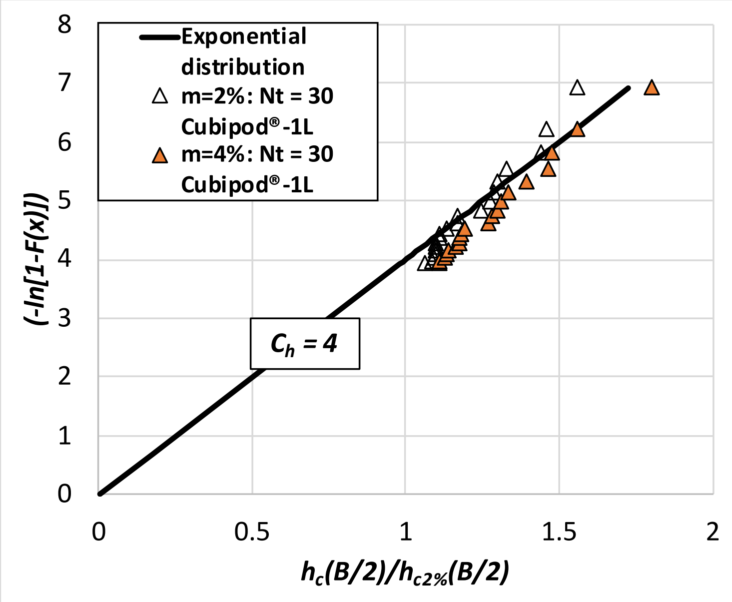

Fig. 18. Example of cumulative distribution function of $h_c(B/2)$ in equivalent probability plot.

6. Estimating overtopping flow velocity (OFV) on mound breakwaters

6.1. Overtopping flow velocity (OFV) exceeded by 2% of incoming waves

In Section 2, methods found in the literature to estimate OFV exceeded by 2% of the incoming waves, $u_{c2\%}(B/2)$, were described. Most of them (*Mares-Nasarre et al., 2019*; *Schüttrumpf and Van Gent, 2003*) were based on the correlation between the statistics of OLT and OFV. This means that $h_{c2\%}(B/2)$ needs to be estimated first with the subsequent accumulated errors later. In this study, a new formula was developed using the experimental database and considering the four input dimensionless explanatory variables described in Section 4 (m, R_c/H_{m0}, $Ir_{m-1,0}$ and h_s/H_{m0}).

Based on the trends observed in the simulations conducted with the NN models in Section 4.4, the following 5-parameter formula is proposed to estimate $u_{c2\%}(B/2)/(H_{m0}/T_{m-1,0})$

$$\frac{u_{c2\%}(B/2)}{\left(\frac{H_{m0}}{T_{m-1,0}}\right)} = D1 + D2\,m + D3\left(\frac{R_c}{H_{m0}} - 1\right) + D4\,{Ir_{m-1,0}}^2 + D5\,\frac{h_s}{H_{m0}} \geq 0 \qquad (15)$$

where *D1*, *D2*, *D3*, *D4* and *D5* are coefficients to be calibrated. The procedure described in Section 5.1 is performed in order to assess the significance of the four explanatory variables. Figures 19 to 21 show the evolution of the median value and 90% confidence band of the R^2_{adj} depending on the number of explanatory variables considered in Eq. (15) for each armor layer model. The explanatory variable which maximized R^2_{adj} in each step is indicated and the final number of selected explanatory variables to be included in Eq. (15) is highlighted in red.

The explanatory variable $Ir_{m-1,0}$ explained the highest percentage of the variance. All the explanatory variables were significant and were included in the model. Finally, the significance of the constant term (*D1*) was assessed; $D1 \neq 0$ was proposed for the three armor layers.

The number of significant figures in the empirical coefficients in the fitted model is based on their variability from the bootstrapping resamples. One significant figure was proposed for *D1*, *D2*, *D3* and *D5* ($9\% \leq CV \leq 40\%$) whereas a maximum of two significant figures were recommended for *D4* ($5\% \leq CV \leq 9\%$). Table 4 lists the final coefficients as well as the goodness-of-fit metrics for Eq. (15) corresponding to the three armor layers.

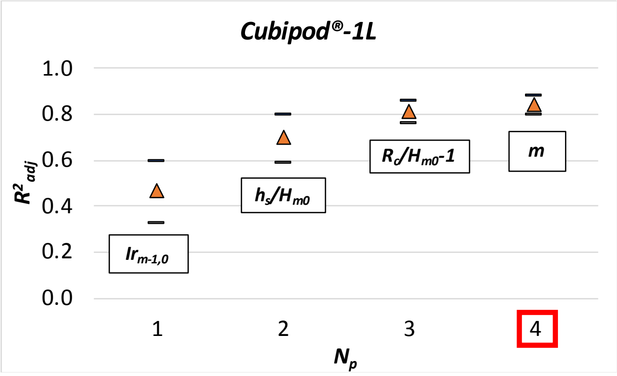

Fig. 19. Influence of the number of explanatory (N_p) variables on R^2_{adj} for Cubipod®-1L to estimate $u_{c2\%}(B/2)/(H_{m0}/T_{m-1,0})$.

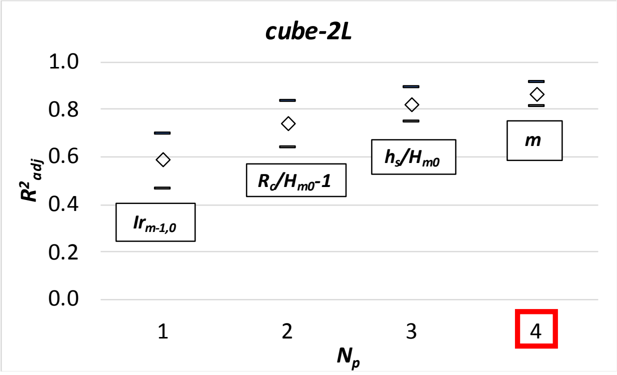

Fig. 20. Influence of the number of explanatory (N_p) variables on R^2_{adj} for cube-2L to estimate $u_{c2\%}(B/2)/(H_{m0}/T_{m-1,0})$.

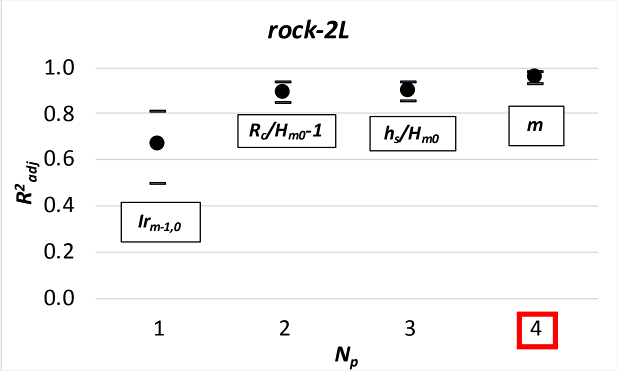

Fig. 21. Influence of the number of explanatory (N_p) variables on R^2_{adj} for rock-2L to estimate $u_{c2\%}(B/2)/(H_{m0}/T_{m-1,0})$.

Armor layer	*D1*	*D2*	*D3*	*D4*	*D5*	*r*	*R^2*	*bias*
Cubipod®-1L	2	20	-2	0.20	-1	0.920	0.832	-0.014
cube-2L	4	-30	-2	0.20	-1	0.917	0.845	0.011
rock-2L	2	-30	-3	0.25	-0.5	0.972	0.934	-0.023

Table 4. Coefficients and goodness-of-fit metrics for Eq. (15).

The measured and estimated $u_{c2\%}(B/2)/(H_{m0}/T_{m-1,0})$ with Eq. (15) using the coefficients given in Table 4 in shown in Figure 22. The 90% error band is also indicated. The agreement was good (R^2 = 0.866).

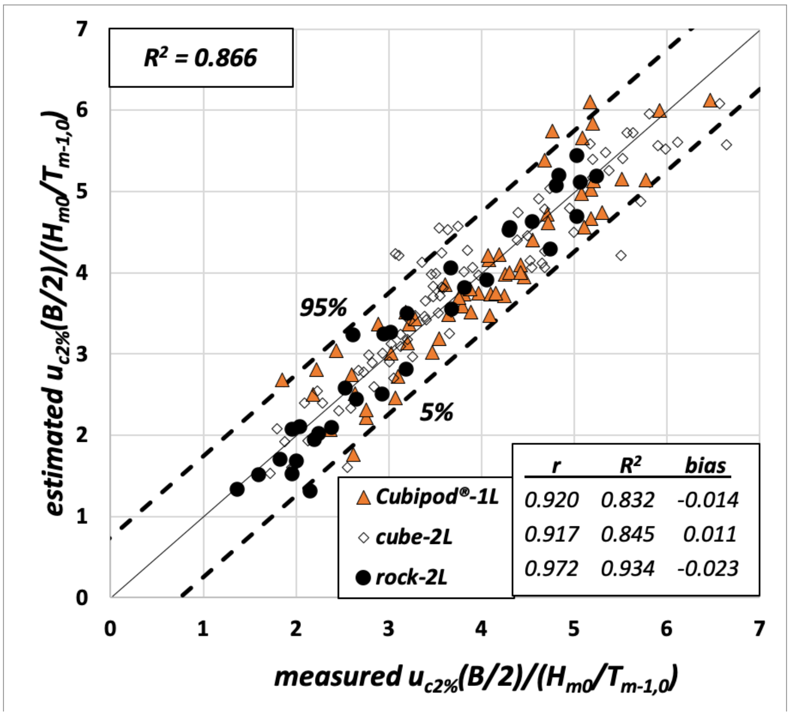

Fig. 22. Comparison between measured and estimated dimensionless $u_{c2\%}$(B/2) using Eq. (15) and Table 4.

Assuming a Gaussian error distribution, the 90% error band can be estimated as

$$\left.\frac{u_{c2\%}(B/2)}{(H_{m0}/T_{m-1,0})}\right|_{5\%}^{95\%} = \frac{u_{c2\%}(B/2)}{(H_{m0}/T_{m-1,0})} \pm 0.744 \qquad (16)$$

6.2. Distribution function for extreme values of overtopping flow velocity (OFV)

Similar to Section 5.2, the OFV events during the most severe wave storms are characterized here. Thus, the distribution function of $u_c(B/2)$ with exceedance probabilities below 2% was studied in this section. *Mares-Nasarre et al.* (*2019*) recommended the Rayleigh distribution to describe the distribution function of $u_c(B/2)$ with exceedance probabilities below 2%. Here, best results were also obtained with the Rayleigh distribution given as

$$F\left(\frac{u_c(B/2)}{u_{c2\%}(B/2)}\right) = 1 - exp\left(-C_u\left[\frac{u_c(B/2)}{u_{c2\%}(B/2)}\right]^2\right) \tag{17}$$

where C_u is an empirical coefficient to be calibrated. *Mares-Nasarre et al.* (*2019*) proposed C_u =3.6 when m = 2%. The calibration procedure described in Section 5.2 is also applied here. Note that $u_{c2\%}(B/2)$ estimated with Eq. (15) together coefficients in Table 4 were used to simulate the design phase conditions. The initial calibrated coefficients were C_u = 3.62 for m = 2% and C_u = 3.46 for m = 4%. Since C_u values were similar for both bottom slopes, the non-parametric Mood Median Test was performed to determine if the difference between the median values of C_u was significant. The null hypothesis (H_0) corresponded to both medians being equal; H_0 was not rejected with a significance level α = 0.05. Hence, the final value C_u = 3.5 was proposed for the two bottom slopes. The bottom slope does not influence C_u but it does influence the estimation of $u_{c2\%}(B/2)$. Comparison between measured and estimated $u_c(B/2)$ using Eq. (17) with C_u = 3.5 is shown in Figure 23. The 90% error band is also indicated. A good agreement (R^2 = 0.812) was obtained.

It was observed that *MSE* rose for larger values of $u_c(B/2)/(H_{m0}/T_{m-1,0})$. Thus, the methodology proposed by *Herrera and Medina* (*2015*) was used here to estimate the 90% error band. Assuming a Gaussian error (□) distribution with 0 mean and variance calculated as

$$\sigma^2(\varepsilon) = 0.08\frac{u_c(B/2)}{(H_{m0}/T_{m-1,0})} \tag{18}$$

The 90% error band is obtained as

$$\left.\frac{u_c(B/2)}{(H_{m0}/T_{m-1,0})}\right|_{5\%}^{95\%} = \frac{u_c(B/2)}{(H_{m0}/T_{m-1,0})} \pm 0.46\sqrt{\frac{u_c(B/2)}{(H_{m0}/T_{m-1,0})}} \tag{19}$$

Figure 24 illustrates the fitting of two sample datasets in a Rayleigh probabilistic plot.

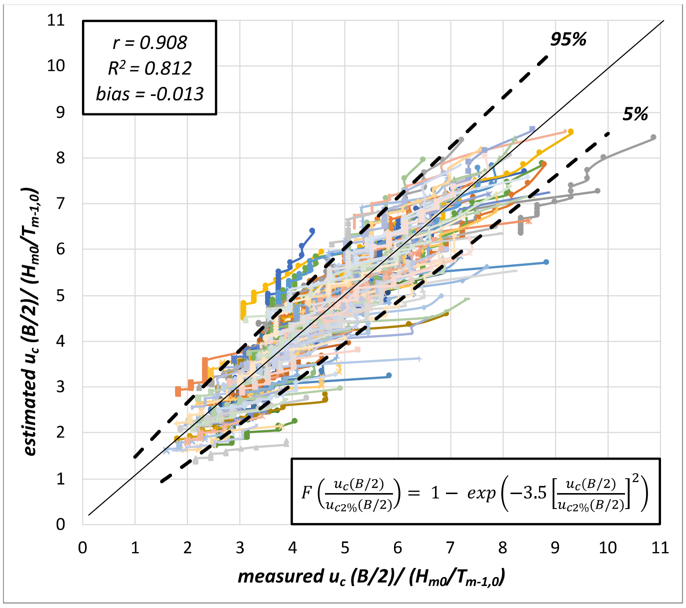

Fig. 23. Comparison between measured and estimated dimensionless $u_c(B/2)$ using Eq. (19) with C_u = 3.5.

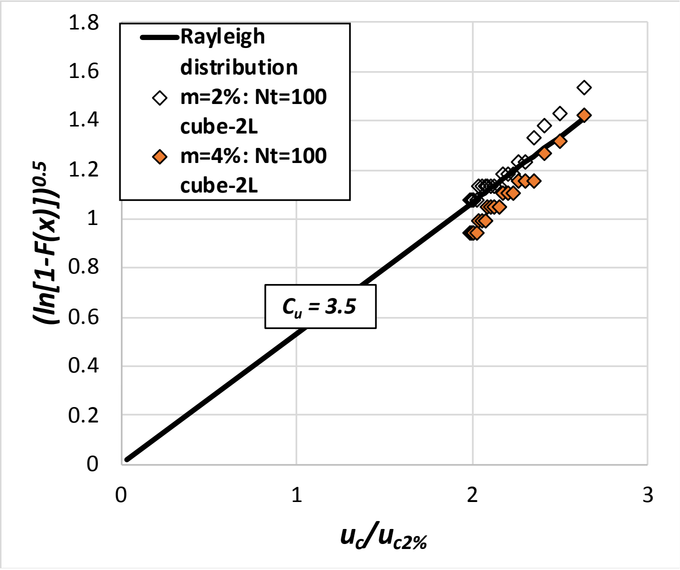

Fig. 24. Example of the cumulative distribution function of $u_c(B/2)$ in a Rayleigh probability plot.

7. Evaluation of the influence of the explanatory variables

As shown in Sections 5 and 6, the four selected explanatory variables (m, R_c/H_{m0}, $Ir_{m-1,0}$ and h_s/H_{m0}) were found to be significant when estimating $h_{c2\%}(B/2)$ and $u_{c2\%}(B/2)$. Nevertheless, the influence of h_s/H_{m0} on $h_{c2\%}(B/2)$ and m on $u_{c2\%}(B/2)$ was low. In this section, the performance of Eq. (9) and (15) is assessed when h_s/H_{m0} in Eq. (9) and m in Eq. (15) are disregarded. Table 5 presents the calibrated coefficients as well as the goodness-of-fit metrics for Eq. (9) when h_s/H_{m0} is not included in the model ($C5$ = 0) for the three armor layers.

Armor layer	*C1*	*C2*	*C3*	*C4*	*C5*	*r*	R^2	*bias*
Cubipod®-1L	0	-4	-1/3	0.085	0	0.949	0.900	0.008
cube-2L	0	-2	-0.3	0.075	0	0.902	0.804	0.067
rock-2L	0.3	-10	-0.45	0.075	0	0.947	0.875	0.194

Table 5. Sensitivity of the coefficients and goodness-of-fit metrics for OLT-Eq. (11) when h_s/H_{m0} is disregarded.

When comparing Tables 3 and 5, the relative variation (Δ%) of the coefficients are: *C1* (0 ≤ Δ% ≤ 11%), C2 (Δ%=0), C3 (Δ%=0) and *C4* (6% ≤ Δ% ≤ 12%). Most of the coefficients gave the same values. Regarding the goodness of fit, R^2 decreased around 2% when $C5$ = 0.

Table 6 lists the calibrated coefficients as well as the goodness-of-fit metrics for Eq. (15) when m is not included in the model ($D2$ = 0) for the three armor layers.

Armor layer	*D1*	*D2*	*D3*	*D4*	*D5*	*r*	R^2	*bias*
Cubipod®-1L	3	0	-2	0.2	-1	0.909	0.785	0.068
cube-2L	2	0	-2	0.2	-0.5	0.901	0.796	-0.018
rock-2L	1	0	-3	0.2	-0.2	0.943	0.872	-0.039

Table 6. Sensitivity of the coefficients and goodness-of-fit metrics for OFV-Eq. (17) when m is disregarded.

When comparing Tables 4 and 6, the relative variation (Δ%) of the coefficients are: D*1* (Δ% =50%), D3 (Δ%=0), D4 (0 ≤ Δ% ≤ 20%) and *D5* (0 ≤ Δ% ≤ 50%). R^2 decreased around 6% when $D2$ = 0. Note that the influence of m is also included in the model by the wave conditions, H_{m0}. Thus, m is still relevant even if it is not an explicit explanatory variable in the model.

From the results in Tables 5 and 6, it can be concluded that the performance of Eq. (9) and (15) is still satisfactory when removing h_s/H_{m0} and m, respectively. However, it should be noted that such explanatory variables were statistically significant as described in Sections 5 and 6.

8. Conclusions

Mound breakwater design is evolving due to the social concerns about the impact of coastal structures and the rising sea levels as well as stronger wave conditions caused by climate change. These drivers of change have led to reduced design crest freeboards and increased overtopping risks. In this context, the OLT and OFV on the breakwater crest has become relevant to assess the hydraulic stability of the armored crest and the pedestrian safety on the breakwater crest.

In this study, 235 physical tests reported in *Mares-Nasarre et al.* (*2019* and *2020a*) were used to propose empirical models to estimate OLT and OFV. The 2D tests measured OLT and OFV on overtopped mound breakwaters with three armor layers (Cubipod®-1L, cube-2L and rock-2L) in depth-limited breaking wave conditions with two bottom slopes (m = 2% and m = 4%) and armor slope tanα=2/3.

Sea bottom slope, dimensionless crest freeboard, Iribarren number related to wave steepness and dimensionless water depth (m, R_c/H_{m0}, $Ir_{m-1,0}$ and h_s/H_{m0}) were the selected explanatory variables to estimate OLT and OFV exceeded by 2% of the incoming waves in the middle of the breakwater crest, $h_{c2\%}(B/2)$ and $u_{c2\%}(B/2)$. Eqs. (11) and (17) with five coefficients are proposed to estimate dimensionless OLT ($h_{c2\%}(B/2)/H_{m0}$) and OFV ($u_{c2\%}(B/2)/(H_{m0}/T_{m-1,0})$, respectively, using the four dimensionless explanatory variables. The coefficients to be used in Eqs. (9) and (15), as well as the goodness-of-fit metrics for Cubipod®-1L, cube-2L and rock-2L armors, are given in Tables 3 and 4, respectively; the agreement between measured and estimated $h_{c2\%}(B/2)$ and $u_{c2\%}(B/2)$ was good ($0.866 \leq R^2 \leq 0.876$)

Dimensionless crest freeboard, R_c/H_{m0}, was the most significant explanatory variable to describe OLT whereas the Iribarren number related to wave steepness, $Ir_{m-1,0}$, was the most significant variable to describe OFV*;* the bottom slope (m) had a significant influence on $h_c(B/2)$ and $u_c(B/2)$.

In order to better describe the OLT and OFV during the most severe wave storms, the 1-parameter Exponential and Rayleigh distribution functions were used to estimate OLT and OFV values, respectively, with exceedance probabilities below 2%, $h_c(B/2)$ and $u_c(B/2)$. The recommended coefficients for the 1-parameter Exponential distribution and the Rayleigh distributions were C_h = 4 for Eq. (13) and C_u = 3.5 for Eq. (17), respectively; the agreement was good ($0.803 \leq R^2 \leq 0.812$) between the measured and estimated $h_c(B/2)$ and $u_c(B/2)$ given by Eqs. (13) and (17) when using C_h = 4 and C_u = 3.5, respectively.

Acknowledgements

The authors thank the three anonymous reviewers for their comments and suggestions. The authors acknowledge the financial support from the Spanish *Ministerio de Economía* *y Competitividad* and *Fondo Europeo de Desarrollo Regional* (FEDER) under grant RTI2018-101073-B-I00. The first author was also financially supported through the FPU program (*Formación de Profesorado Universitario*) funded by the Spanish *Ministerio de Educación, Cultura y Deporte* under grant FPU16/05081. The authors thank Debra Westall for revising the manuscript.

Appendix A. Data used in this study: $h_{c2\%}(B/2)$ and $u_{c2\%}(B/2)$

This appendix provides the test matrix used in this study as well as the observed OLT and OFV exceeded by 2% of the incoming waves in the middle of the breakwater crest ($h_{c2\%}(B/2)$ and $u_{c2\%}(B/2)$, respectively). Wave runs of N_w = 1,000 waves were generated following a JONSWAP spectrum (γ = 3.3). m represents the bottom slope, H_{m0} and $T_{m-1,0}$ are the incident spectral significant wave height and the spectral period at a distance of 3 times the water depth from the toe of the structure, R_c is the crest freeboard and h_s is the water depth at the toe of the structure. Tables 7 to 9 present the data from the tests performed with the models with Cubipod®-1L, cube-2L and rock-2L, respectively.

Test #	**m (%)**	**H_{m0} (mm)**	**$T_{m-1,0}$ (s)**	**R_c (mm)**	**h_s (mm)**	**$h_{c2\%}(B/2)$ (mm)**	**$u_{c2\%}(B/2)$ (mm/s)**
1	2	93	1.04	120	200	6	-
2	2	101	1.12	121	200	8	-
3	2	107	1.13	121	200	11	-
4	2	112	1.12	121	200	13	-
5	2	119	1.19	121	200	16	-
6	2	125	1.22	122	200	18	-
7	2	129	1.25	122	200	19	-
8	2	133	1.30	122	200	21	-
9	2	135	1.31	122	200	24	-
10	2	136	1.28	122	200	25	-
11	2	142	1.41	122	200	27	-
12	2	142	1.40	120	200	29	-
13	2	143	1.42	120	200	30	-
14	2	76	1.42	120	200	12	-
15	2	102	1.59	120	200	18	-

Test #	m (%)	H_{m0} (mm)	$T_{m-1,0}$ (s)	R_c (mm)	h_s (mm)	$h_{c2\%}(B/2)$ (mm)	$u_{c2\%}(B/2)$ (mm/s)
16	2	111	1.59	120	200	23	-
17	2	118	1.63	121	200	28	-
18	2	125	1.64	121	200	33	-
19	2	133	1.73	121	200	33	-
20	2	136	1.85	122	200	39	-
21	2	140	1.86	123	200	37	-
22	2	142	1.88	120	200	40	-
23	2	145	1.88	121	200	39	-
24	2	147	1.87	122	200	40	-
25	2	149	1.98	123	200	43	-
26	2	75	0.93	70	250	8	-
27	2	84	1.03	70	250	13	-
28	2	91	1.04	70	250	17	230
29	2	102	1.10	70	250	23	255
30	2	110	1.08	71	250	26	279
31	2	117	1.11	71	250	29	279
32	2	124	1.16	71	250	33	279
33	2	133	1.23	71	250	38	327
34	2	138	1.26	72	250	42	352
35	2	145	1.33	73	250	44	352
36	2	152	1.38	74	250	47	352
37	2	157	1.40	75	250	51	425
38	2	162	1.46	77	250	52	425
39	2	164	1.45	78	250	53	425
40	2	167	1.47	80	250	54	449

Test #	***m*** **(%)**	**H_{m0} (mm)**	**$T_{m-1,0}$ (s)**	**R_c (mm)**	**h_s (mm)**	**$h_{c2\%}(B/2)$ (mm)**	**$u_{c2\%}(B/2)$ (mm/s)**
41	2	76	1.42	71	250	15	-
42	2	88	1.52	72	250	24	-
43	2	99	1.62	70	250	35	-
44	2	109	1.62	70	250	42	-
45	2	118	1.68	71	250	48	-
46	2	128	1.72	72	250	59	-
47	2	137	1.84	70	250	54	-
48	2	145	1.92	72	250	66	-
49	2	149	1.83	74	250	71	-
50	2	155	1.90	70	250	81	-
51	2	160	1.97	70	250	80	-
52	2	164	1.94	71	250	79	-
53	2	167	2.04	71	250	73	-
54	4	100	1.04	120	200	4	-
55	4	109	1.12	120	200	5	-
56	4	116	1.18	120	200	7	182
57	4	123	1.19	120	200	10	230
58	4	129	1.24	120	200	12	255
59	4	139	1.32	120	200	12	303
60	4	142	1.33	120	200	16	352
61	4	147	1.34	120	200	20	400
62	4	155	1.41	121	200	21	449
63	4	156	1.40	121	200	25	473
64	4	160	1.41	122	200	28	473
65	4	165	1.48	122	200	28	498

Test #	m (%)	H_{m0} (mm)	$T_{m-1,0}$ (s)	R_c (mm)	h_s (mm)	$h_{c2\%}(B/2)$ (mm)	$u_{c2\%}(B/2)$ (mm/s)
66	4	91	1.60	120	200	8	206
67	4	103	1.64	120	200	18	255
68	4	113	1.76	120	200	21	303
69	4	121	1.74	121	200	25	327
70	4	130	1.87	120	200	29	400
71	4	136	1.88	121	200	29	400
72	4	142	1.77	122	200	33	425
73	4	151	1.74	120	200	35	449
74	4	158	1.71	122	200	35	473
75	4	79	0.94	70	250	1	-
76	4	85	1.18	70	250	6	157
77	4	89	1.03	70	250	11	206
78	4	98	1.08	70	250	16	279
79	4	108	1.10	70	250	19	303
80	4	116	1.15	70	250	21	352
81	4	124	1.17	70	250	23	376
82	4	130	1.26	71	250	25	425
83	4	136	1.24	70	250	32	425
84	4	146	1.33	71	250	34	425
85	4	154	1.39	72	250	36	473
86	4	161	1.39	73	250	39	498
87	4	168	1.43	75	250	40	522
88	4	175	1.48	77	250	40	498
89	4	180	1.48	80	250	46	498
90	4	69	1.42	70	250	5	-

Test #	*m* (%)	H_{m0} (mm)	$T_{m-1,0}$ (s)	R_c (mm)	h_s (mm)	$h_{c2\%}(B/2)$ (mm)	$u_{c2\%}(B/2)$ (mm/s)
91	4	80	1.53	70	250	18	230
92	4	89	1.60	70	250	22	255
93	4	101	1.73	70	250	28	303
94	4	111	1.72	70	250	35	327
95	4	119	1.76	71	250	40	352
96	4	132	1.90	70	250	45	352
97	4	138	1.84	70	250	46	352
98	4	150	2.06	72	250	50	376
99	4	157	1.98	74	250	50	376
100	4	166	2.04	77	250	54	425
101	4	174	2.15	81	250	52	522
102	4	180	2.14	86	250	55	498

Table 7. Data from the tests conducted with the Cubipod®-1L armored model.

Test #	*m* (%)	H_{m0} (mm)	$T_{m-1,0}$ (s)	R_c (mm)	h_s (mm)	$h_{c2\%}(B/2)$ (mm)	$u_{c2\%}(B/2)$ (mm/s)
1	2	67	0.95	112	250	3	-
2	2	75	0.99	112	250	6	-
3	2	85	1.05	112	250	12	157
4	2	85	1.05	112	250	12	206
5	2	101	1.08	112	250	16	230
6	2	108	1.10	111	250	20	279
7	2	117	1.17	111	250	21	279
8	2	127	1.26	112	250	22	327
9	2	134	1.25	112	250	24	352
10	2	142	1.34	112	250	25	376

Test #	***m* (%)**	**H_{m0} (mm)**	**$T_{m-1,0}$ (s)**	**R_c (mm)**	**h_s (mm)**	**$h_{c2\%}(B/2)$ (mm)**	**$u_{c2\%}(B/2)$ (mm/s)**
11	2	147	1.38	112	250	29	425
12	2	153	1.38	113	250	28	425
13	2	157	1.40	111	250	25	376
14	2	160	1.45	112	250	31	425
15	2	69	1.43	111	250	3	-
16	2	81	1.57	112	250	15	-
17	2	94	1.58	112	250	25	230
18	2	104	1.63	112	250	28	279
19	2	113	1.79	111	250	33	327
20	2	122	1.72	111	250	39	327
21	2	132	1.87	112	250	45	376
22	2	140	1.90	112	250	49	449
23	2	144	1.90	113	250	41	449
24	2	150	1.91	115	250	59	522
25	2	157	2.04	116	250	58	643
26	2	163	2.05	111	250	69	522
27	2	67	0.89	61	300	6	-
28	2	75	0.94	61	300	12	-
29	2	83	0.99	61	300	19	-
30	2	92	1.02	61	300	25	206
31	2	100	1.07	62	300	31	255
32	2	109	1.12	62	300	33	303
33	2	115	1.03	62	300	36	327
34	2	124	1.17	62	300	40	376
35	2	129	1.22	62	300	42	376

Test #	*m* (%)	H_{m0} (mm)	$T_{m-1,0}$ (s)	R_c (mm)	h_s (mm)	$h_{c2\%}(B/2)$ (mm)	$u_{c2\%}(B/2)$ (mm/s)
36	2	139	1.28	63	300	48	376
37	2	145	1.27	63	300	51	400
38	2	153	1.34	64	300	53	352
39	2	162	1.43	61	300	57	400
40	2	166	1.42	63	300	57	425
41	2	172	1.43	64	300	62	449
42	2	178	1.50	66	300	64	522
43	2	69	1.42	68	300	18	-
44	2	80	1.52	61	300	28	-
45	2	92	1.63	61	300	36	279
46	2	101	1.63	61	300	43	352
47	2	112	1.78	62	300	50	376
48	2	119	1.75	63	300	55	376
49	2	130	1.89	61	300	64	400
50	4	106	1.14	161	200	4	182
51	4	114	1.18	161	200	8	182
52	4	120	1.18	161	200	11	182
53	4	125	1.27	161	200	13	206
54	4	132	1.27	161	200	16	230
55	4	139	1.33	161	200	19	279
56	4	144	1.34	161	200	23	303
57	4	151	1.39	161	200	25	327
58	4	154	1.40	161	200	27	352
59	4	158	1.41	161	200	29	352
60	4	162	1.47	161	200	29	376

Test #	***m* (%)**	**H_{m0} (mm)**	**$T_{m-1,0}$ (s)**	**R_c (mm)**	**h_s (mm)**	**$h_{c2\%}(B/2)$ (mm)**	**$u_{c2\%}(B/2)$ (mm/s)**
61	4	102	1.63	161	200	9	-
62	4	112	1.70	161	200	15	230
63	4	120	1.74	161	200	22	279
64	4	131	1.87	161	200	26	352
65	4	136	1.80	162	200	28	352
66	4	146	1.76	162	200	30	376
67	4	152	1.72	162	200	36	400
68	4	158	1.73	161	200	33	425
69	4	163	1.70	162	200	36	449
70	4	166	1.76	163	200	42	522
71	4	97	1.06	111	250	5	157
72	4	106	1.10	111	250	7	206
73	4	115	1.17	111	250	10	255
74	4	123	1.24	111	250	15	303
75	4	130	1.30	111	250	24	327
76	4	136	1.24	111	250	26	327
77	4	146	1.33	111	250	30	400
78	4	154	1.39	112	250	33	376
79	4	161	1.39	112	250	33	425
80	4	168	1.43	112	250	40	400
81	4	175	1.48	113	250	41	425
82	4	180	1.48	114	250	41	425
83	4	89	1.60	111	250	3	-
84	4	101	1.73	111	250	9	182
85	4	111	1.72	111	250	17	230

Test #	***m* (%)**	**H_{m0} (mm)**	**$T_{m-1,0}$ (s)**	**R_c (mm)**	**h_s (mm)**	**$h_{c2\%}(B/2)$ (mm)**	**$u_{c2\%}(B/2)$ (mm/s)**
86	4	119	1.76	111	250	27	303
87	4	132	1.90	111	250	34	327
88	4	138	1.84	112	250	39	352
89	4	150	2.06	111	250	43	376
90	4	157	1.98	112	250	41	425
91	4	166	2.04	114	250	43	425
92	4	174	2.15	117	250	56	449
93	4	180	2.14	111	250	61	473

Table 8. Data from the tests conducted with the cube-2L armored model.

Test #	***m* (%)**	**H_{m0} (mm)**	**$T_{m-1,0}$ (s)**	**R_c (mm)**	**h_s (mm)**	**$h_{c2\%}(B/2)$ (mm)**	**$u_{c2\%}(B/2)$ (mm/s)**
1	2	105	1.13	151	200	6	-
2	2	110	1.12	152	200	8	133
3	2	117	1.17	151	200	11	182
4	2	86	1.50	151	200	8	-
5	2	98	1.59	151	200	18	182
6	2	108	1.58	151	200	23	206
7	2	117	1.70	152	200	28	279
8	2	122	1.67	152	200	33	279
9	2	72	0.89	102	250	3	-
10	2	81	0.99	101	250	14	-
11	2	89	1.01	102	250	19	-
12	2	98	1.06	101	250	32	206
13	2	108	1.12	101	250	39	255
14	2	114	1.11	101	250	47	303

Test #	m (%)	H_{m0} (mm)	$T_{m-1,0}$ (s)	R_c (mm)	h_s (mm)	$h_{c2\%}(B/2)$ (mm)	$u_{c2\%}(B/2)$ (mm/s)
15	2	121	1.17	102	250	52	327
16	2	74	1.42	101	250	17	-
17	2	85	1.52	101	250	28	206
18	2	98	1.62	101	250	36	303
19	2	108	1.62	101	250	45	303
20	2	116	1.73	101	250	49	352
21	2	126	1.72	101	250	54	352
22	4	123	1.25	151	200	3	157
23	4	130	1.26	151	200	5	206
24	4	137	1.31	151	200	15	230
25	4	143	1.34	151	200	15	255
26	4	102	1.69	151	200	5	157
27	4	112	1.73	151	200	7	206
28	4	120	1.74	151	200	23	255
29	4	130	1.89	151	200	23	327
30	4	91	1.08	101	250	3	182
31	4	100	1.08	101	250	8	182
32	4	109	1.18	101	250	10	182
33	4	116	1.15	101	250	17	206
34	4	126	1.26	101	250	19	255
35	4	89	1.53	101	250	9	-
36	4	101	1.70	101	250	16	255
37	4	111	1.72	101	250	20	279
38	4	124	1.91	101	250	34	327
39	4	129	1.86	101	250	41	352

Test #	**m (%)**	**H_{m0} (mm)**	**$T_{m-1,0}$ (s)**	**R_c (mm)**	**h_s (mm)**	**$h_{c2\%}(B/2)$ (mm)**	**$u_{c2\%}(B/2)$ (mm/s)**
40	4	138	1.90	102	250	43	352

Table 9. Data of the tests conducted with the rock-2L armored model.

Notation

Acronyms:

AWACS	= Active Wave Absorption System
bias	= Relative bias
LASA-V	= Local Approximation using Simulated Annealing (*Figueres and Medina, 2005*)
LPC-UPV	= Laboratory of Ports and Coasts (UPV)
MSE	= Mean squared error
MWL	= Mean water level
NN	= Neural Network
OLT	= Overtopping layer thickness
OFV	= Overtopping flow velocity
r	= Correlation coefficient
R^2	= Coefficient of determination
R^2_{adj}	= Adjusted coefficient of determination
UPV	= Universitat Politècnica de València (ES)

Symbols:

B = crest width

$\cot\alpha$ [-] = armor slope

$Dn50$ [m] or [cm] = $(W_{50}/\rho)^{1/3}$, nominal diameter

e_i = estimated values

$\bar{e}$ = average of the estimated values

g [m/s^2] = gravitational acceleration

h_s [m] or [cm] = water depth

$h_{A2\%}(z_A)$ [m] or [cm] = run-up layer thickness exceeded by 2% of the incoming waves

$h_c(x_c)$ [m] or [cm] = overtopping layer thickness with exceedance probabilities below 2%

$h_{c2\%}(x_c)$ [m] or [cm] = overtopping layer thickness exceeded by 2% of the incoming waves

H_{m0} [m] or [cm] $=4(m_0)^{0.5}$, spectral wave height

$H_{m0,g}$ [m] or [cm] = spectral wave height in the wave generation zone

$H_{m0,i}$ [m] or [cm] = incident spectral wave height

$H_{m0,m}$ [m] or [cm] = measured spectral wave height

$H_{m0,r}$ [m] or [cm] = reflected spectral wave height

H_s [m] or [cm] = significant wave height or average wave height of the highest one-third waves, $H_{1/3}$

$Ir_{m-1,0}$ [-]	= $\xi_{-1,0} = tan\alpha/(H_{m0}/L_{m-1,0})^{0.5}$, Iribarren number or surf similarity parameter calculated with H_{m0} and $T_{m-1,0}$
K_r [-]	= $H_{m0,r}/ H_{m0,i}$, reflection coefficient
$L_{m-1,0}$ [m] or [cm]	= $gT_{m-1,0}^2/2\pi$, deep water wave length based on the spectral period, $T_{m-1,0}$
L_{0p} [m] or [cm]	= $gT_p^2/2\pi$, deep water wave length based on the peak period, T_p
m [-]	= bottom slope
m_i	= i-th spectral moment
N_h [-]	= number of neurons in the hidden layer of NNs
N_i [-]	= number of neurons in the input layer of NNs
N_o [-]	= number of neurons in the output layer of NNs
N_{ob} [-]	= number of observations
o_i	= observed values
P [-]	= number of free parameters in NNs
R_c [m] or [cm]	= crest freeboard
$Ru_{2\%}$ [m] or [cm]	= wave run-up height exceeded by 2% of the incoming waves
s_{0p} [-]	=H_{s0}/L_{0p}, deep water wave steepness based on the peak period, T_{p0}
$S(f)$	= wave spectrum

t [s] = time

$T_{m-1,0}$ [s] = m_{-1}/m_0, spectral wave period based on the spectral moment, m_{-1}

T_p [s] = peak wave period

T_{p0} [s] = deep waters peak wave period

T-BLIND [-] = subset used for blind testing

TEST [-] = 15%*TR*, subset used for cross validation of the trained NNs as part of the Early Stopping Criterion

TR [-] = subset used for training NNs

TRAIN [-] = 70%*TR*, subset used for the formal training of NNs as part of the Early Stopping Criterion

VAL [-] = 15%*TR*, subset used for validation during the training of NNs as part of the Early Stopping Criterion

$u_{A2\%}(z_A)$ [m/s] or [cm/s] = run-up velocity

$u_c(x_c)$ [m/s] or [cm/s] = overtopping velocity with exceedance probabilities below 2%

$u_{c2\%}(x_c)$ [m/s] or [cm/s] = overtopping velocity exceeded by 2% of the incoming waves

x_c [m] or [cm] = horizontal coordinate along the crest from the seaward edge

x_e = estimated value given by the linear regression

z_A [m] or [cm] = elevation on the MWL

ε [-] = error, difference between the estimated and the measured value

α [º] or [rad] = angle of the slope

Δ% = relative variation of the empirical coefficients

γ [-] = parameter of the JONSWAP spectrum

γ_b [-] = berm factor

γ_f [-] = roughness factor

γ_β [-] = obliquity factor

μ [-] = friction factor of dike crests according to *Schüttrumpf et al. (2002)*

References

Abt, S.R., Wittier, R.J., Taylor, A., Love, D.J., 1989. Human stability in a high flood hazard zone. JAWRA J. Am. Water Resour. Assoc. 25, 881–890. https://doi.org/10.1111/j.1752-1688.1989.tb05404.x

Argente, G., Gómez-Martín, M.E., Medina, J.R., 2018. Hydraulic stability of the armor layer of overtopped breakwaters. J. Mar. Sci. Eng. 6, 1–13. https://doi.org/10.3390/jmse6040143

Bae, H.U., Yun, K.M., Yoon, J.Y., Lim, N.H., 2016. Human stability with respect to overtopping flow on the breakwater. Int. J. Appl. Eng. Res. 11, 111–119.

Battjes, J.A., Groenendijk, H.W., 2000. Wave height distributions on shallow foreshores. Coast. Eng. 40, 161–182. https://doi.org/10.1016/S0378-3839(00)00007-7

Camus, P., Tomás, A., Díaz-Hernández, G., Rodríguez, B., Izaguirre, C., Losada, I.J., 2019. Probabilistic assessment of port operation downtimes under climate change. Coast. Eng. 147, 12–24. https://doi.org/10.1016/j.coastaleng.2019.01.007

Endoh, K., Takahashi, S., 1995. Numerically modeling personnel danger on a promenade breakwater due to overtopping waves, in: Proc. 24th International Conference on Coastal Engineering. pp. 1016–1029.

EurOtop. A manual on wave overtopping of sea defences and related structures. An overtopping manual largely based on European research but for worldwide Application, 2018. Van der Meer, J. W.; Allsop, N.W.H.; Bruce, T.; De Rouck, J.; Kortenhaus, A.; Pullen, T.; Schüttrumpf, H.; Troch, P.; Zanuttigh, B. www.overtopping-manual.com.

Figueres, M., Medina, J.R., 2005. Estimating incident and reflected waves using a fully nonlinear wave model, in: Proc. 29th International Conference on Coastal Engineering. Lisboa (Portugal), pp. 594–603. https://doi.org/10.1142/9789812701916-0047

Formentin, S.M., Gaeta, M.G., Palma, G., Zanuttigh, B., Guerrero, M., 2019. Flow Depths and Velocities across a Smooth Dike Crest. Water 11, 2197. https://doi.org/10.3390/w11102197

Formentin, S.M., Zanuttigh, B., van der Meer, J.W., 2017. A Neural Network Tool for Predicting Wave Reflection, Overtopping and Transmission. Coast. Eng. J. 59, 1750006-1-1750006–31. https://doi.org/10.1142/S0578563417500061

Goda, Y., 1985. Random Seas and Design of Maritime Structures. University of Tokyo Press, Tokyo, Japan.

Gómez-Martín, M.E., Medina, J.R., 2014. Heterogeneous Packing and Hydraulic Stability of Cube and Cubipod Armor Units. J. Waterw. Port, Coastal, Ocean Eng. 140, 100–108. https://doi.org/10.1061/(ASCE)WW.1943-5460.0000223

Herrera, M.P., Gómez-Martín, M.E., Medina, J.R., 2017. Hydraulic stability of rock armors in breaking wave conditions. Coast. Eng. 127, 55–67. https://doi.org/10.1016/j.coastaleng.2017.06.010

Herrera, M.P., Medina, J.R., 2015. Toe berm design for very shallow waters on steep sea bottoms. Coast. Eng. 103, 67–77. https://doi.org/10.1016/j.coastaleng.2015.06.005

Hughes, S.A., Thornton, C.I., Van der Meer, J.W., Scholl, B., 2012. Improvements in describing wave overtopping processes. Proc. 33rd Int. Conf. Coast. Eng. [SI], 1–15. https://doi.org/10.9753/icce.v33.waves.35

Lorke, S., Scheres, B., Schüttrumpf, H., Bornschein, A., Pohl, R., 2012. Physical model tests on wave overtopping and flow processes on dike crests influenced by wave-current interaction. Coast. Eng. Proc. 1–13. https://doi.org/10.9753/icce.v33.waves.34

Mansard, E.P.D., Funke, E.R., 1980. The Measurement of Incident and Reflected Spectra Using a Least squares Method, in: Proc. 17th International Conference on Coastal Engineering. ASCE, pp. 154–172.

Mares-Nasarre, P., Argente, G., Gómez-Martín, M.E., Medina, J.R., 2019. Overtopping layer thickness and overtopping flow velocity on mound breakwaters. Coast. Eng. 154, 103561. https://doi.org/10.1016/J.COASTALENG.2019.103561

Mares-Nasarre, P., Gómez-Martín, M.E., Medina, J.R., 2020a. Influence of mild bottom slopes on the overtopping flow over mound breakwaters under depth-limited breaking wave conditions. J. Mar. Sci. Eng. 8. https://doi.org/10.3390/JMSE8010003

Mares-Nasarre, P., Molines, J., Gómez-Martín, M.E., Medina, J.R., 2020b. Individual wave overtopping volumes on mound breakwaters in breaking wave conditions and gentle sea bottoms. Coast. Eng. 159, 103703. https://doi.org/10.1016/j.coastaleng.2020.103703

Melby, J.A., 1999. Damage progression on Rubble Mound Breakwaters. Vicksburg, MS, USA. Also Ph.D. Thesis, University of Delaware, Newark, DE, USA.

Molines, J., Herrera, M.P., Medina, J.R., 2018. Estimations of wave forces on crown walls based on wave overtopping rates. Coast. Eng. 132, 50–62. https://doi.org/10.1016/j.coastaleng.2017.11.004

Molines, J., Medina, J.R., 2016. Explicit wave-overtopping formula for mound breakwaters with crown walls using CLASH neural network-derived data. J. Waterw. Port, Coast. Ocean Eng. 142. https://doi.org/10.1061/(ASCE)WW.1943-5460.0000322

Molines, J., Medina, J.R., 2015. Calibration of overtopping roughness factors for concrete armor units in non-breaking conditions using the CLASH database. Coast. Eng. 96, 62–70. https://doi.org/10.1016/j.coastaleng.2014.11.008

Nørgaard, J.Q.H., Lykke Andersen, T., Burcharth, H.F., 2014. Distribution of individual wave overtopping volumes in shallow water wave conditions. Coast. Eng. 83, 15–23. https://doi.org/10.1016/j.coastaleng.2013.09.003

Sandoval, C., Bruce, T., 2017. Wave overtopping hazard to pedestrians: video evidence from real accidents, in: Proc. Of Coasts, Marine Structures and Breakwaters 2017. Realising the Potential. Liverpool Waterfront, UK, pp. 501–512.

Schüttrumpf, H., Möller, J., Oumeraci, H., 2002. OVERTOPPING FLOW PARAMETERS ON THE INNER SLOPE OF SEADIKES, in: Proc. 28th International Conference on Coastal Engineering. World Scientific Publishing Company, pp. 2116–2127. https://doi.org/10.1142/9789812791306_0178

Schüttrumpf, H., Van Gent, M.R.A., 2003. Wave overtopping at seadikes, in: Coastal Structures 2003 - Proceedings of the Conference. pp. 431–443.

The MathWorks Inc., 2019. MATLAB®.

Theil, H., 1961. Economic forecasts and policy. North, Amsterdam (Holland).

van Bergeijk, V.M., Warmink, J.J., van Gent, M.R.A., Hulscher, S.J.M.H., 2019. An analytical model of wave overtopping flow velocities on dike crests and landward slopes. Coast. Eng. 149, 28–38. https://doi.org/10.1016/j.coastaleng.2019.03.001

van der Meer, J.W., Hardeman, B., Steendam, G.J., Schüttrumpf, H., Verheij, H., 2010. FLOW DEPTH AND FLOW VELOCITY AT CREST AND LANDWARD SLOPE OF A DIKE, IN THEORY AND WITH THE WAVE OVERTOPPING SIMULATOR. Coast. Eng. Proc. [SI]. https://doi.org/https://doi.org/10.9753/icce.v32.structures.10

van Gent, M.R.A., 2002. WAVE OVERTOPPING EVENTS AT DIKES, in: Scientific, W. (Ed.), Proc. 28th International Conference on Coastal Engineering. World Scientific Publishing Company, Cardiff, UK, pp. 2203–2215. https://doi.org/10.1142/9789812791306_0185

van Gent, M.R.A., 2001. Wave Runup on Dikes with Shallow Foreshores. J. Waterw. Port, Coastal, Ocean Eng. 127, 254–262. https://doi.org/10.1061/(ASCE)0733-950X(2001)127:5(254)

van Gent, M.R.A., 1999. Physical model investigations on coastal structures with shallow foreshores. 2D model tests with single and double-peaked wave energy spectra. Delft (The Netherlands).

van Gent, M.R.A., van den Boogaard, H.F.P., Pozueta, B., Medina, J.R., 2007. Neural network modelling of wave overtopping at coastal structures. Coast. Eng. 54, 586–593. https://doi.org/10.1016/j.coastaleng.2006.12.001

Verhagen, H.J., van Vledder, G., Arab, S.E., 2008. A practical method for design of coastal structures in shallow water, in: Proc. 31st International Conference on Coastal Engineering. World Scientific Publishing Company, pp. 2912–2922. https://doi.org/https://doi.org/10.1142/9789814277426_0241

5. **Mares-Nasarre, P., van Gent, M.R.A, 2020. Oblique Wave Attack on Rubble Mound Breakwater Crest Walls of Finite Length. Water 12, Article number 353. https://doi.org/10.3390/w12020353**

Oblique Wave Attack on Rubble Mound Breakwater Crest Walls of Finite Length

Patricia Mares-Nasarre [1,] * and Marcel R.A. van Gent[2]

[1]Lab. Ports and Coasts, Institute of Transport and Territory, Universitat Politècnica de València; patmana@cam.upv.es

[2]Department Coastal Structures & Waves, Deltares; marcel.vangent@deltares.nl

***** Corresponding author: patmana@cam.upv.es

Abstract:

Rubble mound breakwaters usually present a crest wall to increase the crest freeboards without a large increase of the consumption of material. Methods in the literature to design crest walls are based on estimates of the wave loads. These methods are focused on the maximum loading that attacks a single position of the crest wall. In practice, crest walls have a finite length. Since the maximum loading does not occur at the same instant over the entire length of the crest wall for oblique waves, these methods overestimate the loading in the situation of oblique waves. Wave loads under oblique wave attack have been measured in physical model tests. A method to account for the effect of the finite length of crest walls has been developed, and design guidelines have been derived. The results of this study in combination with the existing methods in the literature to estimate the wave forces enable a more advanced design of crest walls.

Keywords: crown wall; crest wall; oblique waves; rubble mound breakwaters; wave loading; forces

1. Introduction

Crest walls are usually built on top of rubble mound breakwaters to achieve higher crest freeboards without a severe increase in the amount of granular material needed. They also protect the crest, improve the accessibility, and provide space for equipment and infrastructure. Crest walls, also called crown walls, are built with concrete and are located on top of the core. During storms, crest walls are impacted by waves, experiencing both (horizontal) forces at the front of the crest wall and (vertical uplift) forces underneath the crest wall. Such wave loads on crest walls determine their size, since crest walls are designed to allow minimal or no displacements under extreme wave conditions. Thus, an accurate prediction of wave loads on crest walls is essential for their design.

Guidelines for crest walls design *[1–3]* exist, but they are only valid within their range of tested cross sections. In *[4]*, a numerical model is presented to estimate wave loads on the crest walls of rubble mound breakwaters. This model provides valuable estimates of the wave loads for cross-sections that have not been tested before (under perpendicular wave attack). Oblique wave attack has been proven to affect the wave loads on crest walls in *[3,5]*. *[5]* conducted a systematic study on the reduction of the wave loads on crest walls due to the obliqueness of waves and derived a method to account for such an effect.

All the studies related to wave loads on crest walls on rubble mound breakwaters are focused on the (horizontal or vertical) forces that attack the breakwater cross-section (maximum loading). In practice, a crest wall on a rubble mound breakwater has a finite length (e.g., with expansion joints between two parts of the crest wall). If the maximum loading on a single position is used for the entire length of the crest wall, the loading will be overestimated for situations with oblique waves, because the maximum loading does not occur at the same time over the entire length of the crest wall. In other words, methods in the literature assume a rectangle-shaped force diagram all along the crest wall length. This means that the actual reduction in the forces on the entire crest wall due to the oblique waves is more significant than simply applying the method proposed by *[3,5]*, which is valid for one position (chainage) along the breakwater. Therefore, this study is focused on the influence of finite length on crest walls under oblique wave attack.

The structure of this paper is as follows. In Section 2, a brief overview of the methods in the literature to estimate wave forces on crest walls is presented. A summary of the findings in *[5]* is given, since it is the only systematic study found in the literature on the reduction of the wave loads on crest walls due to the oblique wave attack. In Section 3, the physical model tests are described. Here, the tests conducted by *[5]* in a wave basin are used. In Section 4, the analysis of the tests results is presented. The temporal shape of the force events is described and transformed into the space domain. The actual force that attacks the crest wall is integrated, and a length coefficient is proposed in order to account the force reduction due to the length of the crest wall. Finally, in Section 5, conclusions are drawn.

2. Oblique Wave Attack on Forces on Rubble Mound Breakwaters Crest Walls

Sliding is the most common failure mode for crest walls on mound breakwaters. The crest wall is stable when the horizontal force that attacks the structure is lower than the friction resistance, which may be affected by the ascending uplift. The stability of the crest wall for the sliding failure mode is guaranteed by building the crest wall with enough weight. The required size of crest walls is usually determined in physical model tests in wave flumes or wave basins. Before such tests, a first approximation of the needed size of the crest wall must be done by estimating the wave loads. The better the approximation, the shortest the test campaign and the lower the costs. Estimates of wave loads can be obtained from both numerical models and empirical expressions.

An extensive literature exists on methods to estimate forces on crest walls on mound breakwaters. The first approaches were empirical expressions *[1,6–12]* derived from experimental campaigns. Several proposals *[1,3,5,7,10,12]* were based on the estimates of virtual wave run-up levels ($Ru_{2\%}$), which are the wave run-up levels that would be reached in the case of extending the armor layer. More recent methods use numerical models *[4]* and neural networks estimations *[2]*. All the mentioned methods except *[3]* and *[5]* are based on physical model tests in wave flumes with perpendicular wave attack or the numerical modeling of structures under perpendicular wave attack.

[5] was the first systematic study on the effect of oblique waves on the wave loads on crest walls of rubble mound breakwaters. *[5]* conducted physical model tests in a wave basin using wave attack angles β = 0°, 15°, 30°, 60, 45°, and 75°, where β = 0° corresponds to perpendicular wave attack. Two crest walls geometries (with and without a key) and two wave steepness ($s_{m-1,0} = 2\pi H_s/gT_{m-1,0}^2 = 0.018$ and 0.048, which tested H_s as the significant wave height and $T_{m-1,0} = m_{-1}/m_0$ as the spectral wave period). *[5]* derived new estimators for the horizontal and vertical forces exceeded by 0.1% of the incoming waves ($F_{H,0.1\%}$ and $F_{V,0.1\%}$) based on $Ru_{2\%}$ (see Equations (1) and (2)).

$$F_{H,0.1\%} = K_{e,H}\,\rho\,g\,H_{wall}\,(Ru_{2\%} - A_C) \tag{1}$$

$$F_{V,0.1\%} = K_{e,V}\,c_{F,v}\,\rho\,g\,B_{wall}\,(Ru_{2\%} - 0.75\,A_C)\left(1 - \left[\frac{F_b}{A_C}\right]^{0.5}\right) \tag{2}$$

where $K_{e,H} = 1.6$, $K_{e,v}$ and $c_{F,v}$ are empirical coefficients, ρ is the density, g is the gravity acceleration, H_{wall} is the height of the crest wall including the key (if any), A_C is the crest level of the armor in front of the crest wall, B_{wall} is the width of the crest wall including the key (if any), and F_b is the level of the bottom of the base plate of the crest wall above the still water level. $K_{e,v}$ was calibrated as a function of the $s_{m-1,0}$; $K_{e,v} = 2.4$ for $s_{m-1,0} = 0.018$; and $K_{e,v} = 1.6$ for $s_{m-1,0} = 0.048$ ($F_{v,0.1\%} = (2.88\text{-}32 s_{op})\,F_{v,2\%}$, see *[3]*). $c_{F,v}$ includes the reduction of the vertical forces due to the presence of a key; $c_{F,v} = 0.4$ includes those for the crest wall configuration without key, and $c_{F,v}$ = 0.3 includes those for the crest wall configuration with a key.

[5] included the effect of oblique waves through $Ru_{2\%}$. Equation (3) given in *[13,14]* was proposed to estimate $Ru_{2\%}$.

$$\begin{cases} \dfrac{Ru_{2\%}}{\gamma\, H_s} = c_0 \xi_{m-1,0} \quad for\ \xi_{m-1,0} \leq p \\ \dfrac{Ru_{2\%}}{\gamma\, H_s} = c_1 - \dfrac{c_2}{\xi_{m-1,0}}\ for\ \xi_{m-1,0} \geq p \end{cases} \tag{3}$$

where $\gamma = \gamma_f\, \gamma_\beta$ is the reduction factor to take into account the effect of both the roughness and the oblique wave attack, respectively, $\xi_{m-1,0} = tan\alpha/(2\pi H_s/gT_p^2)^{0.5}$ is the surf-similarity parameter or Iribarren number, c_0 = 1.45, c_1 = 5.0, $c_2 = 0.25\ c_1^2/c_0$, and $p = 0.5c_1/c_0$. *[5]* used γ_f = 0.45 for the double-layer rock armor and proposed a new expression for γ_β.

$$\gamma_\beta = 0.5\ cos^2\beta + 0.5 \tag{4}$$

where β is the wave direction at the toe of the structure, where $\beta = 0°$ corresponds to perpendicular wave attack.

The mentioned methods propose expressions to calculate the maximum wave loading of the crest wall in a single position (chainage) along its length. No methods that incorporate the effect of finite length in the estimation of the wave loading of the crest walls on mound breakwaters are known.

3. Experimental Methodology

3.1. Test Set-Up

In this study, the tests by *[5]* are used. Those tests were conducted in the Delta Basin (50m × 50m) at Deltares, Delft. Waves were generated using a multi-directional wave board composed of 100 paddles and equipped with both active absorption and second-order wave steering. This means that the motion of the paddles compensates for the wave reflected by the structure in order to prevent them from re-reflecting on the wave paddles and that the second-order effects of the first lower and higher harmonics of the wave field are considered, ensuring that the generated waves resemble waves that occur in nature.

The experimental set-up in the wave basin is illustrated in Figure 1. A structure with a width of 18.3 m was built with an angle of 37.5° between the model and the wave generator. Gravel beaches were built on both sides of the model to ensure wave damping in the basin.

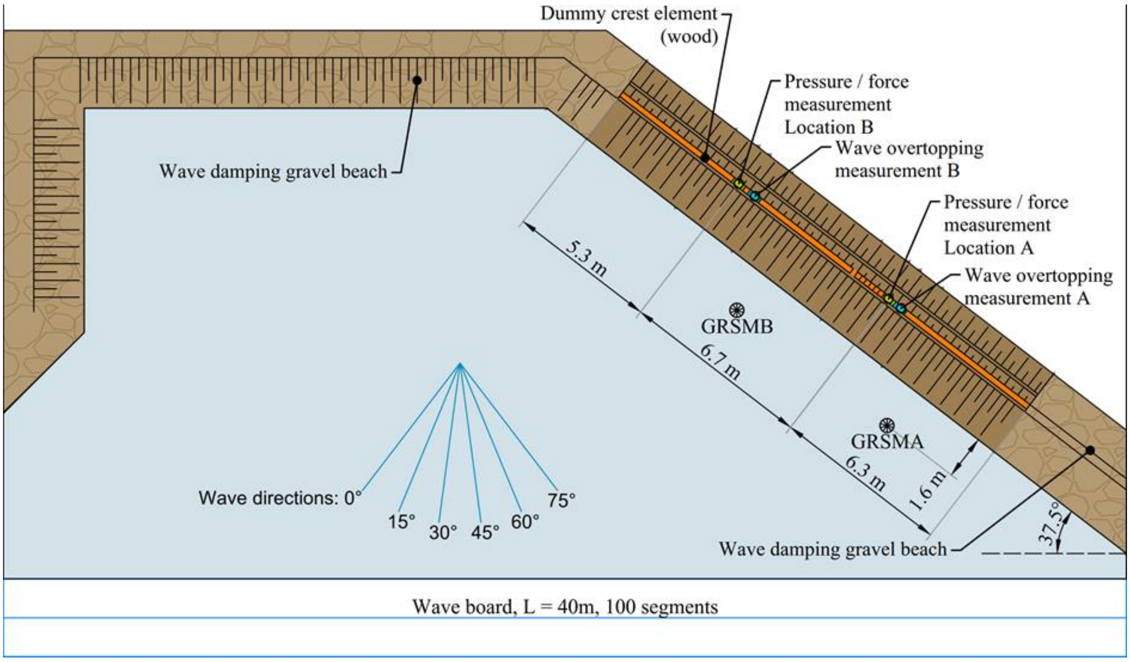

Figure 1. Tests set-up in the wave basin *[5]*.

The tested cross-section corresponds to a rubble mound breakwater with 1:2 slope and two crest walls configurations. The model cross-section is depicted in Figure 2. A double-layer rock armor with high density stones (Δ = 2.69) is used in order to limit the armor damage during the tests while keeping a realistic size of the stones. A 1:1.5 slope was used in the rear side of the structure.

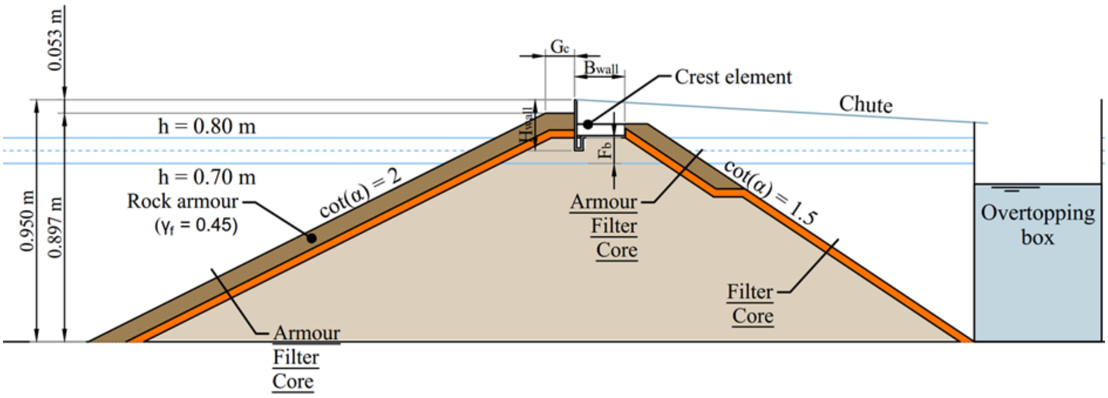

Figure 2. Tested cross-section [5].

Figure 3 presents the two crest wall configurations used in the tests, made of aluminum, as well as the location of the pressure transducers. The two crest walls configurations are identical except for the key placed at the intersection between the front wall and the bottom of the crest wall. The presence of a key is desirable from the geotechnical perspective, since the passive earth pressure is increased. Crest wall A does not present the key, while Crest wall B does. Pressures were measured at the front side of the crest wall and underneath it for both crest wall configurations using 18 pressure transducers. These transducers have a frequency response of 5 kHz, an accuracy of 0.06% of the full scale (Best Straight Line), and a range of 350 mBar. In Crest wall A, five pressure transducers were located in the front wall, and three pressure transducers were placed in the baseplate. In Crest wall B, two additional pressure transducers were located: one in the front wall and one in the baseplate. No movement of crest walls was ensured by fixing them to steel frames, as shown in Figure 4.

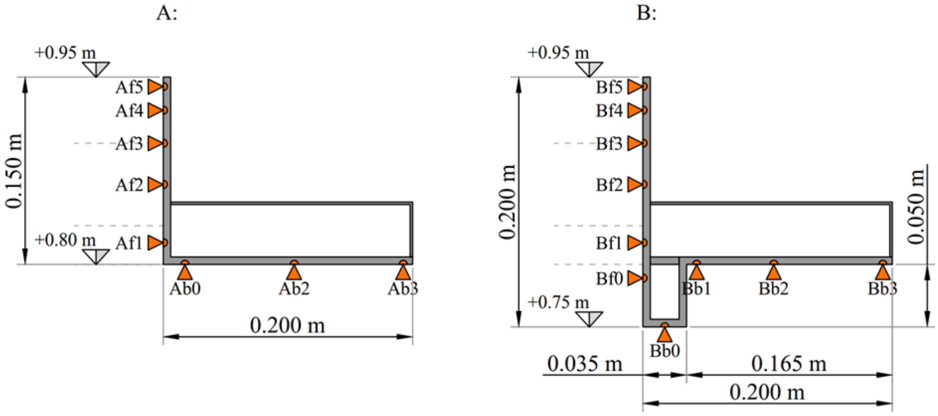

Figure 3. Tested crest wall cross-sections and location of the pressure transducers *[5]*.

Figure 4. Experimental set-up during a test with oblique waves.

Waves were measured using directional wave gauges (GRSM) at two locations in front of the model so the incident and reflected waves could be separated. The directional wave gauges were located to be in the same line as the measurement cross-sections for a wave angle of 37.5°, which is the average of all the tested angles and perpendicular to the wave paddle (see Figure 1). Small variations observed between both measurement points were accounted for in the following analysis; measurements of GRSM-A were used for Test section A, and measurements of GRSM-B were used for Test section B. In following analysis, incident waves at these locations at the toe were used. The spectral significant wave height ($H_s = H_{m0} = 4\sqrt{m_0}$) and the spectral mean wave period ($T_{m-1,0} = m_{-1}/m_0$) were obtained from the measured wave energy spectra. $T_{m-1,0}$ was first found to better describe the influence of wave energy spectra on wave run-up and overtopping in *[13,14]*. Later, $T_{m-1,0}$ was applied as the best wave period to describe other interaction processes between waves and coastal structures, see for instance *[15]*. Thus, this spectral wave period was also used in this study. The mean overtopping discharge was also measured in *[5]*, using two overtopping chutes and boxes (see Figure 5).

Parameter	**Symbol**	**Value/Range**
Seaward side slope angle (-)	$\cot\alpha$	2
Dimensionless crest freeboard (-)	R_c/H_s	0.84–1.60
Ratio crest level of crest wall and armor (-)	R_c/A_c	1.27–1.55
Dimensionless level of base plate (-)	F_b/H_s	0–0.56
Wave height over water depth ratio (-)	H_s/h_s	0.13–0.27
Surf similarity parameter (-)	$\xi_{m-1,0}$	2.3 and 3.7
Number of waves (-)	N	1000
Wave angles at the toe (°)	β	0–75
Incident wave height (m)	H_s	0.10–0.19
Water depth at the toe (m)	h_s	0.70–0.80
Crest wall freeboard (m)	R_C	0.15–0.25
Crest level of the armor layer crest (m)	A_C	0.097–0.197
Crest width of the armor layer (m)	G_C	0.114
Level base plate relative to the wave level (m)	F_b	0–0.10
Height of the crest wall (m)	H_{wall}	0.15 and 0.2
Width of the crest wall (m)	B_{wall}	0.20

Table 1. Summary of the parameter ranges of the test program.

Runs of 1000 random waves were generated following a JONSWAP wave spectrum (peak enhancement factor of 3.3). Each configuration was tested with a constant value of $s_{m-1,0}$ = 0.018 or 0.048. Six wave directions were considered β = 0°, 15°, 30°, 60, 45°, and 75°, where β = 0° corresponds to the perpendicular wave attack. Three water depths, h_s = 0.70, 0.75, and 0.80 m, and crest freeboards, R_C = 0.15, 0.20 and 0.25 m, were used. For the lowest h_s, only the perpendicular waves were tested, since most of the conditions with oblique waves would not have caused forces on the crest walls. In total, 30 tests were used in this study. Table 1 summarizes the main experimental ranges in these tests.

3.2. Test Results

As previously mentioned, 18 pressure transducers were used to measure the pressure signals on the crest walls. Their sampling frequency was 1000 Hz. Before a test, the transducers were set to zero, so the measurements were relative to the pressures caused by the still water level and hydrostatic forces were not included in the measurements. This is especially relevant for Crest wall B, since the key is submerged during the tests with the higher water depth.

Each pressure transducer provided a point of pressure (kN/m^2). The pressure distribution along the front and base of the crest wall was obtained by assembling the points of pressure (see Figure 5). The pressure distribution was extrapolated toward the edges of the crest wall. Pressure transducers were located as close as possible to the edges of the crest wall to minimize extrapolation, and the extrapolated pressures were set to a lower limit of 0. In Figure 6, the extrapolation zone is indicated with blue dashed lines. The pressure distribution was integrated along the front and base of the crown wall to obtain the force on the crest wall. It resulted in a horizontal force on the front of the crest wall (F_H) and a vertical force on its base (F_V).

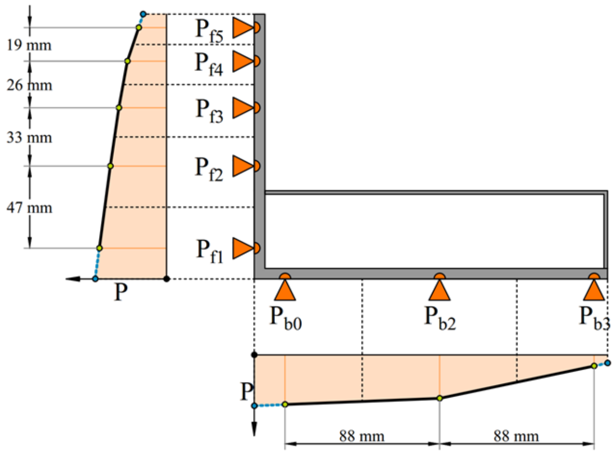

Figure 5. Pressure integration principle *[5]*.

In this study, the temporal shape of the (horizontal and vertical) force events was studied. Thus, the duration of the force events and the time of the peak (t_{peak}) was determined. The start, t_{peak}, and end of the force events were determined for both horizontal and vertical forces. They were extracted in three steps: (1) peaks were identified applying the Peaks-Over-Threshold method; in case of two peaks closer than 0.5 s, only the maximum was considered; (2) zero-up and zero-down crossing points were determined using a threshold of 2 to account the points slightly above zero and related to each peak as the start and end points of the force event; and (3) correction was applied in case the start and end points were located even more above zero. If two peaks presented the same start or end point, it was replaced by the minimum value between both peaks. The duration is calculated as the difference between the start and end of the force event. The exceedance values used in this study are not based on the total number of force peaks but rather on the number of waves within a test. Note that some vertical force registers were discarded, since the events were too low to be distinguished. Therefore, 59 duration values (29 for Crest wall A + 30 for Crest wall B) were obtained for the horizontal forces, while 47 (22 for Crest wall A + 25 for Crest wall B) were identified for vertical forces. An example of the determination of beginning and ending points is displayed in Figure 6 for vertical forces of Test #10 on Crest wall A.

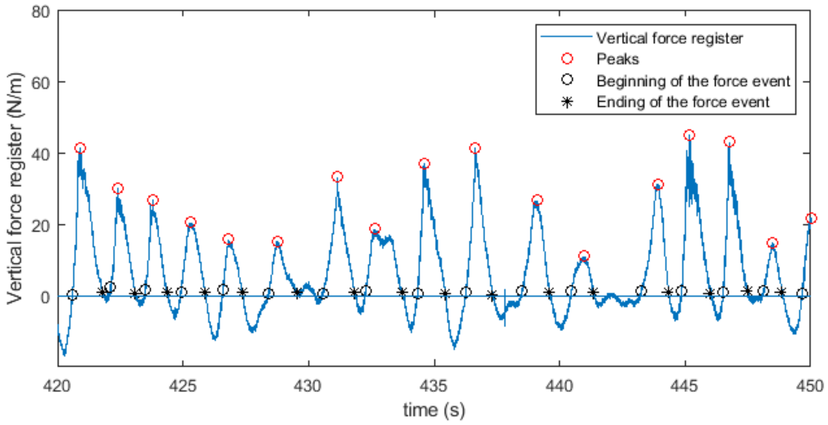

Figure 6. Example of determination of beginning, peak, and ending point for vertical forces of Test #10 on Crest wall A.

As *[5]* pointed out, it is common practice to assume that the maximum value registered in tests is the maximum (horizontal or vertical) force, which lasts 1000 waves (force exceeded by 0.1% of the incoming waves) *[1,2,11]*. However, the smaller the exceedance probability, the more hampered the value is by the coincidence within a test. Thus, *[5]* compared the maximum forces (peak of the force event) within a test (forces exceeded by 0.1% of the incoming waves) with the forces exceeded by 2% of the incoming waves. An almost constant ratio was observed for the horizontal forces and for many vertical forces. Here, a similar comparison is conducted for the duration and the position of the peak (t_{peak}) to determine whether the force event exceeded by 2% of the incoming waves is a valid approach to describe the shape of the maximum force events (see Figure 7).

In order to assess the correlation between the variables, the correlation coefficient ($-1 \leq r \leq 1$) was used. Here, the higher the absolute value of r, the higher the correlation.

$$r = \frac{\sum_{i=1}^{N_o}(t_i - \bar{t})(e_i - \bar{e})}{\sqrt{\sum_{i=1}^{N_o}(t_i - \bar{t})^2 \sum_{i=1}^{N_o}(e_i - \bar{e})^2}} \tag{5}$$

where N_o is the number of observations, t_i are the first variable observations, e_i are the corresponding observations of the second variable, and $\bar{t}$ and $\bar{e}$ are the average values of both variables.

As shown in Figure 7, reasonable correlation (r = 0.790) was found for the duration of the horizontal force events exceeded by 0.1% and 2% of the incoming waves ($duration_{H,0.1\%}$ and $duration_{H,2\%}$). Poor correlation ($0.148 \leq r \leq 0.392$) was observed for the duration of the vertical force events exceeded by 0.1% and 2% of the incoming waves ($duration_{V,0.1\%}$ and $duration_{V,2\%}$), as well as for the position of the peak (*tpeak*) of both horizontal and vertical force events exceeded by 2% and 0.1% of the incoming waves. As a result, it was decided to conduct the following analysis using the force events exceeded by 0.1% of the incoming waves.

4. Results

In this section, the temporal shape of the (horizontal and vertical) force events is discussed. A triangle-shaped model is proposed. Therefore, the base width and the height of that triangle are needed to characterize the temporal shape. The formulas given in [5] are used to estimate the maximum loading (height) for both the horizontal and the vertical forces. Formulas to calculate the duration of the force events and the velocity at which the force events travel along the structure are proposed. This way, the duration is transformed into the space domain (base width); a force diagram along the longitudinal dimension of the crest wall is obtained. This study assumes that the force received by a point of the crest wall in a certain instant is at some point of the spatial force diagram, and the rest of the points receive forces according to the shape of that diagram. The force diagram is integrated to estimate the actual force that attacks the crest wall, including the finite length effect. Such force is compared to the force obtained using the existing methods and a coefficient to account for the effect of finite length on crest walls under oblique wave attack is given.

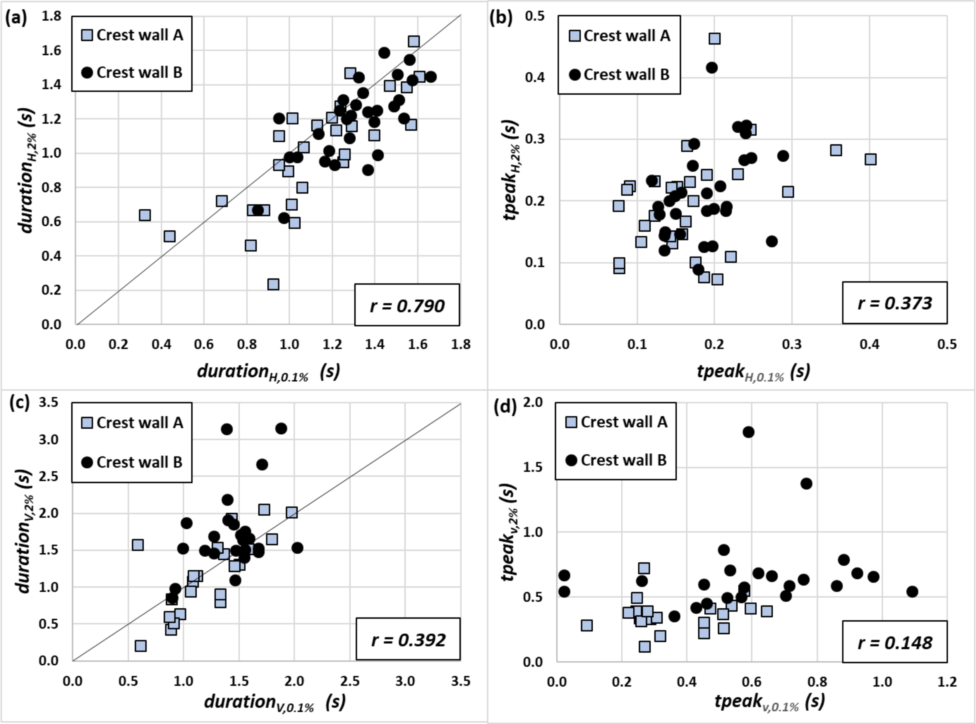

Figure 7. Comparison between: (a) duration of the horizontal force event exceeded by 0.1% and 2% of incoming waves ($duration_{H,0.1\%}$ and $duration_{H,2\%}$), (b) position of the peak of the horizontal force event exceeded by 0.1% and 2% of incoming waves ($tpeak_{H,0.1\%}$ and $tpeak_{H,2\%}$), (c) duration of the vertical force event exceeded by 0.1% and 2% of incoming waves ($duration_{V,0.1\%}$ and $duration_{V,2\%}$), and (d) position of the peak of vertical force event exceeded by 0.1% and 2% of incoming waves ($tpeak_{V,0.1\%}$ and $tpeak_{V,2\%}$).

4.1. Temporal Shape of Force Events

In this section, the temporal shape of the force events is discussed and parameterized. In Figure 8, typical registers for horizontal and vertical forces are presented.

In Section 3.2, it was decided to analyze the maximum force event in each test (force events exceeded by 0.1% of the incoming waves). The maximum force event is extracted for each test, and a new register is created grouping them (Extracted register, from now). A five-second spacing was left between the events in order to allow for the afterwards analysis. Figure 9 shows a fragment of such an Extracted register.

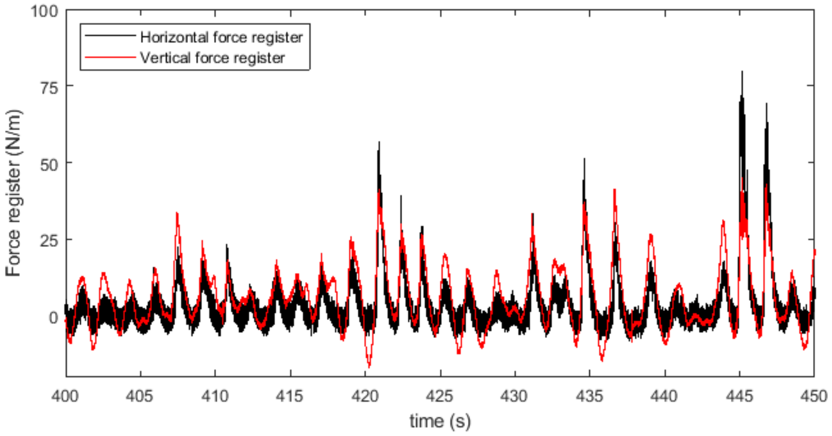

Figure 8. Typical register for horizontal and vertical forces (Test #10, Crest wall A).

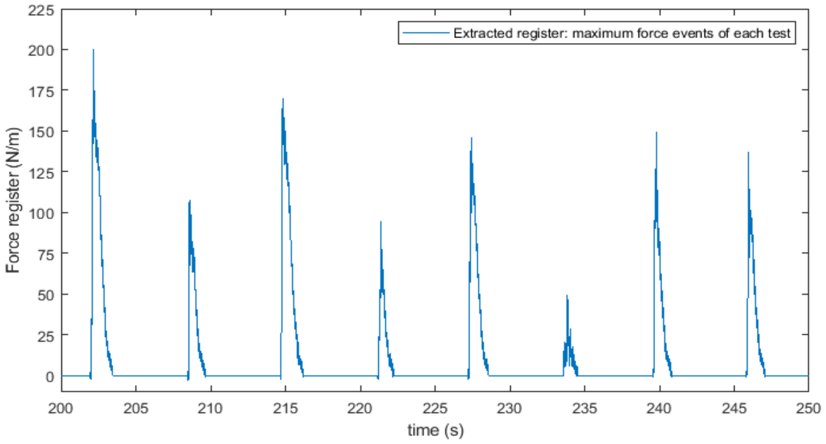

Figure 9. Extracted register made by grouping the maximum force events of each test (horizontal forces).

A triangle-shaped model is proposed for the temporal shape of the force events. In order to assess the goodness of fit of such a model, the correlation between the Extracted register and a new triangle-shaped register is evaluated. The new triangle-shaped register is created using the measured duration and the measured peak values of the forces. The location of the peak value of the force ($tpeak_{0.1\%}$) is calculated as function of the duration of the horizontal or vertical force event ($duration_{0.1\%}$), as shown in Equation (6).

$$tpeak_{0.1\%} = K_{peak}\ duration_{0.1\%} \tag{6}$$

where K_{peak} is an experimental coefficient. K_{peak} is calibrated for both horizontal and vertical forces in order to maximize the correlation with the Extracted register. $K_{peak} = 0.1$ and $K_{peak} = 0.35$ are obtained for horizontal and vertical forces, respectively; $0.912 \leq r \leq 0.924$. Figure 10 shows the superposition of the Extracted register (the actual maximum force events) and the triangle-shaped model.

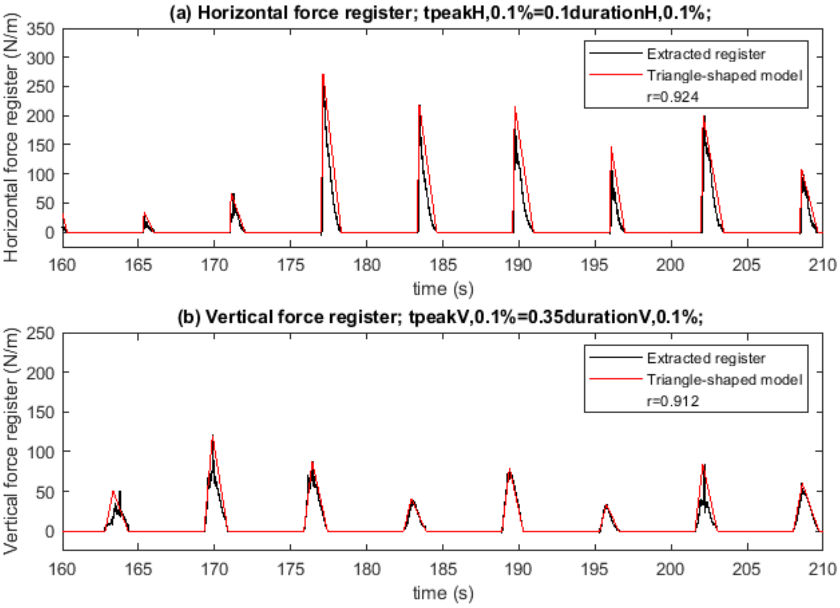

Figure 10. Comparison of Extracted register (the actual maximum force events) and the triangle-shaped model using the measured $F_{H,0.1\%}$, $F_{V,0.1\%}$, and $duration_{0.1\%}$ for: (a) horizontal forces, and (b) vertical forces.

4.2. Duration of Force Events

As mentioned in Section 3.2, 59 values (29 for Crest wall A + 30 for Crest wall B) and 47 (22 for Crest wall A + 25 for Crest wall B) of the duration corresponding to the force exceeded by 0.1% of incoming waves ($duration_{0.1\%}$) were obtained for the horizontal ($duration_{H,0.1\%}$) and vertical ($duration_{V,0.1\%}$) forces, respectively. $duration_{H,0.1\%}$ and $duration_{V,0.1\%}$ corresponding to the same test were compared in order to determine if they present the same behavior. Note that 47 $duration_{0.1\%}$ values could be compared (i.e., the minimum number of $duration_{0.1\%}$ values, which corresponds to the vertical forces). Figure 11 compares $duration_{H,0.1\%}$ and $duration_{V,0.1\%}$ corresponding to the same test.

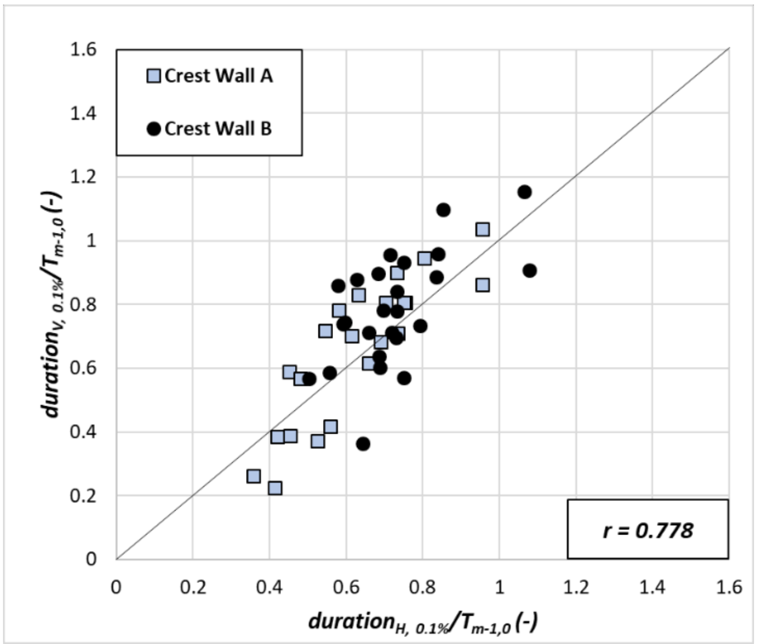

Figure 11. Comparison between the measured dimensionless *duration*$_{0.1\%}$ (*duration*$_{0.1\%}/T_{m-1,0}$) for horizontal and vertical forces.

Reasonable correlation was observed (r = 0.778) between $duration_{H,0.1\%}$ and $duration_{V,0.1\%}$. Thus, it is reasonable to analyze them together. Equation (7) was proposed to estimate $duration_{0.1\%}$, based on the difference between $Ru_{2\%}$ and A_C.

$$duration_{0.1\%} = 5\sqrt{H_{wall}\,\frac{\gamma_\beta\,(Ru_{2\%} - A_C)}{H_s}} \tag{7}$$

Note that if $A_C \geq Ru_{2\%}$, no waves reach the crest, which leads to $duration_{0.1\%} = 0$. Equation (7) also shows that the duration of the force event increases for the larger crest walls (H_{wall}); larger crest walls are a bigger obstacle to dissipating phenomena (infiltration and wave overtopping), such that the water remains longer at the breakwater crest. Equation (7) is valid within the ranges $0.260 \leq \gamma_\beta\,(Ru_{2\%} - A_C)/H_s \leq 0.863$. In order to assess the goodness of fit, r and the relative mean squared error ($rMSE$) were used.

$$rMSE = \frac{MSE}{var} = \frac{\frac{1}{N_o}\sum_{i=1}^{N_o}(t_i - e_i)^2}{\frac{1}{N_o}\sum_{i=1}^{N_o}(t_i - \bar{t})^2} \tag{8}$$

where MSE is the mean squared error, var is the variance of the target values, N_o is the number of observations, t_i and e_i are the target and estimated values, respectively, and $\bar{t}$

is the average of the target values. The variation coefficient (*CV*) of the data was also calculated as $CV = \sigma/\mu$, where σ is the standard deviation of the observations and μ is the observations' mean.

Figure 12 compares the measured and estimated dimensionless duration ($duration_{0.1\%}/T_{m-1,0}$) using Equation (7), as well as the 90% confidence interval. Here, $r = 0.726$ and $rMSE = 0.472$.

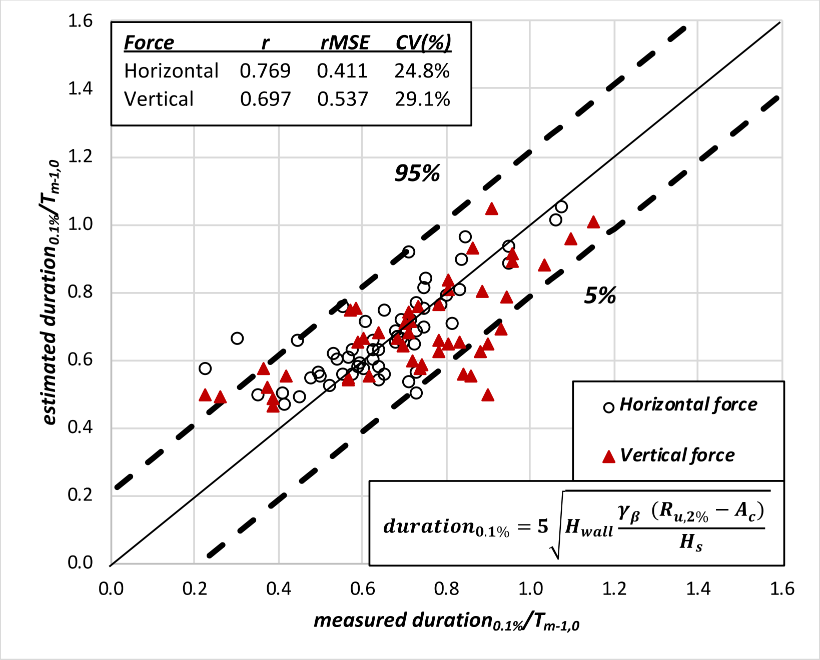

Force	r	rMSE	CV(%)
Horizontal	0.769	0.411	24.8%
Vertical	0.697	0.537	29.1%

$$duration_{0.1\%} = 5\sqrt{H_{wall}\frac{\gamma_\beta\,(R_{u,2\%} - A_c)}{H_s}}$$

Figure 12. Comparison between the measured and estimated dimensionless *duration*$_{0.1\%}$ using Equation (7).

The *MSE* remained stable with increasing values of $duration_{0.1\%}/T_{m-1,0}$. Thus, the 90% confidence interval was calculated based on the variance of the error ($var(\varepsilon) = 0.0167$). Assuming a Gaussian error distribution, the confidence interval is obtained as

$$\left.\frac{duration_{0.1\%}}{T_{m-1,0}}\right|_{5\%}^{95\%} = \frac{duration_{0.1\%}}{T_{m-1,0}} \pm 1.64\sqrt{var(\varepsilon)} = \frac{duration_{0.1\%}}{T_{m-1,0}} \pm 0.212 \qquad (9)$$

Similar to Section 4.1, the correlation between the Extracted register and a new triangle-shaped register was assessed. Here, the triangle-shaped register was created using the estimated $F_{H,0.1\%}$, $F_{V,0.1\%}$, and $duration_{0.1\%}$ using the method in *[5]* (Equations (1) to (4)) and Equation (7). $tpeak_{0.1\%}$ in Equation (6) was again calibrated by maximizing the correlation; $K_{peak} = 0.15$ and $K_{peak} = 0.35$ were obtained for horizontal and vertical forces, respectively; $0.874 \leq r \leq 0.879$. Figure 13 shows the superposition of the Extracted register (the actual maximum force events) and the triangle-shaped model generated with the estimated $F_{H,0.1\%}$, $F_{V,0.1\%}$, and $duration_{0.1\%}$. Note that if $(Ru_{2\%} - A_C) \leq 0$ or $(Ru_{2\%} - 0.75A_C) \leq 0$, $F_{H,0.1\%}$ or $F_{V,0.1\%}$ result in 0, respectively.

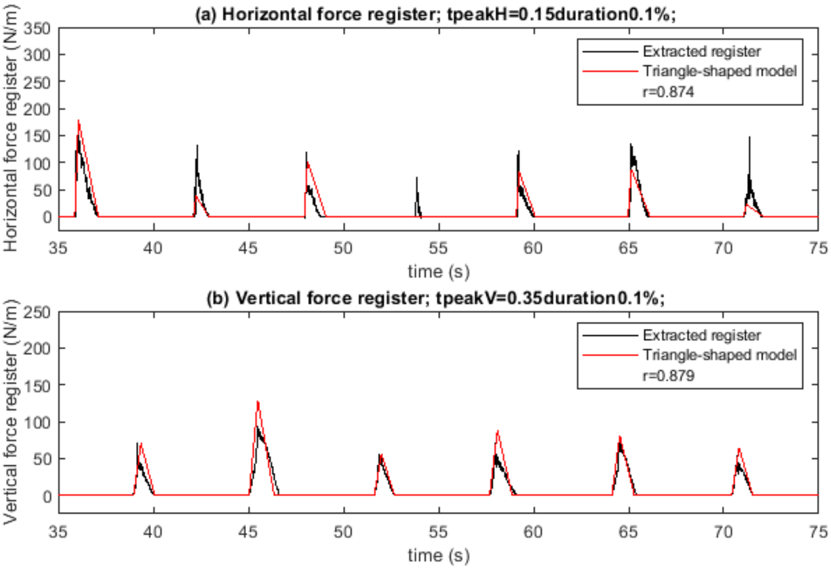

Figure 13. Comparison of Extracted register (the actual maximum force events) and the triangle-shaped model using the estimated $F_{H,0.1\%}$, $F_{V,0.1\%}$, and *duration*$_{0.1\%}$ for (a) horizontal forces and (b) vertical forces.

4.3. Travel Time and Velocity of Force Events

As discussed in Section 4.1, a triangle-shaped model is adopted for the time evolution of both horizontal and vertical force events. Since the area of a triangle depends on the base ($duration_{0.1\%}$) and the height (maximum loading), the method proposed in *[5]* (Equations (1) to (4)) and Equation (7) can be used to estimate the area of the actual force in the time domain. In order to transform the temporal shape into the space domain, the velocity (v_F) at which the force event travels is needed. To assess v_F, the travel time of the force events between the two measurement points was obtained. v_F was calculated dividing the distance between the measurement points (6.7 m) between the travel time.

In order to extract the travel time from the experimental registers, the register measured at point B (see Figure 1) was moved forward in steps of 0.01 s from 0 s (no displacement) to 5 s. For each step, the correlation between Register A and the displaced Register B was calculated. The travel time corresponded to the displacement time, which maximizes the correlation. This procedure could not be applied to three out of the 30 analyzed vertical force registers, since they were too low. Thus, 57 travel time values (30 values for horizontal forces and 27 for vertical forces) were obtained. Figure 14 shows an example of the exposed procedure for the horizontal force registers in Test #5, whereas Figure 15 presents a comparison between Register A and the original and displaced Register B until the travel time, which maximizes the correlation for Test #5.

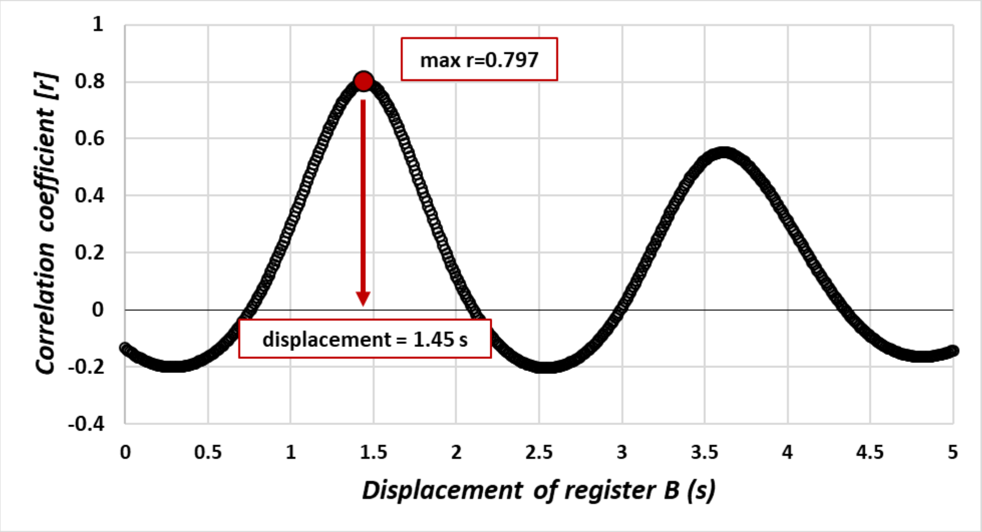

Figure 14. Example of the procedure to determine the travel time between the two measurement points (Test #5).

Once the travel time was determined for both the horizontal and vertical forces, the travel time values corresponding to the same test were compared to determine whether the behavior was equal for both types of forces (see Figure 16). In total, 27 pairs of values could be compared (minimum number of travel time values, which corresponds to those available from measured vertical forces).

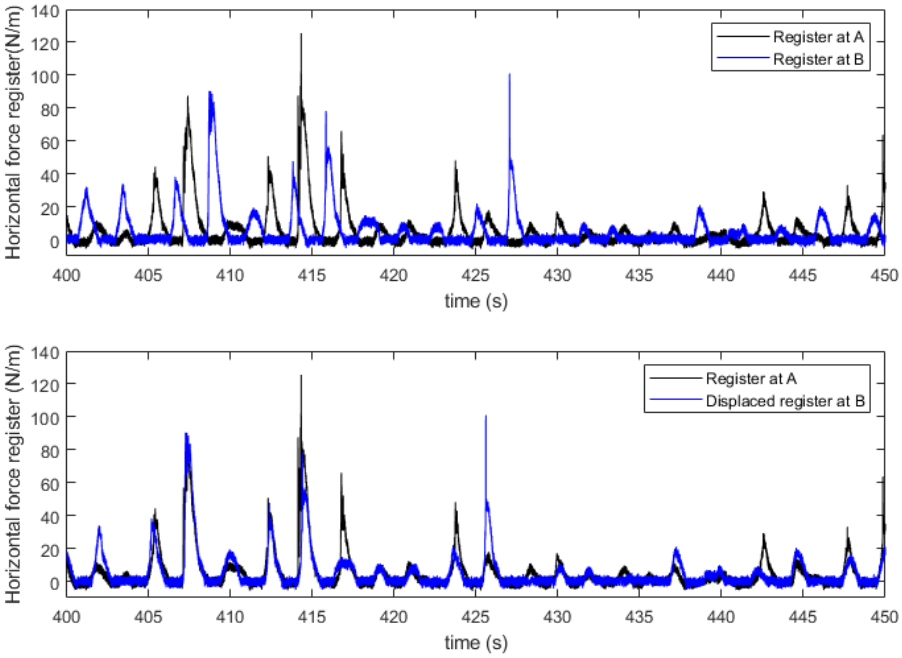

Figure 15. Example of applying the maximum correlation travel time to displace the register at measurement point B (Test #5).

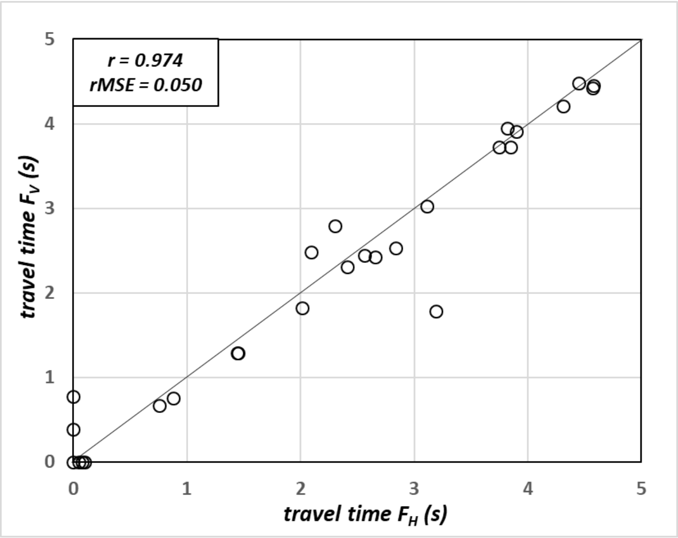

Figure 16. Comparison between the travel time of horizontal and vertical force events corresponding to the same test.

As shown in Figure 16, a very good agreement between the travel time of both horizontal and vertical force events corresponding to the same test was found ($r = 0.974$; $rMSE = 0.050$). Therefore, it is reasonable to analyze the travel time for horizontal and vertical forces together.

v_F was determined by dividing the distance between the two measurement points (6.7 m) between the obtained travel time. The higher the angle, the lower the observed velocity. Note that the travel time for tests with perpendicular waves was zero, since the crest wall is impacted by the whole wave front at the same time. Thus, the tests with perpendicular wave attack could not be used to analyze v_F; 45 v_F values were obtained.

A very high correlation was observed between the dimensionless velocity of the maximum force along the structure ($v_F/(g\ h_s)^{0.5}$, where h_s is the water depth at the toe of the structure) and sinβ ($r = 0.826$). Therefore, Equation (10) was proposed for $v_F/(g\ h_s)^{0.5}$

$$\frac{v_F}{(g\ h_s)^{0.5}} = \frac{0.2}{sin^{1.2}\beta\ {s_{m-1,0}}^{0.3}} \tag{10}$$

Equation (10) is valid for $15° \leq \beta \leq 75°$ and $0.018 \leq s_{m-1,0} \leq 0.048$. Figure 17 presents the comparison between the measured and estimated dimensionless velocity $v_F/(g\ h_s)^{0.5}$ with Equation (10), as well as the 90% confidence interval. Here, 93.4% of the variance was explained by the model.

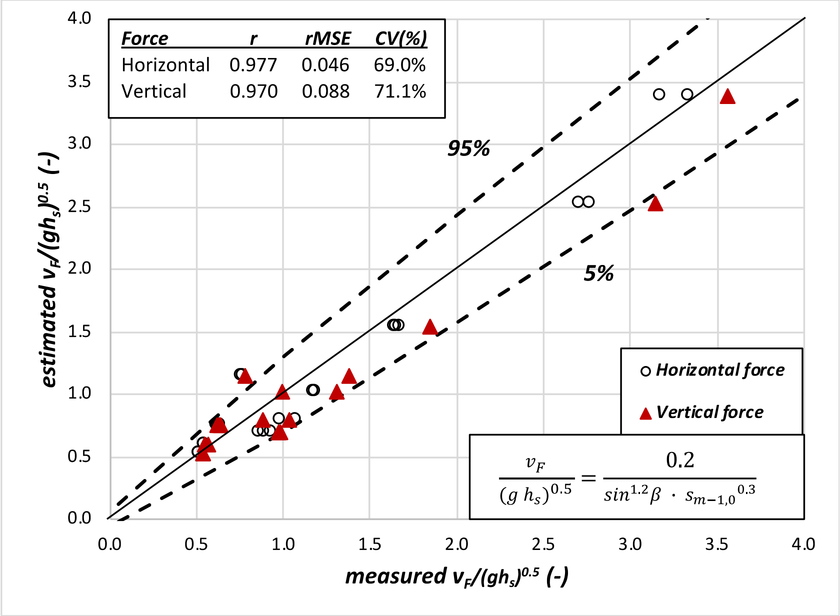

Figure 17. Comparison between the measured and estimated $v_F/(g\ h_s)^{0.5}$ using Equation (10).

The 90% confidence interval is calculated following the methodology given in *[16]*. As the *MSE* increases with increasing $v_F/(g\ h_s)^{0.5}$, the variance of the error ($var(\varepsilon)$) is calculated as

$$var(\varepsilon) = 0.035\left[\frac{v_F}{(g\ h_s)^{0.5}}\right] \tag{11}$$

Assuming a Gaussian error distribution, the 90% confidence interval for $v_F/(g\ h_s)^{0.5}$ estimated using Equation (10) is given in Equation (12).

$$\left.\frac{v_F}{(g\ h_s)^{0.5}}\right|_{5\%}^{95\%} = \frac{v_F}{(g\ h_s)^{0.5}} \pm 0.31\sqrt{\frac{v_F}{(g\ h_s)^{0.5}}} \tag{12}$$

4.4. Integration of the Actual Force

The triangle-shaped force diagram along the longitudinal dimension of the crest wall was obtained for both the horizontal and vertical force events using the method proposed in *[5]* to calculate the maximum loading (Equations (1) to (4)) and Equations (7) and (10) to estimate $duration_{0.1\%}$ and v_F. The actual force ($AF_{0.1\%}$) that attacks the structure can be calculated using the formula for the triangle area,

$$AF_{0.1\%} = 0.5\ (duration_{0.1\%}\ v_F)\ F_{0.1\%} \tag{13}$$

where $F_{0.1\%}$ is the maximum estimated loading for the horizontal or vertical force with *[5]*. Equation (13) is valid while the length of the crest wall (L_{crest}) is higher than the width of the force event ($duration_{0.1\%}\ v_f$). If $duration_{0.1\%}\ v_f > L_{crest}$, the considered portion of the area within the triangle needs to be the maximum possible value to obtain the dominant force (see the right panel of Figure 18). For every case, 20 values of L_{crest} were considered. $L_{crest} = K_A\ duration_{0.1\%}\ v_f$, where K_A was varied from 0.05 to 1 in steps of 0.05. The maximum area within the triangle was numerically integrated for every case and L_{crest}. Similar to the estimated $AF_{0.1\%}$, the measured $AF_{0.1\%}$ was obtained as the maximum numerically integrated area from the force register in the space domain. For the numerical integration, the following steps were performed: (1) a vector with the same length as the time register is created, and all its values are set equal to the time step (0.001 s in this study), (2) the vector is multiplied by the measured velocity, (3) the cumulative sum is determined, and (4) the force register is numerically integrated over this new space vector. Figure 19 shows the comparison between the measured and estimated $AF_{0.1\%}$ using the method in *[5]* (Equations (1) to (4)) and Equations (7) and (10). Here, $r = 0.938$ and $rMSE = 0.945$.

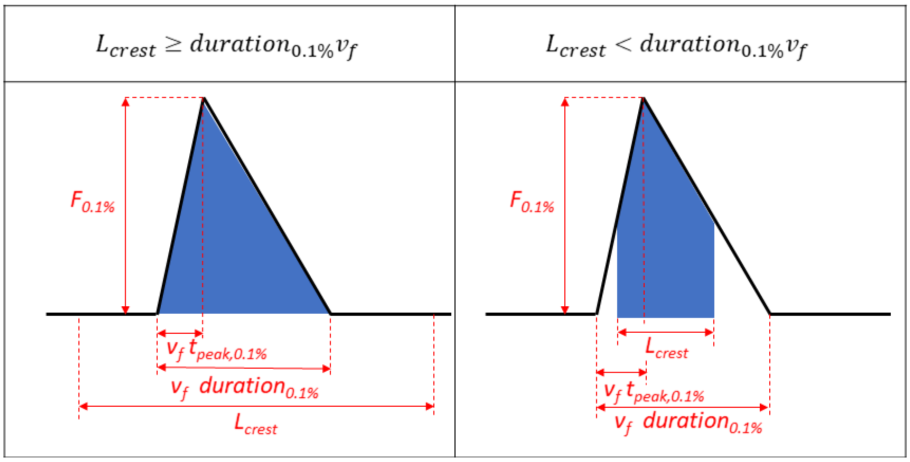

Figure 18. Possible situations when calculating *AF*$_{0.1\%}$.

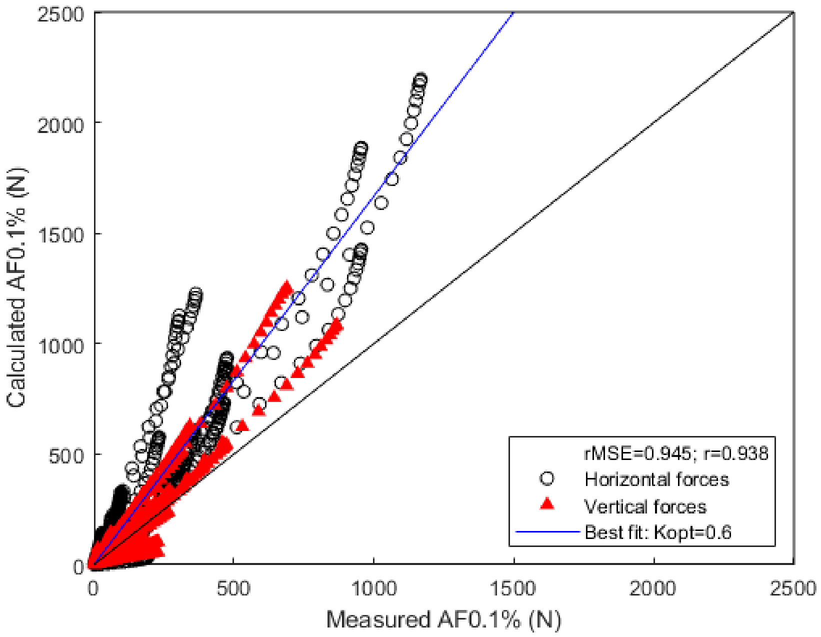

Figure 19. Comparison between the measured and estimated *AF*$_{0.1\%}$ using Equations (1) to (4), (7), and (10).

Every alignment of points in Figure 19 represents the $AF_{0.1\%}$ variation for one test due to the different values of K_A. As shown in Figure 19, the proposed method is on the conservative side. In order to obtain the best fitting approach, $AF_{0.1\%}* = K_{opt}\ AF_{0.1\%}$ is considered where $AF_{0.1\%}*$ is the best fit estimated $AF_{0.1\%}$ and K_{opt} is a coefficient to be calibrated. K_{opt} was calibrated by minimizing the *rMSE*. The best fit was obtained for $K_{opt} = 0.6$ with *rMSE* = 0.133. Figure 20 presents the comparison between the measured $AF_{0.1\%}$ and estimated $AF_{0.1\%}*$ using the method in *[5]* (Equations (1) to (4)) and Equations (7) and (10) with $K_{opt} = 0.6$, as well as the 90% confidence interval.

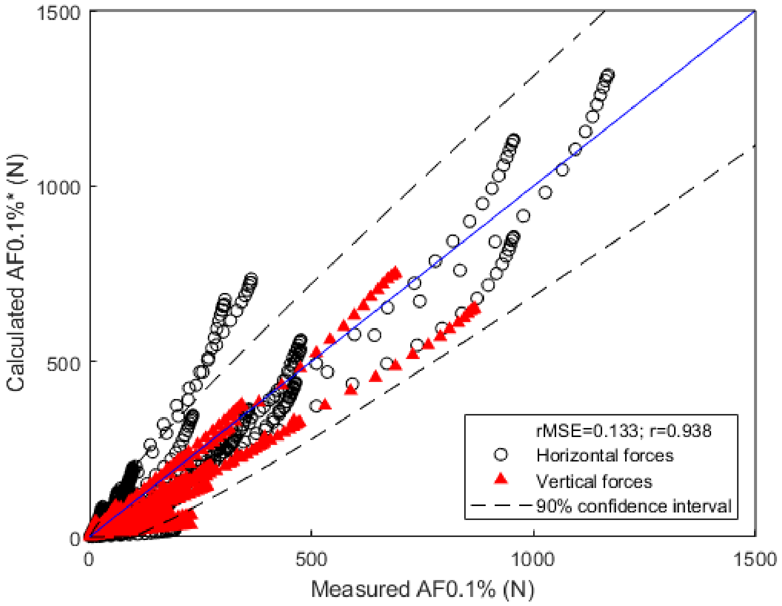

Figure 20. Comparison between the measured $AF_{0.1\%}$ and estimated $AF_{0.1\%}*$ using Equations (1) to (4), (7), and (10) with $K_{opt} = 0.6$, as well as the 90% confidence interval.

Similar to Section 4.3, since the *MSE* increases with increasing $AF_{0.1\%}*$, $var(\varepsilon)$ is calculated as

$$var(\varepsilon) = 36.5\ AF_{0.1\%}{}^{*} \tag{14}$$

Assuming a Gaussian error distribution, the 90% confidence interval for $AF_{0.1\%}*$ is given in Equation (15).

$$AF_{0.1\%}{}^{*}\Big|_{5\%}^{95\%} = AF_{0.1\%}{}^{*} \pm 9.91\sqrt{AF_{0.1\%}{}^{*}} \tag{15}$$

4.5. Length Coefficient

The goal of this study was to propose a reduction coefficient to directly multiply to the force obtained with the methods in the literature to account for the effect of the finite length of crest walls under oblique wave attack. Methods in the literature provide the maximum force that attacks a chainage of the crest wall ($F_{0.1\%}$). They assume that the whole crest wall is attacked by this maximum force; a rectangle-shaped diagram along the whole crest wall length is assumed, as illustrated in the left panel of Figure 21. Thus, the total force $AF_{0.1\%}$ on a crest wall section is generally estimated by multiplying $F_{0.1\%}$ by the length of the crest wall (L_{crest}). Figure 21 illustrates the horizontal force diagrams along the crest wall as generally applied compared to the method proposed in the present study. As previously mentioned, vertical force diagrams were defined in the same way. The length coefficient (γ_L) was calculated by dividing $AF_{0.1\%}$ estimated using the results of the present study ("triangular shape") with the best fitting approach by the $AF_{0.1\%}$ without the finite length effect ("rectangular shape"). Equation (16) is derived

$$\gamma_L = \frac{0.6 \cdot 0.5\ (duration_{0.1\%}\ v_F)\ F_{0.1\%}}{L_{crest}\ F_{0.1\%}} = 0.24 \frac{\sqrt{H_{wall}\ \gamma_\beta\ (Ru_{2\%} - A_c)}}{L_{crest}\ {H_s}^{0.5}\ sin^{1.2}\beta\ {s_{m-1,0}}^{0.3}} \tag{16}$$

where Equation (3) is used for $Ru_{2\%}$ and Equation (4) is used for γ_β. Thus, Equation (16) is only valid if $L_{crest} \geq (duration_{0.1\%}\ v_F)$.

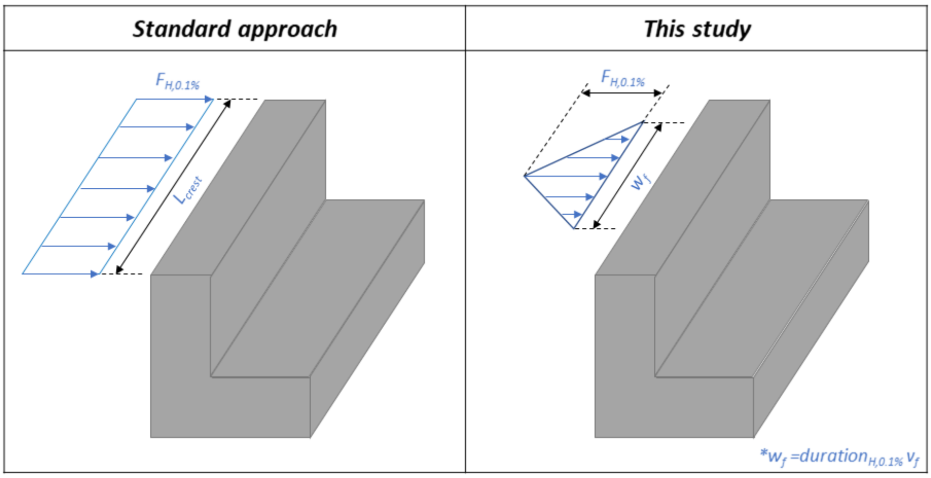

Figure 21. Example of the horizontal force diagram along the longitudinal dimension of the crest wall assumed by the standard method (left panel) and the present study (right panel).

As mentioned in Section 4.4, when $duration_{0.1\%}\, v_f > L_{crest}$, the considered portion of the area within the triangle needs to be the maximum (see Figure 18). Since the area calculation is not direct, a new equation is derived. Cases within the tested experimental ranges were generated. $s_{m-1,0} = 0.02$ and 0.04, $\beta = 15°, 30°, 45°, 60°$, and $75°$, $h_s = 0.77$ m, $A_C = 0.12$ m and $H_{wall} = 0.15$ and 0.20 m were considered. Values for H_s were selected such that the generated cases remain within the experimental range of tested values for $Ru_{2\%}/A_C$. Test conditions were used for cross-validation. Both the generated cases and the test conditions cases were applied to five lengths of the crest wall ($L_{crest} = 2.25$ m, 5 m, 10 m, 15 m, and 20 m on the scale of the model). Thus, 187 generated cases and 235 test conditions were used to illustrate the obtained method. The considered values of L_{crest} went from approximately the smallest $L_{m-1,0}$ until $2L_{m-1,0}$ of the highest $L_{m-1,0}$.

$F_{H,0.1\%}$ and $F_{V,0.1\%}$ were calculated using the methodology given in *[5]* (Equations (1) to (4)). Note that $K_{e,v}$ needed to be interpolated for the generated cases ($K_{e,v} = 2.35$ and 1.81 for $s_{m-1,0} = 0.02$ and 0.04, respectively). $AF_{0.1\%}$ using the results of this study were obtained with the best fitting option ($K_{opt} = 0.6$) with Equations (7) and (10). The reduction factor γ_L is calculated by dividing $AF_{0.1\%}$ obtained with the results from this study ("triangular shape") by the $AF_{0.1\%}$ calculated with the generally applied method ("rectangular shape" with the maximum force acting on the entire crest wall at the same instant).

The same trend was observed in γ_L for both horizontal and vertical force events. Equation (17) was proposed based on the generated cases. Thus, for relatively short crest walls with $L_{crest} < (duration_{0.1\%}\, v_F)$, the following expression is proposed:

$$\gamma_L = 6.5 \left[\frac{A_C}{H_s}\right]^2 \left[\frac{\left(\gamma_\beta\, Ru_{2\%} - A_C\right)}{L_{crest}}\right]^{0.65} \tag{17}$$

where Equation (3) is used for $Ru_{2\%}$ and Equation (4) is used for γ_β, which accounts for the effect of oblique wave attack. The reduction factor expressed by Equations (16) and (17) are valid within the ranges $0.541 \leq A_C/Hs \leq 1.102$; $0 \leq (\gamma_\beta\, Ru_{2\%} - A_C)/L_{crest} \leq 0.045$. Since Equations (16) and (17) do not depend on $F_{0.1\%}$, they are applicable independently on the method used to estimate $F_{0.1\%}$. Note that the higher the wave attack angle, the lower γ_L and the higher the reduction on the crest wall forces. Figure 22 compares the goal γ_L and the estimated γ_L using Equation (17) for (a) horizontal forces and (b) vertical forces, as well as the 90% confidence interval. Open symbols correspond to the generated cases, while closed symbols correspond to the test conditions cases used as cross-validation.

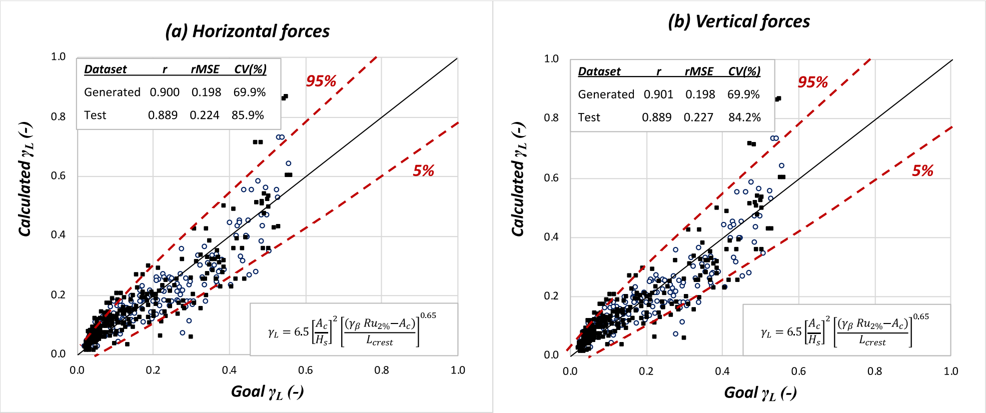

Figure 22. Comparison between the goal γ_L and the estimated γ_L with Equation (16), as well as the 90% confidence interval for (a) horizontal forces and (b) vertical forces. Generated cases correspond to open symbols, while test conditions correspond to closed symbols.

Similar to Section 4.3 and 4.4, $var(\varepsilon)$ is calculated as

$$var(\varepsilon) = 0.019\,\gamma_L \tag{18}$$

Assuming a Gaussian error distribution, the 90% confidence interval for γ_L is given by

$$\gamma_L|_{5\%}^{95\%} = \gamma_L \pm 0.23\sqrt{\gamma_L} \tag{19}$$

Note that the confidence interval was calculated for the generated cases. The agreement is rather good for both the generated cases and the test conditions ($0.198 \leq rMSE \leq 0.227$).

5. Conclusions

To estimate the forces on a crest wall of a rubble mound structure, the predicted maximum force at a single position (chainage) is normally assumed to act on the entire length of the crest wall. For perpendicular wave attack, this is a reasonable approach. However, for oblique wave attack, the maximum loading is not acting on the entire length of the crest wall at the same instant. Since crest walls have a finite length, assuming that the maximum wave loading acts at the same instant over the entire length of the crest wall leads to an overestimation of the actual forces on crest walls under oblique wave attack. This study describes a method to account for the effect of the finite length of crest walls on the forces caused by oblique wave attack.

The physical model tests conducted by *[5]* in a wave basin were used. A triangular shape is applied to model the temporal shape of the (horizontal and vertical) force events (exceeded by 0.1% of the incoming waves) with $0.912 \leq r \leq 0.924$. It was found that the duration of the force events ($duration_{0.1\%}$) (base of the triangle) is the same for both horizontal and vertical forces. Equation (7) is proposed to estimate the duration of the force events ($rMSE = 0.472$). Equation (6) is derived to estimate the position of the peak within the force event; the rising time of the horizontal forces is faster than for the vertical forces. The method proposed in *[5]* was suggested to calculate the maximum loading ($F_{0.1\%}$). The agreement between the calculated and measured force register was good ($0.874 \leq r \leq 0.879$).

The temporal shape of the force events was transformed into the space domain by means of the velocity at which the force event travels along the structure (v_f). To this end, the travel time between two measurement points was determined, and v_f was obtained by dividing the distance between both points between the travel time. The same travel time and v_f were obtained for horizontal and vertical forces. The travel time obviously is 0 for perpendicular wave attack, since the whole crest wall is impacted by the wave in the same instant. Equation (10) was proposed to calculate v_f for oblique wave attack with a rather high accuracy ($rMSE = 0.066$).

The actual force on the entire crest wall with a finite length ($AF_{0.1\%}$) was obtained using a triangular shape in the space domain. The adopted approach resulted in conservative estimates of the reduction due to the finite length of crest walls under oblique wave attack. The best fit for actual force on the entire crest wall with a finite length ($AF_{0.1\%}$) resulted in 60% of the triangular shape ($K_{opt} = 0.6$) with $rMSE = 0.133$.

A new reduction factor (γ_L) was defined as the ratio between $AF_{0.1\%}$ estimated using the findings of the present study and the maximum force acting against the crest wall ($F_{0.1\%}\ L_{crest}$). Equations (16) and (16) were proposed to directly estimate γ_L for both horizontal and vertical forces. Equation (16) is valid if $L_{crest} \geq (duration_{0.1\%}\ v_F)$. Equation (17) was developed to account for relatively short crest walls $L_{crest} < (duration_{0.1\%}\ v_F)$. To obtain Equation (17), the methodology developed in this study using the best fit approach ($K_{opt} = 0.6$) was applied on two data sets: (1) generated cases within the experimental ranges with five values of the length of the crest wall (L_{crest}) and (2) tests conditions with five values of L_{crest}. The forces on the entire crest wall with finite length ($AF_{0.1\%}$) were also calculated using the generally applied method ($AF_{0.1\%} = F_{0.1\%}\ L_{crest}$). Equation (17) was derived using dataset (1), while dataset (2) was used for cross-validation ($0.198 \leq rMSE \leq 0.227$). Since the derived reduction factor, expressed by Equations (16) and (17), does not depend on $F_{0.1\%}$, Equations (16) and (17) are applicable independently on the estimator used for $F_{0.1\%}$.

The expressions proposed in this study are valid within the ranges of the present tests ($0.84 \leq R_c/H_s \leq 1.6$; $1.27 \leq R_c/A_c \leq 1.55$; $0 \leq F_b/H_s \leq 0.56$; $0.13 \leq H_s/h_s \leq 0.27$). It is encouraged to check their validity out of the experimental ranges of this study, paying special attention to the effect of wave characteristics on the shape of the force events, different crest wall geometries, and armor layers (1:2 rock armored slopes).

This study has illustrated how large the reduction in the required size of the crest wall can be if the finite length of the crest wall is taken into account in oblique wave attack conditions. Therefore, it is recommended to take into account not only the reduction in the maximum forces due to oblique waves, but also the reduction due to the fact that the maximum forces do not occur at the same instant over the entire length of crest walls on rubble mound breakwaters.

Author Contributions: P.M.-N. performed the data analysis, was responsible for the model conceptualization, and drafted the original manuscript. M.R.A.v.G. conceived the research topic, designed the research plan, supervised the investigation, and reviewed and approved the manuscript.

Funding: The first author was financially supported by the *Ministerio de Educación, Ciencia y Deporte* through the FPU program (*Formación de Profesorado Universitario)* under grant FPU16/05081.

Acknowledgments: The first author was financially supported by the *Ministerio de Educación, Ciencia y Deporte* through the FPU program (*Formación de Profesorado Universitario)* under grant FPU16/05081.

Conflicts of Interest: The authors declare no conflict of interest. The funders had no role in the design of the study; in the collection, analyses, or interpretation of data; in the writing of the manuscript, or in the decision to publish the results.

References

[1] Pedersen, J. Wave forces and overtopping on crown walls of rubble mound breakwaters—An experimental study. PhD thesis, Aalborg University, Denmark, 1996.

[2] Molines, J.; Herrera, M.P.; Medina, J.R. Estimations of wave forces on crown walls based on wave overtopping rates. *Coast. Eng.* 2018, *132*, 50–62.

[3] Van Gent, M.R.A.; Van der Werf, I.M. Prediction method for wave overtopping and wave forces on rubble mound breakwater crest walls; In Proceedings of the Coastal Structures, Hannover, Germany, 30th September to 2nd October, 2019.

[4] Jacobsen, N.G.; Van Gent, M.R.A.; Capel, A.; Borsboom, M. Numerical prediction of integrated wave loads on crest walls on top of rubble mound breakwaters. *Coast. Eng.* 2018, *142*, 110–124.

[5] Van Gent, M.R.; Van Der Werf, I.M. Influence of oblique wave attack on wave overtopping and forces on rubble mound breakwater crest walls. *Coast. Eng.* 2019, *151*, 78–96.

[6] Jensen, O.J. A Monograph of Rubble Mound Breakwaters.Available online: https://repository.tudelft.nl/islandora/object/uuid%3A133be463-5f43-45cd-9115-3ef9ebe245b3 (accessed on 26 January 2020).

[7] Günbak, A.R.; Gökce, T. Wave screen stability of rubble mound Breakwaters. In Proceedings of the International Symposium of Maritime Structure in the Mediterranean Sea, Athens, Greece, 1984.

[8] Günbak, A.R. Damage of Tripoli harbor north west breakwater. In Design and Construction of Mounds for Breakwaters and Coastal Protection; P. Brunn, Elsevier: Amsterdam, The Netherlands, 1985, pp. 676–695.

[9] Martin, F.L. *Experimental Study of Wave Force on Rubble Mound Breakwater Crown Walls*; PIANC Bulletin: Brussels, Belgium, 1999.

[10] Martin, F.L.; Losada, M. Ángel; Medina, R. Wave loads on rubble mound breakwater crown walls. *Coast. Eng.* 1999, *37*, 149–174.

[11] Molines, J. Wave overtopping on Crown Wall Stability of Cube and Cubipod armored Mound Breakwaters. PhD thesis, Universitat Politècncia de València, Spain, 2016.

[12] Nørgaard, J.Q.H.; Andersen, T.L.; Burcharth, H.F. Wave loads on rubble mound breakwater crown walls in deep and shallow water wave conditions. *Coast. Eng.* 2013, *80*, 137–147.

[13] Van Gent, M.R.A. Report H3608. Physical model investigations on coastal structures with shallow foreshores; 2D model test with single and double-peaked wave energy spectra. Available online: https://repository.tudelft.nl/islandora/object/uuid:1b4729de-2e86-4b8a-98d5-48d8e07d5902?collection=research (accessed on 26 January 2020).

[14] Van Gent, M.R.A. Wave Run-Up on Dikes with Shallow Foreshores. *27th International Conference on Coastal Engineering (ICCE)* 2001, *127*, 2030–2043.

[15] Mares-Nasarre, P.; Argente, G.; Gómez-Martín, M.E.; Medina, J.R. Overtopping layer thickness and overtopping flow velocity on mound breakwaters. *Coast. Eng.* 2019, *154*, 103561.

[16] Herrera, M.P.; Medina, J.R. Toe berm design for very shallow waters on steep sea bottoms. *Coast. Eng.* 2015, *103*, 67–77.